



HAL
open science

The Role of SHH Signaling in Regulating Species-Specific Jaw Size

Zuzana Vavrušová

► **To cite this version:**

Zuzana Vavrušová. The Role of SHH Signaling in Regulating Species-Specific Jaw Size. Development Biology. Université Paris-Saclay, 2021. English. NNT : 2021UPASL051 . tel-04175259

HAL Id: tel-04175259

<https://theses.hal.science/tel-04175259v1>

Submitted on 2 Aug 2023

HAL is a multi-disciplinary open access archive for the deposit and dissemination of scientific research documents, whether they are published or not. The documents may come from teaching and research institutions in France or abroad, or from public or private research centers.

L'archive ouverte pluridisciplinaire **HAL**, est destinée au dépôt et à la diffusion de documents scientifiques de niveau recherche, publiés ou non, émanant des établissements d'enseignement et de recherche français ou étrangers, des laboratoires publics ou privés.

The role of SHH signaling in regulating species-specific jaw size

*Le rôle de la signalisation SHH dans la régulation
de la taille de la mandibule spécifique à l'espèce*

Thèse de doctorat de l'université Paris-Saclay

École doctorale n°568 : signalisations et réseaux intégratifs en biologie
(Biosigne)

Spécialité de doctorat : Aspects moléculaires et cellulaires de la biologie
Unité de recherche : Université Paris-Saclay, CNRS, Institut des neurosciences Paris-Saclay,
91190, Gif-sur-Yvette, France
Réfèrent : Faculté de médecine

Thèse soutenue en visioconférence totale le 26-08-2021, par

Zuzana VAVRUŠOVÁ

Composition du Jury

Jennifer L. FISH

Assistant Professor, University of Massachusetts
Lowell - Department of Biological Science

Présidente

Anne PLESSIS

Professeure, Université de Paris - Institut Jacques
Monod UMR 7592 CNRS

Rapporteuse & Examinatrice

Paul A. TRAINOR

Professor, University of Kansas School of Medicine
- Department of Anatomy & Cell Biology

Rapporteur & Examineur

Anne-Hélène MONSORO-BURQ

Professeure, Université Paris-Saclay IUF - Institut
Curie U1021

Examinatrice

Direction de la thèse

Sophie E. CREUZET

Directrice de Recherche CNRS, Institut des
Neurosciences Paris-Saclay CNRS-UMR-9197

Directrice de thèse

Richard A. SCHNEIDER

Professor, University of California San Francisco
(UCSF) - Orthopaedic surgery department

Co-Directeur de thèse

Dedication and acknowledgements

This thesis is dedicated to the memory of my beloved grandparents and father who passed away before I finished my doctoral studies; to my mother who taught me that education is the biggest gift we can get and sacrificed so much to give me this opportunity she didn't have; to my uncle without whom I would have never been able follow my dream; to my sisters who encouraged all my endeavors and explorations; and to my partner who supported me unconditionally in every possible way and is my everyday inspiration to do better.

I wish to thank all my family, for their encouragement throughout the years; my mentors, Rich, who instilled knowledge and confidence in me to be a writer, a storyteller, a teacher, and a scientist, and Sophie, who was indispensably a role model to me; the members of my committee, who helped strengthen my weaknesses; and my international reinforcing circle of friends, who emboldened me on this journey from many different countries.

To all these people, I give my sincerest gratitude and appreciation. I could not have accomplished this journey without you.

Table of Contents

LIST OF FIGURES.....	vi
LIST OF TABLES.....	xii
CHAPTER 1: CELLULAR MECHANISMS UNDERLYING THE EVOLUTION OF SIZE AND SHAPE IN THE VERTEBRATE JAW	1
INTRODUCTION.....	2
HISTORY OF SIZE, SHAPE, TIME, AND SCALING	4
SCALING CAN BE ACHIEVED AT DIFFERENT DEVELOPMENTAL STAGES	8
TISSUE PATTERNING	11
MORPHOGENS	13
JAW COMPLEX DEVELOPMENT.....	17
VERTEBRATE JAW – SIZE AND SHAPE.....	19
JAW TISSUES: CELLULAR ORIGINS	20
NEURAL CREST MESENCHYME AND MOLECULAR MECHANISMS UNDERLYING JAW PATTERNING.....	22
SONIC HEDGEHOG SIGNALING	28
QUAIL-DUCK CHIMERAS.....	32
JAW SIZE AND SHAPE – EARLY DEVELOPMENTAL MECHANISMS	34
FIGURES	36
CHAPTER 2: DECIPHERING THE NEURAL CREST CONTRIBUTION TO CEPHALIC DEVELOPMENT WITH AVIAN EMBRYOS.....	63
INTRODUCTION.....	64
MATERIALS	67
<i>Manipulation of Fertilized Eggs.....</i>	<i>67</i>
<i>Tools for Microinjection and Microsurgery</i>	<i>68</i>
<i>Solutions.....</i>	<i>68</i>
<i>In Ovo Electroporation.....</i>	<i>68</i>
METHODS	69
<i>Self-Made Micro-Scalpels and Transfer Pipettes for Surgery and Electroporation</i>	<i>69</i>
<i>Embryo Incubation</i>	<i>69</i>
<i>Preparation and Visualization of Avian Embryos</i>	<i>70</i>
<i>Generation of Quail-Chick Chimeras</i>	<i>70</i>
<i>Transfection of Neural Crest Cells Prior to Xenotransplantation.....</i>	<i>71</i>
NOTES	72
FIGURES	79
CHAPTER 3: DIFFERENTIAL REGULATION OF SHH SIGNALING AND THE DEVELOPMENTAL CONTROL OF SPECIES-SPECIFIC JAW SIZE THROUGH GAS1 EXPRESSION	86
INTRODUCTION.....	87
RESULTS.....	91
<i>Species-specific differences in mandibular primordia arise early and progress during development.....</i>	<i>91</i>
<i>SHH pathway activation is species-specific and dose-dependent</i>	<i>93</i>
<i>Response to SHH treatments is NCM-mediated and context dependent</i>	<i>95</i>
<i>Changes in Gas1 expression affect mandibular primordia size in vivo.....</i>	<i>97</i>
DISCUSSION	98
<i>Early developmental parameter values establish species-specific jaw size.....</i>	<i>98</i>
<i>Higher transcriptional activity in quail correlates with smaller mandibular primordia.....</i>	<i>100</i>
<i>Activation of the SHH pathway is species-specific.....</i>	<i>101</i>
<i>Gas1 affects the species-specific development of the mandibular primordia.....</i>	<i>102</i>
MATERIALS AND METHODS.....	103
<i>The Use of Avian Embryos.....</i>	<i>103</i>
<i>Generation of Chimeric Embryos.....</i>	<i>104</i>
<i>Isolation of Mandibular Primordia</i>	<i>105</i>
<i>Quantification of Mandibular Mesenchyme.....</i>	<i>105</i>
<i>Extraction of RNA</i>	<i>106</i>

<i>Quantification of Total RNA Yield</i>	108
<i>Quantification of Sox10⁺ Cell Population</i>	108
<i>Modelling Relative Population Size</i>	108
<i>Preparation of cDNA Libraries</i>	109
<i>Designing and Testing Primers for qRT-PCR</i>	109
<i>Analysis of Gene Expression by qRT-PCR</i>	112
<i>Culture of Mandibular Primordia and Biochemical Treatments</i>	113
<i>Generating Probes for In Situ Hybridization</i>	115
<i>Analysis of Gas1 Expression by In Situ Hybridization</i>	115
<i>Cloning Full-Length Gas1</i>	116
<i>Preparation of Micropipettes</i>	117
<i>The Use of Cell Culture and Generation of Stable Gas1-Expressing Lines</i>	117
<i>Electroporation</i>	119
<i>Treatment with Doxycycline</i>	121
<i>Injections with Vivo-Morpholinos</i>	122
<i>Staining with Hoechst Dye</i>	122
<i>Capture and Adjustment of Images</i>	123
<i>Methods for Determining Statistical Significance</i>	123
FIGURES.....	125
TABLES.....	146
CHAPTER 4: RT-PCR ANALYSIS PYTHON SCRIPT FOR COMMONLY USED METHODS	178
INTRODUCTION.....	179
SCRIPT.....	181
CHAPTER 5: CONCLUDING REMARKS	228
CONCLUDING REMARKS.....	229
REFERENCES	232
APPENDIX I: ADDITIONAL METHODS	268
INTRODUCTION.....	269
CUBIC CLEARING.....	269
IMAGING – SELECTIVE PLANE ILLUMINATION MICROSCOPE.....	271
APPENDIX II: OTHER PUBLICATIONS	274
APPENDIX III: SYNTHESIS	328

List of Figures

- FIGURE 1: EMBRYOLOGY THEORY OF ERNST HAECKEL.** ONTOGENY RECAPITULATES PHYLOGENY (I.E., RECAPITULATION THEORY), ADULT EVOLUTIONARY STAGES OF “SIMPLER” FORMS (I.E., ANIMAL SPECIES), HERE FISH, FROG, AND BIRD, ARE RECAPITULATED DURING DEVELOPMENTAL STAGES OF MORE COMPLEX SPECIES (I.E., PIG)..... 36
- FIGURE 2: FORM AND GROWTH IN CARTESIAN COORDINATES SYSTEMS.** D'ARCY WENTWORTH THOMPSON'S COMPARATIVE ILLUSTRATIONS OF CRANIAL ONTOGENETIC SHAPE CHANGES (FIGURES 404 TO 407 RE-DRAWN FROM (THOMPSON, 1917)). **(A)** CARTESIAN COORDINATES OF A HUMAN SKULL. **(B)** NETWORK OF CARTESIAN COORDINATES OF A CHIMPANZEE'S SKULL AS A PROJECTION OF COORDINATES IN **(A)**. **(C)** CHIMPANZEE'S SKULL WITH CORRESPONDING CARTESIAN COORDINATES FROM **(B)**. **(D)** TRANSFORMATION OF THE CARTESIAN COORDINATES IN **(A)** FOR A SKULL OF BABOON. SAME ORDER OF TRANSFORMATION IS USED TO TRANSFORM COORDINATES FROM **(A)** TO **(C)** AND **(D)** WITH THE ONLY VARIABILITY BEING INCREASED INTENSITY OR DEGREE OF DEFORMATION..... 38
- FIGURE 3: EIGHT CATEGORIES OF HETEROCHRONY** (FIGURE 2 FROM (DE BEER, 1940)). EACH GRAPH REPRESENTS A DIAGRAM OF THE RELATIONS OF ONTOGENY (FROM BOTTOM TO TOP) AND PHYLOGENY (I.E., ANCESTOR-DESCENDANT SEQUENCE; FROM LEFT TO RIGHT). THE VERTICAL LINES REPRESENT SUCCESSIVE ONTOGENIES AND THICK BLACK LINES DENOTE AN EVOLUTIONARY NOVELTY. ACTUAL MODES OF HETEROCHRONY (RETARDATION, NEOTENY, HYPERMORPHOSIS, AND ACCELERATION), AS DESCRIBED BY GOULD (GOULD, 1977), ARE HIGHLIGHTED IN GRAY. 40
- FIGURE 4: GOULD'S EVOLUTIONARY CLOCK MODEL TO REPRESENT DIFFERENT MODES OF HETEROCHRONY** (FIGURE 33 AND 35 RE-DRAWN FROM (GOULD, 1977)). **(A)** GOULD'S MODEL REPRESENTED CORRELATIONS BETWEEN SIZE, SHAPE, AND AGE DURING ONTOGENY AND PHYLOGENY. **(B)** HETEROCHRONY DOMAINS FOR THE AGE SCALE (I.E., ACCELERATED AND RETARDED), THE SHAPE SCALE (I.E., PAEDOMORPHIC AND RECAPITULATORY), AND THE SIZE SCALE (I.E., SMALLER AND LARGER). 42
- FIGURE 5: AMPHIBIAN EGG ASYMMETRY.** THE EGG DIVISION (BLACK DASHED LINE) ALONG THE PLANE OF FIRST CLEAVAGE INTO TWO BLASTOMERES (I.E., EACH BLASTOMERE CONTAINS HALF OF THE GRAY CRESCENT) RESULTS IN TWO NORMAL EMBRYOS (**LEFT**). WHEN ONLY ONE OF THE BLASTOMERES RECEIVES THE GRAY CRESCENT, IT ALONE CAN UNDERGO NORMAL DEVELOPMENT AND FORM NORMAL EMBRYO. THE SECOND HALF IS ARRESTED IN VEGETATIVE STATE (**RIGHT**). (SPEMANN, 1938)..... 44
- FIGURE 6: SPEMANN ORGANIZER – INDUCTION OF A SECONDARY BODY AXIS BY DORSAL BLASTOPORE LIP TISSUE TRANSPLANT.** DORSAL LIP TISSUE FROM EARLY GASTRULA OF AN UNPIGMENTED DONOR (LIGHT PURPLE) IS TRANSPLANTED INTO A PIGMENTED HOST AT THE SAME DEVELOPMENTAL STAGE. THE TISSUE IS TRANSPLANTED OPPOSITE TO DORSAL LIP (I.E., VENTRAL), INTO A REGION NORMALLY SPECIFYING INTO VENTRAL EPIDERMIS. HOST (TAUPE) AND DONOR (PURPLE) CELLS CONTRIBUTES TO THE FORMATION OF SECONDARY AXIS (INCLUDING NEURAL TUBE, NOTOCHORD, AND SOMITES). SECOND EMBRYOS FORMS AND IS JOINED WITH THE FIRST ONE FORMING SIAMESE TWINS. (SPEMANN AND MANGOLD, 1924)..... 46
- FIGURE 7: TURING'S “REACTION-DIFFUSION” (RD) SYSTEM IN COMPARISON WITH MORPHOGEN GRADIENT.** **(A)** MORPHOGEN GRADIENT IS FORMED BY DIFFUSION FROM A SINGLE SOURCE (X) (I.E., MORPHOGEN PRODUCING CELLS/TISSUE). CELLS RESPOND TO ITS CONCENTRATION WHICH GIVES THEM THEIR POSITIONAL IDENTITY FROM THE SOURCE. THE GRADIENT AND THUS CELL RESPONSE AND THE TISSUE PATTERNING ARE VERY LIMITED AND DEPENDENT ON THE MORPHOGEN PRODUCING CELLS (I.E., SOURCE). **(B)** BY ADDING ANOTHER MORPHOGEN (HERE Y) THAT IS FORMING SECOND GRADIENT BY DIFFUSION, THE COMPLEXITY OF TISSUE PATTERNING IS INCREASED AND CAN BECOME MORE COMPLEX. **(C)** ONLY BY ADDING INTERACTION BETWEEN MORPHOGENS AND WITH ITSELF (BROWN AND PURPLE ARROWS), THE SYSTEM BECOMES SELF-REGULATING AND HIGHLY COMPLEX. BASED ON (KONDO AND MIURA, 2010; LANDGE ET AL., 2020; MEINHARDT, 2012; TURING, 1952)..... 48
- FIGURE 8: MODULES INVOLVED IN TISSUE PATTERNING.** PATTERNING MECHANISMS USUALLY INVOLVE INTERACTIONS AT MULTIPLE LEVELS: SOURCE, DISTRIBUTION, TRANSPORT, DETECTION, TRANSDUCTION, AND RESPONSE..... 50
- FIGURE 9: PRIMARY ARCHITECTURE OF A GENERALIZED VERTEBRATE EMBRYO CRANIUM.** THE CRANIUM IS COMPOSED OF THE NEUROCRANIUM, DERMATOCRANIUM, AND VISCEROCRANIUM. THE NEUROCRANIUM PROTECTS BRAIN AS WELL AS SENSE ORGANS AND FIRST FORM AS CARTILAGE. THE

VISCEROCRANIUM IS CARTILAGINOUS SKELETON COMPOSED OF SEVEN ARCHES (1–7), THE MANDIBULAR (MD), HYOID (HY), AND FIVE BRANCHIAL (BA). THE DERMATOCRANIUM CONSISTS OF CRANIAL VAULT, PALATE BONES, AND TOOTH BEARING BONE ELEMENTS. NEURAL CREST MESENCHYME CONTRIBUTES TO THE DEVELOPMENT OF ALL THREE CRANIAL PARTS (I.E., NEUROCRANIUM, DERMATOCRANIUM, AND VISCEROCRANIUM) WHEREAS MESODERM CONTRIBUTES TO DEVELOPMENT OF THE NEUROCRANIUM AND DERMATOCRANIUM. BASED ON (KURATANI, 2005, 2012)..... 52

FIGURE 10: THE EVOLUTIONARY ADAPTABILITY AND CELLULAR ORIGIN OF VERTEBRATE JAW. THE AMNIOTE JAW SKELETON, ESPECIALLY VERTEBRATE, DISPLAYS AN ASTONISHING ARRAY OF SIZE, SHAPE, AND FUNCTION. THE JAWS OF DIFFERENT SPECIES REPRESENT THE CAPACITY OF ADAPTATION THAT THE TISSUE RESPONSIBLE FOR ITS DEVELOPMENT CAN ACHIEVE. THE AMNIOTE JAW SKELETON IS DERIVED UNIQUELY FROM NEURAL CREST (LIGHT BLUE) WHILE SOME PARTS OF THE SKULL ARE DERIVED FROM MESODERM (ORANGE). **(A)** THE FUNCTIONAL UPPER JAW OF BIRDS AND REPTILES (HERE EXAMPLE OF CHICK) CONSISTS OF DERMAL BONES THAT INCLUDE THE PREMAXILLA, MAXILLA, AND PALATINE. THE LOWER JAW ALSO CONTAINS SEVERAL DERMAL BONES THAT SURROUND MECKEL’S CARTILAGE INCLUDING THE SPENIAL, DENTARY, ANGULAR, AND SURANGULAR. **(B)** IN MAMMALS, THE UPPER JAW CONSISTS OF THE SAME DERMAL BONES (I.E., PREMAXILLA, MAXILLA, AND PALATINE) AS IN BIRDS AND THE LOWER JAW IS EXTENSIVELY REDUCED TO A SINGLE BONE SURROUNDING MECKEL’S CARTILAGE, THE DENTARY. DESPITE THE MARVELOUS ARRAY OF FORMS AND COUNTLESS ADAPTATION TO EVERY CONCEIVABLE ECOLOGICAL ENVIRONMENT, THE EMBRYONIC ORIGINS OF THE JAW ARE HIGHLY CONSERVED ACROSS AMNIOTES. **(C)** SCHEMATIC OF A GENERALIZED AMNIOTE EMBRYO IN A TRANSVERSE SECTION PLANE THROUGH THE MIDBRAIN-HINDBRAIN BOUNDARY SHOWING EMBRYONIC PRECURSORS, CELL LINEAGES, CELL TYPES, CELL-CELL INTERACTIONS (VERTICAL ARROWS), AND TISSUE DERIVATIVES THAT CONTRIBUTE TO THE DEVELOPMENT AND FORMATION OF FUNCTIONAL JAW APPARATUS. MODIFIED AND ADAPTED FROM (EALBA ET AL., 2015; FISH AND SCHNEIDER, 2014A). 54

FIGURE 11: MULTIPLE EMBRYONIC POPULATIONS CONTRIBUTE TO THE FORMATION OF AMNIOTE JAW COMPLEX. NEURAL CREST MESENCHYME (NCM) SUB-POPULATION IS RESPONSIBLE FOR THE FORMATION OF THE CRANIOFACIAL SKELETAL SYSTEM AND MUSCLE AND CONNECTIVE TISSUE OF THE HEAD. **(A)** ETHIDIUM BROMIDE STAINING OF A QUAIL EMBRYO AT EMBRYONIC STAGE (HH) 9.5, DORSAL VIEW. **(C)** AT HH9.5 (PRIOR TO MIGRATING ALONGSIDE PARAXIAL MESODERM (M; ORANGE)) CRANIAL NCM (LIGHT BLUE) DELAMINATES FROM MID-DIENCEPHALON (I.E., THE FOREBRAIN (FB) AND MIDBRAIN (MB)) DOWN TO RHOMBOMERE 2 (R2) AND RHOMBOMERE 4 (R4) AND 6 (R6). **(B)** FRONTAL VIEW OF A QUAIL EMBRYO AT HH25 WITH VISIBLE FRONTONASAL (FN), MAXILLARY (MX), AND MANDIBULAR (MA) PRIMORDIA; WHITE LINE INDICATES SAGITTAL SECTION PLANE FOR **(D)**. **(D)** DIFFERENT EMBRYONIC POPULATION CONTRIBUTIONS ARE SCHEMATIZED, SAGITTAL VIEW OF A HH25 QUAIL EMBRYO WHERE THE FRONTONASAL (FN), MAXILLARY (MX), MANDIBULAR (MA), AND HYOID (HY) PRIMORDIA ARE POPULATED BY NEURAL CREST (LIGHT BLUE) SURROUNDED BY SURFACE ECTODERM (SE; TAN), PHARYNGEAL ENDODERM (PE; YELLOW), AND FOREBRAIN NEUROEPITHELIUM (FB; DARK BLUE). THE JAW COMPLEX CONTAINS CONTRIBUTIONS FROM NEURAL CREST, NASAL PLACODE (NP), CRANIAL GANGLIA (V, VII, IX), AND MESODERM (M). MODIFIED AND ADAPTED FROM (SCHNEIDER, 1999, 2005; SCHNEIDER ET AL., 2001) 56

FIGURE 12: SONIC HEDGEHOG (SHH) SIGNALING CASCADE. ON-STATE: SHH-INDUCED INTERNALIZATION OF PATCHED 1 (PTCH1) RECEPTOR LEADS TO ACTIVATION OF SMOOTHENED (SMO) WHICH RESULTS IN STABILIZATION AND NUCLEAR ACCUMULATION OF GLI FAMILY MEMBERS. GLI ACTIVATORS BIND TO GACCACCCA MOTIF TO REGULATE TRANSCRIPTION OF TARGET GENES INVOLVED IN A VARIETY OF PROCESSES SUCH AS SHH SIGNALING POSITIVE FEEDBACK, NEGATIVE FEEDBACK, PROLIFERATION, SELF-RENEWAL, SURVIVAL, AND EMT. **OFF-STATE:** PTCH1 INTERNALIZES SMO WHICH IS FOLLOWED BY GLI FAMILY MEMBERS DEGRADATION (GLI1) OR CLEAVAGE (GLI2 AND 3) INTO REPRESSOR FORM (GLI-R). GLI-R IS TRANSLOCATED INTO THE NUCLEUS AND TARGET GENE TRANSCRIPTION IS REPRESSED. 58

FIGURE 13: THE ORIGINS OF SPECIES-SPECIFIC JAW PATTERNING. (A) TO GENERATE QUAIL-DUCK CHIMERAS ("QUICK"), QUAIL (GREEN SQUARE) AND DUCK (PINK CIRCLE) EMBRYOS ARE STAGE-MATCHED FOR SURGERY AT HH9.5 (YELLOW TRIANGLE) BY INCUBATING THEIR EGGS FOR DIFFERENT TIMES. DONOR AND HOST CELLS SUBSEQUENTLY DIVERGE IN STAGE DUE TO THEIR DIFFERENT RATES OF MATURATION. **(B)** QUAIL (I.E., DONOR) CELLS REMAIN ACCELERATED BY APPROXIMATELY THREE STAGES WITHIN 2 DAYS AFTER SURGERY RELATIVE TO THE DUCK HOST . BILATERAL NEURAL FOLDS, CONTAINING PRESUMPTIVE QUAIL NEURAL CREST, FROM MID-DIENCEPHALON (DI) TO RHOMBOMERE 2 (R2) OF THE HINDBRAIN (DARK GREEN), ARE TRANSPLANTED FROM QUAIL INTO A DUCK HOST. **(C)** SAGITTAL SECTION IN A CHIMERIC QUICK THROUGH THE MAXILLARY (I.E., MAXILLA) AND MANDIBULAR (I.E., MANDIBLE)

REGION SHOWING QUAIL DONOR CELLS STAINED WITH QcPN (BLACK NUCLEI). DUCK-HOST EPITHELIUM (I.E., SURFACE ECTODERM, LIGHT BROWN), PHARYNGEAL ENDODERM (YELLOW), AND MYOGENIC MESENCHYME ARE UNLABELED. ALTHOUGH NEURAL-CREST MESENCHYME ORIGIN, THE HYOID ARCH IS ALSO NEGATIVE SINCE ITS PRECURSORS FROM R4 WERE NOT TRANSPLANTED. MODIFIED AND ADAPTED FROM (FISH AND SCHNEIDER, 2014B; NODEN AND SCHNEIDER, 2006A; SCHNEIDER, 2018B). 60

FIGURE 14: INSTRUMENTS AND MATERIAL REQUIRED FOR EMBRYONIC MANIPULATION IN AVIAN EMBRYOS.

(A) EGG HOLDER FOR HORIZONTAL INCUBATION OF CHICK EGG. (B) EGG TEE USED TO OPERATE QUAIL EMBRYO IN OVO. (C) TOOLS REQUIRED FOR EMBRYONIC MICROSURGERY: (A) CURVED AND (B) PASCHEFF'S SCISSORS, (C) SKIMMER TO COLLECT EMBRYOS, (D) TRANSPLANTATION SPOON, (E) FORCEPS, (F) MICRO-SCALPEL HOLDER. (D) CHICK EMBRYO AT 8 SOMITE STAGE (SS) ON THE YOLK: THE NEURAL FOLD IS DELINEATED WITH RED DASHED LINES. (E) INJECTION OF INDIA INK UNDER THE BLASTODERM HELPS TO VISUALIZE THE EMBRYONIC STRUCTURES; TO ACCESS THE EMBRYO, THE VITELLINE MEMBRANE COVERING THE CEPHALIC REGION IS INCISED AND DEFLECTED. (F) THE CEPHALIC NEURAL CREST (CNC) IS FIRST INCISED ON THE RIGHT-HAND SIDE FROM THE LEVEL OF R2, AND THEN PROGRESSIVELY REMOVED UNTIL BEING COMPLETELY ABLATED. (G) BILATERAL ABLATION OF THE CNC: THE REMOVED TERRITORY CORRESPONDS TO THE NEURAL CREST CELL (NCC), WHICH ARE FATED TO FORM THE CRANIOFACIAL SKELETON. (H) AFTER TRANSPLANTATION, OPENING IN THE SHELL IS SEALED WITH TAPE BEFORE RE-INCUBATING CHICK EMBRYOS..... 79

FIGURE 15: QUAIL-CHICK XENOTRANSPLANTATION OF DISCRETE CEPHALIC NEURAL CREST (CNC) TERRITORIES: UNRAVELING THE MIGRATION OF CNC CELLS.

(A, B) INTERSPECIFIC EXCHANGE BETWEEN QUAIL AND CHICK EMBRYOS INVOLVING (A) THE POSTERIOR DIENCEPHALIC (DI) NEURAL CREST (NC) CELLS, AND (B) THE MIGRATION OF THE CELLS IN THE NASOFRONTAL BUD, 24 HOURS AFTER THE GRAFT. (C, D) XENOGRAFT (C) AT RHOMBOMERE (R) 3 LEVEL, AND (D) THE DISPERSAL OF NC R3 CELLS IN THE FIRST AND SECOND BRANCHIAL ARCHES (BA). (E) COLOR-CODED FATE MAP RESULTING FROM THE SYSTEMATIC EXPLORATION OF THE MIGRATION ROUTES OF THE CNC. (F, G) COLONIZING OF THE (F) PERIOCCULAR REGION AND (G) SECOND BA, BY THE DI AND R3 NC CELLS, RESPECTIVELY. (H-L) ASIDE FROM THE ELUCIDATION OF NC CELL MIGRATION, THE QUAIL-CHICK SYSTEM CAN REVEAL THE LONG-TERM FATE AND DERIVATIVES OF THE TRANSPLANTED CELLS. (J) XENOGRAFT INVOLVING R1 AND R2 NC CELLS, (H) AT NEURULA STAGE. (I) PIGMENT PATTERN IN E18 CHIMERA. (J-L) MUSCULOSKELETAL DERIVATIVES OF THE GRAFTED CELLS: MASSIVE CONTRIBUTION OF QUAIL NCC CELLS TO (J) BONY TISSUES IN THE DENTARY, (K) CARTILAGE IN THE RETROOCULAR PROCESS, AND (L) TENDINOUS INSERTION OF PTERYGOIDEUS MUSCLE. (A,B) ARE REPRODUCED FROM CREUZET ET AL. (2005B); (C,D) FROM CREUZET ET AL. (2005A). 81

FIGURE 16: UNILATERAL AND BILATERAL ELECTROPORATION OF THE CEPHALIC NEURAL CREST (CNC).

(A) CLASSICAL SYSTEM OF TWO ELECTRODES, INVOLVING A CATHODE AND AN ANODE, TO FLANK THE NEURAL GROOVE AND TRIGGER A UNILATERAL TRANSFECTION. (B) AN E2 (HH10) CHICK EMBRYO SHOWING THE GFP ACTIVITY AFTER A UNILATERAL ELECTROPORATION OF THE NEURAL CREST (NC) CELLS EXTENDING FROM RHOMBOMERE (R) 3 TO R8. (C) THE SAME EXPERIMENT OBSERVED AT E2.5 (HH14) SHOWING THE ELECTROPORATED CELLS MIGRATING TOWARDS THE BRANCHIAL ARCHES (BA). (D) THE TRIPLEX ELECTRODE SYSTEM INVOLVING ONE CATHODE WITH TWO ANODES DEVISED TO TRIGGER A BILATERAL TRANSFER OF THE ELECTROPORATED CONSTRUCT (CREUZET ET AL., 2002A). (E) A TOP VIEW OF A 6-SOMITE STAGE (SS) CHICK EMBRYO WHERE THE ANATOMICAL LANDMARKS OF THE CNC VERSUS THE FACIAL NC (FNC) ARE DELINEATED. (F) THE SAME EMBRYO IN WHICH THE FNC HAS BEEN BILATERALLY ELECTROPORATED AT 4SS, WITH A CONSTRUCT DRIVING THE EXPRESSION OF GFP IN FNC CELLS. (G) AT 8SS, THE ELECTROPORATED FNC CELLS START TO MIGRATE AWAY FROM THE NEURAL PRIMORDIUM. (H) SECTION PERFORMED ON 12SS EMBRYO, SHOWING THAT ONLY THE NC CELLS BENEFIT THE ELECTROPORATION, LEAVING THE SUPERFICIAL ECTODERM ALONG WITH THE ADJACENT NEUROEPITHELIUM UNTRANSFECTED. (E-H) ARE REPRODUCED FROM (AGUIAR ET AL., 2014). 83

FIGURE 17: SPECIES-SPECIFIC VARIATION AT EARLY EMBRYONIC STAGES.

(A) THE HAMBURGER-HAMILTON (HH) STAGING SYSTEM (I.E., EMBRYONIC STAGE) FUNCTIONS INDEPENDENT OF TIME (I.E., ABSOLUTE TIME), AND INSTEAD RELIES ON EXTERNAL MORPHOLOGICAL CHARACTERS (I.E., DEVELOPMENTAL TIME). THUS, DUCK (VIOLET ●), CHICK (YELLOW ◊), AND QUAIL (GREEN ◻) EMBRYOS CAN BE ALIGNED AT EQUIVALENT STAGES BY INCUBATING THEM FOR DIFFERENT LENGTHS OF TIME. IN OVO DAY REPRESENTS THE NUMBER OF INCUBATION DAYS NEEDED TO REACH EQUIVALENT STAGES FOR EACH SPECIES. (B) TO GENERATE QUAIL-DUCK CHIMERAS ("QUICK"), QUAIL AND DUCK EMBRYOS ARE STAGE-MATCHED FOR SURGERY AT HH9.5 (I.E., POST-SURGERY DAY 0, ▼*) BY INCUBATING THEIR EGGS FOR DIFFERENT TIMES (SEE PANEL A ABOVE). BILATERAL NEURAL FOLDS FROM THE MID-DIENCEPHALON (DI)

TO RHOMBOMERE 2 (R2) OF THE HINDBRAIN (DARK GREEN), WHICH GENERATE NEURAL CREST MESENCHYME (NCM), ARE TRANSPLANTED FROM QUAIL TO DUCK. QUAIL DONOR NCM (GREEN CELLS) MIGRATES (GREEN ARROWS) INTO MANDIBULAR PRIMORDIA BETWEEN HH10 AND HH15. DUE TO ITS FASTER RATE OF MATURATION, QUAIL NCM DEVELOPS APPROXIMATELY THREE STAGES AHEAD OF THE SLOWER-MATURING DUCK HOST WITHIN TWO DAYS POST-SURGERY. QUAIL NCM RECEIVES CUES FROM AND INTERACTS WITH DUCK-HOST DERIVED EPITHELIUM (VIOLET ARROWS). **(C)** MANDIBULAR MESENCHYME (MM) POPULATION AT HH18, HH21, HH24, AND HH27 IN DUCK (VIOLET), CHICK (YELLOW), AND QUAIL (GREEN) EMBRYOS. **(D)** MANDIBULAR PRIMORDIA (MP) TOTAL RNA EXTRACTION AT HH15, HH18, HH21, HH24, AND HH27 IN DUCK (VIOLET), CHICK (YELLOW), AND QUAIL (GREEN) EMBRYOS AND AT HH21 AND HH24 IN QUACK (BLUE) EMBRYOS. **(E)** CONTENT OF TOTAL RNA PER MANDIBULAR PRIMORDIA CELL AT HH18, HH21, HH24, AND HH27 IN DUCK (VIOLET), CHICK (YELLOW), AND QUAIL (GREEN) EMBRYOS. **(F)** MANDIBULAR PRIMORDIA (MP) RNA EXTRACTION RATIOS COMPARING DUCK TO QUAIL AT HH18, HH21, HH24, AND HH27. **(G)** RELATIVE MANDIBULAR MESENCHYME POPULATION SIZE MODELLING AT HH15, HH18, HH21, HH24, AND HH27 IN DUCK (VIOLET) AND QUAIL (GREEN) EMBRYOS USING THE NUMBER OF MIGRATORY NCM CELLS, CELL CYCLE LENGTH, AND ABSOLUTE TIME. **(H)** RELATIVE MANDIBULAR MESENCHYME POPULATION SIZE BASED ON DUCK TO QUAIL RATIOS FOR IN VIVO (WHITE) AND MODEL (BLACK) DATA AT HH18, HH21, HH24, AND HH27..... 125

FIGURE 18: EXPRESSION OF SHH PATHWAY MEMBERS AND PATHWAY ACTIVATION IN MANDIBULAR PRIMORDIA OF DUCK, CHICK, QUAIL, AND CHIMERIC QUACK. RELATIVE MRNA LEVELS OF **(A) SHH**, **(B) PTCH1**, **(C) GAS1**, AND **(D) GLI1** IN MANDIBULAR PRIMORDIA OF DUCK (VIOLET), CHICK (YELLOW), AND QUAIL (GREEN) AT HH15, HH18, HH21, HH24, AND HH27 AND AT HH21 AND HH24 OF QUACK (BLUE) EMBRYOS. EXPRESSION LEVELS WERE ASSAYED BY QRT-PCR AND NORMALIZED TO *R18S*. SIGNIFICANCE IS SHOWN (P-VALUE < 0.02, N ≥ 6 FOR EACH GROUP AND DATA POINT, AND ERROR BARS REPRESENT SEM) FOR COMPARISONS BETWEEN DIFFERENT SPECIES AT THE SAME EMBRYONIC STAGE (I.E., DIAMOND SYMBOL FOR DUCK VERSUS CHICK, ASTERISK SYMBOL FOR DUCK VERSUS QUAIL, FULL CIRCLE SYMBOL FOR QUAIL VERSUS CHICK, AND VIOLET ASTERISK SYMBOL FOR DUCK VERSUS QUACK). FOR QUAIL VERSUS QUACK, SIGNIFICANCE IS SHOWN (GREEN ASTERISK SYMBOL) AT HH21 AND DENOTES THE COMPARISON OF HH24 QUAIL VERSUS HH21 QUACK, AND AT HH24 FOR THE COMPARISON OF HH27 QUAIL VERSUS HH24 QUACK. SHH PATHWAY ACTIVATION AS REPRESENTED BY RATIOS OF **(E) SHH TO PTCH1** AND **(F) SHH TO GLI1** MRNA LEVELS FOR DUCK, CHICK, AND QUAIL AT HH15, HH18, HH21, HH24, AND HH27 AND QUACK AT HH21 AND HH24. SIGNIFICANCE IS SHOWN FOR COMPARISONS BETWEEN SPECIES AS DENOTED BY BRACKETS AND P-VALUES ARE AS INDICATED. N ≥ 6 FOR EACH GROUP AND DATA POINT, AND ERROR BARS REPRESENT SEM. 128

FIGURE 19: EFFECTS OF INHIBITION AND ACTIVATION OF THE SHH PATHWAY IN MANDIBULAR PRIMORDIA OF DUCK, CHICK, AND QUAIL. MANDIBULAR PRIMORDIA FROM DUCK (VIOLET), CHICK (YELLOW), AND QUAIL (GREEN) EMBRYOS WERE HARVESTED AT HH21, PLACED IN CULTURE, AND TREATED WITH CYCLOPAMINE (CYCL, DARK GREY) TO INHIBIT THE SHH PATHWAY OR WITH FIVE SERIAL DILUTIONS OF RECOMBINANT (R) SHH PROTEIN (LIGHT GREY) TO ACTIVATE THE SHH PATHWAY. BOX PLOTS SHOW RELATIVE LEVELS OF MRNA EXPRESSION (ON THE Y-AXIS IN LOG₂ SCALE) FOR SHH PATHWAY MEMBERS INCLUDING **(A) PTCH1**, **(B) GAS1**, **(C) GLI1**, **(D) GLI2**, AND **(E) GLI3** 24 HOURS AFTER TREATMENT. CONTROL (CTRL, WHITE) AND TREATMENT GROUPS ARE SHOWN ON THE X-AXIS. EXPRESSION LEVELS WERE ASSAYED BY QRT-PCR AND NORMALIZED TO *R18S*. SIGNIFICANCE IS SHOWN FOR COMPARISONS BETWEEN CONTROL AND TREATMENT GROUPS (I.E., CYCLOPAMINE OR RSHH) WITHIN THE SAME SPECIES AS INDICATED BY COLORED SHADING AND BY THE FOLLOWING SYMBOLS FOR P-VALUES: * P < 0.05, ** P < 0.01, *** P < 0.001, AND **** P < 0.0001. P-VALUES ≥ 0.05 WE CONSIDERED NOT SIGNIFICANT (NS). N ≥ 4 FOR EACH GROUP AND DATA POINT. 130

FIGURE 20: EXPRESSION OF GAS1 IN MANDIBULAR PRIMORDIA AT EARLY DEVELOPMENTAL STAGES. WHOLE MOUNT *IN SITU* HYBRIDIZATION SHOWING *GAS1* EXPRESSION (PURPLE

STAIN) IN MANDIBULAR PRIMORDIA FROM (A) DUCK, (B) CHICK, AND (C) QUAIL AT HH21; AND IN (D) DUCK, (E) CHICK, AND (F) QUAIL AT HH27..... 132

FIGURE 21: EFFECTS OF SHH PATHWAY ACTIVATION AND *GAS1* OVEREXPRESSION IN CELL CULTURE. (A) RELATIVE LEVELS OF MRNA EXPRESSION (ON THE Y-AXIS IN LOG₂ SCALE) FOR *GAS1*, *PTCH1*, AND *GLI1* IN CHICK FIBROBLASTS (I.E., DF-1) 24 HOURS (H) AFTER TREATMENT WITH FIVE SERIAL DILUTIONS OF RECOMBINANT (R) SHH PROTEIN. (B) RELATIVE *GAS1* MRNA LEVELS IN CHICK FIBROBLASTS 24 HOURS AFTER DOXYCYCLINE (DOX)-INDUCTION OF A STABLY INTEGRATED CHICK *GAS1* OVEREXPRESSION VECTOR. NUMBER OF CHICK *GAS1*-POSITIVE CELLS 72 HOURS AFTER INDUCTION WITH DOX. (C) RELATIVE *GAS1* MRNA LEVELS IN CHICK FIBROBLASTS 24 HOURS AFTER DOX-INDUCTION OF A STABLY INTEGRATED QUAIL *GAS1* OVEREXPRESSION VECTOR. NUMBER OF QUAIL *GAS1*-POSITIVE CELLS 72 HOURS AFTER INDUCTION WITH DOX. (D) RELATIVE LEVELS OF MRNA EXPRESSION FOR *GAS1*, *PTCH1*, AND *GLI1* IN CHICK FIBROBLASTS 48 HOURS AFTER TREATMENT WITH SERIAL DILUTIONS OF RSHH PROTEIN. RELATIVE LEVELS OF MRNA EXPRESSION FOR *GAS1*, *PTCH1*, AND *GLI1* IN CHICK FIBROBLASTS 48 HOURS AFTER DOX-INDUCTION OF A STABLY INTEGRATED *GAS1* OVEREXPRESSION VECTOR (SERIAL DILUTION) AND TREATMENT WITH RSHH PROTEIN (CONTROL 0 NG/ML IN WHITE AND 100 NG/ML DARK GREY). EXPRESSION LEVELS WERE ASSAYED BY QRT-PCR AND NORMALIZED TO *R18S*. SIGNIFICANCE IS SHOWN FOR COMPARISONS BETWEEN CONTROL AND TREATMENT GROUPS AS DENOTED BY BRACKETS AND P-VALUES ARE AS INDICATED. P-VALUES ≥ 0.05 ARE CONSIDERED NOT SIGNIFICANT (NS). N ≥ 2 FOR EACH GROUP AND DATA POINT, AND ERROR BARS REPRESENT SEM..... 134

FIGURE 22: EFFECTS OF *GAS1* OVEREXPRESSION AND KNOCKDOWN IN DUCK AND QUAIL EMBRYOS. (A) MESENCHYMAL CELL NUMBER IN DUCK MANDIBULAR PRIMORDIA FOLLOWING BILATERAL *IN OVO* ELECTROPORATION OF A STABLY INTEGRATING AND DOXYCYCLINE (DOX)-INDUCIBLE *GAS1* OVEREXPRESSION (OE) VECTOR INTO NCM AT HH8.5. *GAS1* OVEREXPRESSION WAS INDUCED WITH 50 NG/ML OF DOX AT HH15 AND MANDIBULAR PRIMORDIA WERE COLLECTED AT HH18, HH21, AND HH24. (B) DISSECTED DUCK MANDIBULAR PRIMORDIA IN WHOLE MOUNT AT HH18 FOLLOWING BILATERAL *IN OVO* ELECTROPORATION OF A *GAS1* OVEREXPRESSION VECTOR INTO NCM AT HH8.5. (C) *GAS1*-POSITIVE NCM CAN BE VISUALIZED BY MSCARLET FLUORESCENCE (RFP). *GAS1* OVEREXPRESSION CAN BE SEEN (D) IN WHOLE MOUNT AND (E) WITH RFP AT HH21, AND (F) IN WHOLE MOUNT AND (G) WITH RFP AT HH24. (H) MESENCHYMAL CELL NUMBER IN QUAIL MANDIBULAR PRIMORDIA FOLLOWING BILATERAL *IN OVO* ELECTROPORATION OF A *GAS1* OVEREXPRESSION VECTOR INTO NCM AT HH8.5. *GAS1* OVEREXPRESSION WAS INDUCED WITH DOX AT HH15 AND MANDIBULAR PRIMORDIA WERE COLLECTED AT HH18, HH21, AND HH24. (I) QUAIL EMBRYO IN WHOLE MOUNT AT HH27 FOLLOWING UNILATERAL *IN OVO* ELECTROPORATION OF A *GAS1* OVEREXPRESSION VECTOR INTO NCM AT HH8.5 AND INDUCTION WITH DOX AT HH15. THE TREATED SIZE APPEARS SMALLER (WHITE ARROW) THAN THE CONTRALATERAL CONTROL SIDE. (J) UNILATERAL DISTRIBUTION OF *GAS1*-POSITIVE NCM CAN BE VISUALIZED BY RFP ON ONE SIDE OF THE EMBRYO. HIGHER MAGNIFICATION VIEW OF QUAIL MANDIBULAR PRIMORDIA (DASHED LINES) IN (K) WHOLE-MOUNT AND (L) WITH RFP SHOWING A SIZE REDUCTION ON THE TREATED (ARROW) VERSUS CONTROL SIDE. (M) QUAIL EMBRYO IN WHOLE MOUNT AT HH27 FOLLOWING UNILATERAL *IN OVO* INJECTION OF A CONTROL ANTI-GFP MORPHOLINO (MO) AT HH18. AT HIGHER MAGNIFICATION IN (N) WHOLE-MOUNT AND (O) IN SCHEMATIC VIEW, THE MANDIBULAR PRIMORDIA (DASHED LINES) APPEAR THE SAME SIZE ON THE TREATED (STRIPED) AND CONTROL (GREEN) SIDES. (P) QUAIL EMBRYO IN WHOLE MOUNT AT HH27 FOLLOWING UNILATERAL *IN OVO* INJECTION OF AN ANTI-*GAS1* MORPHOLINO (MO) AT HH18. AT HIGHER MAGNIFICATION IN (Q) WHOLE-MOUNT AND (R) IN SCHEMATIC VIEW, THE MANDIBULAR PRIMORDIA (DASHED LINES) APPEAR SMALLER ON THE TREATED (STRIPED) VERSUS CONTROL (GREEN) SIDES. SIGNIFICANCE IS SHOWN FOR COMPARISONS BETWEEN CONTROL AND TREATMENT GROUPS AS DENOTED BY BRACKETS AND P-VALUES ARE AS

INDICATED. P-VALUES ≥ 0.05 ARE CONSIDERED NOT SIGNIFICANT (NS). N ≥ 2 FOR EACH GROUP AND DATA POINT. ERROR BARS REPRESENT SEM..... 136

List of Tables

TABLE 1. DUCK, CHICK, AND QUAIL INCUBATION TIMES.....	146
TABLE 2. MANDIBULAR PRIMORDIA INCUBATION TIMES IN TRYPSIN-PANCREATIN SOLUTION.....	147
TABLE 3. QUANTIFICATION OF SOX10-POSITIVE DELAMINATED NC PROGENITORS IN THE MIDBRAIN OF CHICK EMBRYOS AT HH10.....	148
TABLE 4. MANDIBULAR MESENCHYME POPULATION SIZE IN DUCK, CHICK, AND QUAIL EMBRYOS.....	149
TABLE 5. MANDIBULAR PRIMORDIA TOTAL RNA YIELD IN DUCK, CHICK, QUAIL, AND QUACK EMBRYOS	150
TABLE 6. RNA CONTENT PER CELL IN MANDIBULAR PRIMORDIA.....	151
TABLE 7. MANDIBULAR MESENCHYME POPULATION SIZE MODELING IN DUCK AND QUAIL EMBRYOS	152
TABLE 8. DUCK/QUAIL TOTAL RNA EXTRACTION RATIOS	153
TABLE 9. DUCK/QUAIL MANDIBULAR MESENCHYME POPULATION SIZE RATIOS	154
TABLE 10. SHH PATHWAY ACTIVATION IN DUCK, CHICK, QUAIL, AND QUACK MANDIBULAR PRIMORDIA	155
TABLE 11. SHH PATHWAY MEMBERS MRNA LEVELS IN DUCK, CHICK, QUAIL, AND QUACK MANDIBULAR PRIMORDIA.....	156
TABLE 12. SHH PATHWAY MEMBERS MRNA LEVELS IN DUCK, CHICK, AND QUAIL MANDIBULAR PRIMORDIA EXPLANT CULTURES.....	158
TABLE 13. SHH PATHWAY MEMBERS MRNA LEVELS IN DF1 CELL CULTURES WITH STABLY INTEGRATED DOX-INDUCIBLE GAS1 CONSTRUCT AFTER 24 HOURS OF DOXYCYCLINE HYCLATE (DOX) TREATMENT	160
TABLE 14. NUMBER OF CELLS COUNTED IN 6-WELL PLATE AFTER 72 HOURS OF DOXYCYCLINE HYCLATE (DOX) TREATMENT IN DF1 CELL LINES WITH STABLY INTEGRATED DOX-INDUCIBLE GAS1.....	161
TABLE 15. SHH PATHWAY MEMBERS MRNA LEVELS IN DF1 CELLS AFTER 24 HOURS OF RECOMBINANT SHH (RSHH) TREATMENT	162
TABLE 16. SHH PATHWAY MEMBERS MRNA LEVELS IN DF1 CELLS WITH STABLY INTEGRATED DOX-INDUCIBLE GAS1 CONSTRUCT AFTER 48 HOURS OF DOXYCYCLINE HYCLATE (DOX) AND RECOMBINANT SHH (RSHH) TREATMENT.....	163
TABLE 17. QRT-PCR PRIMER SEQUENCES	166
TABLE 18. GAS1 IN SITU PROBES PRIMER SEQUENCES	167
TABLE 19. VIVO-MORPHOLINO OLIGO SEQUENCES	168
TABLE 20. P-VALUES FOR <i>IN VIVO</i> SAMPLES (SIGNIFICANT VALUES HIGHLIGHTED IN GRAY)	169
TABLE 21. P-VALUES FOR MANDIBULAR PRIMORDIA EXPLANT CULTURES TREATED WITH RECOMBINANT SHH PROTEIN (SIGNIFICANT VALUES HIGHLIGHTED IN GRAY).....	172
TABLE 22. P-VALUES FOR DF1 CELL CULTURES WITH STABLY INTEGRATED DOX-INDUCIBLE GAS1 CONSTRUCT AFTER 24 HOURS OF DOXYCYCLINE HYCLATE (DOX) TREATMENT (SIGNIFICANT VALUES HIGHLIGHTED IN GRAY).....	173
TABLE 23. P-VALUES FOR DF1 CELL CULTURES WITH STABLY INTEGRATED DOX-INDUCIBLE GAS1 CONSTRUCT AFTER 24 AND 48 HOURS OF RECOMBINANT SHH (RSHH) PROTEIN TREATMENT (SIGNIFICANT VALUES HIGHLIGHTED IN GRAY).....	174
TABLE 24. P-VALUES FOR DF1 CELL CULTURES WITH STABLY INTEGRATED DOX-INDUCIBLE GAS1 CONSTRUCT AFTER 48 HOURS OF DOXYCYCLINE HYCLATE (DOX) AND/OR RECOMBINANT SHH (RSHH) PROTEIN TREATMENT (SIGNIFICANT VALUES HIGHLIGHTED IN GRAY).....	175
TABLE 25. MANDIBULAR MESENCHYME POPULATION SIZE IN DUCK AND QUAIL EMBRYOS WITH GAS1 OVER-EXPRESSION.....	176

Chapter 1: Cellular mechanisms underlying the evolution of size and shape in the vertebrate jaw

Introduction

Since Aristotle, biologists strived to categorize species based on the aspect of the outward appearance (shape, structure, color, size, and pattern), i.e., eidonomy, and their structure and form of the internal parts, i.e., anatomy. The effort to do so was predominantly motivated by the narcissistic belief of "Scala naturæ" (i.e., great chain of being), an idea first enunciated by Aristotle or should we say belief, that all life on earth is inferior to "man" (Russell, 1916). Each organism was described and categorized based on the theory that there is a hierarchy of forms that could be constructed from "simpler" to more complex with the "man" at the top. Ernst Haeckel, one of the major proponents of this philosophy, believed in the law of recapitulation. He believed that all animal forms are recapitulated during human development and that at any stage one of the "simpler or inferior" animal forms is produced (Figure 1) (Gould, 1977). Eventually, evidence against the idea of recapitulation (i.e., belief that "Ontogeny recapitulates phylogeny") accumulated and its stronghold on evolutionary as well as developmental thought was overturned (de Beer, 1958; Garstang, 1922; Hall, 2000a).

Aristotle, the said founder of comparative anatomy, also made a real start with comparative embryology. He was the first to describe the development of the chick as it appears to the naked eye. One of Aristotle's greatest service to morphology is his clear acknowledgment of the Bauplan (i.e., body plan) unity held throughout each of the great groups (i.e., man, viviparous quadrupeds, oviparous quadrupeds, birds, and fishes) which later led to the recognition of what is now called the homology of parts (Russell, 1916).

The noticeable resemblances of one animal to another, the possibility of organizing them into a system, as well as the concept of all-pervading plan of structure lead to the thought of blood-

relationship and that group of species might be descended from a common ancestor (Russell, 1916; Strickland, 2005). Immanuel Kant, another great philosopher, suggested the possibility that the whole organic realm is derived from one parent form (he even considered the possibility of inorganic matter), he writes: "The agreement of so many genera of animals in a certain common schema, which appears to be fundamental not only in the structure of their bones, but also in the disposition of their remaining parts – so that with an admirable simplicity of original outline, a great variety of species has been produced by the shortening of one member and the lengthening of another, the involution of this part and the evolution of that – allows a ray of hope, however faint, to penetrate into our minds, that here something may be accomplished by the aid of the principle of the mechanism of Nature (without which there can be no natural science in general). This analogy of forms, which with all their differences seem to have been produced according to a common original type, strengthens our suspicions of an actual relationship between them in their production from a common parent, through the gradual approximation of one animal-genus to another – from those in which the principle of purposes seems to be best authenticated, *i.e.*, from man down to the polype, and again from this down to mosses and lichens, and finally to the lowest stage of Nature noticeable by us, *viz.*, to crude matter" (Kant, 1790; Russell, 1916).

Human arrogance and need for superiority led to denial of adaptations as a way of radiation for filling ecological niches by embryologists for very long time – the idea that diversity wasn't just a byproduct of a developmental arrest in humankind was hard to grasp by many recapitulationists. They had to acknowledge that there is a possibility that biological forms may reflect their evolutionary roots as well as the current pressures of survival and adaptation. This important change in how evolution is perceived by many philosophers was provoked by

the publication of the masterpiece *On the Origin of Species* by Charles Darwin's in 1859.

Charles Darwin was among the first to argue that by natural selection, the struggle for survival, and the opportunity that different species have had shaped their form. The morphology and function coincided over generations and healthy population of species that were able to adapt with their environment survived. Such a process of selection by functionality is responsible for the diversity of life on earth, as Darwin wrote, "endless forms most beautiful, and most wonderful, have been, and are being, evolved" (Darwin, 1859).

History of Size, Shape, Time, and Scaling

Scientists have been fascinated for centuries by the fact that anatomical proportions, like size and shape, are so robustly maintained in individuals even though they can vary enormously, both within a species as well as between members of related taxa. How are these differences established during development and how do they change in the course of evolution? What processes and mechanisms allow different structures of the early embryo to augur their later use and function in adults? These fundamental biological questions intrigued scientists since Aristotle and there is a long history of efforts and approaches to find the answers to them.

Scientists such as Cuvier, Goethe, Geoffroy, Buffon, Serres, Savigny, Lamarck, and Owen tried to link morphology and function by observations of the adult body plan. They conducted very detailed comparative studies, in the pre-evolutionary era, that outlined the fundamentals for comparative methods used to study variation in morphology and species adaptation (Appel, 1987; Russell, 1916). These studies led to neologisms like "analogy" (i.e., similarity due to convergent evolution) and "homology" (i.e., traits found in different organisms that are inherited from a common ancestor) that were defined by Owen in his work on description of

the vertebrate skull (Owen, 1848). The precision of his language enabled a discussion in the scientific field about the origins, form, and function of structures across taxa.

In the highly influential monumental book *On Growth and Form*, originally published in 1917, D'Arcy Thompson encapsulated the origin of diversity of body shape and size. Thompson discussed and expanded, in a comprehensive manner, the inseparable connection between morphology and function. Thompson perceived morphology as simple geometry – as a consequence of body Cartesian coordinates systems (Figure 2). He argued that allometric difference in coordinate scale would result in changes in body plan proportion and likely act as a major driving force for evolutionary heterogeneousness. He was critical of other zoologists for not using the physical or mathematical sciences and mathematical language for describing biological processes: “Even now the zoologist has scarce begun to dream of defining in mathematical language even the simplest organic forms. When he meets with a simple geometrical construction, for instance in the honeycomb, he would fain refer it to psychical instinct, or to skill and ingenuity, rather than to the operation of physical forces or mathematical laws; when he sees in snail, or nautilus, or tiny foraminiferal or radiolarian shell a close approach to sphere or spiral, he is prone of old habit to believe that after all it is something more than a spiral or a sphere, and that in this 'something more' there lies what neither mathematics nor physics can explain.” (Thompson, 1917). Both Darwin's and Thompson's work argued that all life forms are perfect in the size and shape they are present (i.e., form shaped by evolutionary pressure driven by natural selection).

Other biologists eager to address similar biological questions on size and shape include John Haldane and Julian Huxley. Haldane, again as Thompson, criticized zoologists for neglecting one of the most obvious differences between species, their difference in size. He wrote in *On*

Being the Right Size, "In a large textbook of zoology before me I find no indication that the eagle is larger than the sparrow, or the hippopotamus bigger than the hare, though some grudging admissions are made in the case of the mouse and the whale. But yet it is easy to show that a hare could not be as large as a hippopotamus or a whale as small as a herring. For every type of animal there is a most convenient size, and a large change in size inevitably carries with it a change of form." (Haldane, 1926). Huxley included the mathematical representations of morphological transformations. He introduced the neologism, allometry, which he used to explain the relationship of body size to shape. The big question many wanted to answer was, how is allometry established and maintained during development? Their research and thinking was fueled by the curiosity for understanding developmental mechanisms responsible for the differences that correlate the growth of body parts at different rates to change of body proportions (Coppinger and Schneider, 1995; Gayon, 2000; Gould, 1966, 1981; Hersh, 1934; Huxley, 1932, 1950; Huxley and Teissier, 1936; Lumer, 1940; Lumer et al., 1942; Needham and Lerner, 1940; Stern and Emlen, 1999; von Bonin, 1937).

One of the most important contributions to evolutionary developmental biology was made by Gavin de Beer who emphasized the importance of possible changes in the timing of developmental events in correlation to size and shape. He wrote "By acting at different rates, the genes can alter the time at which certain structures appear...This conclusion ...enables us to see how changes and indeed reversals in the order of development of structures can take place...To this phenomenon the term heterochrony may be applied." (de Beer, 1954).

Heterochrony, initially introduced by Ernst Haeckel as an exception for individual organs, a genetically controlled difference in timing and/or duration of a developmental process of an organism in comparison to its ancestor or another organism/species, leads to changes in

morphology (i.e., size, shape, presence or absence of certain organs or features). de Beer argued that the paedomorphosis (i.e., adults descendant display/retain traits previously seen only in the juvenile ancestor), a result of neoteny (i.e., juvenilization of adults by slowed or delayed physiological/somatic development) as well as progenesis (i.e., reaching sexual maturity, by accelerating sexual development, while still in the juvenile form of the ancestors), increases morphological evolvability and diversification which allows for large, rapid phenotypic change and accounts for the origin of many taxa (including higher taxa): "A species undergoing paedomorphosis will find itself in possession of a number of genes whose functions were to control characters which no longer appear, since the old adult characters will be lost in neoteny, and old structures will be replaced by new ones in deviation. It is, therefore, possible to imagine that these 'unemployed' genes are available for new variation, and that paedomorphosis may contribute directly to an increase of genetic and evolutionary plasticity in this way" (Brigandt, 2006; de Beer, 1930, 1954; Gould, 1977; Hall, 1984, 2000a; Ridley, 1985; Schneider, 2018a).

Some of the most notable allometric studies that characterized size and shape in relation to growth were done by Stephen Jay Gould. He summarized the history of the relationship of development and evolution in his masterpiece *Ontogeny and Phylogeny* where he also revisited and criticized de Beer's schema for heterochrony. Gould disagreed with the classification of de Beer's four types of heterochrony, de Beer presented eight modes of heterochrony, but only four of them are types of heterochrony (i.e., acceleration, hypermorphosis, neoteny, and retardation) (Figure 3). Gould wrote "If heterochrony is the basis of classification, then we must assume that the eight modes refer to quantitative, temporal displacements, not to the qualitative introduction of evolutionary novelties. Starting with the

1940 edition, de Beer presents his famous chart of the eight modes (Figure 29); the verbal descriptions are identical in all editions. Of the eight modes, four have nothing to do with heterochrony; and of these four, three are identical." (Gould, 1977).

Gould presented his evolutionary clock model that included size, shape, and time (i.e., age). Each parameter can be altered separately without changing the others which generates enough plasticity in the model to represent all de Beer's types of heterochrony (Figure 4) (Brigandt, 2006; Gould, 1977; Hall, 1984, 2000a; Schneider, 2018a). The biggest drawback of Gould's model is its static nature as it is unable to realistically represent such dynamic biological processes that are happening during development. Two years later, Pere Alberch, George F. Oster, and David B. Wake collaborated with Gould to develop a quantitative method for describing the relationship between heterochronic changes in ontogeny and phyletic trends. Their collaborative effort to make Gould's clock model more dynamic was presented in *Size and Shape in Ontogeny and Phylogeny* where they introduced differential equations as a way to describe and include the dynamic process of development in mathematical terms. This work became highly cited and was a success in their attempt to stimulate others. "We hope that our attempts to construct a quantitative theory will stimulate others to delve more deeply below the level of pure phenomenology and come to grips with the central issue underlying evolutionary diversification of size and shape – that is, the morphogenetic unfolding of genetic programs in ontogeny and their alteration in the course of phyletic evolution" (Alberch et al., 1979).

Scaling Can be Achieved at Different Developmental Stages

The anatomical structure of animals belonging to a particular taxon share a common body

plan with a variation that follows normal distribution. The fundamental body plan of a phylum is often altered in size and/or proportion. Individuals of the same taxa and those among more closely related taxa have a more similar/conserved common body plan. Not only are there identical (i.e., homologous) structures present, but they are often in relative proportion, a phenomenon known as scaling. Organs and tissues of many organisms vary a lot in size, but very little in their morphology. They appear to be scaled versions of a common pattern or template. Such scaling involves species-specific adjusting of the intrinsic scale of spatial patterns of gene expression, because even a small genetic change affecting developmental time could result in a very significant phenotypic variation or transformation in size or shape, an idea that Goldschmidt already presented in the early 20th century when he discovered genes that alter the rate of development (Goldschmidt, 1938). Thus, the proper initiation and order of expression for genes responsible for developmental timing is necessary to size the system (i.e., organism, tissues, organs) properly. The identification and answering the question of when, where, and what mechanisms are responsible for the regulation of pattern scaling at the tissue, organ, and organism level during development is one of the long-standing challenges in biology. Huxley, similarly to Goldschmidt, emphasized the importance of studying time and the timing of gene expression during development when asking biological questions about scaling, and proposed the possibility of one gene controlling two or more different growth processes; as he wrote "...we may hope for a fuller understanding of the processes involved in changes of proportion. One alteration in a single rate-gene may delay the first formation of an organ and also decrease the growth-coefficient once it is formed. Further, although the processes of histo-differentiation do not seem to follow the same laws of relative growth as those of auxano-differentiation, the quantitative intensity of the two kinds of growth-

processes may well be controlled by the same genes." *

He also proposed possible genetic mechanisms, "...

(a) mutations affecting the primary gradient of the early embryo, on which the time-relations of antero-posterior differentiation depend;

(b) mutations affecting specific rate-genes;

(c) mutations affecting specific 'time-genes' – genes controlling time of onset and not rate of processes",

that should be considered while looking for answers to how evolutionary changes in relative size (i.e., scaling) are established during development. Many biologists were eager to have more in-depth answers and to know what genes govern the developmental mechanisms regulating size and shape (Huxley, 1932).

In the past three decades, as a result of the accessibility of molecular-level data, *in vivo* gene expression manipulations together with mathematical modeling and cutting-edge technology for imaging, there was a rapid progress in the field of developmental biology. Scientists have uncovered the near complete list of evolutionally conserved genes that are responsible for animal body plan specification, have shed some light on scaling mechanisms in several systems

* *histodifferentiation*, "tissue differentiation and the assumption of the definitive general form-plan" (i.e., tissue/organ differentiation from an undifferentiated group of cells), is followed by *auxano-differentiation*, the phase of growth during which "quantitative growth-changes in proportions" Huxley, J.S., 1932. Problems of Relative Growth. Methuen, London.

and tissues, and gained a deeper understanding of the mechanisms (molecular and cellular) that unite time, size, and shape during ontogeny and phylogeny.

Scaling of embryos, tissues, and organs can be achieved at different time points throughout development and continue post-embryonically. There is a possibility for an initial pattern to be established very early in development when the embryo is a set size which can be followed by differential yet proportional embryonic growth. However, it isn't uncommon that embryos, even of closely related taxa, vary a lot in size at the time the tissue patterning is established. Despite the size differences at the time of patterning, their anatomical and cellular structures are scaled properly. This suggests the possible mechanism to achieve a size-invariant output involves modifications of the patterning mechanisms themselves. One of the most studied and explored patterning mechanism is morphogen gradient that had been explored by many scientists for decades.

Tissue Patterning

How and through what mechanisms is tissue patterning established during development of multicellular organisms? How is it possible that invariant phenotypes are generated by many developmental processes in such a wide scope of ecological conditions? Those are the questions that many, not only, biologists have asked. Since the early days of embryology many were fascinated by the marvelous consistency of body plan development. That kind of robustness to environmental, stochastic, and genetic variation and mechanistic foundations is a fundamental biological property of cells and organisms and is of long-standing interdisciplinary interest (Barkai and Ben-Zvi, 2009; Braendle and Félix, 2008; Waddington, 1942; Wagner, 2005).

Those questions were approached by scientists from both theoretical as well as experimental perspectives. At the beginning of the 20th century, Hans Spemann experimentally tested the plasticity of embryonic development and its ability to overcome extreme perturbation using clawed frog embryos (*Xenopus laevis*) and newt embryos (*Triturus taeniatus* and *Triturus cristatus*). Spemann used a baby hair to cut in half a newt embryo, separating the dorsal end from the ventral end. The dorsal half of the embryo continued proper tadpole development, although it was smaller (i.e., scaled down) in size, while the ventral half was left in vegetative state (Figure 5) (Spemann, 1938; Spemann and Mangold, 1924).

In 1924, Hilde Mangold performed dorsal blastopore lip transplantation experiments resulting in a complete secondary axis formation and Siamese twins (Figure 6). In some experiments, Mangold transplanted tissue between two different species. This was an elegant method that enabled Mangold to differentiate the donor (*Xenopus cristatus*) and host (*Xenopus taeniatus*) cells and follow cell fate as well as tissue contributions as cells from these species exhibit differences in pigmentation that persist throughout the course of development. The secondary axis cell contributions derived mostly from the host, with a very small fraction coming from the donor (i.e., unpigmented) cells. The donor cells re-specified the fate of host-tissue by providing cues necessary and sufficient for full embryonic axis formation. The region of embryonic tissue carrying such a specifying capacity (i.e., the dorsal blastopore lip of the early gastrula embryo) was later named after Spemann as the Spemann Organizer (Spemann and Mangold, 1924). Those two experiments demonstrated the capacity of the embryo to adapt and tolerate an extreme perturbation in initial size and tissue disruption and scale the morphological patterns in response to these interventions.

In 1942, Conrad Waddington proposed the concept of canalization (i.e., invariance of a

population to produce wild-type phenotype in the face of genetic or environmental perturbations), as a form of developmental stability and evolutionary robustness (Waddington, 1940, 1942, 1957). As he wrote: "In multi-cellular organisms the development of tissues and organs commonly exhibits a balance between flexibility and inflexibility; while a sufficient external stress will cause development to diverge and reach some unusual end-result, there are counteracting tendencies to attain the normal adult condition even in the face of disturbing influences. This condition, which has been referred to as the 'canalization of development', must be regarded as a result of the complex interactions between the numerous gene-controlled processes by which development is brought about."

Morphogens

During development, cell organization through growth, migration, and differentiation gives rise to tissues. This process of patterning is governed by molecule secretion together with cell-cell interactions which results in unique cell fate (i.e., tissue pattern). The complexity of the gene networks and changes in epigenetics generate flexibility that can modify physical properties and/or behaviors of cells. These self-propagating entities (i.e., morphogens) produce domains of chemical and/or mechanical signals that evolve and change with developmental time. One of the most influential theoretical frameworks describing "a system of chemical substances, called morphogens, reacting together and diffusing through a tissue" was devised by Alan Turing. In his work, *The Chemical Basis of Morphogenesis*, Turing made the connection between development and pattern formation and physical laws and chemical reactions (Turing, 1952). Turing described a hypothetical chemical reaction that could result in the initially chemically uniform system (i.e., embryo) spontaneously breaking symmetry and generating stable spatial patterns. Turing's "reaction-diffusion" system's key characteristic is

that even very small transient differences in a morphogen concentration, while considering five important points, can be amplified very quickly, and propagated over large distances. As he writes: "...the concentrations and diffusibilities of each substance have to be given at each point. In determining the changes of state, one should take into account

- (i) The changes of position and velocity as given by Newton's laws of motion.
- (ii) The stresses as given by the elasticities and motions, also taking into account the

osmotic pressures as given from the chemical data.

- (iii) The chemical reactions.

- (iv) The diffusion of the chemical substances. The region in which this diffusion is

possible is given from the mechanical data."

By adjusting the system's parameters, an astonishing amount of ordered patterns observed in the nature, such as plant vasculature, leopard's spots, zebra or fish stripes, pigmentation patterns of bird feathers and seashells, the segmentation of *Drosophila* embryos, spacing of mammalian hair, or limb patterning can be mathematically modeled (Figure 7) (Bieler et al., 2011; Dimitrov and Zucker, 2006; Holloway, 2010; Kauffman et al., 1978; Kondo and Asai, 1995; Kondo and Miura, 2010; Meinhardt et al., 2003; Nagorcka and Mooney, 1982, 1985; Newman and Frisch, 1979; Raspopovic et al., 2014; Richardson et al., 1990; Sheth et al., 2012; Turing, 1952; Yamaguchi et al., 2007). The biggest challenge was not to identify the mechanism, but the morphogens that are responsible for it.

Recent advances in computer science and computer simulations as well as in genetics,

molecular biology, and experimental manipulations (especially in vertebrate systems) enabled the identification of morphogens relevant to tissue patterning and provided direct evidence that Turing's reaction-diffusion system is used as a tissue patterning strategy during development. Some tissue patterning strategies that were initially thought to involve reaction-diffusion systems involve a combination of other mechanisms and are not as simple as a two-component (i.e., activator – inhibitor) system. Some tissue patterns are not achieved by secreted molecules but by cell-cell interactions (short- and long-range) that can induce the desired cell behavior (DasGupta and Fuchs, 1999; Huelsken et al., 2001; Jiang et al., 1999; Jung et al., 1998; Nakamasu et al., 2009; Paré et al., 2014; Sick et al., 2006; Watanabe and Kondo, 2015; Zallen and Wieschaus, 2004; Zhang et al., 2012).

There are at least two main patterning mechanisms operating during development, positional information and mechanical self-organization. Probably one of the simplest ways of establishing tissue pattern and size involves cell differentiation while the cells acquire their positional identity and information within the tissue/group of cells. This can result a cell or group of cells adopting a certain fate or exhibiting a phenotype with regard to their position withing a mechanical or chemical gradient that they are exposed to (Figure 7). A fundamental principle of this patterning model is the capacity of cells to be sensitive to a very small change in morphogen and/or chemotactic agent concentration and adopt/exhibit cell different fates (i.e., specification) by activating very intricate gene regulatory networks that can involve multiple signaling pathways (Tostevin et al., 2007; Wolpert, 1969, 1996). There is no requirement of the system to be prepatterned and only mirroring the morphogen gradient as it is the case of simple gradient patterning model (Figure 7).

Acquisition of a cell fate as a response to a precise position within a morphogen gradient is

very common in development and is fundamental to the determination of embryonic axes (anterior-posterior, dorsal-ventral, as well as left-right) and contributes to a specified body plan. A very classic example of body segmentation during development is the *Drosophila* segmented body plan. The anterior-posterior axis is established by the Bicoid morphogen gradient leading to *gap and pair-rule* striped pattern gene expression, which pre-sages the identity of body segments (Driever and Nüsslein-Volhard, 1988; Nüsslein-Volhard and Wieschaus, 1980; Riddihough and Ish-Horowicz, 1991; Small et al., 1991). Rather than using only single patterning mechanisms, the tissues are specified by a combination of multiple systems of activators and inhibitors where the geometry, cell position, as well as the mechanical and chemical gradients play a role. Specification of germ layers (i.e., endoderm, mesoderm, and ectoderm) involves many cellular and molecular mechanisms such as conserved gastrulation movements (epiboly, internalization, convergence, and extension) that drive well defined morphological tissue transformations; cellular mechanisms that include cell migration, intercalation, epithelial mesenchymal transition (EMT), and cell shape changes; chemical signals emerging from discrete locations (i.e., signaling centers) within the embryo. All mentioned mechanisms together ensure the correct timing of induction and positioning of germ layers in the developing embryo (Solnica-Krezel and Sepich, 2012).

Over-all the presence of a morphogen is one of the most classic patterning mechanisms that is in many cases accompanied by an additional combination of mechanisms such as molecule secretion. The signal (i.e., morphogen) is secreted by a group of cells or tissue (i.e., signaling center) and becomes more diluted further from its source. Target tissue (i.e., cells capable of responding to the input signal) respond by activating distinct signaling pathways and thus transcription of target genes in a concentration-dependent manner resulting in defined cell

fates that vary based on specific morphogen concentration. Morphogens can be scaled to embryo size by several mechanisms (external and/or internal to the target cell population) that include:

1. Changes in the amount of morphogen production.
2. Changes in ligand decay rate and/or diffusion.
3. Two opposing gradients.
4. Cell-autonomous manner (i.e., changes in the sensitivity of the target cell to the morphogen levels).

Thus, for many developmental patterning systems the origin of patterning could be generated on one or a combination of multiple levels, the source (i.e., tissue that generates the morphogen signal), distribution (i.e., morphogen release and/or secretion), transportation (i.e., morphogen diffusion throughout the tissue), and detection (i.e., morphogen detection and signal transduction in the cells sensitive to the input signal) (Figure 8).

Jaw Complex Development

The evolution of vertebrate jaw skeleton involves two distinct systems, the viscerocranium (i.e., cartilaginous skeleton including jaws, gill arches, and their derivatives) and dermatocranium (i.e., cranial vault, palate bones, and tooth bearing bone elements) (Figure 9) (Hall, 2005a; Noden and Schneider, 2006b). The composite elements of the head and jaw skeleton is especially striking during development. The pre-formed cartilaginous structure of the viscerocranium is typically replaced by bone through ossification (endochondral and perichondral) (Hall, 1980a; Hall, 1981, 2005b; Hall and Miyake, 2000; Helms and Schneider,

2003; Mina et al., 1994; Patterson, 1977; Schneider, 2018b; Thorogood et al., 1986).

Chondrocyte maturation is typically followed by their apoptosis and subsequent vasculature invasion bringing nutrients and minerals into the tissue where the cartilage is replaced by bone in the endochondral ossification process. Some recent studies showed that chondrocytes may contribute directly to bone showing that chondrocyte death is not necessary in the process of endochondral bone formation (Almubarak et al., 2016; Bahney et al., 2014; Jing et al., 2015; Marconi et al., 2020; Park et al., 2015; Yang et al., 2014a; Yang et al., 2014b; Zhou et al., 2014).

The viscerocranium is derived from a series of pharyngeal arches (Figure 9) that support the gill apparatus. Each arch consists of skeletal portions and includes muscular, nervous, as well as vascular components (Noden and Schneider, 2006b). First, the oropharyngeal (op) arch forms the jaws (Cerny et al., 2004; Kuratani et al., 2013; Noden and Schneider, 2006b). Evolutionary, the emergence of vertebrate jaws probably facilitated a change in the way of predation (from passive to active) (Northcutt, 2005; Northcutt and Gans, 1983). The upper jaw consists of dermal bones that includes the premaxilla, maxilla, and palatine. The lower jaw also contains multiple dermal bones including the dentary, angular, surangular, and splenial which surround the Meckel's [cartilage \(Figure 10A, 10B\)](#) (Eames et al., 2004; Moore, 1981; Smith and Schneider, 1998).

In contrast, jaw components of the dermatocranium develop as mesenchymal condensations that undergo intramembranous ossification and differentiate directly into bone, called dermal bones (Hall, 1980a; Hall, 1981, 2005b; Hall and Miyake, 2000; Helms and Schneider, 2003; Mina et al., 1994; Patterson, 1977; Schneider, 2018b; Thorogood et al., 1986).

Bone formation via intramembranous ossification consists of mesenchymal cell condensation

together with the secretion of osteoid (i.e., a dense extracellular matrix) that is especially rich in collagen I (Beresford, 1993; Hall and Miyake, 1992). Osteoid secretion is followed by its mineralization which is the result of the incorporation into the tissue of calcium phosphate crystals, sourced from the vasculature network, providing stiffness to the very fibrous tissue. During cartilage formation, extracellular matrix rich in collagen II is secreted from mesenchymal cell condensations which results in the production of a tissue without vasculature (Hall, 2005b; Hall and Williams, 1983; Patterson, 1977; Smith and Thorogood, 1983; Thorogood, 1983). Such a process results in tissue expansion and chondrocyte separation by extensive amount of the extracellular matrix.

Vertebrate Jaw – Size and Shape

The evolutionary adaptability, functional significance, and easily measurable geometry of the vertebrate skull are some of the many reasons for intensive research that has been done to understand size and shape (e.g., chick and mouse skull in Figure 10A, 10B). The vertebrate jaws especially display an astonishing array of size, shape, and functions. The jaws of different species represent the capacity of adaptation that the tissue responsible for its development is able to achieve (de Beer, 1937; Hanken and Hall, 1984; Sánchez-Villagra and Smith, 1997; Schneider, 2015, 2018b; Smith and Hall, 1993; Woronowicz and Schneider, 2019; Zusi, 1993). The main focus of developmental studies have included the characterization of genes that affect skeletal patterning, the study of tissue interactions that are necessary and sufficient for mesenchymal cell differentiation into cartilage and bone, what mechanisms and gene networks are involved in species-specific jaw patterning, as well as studies of morphogens that regulate tissue outgrowth (Abzhanov et al., 2004; Abzhanov and Tabin, 2004; Andres, 1949; Balling et al., 1989; Barlow and Francis-West, 1997; Bee and Thorogood, 1980; Couly et al.,

2002a; Creuzet et al., 2002a; Crump et al., 2004; Depew et al., 2002; Dunlop and Hall, 1995; Ferguson et al., 2000; Francis-West et al., 1998; Francis-West et al., 2003; Gendron-Maguire et al., 1993; Grammatopoulos et al., 2000; Hall, 1980b, 1982, 1987; Hu et al., 2003; Hunt et al., 1998; Kimmel et al., 2005; Liu et al., 2005; Lufkin et al., 1992; Marcucio et al., 2005; Merrill et al., 2008; Mitsiadis et al., 2006; Noden, 1983b; Pasqualetti et al., 2000; Qiu et al., 1997; Richman and Tickle, 1989; Richman and Tickle, 1992; Rijli et al., 1993; Schilling, 1997; Schneider and Helms, 2003; Schneider et al., 2001; Schowing, 1968; Shigetani et al., 2000; Smith and Schneider, 1998; Thorogood, 1987; Thorogood et al., 1986; Tucker and Lumsden, 2004; Tyler, 1978, 1983; Wagner, 1959; Wilson and Tucker, 2004; Wu et al., 2006; Wu et al., 2004).

The variation of size and shape in vertebrate skulls and especially jaws is astonishing, yet all vertebrates share common well conserved developmental mechanisms, evolutionary origins, and tissue patterning resulting in homologous tissue components (de Beer, 1930; Goodrich, 1913, 1930).

Jaw Tissues: Cellular origins

The evolutionary origins of the jaw complex have been studied for centuries and are well established, but which cells from the early embryo are responsible for jaw development? Studies have shown that all three germ layers (i.e., endoderm, mesoderm, and ectoderm) contribute to the development of the jaws (Figure 10C). Although, the major contributor to the craniofacial development, the neural crest mesenchyme (NCM), is ectodermal origin. Cells derived from four tissues (i.e., NCM, paraxial mesoderm, surface ectoderm, and pharyngeal endoderm) must interact together throughout development to produce a complex musculoskeletal structure that is able to function properly and has very unique, species-

specific, size and shape. The development of a functional jaw complex is a multidimensional dynamic process that involves precisely controlled mechanisms regulating cell cycle, cell size, cell fate, cell number, tissue and cell metabolism, and more. Deciphering mechanisms that govern the proliferation, migration, and differentiation of the jaw precursor cell population is indispensable to understand how functional, species-specific, vertebrate jaws are established during development.

Bones of the face are derived from embryonic tissue surrounding the stomodeum (i.e., an ectodermal depression of the oral region which develops into the oral cavity). The first, oropharyngeal, arch consists of maxillary (lateral to the stomodeum) and mandibular (inferior to the stomodeum) prominences. The maxillary processes give rise to a portion of the upper jaw as well as the secondary palate. The mandibular processes give rise to the lower jaw (Fish and Schneider, 2014b; Fish et al., 2014; Schneider, 2005; Schneider et al., 1999). The frontonasal process together with lateral and medial nasal processes develop into the primary palate and the mid and upper face (Hu and Marcucio, 2012; Hu et al., 2003).

These prominences must interact together throughout facial development in order to give rise to a very complex morphological structure. Thus, there is significant potential for the introduction of patterning and morphogenetic errors. It has been previously shown that craniofacial development depends on the mutual interactions between NCM, which provides facial skeletogenic cells, and the ectodermal and endodermal tissues, which provide trophic and patterning cues for head development (Figure 10C). Defects in the craniofacial structure and particularly in palatal formation are one of the most common birth defects (Cordero et al., 2002; Couly et al., 2002a; Creuzet et al., 2005a; Creuzet et al., 2002a; Creuzet et al., 2004b; Creuzet et al., 2005b; Eames and Schneider, 2005; Schneider, 2005, 2018a; Schneider et al.,

1999).

Neural Crest Mesenchyme and Molecular Mechanisms Underlying Jaw Patterning

At early developmental stages, the oropharyngeal arches are populated by NCM. In the neurula stage embryo, NCM is specified in the dorsal neural fold, bulging between the neural plate and the non-neural ectoderm (Figure 10C, light blue cells). NCM delaminates, by a mechanism of epithelial to mesenchymal transformation, and migrates extensively from the neural primordium along definite pathways to colonize specific sites, where they differentiate into a large variety of cell types (Baker and Bronner-Fraser, 1997; Bronner-Fraser, 1994; Hörstadius and Hörstadius, 1950; Noden and Schneider, 2006a; Saint-Jeannet, 2006; Selleck and Bronner-Fraser, 1995; Selleck and Bronner-Fraser, 1996; Theveneau and Mayor, 2012; Tosney, 1982). Apart from the craniofacial skeleton, NCM derivatives include the neurons and glial cells of the peripheral nervous system, the pigment cells, and endocrine cells such as the adrenal medulla and calcitonin-producing cells (Le Douarin and Kalcheim, 1999; Le Douarin et al., 2004; Schneider, 2018b). In the jaw apparatus NCM derivatives include cartilage, bone, tendon, and muscle connective tissues (Figure 10C) (Couly et al., 1993a; Dupin et al., 2010; Jheon and Schneider, 2009; Jiang et al., 2002; Le Lièvre, 1978; Le Lièvre and Le Douarin, 1975a; McBratney-Owen et al., 2008; Morriss-Kay, 2001; Noden, 1978b; Noden and Schneider, 2006a; Yoshida et al., 2008).

The process of NCM migration appears to be governed by chemoattractant gradients of many molecules such as fibroblast growth factors (FGFs), vascular endothelial growth factors (VEGFs), and others that attract NCM to elected sites. It is still unknown whether the chemokine gradient is sufficient to carry out these long-range migrations of the NCM (Creuzet et al.,

2004b; McLennan et al., 2015a, b; Olesnicky Killian et al., 2009; Shellard and Mayor, 2016). Other data suggest that the long-range migration of NCM is driven by contact inhibition (Kulesa et al., 2004; Roycroft and Mayor, 2016; Shellard and Mayor, 2016; Theveneau and Mayor, 2012; Trainor et al., 2002). Another mechanism involved in NCM migration is the presence of repulsive signals that are mediated by ephrin/Eph and neuropilin/semaphorin signaling (Gammill et al., 2007; Golding et al., 2000; Minoux and Rijli, 2010). As previously mentioned, the patterning of the jaw including NCM migration is most likely driven by a combination of all three mechanisms – contact inhibition together with chemoattraction and chemo-repulsion.

There is a very specific NCM sub-population, that is responsible for the formation of the craniofacial skeletal system and muscle and connective tissue of the head, extending from mid-diencephalon (fb and mb) down to rhombomere 2 (r2) and rhombomere 4 (r4) and 6 (r6) in an early developing embryo (Figure 11) (Baroffio et al., 1988; Couly et al., 1992; Dupin et al., 2010; Etchevers et al., 1999b; Etchevers et al., 2001; Le Lièvre and Le Douarin, 1975a; Noden, 1978a, 1983a, 1988; Noden and Trainor, 2005).

Patterning of the jaws is carried out using conserved gene regulatory networks and molecular mechanisms that the NCM population uses to establish its positional identity. The basic dorsoventral, proximodistal, and mediolateral layout of the jaws and the underlying patterning mechanisms are very well conserved despite the astonishing array of craniofacial forms present in nature. Differences in jaw size and shape can be achieved by many molecular mechanisms that have been reported in a wide array of studies and may include changes in protein coding sequences, expression domains of ligands and receptors, differences in the timing or levels of gene expression, and the intrinsic cellular sensitivity (i.e., differences in the target cell response)

(Abzhanov and Tabin, 2004; Depew and Compagnucci, 2008; Ealba et al., 2015; Fish et al., 2014; Hanken and Hall, 1993; Mallarino et al., 2011; Schoenebeck et al., 2012).

Interestingly, compared to the anteroposterior patterning of the trunk or proximodistal patterning of the limb that is established by overlapping Hox expression domains, the first pharyngeal arch prominences (frontonasal, maxillary, and mandibular) are Hox-free (Hunt et al., 1991; Hunt and Krumlauf, 1992; Trainor and Krumlauf, 2000, 2001; Wilkinson et al., 1989). The early developmental mechanism regulating NCM together with precisely timed interactions between mesenchyme and epithelium in the developing primordia are responsible for proper jaw patterning. These epithelial-mesenchymal signaling interactions include homeobox family transcription factors such as *Msx*, *Barx*, *Prx*, or *Dlx*. Perturbation to expression of those homeobox genes can result in homeotic transformation and change of identity demonstrating the existence of a family of transcription factors acting as master regulators during craniofacial patterning (Alappat et al., 2003; Beverdam et al., 2002; Depew et al., 1999; Depew et al., 2002; Depew et al., 2005; Jeong et al., 2008; Kuraku et al., 2010) (Liu et al., 1997; Minoux and Rijli, 2010; Qiu et al., 1997; Qiu et al., 1995; Richman and Lee, 2003; Sato et al., 2008; Shigetani et al., 2000; Shigetani et al., 2002; Talbot et al., 2010; Trainor et al., 2002).

The dorsoventral polarity of the jaws is also established by epithelial-mesenchymal signaling interactions. These interactions are triggered by retinoic acid (RA) expression in the frontonasal processes followed by a series of signaling events (including expression of *endothelin-1* and *Fgf8*, signals instrumental in activating *Dlx* genes) involving the surface ectoderm, neuroepithelium, and NCM to establish sonic hedgehog (SHH) expression domain in the forebrain (Lee et al., 2001c; Schneider et al., 2001; Song et al., 2004). NCM respond to SHH expression in the forebrain and communicate the signal to the surface ectoderm. Epithelial-

mesenchymal interactions between the surface ectoderm and NCM further establish the Frontonasal Ectodermal Zone (FEZ), a signaling center in which a FGF8 and SHH signaling domains are precisely separated. RA signaling is responsible for maintaining FGF8 and SHH expression domains present in both the surface ectoderm and the neuroepithelium. Experimental manipulations of the FEZ results in numerous dorsoventral axes formation and production of multiple upper aspects of the jaws (Hu and Marcucio, 2009a, b, 2012; Hu et al., 2003; Parsons et al., 2011; Schneider et al., 2001; Song et al., 2004).

The anteroposterior polarity of the jaw skeleton is established through interactions, mediated by SHH signaling, between the pharyngeal endoderm and NCM. These interactions are also necessary for cartilage induction in the jaw (Brito et al., 2006; Couly et al., 2002a; Helms and Schneider, 2003).

Interventions into the pharyngeal endoderm result in craniofacial malformations. Ablation of small regions of the pharyngeal endoderm prevents the formation of Meckel's cartilage, the angular bone, quadrate bone, the nasal capsule, as well as elements of the upper jaw. Rotation of the pharyngeal endoderm results in ectopic reoriented cartilaginous elements. Moreover, manipulation by inhibition into BMP signaling and simultaneous exogenous RA source results in ectopic egg tooth formation. Furthermore, grafting fibroblasts expressing SHH into an early embryo (5-8 somite stage) result in caudolateral lower jaw duplication. The ectopic source of SHH in caudal ectoderm mimics oral epithelial expression which leads to formation of an extra organizing center and the induction of mirror-image supernumerary lower jaws. These and many other experiments together underline that the epithelium plays an essential role in the establishment of jaw patterning during development (Abzhanov and Tabin, 2004; Ahlgren and Bronner-Fraser, 1999; Ahlgren et al., 2002; Brito et al., 2008; Chong et al., 2012; Hu et al., 2015a;

Lee et al., 2001a; Richman and Lee, 2003; Schneider et al., 2001; Sheehan-Rooney et al., 2013).

Besides contributing to establishing three main head tissues (i.e., bone, cartilage, and tendon), the NCM is responsible for the species-specific development of the jaws. Its ability to dictate species-specific information on size and shape has been shown primarily through tissue transplant experiments between many vertebrate species including birds, mice, frogs, and salamanders. These interspecific grafting experiments of the neural fold containing pre-migratory NCM have revealed the cell-autonomous character of the jaw morphogenic program (Andres, 1949; Lwigale and Schneider, 2008; Mitsiadis et al., 2006; Mitsiadis et al., 2003; Noden and Schneider, 2006b; Schneider and Helms, 2003; Tucker and Lumsden, 2004; Wagner, 1959). In addition, chimeric transplant experiments enabled the discovery of molecular mechanisms involved in jaw patterning and characterization of NCM mediated gene expression as well as its capacity to dictate the timing of gene expression in the adjacent epithelium (Ealba et al., 2015; Eames and Schneider, 2005; Fish and Schneider, 2014b; Hall et al., 2014; Merrill et al., 2008; Schneider, 2005; Schneider and Helms, 2003; Solem et al., 2011; Tokita and Schneider, 2009). Furthermore, interspecific together with intraspecific tissue transplants revealed the osteogenic character of the NCM and not its adjacent epithelium. Proper jawbone development is dependent on numerous unidirectional and bidirectional signaling interactions. Those interactions are NCM-mediated and precisely timed (Fish and Schneider, 2014b; Griffin et al., 2013; Hall, 1981; Merrill et al., 2008; Tyler and Hall, 1977). Craniofacial muscle patterning (muscle origins and insertions) is also governed by the NCM (i.e., NCM-derived tendon and connective tissues) despite their prechordal and unsegmented cranial paraxial mesoderm origins (Diogo et al., 2015; Evans and Noden, 2006; Grenier et al., 2009; Lescroart et al., 2015; Noden, 1983a, b; Noden and Francis-West, 2006; Noden et al.,

1999; Noden and Trainor, 2005; Olsson et al., 2001; Rinon et al., 2007; Sadaghiani and Thiebaud, 1987; Sambasivan et al., 2011; Solem et al., 2011; Tokita and Schneider, 2009; Trainor and Tam, 1995; Trainor et al., 1994).

The establishment of proper jaw size and shape is crucial to maintaining structural as well as functional identity of the jaw complex. Thanks to a combination of experimental embryology and classical comparative methods, many of the underlying molecular mechanisms responsible for subtle species-specific size and shape changes to the chondrogenic and skeletogenic elements of the craniofacial structures have been examined and characterized.

Those studies have revealed that multiple signaling pathway are involved in modulating jaw properties (i.e., width, depth, and length) by the establishment of species-specific gene expression patterns. BMP signaling has been shown to affect the depth and width, while calmodulin-dependent pathway seems to manage upper jaw length, and TGF β and WNT signaling have been implicated in the size and shape regulation of the upper jaw. Additionally, factors such as SHH or FGF appear to be associated with the species-specific shape and outgrowth of the jaw skeleton (Abzhanov et al., 2006; Abzhanov et al., 2004; Abzhanov and Tabin, 2004; Ashique et al., 2002a; Bhullar et al., 2015b; Brugmann et al., 2007; Brugmann et al., 2010; Doufexi and Mina, 2008; Fish et al., 2011; Foppiano et al., 2007; Grant et al., 2006; Havens et al., 2008; Hu and Marcucio, 2009b, 2012; Hu et al., 2015a; Hu et al., 2015b; Lamichhaney et al., 2015; MacDonald et al., 2004; Mallarino et al., 2011; Mina et al., 2002; Richman et al., 1997; Rowe et al., 1992; Schneider, 2007; Schneider et al., 1999; Schneider et al., 2001; Szabo-Rogers et al., 2008; Wu et al., 2006; Wu et al., 2004; Young et al., 2010; Young et al., 2014).

Sonic Hedgehog Signaling

The *hedgehog* (HH) gene was first discovered by genetic screens in *Drosophila melanogaster*. It obtained its name based on the appearance of embryos with null alleles of *hh*, in which denticles were similar to hedgehog spines. Its molecular characterization, as a secreted molecule, happened 12 year later and revealed its ability to induce patterning. Moreover, it's mammalian homologs, *sonic hedgehog*, *Indian hedgehog*, and *desert hedgehog*, were discovered together with their essential role in body organization during development (Chang et al., 1994; Echelard et al., 1993; Hu and Marcucio, 2009a; Ingham and McMahon, 2001; Krauss et al., 1993; Nusslein-Volhard and Wieschaus, 1980; Riddle et al., 1993; Roelink et al., 1994). Normal embryonic development is dependent on the evolutionarily conserved SHH signaling pathway. Moreover, SHH signaling is vital for adult tissue homeostasis, renewal, and regeneration (Briscoe and Thérond, 2013).

As previously described, SHH is a key secreted molecule implicated in the induction of skeletal patterning in the head from several signaling centers (prechordal plate, forebrain, as well as the pharyngeal endoderm). SHH acts in a concentration- and time-dependent manner to initiate cellular responses, ranging from proliferation and survival to differentiation and cell fate specification, necessary for proper tissue patterning through target gene transcription. Deregulation of *Shh* expression leads to severe disruption of proper craniofacial patterning during development (Ahlgren and Bronner-Fraser, 1999; Ahlgren et al., 2002; Billmyre and Klingensmith, 2015; Briscoe and Thérond, 2013; Brito et al., 2006; Chiang et al., 1996; Chong et al., 2012; Jeong et al., 2004; Xu et al., 2015).

During lower jaw development, *Shh* is expressed in the oropharyngeal endoderm (i.e.,

epithelium). SHH is synthesized as a precursor protein which undergoes autocatalytic cleavage, cholesterol modification at the carboxy terminus, and palmitoylation at the amino terminus prior to being released from the cell surface through the combined actions of Dispatched and Scube2. SHH is trafficked through the tissue (i.e., diffused) by interacting with cell surface proteins such as low-density lipoprotein receptor-related protein 2 (LRP2) and Glypican family of heparan sulfate proteoglycans (GPC1-6). SHH initiates mesenchymal cell responses through binding to the canonical receptor Patched (PTCH1) and the co-receptors cell adhesion molecule-related/downregulated by oncogenes (CDON) and brother of CDON (BOC), as well as growth arrest-specific 1 (GAS1) (Figure 12). SHH binding to its receptor PTCH1 results in de-repression of Smoothened (SMO) followed by SMO accumulation in cilia and phosphorylation of its cytoplasmic tail. Downstream signal transduction is mediated by SMO through transcriptional factors, the GLI proteins (known as Cubitus interruptus in *D. melanogaster*). Activation of SMO results in an increase GLI-SUFU dwell time in the cilia. The GLI-SUFU complex is dissociated within the cilia and GLI-activator proteins trafficked through cilia to the nucleus. This process is dependent in part on the kinesin-family protein 7 (KIF7) molecule and enables the GLI protein bypass proteolytic processing which ultimately leads to the activation of target gene transcription. In the absence of SHH and inhibition of SMO by PTCH1, GLI proteins traffic through cilia where they are sequestered by SUFU and KIF7. Subsequently, they are phosphorylated by protein kinase A (PKA), glycogen synthase kinase 3 β (GSK3 β), and casein kinase I (CKI). Thereafter, GLIs are processed into transcriptional repressors (GLI2R and GLI3R) or targeted by E3 ubiquitin ligase β -TrCP for degradation (Figure 2) (Allen et al., 2011; Allen et al., 2007; Atwood et al., 2013; Beachy et al., 2010; Carballo et al., 2018; Choudhry et al., 2014; Izzi et al., 2011; Kaesler et al., 2000; McLellan et al., 2008; Nusslein-

Volhard and Wieschaus, 1980; Shimeld et al., 2007; Tenzen et al., 2006; Wilson and Chuang, 2010; Xavier et al., 2016). GLI2 and GLI3 are bifunctional transcription factors (i.e., can activate or inhibit transcription) and their regulation through cytoplasmic processing together with nuclear translocation are key to the SHH signaling cascade. GLI1 has diverged from GLI2 and GLI3 and lacks a transcriptional repressor domain, thus, it possesses only transcriptional activator functions. The GLI proteins belong to the C2H2-type zinc finger (ZF) subclass of the GLI-Kruppel family (i.e., subclass characterized by the presence of ZF motif in their DNA that enables binding to 5'-GACCACCCA-3' consensus sequence). For all three (i.e., GLI1, 2, and 3) the protein structure characteristics are similar, a highly conserved ZF motif centrally located, a shorter N-terminal domain, and a longer C-terminal domain. The latter two are extensively modified during post-transcriptional processing which result in a specific trafficking through the cell and ultimately a specific response to the input signal (i.e., SHH) (Kinzler et al., 1988; Kinzler and Vogelstein, 1990; Sasaki et al., 1999).

Research over the past 20 years has revealed many diverse mechanisms and functions through which the SHH pathway acts during development. The ligand and core pathway unit identification across many species throughout branches of the bilaterian family underline its significance and deep evolutionary origin. One of the best-studied functions of the SHH pathway during development is its tissue polarizing activity in the limb bud and in neural progenitor patterning, in which the six different cell types are established due to the SHH gradient (Briscoe and Ericson, 2001; Cohn and Tickle, 1996; Dessaud et al., 2008; Jessell, 2000). It has also been reported that neural tube patterning is scaled to size in different embryos to reflect the scaling that is necessary to achieve proper tissue size establishment during development (Uygur et al., 2016).

Furthermore, SHH binding to its co-receptors, CDON, BOC, and GAS1 had been studied more deeply and has revealed very important mechanisms through which the SHH pathway promotes signal transduction (i.e., cell behavior such as cell survival or proliferation) during embryogenesis has been characterized (Allen et al., 2011; Allen et al., 2007; Cole and Krauss, 2003; Izzi et al., 2011; Martinelli and Fan, 2007; Tenzen et al., 2006). For example, SHH binding to the CDON co-receptor appears to be a mechanism by which SHH signaling promotes cell survival (Delloye-Bourgeois et al., 2014). GAS1 appears to act cooperatively with PTCH1 in order to transform the SHH concentration gradient into its morphogenic activity gradient. These findings incite the idea that GAS1 may coordinate cell proliferation and differentiation which can directly impact how biological patterns are created during development (Martinelli and Fan, 2007). Furthermore, the ligand-binding component of BOC, CDON, and GAS1 is required for SHH-mediated cell proliferation (Izzi et al., 2011). The important role of these three co-receptors in craniofacial development has been demonstrated in many studies. The simultaneous genetic removal of all three co-receptors (i.e., *Cdon*, *Boc*, and *Gas1*) results in alobar holoprosencephaly. In the context of other holoprosencephaly gene mutations, *Boc* has been shown to act as a holoprosencephaly modifier affecting the severity of the phenotype and contributing to the phenotypic differences that can be observed in different genetic backgrounds. Additionally, human holoprosencephaly patients have been diagnosed with mutations in these SHH co-receptors genes (Allen et al., 2011; Bae et al., 2011; Cole and Krauss, 2003; Echevarría-Andino and Allen, 2020; Hong and Krauss, 2018; Hong et al., 2017; Ribeiro et al., 2010; Seppala et al., 2007; Seppala et al., 2014; Xavier et al., 2016; Zhang et al., 2011; Zhang et al., 2006).

Despite the advances made to understand many components of the pathway, there are still

gaps in our knowledge of SHH signaling. Addressing unanswered questions about the SHH pathway is crucial for understanding its full developmental and evolutionary potential that might give much needed insight for developing therapeutic strategies to target medical conditions caused by its dysregulation.

Quail-Duck Chimeras

Research using avians as model organisms has been especially important in identifying mechanisms and factors that affect skeletal size and shape. In particular, exceptional variability in size and shape is apparent in bird beak development. Studies have shown that differential domains of *Bmp4* in beak progenitor cells account for variation in beak shape (i.e., width and depth) among birds. Additionally, a calmodulin-dependent pathway governs beak length. The shape and outgrowth of the beak skeleton is suggested to be dependent on signaling factors, including SHH, FGFs, BMPs, and WNTs, that are secreted from the epithelial tissue (Abzhanov et al., 2006; Abzhanov et al., 2004; Abzhanov and Tabin, 2004; Ashique et al., 2002a, b; Bhullar et al., 2015a; Brugmann et al., 2007; Brugmann et al., 2010; Doufexi and Mina, 2008; Fish and Schneider, 2014b; Foppiano et al., 2007; Grant et al., 2006; Havens et al., 2008; Helms and Schneider, 2003; Hu and Marcucio, 2009a, 2012; Hu et al., 2015a; Hu et al., 2015b; MacDonald et al., 2004; Mina et al., 2002; Richman et al., 1997; Rowe et al., 1992; Schneider, 2005, 2007, 2015; Schneider et al., 1999; Schneider et al., 2001; Shen et al., 1997; Szabo-Rogers et al., 2008; Woronowicz et al., 2018; Woronowicz and Schneider, 2019; Wu et al., 2006; Wu et al., 2004; Young et al., 2014).

Scientists have taken on the advantage of avian embryo accessibility and through chimeric transplantation gained more insight into molecular and cellular mechanisms responsible for

development of the unique (i.e., species-specific) morphological and/or behavioral features of the craniofacial structures. We use the chimeric system to exploit the molecular mechanisms underlying the species-specific development of the jaws between Japanese quail (*Coturnix coturnix japonica*) and white Pekin duck (*Anas platyrhynchos*) (Figure 13) (Ealba and Schneider, 2013; Fish and Schneider, 2014b; Fish and Schneider, 2014c; Jheon and Schneider, 2009; Lwigale and Schneider, 2008; Schneider, 2005, 2007, 2015, 2018b; Schneider and Helms, 2003).

Quail-duck chimeric transplants exploit inherent differences in developmental rate (Figure 13A), and show that a cell-autonomous, NCM mediated developmental program, dictates the timing of epithelial-mesenchymal signaling. Unilateral NCM transplants enable the comparison of donor- and host-derived tissues within the same embryo (Eames and Schneider, 2005, 2008; Fish and Schneider, 2014a, b; Fish and Schneider, 2014c; Fish et al., 2014; Lwigale and Schneider, 2008; Solem et al., 2011; Tokita and Schneider, 2009; Tucker and Lumsden, 2004; Woronowicz et al., 2018). The quail-duck chimeric system is very powerful in determining the NCM-mediated gene expression throughout craniofacial development. A major advantage lies in the difference in their developmental rate, for quail 17 versus duck 28 days from fertilization to hatching. The asynchronous development of the two (i.e., duck and quail) cell populations provides a way to screen donor versus host (i.e., species-specific) gene expression levels, tissue patterning, cell differentiation, growth rate, as well as the timing of developmental events (Figure 13B, 13C) (Fish and Schneider, 2014a; Fish et al., 2014; Hall et al., 2014; Lwigale and Schneider, 2008; Schneider, 1999, 2018a). For example, a unilateral NCM transplant from quail, which hatch in 17 days, to duck, which hatch in 28 days, shows that precocial bone forms in the mandibular mesenchyme on the quail (i.e., donor) side a full three developmental stages earlier than on the contralateral duck (i.e., host) side (Merrill et al., 2008).

Such chimeric transplant systems shed light on the timing of bidirectional signaling events and underscore the dominant role of the NCM in dictating the timing of developmental processes like intramembranous ossification.

The ability of NCM to govern the levels, spatial pattern, as well as the timing of gene expression in a species-specific way likely regulates the proliferation, differentiation, and growth of jaw skeletal progenitors which ultimately establishes the size and shape of the cartilage and bone.

Jaw Size and Shape – Early Developmental Mechanisms

The development of species-specific jaw morphology begins with the genesis of NCM. The developmental mechanisms that control morphogenetic events (i.e., NCM induction, specification, regionalization, cell division while maintaining pluripotency, delamination, and migration to elected sites) are highly conserved across vertebrates (Betancur et al., 2010; Bronner-Fraser, 2008; Couly et al., 1993a; Depew and Olsson, 2008; Köntges and Lumsden, 1996; Le Lièvre and Le Douarin, 1975a; Nikitina et al., 2008; Noden, 1978b; Northcutt, 2005; Schneider et al., 2001). However, there is still the unanswered question, when, where, and through what mechanisms in early embryo development are species-specific differences established?

It has been previously shown that duck have about 15 % more NCM at the midbrain/hindbrain region from which NC cells migrate into the mandibular arch to give rise to the jaw. By HH20, the slightly larger progenitor cell population in duck becomes two-fold difference in cell number in the mandibular arch of duck compared to quail. The difference in mandibular mesenchyme population size could be explained by taking into account that duck and quail have different (i.e., species-specific) cell cycle length (13.5 versus 11 hours) together with

absolute time (i.e., time each species need to reach specific stage). The results show that duck NCM cells are proliferating relatively more than those of quail. NCM maintains its intrinsic species-specific rate of maturation that enables the deployment of cellular mechanisms that ultimately reflect the species-specific difference in jaw size between duck and quail (Fish and Schneider, 2014b; Fish et al., 2014; Schneider, 2015, 2018a).

The coordination of cell proliferation together with cell migration is crucial in development. The NCM exhibits internal patterns of proliferation and migration that are species-specific and have a memory effect (i.e., intrinsic mechanisms are maintain in chimeras). It is known that *Shh* deregulation results in atypical mandible size and that manipulation of the SHH pathway can directly affect cell proliferation. Therefore, understanding whether there are species-specific differences in SHH signaling that might be related to jaw size is crucial to determine its potential to modulate jaw size during development, disease, and evolution.

Figures

Figure 1: Embryology theory of Ernst Haeckel. Ontogeny recapitulates phylogeny (i.e., recapitulation theory), adult evolutionary stages of "simpler" forms (i.e., animal species), here fish, frog, and bird, are recapitulated during developmental stages of more complex species (i.e., pig).

Haeckel's law of recapitulation

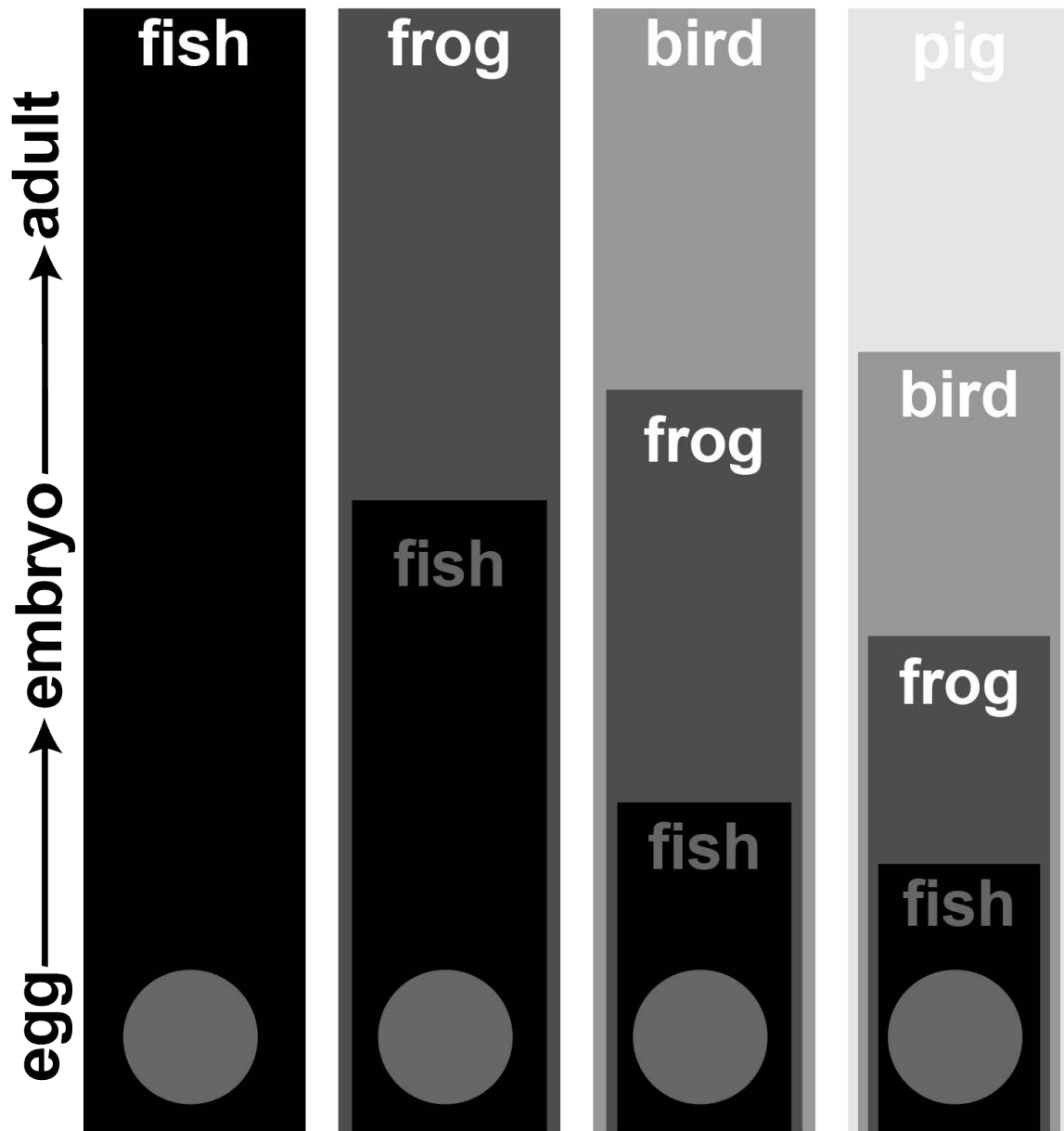


Figure 2: Form and growth in Cartesian coordinates systems. D'Arcy Wentworth Thompson's comparative illustrations of cranial ontogenetic shape changes (Figures 404 to 407 re-drawn from (Thompson, 1917)). **(A)** Cartesian coordinates of a human skull. **(B)** Network of Cartesian coordinates of a chimpanzee's skull as a projection of coordinates in **(A)**. **(C)** Chimpanzee's skull with corresponding Cartesian coordinates from **(B)**. **(D)** Transformation of the Cartesian coordinates in **(A)** for a skull of baboon. Same order of transformation is used to transform coordinates from **(A)** to **(C)** and **(D)** with the only variability being increased intensity or degree of deformation.

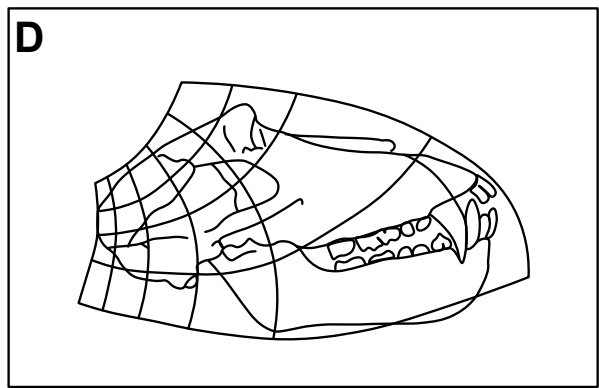
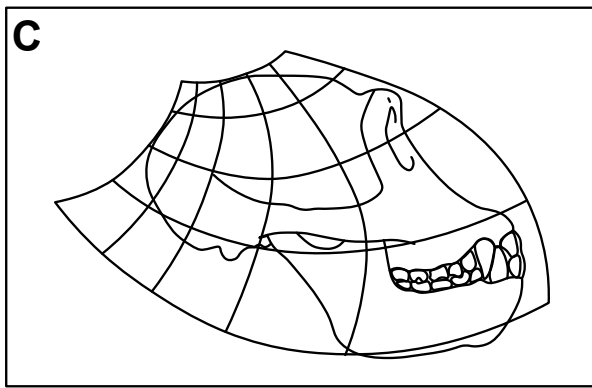
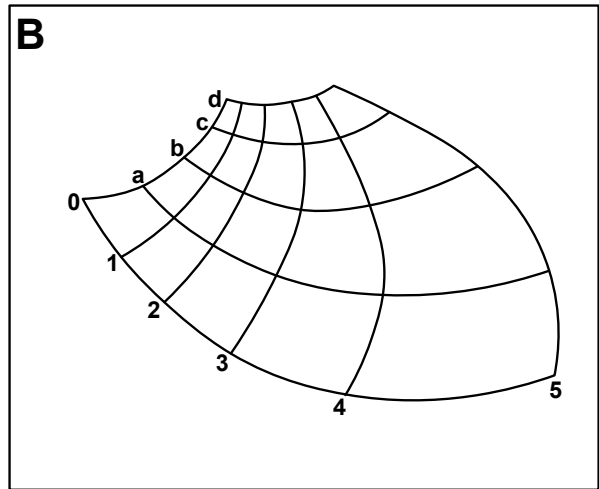
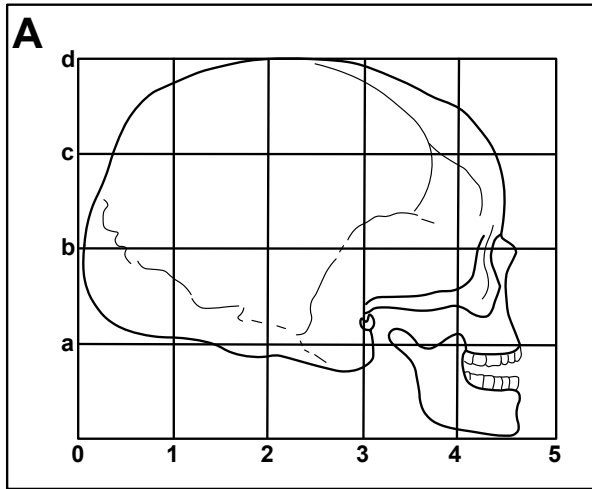


Figure 3: Eight categories of heterochrony (Figure 2 from (de Beer, 1940)). Each graph represents a diagram of the relations of ontogeny (from bottom to top) and phylogeny (i.e., ancestor-descendant sequence; from left to right). The vertical lines represent successive ontogenies and thick black lines denote an evolutionary novelty. Actual modes of heterochrony (retardation, neoteny, hypermorphosis, and acceleration), as described by Gould (Gould, 1977), are highlighted in gray.

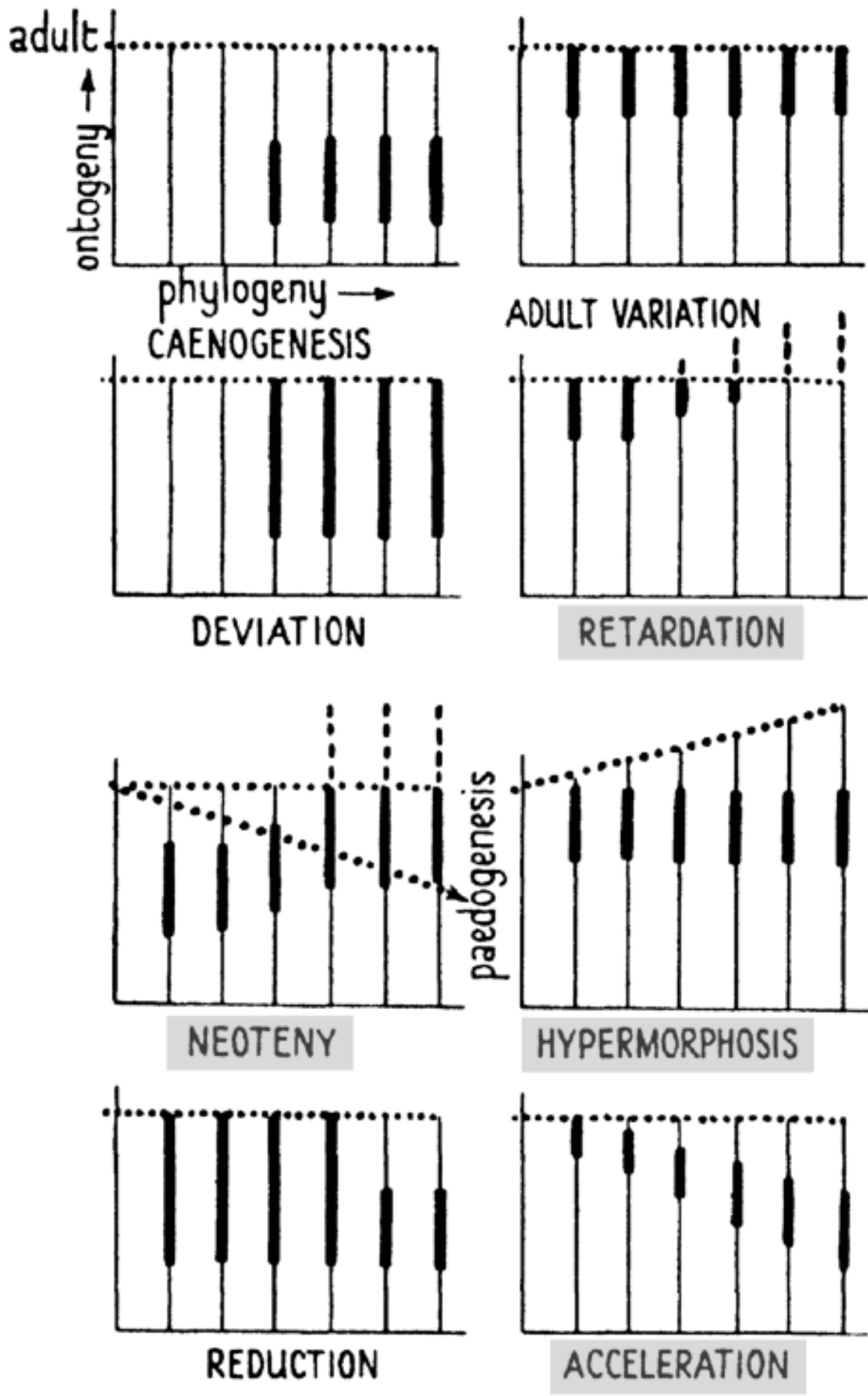


Figure 4: Gould's evolutionary clock model to represent different modes of heterochrony (Figure 33 and 35 re-drawn from (Gould, 1977)). **(A)** Gould's model represented correlations between size, shape, and age during ontogeny and phylogeny. **(B)** Heterochrony domains for the age scale (i.e., accelerated and retarded), the shape scale (i.e., paedomorphic and recapitulatory), and the size scale (i.e., smaller and larger).

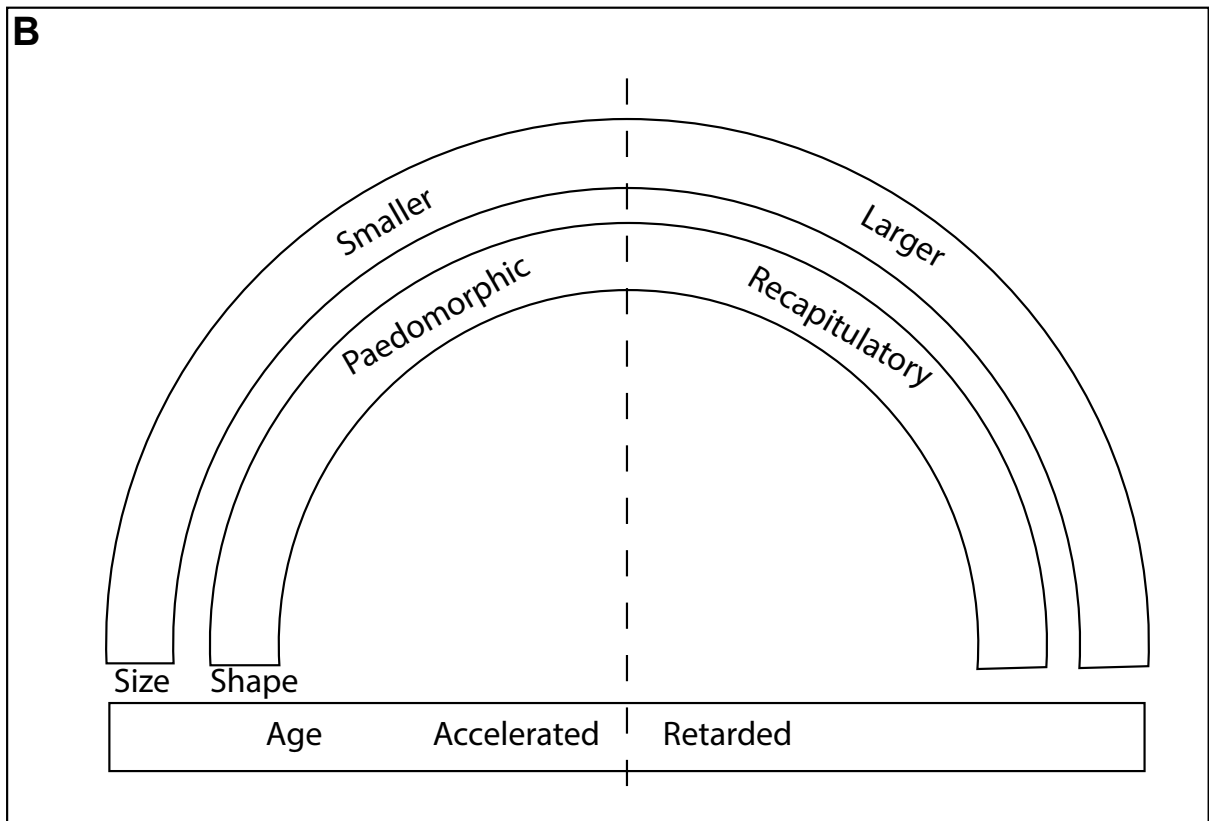
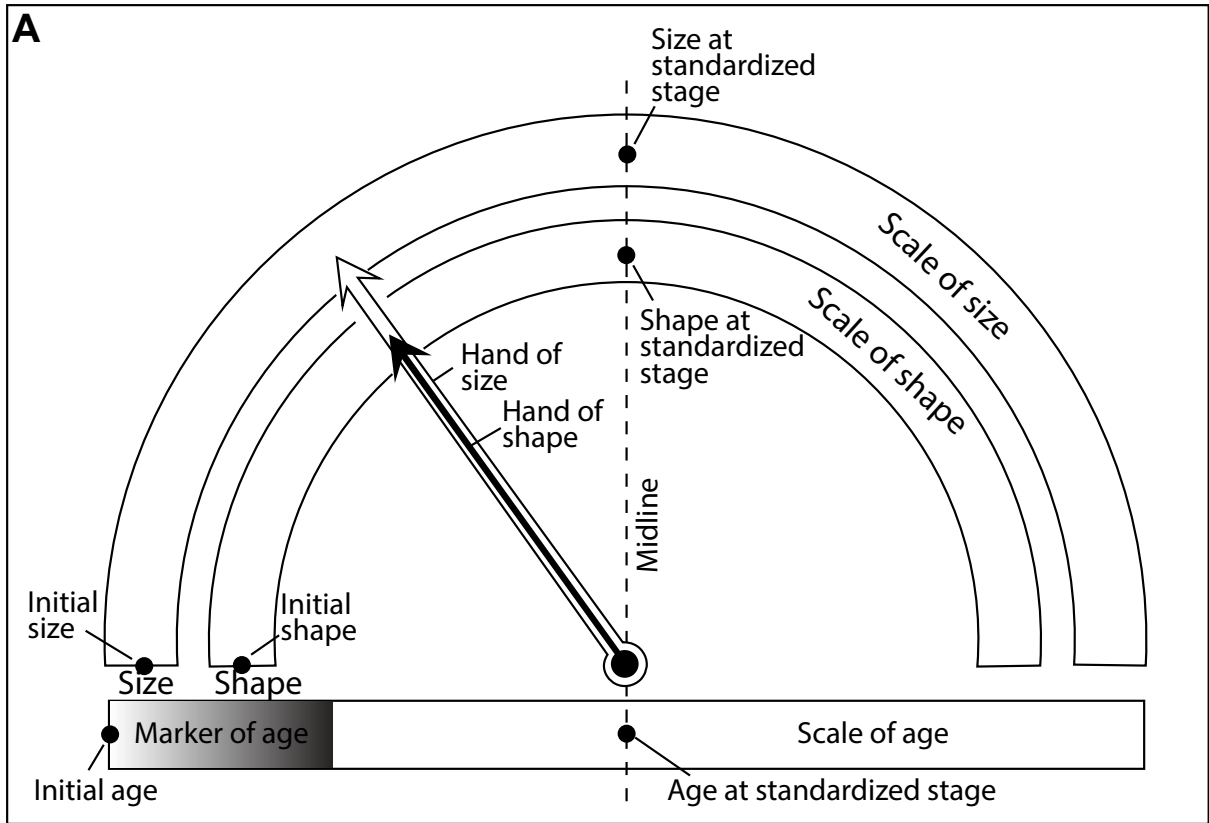


Figure 5: Amphibian egg asymmetry. The egg division (black dashed line) along the plane of first cleavage into two blastomeres (i.e., each blastomere contains half of the gray crescent) results in two normal embryos (**left**). When only one of the blastomeres receives the gray crescent, it alone can undergo normal development and form normal embryo. The second half is arrested in vegetative state (**right**). (Spemann, 1938)

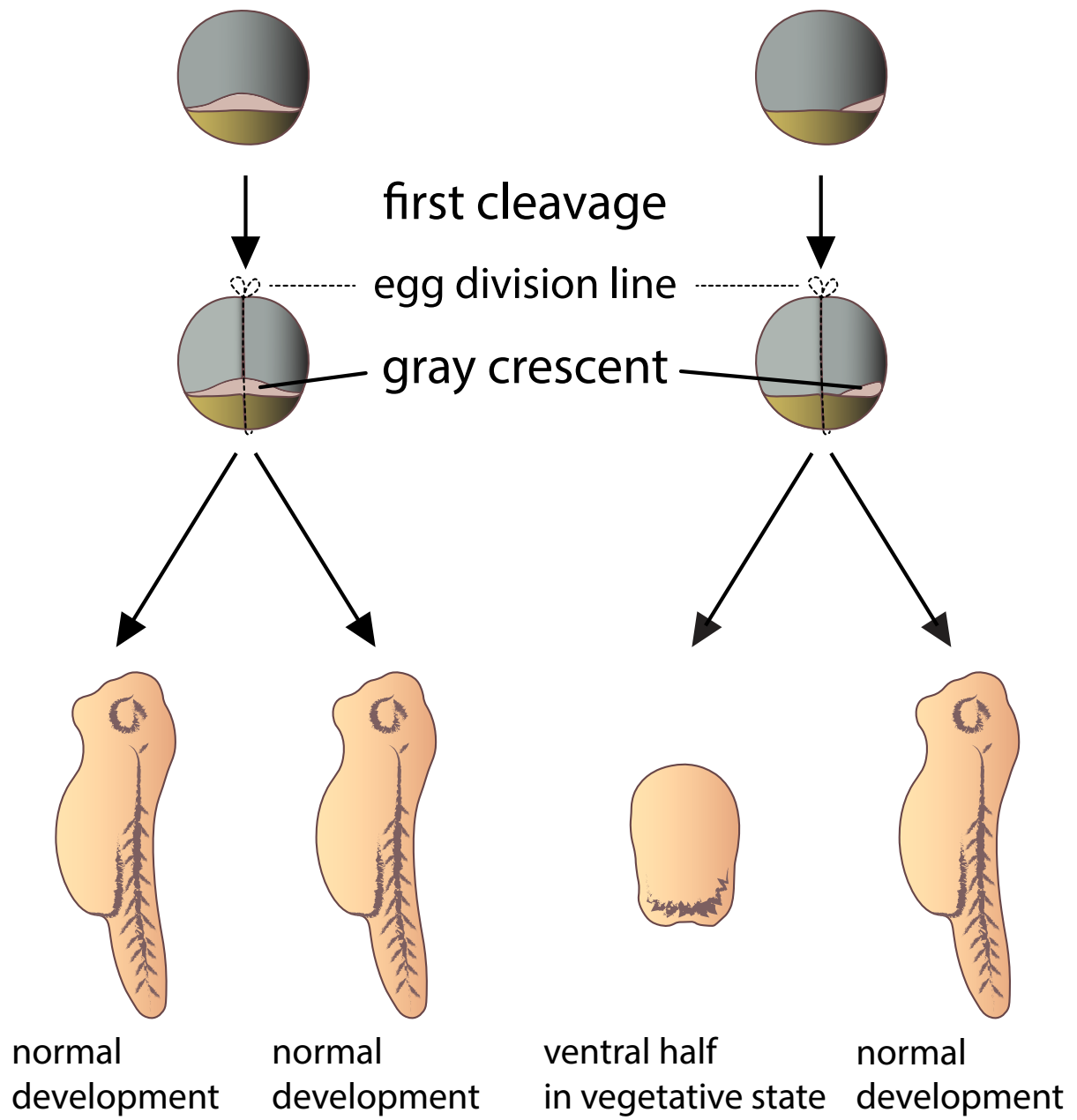


Figure 6: Spemann organizer – induction of a secondary body axis by dorsal blastopore lip tissue transplant. Dorsal lip tissue from early gastrula of an unpigmented donor (light purple) is transplanted into a pigmented host at the same developmental stage. The tissue is transplanted opposite to dorsal lip (i.e., ventral), into a region normally specifying into ventral epidermis. Host (taupe) and donor (purple) cells contributes to the formation of secondary axis (including neural tube, notochord, and somites). Second embryos forms and is joined with the first one forming Siamese twins. (Spemann and Mangold, 1924)

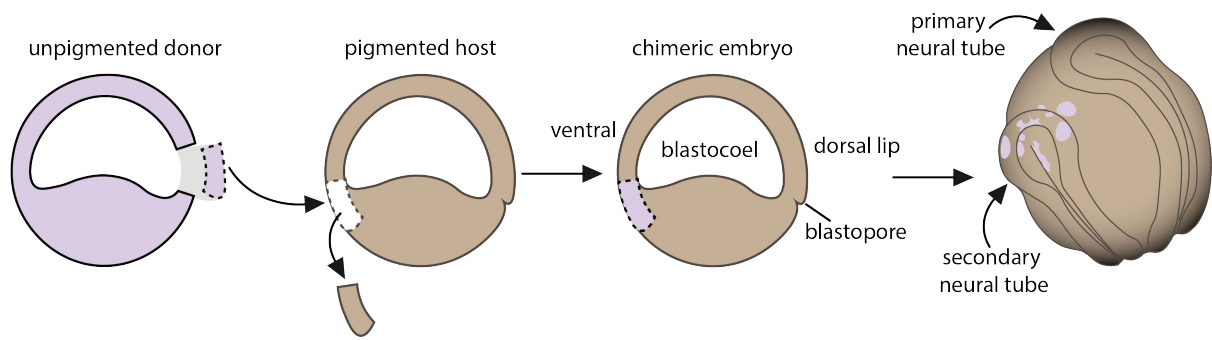


Figure 7: Turing’s “reaction-diffusion” (RD) system in comparison with morphogen gradient. (A) Morphogen gradient is formed by diffusion from a single source (X) (i.e., morphogen producing cells/tissue). Cells respond to its concentration which gives them their positional identity from the source. The gradient and thus cell response and the tissue patterning are very limited and dependent on the morphogen producing cells (i.e., source). **(B)** By adding another morphogen (here Y) that is forming second gradient by diffusion, the complexity of tissue patterning is increased and can become more complex. **(C)** Only by adding interaction between morphogens and with itself (brown and purple arrows), the system becomes self-regulating and highly complex. Based on (Kondo and Miura, 2010; Landge et al., 2020; Meinhardt, 2012; Turing, 1952).

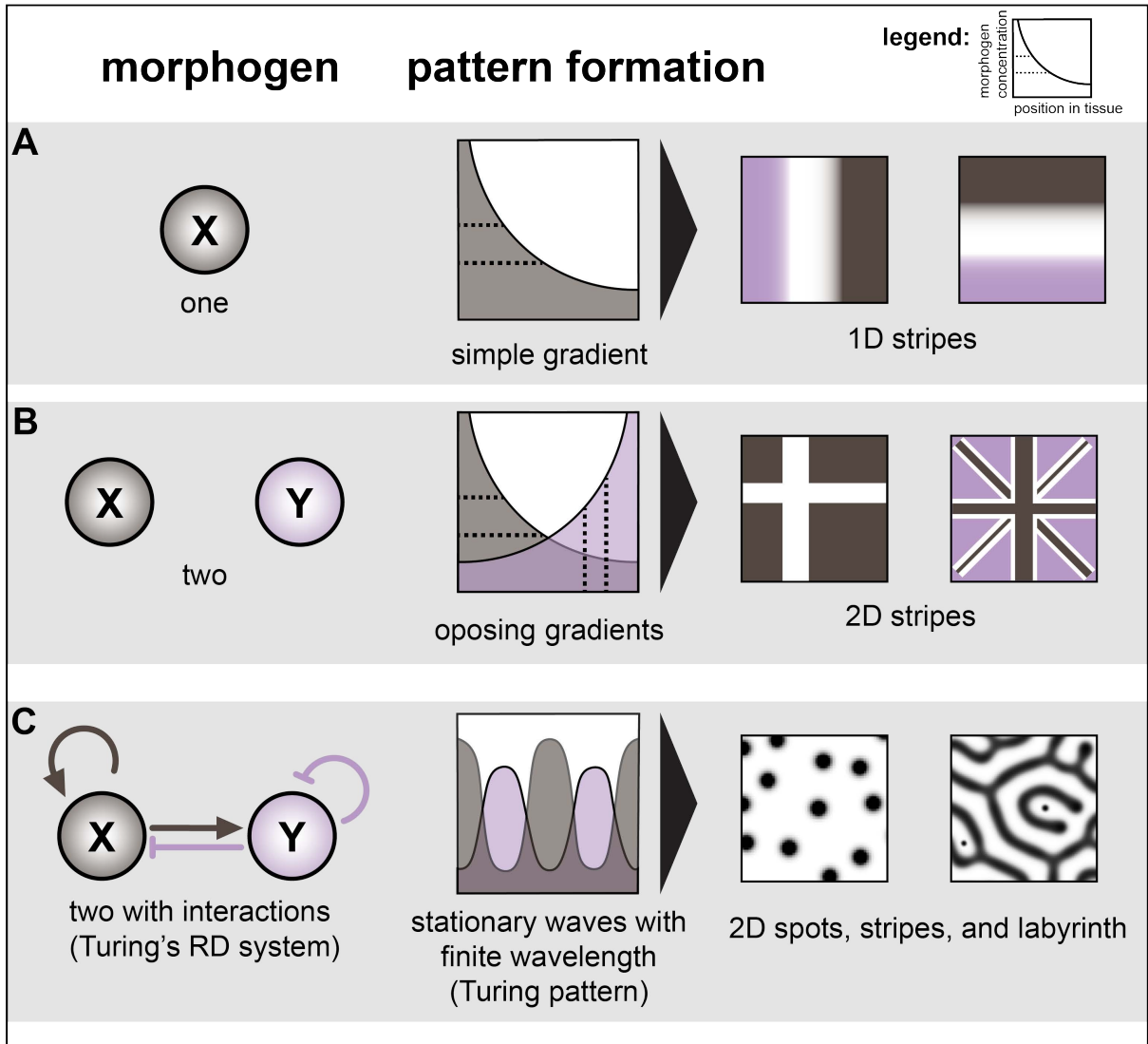


Figure 8: Modules involved in tissue patterning. Patterning mechanisms usually involve interactions at multiple levels: Source, distribution, transport, detection, transduction, and response.

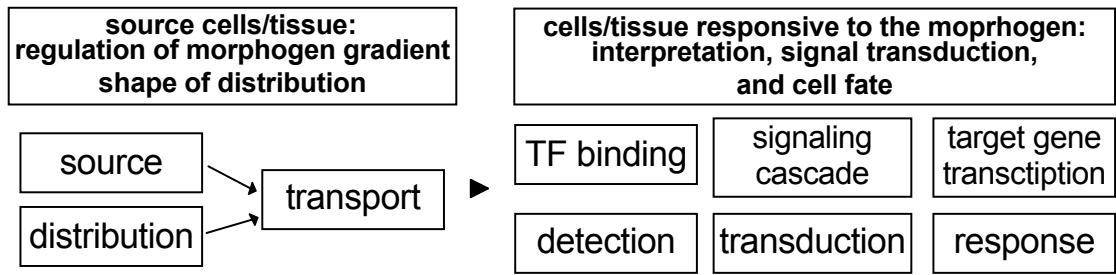


Figure 9: Primary architecture of a generalized vertebrate embryo cranium. The cranium is composed of the neurocranium, dermatocranium, and viscerocranium. The neurocranium protects brain as well as sense organs and first form as cartilage. The viscerocranium is cartilaginous skeleton composed of seven arches (1–7), the mandibular (md), hyoid (hy), and five branchial (ba). The dermatocranium consists of cranial vault, palate bones, and tooth bearing bone elements. Neural crest mesenchyme contributes to the development of all three cranial parts (i.e., neurocranium, dermatocranium, and viscerocranium) whereas mesoderm contributes to development of the neurocranium and dermatocranium. Based on (Kuratani, 2005, 2012)

Primary architecture of generalized vertebrate embryo cranium

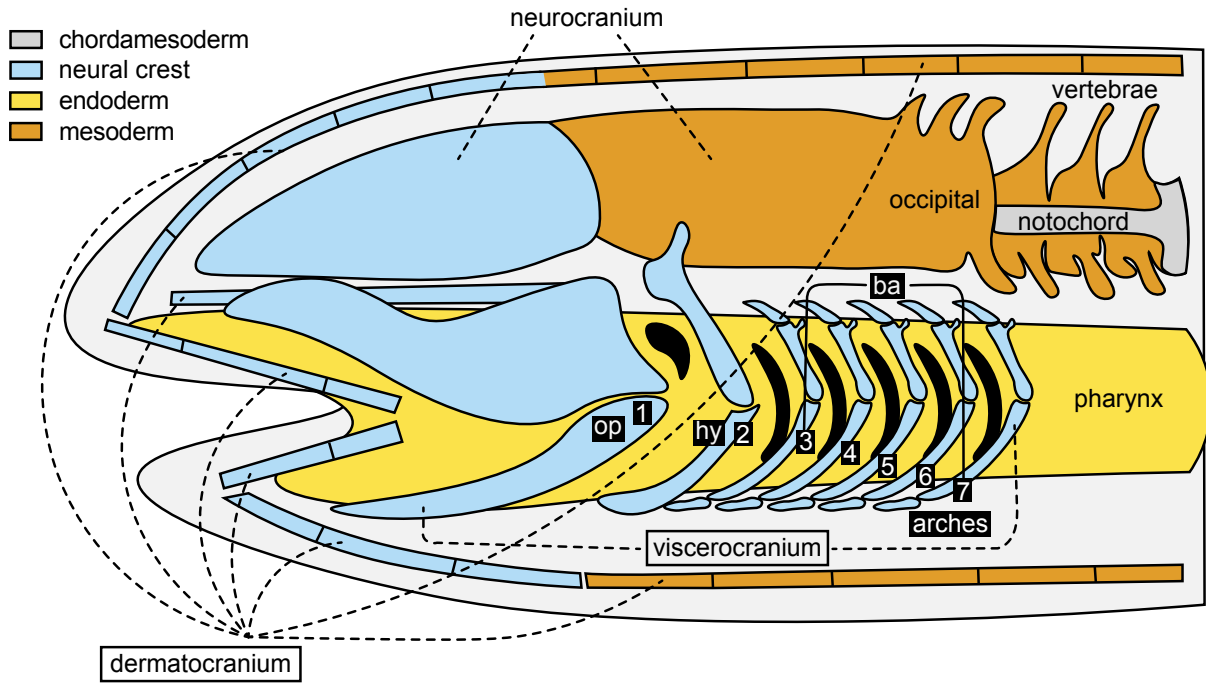


Figure 10: The evolutionary adaptability and cellular origin of vertebrate jaw. The amniote jaw skeleton, especially vertebrate, displays an astonishing array of size, shape, and function. The jaws of different species represent the capacity of adaptation that the tissue responsible for its development can achieve. The amniote jaw skeleton is derived uniquely from neural crest (light blue) while some parts of the skull are derived from mesoderm (orange). **(A)** The functional upper jaw of birds and reptiles (here example of chick) consists of dermal bones that include the premaxilla, maxilla, and palatine. The lower jaw also contains several dermal bones that surround Meckel's cartilage including the splenial, dentary, angular, and surangular. **(B)** In mammals, the upper jaw consists of the same dermal bones (i.e., premaxilla, maxilla, and palatine) as in birds and the lower jaw is extensively reduced to a single bone surrounding Meckel's cartilage, the dentary. Despite the marvelous array of forms and countless adaptation to every conceivable ecological environment, the embryonic origins of the jaw are highly conserved across amniotes. **(C)** Schematic of a generalized amniote embryo in a transverse section plane through the midbrain-hindbrain boundary showing embryonic precursors, cell lineages, cell types, cell-cell interactions (vertical arrows), and tissue derivatives that contribute to the development and formation of functional jaw apparatus. Modified and adapted from (Ealba et al., 2015; Fish and Schneider, 2014a).

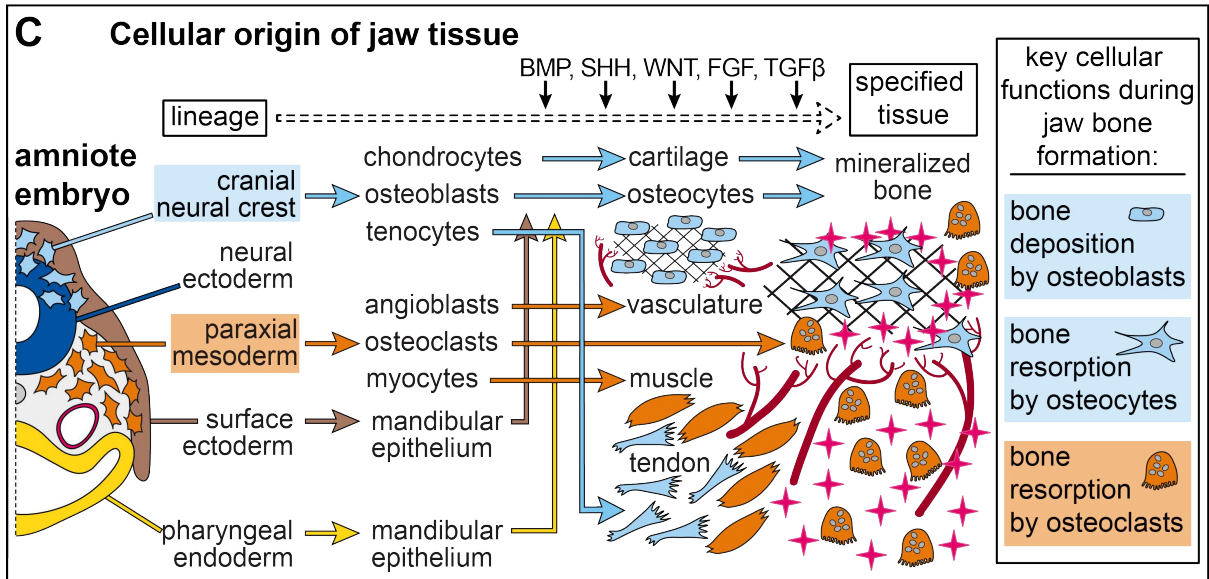
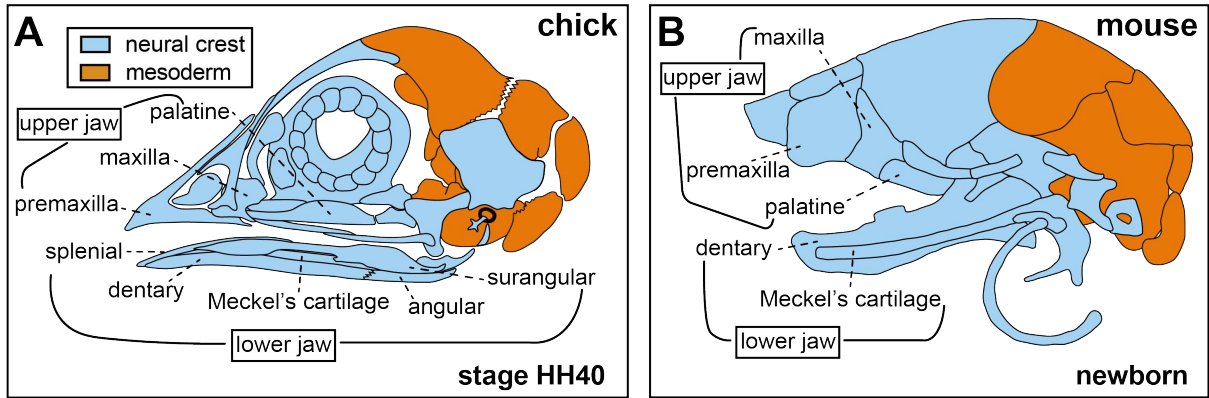


Figure 11: Multiple embryonic populations contribute to the formation of amniote jaw complex. Neural crest mesenchyme (NCM) sub-population is responsible for the formation of the craniofacial skeletal system and muscle and connective tissue of the head. **(A)** Ethidium bromide staining of a quail embryo at embryonic stage (HH) 9.5, dorsal view. **(C)** At HH9.5 (prior to migrating alongside paraxial mesoderm (m; orange)) cranial NCM (light blue) delaminates from mid-diencephalon (i.e., the forebrain (fb) and midbrain (mb)) down to rhombomere 2 (r2) and rhombomere 4 (r4) and 6 (r6). **(B)** Frontal view of a quail embryo at HH25 with visible frontonasal (fn), maxillary (mx), and mandibular (ma) primordia; white line indicates sagittal section plane for **(D)**. **(D)** Different embryonic population contributions are schematized, sagittal view of a HH25 quail embryo where the frontonasal (fn), maxillary (mx), mandibular (ma), and hyoid (hy) primordia are populated by neural crest (light blue) surrounded by surface ectoderm (se; tan), pharyngeal endoderm (pe; yellow), and forebrain neuroepithelium (fb; dark blue). The jaw complex contains contributions from neural crest, nasal placode (np), cranial ganglia (V, VII, IX), and mesoderm (m). Modified and adapted from (Schneider, 1999, 2005; Schneider et al., 2001)

quail

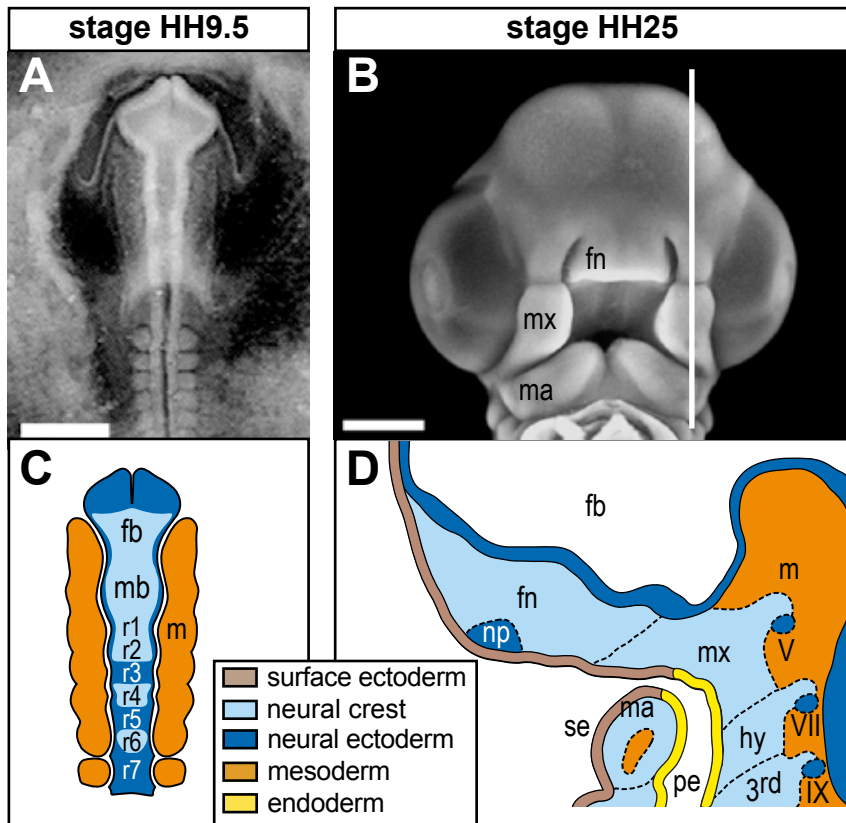


Figure 12: Sonic hedgehog (Shh) signaling cascade. On-state: Shh-induced internalization of Patched 1 (Ptch1) receptor leads to activation of Smoothed (SMO) which results in stabilization and nuclear accumulation of GLI family members. GLI activators bind to GACCACCCA motif to regulate transcription of target genes involved in a variety of processes such as Shh signaling positive feedback, negative feedback, proliferation, self-renewal, survival, and EMT. **Off-state:** PTCH1 internalizes SMO which is followed by GLI family members degradation (GLI1) or cleavage (GLI2 and 3) into repressor form (GLI-R). GLI-R is translocated into the nucleus and target gene transcription is repressed.

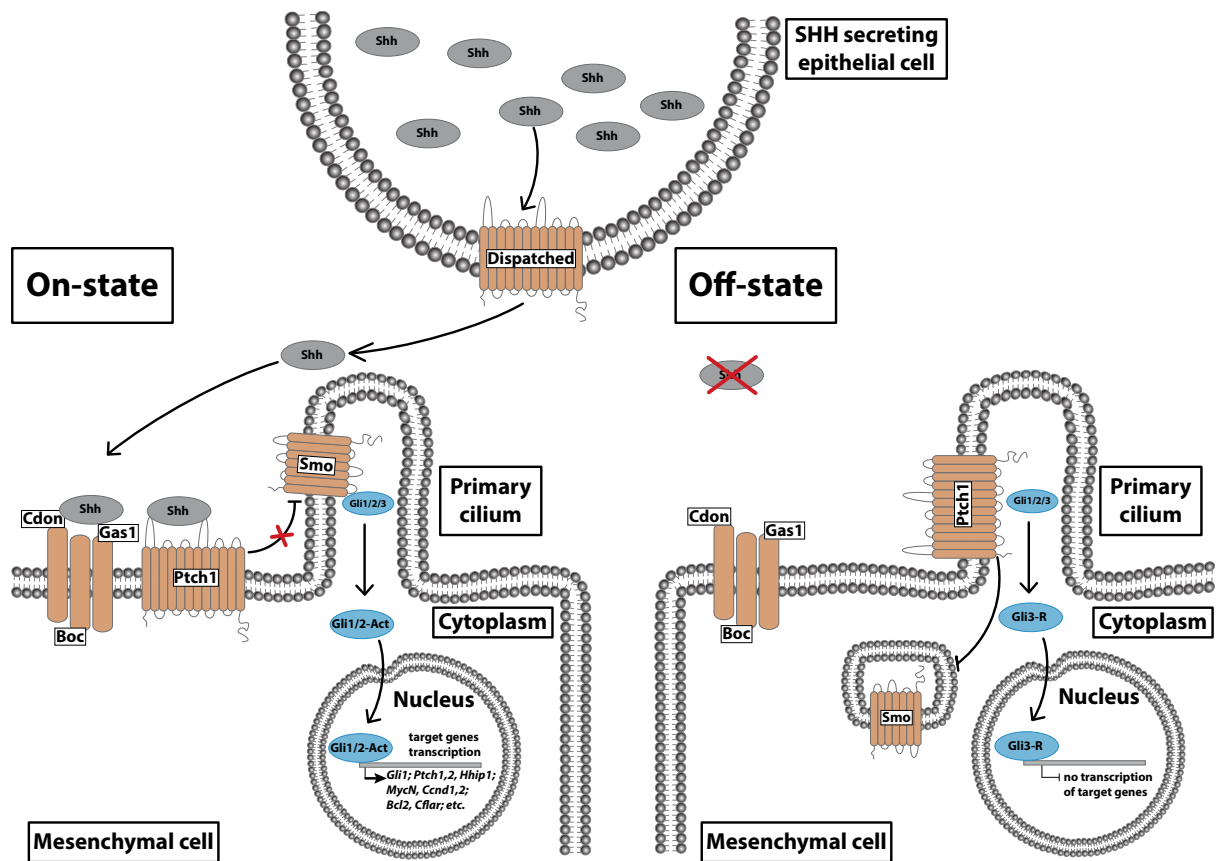
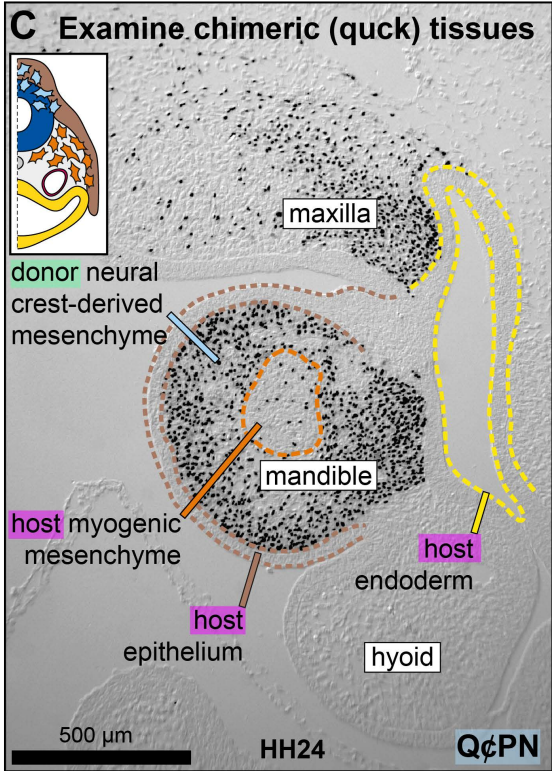
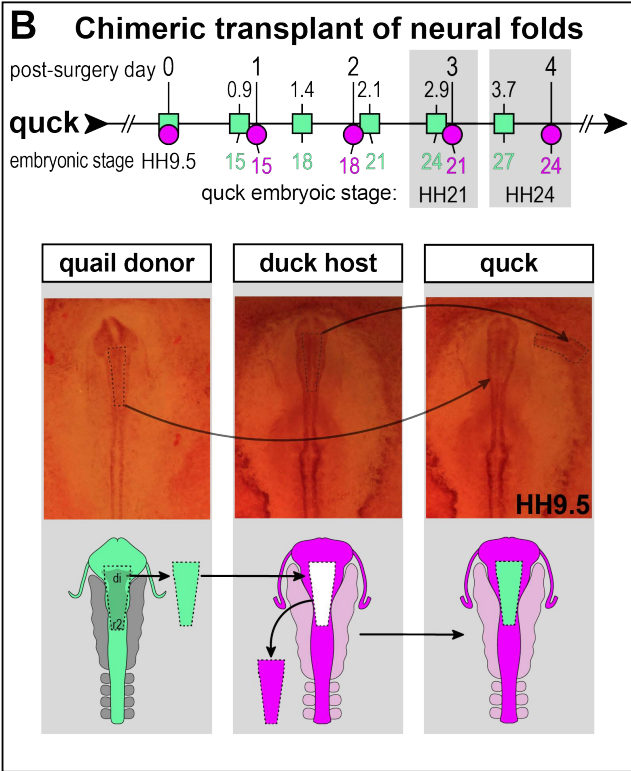
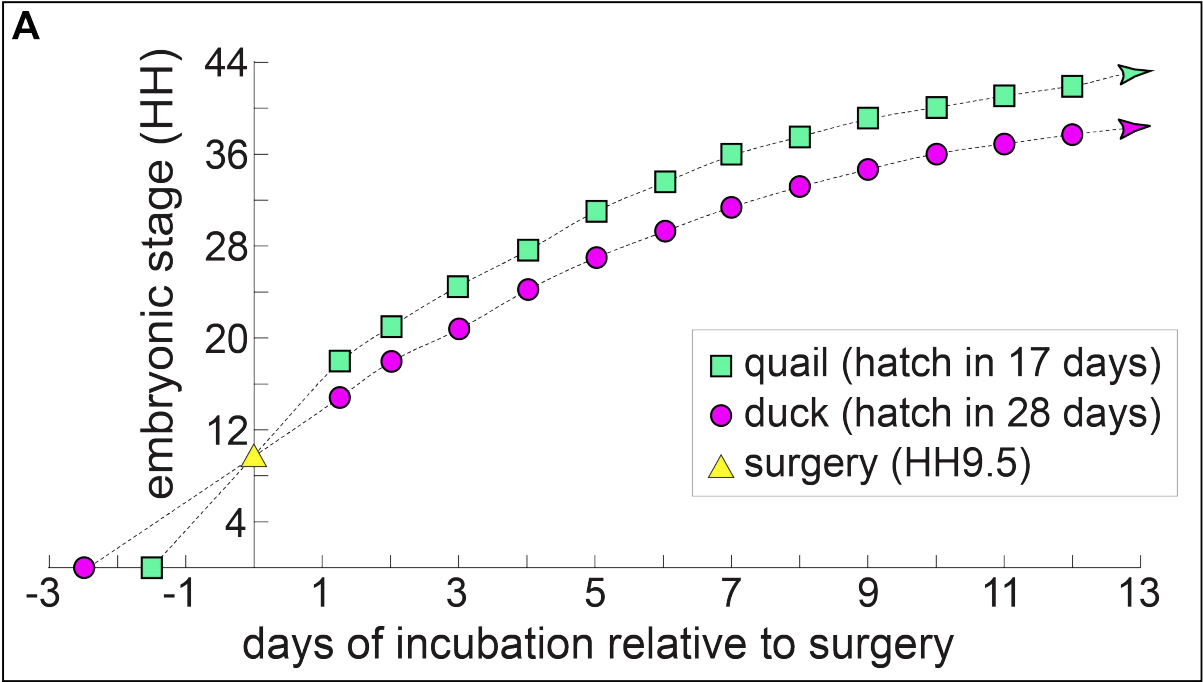


Figure 13: The origins of species-specific jaw patterning. (A) To generate quail-duck chimeras ("quck"), quail (green square) and duck (pink circle) embryos are stage-matched for surgery at HH9.5 (yellow triangle) by incubating their eggs for different times. Donor and host cells subsequently diverge in stage due to their different rates of maturation. **(B)** Quail (i.e., donor) cells remain accelerated by approximately three stages within 2 days after surgery relative to the duck host. Bilateral neural folds, containing presumptive quail neural crest, from mid-diencephalon (di) to rhombomere 2 (r2) of the hindbrain (dark green), are transplanted from quail into a duck host. **(C)** Sagittal section in a chimeric quck through the maxillary (i.e., maxilla) and mandibular (i.e., mandible) region showing quail donor cells stained with Q \dagger PN (black nuclei). Duck-host epithelium (i.e., surface ectoderm, light brown), pharyngeal endoderm (yellow), and myogenic mesenchyme are unlabeled. Although neural-crest mesenchyme origin, the hyoid arch is also negative since its precursors from r4 were not transplanted. Modified and adapted from (Fish and Schneider, 2014b; Noden and Schneider, 2006a; Schneider, 2018b).



Chapter 2: Deciphering the neural crest contribution to cephalic development with avian embryos

(In collaboration with Moussab Alrajeh and Sophie E. Creuzet and published as a book chapter in *Neural Crest Cells Methods and Protocols*. Quentin Schwarz and Sophie Wiszniak (editors))

Introduction

As a multipotent and highly plastic cell population, endowed with strong migratory and regenerative properties, the neural crest is difficult to handle at both cellular and molecular levels. Approaches allowing us to track and observe neural crest cells, to decrypt their fate and interplay with their environment, and to assess their morphogenetic movements are particularly powerful in understanding the biology of this unique structure.

Since the discovery of the neural crest 150 years ago (His, 1868), diverse methods have been devised to track neural crest dispersal and interaction in the developing embryo. However, the approaches based on intrinsic natural markers such as pigment granules, yolk inclusions, or cell size had severe restrictions with limited resolution at single-cell level. These drawbacks compromised the long-term fate mapping of cell lineages and hampered the systematic explorations of developmental processes. Similarly, vital stains were also widely used in an attempt to follow cell behavior during embryonic development. However, these marking techniques suffered from the propensity of vital dyes to diffuse, a drawback that eventually casted doubt on cell tracking accuracy and reliability.

When the quail-chick system came on the scene, much of the current knowledge on the neural crest was gained in lower vertebrates (Hörstadius, 1950). The xeno-association between quail and chick was devised for the dual purpose of exploiting (1) the developmental and morphological similarities between the two species and (2) the structural differences between the nuclei in both species. At cellular level, quail cells harbor a structural singularity, which made their interphasic nuclei easily recognizable after nucleic acid staining. While the latter are tagged by a spot of heterochromatin, densely packed around the nucleolus, chick cells

exhibit an even dispersal of heterochromatin throughout the nucleus, leaving the nucleolus almost indistinguishable.

As soon as the quail-chick system was devised (Le Douarin, 1969), it became manifest that this model could be a critical asset for the comprehensive exploration of neural crest cell contribution to embryogenesis in higher vertebrates. The research community readily espoused this thriving model, so that the evocation of the quail-chick chimeras became closely related to the neural crest. In terms of contribution, the field owes a significant debt to this model. In the head, the cephalic neural crest generates a vast and very plastic mesenchyme, the mesectoderm, which differentiates into connective tissues and chondrogenic and osteogenic cells. The quail-chick system has revealed the wealth of neural crest cell derivatives at cephalic level, their prime skeletogenic role, along with the multi-systemic and synergic contribution of its connective, perivascular, and neural derivatives. The cephalic neural crest forms much of the craniofacial skeleton including the skull, the upper and lower jaws, and hypobranchial skeleton. Aside from skeletal derivatives, the cephalic neural crest also contributes to the elaboration of the facial and cerebral vascular tree: cephalic neural crest cells give rise to the pericytes lining the facial and cerebral capillaries in the forebrain, the adventitial perivascular cells forming the tunicae of aortic arches, as well as the conotruncus, heart septum, and sigmoid valves. Through its cardiac and perivascular derivatives, the cephalic neural crest participates in the homeostasis of the craniofacial structures (Couly et al., 1996; Couly et al., 1993b; D'amico-Martel and Noden, 1983; Etchevers et al., 1999a; Etchevers et al., 2001; Kontges and Lumsden, 1996; Le Lièvre and Le Douarin, 1974; Le Lièvre and Le Douarin, 1975b).

From a developmental standpoint, the cephalic neural crest exerts an essential structural role

in building up skeletal, vascular, and cephalic structures. Altogether, these observations have casted a new light on the evolutionary implications of the cephalic neural crest in the elaboration of an "achordal" skeleton and an innovative vascular circuitry to protect and support the demanding requirement in oxygen of the growing brain. By the way, these investigations have emphasized the paramount role of the neural crest in the emergence of a "new head" over vertebrate evolution (Gans and Northcutt, 1983) and further substantiated the notion that the neural crest can be considered as a fourth germ layer (Hall, 2000b).

With the advent of the molecular era, the chick embryo, which was a fantastic model for lineage studies, was regarded as obsolete due to the lack of relevant approaches to drive transgenesis. However, this model took a new lease of life when the electrical pulse-based transfection, first devised *in vitro*, was astutely designed to allow *in ovo* electroporation (Muramatsu et al., 1997). Thanks to the accessibility of the avian embryo at a range of developmental stages, *in ovo* electroporation can be performed in stage-, space-, and tissue-specific manner with an unparalleled spatiotemporal precision.

By combining the cell tracking technique by xenotransplantation with local transfection using *in ovo* electroporation, our experimental strategy has revealed and documented the so far unperceived role of the cephalic neural crest in brain development and patterning (Creuzet, 2009b). Over the last years, the investigations led by our group have shown that the cephalic neural crest, aside from its structural role in head development, also exerts a potent morphogenetic effect on the brain and sense organs (Creuzet et al., 2004a; Creuzet, 2009a; Creuzet et al., 2006). The absence of cephalic neural crest, responsible for building up the craniofacial skeleton, results in the absence of facial skeleton together with severe defects of mid- and forebrain development leading to anencephaly. Some of the molecular determinant regulators

required to convey this morphogenetic effect have been identified (Aguiar et al., 2014; Cases et al., 2013; Creuzet et al., 2016; Garcez et al., 2014). The results gleaned from this experimental design have demonstrated that the cephalic neural crest regulates early brain patterning and acts as a forebrain organizer. These data support the promising picture that the emergence of the neural crest at the dawn of vertebrate evolution, required for the formation of a “new head” in craniates, has also been critical for the development of a “new brain” (Creuzet, 2009a). These notions provide a novel conceptual framework: they have profound implications in developmental biology. From a biomedical standpoint, these data also suggest that the spectrum of neurocristopathies is broader than expected. In humans, the association of neurological deficiencies with craniofacial defects points to the importance of reciprocal interactions between the cephalic neural crest and the anterior cephalic neuroepithelium. Therefore, demonstrating the functional link between the development of the brain and sophistication of its functions may pave the way for revisiting the aetiology of brain malformations and some neurological disorders, which are multifactorial and polygenic, in the light of cephalic neural crest dysfunctions.

Materials

Manipulation of Fertilized Eggs

1. Freshly laid eggs from chick (*Gallus gallus*, JA57) and quail (*Coturnix japonica*) strains (see Note 1).
2. Self-made chick egg holder (individual and slat) in plexiglass (Figure 14A).
3. Self-made 3D-printed quail holder (Figure 14B).
4. Leica stereomicroscope.
5. Halogen optic illuminator equipped with swan neck lightguides.

6. Incubators equipped with programmable timer switch.

Tools for Microinjection and Microsurgery

1. 230-mm-long Pasteur pipettes to make micro-scalpels.
2. Gas burner.
3. Flexible plastic tub (internal diameter, 0.8 mm; outer diameter, 2.4 mm).
4. Plastic tips.
5. 50 mm-wide transparent adhesive tape.
6. 1 ml syringe.
7. Perpendicularly bent needle (26 G, 0.45 x 12 mm).
8. Forceps (Figure 14C).
9. Curved scissors (Figure 14C).
10. Pascheff's scissors (Figure 14C).
11. Skimmer and transplantation spoon (Figure 14C).

Solutions

1. India ink.
2. Phosphate-buffered saline (PBS) solution supplemented with Penicillin-Streptomycin.
3. 70% ethanol.
4. Solution of exogenous nucleic acids, contrasted with Fast Green FCF for easier injection.

In Ovo Electroporation

1. Square electroporator (i.e., BTX ECM 830).
2. Cables and contact hooks.
3. Self-made club-shaped stainless-steel electrodes.

4. Self-made 3D-printed electrode holder.
5. Manual control micromanipulator with a tilting base.

Methods

Self-Made Micro-Scalpels and Transfer Pipettes for Surgery and Electroporation

1. Adapt micro-scalpel design to each type of tissue manipulation (Conrad et al., 1993; Couly et al., 2002b; Creuzet et al., 2002b; Douarin et al., 2008; Ruhin et al., 2003).
2. Glass micro-scalpels are made by stretching Pasteur pipettes over a burner so that the tip of the hand-drawn out pipette is under the limit of capillary (see Note 2).
3. Transfer pipettes are made by stretching Pasteur pipettes over a burner so that the tip diameter allows collection and transfer of tissues between donor and recipient embryos or injection of liquid solutions into tissue lumen prior to electroporation.
4. Couple the glass-made transfer pipettes to a flexible plastic tube for mouth use, or alternatively attach the transfer pipettes to Spemann pipettes (Fish and Schneider, 2014a; Lwigale and Schneider, 2008; Schneider, 1999).

Embryo Incubation

1. After delivery, unpack and quickly wipe eggs with 70% ethanol.
2. Store eggs in a cold room or refrigerator with temperature set at 14 °C before incubation (see Notes 1 and 3).
3. Acclimate them to room temperature, for 1.5 h, before putting eggs into the incubator, to minimize temperature shock.
4. Incubate quail and chick embryos at 38 ± 0.5 °C with 45% of humidity for successful development (see Notes 4–7) (Hamburger and Hamilton, 1951; Zacchei, 1961).

Preparation and Visualization of Avian Embryos

1. Incubate eggs in a horizontal position and mark the top point with a pencil as the embryos rotate to the top of the yolk (Figure 14A-B) (see Note 8).
2. Perform all embryo manipulation under a stereo microscope equipped with a camera for surgery recording.
3. Pierce the blunt end of the egg with fine scissors to empty an air chamber. Allow approximately 2 ml of albumen to run from the egg which will drop down the position of the embryo and create enough space above the blastoderm to open the shell without ripping the embryo. Alternatively, poke at the narrow pole of the egg, and remove 1–2 ml of albumen with an 18G syringe.
4. Seal the hole with a piece of transparent tape or a drop of paraffin.
5. Cut a window in the shell along the top of the egg with curved scissors.
6. Enhance visualization of transparent embryos by injecting India ink diluted in PBS (1:20) under the blastoderm to contrast the cell density of embryonic tissue, hence helping the visualization of anatomical landmarks (Figure 14D-E). Soak the vitelline membrane, with sterile PBS supplemented with antibiotics, to prevent embryo desiccation.
7. Precisely stage embryos by referring to specific timetables and then further refine staging by counting somite pairs (see Note 9).
8. Seal the shell with a transparent tape to prevent desiccation and place back in the incubator.

Generation of Quail-Chick Chimeras

1. Remove appropriately staged embryos from the incubator, and place and stabilize the host egg/embryo on an appropriate holder. Remove tape.

2. Incise vitelline membrane using a micro-scalpel in order to access the region of interest (Figure 14E – G).
3. Make a bilateral longitudinal slit through the ectoderm and between the tube and paraxial mesoderm (Figure 14F – G).
4. Progressively cut the whole region of interest using micro-scalpel (see Notes 10 and 11).
5. Once the graft is separated from the donor, remove the tape from host embryo.
6. Use a micro-scalpel to excise the matching region from the host embryo.
7. Push away the excised region.
8. Gently suck out the graft from donor egg, using an appropriately sized micropipette.
9. Carefully transfer the graft into host egg.
10. Implant the donor graft in the elected site using the micro-scalpel.
11. Add a small volume of sterile PBS on top of the host embryo.
12. Seal the window of recipient embryo with transparent tape.
13. Place the egg back into the incubator.
14. Let embryo develop until the desired stage for phenotype analysis (see Note 12).

Transfection of Neural Crest Cells Prior to Xenotransplantation

1. Remove appropriately staged embryos from the incubator and place and stabilize the host egg/embryo on an appropriate holder. Remove tape.
2. Fill the tip of a glass transfer micropipette with the solution containing exogenous nucleic acid sequences (see Notes 13 and 14).
3. Contrast the solution of nucleic acids with Fast Green FCF (1:10,000) in order to enhance and more precisely control the site of injection.

4. Carefully position the tip of the transfer micropipette in the neural groove.
5. Gently blow the solution containing the exogenous nucleic acid sequences to deposit the solution in the lumen of the closing neural tube. Carefully withdraw the micropipette.
6. Attach unilateral or bilateral electroporation electrodes to the micromanipulator (Figure 16A, D) (see Notes 15 – 17).
7. Place the electrodes on the vitelline membrane.
8. For unilateral electrodes set the two-golf club-headed electrodes flanking the target area around 5 – 6 mm apart.
9. For bilateral electrodes set the two golf club-headed anodes laterally, flanking the target area (Creuzet, 2009b). Place the sharp-end cathode 5 – 6 mm distant from anodes rostral to the anterior neuropore.
10. Moisten the electrodes with PBS to homogenize the electrical field and enhance the efficiency of electroporation.
11. Connect the electrode system with contact hooks and cables to square pulse-delivering generator.
12. Trigger 5 iterative electrical pulses of 22 V (duration 50 ms, interval 500 ms).
13. Clean electrodes with a brush after each electroporation to preserve their conductivity.
14. Drop a small volume of sterile PBS on top of the embryo.
15. Seal the shell with a transparent tape to prevent desiccation.

Notes

1.

Fertilized quail and chick eggs are usually available from local farms or breeders. Cold storage

keeps embryos arrested at very early stage of development. The eggs can be stored at 14 °C for about 1 week.

2.

Adapt the design of micro-scalpels to each type of tissue manipulation. Micro-scalpels made with glass are suitable for very delicate excision of neural crest cell domains. As the glass does not retain embryonic material, the micro-scalpel makes very neat incisions and remains sharpened over many operations. Glass micro-scalpels are particularly suitable for ablation or transplantation of neural crest cells and, more specifically, for operations involving very small neural crest territories (Creuzet et al., 2002b; Creuzet et al., 2004a) (Figure 15). For operations involving the neural tube plus neural crest, micro-scalpels that are metal made by honing steel needle on an Arkansas stone may be more convenient as they are more robust (Douarin et al., 2008). Alternatively, micro-scalpels can be made up (1) with tungsten sharpened by electrolysis in a 0.5 M KOH solution (Conrad et al., 1993) or (2) with honed entomology needles. The latter can be subsequently folded or clubbed to deeply implant embryonic tissues (Couly et al., 2002b; Ruhin et al., 2003). Another possibility is flame-sharpened tungsten needle made by cutting tungsten wire in half which is then inserted inside the tapered end of Pasteur pipette filled with hot glue gun, bent to an angle of 45° using a pair of forceps, and sharpened using a propane fuel cylinder (Lwigale and Schneider, 2008). Flame-sharpened tungsten needle micro-scalpels are very thin and extremely resistant and can be repeatedly flame-sterilized so they can be used until they are blunt.

3.

Choose fast-growing quail and chick strains in order to synchronize the stages of development between donor and recipient embryos. Such strains include the quail strain (*Coturnix coturnix*

japonica) and JA57 domestic chick (*Gallus gallus domesticus*), which are particularly resistant and commonly used strains in food industry with a high rate of hatching.

4.

For manipulation of neural crest, it is recommended to incubate quail and chick embryos until stage-matched at Hamburger-Hamilton (HH) stage 8. Quail and chick have slightly different maturation rates (i.e., from fertilization quail hatch in 17 days and chick in 21 days), but early in development, these differences are subtle. To perform the surgery at stage HH8 embryos, the incubation time is approximately 29 h.

5.

Adequate humidity is crucial for successful development and cannot be overemphasized. Refill water containers regularly and monitor the humidity as well as the temperature in the incubators.

6.

Maintain incubator humidity about 45% throughout ontogenesis: it must amount to 75 – 85% as the embryos near hatching age.

7.

Clean incubators regularly to minimize bacterial and/or yeast contamination (use 10% bleach and soap water, rinse with freshwater, and then let the incubator dry for at least 12 h).

8.

Design egg holders according to the operation. Holders can be of several types, multiple wire tongs, wooden circles, or egg trays, that are used for egg storage in most of the households. Some specific devices have been developed in our laboratory to fulfill the requirement of *in*

ovo manipulation for both chick and quail eggs (Figure 14A – B).

9.

Stage embryos according to external morphological characters (Hamburger and Hamilton, 1951). In addition to Hamburger and Hamilton (HH) staging, other timetables from Eyal-Giladi and Kochav (Eyal-Giladi and Kochav, 1976), Zacchei (Zacchei, 1961), or more recent Ainsworth et al. (Ainsworth et al., 2010) may be used to precisely stage either chick or quail embryos. Although the HH staging system is dedicated for chick staging, it may also be routinely used when classifying quail embryos. However, during the early phases of development, when cephalic neural crest manipulation is performed, embryos subjected to micro-surgery are staged by counting the number of somite pairs flanking the neural tube, and their developmental stage is expressed as somite stage (ss).

10.

Operate the neural fold by referring to topographical land-marks based on the previously published fate maps of the neural primordium (Figure 15E) (Couly and Le Douarin, 1988; Couly and Le Douarin, 1985, 1987).

11.

Perform neural crest cell exchange at very precise time point during development. Neural crest cell grafting needs to be performed before neural crest cell population begins migration when cells are still attached to neural primordium, at the border of the neural plate. Neural crest cell formation and delamination are first initiated at cephalic level at stage HH8.5 (i.e., 5–6 somites, 29 h) (Le Lièvre and Le Douarin, 1974; Le Lièvre and Le Douarin, 1975b) and continue progressively to caudal levels (Catala et al., 2000) (E4.5 and E5 in quail and chick embryos,

respectively).

12.

After xenotransplantation, the “quail pedigree” of transplanted cells is easily recognized from the recipient chick at the single-cell level and at any developmental stage upon classical Feulgen-Rossenbeck’s staining (Feulgren and Rossenbeck, 1924) or immunocytochemistry using QCPN antibody (Carlson and Carlson, Univ. of Michigan). By the virtue of its stability, the heritable cell marker offers the possibility to enlighten the developmental continuum leading a cell population from the site of its origin to the final destination of their progenies, no matter the state of differentiation (Figure 15).

13.

Nucleic acids in the form of expression plasmids or retroviral vectors are useful for transient or permanent gain-of-function experiments, respectively. The main drawback of plasmids resides in the nonpermanent integration in the transfected-derived cells, thus leading to progressive loss of the vector and finally turning off the foreign gene expression (whose kinetics tightly depend on the proliferative rate of the recipient tissue). In contrast, the use of retroviruses that randomly integrate into the host genome by means of their long terminal repeat sequences ensures a stable transfection of the exogenous DNA. An elegant approach to limit the spread of retroviral contamination in quail-chick chimeras is to exploit the species-restricted infectious ability of viruses into either a permissive or repellent species environment provides. For ectopic expression, constructs may be used at the concentration ranging from 1 to 4 $\mu\text{g}/\mu\text{l}$ in PBS.

14.

For loss-of-function experiments, we recommend RNA interference to drive gene silencing. Up to four genes can be manipulated at once (Garcez et al., 2014), which provides a critical asset for dissecting the epistasis in molecular networks (Pekarik et al., 2003; Stoeckli, 2006). Double-stranded RNA used for gene silencing must be adjusted at a working concentration varying between 200 and 500 ng/ μ l in PBS.

15.

Electroporation allows an instantaneous and highly efficient penetration of the nucleic acid vectors into cells (Muramatsu et al., 1997). Based upon a transient permeabilization of the cell membrane by an electrical impulse, this technique exploits polarized electrical fields to orient the exogenous nucleic acids toward the targeted cells and trap them in their cytoplasm. According to the principles, the interposition of an epithelium between the nucleic acid solution and the cathode results in the directional transfer of the foreign nucleic sequence into the epithelial cells. Firstly devised *in vitro*, this technique has been successfully adapted to *in vivo* transfection since the mid-1990s by turning a unique pulse of high voltage, with an exponential decay, into a series of iterative low-voltage square pulses (Momose et al., 1999; Muramatsu et al., 1997; Ogino and Yasuda, 1998).

16.

A problem raised by the electroporation of the cephalic neural crest cells is that the cells emanating from the strands of neural folds merge along the dorsal midline before migrating bilaterally. As a consequence, the "control" and "experimental" sides receive a substantial contribution of transfected and untransfected cells that can strongly bias the interpretation of resulting phenotypes. To circumvent this limitation, the unilateral electroporation of the neural

fold (Figure 16A – C) may be followed by the bilateral transplantation of the transfected tissues. In such a case, two donor embryos can be used: one for the right and another for the left neural fold (see (Creuzet et al., 2002b) for technical description). For example, transfected quail neural folds can be bilaterally engrafted into a recipient “experimental” embryo. In parallel, the contralateral neural folds that have been electroporated but remained untransfected can be bilaterally implanted into a recipient “control” embryo. In spite of being technically challenging, this procedure can precisely correlate the forced gene expression to the fate of the transfected cells and enables discrimination of the fate of the targeted graft-derived cells from the untransfected host environment (Creuzet et al., 2002b). In addition, as “control” and “experimental” embryos contain the sibling neural fold, the morphological and functional defects are therefore strictly attributable to the activity of the foreign gene.

17.

An alternative way to manage bilateral transfection at once is to generate a triangular electric field by using a triplex of electro-des (e.g., one anode, rostral, and two cathodes, lateral), which yields the bilateral dispersion of the nucleic acid sequences (Figure 16D – H) (Creuzet et al., 2002b). When combined to quail-chick xenotransplantation, this strategy turned out to be particularly useful to decipher the molecular basis of neural crest cell interactions in craniofacial development. It was also decisive to document the trophic effect exerted by the cephalic neural crest on brain development and identify neural crest cell-dependent pathways and the cognate mediators involved in the sophistication of the preotic brain (Aguiar et al., 2014; Creuzet, 2009b; Creuzet et al., 2016; Garcez et al., 2014).

Figures

Figure 14: Instruments and material required for embryonic manipulation in avian embryos. (A) Egg holder for horizontal incubation of chick egg. **(B)** Egg tee used to operate quail embryo in ovo. **(C)** Tools required for embryonic microsurgery: (a) curved and (b) Pascheff's scissors, (c) skimmer to collect embryos, (d) transplantation spoon, (e) forceps, (f) micro-scalpel holder. **(D)** Chick embryo at 8 somite stage (ss) on the yolk: the neural fold is delineated with red dashed lines. **(E)** Injection of India ink under the blastoderm helps to visualize the embryonic structures; to access the embryo, the vitelline membrane covering the cephalic region is incised and deflected. **(F)** The cephalic neural crest (CNC) is first incised on the right-hand side from the level of r2, and then progressively removed until being completely ablated. **(G)** Bilateral ablation of the CNC: the removed territory corresponds to the neural crest cell (NCC), which are fated to form the craniofacial skeleton. **(H)** After transplantation, opening in the shell is sealed with tape before re-incubating chick embryos.

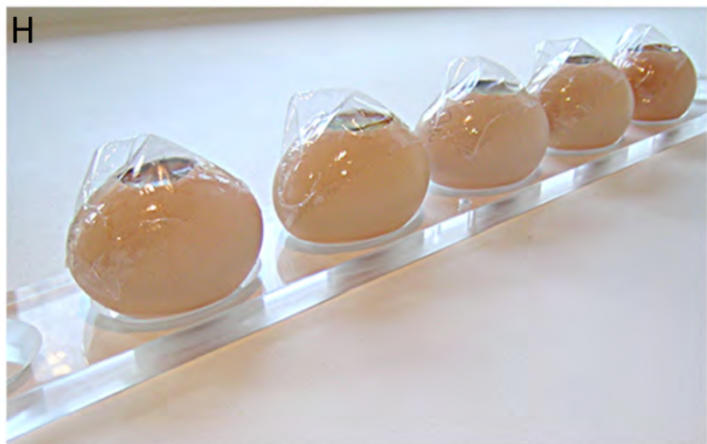
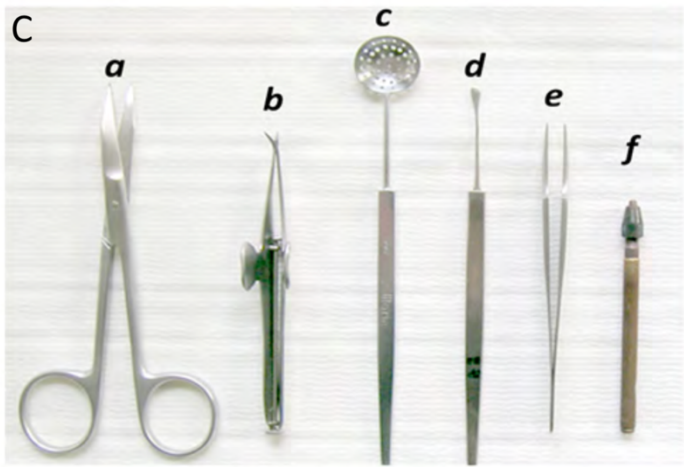
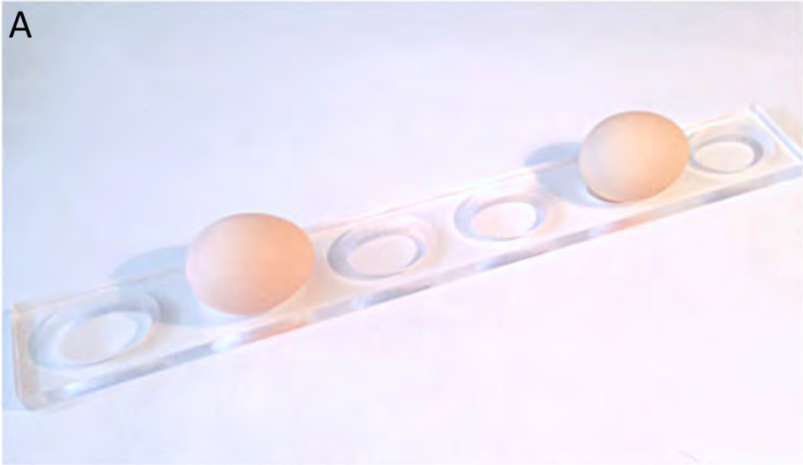


Figure 15: Quail-chick xenotransplantation of discrete cephalic neural crest (CNC) territories: unraveling the migration of CNC cells. (A, B) Interspecific exchange between quail and chick embryos involving **(A)** the posterior diencephalic (Di) neural crest (NC) cells, and **(B)** the migration of the cells in the nasofrontal bud, 24 hours after the graft. **(C, D)** Xenograft **(C)** at rhombomere (r) 3 level, and **(D)** the dispersal of NC r3 cells in the first and second branchial arches (BA). **(E)** Color-coded fate map resulting from the systematic exploration of the migration routes of the CNC. **(F, G)** Colonizing of the **(F)** periocular region and **(G)** second BA, by the Di and r3 NC cells, respectively. **(H-L)** Aside from the elucidation of NC cell migration, the quail-chick system can reveal the long-term fate and derivatives of the transplanted cells. **(J)** Xenograft involving r1 and r2 NC cells, **(H)** at neurula stage. **(I)** Pigment pattern in E18 chimera. **(J-L)** Musculoskeletal derivatives of the grafted cells: massive contribution of quail NCC cells to **(J)** bony tissues in the Dentary, **(K)** cartilage in the retroocular process, and **(L)** tendinous insertion of Pterygoideus muscle. **(A,B)** are reproduced from Creuzet et al. (2005b); **(C,D)** from Creuzet et al. (2005a).

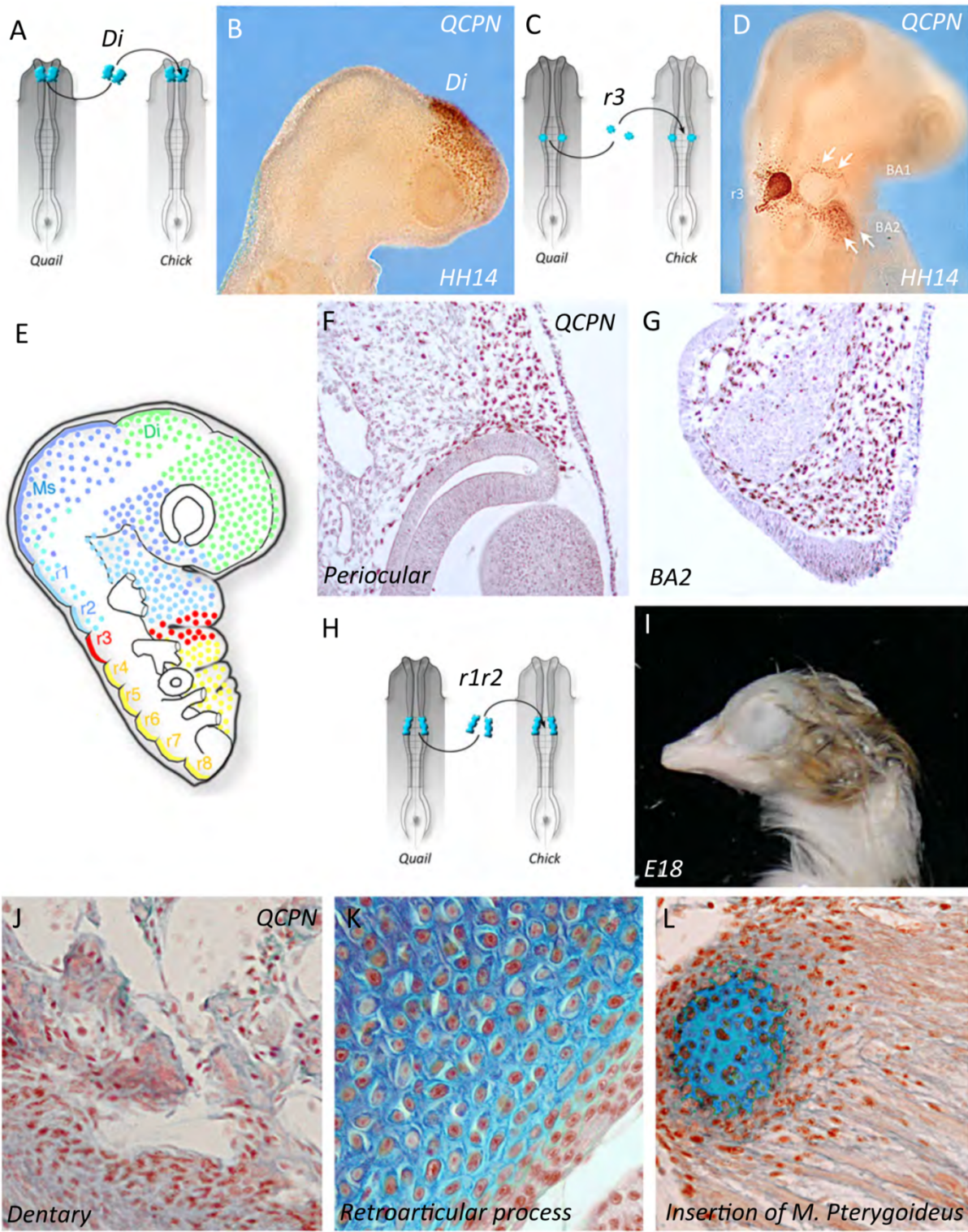
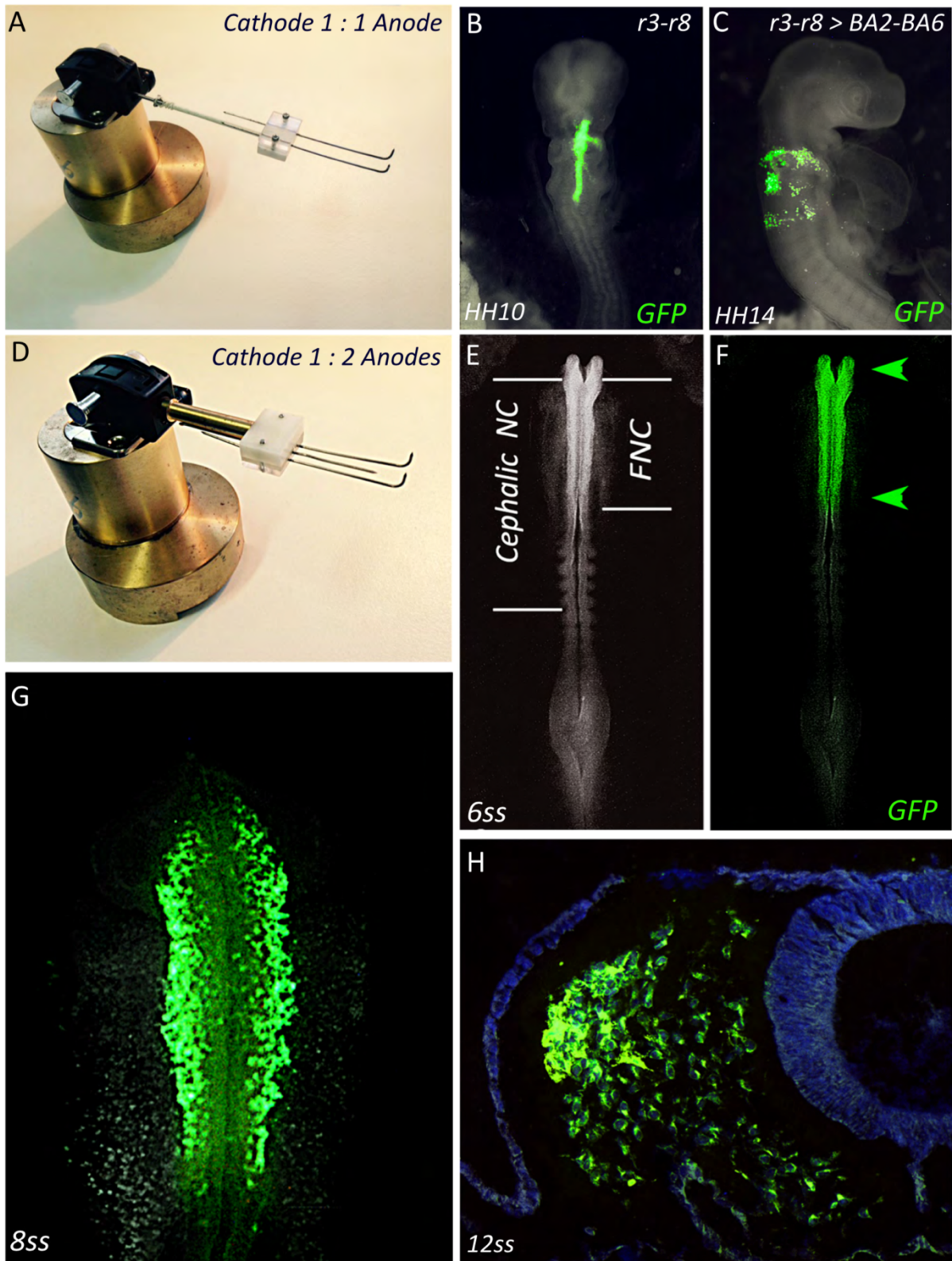


Figure 16: Unilateral and bilateral electroporation of the cephalic neural crest (CNC). (A)

Classical system of two electrodes, involving a cathode and an anode, to flank the neural groove and trigger a unilateral transfection. **(B)** An E2 (HH10) chick embryo showing the GFP activity after a unilateral electroporation of the neural crest (NC) cells extending from rhombomere (r) 3 to r8. **(C)** The same experiment observed at E2.5 (HH14) showing the electroporated cells migrating towards the branchial arches (BA). **(D)** The triplex electrode system involving one cathode with two anodes devised to trigger a bilateral transfer of the electroporated construct (Creuzet et al., 2002a). **(E)** A top view of a 6-somite stage (ss) chick embryo where the anatomical landmarks of the CNC versus the facial NC (FNC) are delineated. **(F)** The same embryo in which the FNC has been bilaterally electroporated at 4ss, with a construct driving the expression of GFP in FNC cells. **(G)** At 8ss, the electroporated FNC cells start to migrate away from the neural primordium. **(H)** Section performed on 12ss embryo, showing that only the NC cells benefit the electroporation, leaving the superficial ectoderm along with the adjacent neuroepithelium untransfected. **(E-H)** are reproduced from (Aguiar et al., 2014).



Chapter 3: Differential regulation of SHH signaling and the developmental control of species-specific jaw size through Gas1 expression

(In collaboration with Daniel B. Chu, An Nguyen, Jennifer L. Fish, and Richard A. Schneider and submitted to Development)

Introduction

Animals belonging to a given taxon typically share a conserved body plan that contains equivalent (i.e., homologous) structures. Such structures often appear to be iterative versions of a common template that can vary in relative size and/or proportions along a normal distribution, which is a phenomenon known as allometry or biological scaling (Gayon, 2000; Gould, 1966; Huxley, 1932; Huxley and Teissier, 1936; Schneider, 2018a; Stern and Emlen, 1999; Thompson, 1917; Woodger, 1945; Young et al., 2014). For purposes of functional morphology, the proper scaling of structures is robustly maintained during the development of individuals even though the size of these same structures can vary enormously both within a species and among members of related taxa (Haldane, 1926; Russell, 1916; Smith et al., 2015). Additionally, tissue regeneration and transplantation experiments indicate that structures retain intrinsic mechanisms enabling them to know their proper size and to regulate growth (Leevers and McNeill, 2005; Fish et al., 2014; Uygur et al., 2016; Schneider, 2018a). But how these intrinsic mechanisms function and how they potentiate normal to abnormal phenotypic variation in size, is poorly understood. Moreover, molecular and cellular processes that enable early embryos to establish growth trajectories in support of requisite adult form and function remain to be identified especially as a means to understand etiologies of disease and mechanisms of evolution (Schneider, 2015; Woronowicz and Schneider, 2019).

On the molecular level, biological scaling likely involves species-specific modulations to intrinsic levels and patterns of gene expression that affect the behaviors of cells and the corresponding growth of tissues and organs. Such ideas emerged in the first half of the 20th century with the discovery of genes that alter the timing and rates of development (de Beer, 1954; Goldschmidt, 1938; Goldschmidt, 1940; Huxley, 1932), and they led to theories and

quantitative methods during the rebirth of evolutionary developmental biology in the 1970s predicting how even small changes affecting developmental time and rates could generate significant phenotypic variation and transformations in size (Alberch et al., 1979; Gould, 1977; Hall, 1984; Keyte and Smith, 2014; Klingenberg, 1998; McKinney, 1988; Smith, 2003). In this context, molecules that act as morphogens seem to play a key role, especially when genetic changes alter their expression levels, source (i.e., cells that produce the morphogen), distribution (i.e., release of the morphogen), transportation (i.e., diffusion of the morphogen), and detection (i.e., cellular sensitivity to the morphogen) within the local environment (Ben-Zvi and Barkai, 2010; Cheung et al., 2014; Gurdon and Bourillot, 2001; Gurdon et al., 1999; Oster et al., 1988; Tostevin et al., 2007). One well studied example is the classic morphogen Sonic Hedgehog (SHH), which elicits cellular proliferation or differentiation responses in a concentration-dependent manner that pattern and scale organs such as the limb bud, neural tube, and craniofacial primordia (Briscoe et al., 2001; Dessaud et al., 2008; Dessaud et al., 2007; Echelard et al., 1993; Ericson et al., 1997; Ericson et al., 1995; Hu and Marcucio, 2009; Laufer et al., 1994; López-Martínez et al., 1995; McLellan et al., 2008; Riddle et al., 1993; Schneider et al., 2001; Summerbell et al., 1973; Uygur et al., 2016; Xu et al., 2015; Yang et al., 1997; Young et al., 2010; Zeng et al., 2001).

SHH binds to the canonical receptor Patched (PTCH1) and the co-receptors Cell adhesion molecule-related/Downregulated by ONcogenes (CDON) and Brother Of Cdon (BOC), as well as Growth Arrest-Specific 1 (GAS1) (Beachy et al., 2010; Choudhry et al., 2014; Izzi et al., 2011; Tenzen et al., 2006). The binding of PTCH1 by SHH results in de-repression and accumulation of Smoothened (SMO), and signal transduction through the Glioma-associated oncogene (GLI) transcription factors (Alcedo and Noll, 1997; Murone et al., 1999; Quirk et al., 1997; Taipale

et al., 2002; van den Heuvel and Ingham, 1996; Wilson and Chuang, 2010). GLI2 and GLI3 are bifunctional transcription factors that can either activate or inhibit transcription whereas GLI1 lacks a transcriptional repressor domain and can only function as a transcriptional activator (Bai et al., 2002; Bai and Joyner, 2001; Hui and Angers, 2011; Lee et al., 1997; Marigo et al., 1996; Matisse and Joyner, 1999; Mo et al., 1997; Wang et al., 2000). The binding of CDON, BOC, and GAS1 by SHH promotes cell survival, proliferation, and differentiation, which ultimately can affect the size and shape of organs (Allen et al., 2007; Delloye-Bourgeois et al., 2014; Izzi et al., 2011; Martinelli and Fan, 2007).

In the current study, we tested if differential regulation of the SHH pathway can account for species-specific scaling of the developing jaw primordia by comparing expression of pathway members in duck, chick, and quail, which are three species of birds with distinctly different jaw sizes (i.e., from relatively large to small) and rates of maturation (Fig 1A). We analyze embryonic stages starting when neural crest mesenchyme (NCM), which are the jaw precursor cells (Jheon and Schneider, 2009; Le Lièvre, 1978; Noden, 1978), first arrive in the mandibular primordia and then undergo their patterned outgrowth. NCM controls species-specific jaw size (Schneider, 2005; Schneider, 2015; Schneider, 2018b; Schneider and Helms, 2003) and previously we have shown that mechanisms contributing to the larger jaw size of duck versus quail include the allocation of approximately 15% more jaw progenitors to the mandibular primordia during early stages of migration and a longer cell cycle length (13.5 hours in duck and 11.0 hours in quail). When taken alongside equivalent rates of proliferation over a period of 45 hours in duck versus 32 hours in quail (i.e., the amount of absolute time over comparable stages), this translates into a twofold difference in cell number by HH20 (Fish et al., 2014). NCM also exerts species-specific control over multiple signaling pathways during later stages of cell

proliferation and skeletal differentiation that directly affect jaw size (Ealba et al., 2015; Eames and Schneider, 2008; Fish and Schneider, 2014b; Hall et al., 2014; Merrill et al., 2008). Signaling interactions between NCM and the epithelium of the pharyngeal endoderm, which secretes SHH, promote the patterned outgrowth of the mandibular primordia and establish the anteroposterior polarity of the jaw skeleton (Abzhanov and Tabin, 2004; Brito et al., 2006; Couly et al., 2002; Graham et al., 2005; Helms and Schneider, 2003; Moore-Scott and Manley, 2005). Similarly, SHH is associated with species-specific shape and outgrowth of the face (Hu and Marcucio, 2012; Hu et al., 2015a; Hu et al., 2015b; Schneider et al., 2001; Young et al., 2010) and disruptions to SHH co-receptors as well as other pathway members can result in micrognathia and other jaw defects especially in association with holoprosencephaly (Allen et al., 2011; Bae et al., 2011; Cole and Krauss, 2003; Dennis et al., 2012; Echevarría-Andino and Allen, 2020; Hong et al., 2017; Hui and Angers, 2011; Melnick et al., 2005; Mo et al., 1997; Pineda-Alvarez et al., 2012; Ribeiro et al., 2010; Roessler and Muenke, 2010; Seppala et al., 2007; Seppala et al., 2014; Xavier et al., 2016; Zhang et al., 2011; Zhang et al., 2006). But the extent to which the SHH pathway is differentially regulated by NCM and whether changes to its regulation might affect the species-specific growth of the jaw primordia are still unclear.

We performed a comparative analysis of the developing mandibular primordia of duck, chick, and quail from embryonic stages (HH) 15 to HH27 (Hamburger and Hamilton, 1951) and found species-specific differences in the size of NCM population at each stage based on total RNA yield and cell number. We quantified expression of *Shh*, *Ptch1*, *Cdon*, *Boc*, *Smo*, *Gas1*, *Gli1*, *Gli2*, and *Gli3* in mandibular primordia of duck, chick, quail, and chimeras in which we transplanted NCM from quail to duck (i.e., quack) (Figure 17B). Our strategy uncovers stage- and species-specific expression levels for key pathway members but not others, identifies

stage- and species-specific levels of pathway activation, and reveals that these differences are NCM-mediated since donor NCM maintains its quail-like expression in duck hosts. We also test if duck, chick, and quail have an intrinsic species-specific response to SHH signaling by culturing explants of mandibular primordia and treating them with different levels of recombinant SHH protein or pathway inhibitor. These pathway activation and inhibition experiments reveal a species-specific response to SHH signaling, with the SHH co-receptor Gas1 being most sensitive to manipulations. This is in contrast to in vitro studies that we perform in parallel using chick fibroblasts where we observe a minimal response to the same treatments, which indicates that sensitivity to SHH signaling and the response of Gas1 is context dependent. *In ovo* overexpression and knockdown of Gas1 in NCM alters cell number and/or mandible size. Overall, our work suggests that species-specific changes in the response of NCM to SHH signaling and the differential regulation of Gas1 expression may be a mechanism through which NCM controls jaw size during development, disease, and evolution.

Results

Species-specific differences in mandibular primordia arise early and progress during development

To compare the size of mandibular primordia in duck, chick, and quail embryos, we quantified the amount of mandibular mesenchyme (MM) in HH18, HH21, HH24, and HH27 embryos (Figure 17C). We observe significant differences (n and p-values in Tables 4 and 20) in mandibular mesenchyme population size among all three species for every embryonic stage. Mandibular mesenchyme population size is significantly larger in duck and chick than in quail throughout the developmental stages with duck being the largest.

We also quantified total RNA in the mandibular primordia (MP) in HH15, HH18, HH21, HH24,

and HH27 duck, chick, and quail embryos (Figure 17D) as well as in HH21 and HH24 quack embryos. RNA yield is significantly higher (n and p-values in Tables 5 and 20) in duck than in chick and quail, and chick RNA yield is significantly higher than quail at HH21, HH24, and HH27. Quack RNA yield is significantly higher than quail at HH24.

To assess overall amount of gene expression in the mandibular primordia, we used the ratios of RNA yield to cell counts and discovered that activity per cell (i.e., mandibular primordia RNA content) is higher in quail than in duck and chick (Figure 17E, values in Table 6). Throughout HH18 to HH27, RNA content per cell decreases for all three species.

To evaluate the rate at which mandibular mesenchyme population size and the total amount of RNA extracted from mandibular primordia increases over time in duck and quail we calculated duck to quail mandibular mesenchyme population size ratios (Figure 17H) at HH18, HH21, HH24, and HH27 as well as mandibular primordia RNA extraction ratios (Figure 17F) at HH15, HH18, HH21, HH24, and HH27. The mandibular mesenchyme population size ratio is lowest at HH18 and highest at HH21 with very small changes over development (values in Table 9). The mandibular mesenchyme population is on average 4.1-fold larger in duck than quail. The mandibular primordia RNA extraction ratio is about the same from HH15 to HH27 (values in Table 8) with an average of 2.4. Thus, duck have about 2.4 times more total RNA per mandibular primordia than quail do and the rate at which the amount of total RNA extracted from mandibular primordia increases over time is equivalent in duck and quail.

To determine whether differences in the mandibular mesenchyme population size between duck and quail are due to differences in cell cycle length, size of the migratory NCM population (Fish et al., 2014), and/or the absolute time (i.e., the time that each species takes to reach each

successive developmental stage, Figure 17A) we modeled relative mandibular mesenchyme population size, using the number of migratory NCM, cell cycle length, and absolute time (Figure 17G, Table 7). We compared modeled data to the population size *in vivo* (Figure 17H, Table 8) and we were able to replicate the relative mandibular mesenchyme population size for duck and quail. The size of the migratory NCM population was identified in HH10 chick embryos by the presence of *Sox10* expression. Quantification of *Sox10*-positive cells reveals that chick have an average of 87.1 NCM cells (values in Table 3) emigrating from the midbrain, which is lower than what we observed previously for duck and quail (Fish et al., 2014).

SHH pathway activation is species-specific and dose-dependent

Previous studies have shown that SHH regulates growth and proliferation of the mandibular primordia (Brito et al., 2008; Roper et al., 2009; ten Berge et al., 2001) and that *Shh* is expressed in similar domains (i.e., in the pharyngeal endoderm) in duck and quail embryos (Fish et al., 2014). To test the hypothesis that species-specific expression of SHH pathway members underlies the differential rates of proliferation that ultimately affect mandibular mesenchyme population size, we compared the expression of SHH pathway members and targets among duck, chick, quail, and chimeric quack mandibular primordia during development. We quantified the relative expression of key components including *Shh*, *Ptch1*, *Gas1*, *Gli1* (Figure 18A to 18D), *Boc*, *Cdon*, *Smo*, *Gli2*, and *Gli3* (Supplemental Figure 1) in duck, chick, and quail mandibular primordia at HH15, HH18, HH21, HH24, and HH27, and quack at HH21 and HH24. We find stage- and species-specific differences in many genes with the most striking difference in the relative expression of *Gas1*. *Gas1* is approximately 25 to 75 times higher in duck than in chick and quail with this difference increasing from HH15 to HH27 (Figure 18C). For all significant comparisons between species $p < 0.02$, and n and p -values are listed in Tables 11

and 20.

To assess if there are species-specific differences in SHH pathway activation among duck, chick, quail, and quack mandibular primordia, we calculated gene expression ratios for *Shh* to *Ptch1* (Figure 18E) and *Shh* to *Gli1* (Figure 18F) at HH15, HH18, HH21, HH24, and HH27. For *Shh* to *Ptch1* ratios we observe significantly higher pathway activation in duck from HH15 to HH24 compared to quail and chick, with quail having the lowest pathway activation. For *Shh* to *Gli1* ratios we observe significantly higher activity for chick and quail at HH15 compared to duck and the activity becomes significantly higher in duck from HH18 to HH24 (n and p-values in Tables 10 and 20).

To determine if there are intrinsic species-specific differences in sensitivity to SHH signaling (i.e., a dose-response to the same amount of pathway activator and/or inhibitor), we cultured explants of HH21 mandibular primordia from duck, chick, and quail and treated them with various concentrations of recombinant (r) SHH protein (i.e., pathway activator) or cyclopamine (i.e., pathway inhibitor). After 24 hours of treatment, we quantified relative expression of *Ptch1*, *Gas1*, *Gli1*, *Gli2*, *Gli3* (Figure 19), *Shh*, *Boc*, *Cdon*, and *Smo* (Supplemental Figure 2A to 2D). We find that duck and chick show a greater response to SHH treatments compared to quail for both *Ptch1* (Figure 19A) and *Gli1* (Figure 19C). The response of these two target genes to cyclopamine treatments is similar in all three species. Most SHH pathway members exhibit species-specific differences in their relative expression with the exception of *Shh* (Supplemental Figure 2A) and *Smo* (Supplemental Figure 2D) for which we observe no significant differences in relative expression between control and any treatment group for any species. Notably, we observe the greatest interspecies sensitivity to SHH pathway manipulations with *Gas1* (Figure 19B). *Gas1* expression is significantly different starting at 0.1

ng/mL of SHH protein for quail, and at 100 ng/mL for chick compared to control, whereas there is no significant difference at any concentration of SHH for duck. By contrast, *Gas1* expression is significantly increased in duck and chick when treating with cyclopamine and there is no significant difference in quail (n and p-values for all genes and species are in Tables 12 and 21).

To understand the spatial expression of *Gas1*, we performed in situ hybridization in HH21 and HH27 duck, chick, and quail mandibular primordia (Figure 20). We find that *Gas1* expression is symmetrical for all three species with one lateral domain on each side at HH21 and two distinct domains at HH27 (one lateral domain on each side of the mandibular primordia and one medial domain).

Response to SHH treatments is NCM-mediated and context dependent

To test if the response to changes in SHH pathway activation is mediated by the context of the mandibular primordia or instead a cell-autonomous effect, we treated chick fibroblasts (i.e., DF-1 cells) with the same varying concentrations of rSHH protein as mandibular primordia explant cultures. While treating with rSHH for 24 hours results in SHH pathway activation in chick fibroblasts (i.e., *Ptch1* expression significantly increased at 1000 ng/mL), there is no significant difference in *Gli1* or *Gas1* expression compared to control (i.e., 0 ng/mL of rSHH) (Figure 21A). Thus, treating chick fibroblasts with rSHH protein is not sufficient to alter expression and suggests that the SHH pathway response is specific to developmental context of the mandibular primordia. n and p-values for all genes and treatments are in Tables 15 and 23.

To determine if variation in the levels of *Gas1* expression can affect cell number, we

overexpressed chick and quail *Gas1* in chick fibroblasts. We overexpressed *Gas1* in chick fibroblasts using a doxycycline (dox)-inducible promoter system that we have characterized previously (Chu et al., 2020) and by titrating the concentrations of dox. We confirmed chick (Figure 21B, left panel) and quail (Figure 21C, left panel) *Gas1* overexpression by qRT-PCR after 24 hours (h) of treatment, and we quantified expression of *Boc*, *Cdon*, *Smo*, *Ptch1*, *Gli1*, *Gli2*, and *Gli3* (Supplemental Figure 3A). We do not observe any changes to the expression of these genes with the exception of *Smo* when *Gas1* is overexpressed following treatments with 0.1 ng/mL of dox. We also quantified the number of cells per plate after 72 hours of dox-induction (Figure 21B to 21C, right panel). Our results show no difference in the number of cells per plate in any of the treatment groups for either chick or quail *Gas1* overexpression compared to control (i.e., 0 ng/mL of dox). Thus, *Gas1* overexpression in chick fibroblasts is not sufficient to alter expression of SHH pathway members 24 hours after dox-induction nor alter the number of cells per plate after 72 hours. n and p-values for all genes and treatments are in Tables 13, 14, 20, and 22.

To evaluate if combining *Gas1* overexpression and SHH pathway activation is sufficient to alter the expression of SHH pathway members, we treated *Gas1*-expressing chick fibroblasts with four different concentrations of rSHH together with five different concentrations of dox. Again, we did not observe any change to *Gas1* expression at any rSHH concentration with no dox treatment (Figure 21D, left panel). *Ptch1* and *Gli1* expression was significantly higher at 100 ng/mL, which confirms that the SHH pathway was activated. With *Gas1* over-expression, there is no significant difference in gene expression levels for *Ptch1*, *Gli1* (Figure 21D, right panel), *Boc*, *Cdon*, *Smo*, *Gli2*, and *Gli3* (Supplemental Figure 3B) following any dox treatment with the exception of rSHH at 0 ng/mL for *Cdon* at 10 ng/mL of dox. In addition, for samples at 1, 10,

and 1000 ng/mL of rSHH we observed no significant difference for any of these genes at any dox concentration with the exception of *Gas1*, which is significantly higher for all three rSHH concentrations at 50 ng/mL of dox (data not shown). Thus, *Gas1* over-expression, while able to activate the SHH pathway, is not sufficient to alter the response of members of the SHH pathway in chick fibroblasts. n and p-values for all genes and treatments are in Tables 16, 23, and 24. Taken together, these data suggest that the species-specific response to SHH in mandibular primordia is NCM-mediated and context dependent.

Changes in Gas1 expression affect mandibular primordia size in vivo

Our *in vivo* molecular data together with results from our SHH pathway manipulations in mandibular explant cultures suggest that *Gas1* is key component of the SHH pathway that may mediate species-specific differences in activation, cell number, and jaw size. To test if species-specific differences in levels of *Gas1* expression can affect the size of the mandibular primordia, we altered *Gas1* expression in duck and quail. First, we electroporated our dox-inducible *Gas1* overexpression plasmid bilaterally into the presumptive NCM of duck and quail embryos at HH8.5 and then treated these embryos with dox at HH15. We collected duck and quail embryos at HH18, HH21, and HH24 and quantified the amount of mandibular mesenchyme. We observe a significant reduction in the amount of mandibular mesenchyme in duck *Gas1* OE embryos at HH21 and HH24 (Figure 22A). The extent of *Gas1*-positive overexpression in NCM was validated in whole mount by mScarlet fluorescence (RFP) at HH18 (Figure 22B and 22C), HH21 (Figure 22D and 22E), and HH24 (Figure 22F and 22G). Although not significant ($p < 0.0614$), we observed a trend towards reduction in the amount of mandibular mesenchyme in quail embryos (Figure 22H). n and p-values for all samples are in Tables 20 and 25. To assess the effects of overexpression on mandibular morphology, we also

electroporated *Gas1* overexpression plasmid unilaterally into the right side of presumptive NCM of quail embryos at HH8.5 and then treated these embryos with dox at HH15. By HH27, quail embryos show a clear reduction in the size of the developing jaw on the electroporated side (Figure 22I). Again, we validated the extent of *Gas1*-positive overexpression in NCM in whole mount by RFP (Figure 22J). These differences in the treated versus internal control sides can be seen most clearly at higher magnification (Figure 22K and 22L).

We also knocked-down *Gas1* expression in quail embryos by injecting an anti-*Gas1* morpholino into the right side of the mandibular primordia at HH18. We find that anti-GFP control morpholinos had no observable effect on jaw morphology (Figure 22M) as the left and right sides appear equivalent (Figure 22N and 22O). However, in the anti-*Gas1* morpholino-injected embryos we observed a left-right asymmetry on the treated side of the developing jaw (Figure 22P, 22Q, and 22R). Taken together, our morphological, molecular, and cellular data indicate that changes in the response of NCM to SHH signaling and species-specific differences in *Gas1* expression may be an evolutionary mechanism through which NCM establishes and modulates jaw size.

Discussion

Early developmental parameter values establish species-specific jaw size

In his highly influential book *On Growth and Form*, originally published in 1917, D'Arcy Thompson addressed the origins of changes in anatomical size and shape, and he emphasized the inseparable connection between morphology (i.e., form) and function (Woronowicz and Schneider, 2019). Thompson argued that changes in coordinate scale could alter body plan proportions and act as a major driving force for evolutionary transformations (Thompson,

1917). Such allometry and its mathematical approach (i.e., power law equation) has been used to describe the relationship between measured quantities (e.g., morphogen diffusion rate, gene expression levels, rate of maturation, etc.), model differential growth (i.e., changes in size and shape) of different parts of one organism, as well as compare variation in the same or multiple body parts across species (Huxley, 1924, 1932; Huxley and Teissier, 1936; Longo and Montévil, 2014; Schneider, 2018a).

Our previously published data together with our quantitative analysis of early embryonic stages in three birds with distinct jaw sizes (i.e., duck, chick, and quail) indicate that species-specific differences in the mandibular arch arise very early during development. We have shown that the migratory (i.e., *Sox10*-positive) population of NCM is about 25% larger in duck than in quail (Fish et al., 2014). Surprisingly, the size of migratory NCM in chick does not exactly reflect the intermediate size of the mandibular primordia in chick relative to duck and quail, as the chick *Sox10*-positive population of NCM is about 10% smaller than in quail. This difference, however, could potentially be compensated for in chick by a slightly shorter cell cycle length combined with longer absolute time from fertilization to hatching (21 days in chick compared to 17 days in quail). We have shown that cell cycle length for mandibular mesenchyme is 11 hours in quail and 13.5 hours in duck (Fish et al., 2014) whereas the average cell cycle length for chick has been estimated to be around 10 hours in early generations of cells and depending on the cell type (Morris and Cowan, 1995; Morris et al., 1979; Primmitt et al., 1989; Smith and Schoenwolf, 1987; Venters et al., 2008).

Thus, the initial size of the migratory NCM population that is allocated to the mandibular primordia, the amount of absolute time between developmental stages, and differences in cell cycle length can be major contributing factors to the establishment of species-specific jaw size

(Fish et al., 2014). For this reason, we used a simple power function ($f(x) = ax^b$) to model the relative population size of duck and quail throughout early development and we find that we can replicate mathematically what we observe *in vivo* (Figure 17C, 17G, and 17H). These findings support the conclusion that the regulation of time (both in terms of embryonic stage and absolute), progenitor number, and cell cycle length during development are key parameters for scaling species-specific jaw size throughout evolution (Schneider, 2018a). Similarly, much theoretical and experimental work has also emphasized how varying the values for these types of parameters can directly affect diffusion, condensation, adhesion, differentiation, and other critical biochemical and cell-cell interactions that underlie morphogenesis (Alberch, 1985, 1989; Oster and Alberch, 1982).

Higher transcriptional activity in quail correlates with smaller mandibular primordia

In general, cell intrinsic noise (i.e., variability of biochemical processes within cells) as well as extrinsic variability (e.g., cell size, cell cycle stage, mitochondrial content, phenotypic state transition) can produce gene expression fluctuations between cells and/or tissues (Kalmar et al., 2009; Padovan-Merhar et al., 2015; Phillips et al., 2019). Throughout embryonic development, changes in transcriptional activity, notably decreases, are typical of tissue specification. Our results reveal that transcriptional activity, represented by the RNA content per cell (Figure 16E), is species-specific with quail having notably higher activity than duck and chick. Perhaps the shorter window of development and faster cell cycle in quail relative to duck account for such a phenomenon. Quail might compensate for its smaller number of cells as well as for its faster cell cycle by increasing transcriptional activity as a means to achieve an equivalent level of tissue specification over a much shorter period of time. As expected, we observe a decrease in transcriptional activity over development (i.e., from HH18 to HH27) for

all three species, and this precisely follows the time course we have previously observed for the NCM-mediated shift from proliferation to differentiation in the mandibular primordia (Hall et al., 2014). Therefore, the levels of transcriptional activity and changes in phenotypic states that characterize the developmental progression of the mandibular primordia are similar for all three species, which seemingly achieve the same transcriptional end-points by HH27.

Activation of the SHH pathway is species-specific

Our results reveal that the expression of members and targets of the SHH pathway is species-specific on multiple levels, starting with expression of the ligand, to receptors, and downstream to effectors such as the *Gli* transcription factors. We observe distinct temporal patterns and changes in levels of expression for duck and quail. For example, *Shh*, *Ptch1*, *Gli1*, *Boc*, *Cdon*, *Smo*, *Gli2*, and *Gli3* (Figure 18A, 18B, 18D, and Supplemental Figure 1) shift between HH18 and HH21 from duck having the highest relative expression levels to quail. Interestingly, chick closely follows the gene expression patterns of quail from HH15 to HH18 and shifts to more duck-like expression from HH21 to HH27. Similarly, the ratios that are indicative of SHH pathway activation show chick between duck and quail for *Ptch1* and about the same as quail for *Gli1*. Such results may reflect the observation that the jaw primordia of chick fall somewhere between duck and quail in terms of absolute size, but the jaw primordia of chick and quail are more similar in shape (Smith et al., 2015). Accordingly, we can speculate that the axes of growth that generate species-specific size and shape may be differentially affected by *Ptch1*- versus *Gli*-mediated activation of the SHH pathway. Other studies have shown that various aspects of the SHH pathway can affect tissue size and shape such as changes in *Shh* enhancers (Kvon et al., 2016), variation in levels of SHH ligand, (Xu et al., 2015; Young et al., 2010), differential regulation of SHH receptors (Echevarría-Andino and Allen, 2020; Lopez-Rios et al., 2014), and

transcriptional activity of target genes (Uygur et al., 2016). Our analyses uncover species-specific variation in expression throughout early development and reveal that duck, chick, and quail have their own unique patterns at different hierarchical levels of the SHH pathway. This supports the idea that subtle changes along a continuum of gene expression on various levels, from the ligand to transcription factors, of the SHH signaling pathway can increase variability in its regulatory effects that could ultimately explain such a large variation in the jaw size.

Gas1 affects the species-specific development of the mandibular primordia

Our gene expression analyses as well as activation and inhibition experiments demonstrate that out of all the SHH pathway members that we examined, *Gas1* shows the greatest interspecific variation with the most distinct species-specific patterns detected during early developmental stages (Figure 18, Figure 19, and Figure 20; Supplemental Figure 1 and Supplemental Figure 2). In contrast, our *in situ* hybridization analyses show that the spatial domains of *Gas1* expression appear similar in all three species at HH21 and HH27 (Figure 20). Thus, while the spatial patterns of *Gas1* expression are conserved across species, variation in the levels of expression may contribute to species-specific differences in the growth of the mandibular primordia. Moreover, the species-specific levels in *Gas1* expression correlate with cell cycle length, suggesting there may be a mechanistic relationship between *Gas1* expression and cell cycle length in the mandibular primordia. Duck have the highest levels of *Gas1* expression and the longest cell cycle compared to quail and chick (duck *Gas1* expression is up to 75 times higher than quail depending on stage). We observe the lowest levels of *Gas1* expression in chick, which as noted earlier may have the shortest cell cycle length compared to quail and duck. Our data are consistent with reports from studies in other organisms where *Gas1* has been shown to act as a negative regulator that plays a critical role in growth

suppression by reducing cell proliferation (Sacilotto et al., 2015; Sarkar et al., 2018). Taken together, our results support a model whereby species-specific sensitivity to SHH signaling and differential expression of *Gas1* affects cell cycle length and proliferation dynamics in NCM, which in turn produces distinct growth trajectories and ultimately establishes the size of the mandibular primordia in chick, quail, and duck.

Since its identification in 1988 (Schneider et al., 1988), *Gas1* has been shown to play an important role in a range of biological contexts. For example, *Gas1* inhibits the transition from G₀ to S phase, induces growth arrest through p53 (Del Sal et al., 1995; Del Sal et al., 1992), and functions as a tumor suppressor gene by regulating apoptosis (Zamorano et al., 2004). During embryogenesis, *Gas1* acts as a positive regulator of cell proliferation and survival (Lee and Fan, 2001; Lee et al., 2001b; Liu et al., 2001). Likewise, our overexpression experiments demonstrate that *Gas1* levels are critical for maintaining the amount of NCM and the size of the mandibular primordia. Knocking down *Gas1* expression also affects the size of the mandibular primordia as evidenced by the left-right asymmetry in embryos treated with morpholinos. Future research dedicated to elucidating how differential *Gas1* expression regulates cell number in the mandibular primordia and how *Gas1* modulates growth among different species has the potential to illuminate an important molecular mechanism regulating jaw size during development, disease, and evolution.

Materials and Methods

The Use of Avian Embryos

For all experiments, we adhered to accepted practices for the humane treatment of avian embryos as described in S3.4.4 of the AVMA Guidelines for the Euthanasia of Animals: 2013

Edition (Leary et al., 2013). Fertilized eggs from white Pekin duck (*Anas platyrhynchos*), domestic chick (*Gallus gallus domesticus*), and Japanese quail (*Coturnix coturnix japonica*) were obtained from a commercial supplier (AA Labs, Westminster, CA, USA) and incubated at 37.8 °C and 85 – 87 % humidity until reaching stages appropriate for surgery, manipulations, collection, and/or analysis.

To visualize embryos at early stages, a small amount of sterile 0.5% Neutral Red solution (cat. No. N4638, Sigma-Aldrich, MilliporeSigma, St. Louis, MO, USA) was brushed lightly over the embryo with a blunt glass rod. Embryos were staged using the Hamburger and Hamilton (HH) staging system, a well-established standard that is based on external morphological characters and that is independent of body size and incubation time (Ainsworth et al., 2010; Hamburger and Hamilton, 1951; Hamilton, 1965; Ricklefs and Starck, 1998; Starck and Ricklefs, 1998). Absolute times of incubation to reach a particular embryonic stage for each species are in Figure 16A and Table 1.

Generation of Chimeric Embryos

Quail and duck were incubated until stage matched at HH9.5 (about 32 hours for quail and 55 hours for duck) (Figure 16A). To generate chimeric “quack” embryos, bilateral grafts of neural folds containing presumptive NCM from the anterior hindbrain and midbrain (dark green, Figure 16B) were excised from quail donors and transplanted into stage-matched duck hosts with a comparable region of tissue removed using flame-sharpened tungsten needles (Tungsten wire, cat. No. 7190, A-M Systems, Sequim, WA, USA) and hand-made Spemann pipettes (Fish and Schneider, 2014a). Orthotopic control grafts were performed as done previously (Helms and Schneider, 2003; Lwigale and Schneider, 2008; Noden, 1983b; Schneider, 1999; Schneider et al., 2001). After surgery, eggs were sealed with tape (3M™

Scotch® Transparent Film Tape 600, 3M United States, St. Paul, MN, USA) and placed in the incubator until reaching stages appropriate for collection and analysis.

Isolation of Mandibular Primordia

Using forceps, mandibular primordia were cut along the proximal junction at each side of the maxillary primordia and placed into RNase-free ice-cold 1x PBS (cat. No. BP3991, Fisher Scientific, Hanover Park, IL, USA). For RNA extraction, isolated mandibular primordia were transferred into 1.5 mL microcentrifuge tubes with as little 1x PBS as possible. Samples for RNA extraction were flash frozen on dry ice in 100 % ethanol and stored at -80 °C until ready to process.

Quantification of Mandibular Mesenchyme

Mandibular mesenchyme was quantified in HH18, HH21, HH24, and HH27 duck, chick, and quail embryos. Trypsin-pancreatin solution was made at room temperature by dissolving (i.e., stirring for 15 minutes) 2.25 g of trypsin (Lot# 029K7012, cat. No. T7409-100G, Sigma-Aldrich, MilliporeSigma, St. Louis, MO, USA) and 0.75 g of pancreatin (Lot # SLBP2575V, cat. No. P1625-100G, Sigma-Aldrich, MilliporeSigma, St. Louis, MO, USA) in HBSS (Gibco® Hanks' Balanced Salt Solution, cat. No. 14175095, Thermo Fisher Scientific by Life Technologies Corporation, Grand Island, NY, USA). Pre-made trypsin-pancreatin solution was stored at -20 °C in 5 mL single use aliquots. The solution was thawed prior to dissection, filter sterilized using a 5 mL syringe (cat. No. 309646, BD Vacutainer Labware Medical, Fisher Scientific, Hanover Park, IL, USA) with 0.2 µm filter (cat. No. 431219, Corning Life Sciences Plastic, Lowell, MA, USA), and kept on ice until ready for use.

Isolated mandibular primordia were incubated in 0.5 mL trypsin-pancreatin solution at 4 °C on

a rocker. Incubation length varied for each stages and species due to differences in size. Incubation times are listed in Table 2. The trypsin-pancreatin solution was replaced with 1 mL of ice-cold HBSS to inhibit the enzymatic reaction. Samples were washed for 5 minutes at 4 °C on rocker. The solution was replaced with 1 mL of ice-cold Dulbecco's Modified Eagle's Medium (cat. No. 11965092, Thermo Fisher Scientific by Life Technologies Corporation, Grand Island, NY, USA) and samples were kept on ice.

Mandibular epithelium was removed using two pairs of sharp forceps. Isolated mandibular mesenchyme was transferred into 1.5 mL microcentrifuge tubes containing 200 µL for HH18, 500 µL for HH21 and HH24, and 900 µL for HH27 of Dulbecco's Modified Eagle's Medium; homogenized by pipetting until all clumps were separated into single cells; and kept on ice. Mandibular mesenchyme (i.e., cell number per mandibular primordium) was counted using a hemacytometer (cat. No. 1492, Hausser Scientific Partnership, Fisher Scientific, Hanover Park, IL, USA) in combination with MIPAR software (Sosa et al., 2014; Tyler and Hall, 1977). Mean, SEM, Number of biological replicates for each species and data point are listed in Table 4.

Extraction of RNA

Total RNA was extracted from mandibula primordia at HH15, HH18, HH21, HH24, and HH27, explant tissue cultures, *Gas1* overexpression stable cell lines (DF-1), and whole heads and forelimbs at HH24 using the Arcturus PicoPure RNA Isolation kit (cat. No. KIT0214, Applied Biosystems™, ThermoFisher Scientific by Life Technologies Corporation, Grand Island, NY, USA) and following these steps:

1. RNA extraction
 - a. Whole mandibular primordia and explant tissue culture: 85 µL of extraction buffer

was added to each sample.

- b. Cell culture: Complete media was removed from wells and cells were washed twice with 300 μL of RNase-free 1x PBS. 150 μL of extraction buffer was added per well. Cells were scraped off of the well with 200 μL pipette and transferred into 1.5 mL microcentrifuge tube.

Sample homogenization was carried out in a Bead Mill 24 Homogenizer (cat. No. 15-340-163, Fisher Scientific, Hanover Park, IL, USA) at 4 m/s for 15 s ($C = 1$, $D = 0$). Samples were spun down for 2 minutes at 16,000 RCF then incubated in water bath at 42 °C for 30 minutes. Samples were vortexed for 2 s in the middle of the incubation.

2. RNA isolation

Extraction tubes were pre-treated following manufacturer's directions. 85 μL of RNase-free 70 % ethanol, made by diluting 100 % ethanol (cat. No. BP28184, Fisher Bioreagent, Fisher Scientific, Hanover Park, IL, USA), was added to the tissue/cell extract and mixed by pipetting 20 times up and down. The extract was transferred into pre-conditioned purification column and centrifuged following manufacturer's directions. 180 μL of RNase-free 70 % ethanol was added onto the column and centrifuged for 1 minute at 16,000 RCF. The rest of the protocol was carried out following manufacturer's directions. Residual genomic DNA was removed in on-column step using RNase-free DNase Set (cat. No. 79254, Qiagen, Germantown, MD, USA), 5 μL of DNase I mixed with 35 μL of RDD buffer. Total RNA was eluted in 16 μL of Elution buffer for whole mandibular primordia at HH15 and cell cultures and in 21 μL of Elution buffer for all other tissue.

Concentration and purity of RNA were assessed using a NanoDrop spectrophotometer (model ND-1000, Thermo Fisher Scientific by Life Technologies Corporation, Grand Island, NY, USA) and/or Qubit 4 fluorometer (cat. No. Q33222, Invitrogen, Fisher Scientific, Hanover Park, IL, USA) according to the manufacturer's instructions. Total RNA extracted in Elution buffer was stored at -80 °C.

Quantification of Total RNA Yield

Total RNA yield in mandibular primordia from duck, chick, and quail at HH16, HH18, HH21, HH24, and HH27; and from quack at HH21 and HH24 was calculated using the following equation:

$$\text{total RNA yield } [\eta\text{g}] = \text{total RNA concentration } \left[\frac{\eta\text{g}}{\mu\text{L}} \right] * \text{Elution Buffer volume } [\mu\text{L}]$$

Quantification of Sox10⁺ Cell Population

To quantify the amount of *Sox10*-positive NCM in HH10 chick embryos, we followed our previously published method using *in situ* hybridization (Fish et al., 2014). *Sox10*-positive cells were quantified on three sections through the mandibular primordia for three biological replicates and the resulting number represents the average of all counts.

Modelling Relative Population Size

To model cell counts per mandibular primordia, the size of *Sox10*-positive cell population, cell cycle length, and absolute developmental time were taken into account. The relative cell population size at HH13, HH15, HH18, HH21, HH24, and HH27 in duck and quail was calculated as ax^b , where x represents cell division (i.e., doubling event when a mother cell divides in two daughter cells) and is equal to 2, b represents the number of cell cycles that the cell population

for a particular species is able to go through within a period of time (e.g., from HH18 to HH21) and is calculated as follows $\frac{\text{absolute time [hours] from earlier stage to next stage}}{\text{cell cycle length}}$, and a is the relative cell population at a previous developmental time point (i.e., earlier stage). The starting relative population size at HH13 was set to 1 for quail and calculated for duck by dividing the duck *Sox10*-positive cell population by quail *Sox10*-positive cell population (data values previously published in Fish et al., 2014).

Preparation of cDNA Libraries

Depending on the total RNA amount per sample available 100, 200, or 400 ng of total RNA was reverse transcribed to cDNA in a 20 μ L reverse transcription reaction using 5 μ L of iScript reverse transcription supermix (cat. No. 1708841, Bio-Rad Laboratories - Life Sciences, Hercules, CA, USA), a corresponding volume of total RNA template (calculated with the formula: $\frac{100, 200 \text{ or } 400 [\text{ng}]}{\text{total RNA concentration}[\frac{\text{ng}}{\mu\text{L}}]}$), and sufficient nuclease-free water to bring the total volume up to 20 μ L.

The cDNA synthesis reaction involved four steps: 25 °C for 5 minutes, 42 °C for 30 minutes, 85 °C for 5 minutes, and 4 °C hold in a thermocycler (model C1000 Touch Thermal Cycler, Bio-Rad Laboratories - Life Sciences, Hercules, CA, USA). Lid temperature was set to 105 °C. cDNA libraries were stored at -20 °C.

Designing and Testing Primers for qRT-PCR

Species-specific primers were designed for *Shh*, *Ptc1*, *Cdon*, *Boc*, *Smo*, *Gas1*, *Gli1*, *Gli2*, and *Gli3* using Geneious Prime (Biomatters, San Francisco, CA, USA) (i.e., bioinformatics suite that incorporates Primer 3 (Koressaar and Remm, 2007; Untergasser et al., 2012)). Primer sequences are in Table 17. Design criteria for primers included a product size between 70 and 200 bp

(with optimal being 150 bp); a primer size minimum of 18 bp and maximum of 27 bp (with optimal being 20 bp); a T_m minimum of 50 °C and maximum of 65 °C (with optimal being 60 °C); a GC content minimum of 45% and maximum of 60% (with optimal being 50%); a maximum T_m difference for primer pair of 5 °C; a maximum dimer T_m of 40 °C; a maximum 3' stability of 9; a GC clamp of 1; and a maximum Poly-X of 3. The SantaLucia 1988 formula and salt concentration were set for T_m calculation with concentration settings of 50 mM for monovalent cations, 3 mM for divalent cations, 500 nM for oligos, and 0.8 mM for dNTPs. Gene sequences were checked for SNPs and those regions were avoided. Primer pairs for all genes spanned the same region for all three species. For genes with multiple splice variants, primers were designed to regions present in all known isoforms. To prevent protentional amplification of genomic DNA, all primer pairs, with the exception of *Gas1* (which has a single exon), were designed to span exon-exon junctions. All potential primer pairs were blasted using Primer Blast (Ye et al., 2012) against the genomes of duck, chick, and quail to avoid cross reactivity and amplification of unintended target sequences. Selected primer pairs were ordered from IDT (Integrated DNA Technologies, Coralville, IA, USA) with standard desalting. Lyophilized primers were diluted in an appropriate amount of RNase/DNase free water to make a stock concentration of 100 μ M, which was stored at -20 °C. Prior to use, the stock solution was diluted 1:10 (i.e., working concentration).

To validate species-specific primers, RNA was extracted from whole heads and forelimbs of HH24 duck, chick, and quail embryos as described above. 400 ng of RNA was reverse transcribed to cDNA and cDNA was diluted to a concentration of 2 ng/ μ L (1x). Standard curves with five serial dilutions (1:4, 1:16, 1:64, and 1:256) for each species-specific primer pair were generated from a 25 μ L reaction mixture (1.5 μ L of forward primer at working concentration,

1.5 μL of reverse primer at working concentration, 4 μL of cDNA, 6 μL of RNase/DNase free water, and 12.5 μL of iQ SYBR-Green Supermix (cat. No. 1708884BUN, Bio-Rad Laboratories - Life Sciences, Hercules, CA, USA)), run in technical triplicates on hard-shell PCR white 96-well plates (cat. No. HSP9601, Bio-Rad Laboratories - Life Sciences, Hercules, CA, USA), sealed with optically clear microseal film for PCR plates (cat. No. MSB1001, Bio-Rad Laboratories - Life Sciences, Hercules, CA, USA), and following the protocol described below. Controls for each run included no reverse transcription and no cDNA.

Melt curves were checked for primer specificity (i.e., single product) and for excluding samples with potential genomic DNA contamination. To confirm the correct products size, 1x samples were run on a 1 % Agarose gel (cat. No. BP1356-500, Fisher Bioreagent, Fisher Scientific, Hanover Park, IL, USA) in 1x TAE buffer at 110 V for 30 minutes. The Quick-Load 100bp Ladder (cat. No. N0467S, New England BioLabs, Ipswich, MA, USA) was used as a size reference.

For selected primers, products were amplified in a 25 μL PCR reaction mixture using a thermocycler (model C1000 Touch Thermal Cycler, Bio-Rad Laboratories - Life Sciences, Hercules, CA, USA). PCR reaction reagents included 2.5 μL of 10x Buffer (cat. No. 42-800B3, Apex Biosearch Products, Genesee Scientific, El Cajon, CA, USA), 0.5 μL of dNTPs (cat. No. 17-106, PCR Biosystems, Genesee Scientific, El Cajon, CA, USA), 0.75 μL of MgCl_2 (cat. No. 42-800B3, Apex Biosearch Products, Genesee Scientific, El Cajon, CA, USA), 1.25 μL of DMSO (cat. No. D128-500, Fisher Chemical, Fisher Scientific, Hanover Park, IL, USA), 0.125 μL of Taq (cat. No. 42-800B3, Apex Biosearch Products, Genesee Scientific, El Cajon, CA, USA), 1.25 μL of forward primer at working concentration, 1.25 μL of reverse primer at working concentration, 13.0 μL of DNase/RNase-free water, and 4.375 μL of cDNA at the concentration of 2 ng/ μL . The protocol for product amplification was: Step 1, 94 $^\circ\text{C}$ for 2 minutes; step 2,

94 °C for 2 minutes; step 3, 57.5 °C for 30 seconds; step 4, 72 °C for 1 minute; steps 2 to 4 were repeated 39 times; step 5, hold at 4 °C. Lid temperature was set to 105 °C. To verify primer pair products, PCR product clean up and sequencing was done by Molecular Cloning Laboratories (www.mclab.com, South San Francisco, CA, USA).

Analysis of Gene Expression by qRT-PCR

4.6 µL aliquots of cDNA (1 ng/µL) were prepared and stored in 0.2 mL snap strip PCR tubes with dome caps (cat. No. 490003-692, GeneMate – BioExpress, VWR International, Brisbane, CA, USA) at -20 °C prior to qRT-PCR plates preparation. Only a portion (i.e., volume necessary to run qRT-PCR for selected genes and primer pairs) of the total volume of working solution for each sample was aliquoted and the remaining volume stored in 0.5- or 1.5-mL microcentrifuge tubes at -20 °C until ready for the next usage to prevent the number of freeze-thaw cycles.

qRT-PCR was performed in a C1000 Touch Thermal Cycler with a CFX96 Real-Time System (cat. No. 1855196, Bio-Rad Laboratories - Life Sciences, Hercules, CA, USA). The reaction mixture for each well contained 1.25 µL of forward primer at working concentration, 1.25 µL of reverse primer at working concentration, 2 µg of cDNA (i.e., 2 µL at the concentration of 1 ng/µL), 10 µL of iQ SYBR-Green Supermix (cat. No. 1708884BUN, Bio-Rad Laboratories - Life Sciences, Hercules, CA, USA), containing dNTPs, iTaq DNA polymerase, MgCl₂, SYBR Green I, enhancers, stabilizers, and fluorescein, and 5 µL of RNase-free water. Samples were run in technical duplicates on hard-shell PCR white 96-well plates (cat. No. HSP9601, Bio-Rad Laboratories - Life Sciences, Hercules, CA, USA) sealed with optically clear microseal film for PCR plates (cat. No. MSB1001, Bio-Rad Laboratories - Life Sciences, Hercules, CA, USA) using tested protocol. The protocol steps were following: Step 1, 95 °C for 3 minutes; step 2, 95 °C for 10 seconds;

step 3, 60 °C for 30 seconds and a plate read; steps 2 and 3 were repeated 39 times; step 4, 95 °C for 10 seconds; step 5, melt curve of 60-90 °C for 5 seconds at each 0.5 °C with a plate read. Lid temperature was set to 105 °C. Melt curves were used to assess the specificity of primers and to exclude samples with potential genomic DNA contamination. Gene expression levels were quantified using the Pfaffl method (Pfaffl, 2001). Levels were normalized to *r18s*. A custom python script (see Chapter 4) was developed for data processing in order to manage large numbers of files and to avoid user-introduced error during analysis.

Culture of Mandibular Primordia and Biochemical Treatments

For explant cultures, dissected mandibular primordia were processed as described previously (Eames and Schneider, 2008; Merrill et al., 2008). Briefly, isolated mandibular primordia were placed onto a small circular piece of nitrocellulose membrane filter (cat. No. AAWP04700, MilliporeSigma, St. Louis, MO, USA), which was then transferred to a 50 mm Petri dish containing Dulbecco's Modified Eagle's Medium (DMEM) (cat. No. 11965092, Thermo Fisher Scientific by Life Technologies Corporation, Grand Island, NY, USA). Nitrocellulose membrane filters were cut prior to use with a sterilized metal 6 mm pore diameter punch pliers. Mandibular primordia were positioned into the center of the membrane filter, which was then placed into a transwell plate (cat. No. 3413, Corning Life Sciences Plastic, Lowell, MA, USA) containing 325 µL of complete media (75% Dulbecco's Modified Eagle's Medium, 10% Horse serum (cat. No. 16050122, Thermo Fisher Scientific by Life Technologies Corporation, Grand Island, NY, USA), and 15% chick embryo extract ultrafiltrate (cat. No. C3999, US Biological Life Sciences, Salem, MA, USA) and incubated at 37 °C with 5% CO₂.

To make SHH stock solution lyophilized human recombinant (r) SHH protein (Lot #1362 for mandibular primordia explants and #1371 for cell culture, cat. No. SHH-005/SHH-100, StemRD,

Burlingame, CA, USA) was reconstituted in sterile water to a concentration of 100 ng/ μ L. Stock solution was stored at -80 °C in 7.15 μ L aliquots. 45 μ L aliquots of rSHH protein was diluted in complete media to achieve final concentrations of 0.1, 1, 10, 100, or 1000 ng/mL. To make cyclopamine stock solution, lyophilized Cyclopamine-KAAD (Lot # 2944661, cat. No. 239804, MilliporeSigma, Burlington, MA, USA) was reconstituted following the manufacturer's instructions to a concentration of 4 ng/ μ L and stored at -20 °C in 20 μ L aliquots.

Mandibular primordia were placed with the oral side down on the membrane for control and rSHH treatments, and with the aboral side on the membrane for cyclopamine treatments. 45 μ L of rSHH protein at each concentration were added to the side of each well. rSHH protein was mixed into the complete media by rotating the 24-well plate. For cyclopamine treatment, 40 μ L of complete media was added to the side of each well and 5 μ L of the cyclopamine stock solution was pipetted on top of the mandibular primordia. For control samples, 45 μ L complete media was added to the side of each well. The final volume per well, after adding rSHH protein at each concentration, cyclopamine, or complete media was 370 μ L.

After 24 hours, explants were removed from the transwells and transferred into 50 mm Petri dishes containing RNase-free ice-cold 1x PBS. Explants were carefully detached from the cellulose membrane using a pair of forceps and a 1 mL syringe (cat. No. 329654, BD Vacutainer Labware Medical, Fisher Scientific, Hanover Park, IL, USA) with a 30 gauge by 0.5-inch needle (cat. No. 305106, BD Vacutainer Labware Medical, Fisher Scientific, Hanover Park, IL, USA). Each explant was transferred into a 1.5 mL microcentrifuge tube with snap cap with as little 1x PBS as possible, flash frozen on dry ice, and stored at -80 °C. Harvested explants were processed for qRT-PCR as described above.

Generating Probes for In Situ Hybridization

PCR primers were designed against the coding region of *Gas1* using Primer3 (Untergasser et al., 2012) targeting a conserved region in duck, chick, and quail that would generate a ~650 bp probe. Primers were synthesized with and without T7 RNA polymerase promoter consensus sequence 5'- TAA TAC GAC TCA CTA TAG GG -3' as a primer tail. The forward primer with the T7 RNA polymerase promoter was used to generate sense template and the reverse primer with T7 RNA polymerase promoter was used to generate antisense template. Q5 Hot Start High-Fidelity DNA Polymerase (cat. No. M0493L, New England BioLabs, Ipswich, MA, USA) was used to amplify the templates for *in vitro* transcription. *In vitro* transcription was carried out using T7 RNA polymerase (cat. No. M0251S, New England BioLabs, Ipswich, MA, USA) following the manufacturer's directions with digoxigenin (DIG) RNA Labeling Mix (cat. No. 11277073910, Roche, Basel, Switzerland) to generate DIG labelled probe. RNaseOUT (cat. No. 10777019, Invitrogen, Carlsbad, CA, USA) was used to protect the RNA from degradation during synthesis. *In vitro* transcription was carried out at 37 °C for 2 hours. Following *in vitro* transcription, DNA was degraded using DNase I (cat. No. 4716728001, Roche, Basel, Switzerland). RNA probes were then precipitated with LiCl and ethanol. RNA probes were resuspended in MilliQ water and then mixed with an equal volume of formamide (cat. No. F1085, Spectrum Chemical, New Brunswick, NJ, USA) to stabilize the RNA. Probes were stored at -20 °C until ready for use. Primer sequences for species-specific *Gas1* probes are listed in Table 18.

Analysis of Gas1 Expression by In Situ Hybridization

Mandibular primordia were isolated from duck, chick, and quail embryos at HH21 and HH27 using forceps and placed in RNase-free ice-cold 1x PBS. Samples were transferred into 15 mL

conical tubes and fixed in 4% paraformaldehyde (PFA) at 4 °C for two hours. Samples were washed three times for 30 minutes at room temperature in 1x PBS followed by 30 minutes washes in 25%, 50%, and 75% methanol in 1x PBS and three times in 100% methanol (cat. No. A412-4, Fisher Chemical, Fisher Scientific, Hanover Park, IL, USA). Samples were stored at -20 °C in 100% methanol until processing.

Whole mount *in situ* hybridization was performed following published protocols (Fish et al., 2014; Merrill et al., 2008). A solution of Proteinase K (cat. No. P6556, Sigma-Aldrich, MilliporeSigma, St. Louis, MO, USA) in 1x PBS was used at a concentration of 10 µg/mL for HH21 embryos and 20 µg/mL for HH27 embryos. Incubation times were 25 minutes for HH21 embryos and 15 minutes for HH27 embryos. Following the color reaction, developed for 2 hours at room temperature then for 14 hours at 4 °C, mandibular primordia were imaged on a stereo dissecting microscope under brightfield illumination (model MZFLIII-TS, Leica Microsystems, Buffalo Grove, IL, USA).

Cloning Full-Length Gas1

Full-length cDNA synthesis from RNA was performed using Maxima H Minus reverse transcriptase (cat. No. K1651, Thermo Scientific, Fisher Scientific, Hanover Park, IL, USA) following the manufacturer's directions with 2 µg of total RNA and 100 pmol of d(T)₂₀ VN primer. The cDNA synthesis reaction was carried out at 50 °C for 30 minutes, 55 °C for 10 minutes, 60 °C for 10 minutes, 65 °C for 10 minutes, and 85 °C for 5 minutes. Full length duck, chick, and quail *Gas1* was amplified by PCR in a thermocycler (model 2720 Thermal Cycler Applied Biosystems, Carlsbad, CA, USA) using Q5 Hot Start High-Fidelity DNA Polymerase (cat. No. M0493L, New England BioLabs, Ipswich, MA, USA) and cloned using CloneJET PCR Cloning Kit (cat. No. K1231, Thermo Scientific, Fisher Scientific, Hanover Park, IL, USA). Full-length duck,

chick, and quail *Gas1* were confirmed by Sanger sequencing. *Gas1* was cloned into the pPIDNB plasmid, which integrates into the genome and is doxycycline (dox)-inducible (Chu et al., 2020), using AflIII (cat. No. R0520S, New England BioLabs, Ipswich, MA, USA), PstI (cat. No. R3140S, New England BioLabs, Ipswich, MA, USA), and NEBuilder HiFi DNA Assembly Master Mix (cat. No. E2621L, New England BioLabs, Ipswich, MA, USA). All constructs were verified by Sanger sequencing and midprepped for electroporation and/or transfection using PureLink Fast Low-Endotoxin Midi Kit (cat. No. A36227, Invitrogen, Fisher Scientific, Hanover Park, IL, USA) (Chu et al., 2020). Empty pPIDNB plasmid was used as a control.

Preparation of Micropipettes

Micropipettes for DNA injection were generated using a micropipette puller (model P-87 Flaming/Brown, Sutter Instrument Co., Novato, CA, USA). Borosilicate capillary glass without a filament and with an outside diameter of 1 mm and an inner diameter of 0.75 mm (cat. No. B100 – 75 – 10, Sutter Instrument Co., Novato, CA, USA) was used. Program settings were as follows: Heat = 693, Velocity = 50, Pull = 100, Time = 250, Press = 300.

*The Use of Cell Culture and Generation of Stable *Gas1*-Expressing Lines*

A fibroblast cell line (UMNSAH/DF-1) from embryonic chick (*Gallus gallus*) was obtained from the American Type Culture Collection (cat. No. CRL-12203, ATCC, Manassas, VA, USA) and maintained as directed. DF-1 cells were cultured in complete media (i.e., Dulbecco's Modified Eagle's Medium (DMEM) (cat. No. 10-013-CV, Corning Mediatech Inc., Lowell, MA, USA) supplemented with 10 % Fetal Bovine Serum (FBS) (Lot# 283K18, cat. No. 97068-085, VWR International, Brisbane, CA, USA) and 1x penicillin-streptomycin (cat. No. 15140122, Thermo Fisher Scientific by Life Technologies Corporation, Grand Island, NY, USA)) at 37 °C with 5 % CO₂. Cells were passaged twice a week.

DF-1 cells were transfected with lipofectamine 3000 reagent (cat. No. L3000008, Invitrogen by Life Technologies Corporation, Grand Island, NY, USA) according to the manufacturer's protocol. Transfections for integrating empty pPIDNB, pPIDNB-chick-*Gas1*, or pPIDNB-quail-*Gas1* were carried out in 6-well plates (cat. No. 353046, Corning Life Sciences DI, Corning, NY, USA) in technical duplicates. 500,000 cells were seeded per well 24 hours prior to transfection. Transfections were done using 2.5 µg of plasmid, 2.5 µg of pNano-hyPBase, and 10 µL of P3000 (Chu et al., 2020). Cells were incubated for 12 to 15 hours and then washed with 2 mL of a 0.25 % trypsin solution (cat. No. 25200056, Gibco®, Fisher Scientific, Hanover Park, IL, USA) in 1X EDTA. Transfection efficiency was confirmed by visualizing fluorescence of constitutively active mNeonGreen in the pPIDNB plasmid (Chu et al., 2020) on a Nikon AZ100 C2+ Macro Confocal Microscope (Nikon Instrument, Inc., Melville, NY). Transfected cells from 2 wells (technical duplicates) were seeded into 250 mL cell culture flasks with vented caps (cat. No. 10062-860, VWR International, Brisbane, CA, USA).

Eight days post transfection, complete media was removed, cells were washed with 2 mL of trypsin and incubated in 3 mL of trypsin at room temperature until they started to detach from the bottom of the flask. Trypsin activity was inhibited by adding 5 mL of DMEM with 10% FBS. Cells were pipetted and passed through a 70 µm filter (cat. No. 352235, Corning Life Sciences DI, Reynosa, Tamaulipas, México). Cells were sorted on a FACSAriaII Flow Cytometer (BD Bioscience, San Jose, CA). All debris and dead cells were eliminated using FSC-A and SSC-A gating, doublets were excluded via gating discrimination using FSC-H and FSC-W, and two cell populations per construct (GFP⁺ and GFP⁻) were collected. Voltages used were 181 for FSC, 355 for SSC, and 363 for 530/30 blue C laser. Each cell population was collected into a 15 mL conical tube containing 3 mL of complete media. Three stable cell lines were generated: DF-1

containing an empty pPIDNB expression vector, DF-1 containing the chick *Gas1* pPIDNB expression vector, and DF-1 containing the quail *Gas1* pPIDNB expression vector. Each cell line was split into four flasks and incubated until reaching 90% confluency. Then cells from 3 flasks were detached as described, transferred into 15 mL conical tubes, and spun down at 200 x g for 5 minutes. Supernatant was carefully removed and cells resuspended in 3 mL of complete media. 1 mL of resuspended cells was transferred into a 2 mL cryogenic vial (cat. No. 430659, Corning Life Sciences Plastic, Lowell, MA, USA) and frozen overnight at -80 °C in a NALGENE™ Cryo 1 °C freezing container (cat. No. 5100-0001, Thermo Scientific, Fisher Scientific, Hanover Park, IL, USA) filled with isopropanol (cat. No. 423830025, Acros Organics, Fisher Scientific, Hanover Park, IL, USA). Cells were then stored at -140 °C in liquid nitrogen (CryoPlus™ Storage Systems model 7402, Thermo Scientific, Fisher Scientific, Hanover Park, IL, USA).

To quantify the number of cells per well, DF-1 cells were dissociated and counted using a hemacytometer (cat. No. 1492, Hausser Scientific Partnership, Fisher Scientific, Hanover Park, IL, USA) (Tyler and Hall, 1977). For quantification, DF-1 cells were imaged on a Zeiss Axiovert 40 CLF trinocular inverted microscope (Carl Zeiss AG, Göttingen, Germany) using fluorescence and phase contrast. All cell culture experiments were carried out using the same lot of DF-1 cells.

Electroporation

A DNA solution containing 3 µg/µL pPIDNB (empty or containing *Gas1*), 1 µg/µL pNano-hyPBase plasmid, and 0.5 µL of 1% Fast Green was loaded into a glass micropipette (described above) and delivered with a picospritzer fluid injector (model PV830 Pneumatic PicoPump, cat. No. SYS-PV830, World Precision Instruments, Sarasota, FL, USA). To target the presumptive NCM that migrates into the mandibular primordia (Fish et al., 2014), DNA solution was injected

into the lumen of the dorsal neural folds from the anterior hindbrain to the anterior midbrain of HH8.5 duck and quail embryos. Homemade platinum electrodes (cat. No. 78-0085, Strem Chemicals Inc., Fisher Scientific, Hanover Park, IL, USA) mounted in an Adjustatrod holder (cat. No. 01-925-09, Intracel by Abbotsbury Engineering Ltd., St Ives, UK) were positioned on each side of the area pellucida, centered on the midbrain-hindbrain boundary. The distance between electrodes was set to 5 mm. The electrodes were overlaid with albumin to prevent drying and to facilitate conductivity.

In ovo electroporation was performed using a BEX CUY21EDITII Pulse Generator (cat. No. CUY21EDIT2, BEX CO., LTD, Tokyo, Japan). Unilateral electroporations involved three square pulses delivered at 50 V with 10% decay for 1 ms spaced 50 ms apart followed by five square pulses at 10 V with 20% decay for 50 ms spaced 50 ms apart. Bilateral electroporations involved three square pulses at 50 V with 10% decay for 1 ms spaced 50 ms apart, three square pulses at 50 V with 10% decay for 1 ms spaced 50 ms apart in the reverse polarity, three five square pulses at 10 V with 20% decay for 50 ms spaced 50 ms apart followed by five square pulses at 10 V with 20% decay for 50 ms spaced 50 ms apart in the reverse polarity.

After electroporation, a small amount of albumin was added on top of the embryo to prevent desiccation. Eggs were sealed with tape and incubated at 38.5 °C. After 24 hours, electroporation efficiency was confirmed by visualizing fluorescence *in ovo* of constitutively active mNeonGreen in the pPIDNB plasmid (Chu et al., 2020) on a Nikon AZ100 C2+ Macro Confocal Microscope (Nikon Instrument, Inc., Melville, NY). Eggs were re-sealed with tape, incubated until reaching HH15, and treated with dox (see below).

Treatment with Doxycycline

Stock solution of doxycycline hyclate (dox) (cat. No. 446060250, Acros Organics, Fisher Scientific, Hanover Park, IL, USA) was made up to final concentration of 1 mg/mL in filter sterilized water. Single use 50 μ L aliquots of stock solution were stored at -20 °C.

For cell culture, dox stock solution was diluted to final concentrations of 0.1, 1, 5, 10, or 50 ng/mL in complete media (i.e., DMEM supplemented with 10 % FBS and 1x penicillin-streptomycin). Dox treatment was performed by replacing complete media with prepared complete media containing appropriate dox concentrations. For control samples, complete media was replaced with fresh complete media without dox.

For *in ovo* dox treatments, egg volumes were considered to be 75 mL for duck and 8 mL for quail. A dox working solution was made up by mixing 7.5 μ L for duck and 0.8 μ L for quail of stock (i.e., 1mg/ml) dox solution with 750 μ L for duck and 200 μ L for quail of HBSS (Gibco® Hanks' Balanced Salt Solution, cat. No. 14175095, Thermo Fisher Scientific by Life Technologies Corporation, Grand Island, NY, USA). Prepared working solution was gently pipetted through the egg window onto the vitelline membrane adjacent to the embryo and allowed to diffuse. The final dox concentration was 100 ng/mL. Eggs were sealed with tape and incubated until collection at HH18, HH21, HH24, and HH27. Duck mandibular primordia were isolated and imaged on a stereo dissecting microscope (MZFLIII-TS, Leica Microsystems, Buffalo Grove, IL, USA) under brightfield illumination or epifluorescent illumination to assess the distribution of *Gas1* overexpression as indicated by mScarlet fluorescence. The heads of quail at HH27 were stained with Hoechst (see below) and imaged on a stereo dissection microscope under epifluorescent illumination (MZFLIII-TS, Leica Microsystems, Buffalo Grove, IL, USA).

Injections with Vivo-Morpholinos

In ovo Vivo-Morpholino injections were performed using a 0.5 mM solution of Vivo-Morpholino (quail anti-*Gas1* or control anti-*GFP*) (Gene Tools, LLC, Philomath, OR, USA) in HBSS (Gibco® Hanks' Balanced Salt Solution, cat. No. 14175095, Thermo Fisher Scientific by Life Technologies Corporation, Grand Island, NY, USA) containing 0.01 % phenol red (cat. No. 417240050, Acros Organics, Fisher Scientific, Hanover Park, IL, USA). Vivo-Morpholino sequences are listed in Table 19.

Vivo-Morpholino solution was injected into the right side of quail mandibular primordia at HH18 with pulled glass micropipettes loaded into a PicoNozzle (cat. No. 5430-10, World Precision Instruments, Sarasota, FL, USA) and a picospritzer fluid injector (model PV830 Pneumatic PicoPump, cat. No. SYS-PV830, World Precision Instruments, Sarasota, FL, USA). After injection, eggs were sealed with tape and incubated until reaching HH27. The heads of treated embryos were stained with Hoechst (see below) and imaged on a stereo dissection microscope under epifluorescent illumination (MZFLIII-TS, Leica Microsystems, Buffalo Grove, IL, USA).

Staining with Hoechst Dye

To enhance contrast for phenotypic analysis, whole mount duck and quail embryos were stained with Hoechst 33342 (Lot# RF22228410, cat. No. 62249, Thermo Scientific, Fisher Scientific, Hanover Park, IL, USA). Briefly, a 20 mM stock solution was diluted 1:1000 in 1x PBS to a working solution of 1 µg/mL. Samples were incubated in working solution for 48 hours at 4 °C on a rocker.

Capture and Adjustment of Images

Brightfield and epifluorescent images were acquired with SPOT Insight 2.0 mandibular primordia Firewire Color Mosaic camera (cat. No. IN1820, Model 18.2.x) and SPOT image capture software (SPOT Imag3ing, Diagnostic Instrument, Inc., Sterling Heights, MI, USA). Multiple image planes were combined in Helicon Focus (version 7.6.1 Pro, Helicon Soft Ltd., 2000, Kharkiv, Ukraine). Images were adjusted in Adobe Photoshop 2020 (version 21.2.2) to normalize for exposure, brightness, contrast, saturation, and color balance across samples. Figures were assembled in Adobe Illustrator 2020 (Version 24.2.3). To label data points, the following colors were used: duck = violet/Medium Orchid, # D344DD; chick = yellow/Golden Dream, #F2D33C; quail = green/Magic Mint, #9FF4BA; and quack = blue/Calypso, #3C6B87.

Methods for Determining Statistical Significance

Prism (v.9.1.0) software (GraphPad, San Diego, CA, USA) was used to perform statistical tests and determine significance. Unpaired multiple t-tests were performed at each time point for analysis of total RNA extraction in mandibular primordia, mandibular mesenchyme population size, gene expression levels *in vivo*, as well as gene expression ratios. The Holm-Sidak method was used to correct for multiple comparisons. Ordinary one-way ANOVA was performed for analysis of gene expression following treatments in mandibular primordia explants and DF-1 cells, as well as for quantification of DF-1 cells when comparing different treatments to control samples. The Dunnett's multiple comparison test was used to correct for multiple comparisons. Error bars denote SEM. Multiplicity adjusted p-values were used to determine significance, and p values are indicated on the data points and/or legends of each figure. Formal power analyses were not conducted. The number of biological replicates for each data point and/or treatment group was between 2 and 17, specific number of biological replicates per data point and p-

values are listed in the Tables 20, 21, 22, 23, and 24.

Figures

Figure 17: Species-specific variation at early embryonic stages. **(A)** The Hamburger-Hamilton (HH) staging system (i.e., embryonic stage) functions independent of time (i.e., absolute time), and instead relies on external morphological characters (i.e., developmental time). Thus, duck (violet ●), chick (yellow ◐), and quail (green ◻) embryos can be aligned at equivalent stages by incubating them for different lengths of time. In ovo day represents the number of incubation days needed to reach equivalent stages for each species. **(B)** To generate quail-duck chimeras ("quck"), quail and duck embryos are stage-matched for surgery at HH9.5 (i.e., post-surgery day 0, ▼*) by incubating their eggs for different times (see panel **A** above). Bilateral neural folds from the mid-diencephalon (di) to rhombomere 2 (r2) of the hindbrain (dark green), which generate neural crest mesenchyme (NCM), are transplanted from quail to duck. Quail donor NCM (green cells) migrates (green arrows) into mandibular primordia between HH10 and HH15. Due to its faster rate of maturation, quail NCM develops approximately three stages ahead of the slower-maturing duck host within two days post-surgery. Quail NCM receives cues from and interacts with duck-host derived epithelium (violet arrows). **(C)** Mandibular mesenchyme (MM) population at HH18, HH21, HH24, and HH27 in duck (violet), chick (yellow), and quail (green) embryos. **(D)** Mandibular primordia (MP) total RNA extraction at HH15, HH18, HH21, HH24, and HH27 in duck (violet), chick (yellow), and quail (green) embryos and at HH21 and HH24 in quck (blue) embryos. **(E)** Content of total RNA per mandibular primordia cell at HH18, HH21, HH24, and HH27 in duck (violet), chick (yellow), and quail (green) embryos. **(F)** Mandibular primordia (MP) RNA extraction ratios comparing duck to quail at HH18, HH21, HH24, and HH27. **(G)** Relative mandibular mesenchyme population size modelling at HH15, HH18, HH21, HH24, and HH27 in duck

(violet) and quail (green) embryos using the number of migratory NCM cells, cell cycle length, and absolute time. **(H)** Relative mandibular mesenchyme population size based on duck to quail ratios for in vivo (white) and model (black) data at HH18, HH21, HH24, and HH27.

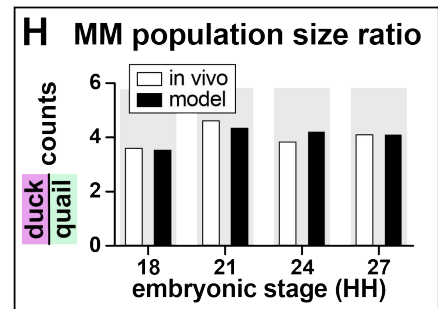
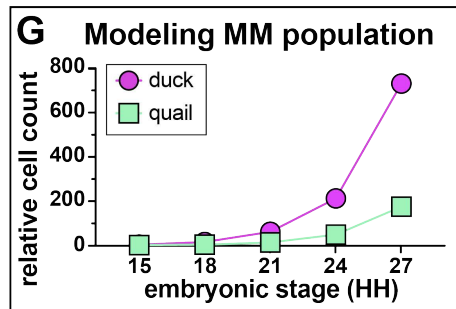
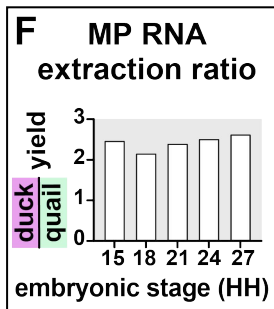
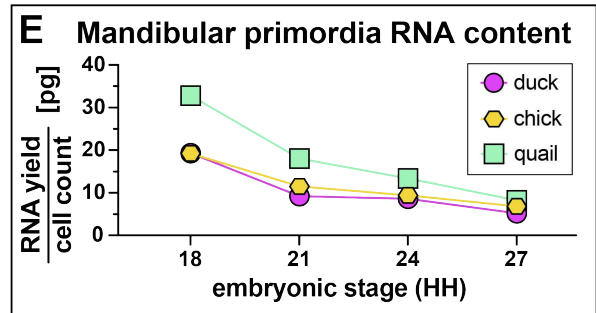
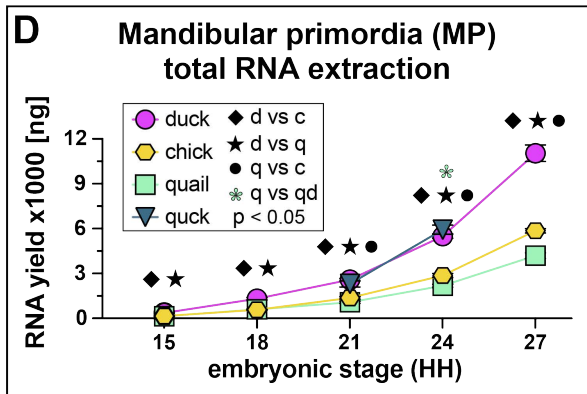
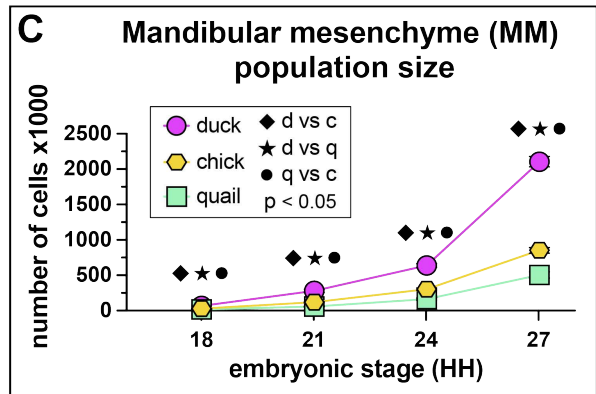
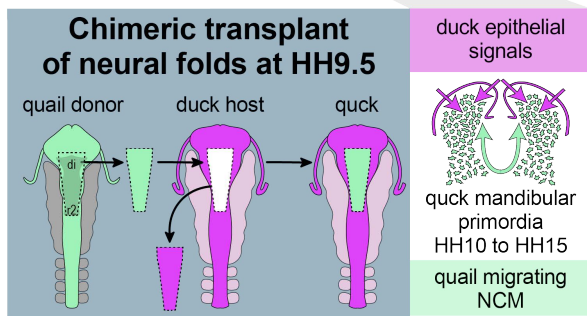
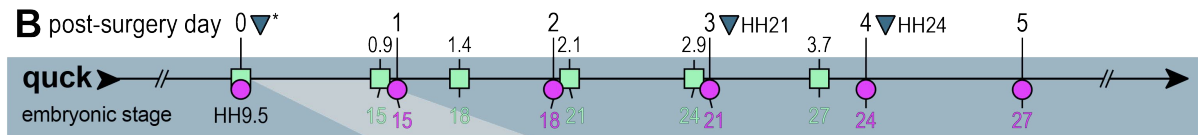
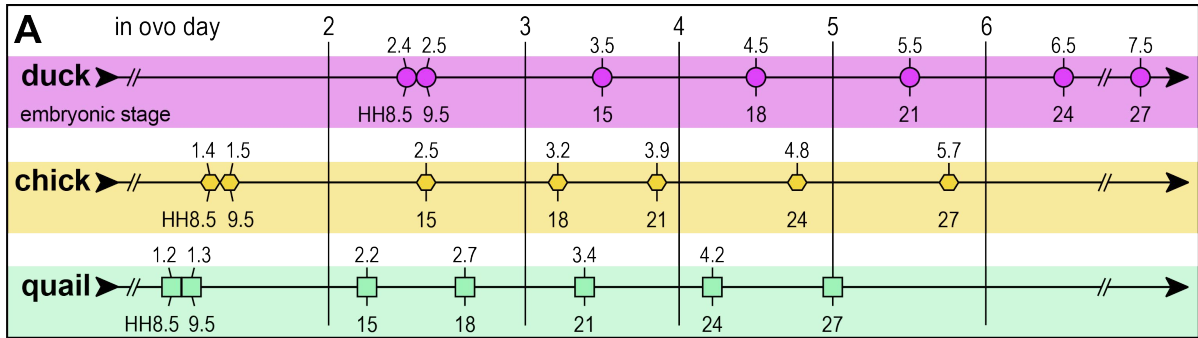


Figure 18: Expression of SHH pathway members and pathway activation in mandibular primordia of duck, chick, quail, and chimeric quck. Relative mRNA levels of **(A) *Shh***, **(B) *Ptch1***, **(C) *Gas1***, and **(D) *Gli1*** in mandibular primordia of duck (violet), chick (yellow), and quail (green) at HH15, HH18, HH21, HH24, and HH27 and at HH21 and HH24 of quck (blue) embryos. Expression levels were assayed by qRT-PCR and normalized to *r18s*. Significance is shown (p -value < 0.02 , $n \geq 6$ for each group and data point, and error bars represent SEM) for comparisons between different species at the same embryonic stage (i.e., diamond symbol for duck versus chick, asterisk symbol for duck versus quail, full circle symbol for quail versus chick, and violet asterisk symbol for duck versus quck). For quail versus quck, significance is shown (green asterisk symbol) at HH21 and denotes the comparison of HH24 quail versus HH21 quck, and at HH24 for the comparison of HH27 quail versus HH24 quck. SHH pathway activation as represented by ratios of **(E) *Shh* to *Ptch1*** and **(F) *Shh* to *Gli1*** mRNA levels for duck, chick, and quail at HH15, HH18, HH21, HH24, and HH27 and quck at HH21 and HH24. Significance is shown for comparisons between species as denoted by brackets and p -values are as indicated. $n \geq 6$ for each group and data point, and error bars represent SEM.

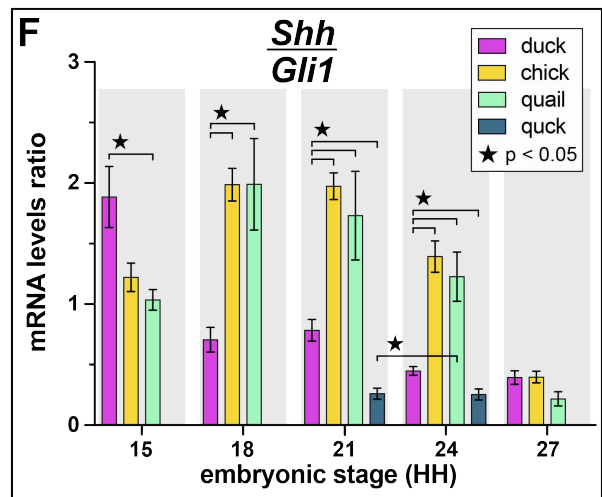
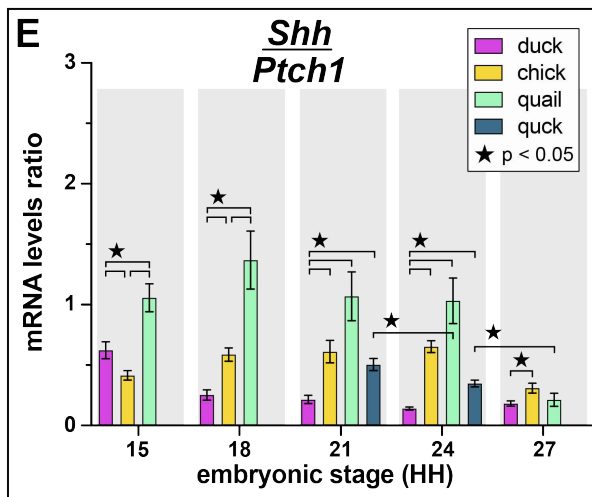
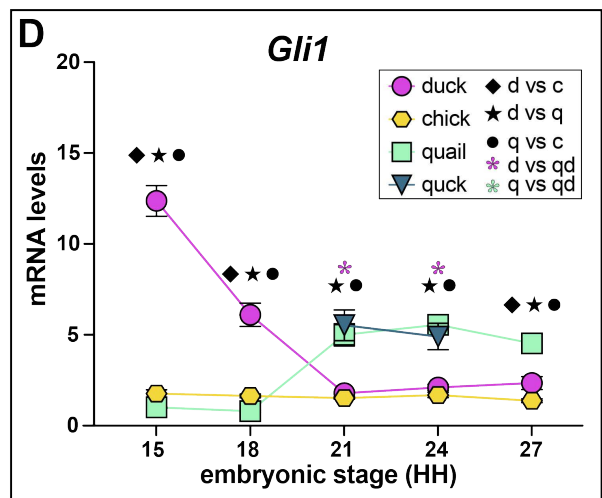
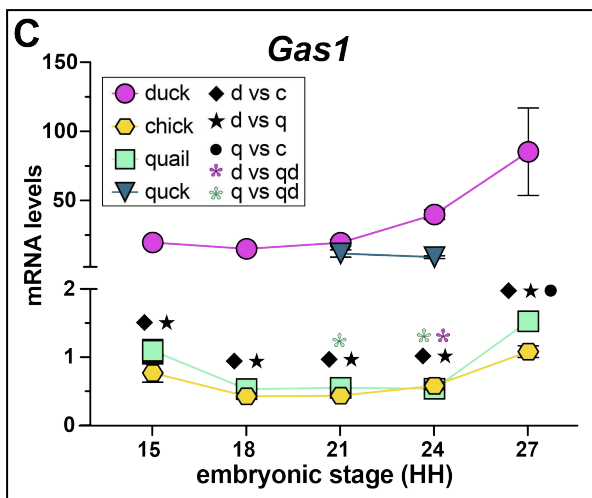
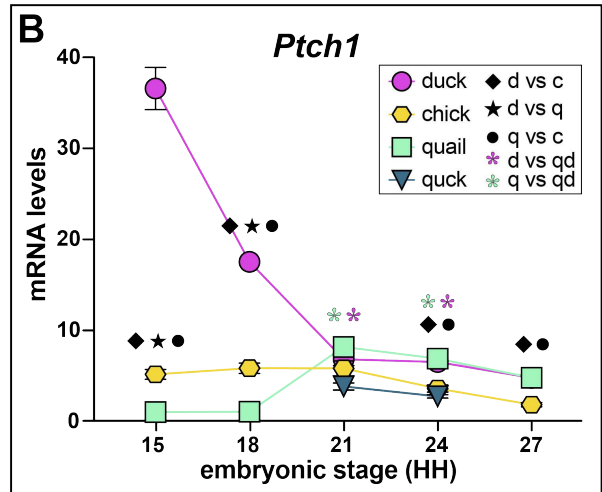
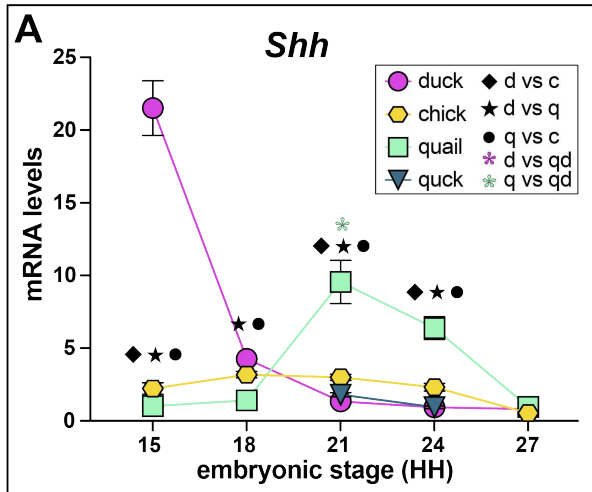


Figure 19: Effects of inhibition and activation of the SHH pathway in mandibular primordia of duck, chick, and quail. Mandibular primordia from duck (violet), chick (yellow), and quail (green) embryos were harvested at HH21, placed in culture, and treated with cyclopamine (cycl, dark grey) to inhibit the SHH pathway or with five serial dilutions of recombinant (r) SHH protein (light grey) to activate the SHH pathway. Box plots show relative levels of mRNA expression (on the y-axis in \log_2 scale) for SHH pathway members including **(A) *Ptch1*, (B) *Gas1*, (C) *Gli1*, (D) *Gli2*, and (E) *Gli3*** 24 hours after treatment. Control (ctrl, white) and treatment groups are shown on the x-axis. Expression levels were assayed by qRT-PCR and normalized to *r18s*. Significance is shown for comparisons between control and treatment groups (i.e., cyclopamine or rSHH) within the same species as indicated by colored shading and by the following symbols for p-values: * $p < 0.05$, ** $p < 0.01$, *** $p < 0.001$, and **** $p < 0.0001$. p-values ≥ 0.05 we considered not significant (ns). $n \geq 4$ for each group and data point.

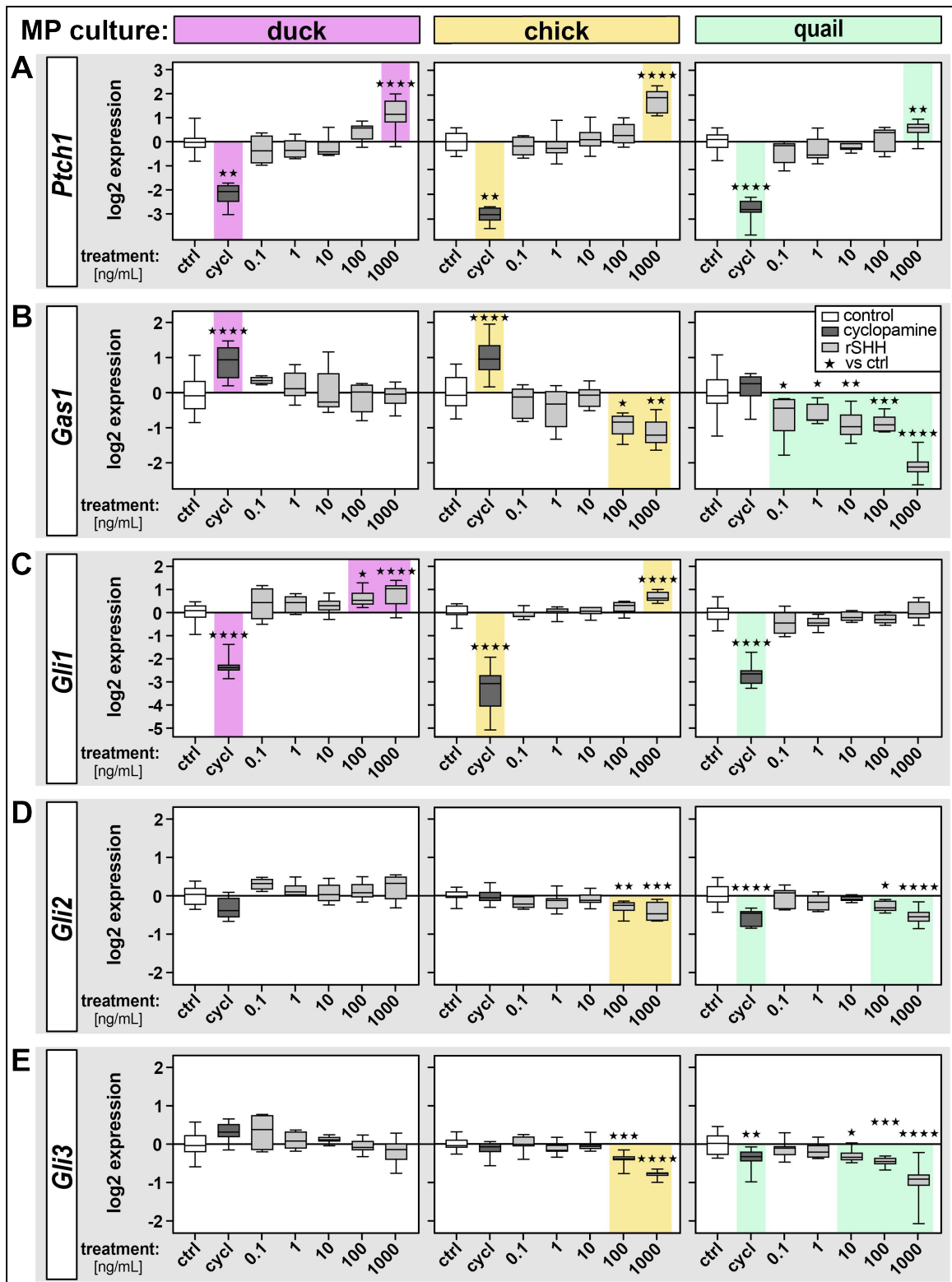


Figure 20: Expression of *Gas1* in mandibular primordia at early developmental stages.

Whole mount *in situ* hybridization showing *Gas1* expression (purple stain) in mandibular primordia from **(A)** duck, **(B)** chick, and **(C)** quail at HH21; and in **(D)** duck, **(E)** chick, and **(F)** quail at HH27.

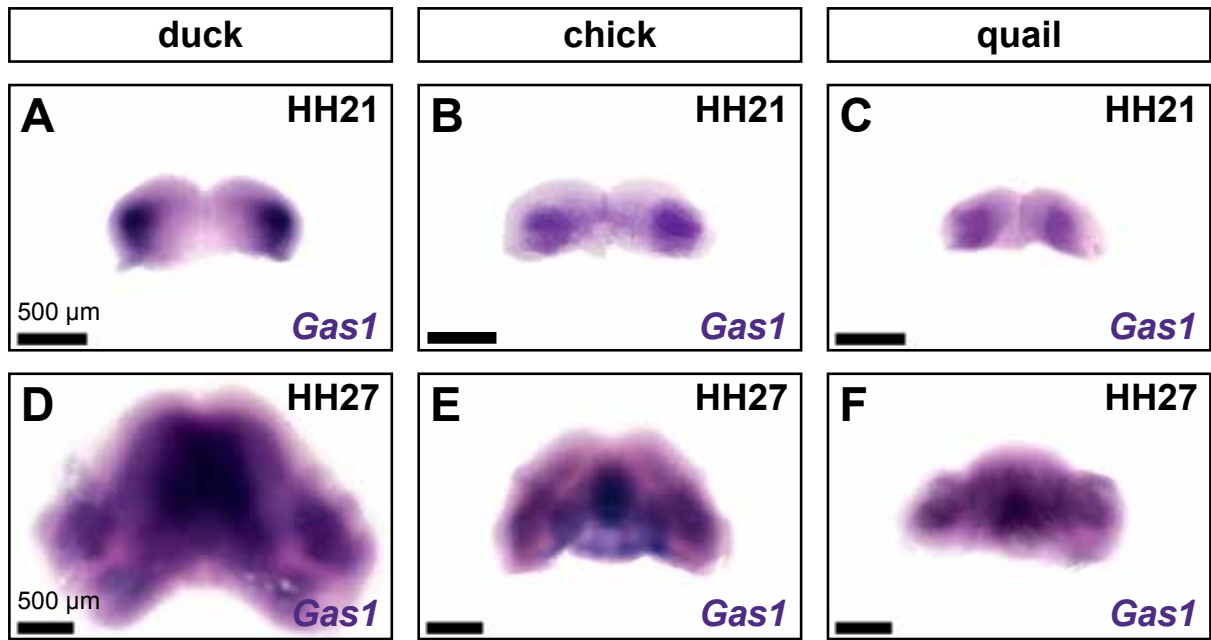


Figure 21: Effects of SHH pathway activation and *Gas1* overexpression in cell culture.

(A) Relative levels of mRNA expression (on the y-axis in \log_2 scale) for *Gas1*, *Ptch1*, and *Gli1* in chick fibroblasts (i.e., DF-1) 24 hours (h) after treatment with five serial dilutions of recombinant (r) SHH protein. **(B)** Relative *Gas1* mRNA levels in chick fibroblasts 24 hours after doxycycline (dox)-induction of a stably integrated chick *Gas1* overexpression vector. Number of chick *Gas1*-positive cells 72 hours after induction with dox. **(C)** Relative *Gas1* mRNA levels in chick fibroblasts 24 hours after dox-induction of a stably integrated quail *Gas1* overexpression vector. Number of quail *Gas1*-positive cells 72 hours after induction with dox. **(D)** Relative levels of mRNA expression for *Gas1*, *Ptch1*, and *Gli1* in chick fibroblasts 48 hours after treatment with serial dilutions of rSHH protein. Relative levels of mRNA expression for *Gas1*, *Ptch1*, and *Gli1* in chick fibroblasts 48 hours after dox-induction of a stably integrated *Gas1* overexpression vector (serial dilution) and treatment with rSHH protein (control 0 ng/mL in white and 100 ng/mL dark grey). Expression levels were assayed by qRT-PCR and normalized to *r18s*. Significance is shown for comparisons between control and treatment groups as denoted by brackets and p-values are as indicated. P-values ≥ 0.05 are considered not significant (ns). $n \geq 2$ for each group and data point, and error bars represent SEM.

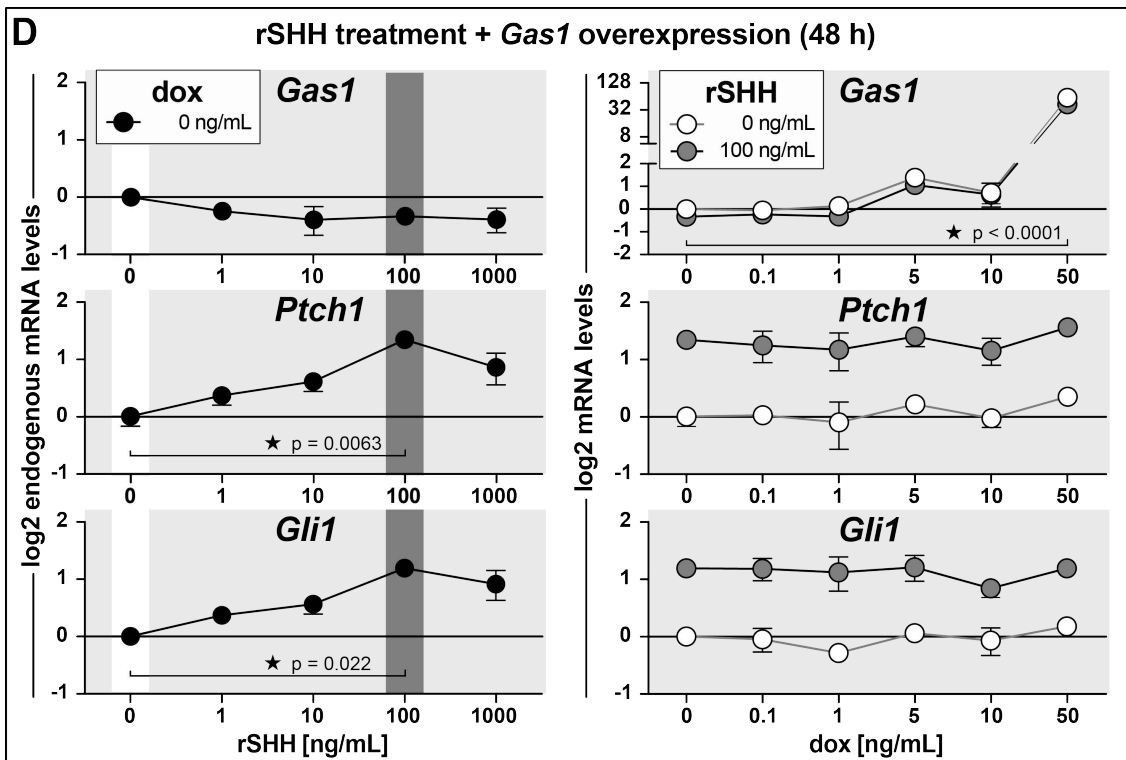
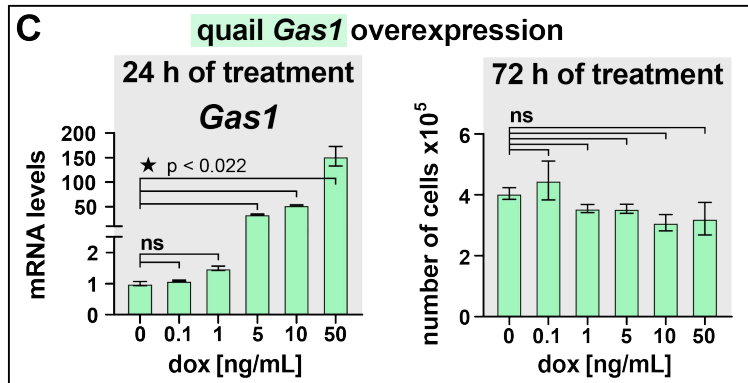
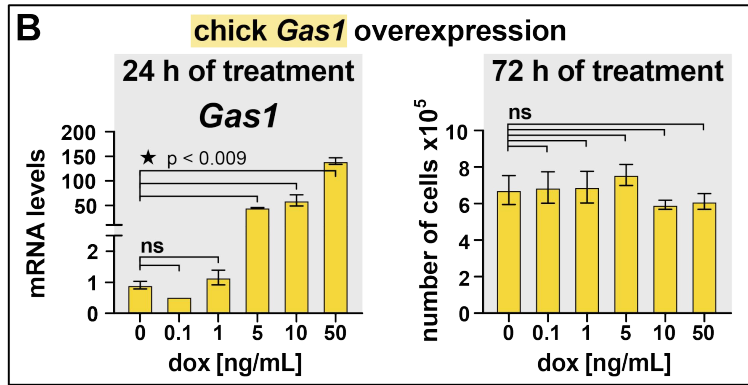
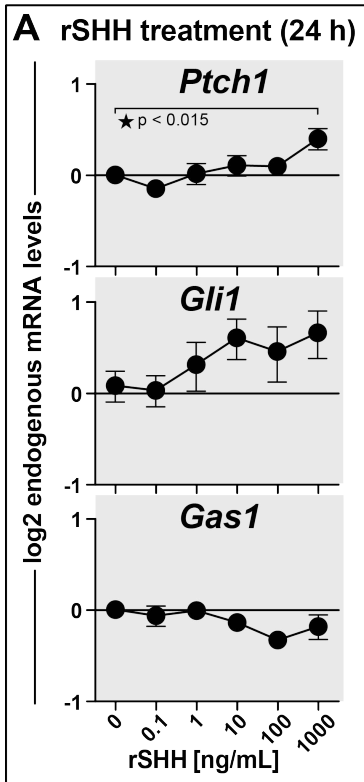
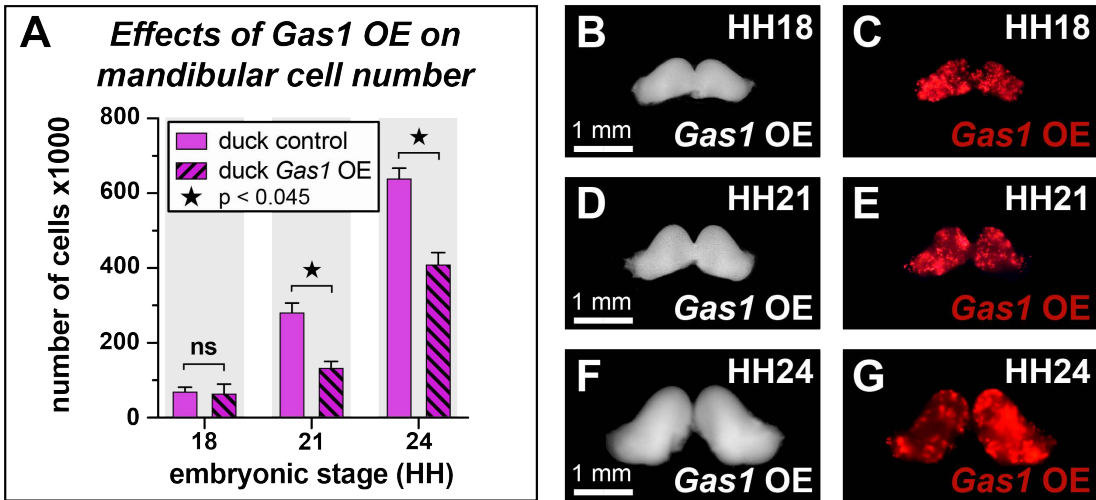


Figure 22: Effects of *Gas1* overexpression and knockdown in duck and quail embryos.

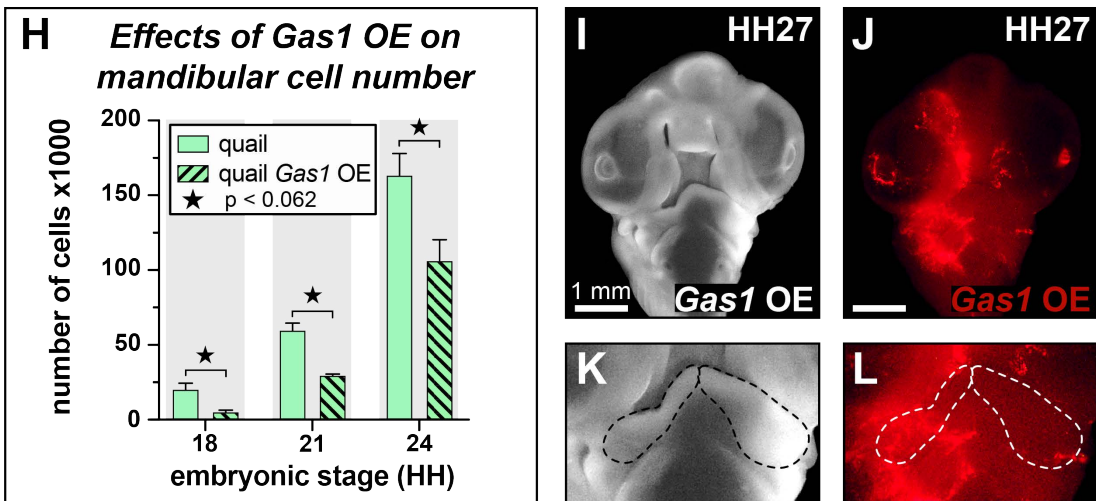
(A) Mesenchymal cell number in duck mandibular primordia following bilateral *in ovo* electroporation of a stably integrating and doxycycline (dox)-inducible *Gas1* overexpression (OE) vector into NCM at HH8.5. *Gas1* overexpression was induced with 50 ng/mL of dox at HH15 and mandibular primordia were collected at HH18, HH21, and HH24. **(B)** Dissected duck mandibular primordia in whole mount at HH18 following bilateral *in ovo* electroporation of a *Gas1* overexpression vector into NCM at HH8.5. **(C)** *Gas1*-positive NCM can be visualized by mScarlet fluorescence (RFP). *Gas1* overexpression can be seen **(D)** in whole mount and **(E)** with RFP at HH21, and **(F)** in whole mount and **(G)** with RFP at HH24. **(H)** Mesenchymal cell number in quail mandibular primordia following bilateral *in ovo* electroporation of a *Gas1* overexpression vector into NCM at HH8.5. *Gas1* overexpression was induced with dox at HH15 and mandibular primordia were collected at HH18, HH21, and HH24. **(I)** Quail embryo in whole mount at HH27 following unilateral *in ovo* electroporation of a *Gas1* overexpression vector into NCM at HH8.5 and induction with dox at HH15. The treated size appears smaller (white arrow) than the contralateral control side. **(J)** Unilateral distribution of *Gas1*-positive NCM can be visualized by RFP on one side of the embryo. Higher magnification view of quail mandibular primordia (dashed lines) in **(K)** whole-mount and **(L)** with RFP showing a size reduction on the treated (arrow) versus control side. **(M)** Quail embryo in whole mount at HH27 following unilateral *in ovo* injection of a control anti-GFP morpholino (MO) at HH18. At higher magnification in **(N)** whole-mount and **(O)** in schematic view, the mandibular primordia (dashed lines) appear the same size on the treated (striped) and control (green) sides. **(P)** Quail embryo in whole mount at HH27 following unilateral *in ovo* injection of an anti-*Gas1* morpholino (MO) at HH18. At higher magnification in **(Q)** whole-mount and **(R)** in schematic

view, the mandibular primordia (dashed lines) appear smaller on the treated (striped) versus control (green) sides. Significance is shown for comparisons between control and treatment groups as denoted by brackets and p-values are as indicated. P-values ≥ 0.05 are considered not significant (ns). $n \geq 2$ for each group and data point. Error bars represent SEM.

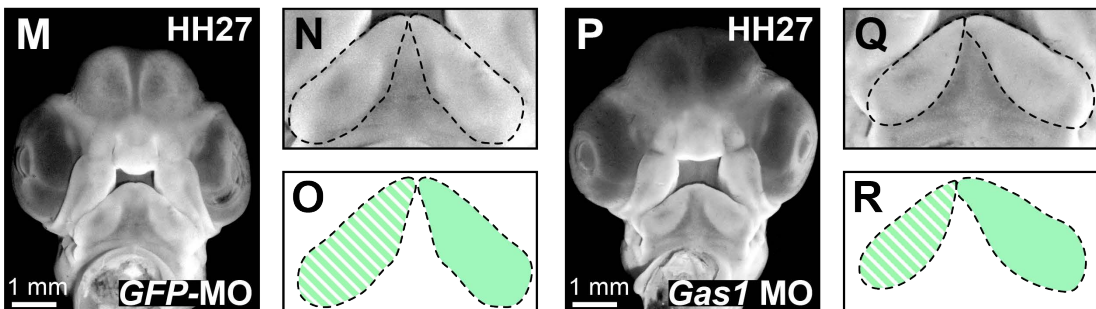
Gas1 over-expression in duck mandibular primordia



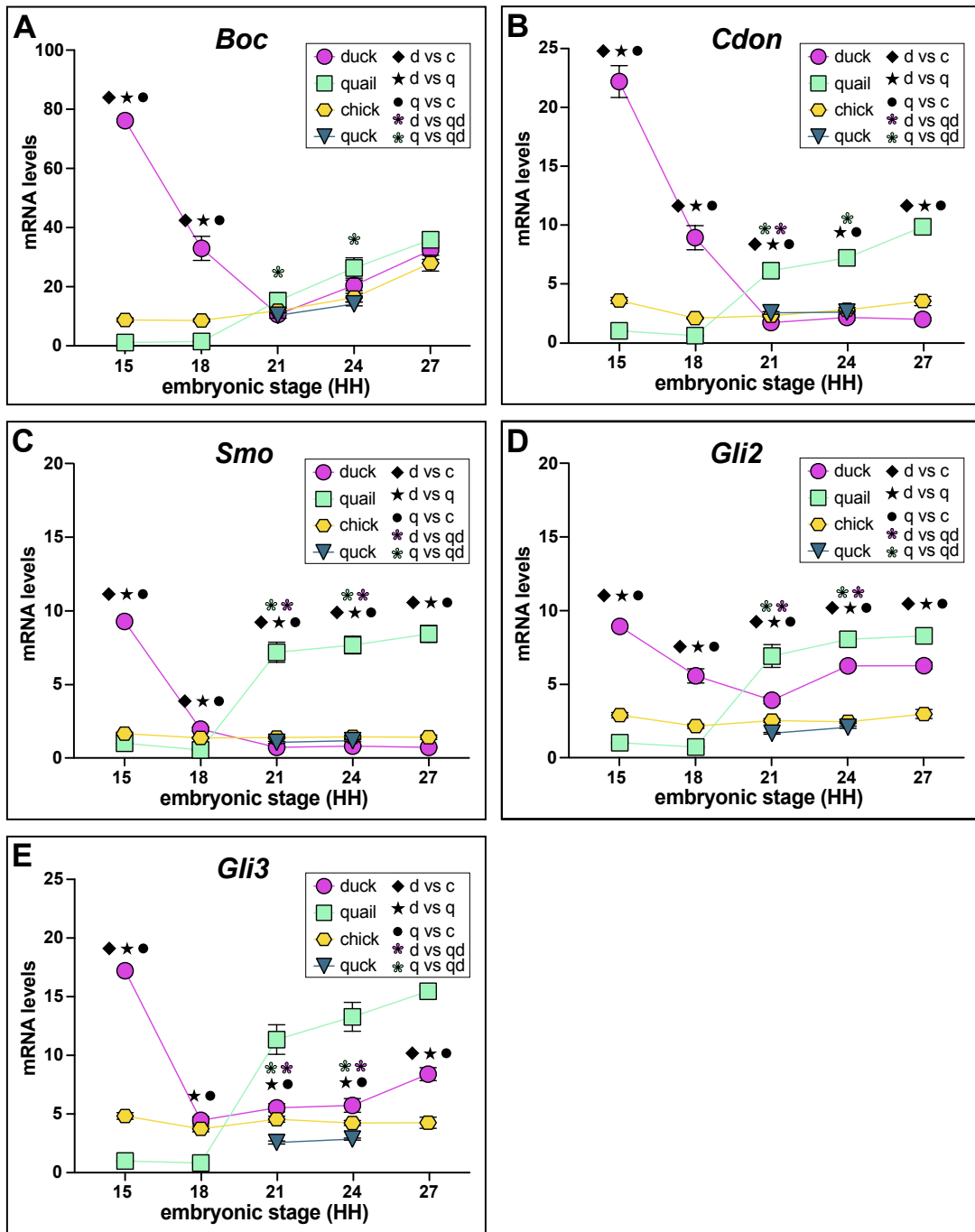
Gas1 over-expression in quail mandibular primordia



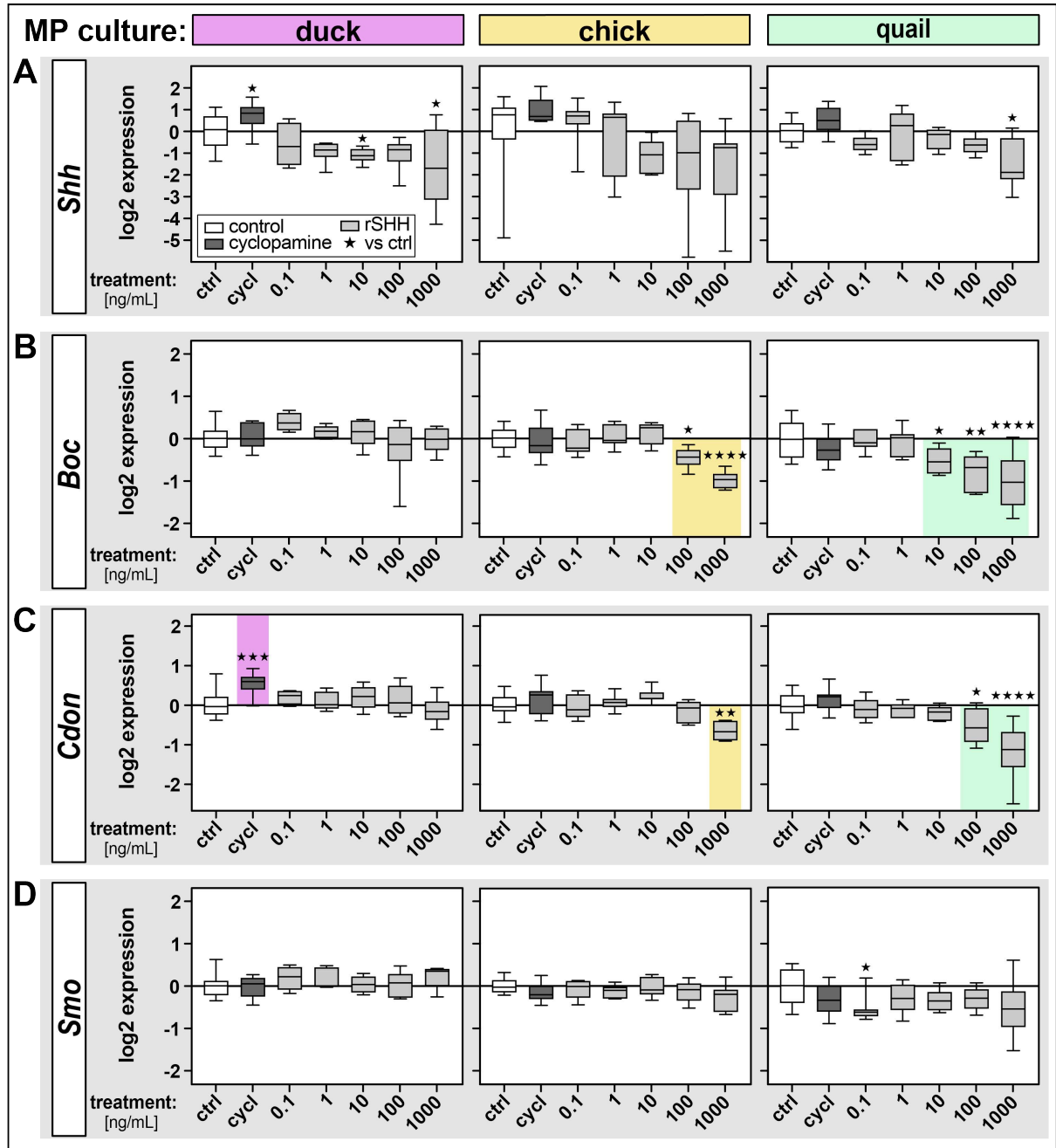
Gas1 morpholino in quail mandibular primordia



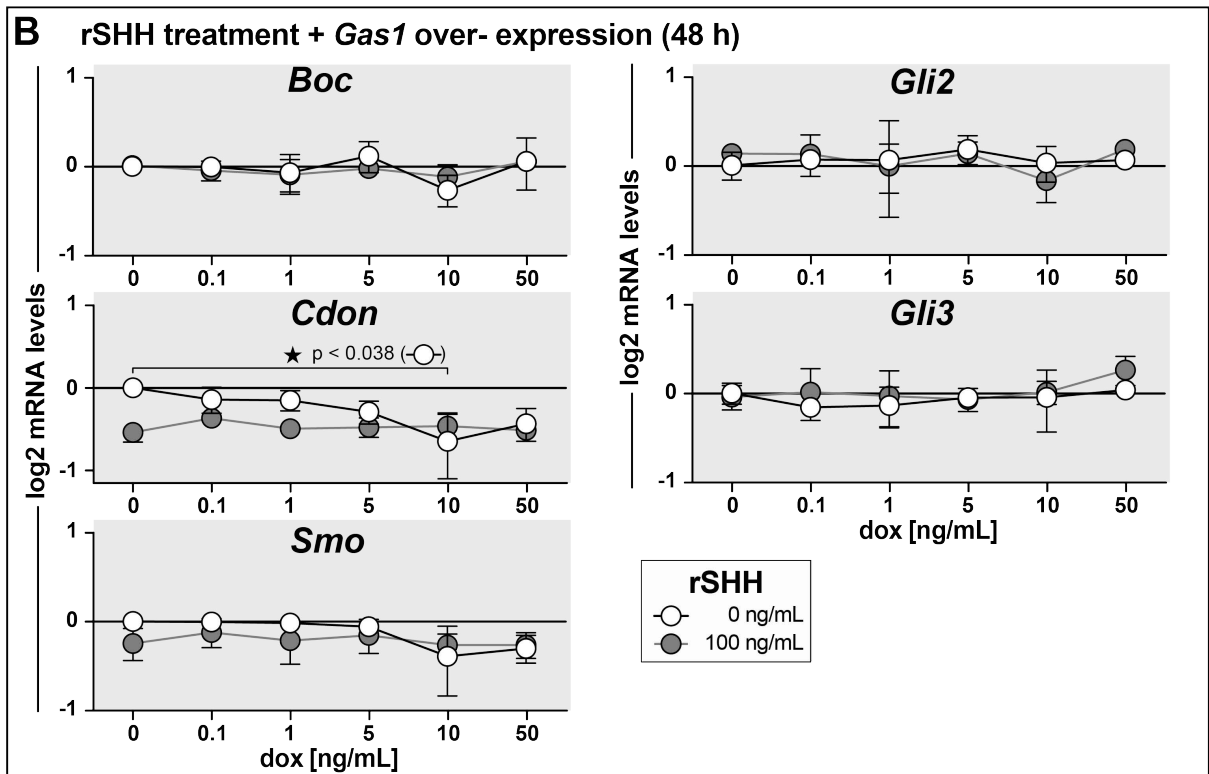
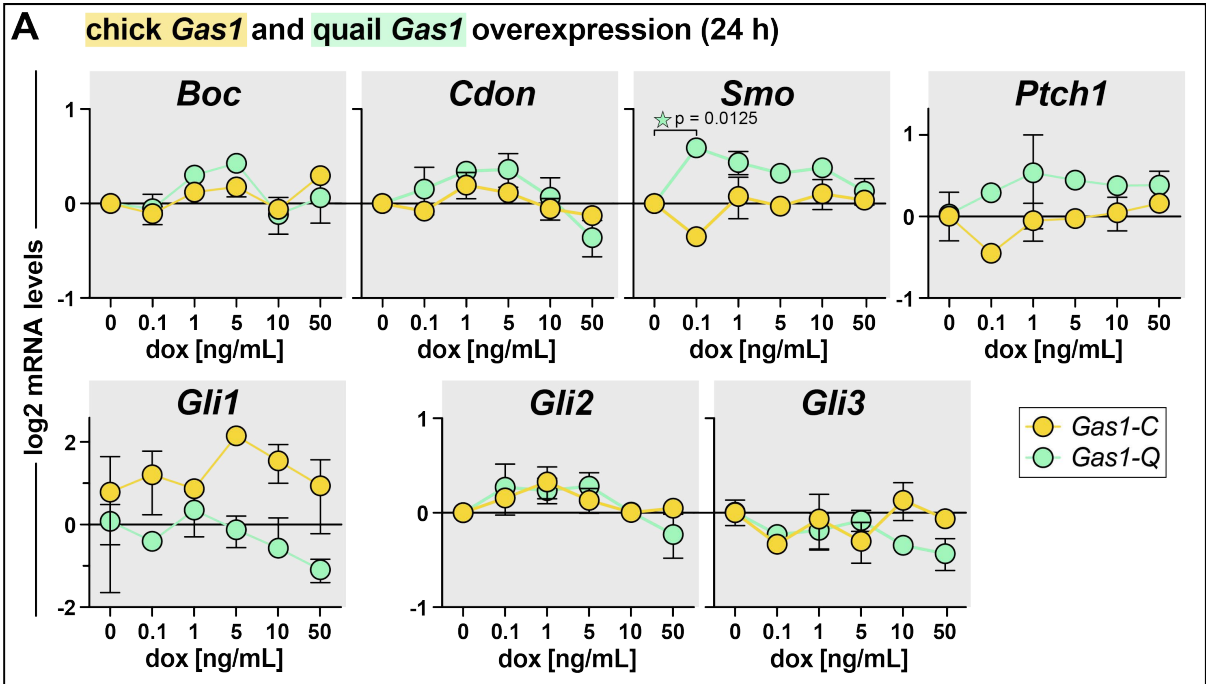
Supplementary Figure 1: Expression of SHH pathway members in mandibular primordia of duck, chick, quail, and chimeric quck. Relative mRNA levels of **(A) *Boc***, **(B) *Cdon***, **(C) *Gli2***, **(D) *Gli3***, and **(E) *Smo*** in mandibular primordia of duck (violet), chick (yellow), quail (green), and quck (blue) at HH15, HH18, HH21, HH24, and HH27. Expression levels were assayed by qRT-PCR and normalized to *r18s*. Significance is shown (p-value < 0.02, n ≥ 6 for each group and data point, and error bars represent SEM) for comparisons between different species at the same embryonic stage (i.e., diamond symbol for duck versus chick, asterisk symbol for duck versus quail, full circle symbol for quail versus chick, and violet asterisk symbol for duck versus quck). For quail versus quck, significance is shown (green asterisk symbol) at HH21 and denotes the comparison of HH24 quail versus HH21 quck, and at HH24 for the comparison of HH27 quail versus HH24 quck.



Supplementary Figure 2: Effects of inhibition and activation of the SHH pathway in mandibular primordia of duck, chick, and quail. Mandibular primordia from duck (violet), chick (yellow), and quail (green) embryos were harvested at HH21, placed in culture, and treated with cyclopamine (cycl, dark grey) to inhibit the SHH pathway or with five serial dilutions of recombinant (r) SHH protein (light grey) to activate the SHH pathway. Box plots show relative levels of mRNA expression (on the y-axis in \log_2 scale) for SHH pathway members including **(A)** *Shh*, **(B)** *Boc*, **(C)** *Cdon*, and **(D)** *Smo* 24 hours after treatment. Control (ctrl, white) and treatment groups are shown on the x-axis. Expression levels were assayed by qRT-PCR and normalized to *r18s*. Significance is shown for comparisons between control and treatment groups (i.e., cyclopamine or rSHH) within the same species as indicated by colored shading and by the following symbols for p-values: * $p < 0.05$, ** $p < 0.01$, *** $p < 0.001$, and **** $p < 0.0001$. p-values ≥ 0.05 we considered not significant. $n \geq 4$ for each group and data point.



Supplementary Figure 3: Effects of SHH pathway activation and *Gas1* overexpression in cell culture. **(A)** Relative levels of mRNA expression (on the y-axis in log₂ scale) for *Boc*, *Cdon*, *Smo*, *Ptch1*, *Gli1*, *Gli2*, and *Gli3* in chick fibroblasts (i.e., DF-1) 24 hours (h) after treatment with five serial dilutions of doxycycline (dox) and induction of a stably integrated chick (yellow) or quail (green) *Gas1* overexpression vector. **(B)** Relative levels of mRNA expression for *Boc*, *Cdon*, *Smo*, *Gli2*, and *Gli3* in chick fibroblasts 48 hours after dox-induction of a stably integrated *Gas1* overexpression vector (serial dilution) and treatment with recombinant (r) SHH protein (control 0 ng/mL in white and 100 ng/mL dark grey). Expression levels were assayed by qRT-PCR and normalized to *r18s*. Significance is shown for comparisons between control (0 ng/mL of rSHH and/or dox) and treatment groups as denoted by brackets and p-values are as indicated. P-values ≥ 0.05 are considered not significant. $n \geq 2$ for each group and data point, and error bars represent SEM.



Tables

Table 1. Duck, chick, and quail incubation times

stage	approximate incubation times [days]		
	duck	chick	quail
HH8.5	2.4	1.4	1.2
HH9.5	2.5	1.5	1.3
HH15	3.5	2.5	2.2
HH18	4.5	3.2	2.7
HH21	5.5	3.9	3.4
HH24	6.5	4.8	4.2
HH27	7.5	5.7	5

Table 2. Mandibular primordia incubation times in trypsin-pancreatin solution

stage	incubation times [min]		
	duck	chick	quail
HH18	20	18	15
HH21	25	20	18
HH24	30	25	23
HH27	40	35	30

Table 3. Quantification of Sox10-positive delaminated NC progenitors in the midbrain of chick embryos at HH10

section	number of Sox10+ cells	average
c1_s4_1	88	
c1_s4_2	91	88.667
c1_s4_3	87	
c2_s6_3	68	
c2_s6_2	84	86.667
c2_s6_1	90	
c3_s5_1	89	
c3_s5_2	86	86
c3_s5_3	83	
total average	87.111	87.111

Table 4. Mandibular mesenchyme population size in duck, chick, and quail embryos

stage	duck			chick			quail		
	mean	SEM	n	mean	SEM	n	mean	SEM	n
HH18	68206.8	10378.0	9	30296.3	2154.3	9	18574.7	3991.7	9
HH21	279777.8	24087.8	12	119858.6	6436.9	11	59793.2	4784.6	9
HH24	638656.6	26323.9	11	305370.4	15696.2	6	163454.6	14439.6	11
HH27	2105453.7	74286.0	18	853886.0	40050.0	11	505857.1	42977.0	7

Table 5. Mandibular primordia total RNA yield in duck, chick, quail, and quck embryos

stage	duck			chick			quail			quck		
	mean	SEM	n	mean	SEM	n	mean	SEM	n	mean	SEM	n
HH15	372.0	28.3	24	162.1	10.4	8	150.5	9.9	19			
HH18	1318.1	82.9	18	584.0	30.9	15	609.5	25.1	19			
HH21	2593.1	83.9	18	1381.3	83.2	18	1079.2	71.4	18	2311.6	201.4	11
HH24	5509.2	141.8	18	2879.4	140.6	16	2188.0	97.4	19	5936.2	304.0	13
HH27	11046.4	553.6	18	5860.4	146.6	18	4196.2	187.8	16			

Table 6. RNA content per cell in mandibular primordia

stage	duck	chick	quail
HH18	19.32	19.28	32.81
HH21	9.27	11.52	18.05
HH24	8.63	9.43	13.39
HH27	5.25	6.86	8.30

Table 7. Mandibular mesenchyme population size modeling in duck and quail embryos

stage	duck			quail		
	hours	population	n° cell cycles	hours	population	n° cell cycles
HH13	0	1.26	0	0	1.00	0
HH15	24	4.31	1.78	12	2.13	1.09
HH18	26	16.37	1.93	12	4.54	1.09
HH21	26	62.19	1.93	18	14.11	1.64
HH24	24	213.26	1.78	20	49.74	1.82
HH27	24	731.28	1.78	20	175.40	1.82

Table 8. Duck/quail total RNA extraction ratios

stage	HH15	HH18	HH21	HH24	HH27
d/q ratio	2.47	2.16	2.40	2.52	2.63

Table 9. Duck/quail mandibular mesenchyme population size ratios

stage	HH18	HH21	HH24	HH27
in vivo	3.67	4.68	3.91	4.16
model	3.61	4.41	4.29	4.17

Table 10. SHH pathway activation in duck, chick, quail, and quck mandibular primordia

stage	duck			chick			quail			quck			
	mean	SEM	n	mean	SEM	n	mean	SEM	n	mean	SEM	n	
<i>Shh / Gli1</i>	HH15	1.89	0.25	13	1.22	0.12	9	1.03	0.09	11	-	-	-
	HH18	0.71	0.10	8	1.99	0.14	13	1.99	0.38	11	-	-	-
	HH21	0.78	0.09	10	1.98	0.11	10	1.73	0.37	7	0.26	0.05	10
	HH24	0.45	0.04	10	1.39	0.13	8	1.23	0.20	9	0.25	0.05	13
	HH27	0.39	0.06	8	0.40	0.05	10	0.22	0.06	6	-	-	-
<i>Shh / Ptch1</i>	HH15	0.62	0.07	13	0.41	0.04	9	1.06	0.12	11	-	-	-
	HH18	0.25	0.04	8	0.59	0.06	13	1.37	0.24	11	-	-	-
	HH21	0.21	0.03	10	0.61	0.09	10	1.07	0.20	7	0.50	0.05	11
	HH24	0.14	0.01	10	0.65	0.05	8	1.03	0.19	9	0.35	0.03	13
	HH27	0.18	0.02	8	0.31	0.04	10	0.21	0.05	6	-	-	-

Table 11. SHH pathway members mRNA levels in duck, chick, quail, and quck mandibular primordia

gene	stage	duck			chick			quail			quck		
		mean	SEM	n	mean	SEM	n	mean	SEM	n	mean	SEM	n
<i>Shh</i>	HH15	21.52	1.88	13	2.24	0.39	9	1.03	0.08	11	-	-	-
	HH18	4.27	0.63	8	3.19	0.22	13	1.42	0.23	11	-	-	-
	HH21	1.35	0.17	10	3.01	0.21	10	9.56	1.48	8	1.81	0.13	11
	HH24	0.94	0.10	10	2.32	0.26	8	6.38	0.79	9	0.95	0.09	13
	HH27	0.82	0.09	8	0.55	0.08	10	0.96	0.26	6	-	-	-
<i>Ptch1</i>	HH15	36.58	2.32	13	5.19	0.54	9	1.03	0.09	11	-	-	-
	HH18	17.55	1.10	8	5.85	0.57	13	1.08	0.08	11	-	-	-
	HH21	6.84	0.69	10	5.84	0.82	10	8.20	0.75	8	3.85	0.38	11
	HH24	6.55	0.44	10	3.63	0.39	8	6.92	0.64	9	2.75	0.19	13
	HH27	4.79	0.70	8	1.86	0.24	10	4.81	0.62	6	-	-	-
<i>Gas1</i>	HH15	19.77	1.68	11	0.77	0.13	9	1.09	0.17	8	-	-	-
	HH18	15.17	1.54	10	0.43	0.04	13	0.53	0.04	8	-	-	-
	HH21	19.50	2.27	8	0.44	0.03	10	0.55	0.06	10	11.74	2.62	10
	HH24	39.97	3.56	8	0.58	0.05	9	0.54	0.07	10	9.07	1.01	13
	HH27	85.33	31.66	10	1.08	0.09	10	1.53	0.04	10	-	-	-
<i>Boc</i>	HH15	76.15	2.47	13	8.75	0.71	9	1.11	0.18	11	-	-	-
	HH18	32.98	4.06	8	8.60	0.57	13	1.46	0.28	11	-	-	-
	HH21	10.60	1.18	10	11.91	0.73	10	15.21	2.73	8	10.31	0.98	11
	HH24	20.48	1.80	10	16.32	1.44	8	26.34	3.43	9	14.17	0.63	13
	HH27	32.32	3.09	8	27.99	2.69	10	35.90	2.27	6	-	-	-
<i>Cdon</i>	HH15	22.20	1.36	13	3.59	0.26	9	1.01	0.03	11	-	-	-
	HH18	8.93	1.02	8	2.09	0.09	13	0.60	0.05	11	-	-	-
	HH21	1.71	0.18	10	2.30	0.12	10	6.12	0.55	8	2.54	0.11	11
	HH24	2.14	0.24	10	2.80	0.19	8	7.22	0.46	9	2.60	0.09	13
	HH27	1.99	0.14	8	3.54	0.39	10	9.85	0.50	6	-	-	-
<i>Smo</i>	HH15	9.28	0.25	13	1.67	0.09	9	1.008	0.0397	11	-	-	-
	HH18	1.96	0.15	8	1.37	0.05	13	0.5501	0.0341	11	-	-	-
	HH21	0.73	0.09	10	1.39	0.09	10	7.1874	0.6809	8	1.06	0.07	11
	HH24	0.82	0.08	10	1.44	0.11	8	7.6792	0.5995	9	1.18	0.06	13
	HH27	0.73	0.05	8	1.42	0.15	10	8.4377	0.5732	6	-	-	-
<i>Glif1</i>	HH15	12.37	0.85	13	1.77	0.21	9	1.01	0.04	11	-	-	-
	HH18	6.10	0.64	8	1.64	0.11	13	0.80	0.06	11	-	-	-
	HH21	1.79	0.18	10	1.53	0.07	10	5.00	0.61	8	5.53	0.84	7
	HH24	2.10	0.17	10	1.69	0.15	8	5.56	0.35	9	4.90	0.73	13
	HH27	2.34	0.35	8	1.37	0.11	10	4.53	0.51	6	-	-	-

Glf2	HH15	8.91	0.38	13	2.88	0.18	9	1.01	0.04	11	-	-	-
	HH18	5.55	0.48	8	2.13	0.15	13	0.72	0.06	11	-	-	-
	HH21	3.90	0.24	9	2.51	0.13	10	6.90	0.78	8	1.65	0.06	11
	HH24	6.23	0.17	8	2.43	0.12	8	8.04	0.51	9	2.06	0.07	13
	HH27	6.25	0.23	8	2.96	0.31	10	8.27	0.40	6	-	-	-
Glf3	HH15	17.21	0.55	13	4.83	0.28	9	1.00	0.02	11	-	-	-
	HH18	4.47	0.31	8	3.74	0.24	13	0.82	0.05	11	-	-	-
	HH21	5.53	0.35	10	4.56	0.25	10	11.34	1.26	8	2.57	0.13	11
	HH24	5.73	0.58	10	4.24	0.20	8	13.29	1.24	9	2.87	0.08	13
	HH27	8.40	0.56	8	4.26	0.48	10	15.47	0.46	6	-	-	-

Table 12. SHH pathway members mRNA levels in duck, chick, and quail mandibular primordia explant cultures

gene	treatment	duck			chick			quail		
		mean	SEM	n	mean	SEM	n	mean	SEM	n
<i>Shh</i>	ctrl	1.14	0.14	17	1.45	0.25	12	1.06	0.10	14
	cycl	1.78	0.25	8	2.11	0.35	8	1.55	0.23	8
	0.1	0.76	0.27	4	1.60	0.30	7	0.71	0.07	7
	1	0.54	0.06	6	1.24	0.33	7	1.14	0.28	7
	10	0.47	0.04	6	0.54	0.10	7	0.84	0.11	6
	100	0.53	0.09	6	0.69	0.25	7	0.66	0.07	7
	1000	0.57	0.16	13	0.53	0.19	7	0.47	0.13	8
	<i>Ptch1</i>	ctrl	1.04	0.08	17	1.04	0.08	12	1.04	0.08
cycl		0.23	0.02	8	0.12	0.01	8	0.15	0.01	8
0.1		0.83	0.18	4	0.93	0.09	7	0.77	0.09	7
1		0.83	0.10	6	0.93	0.16	7	0.84	0.13	7
10		0.87	0.13	6	1.16	0.17	7	0.86	0.04	6
100		1.39	0.14	6	1.33	0.16	7	1.17	0.13	7
1000		2.46	0.25	13	3.44	0.44	7	1.47	0.12	8
<i>Gas1</i>		ctrl	1.08	0.11	17	1.06	0.11	12	1.07	0.11
	cycl	1.93	0.21	8	2.25	0.28	8	1.14	0.10	8
	0.1	1.28	0.05	4	0.87	0.10	7	0.68	0.08	7
	1	1.18	0.14	6	0.76	0.11	7	0.68	0.05	7
	10	1.09	0.24	6	0.90	0.06	7	0.55	0.07	6
	100	0.95	0.11	6	0.52	0.04	7	0.55	0.04	7
	1000	0.95	0.05	13	0.46	0.05	7	0.24	0.02	8
	<i>Boc</i>	ctrl	1.02	0.05	17	1.01	0.05	12	1.04	0.08
cycl		1.06	0.08	8	1.00	0.11	8	0.87	0.08	8
0.1		1.32	0.10	4	0.93	0.08	7	0.97	0.06	7
1		1.12	0.05	6	1.05	0.07	7	0.97	0.08	7
10		1.11	0.10	6	1.13	0.07	7	0.71	0.07	6
100		0.91	0.14	6	0.73	0.04	7	0.61	0.06	7
1000		1.00	0.05	13	0.51	0.03	7	0.54	0.09	8
<i>Cdon</i>		ctrl	1.02	0.06	17	1.02	0.06	12	1.02	0.05
	cycl	1.48	0.10	8	1.15	0.11	8	1.13	0.08	8
	0.1	1.16	0.08	4	0.99	0.08	7	0.95	0.07	7
	1	1.08	0.07	6	1.07	0.06	7	0.92	0.04	7
	10	1.17	0.10	6	1.18	0.06	7	0.88	0.05	6
	100	1.13	0.12	6	0.92	0.06	7	0.75	0.08	7
	1000	0.94	0.06	13	0.65	0.04	7	0.48	0.07	8

<i>Smo</i>	ctrl	1.01	0.04	17	1.01	0.03	12	1.04	0.08	14
	cycl	1.01	0.06	8	0.90	0.05	8	0.82	0.08	8
	0.1	1.16	0.11	4	0.96	0.05	7	0.71	0.07	7
	1	1.12	0.08	6	0.92	0.04	7	0.84	0.07	7
	10	1.04	0.06	6	0.98	0.06	7	0.80	0.06	6
	100	1.05	0.09	6	0.93	0.06	7	0.83	0.06	7
	1000	1.16	0.05	13	0.84	0.07	7	0.77	0.13	8
	<i>Gli1</i>	ctrl	1.03	0.06	17	1.02	0.06	12	1.04	0.08
cycl		0.21	0.03	8	0.12	0.03	8	0.17	0.02	8
0.1		1.42	0.33	4	0.96	0.05	7	0.78	0.10	7
1		1.33	0.13	6	1.02	0.05	7	0.76	0.05	7
10		1.26	0.13	6	1.04	0.05	7	0.89	0.05	6
100		1.57	0.19	6	1.18	0.08	7	0.83	0.05	7
1000		1.84	0.16	13	1.62	0.09	7	1.07	0.11	8
<i>Gli2</i>		ctrl	1.01	0.04	17	1.01	0.03	12	1.02	0.05
	cycl	0.81	0.06	8	0.99	0.05	8	0.69	0.03	8
	0.1	1.24	0.06	4	0.88	0.03	7	0.98	0.07	7
	1	1.12	0.06	6	0.92	0.06	7	0.90	0.05	7
	10	1.06	0.08	6	0.95	0.04	7	0.95	0.02	6
	100	1.10	0.07	6	0.82	0.04	7	0.84	0.03	7
	1000	1.18	0.07	13	0.76	0.05	7	0.70	0.04	8
	<i>Gli3</i>	ctrl	1.03	0.06	17	1.01	0.03	12	1.02	0.05
cycl		1.27	0.08	8	0.92	0.04	8	0.79	0.05	8
0.1		1.30	0.22	4	1.00	0.05	7	0.94	0.06	7
1		1.08	0.07	6	0.92	0.04	7	0.89	0.05	7
10		1.09	0.03	6	0.98	0.04	7	0.81	0.04	6
100		0.97	0.05	6	0.76	0.04	7	0.73	0.02	7
1000		0.89	0.05	13	0.58	0.02	7	0.53	0.06	8

Table 13. SHH pathway members mRNA levels in DF1 cell cultures with stably integrated dox-inducible Gas1 construct after 24 hours of doxycycline hyclate (dox) treatment

gene	dox	Gas1-C			Gas1-Q			gene	Gas1-C			Gas1-Q		
		mean	SEM	n	mean	SEM	n		mean	SEM	n	mean	SEM	n
<i>Ptch1</i>	0	1.00	0.07	2	1.02	0.21	2	<i>Smo</i>	1.00	0.04	2	1.00	0.04	2
	0.1	0.73	0.05	2	1.22	0.06	2		0.79	0.02	2	1.51	0.06	2
	1	0.97	0.15	2	1.45	0.55	2		1.05	0.16	2	1.35	0.11	2
	5	0.98	0.05	2	1.36	0.03	2		0.98	0.02	2	1.25	0.01	2
	10	1.03	0.15	2	1.30	0.02	2		1.08	0.12	2	1.30	0.08	2
	50	1.12	0.07	2	1.31	0.16	2		1.03	0.03	2	1.10	0.11	2
<i>Gas1</i>	0	1.00	0.09	2	1.00	0.05	2	<i>Gli1</i>	1.72	1.41	2	1.06	0.35	2
	0.1	0.59	0.00	2	1.09	0.02	2		2.31	1.13	2	0.76	0.08	2
	1	1.27	0.19	2	1.50	0.05	2		1.82	0.22	2	1.28	0.46	2
	5	30.24	0.36	2	34.74	0.39	2		4.44	0.57	2	0.92	0.24	2
	10	46.08	8.81	2	53.47	0.31	2		2.91	0.91	2	0.67	0.45	2
	50	133.39	4.97	2	152.83	14.18	2		1.91	1.06	2	0.47	0.09	2
<i>Boc</i>	0	1.00	0.03	2	1.00	0.03	2	<i>Gli2</i>	1.00	0.04	2	1.00	0.02	2
	0.1	0.93	0.01	2	0.96	0.11	2		1.11	0.04	2	1.21	0.22	2
	1	1.09	0.07	2	1.23	0.05	2		1.25	0.15	2	1.18	0.11	2
	5	1.13	0.08	2	1.34	0.02	2		1.10	0.10	2	1.22	0.13	2
	10	0.96	0.03	2	0.92	0.12	2		1.00	0.02	2	1.01	0.00	2
	50	1.23	0.02	2	1.04	0.18	2		1.03	0.05	2	0.85	0.14	2
<i>Cdon</i>	0	1.00	0.01	2	1.00	0.01	2	<i>Gli3</i>	1.00	0.04	2	1.00	0.09	2
	0.1	0.95	0.00	2	1.11	0.19	2		0.79	0.00	2	0.85	0.05	2
	1	1.15	0.11	2	1.27	0.01	2		0.96	0.19	2	0.88	0.12	2
	5	1.08	0.04	2	1.28	0.16	2		0.81	0.12	2	0.95	0.07	2
	10	0.96	0.08	2	1.05	0.16	2		1.10	0.15	2	0.79	0.04	2
	50	0.92	0.02	2	0.78	0.10	2		0.96	0.01	2	0.74	0.09	2

Table 14. Number of cells counted in 6-well plate after 72 hours of doxycycline hyclate (dox) treatment in DF1 cell lines with stably integrated dox-inducible Gas1

dox	<i>Gas1-C</i>			<i>Gas1-Q</i>		
	mean	SEM	n	mean	SEM	n
0	674340.30	79731.16	4	404374.98	19182.23	4
0.1	687777.78	86256.14	4	447326.40	63572.87	4
1	690486.13	86948.45	4	355312.50	13432.59	4
5	756979.18	58289.62	4	354409.73	14914.06	4
10	593690.48	24880.28	4	308730.18	26763.42	4
50	611493.05	42838.07	4	322118.08	53244.62	4

Table 15. SHH pathway members mRNA levels in DF1 cells after 24 hours of recombinant SHH (rSHH) treatment

rSHH	<i>Gas1</i>			<i>Ptch1</i>			<i>Gli1</i>		
	mean	SEM	n	mean	SEM	n	mean	SEM	n
0	1.00	0.03	8	1.00	0.02	8	1.06	0.12	8
0.1	0.96	0.07	8	0.90	0.06	8	1.03	0.12	8
1	1.00	0.06	8	1.01	0.08	8	1.25	0.23	8
10	0.91	0.05	8	1.08	0.08	8	1.53	0.23	8
100	0.80	0.05	8	1.07	0.05	8	1.38	0.28	8
1000	0.88	0.08	8	1.32	0.11	8	1.59	0.28	8

Table 16. SHH pathway members mRNA levels in DF1 cells with stably integrated dox-inducible Gas1 construct after 48 hours of doxycycline hyclate (dox) and recombinant SHH (rSHH) treatment

rSHH: 0 ng/mL												
dox	<i>Gas1</i>			<i>Ptch1</i>			<i>Boc</i>			<i>Cdon</i>		
	mean	SEM	n	mean	SEM	n	mean	SEM	n	mean	SEM	n
0	1.00	0.04	2	1.01	0.11	2	1.00	0.05	2	1.00	0.07	2
0.1	0.97	0.08	2	1.02	0.03	2	1.00	0.03	2	0.91	0.10	2
1	1.10	0.11	2	0.94	0.26	2	0.95	0.15	2	0.90	0.08	2
5	2.61	0.55	2	1.16	0.12	2	1.08	0.13	2	0.82	0.08	2
10	1.64	0.57	2	0.99	0.11	2	0.83	0.10	2	0.64	0.17	2
50	60.20	7.61	2	1.28	0.01	2	1.04	0.21	2	0.74	0.10	2
dox	<i>Smo</i>			<i>Gli1</i>			<i>Gli2</i>			<i>Gli3</i>		
	mean	SEM	n	mean	SEM	n	mean	SEM	n	mean	SEM	n
0	1.00	0.06	2	1.00	0.06	2	1.01	0.11	2	1.00	0.08	2
0.1	1.00	0.00	2	0.97	0.14	2	1.05	0.06	2	0.90	0.05	2
1	0.99	0.01	2	0.82	0.03	2	1.05	0.38	2	0.91	0.14	2
5	0.96	0.03	2	1.04	0.01	2	1.14	0.13	2	0.97	0.03	2
10	0.76	0.20	2	0.95	0.16	2	1.02	0.14	2	0.97	0.23	2
50	0.81	0.09	2	1.13	0.01	2	1.05	0.02	2	1.03	0.03	2
rSHH: 1 ng/mL												
dox	<i>Gas1</i>			<i>Ptch1</i>			<i>Boc</i>			<i>Cdon</i>		
	mean	SEM	n	mean	SEM	n	mean	SEM	n	mean	SEM	n
0	0.84	0.01	2	1.29	0.14	2	0.76	0.05	2	0.70	0.15	2
0.1	0.83	0.03	2	1.26	0.15	2	0.75	0.10	2	0.73	0.14	2
1	0.91	0.16	2	1.12	0.14	2	0.77	0.04	2	0.85	0.18	2
5	2.17	0.04	2	1.38	0.04	2	0.80	0.04	2	0.67	0.09	2
10	1.95	0.01	2	1.55	0.00	2	0.90	0.04	2	0.78	0.03	2
50	75.86	11.80	2	0.72	0.16	2	0.59	0.13	2	0.85	0.06	2
dox	<i>Smo</i>			<i>Gli1</i>			<i>Gli2</i>			<i>Gli3</i>		
	mean	SEM	n	mean	SEM	n	mean	SEM	n	mean	SEM	n
0	0.70	0.10	2	1.30	0.00	2	1.00	0.01	2	0.88	0.01	2
0.1	0.69	0.11	2	1.20	0.17	2	1.00	0.15	2	0.88	0.05	2
1	0.65	0.08	2	1.07	0.02	2	0.87	0.12	2	0.82	0.04	2
5	0.66	0.08	2	1.33	0.00	2	1.04	0.06	2	0.84	0.07	2
10	0.77	0.04	2	1.53	0.03	2	1.19	0.04	2	0.99	0.04	2
50	0.75	0.00	2	1.05	0.06	2	0.54	0.13	2	0.77	0.09	2

rSHH: 10 ng/mL												
dox	<i>Gas1</i>			<i>Ptch1</i>			<i>Boc</i>			<i>Cdon</i>		
	mean	SEM	n	mean	SEM	n	mean	SEM	n	mean	SEM	n
0	0.76	0.13	4	1.53	0.18	4	0.86	0.05	4	0.82	0.10	4
0.1	0.79	0.13	4	2.16	0.36	4	1.01	0.10	4	0.73	0.07	4
1	0.75	0.15	4	1.23	0.24	4	0.79	0.11	4	0.87	0.12	4
5	2.10	0.54	4	1.76	0.15	4	0.95	0.08	4	0.76	0.08	4
10	1.80	0.50	4	1.83	0.40	4	0.96	0.14	4	0.76	0.07	4
50	50.10	14.80	4	1.89	0.31	4	0.99	0.14	4	0.84	0.05	4

dox	<i>Smo</i>			<i>Gli1</i>			<i>Gli2</i>			<i>Gli3</i>		
	mean	SEM	n	mean	SEM	n	mean	SEM	n	mean	SEM	n
0	0.85	0.09	4	1.48	0.17	4	0.89	0.07	4	0.89	0.03	4
0.1	0.88	0.10	4	1.79	0.29	4	1.24	0.15	4	1.09	0.16	4
1	0.82	0.02	4	1.51	0.30	4	0.85	0.23	4	0.84	0.09	4
5	0.83	0.04	4	1.78	0.19	4	1.08	0.13	4	1.05	0.08	4
10	0.83	0.04	4	1.84	0.23	4	1.05	0.19	4	1.05	0.16	4
50	0.85	0.07	4	1.63	0.29	4	0.88	0.14	4	1.12	0.17	4

rSHH: 100 ng/mL												
dox	<i>Gas1</i>			<i>Ptch1</i>			<i>Boc</i>			<i>Cdon</i>		
	mean	SEM	n	mean	SEM	n	mean	SEM	n	mean	SEM	n
0	0.79	0.06	4	2.55	0.16	4	1.01	0.04	4	0.69	0.05	4
0.1	0.85	0.04	4	2.38	0.45	4	0.97	0.07	4	0.78	0.04	4
1	0.80	0.04	4	2.26	0.51	4	0.94	0.12	4	0.71	0.05	4
5	2.09	0.46	4	2.64	0.30	4	0.99	0.05	4	0.72	0.06	4
10	1.56	0.38	4	2.23	0.36	4	0.92	0.09	4	0.73	0.08	4
50	42.97	12.04	4	2.96	0.23	4	1.04	0.06	4	0.70	0.02	4

dox	<i>Smo</i>			<i>Gli1</i>			<i>Gli2</i>			<i>Gli3</i>		
	mean	SEM	n	mean	SEM	n	mean	SEM	n	mean	SEM	n
0	0.84	0.11	4	2.29	0.22	4	1.10	0.04	4	0.97	0.09	4
0.1	0.92	0.10	4	2.28	0.31	4	1.10	0.18	4	1.01	0.20	4
1	0.86	0.14	4	2.18	0.45	4	1.00	0.19	4	0.98	0.22	4
5	0.90	0.12	4	2.32	0.36	4	1.10	0.10	4	0.96	0.09	4
10	0.83	0.08	4	1.80	0.19	4	0.89	0.14	4	1.01	0.09	4
50	0.83	0.08	4	2.29	0.15	4	1.14	0.07	4	1.20	0.14	4

rSHH: 1000 ng/mL												
dox	<i>Gas1</i>			<i>Ptch1</i>			<i>Boc</i>			<i>Cdon</i>		
	mean	SEM	n	mean	SEM	n	mean	SEM	n	mean	SEM	n
0	0.76	0.11	4	1.82	0.35	4	0.87	0.12	4	0.72	0.06	4
0.1	0.76	0.11	4	1.25	0.15	4	0.74	0.08	4	0.77	0.07	4
1	0.88	0.12	4	1.62	0.22	4	0.83	0.06	4	0.82	0.04	4
5	1.95	0.38	4	1.63	0.29	4	0.78	0.07	4	0.77	0.02	4
10	1.50	0.17	4	1.63	0.27	4	0.77	0.08	4	0.78	0.05	4
50	49.33	9.93	4	2.18	0.49	4	0.93	0.11	4	0.79	0.06	4

dox	<i>Smo</i>			<i>Gli1</i>			<i>Gli2</i>			<i>Gli3</i>		
	mean	SEM	n	mean	SEM	n	mean	SEM	n	mean	SEM	n
0	0.86	0.12	4	1.89	0.34	4	0.87	0.17	4	0.81	0.08	4
0.1	0.89	0.09	4	1.52	0.20	4	0.57	0.07	4	0.76	0.05	4
1	0.92	0.07	4	1.70	0.06	4	0.77	0.06	4	0.82	0.05	4
5	0.88	0.07	4	1.69	0.27	4	0.79	0.11	4	0.81	0.05	4
10	0.87	0.08	4	1.50	0.14	4	0.57	0.09	4	0.83	0.06	4
50	0.87	0.09	4	2.08	0.32	4	0.89	0.16	4	0.92	0.06	4

Table 17. qRT-PCR primer sequences

	<i>forward primer</i>	<i>reverse primer</i>
<i>r18s</i> duck chick quail	5'- GCG TGT GCC TAC CCT ACG CC -3'	5' - ACG CAA GCT TAT GGC CCG CA -3'
<i>Shh</i> duck chick quail	5'- TGG CAG AGA AGA CCC TAG -3'	5'- TTG CAG CGC TGA GTC ATC -3'
<i>Boc</i> duck chick quail	5'- CAT GCA GCA GTC ACA CGA G -3'	5'- AGT GGA GTC ATC TGG GAG -3'
<i>Cdon</i> duck chick quail	5'- GCC ATC AGT GAC ACT CAG -3'	5'- GGC TGC AGG TGA TTT ATC -3'
<i>Gas1</i> duck chick quail	5'- CCG CTA CAT GGC CTA CTG -3'	5'- CTT GAC CGA CTC GCA GAT -3'
<i>Ptch1</i> duck chick quail	5'- GAA CTC ATC ACA GAA GCA G -3'	5'- GAT CCA CTG CAA AGG AGG -3'
<i>Smo</i> duck chick quail	5'- GAG AAG ATC AAC CTC TTT GC -3'	5'- CTT GCT CTT CTT GAT CCT C -3'
<i>Gli1</i> duck chick quail	5'- TAG TGT TGA CCT GCA GAC -3'	5'- GTG TGG CTG AAC AGA TGC -3'
	5'- TAG CGT TGA CCT GCA GAC -3'	5'- GTG TGG CTA AAC AGT TGC -3'
		5'- GTG TGG CTG AAC AGT TGC -3'
<i>Gli2</i> duck chick quail	5'- GAC AGT TAA GGA TTC CTG C -3'	5'- GAC AGA CAG CTC CAT TAT TC -3'
<i>Gli3</i> duck chick quail	5'- CTC TAC CAT TTC CAC AGC -3'	5'- GGT ACC ATT TCC TAT GAG AG -3'

Table 18. *Gas1* in situ probes primer sequences

		<i>forward primer</i>	<i>reverse primer</i>
<i>Gas1</i>	duck	5'- TAC AAC CAG TAC GCC GAG G -3'	5'- TCG GCT CCT CCT CGT AGT CC -3'
	chick		
	quail		
<i>Gas1-T7</i>	duck	5'- TAA TAC GAC TCA CTA TAG GG TAC AAC CAG TAC GCC GAG G -3'	5'- TAA TAC GAC TCA CTA TAG GG TCG GCT CCT CCT CGT AGT CC -3'
	chick		
	quail		

Table 19. Vivo-Morpholino oligo sequences

quail <i>Gas1</i>	<i>GFP</i>
AGAAGGAGCTGCCGCCTCTGGGAAA	ACAGCTCCTCGCCCTTGCTCACCAT

Table 20. P-values for *in vivo* samples (significant values highlighted in gray)

stage	mandibular primordia (MP) total RNA extraction				
	duck vs chick	duck vs quail	quail vs chick	duck vs quck	quail vs quck
HH15	2.16E-04	4.44E-08	7.44E-01	-	-
HH18	2.18E-08	1.43E-09	7.44E-01	-	-
HH21	2.46E-11	8.00E-15	2.78E-02	2.76E-01	5.39E-01
HH24	1.02E-13	< 1.00E-15	8.96E-04	2.76E-01	5.15E-05
HH27	4.17E-10	4.41E-12	2.60E-07	-	-
stage	mandibular mesenchyme (MM) population size				
	duck vs chick	duck vs quail	quail vs chick	duck vs duck Gas1-oe	quail vs quail Gas1-oe
HH18	2.52E-03	3.92E-04	2.00E-02	8.34E-01	6.14E-02
HH21	8.18E-06	5.11E-07	4.27E-06	2.99E-05	5.70E-02
HH24	7.89E-07	3.56E-12	4.93E-05	1.96E-04	6.14E-02
HH27	4.31E-12	1.41E-11	6.41E-05	-	-
stage	<i>Shh</i> mRNA level				
	duck vs chick	duck vs quail	quail vs chick	duck vs quck	quail vs quck
HH15	< 1.00E-06	< 1.00E-06	7.55E-03	-	-
HH18	8.92E-02	3.61E-04	8.80E-05	-	-
HH21	3.40E-05	4.00E-05	6.50E-04	8.32E-02	1.20E-05
HH24	1.57E-04	6.00E-06	9.44E-04	9.31E-01	9.50E-01
HH27	8.92E-02	5.77E-01	9.22E-02	-	-
stage	<i>Boc</i> mRNA level				
	duck vs chick	duck vs quail	quail vs chick	duck vs quck	quail vs quck
HH15	< 1.00E-06	< 1.00E-06	< 1.00E-06	-	-
HH18	< 1.00E-06	< 1.00E-06	< 1.00E-06	-	-
HH21	5.16E-01	3.06E-01	2.15E-01	8.50E-01	1.14E-04
HH24	2.76E-01	3.06E-01	6.21E-02	2.99E-03	< 1.00E-06
HH27	5.16E-01	3.99E-01	1.22E-01	-	-
stage	<i>Cdon</i> mRNA level				
	duck vs chick	duck vs quail	quail vs chick	duck vs quck	quail vs quck
HH15	< 1.00E-06	< 1.00E-06	< 1.00E-06	-	-
HH18	< 1.00E-06	< 1.00E-06	< 1.00E-06	-	-
HH21	2.88E-02	< 1.00E-06	1.00E-06	1.59E-03	< 1.00E-06
HH24	5.76E-02	< 1.00E-06	< 1.00E-06	6.61E-02	< 1.00E-06
HH27	1.04E-02	< 1.00E-06	< 1.00E-06	-	-
stage	<i>Gas1</i> mRNA level				
	duck vs chick	duck vs quail	quail vs chick	duck vs quck	quail vs quck
HH15	< 1.00E-06	< 1.00E-06	4.06E-01	-	-
HH18	< 1.00E-06	< 1.00E-06	4.06E-01	-	-
HH21	< 1.00E-06	< 1.00E-06	4.06E-01	4.54E-02	4.61E-04
HH24	< 1.00E-06	< 1.00E-06	6.43E-01	< 1.00E-06	4.00E-06
HH27	1.59E-02	1.64E-02	1.19E-03	-	-

stage	<i>Ptch1</i> mRNA level				
	duck vs chick	duck vs quail	quail vs chick	duck vs quack	quail vs quack
HH15	< 1.00E-06	< 1.00E-06	< 1.00E-06	-	-
HH18	< 1.00E-06	< 1.00E-06	< 1.00E-06	-	-
HH21	3.63E-01	4.90E-01	5.49E-02	9.25E-04	8.55E-04
HH24	5.42E-04	8.68E-01	1.46E-03	< 1.00E-06	8.55E-04
HH27	1.01E-03	9.79E-01	3.75E-04	-	-
stage	<i>Smo</i> mRNA level				
	duck vs chick	duck vs quail	quail vs chick	duck vs quack	quail vs quack
HH15	< 1.00E-06	< 1.00E-06	< 1.00E-06	-	-
HH18	7.60E-04	< 1.00E-06	< 1.00E-06	-	-
HH21	1.76E-04	< 1.00E-06	< 1.00E-06	7.65E-03	< 1.00E-06
HH24	6.69E-04	< 1.00E-06	< 1.00E-06	2.28E-03	< 1.00E-06
HH27	1.35E-03	< 1.00E-06	< 1.00E-06	-	-
stage	<i>Gli1</i> mRNA level				
	duck vs chick	duck vs quail	quail vs chick	duck vs quack	quail vs quack
HH15	< 1.00E-06	< 1.00E-06	8.40E-04	-	-
HH18	< 1.00E-06	< 1.00E-06	7.00E-06	-	-
HH21	1.95E-01	9.1E-05	2.10E-05	2.46E-04	9.70E-01
HH24	1.93E-01	< 1.00E-06	< 1.00E-06	3.43E-03	9.35E-01
HH27	3.09E-02	0.00336	7.00E-06	-	-
stage	<i>Gli2</i> mRNA level				
	duck vs chick	duck vs quail	quail vs chick	duck vs quack	quail vs quack
HH15	< 1.00E-06	< 1.00E-06	< 1.00E-06	-	-
HH18	< 1.00E-06	< 1.00E-06	< 1.00E-06	-	-
HH21	7.9E-05	3.00E-03	1.20E-05	< 1.00E-06	< 1.00E-06
HH24	< 1.00E-06	5.63E-03	< 1.00E-06	< 1.00E-06	< 1.00E-06
HH27	< 1.00E-06	1.76E-03	< 1.00E-06	-	-
stage	<i>Gli3</i> mRNA level				
	duck vs chick	duck vs quail	quail vs chick	duck vs quack	quail vs quack
HH15	< 1.00E-06	< 1.00E-06	< 1.00E-06	-	-
HH18	1.04E-01	< 1.00E-06	< 1.00E-06	-	-
HH21	1.04E-01	1.60E-04	2.40E-05	< 1.00E-06	< 1.00E-06
HH24	1.04E-01	5.00E-05	1.20E-05	1.70E-05	< 1.00E-06
HH27	1.35E-04	2.00E-06	< 1.00E-06	-	-
stage	<i>Shh to Ptch1</i> ratios				
	duck vs chick	duck vs quail	quail vs chick	duck vs quack	quail vs quack
HH15	4.73E-02	5.91E-03	6.76E-04	-	-
HH18	1.59E-03	3.49E-03	9.72E-03	-	-
HH21	2.57E-03	6.60E-04	1.10E-01	1.79E-04	1.69E-02
HH24	< 1.00E-06	5.53E-04	1.64E-01	9.00E-06	2.24E-02
HH27	4.73E-02	6.16E-01	1.68E-01	-	-

stage	<i>Shh</i> to <i>Gli1</i> ratios				
	duck vs chick	duck vs quail	quail vs chick	duck vs quack	quail vs quack
HH15	1.01E-01	2.79E-02	6.02E-01	-	-
HH18	6.00E-06	2.93E-02	9.94E-01	-	-
HH21	< 1.00E-06	2.93E-02	8.53E-01	1.07E-04	2.79E-04
HH24	3.00E-06	4.83E-03	8.53E-01	3.98E-03	6.44E-01
HH27	9.51E-01	5.43E-02	1.54E-01	-	-

Table 21. P-values for mandibular primordia explant cultures treated with recombinant SHH protein (significant values highlighted in gray)

control vs		<i>Shh</i> mRNA level			<i>Smo</i> mRNA level		
		duck	chick	quail	duck	chick	quail
rSHH [ng/mL]	cycl	3.05E-02	2.85E-01	7.93E-02	> 1.00E+00	4.73E-01	2.32E-01
	0.1	6.53E-01	9.98E-01	3.81E-01	6.00E-01	9.64E-01	3.06E-02
	1	8.69E-02	9.86E-01	9.98E-01	7.40E-01	6.94E-01	3.46E-01
	10	4.37E-02	8.02E-02	8.54E-01	1.00E+00	1.00E+00	2.46E-01
	100	7.86E-02	1.98E-01	2.55E-01	9.98E-01	7.45E-01	3.30E-01
	1000	2.16E-02	7.85E-02	2.12E-02	1.82E-01	9.97E-02	7.86E-02
control vs		<i>Boc</i> mRNA level			<i>Gli1</i> mRNA level		
		duck	chick	quail	duck	chick	quail
rSHH [ng/mL]	cycl	9.97E-01	1.00E+00	4.51E-01	< 1.00E-04	< 1.00E-04	< 1.00E-04
	0.1	8.15E-02	9.00E-01	9.84E-01	3.72E-01	9.60E-01	7.92E-02
	1	8.60E-01	9.98E-01	9.78E-01	4.61E-01	> 1.00E+00	5.02E-02
	10	9.10E-01	6.97E-01	2.73E-02	7.45E-01	1.00E+00	6.65E-01
	100	8.58E-01	1.83E-02	1.20E-03	3.06E-02	3.01E-01	2.40E-01
	1000	1.00E+00	< 1.00E-04	< 1.00E-04	< 1.00E-04	< 1.00E-04	1.00E+00
control vs		<i>Cdon</i> mRNA level			<i>Gli2</i> mRNA level		
		duck	chick	quail	duck	chick	quail
rSHH [ng/mL]	cycl	1.00E-04	5.23E-01	6.23E-01	7.96E-02	1.00E+00	< 1.00E-04
	0.1	8.31E-01	1.00E+00	9.59E-01	1.51E-01	1.36E-01	9.94E-01
	1	9.93E-01	9.91E-01	8.03E-01	7.47E-01	4.78E-01	3.28E-01
	10	6.54E-01	3.39E-01	5.45E-01	9.92E-01	8.13E-01	8.54E-01
	100	8.99E-01	8.29E-01	1.89E-02	8.78E-01	8.30E-03	3.20E-02
	1000	8.71E-01	1.20E-03	< 1.00E-04	9.99E-02	4.00E-04	< 1.00E-04
control vs		<i>Gas1</i> mRNA level			<i>Gli3</i> mRNA level		
		duck	chick	quail	duck	chick	quail
rSHH [ng/mL]	cycl	< 1.00E-04	< 1.00E-04	9.92E-01	6.90E-02	3.50E-01	6.40E-03
	0.1	9.28E-01	8.34E-01	1.43E-02	1.55E-01	> 1.00E+00	7.74E-01
	1	9.94E-01	5.02E-01	1.33E-02	9.95E-01	4.56E-01	3.56E-01
	10	> 1.00E+00	9.85E-01	1.20E-03	9.89E-01	9.98E-01	4.52E-02
	100	9.76E-01	2.91E-02	7.00E-04	9.92E-01	2.00E-04	9.00E-04
	1000	9.41E-01	9.00E-03	< 1.00E-04	3.99E-01	< 1.00E-04	< 1.00E-04
control vs		<i>Ptch1</i> mRNA level					
		duck	chick	quail			
rSHH [ng/mL]	cycl	2.40E-03	1.80E-03	< 1.00E-04			
	0.1	9.65E-01	9.96E-01	1.63E-01			
	1	9.31E-01	9.98E-01	4.65E-01			
	10	9.71E-01	9.93E-01	6.26E-01			
	100	5.85E-01	7.29E-01	8.33E-01			
	1000	< 1.00E-04	< 1.00E-04	3.90E-03			

Table 22. P-values for DF1 cell cultures with stably integrated dox-inducible *Gas1* construct after 24 hours of doxycycline hyclate (dox) treatment (significant values highlighted in gray)

gene	dox 0 vs	<i>Gas1</i> -C	<i>Gas1</i> -Q	gene	<i>Gas1</i> -C	<i>Gas1</i> -Q
<i>Ptch1</i>	0.1	0.3069	0.9623	<i>Smo</i>	0.3409	0.0125
	1	0.9985	0.6521		0.9858	0.0608
	5	0.9998	0.7991		0.9997	0.1932
	10	0.9997	0.8881		0.9475	0.1054
	50	0.8656	0.8783		0.9997	0.8438
<i>Gas1</i>	0.1	> 0.9999	> 0.9999	<i>Gli1</i>	0.968	0.9309
	1	> 0.9999	> 0.9999		0.9997	0.9797
	5	0.0088	0.0218		0.1994	0.9968
	10	0.0009	0.0025		0.748	0.8538
	50	< 0.0001	< 0.0001		0.9986	0.5902
<i>Boc</i>	0.1	0.7323	0.9986	<i>Gli2</i>	0.7634	0.6894
	1	0.6035	0.4374		0.1974	0.7809
	5	0.2995	0.1702		0.8542	0.6577
	10	0.9523	0.9694		> 0.9999	> 0.9999
	50	0.0515	0.9974		0.9971	0.8717
<i>Cdon</i>	0.1	0.9357	0.9483	<i>Gli3</i>	0.5971	0.5847
	1	0.3499	0.4978		0.9981	0.7224
	5	0.7706	0.4512		0.6611	0.9744
	10	0.9844	0.9985		0.954	0.3125
	50	0.7565	0.6495		0.9984	0.1895

Table 23. P-values for DF1 cell cultures with stably integrated dox-inducible Gas1 construct after 24 and 48 hours of recombinant SHH (rSHH) protein treatment (significant values highlighted in gray)

control vs		dox: 0 ng/mL + rSHH treatment 24h			dox: 0 ng/mL + rSHH treatment 48h		
		<i>Gas1</i>	<i>Ptch1</i>	<i>Gli1</i>	<i>Gas1</i>	<i>Ptch1</i>	<i>Gli1</i>
rSHH [ng/mL]	0.1	9.75E-01	7.96E-01	1.00E+00	-	-	-
	1	1.00E+00	1.00E+00	9.66E-01	8.01E-01	8.89E-01	8.89E-01
	10	7.01E-01	9.15E-01	4.45E-01	4.17E-01	4.47E-01	5.38E-01
	100	6.84E-02	9.40E-01	7.77E-01	5.29E-01	6.30E-03	2.18E-02
	1000	4.64E-01	1.47E-02	3.33E-01	4.20E-01	1.53E-01	1.21E-01

Table 24. P-values for DF1 cell cultures with stably integrated dox-inducible *Gas1* construct after 48 hours of doxycycline hyclate (dox) and/or recombinant SHH (rSHH) protein treatment (significant values highlighted in gray)

0 ng/mL		rSHH: 0 ng/mL + dox treatment 48h			
vs	<i>Gas1</i>	<i>Ptch1</i>	<i>Gli1</i>	<i>Boc</i>	
0.1	> 1.00E+00	> 1.00E+00	> 1.00E+00	> 1.00E+00	
1	> 1.00E+00	1.00E+00	9.95E-01	9.99E-01	
5	1.00E+00	9.99E-01	1.00E+00	9.87E-01	
10	> 1.00E+00	> 1.00E+00	1.00E+00	8.08E-01	
50	< 1.00E-04	9.88E-01	9.99E-01	1.00E+00	
	<i>Cdon</i>	<i>Smo</i>	<i>Gli2</i>	<i>Gli3</i>	
0.1	9.33E-01	> 1.00E+00	1.00E+00	9.87E-01	
1	9.16E-01	1.00E+00	1.00E+00	9.93E-01	
5	5.17E-01	1.00E+00	9.81E-01	1.00E+00	
10	3.78E-02	4.88E-01	> 1.00E+00	1.00E+00	
50	2.04E-01	6.85E-01	1.00E+00	1.00E+00	
0 ng/mL		rSHH: 100 ng/mL + dox treatment 48h			
vs	<i>Gas1</i>	<i>Ptch1</i>	<i>Gli1</i>	<i>Boc</i>	
0.1	> 1.00E+00	9.93E-01	> 1.00E+00	9.98E-01	
1	> 1.00E+00	9.31E-01	9.98E-01	9.76E-01	
5	1.00E+00	1.00E+00	1.00E+00	1.00E+00	
10	1.00E+00	9.06E-01	4.64E-01	9.44E-01	
50	< 1.00E-04	7.79E-01	> 1.00E+00	9.99E-01	
	<i>Cdon</i>	<i>Smo</i>	<i>Gli2</i>	<i>Gli3</i>	
0.1	8.25E-01	9.51E-01	> 1.00E+00	9.99E-01	
1	1.00E+00	1.00E+00	9.71E-01	> 1.00E+00	
5	9.98E-01	9.87E-01	> 1.00E+00	1.00E+00	
10	9.94E-01	1.00E+00	6.84E-01	1.00E+00	
50	1.00E+00	1.00E+00	1.00E+00	4.47E-01	

Table 25. Mandibular mesenchyme population size in duck and quail embryos with Gas1 over-expression

stage	duck Gas1-oe			quail Gas1-oe		
	mean	SEM	n	mean	SEM	n
HH18	62888.9	23888.9	2	5222.2	1206.98	4
HH21	131523.81	15732.7	21	29722.25	833.35	2
HH24	408268.52	30175.1	6	106277.78	14040	4

Chapter 4: RT-PCR analysis python script for commonly used methods

Introduction

Use of the real-time polymerase chain reaction (RT-PCR) to amplify cDNA products that were reverse transcribed from mRNA is one of the most commonly used tools in molecular biology to study gene expression. There are two traditional way of analyzing data from RT-PCR, absolute and relative quantification. In order to accurately quantify the nucleic acid and ensure data reproducibility, proper mathematical model for data analysis as well as data processing with minimal user-introduced error is necessary. With extensive gene expression analysis, the likelihood of human-introduced error is increasing.

Thus, I developed a custom python script to compare and analyze a large set of data from RT-PCR. This script enables analyses of RT-PCR data using three mathematical models, the $2^{-\Delta\Delta C_T}$ (Livak and Schmittgen, 2001), Pfaffl (Pfaffl, 2001), and standard curve method (i.e., called "Spenser's method" in the script). The script was developed in an open-source software Jupyter Notebook (Project Jupyter, <https://jupyter.org/install>).

The following pages include the script code as well as an example of output generated on August 17th, 2020, for *Gli1* gene from DF1 cells and the *r18s* was used as housekeeping gene. The output shown was generated using two .csv files "r18s_u_F2R2_DF1_20190913.csv" and "Gli1_C_F1R1_ES_DF1_20190913.csv".

1 Import packages and libraries to enable qPCR analysis

```
[423]: import pandas as pd
import numpy as np
import matplotlib.pyplot as plt

%matplotlib inline
import glob
import os
import pip
# pip.main(['install', 'eleven'])
from os import listdir #
import eleven
import scipy
from scipy.stats import linregress
from scipy import stats
# # pip.main(['install', 'plotly'])
# import plotly
# import plotly.plotly as py
# import plotly.graph_objs as go
# pip.main(['install', 'seaborn'])
import seaborn as sns
import matplotlib as mpl
import itertools
import math

#outliers
import numpy.ma as ma
from scipy.stats import mstats
from scipy.stats import t, zscore
# pip.main(['install', 'outlier_utils'])
from outliers import smirnov_grubbs

import datetime as dt
```

2 Set path to selected working directory or change your working directory

```
[424]: #save path to the working directory into variable "path" (easier to use through
→the analysis)
# path = '/Users/Zuzka/Documents/Diderot/PhD/UCSF/Science/Shh project/qPCR/
→analysis/'
# path = '/Users/Zuzka/Documents/PhD/UCSF/Science/Shh project/qPCR/analysis/DF1/
→goi/'
```

```

### PATH to the the working directory with GoI files
### PATH_hkg to the working directory with house-keeping gene files
### PATH_plot where the plots will be saved
### PATH_export to save export files
### path to RNA extraction yields csv file

# DF1 cells folder
# path = '/Users/zuzanavavrusova/Documents/PhD/UCSF/Science/Shh_project/qPCR/
→analysis/DF1/goi/'
# path_hkg = '/Users/zuzanavavrusova/Documents/PhD/UCSF/Science/Shh_project/qPCR/
→analysis/DF1/hkg/'
# path_plot = '/Users/zuzanavavrusova/Documents/PhD/UCSF/Science/Shh_project/
→qPCR/analysis/DF1/plots/'
# path_export = '/Users/zuzanavavrusova/Documents/PhD/UCSF/Science/Shh_project/
→qPCR/analysis/DF1/pyth_export/'
# rna = '/Users/zuzanavavrusova/Documents/PhD/UCSF/Science/Shh_project/qPCR/
→analysis/DF1/rna/'

# DF1_201909_13_22_Gas10E_Dox_only_SHH_only folder
path = '/Users/zuzanavavrusova/Documents/PhD/UCSF/Science/Shh_project/qPCR/
→analysis/DF1_201909_13_22_Gas10E_Dox_only_SHH_only/goi/'
path_hkg = '/Users/zuzanavavrusova/Documents/PhD/UCSF/Science/Shh_project/qPCR/
→analysis/DF1_201909_13_22_Gas10E_Dox_only_SHH_only/hkg/'
path_plot = '/Users/zuzanavavrusova/Documents/PhD/UCSF/Science/Shh_project/qPCR/
→analysis/DF1_201909_13_22_Gas10E_Dox_only_SHH_only/plots/'
path_export = '/Users/zuzanavavrusova/Documents/PhD/UCSF/Science/Shh_project/
→qPCR/analysis/DF1_201909_13_22_Gas10E_Dox_only_SHH_only/pyth_export/'
rna = '/Users/zuzanavavrusova/Documents/PhD/UCSF/Science/Shh_project/qPCR/
→analysis/DF1_201909_13_22_Gas10E_Dox_only_SHH_only/rna/'

# DF1_201912_Gas10EDoxShh folder
# path = '/Users/zuzanavavrusova/Documents/PhD/UCSF/Science/Shh_project/qPCR/
→analysis/DF1_201912_Gas10EDoxShh/goi/'
# path_hkg = '/Users/zuzanavavrusova/Documents/PhD/UCSF/Science/Shh_project/qPCR/
→analysis/DF1_201912_Gas10EDoxShh/hkg/'
# path_plot = '/Users/zuzanavavrusova/Documents/PhD/UCSF/Science/Shh_project/
→qPCR/analysis/DF1_201912_Gas10EDoxShh/plots/'
# path_export = '/Users/zuzanavavrusova/Documents/PhD/UCSF/Science/Shh_project/
→qPCR/analysis/DF1_201912_Gas10EDoxShh/pyth_export/'
# rna = '/Users/zuzanavavrusova/Documents/PhD/UCSF/Science/Shh_project/qPCR/
→analysis/DF1/DF1_201912_Gas10EDoxShh/rna/'

# Cmc

```

```

# path = '/Users/zuzanavavrusova/Documents/PhD/UCSF/Science/Shh_project/qPCR/
→analysis/Cmc/goi/'
# path_hkg = '/Users/zuzanavavrusova/Documents/PhD/UCSF/Science/Shh_project/qPCR/
→analysis/Cmc/hkg/'
# path_plot = '/Users/zuzanavavrusova/Documents/PhD/UCSF/Science/Shh_project/
→qPCR/analysis/Cmc/plots/'
# path_export = '/Users/zuzanavavrusova/Documents/PhD/UCSF/Science/Shh_project/
→qPCR/analysis/Cmc/pyth_export/'
# rna = '/Users/zuzanavavrusova/Documents/PhD/UCSF/Science/Shh_project/qPCR/
→analysis/Cmc/rna/'

# Dmc
# path = '/Users/zuzanavavrusova/Documents/PhD/UCSF/Science/Shh_project/qPCR/
→analysis/Dmc/goi/'
# path_hkg = '/Users/zuzanavavrusova/Documents/PhD/UCSF/Science/Shh_project/qPCR/
→analysis/Dmc/hkg/'
# path_plot = '/Users/zuzanavavrusova/Documents/PhD/UCSF/Science/Shh_project/
→qPCR/analysis/Dmc/plots/'
# path_export = '/Users/zuzanavavrusova/Documents/PhD/UCSF/Science/Shh_project/
→qPCR/analysis/Dmc/pyth_export/'
# rna = '/Users/zuzanavavrusova/Documents/PhD/UCSF/Science/Shh_project/qPCR/
→analysis/Dmc/rna/'

# Qmc
# path = '/Users/zuzanavavrusova/Documents/PhD/UCSF/Science/Shh_project/qPCR/
→analysis/Qmc/goi/'
# path_hkg = '/Users/zuzanavavrusova/Documents/PhD/UCSF/Science/Shh_project/qPCR/
→analysis/Qmc/hkg/'
# path_plot = '/Users/zuzanavavrusova/Documents/PhD/UCSF/Science/Shh_project/
→qPCR/analysis/Qmc/plots/'
# path_export = '/Users/zuzanavavrusova/Documents/PhD/UCSF/Science/Shh_project/
→qPCR/analysis/Qmc/pyth_export/'
# rna = '/Users/zuzanavavrusova/Documents/PhD/UCSF/Science/Shh_project/qPCR/
→analysis/Qmc/rna/'

# Whole Mandible (WM) folder
# path = '/Users/zuzanavavrusova/Documents/PhD/UCSF/Science/Shh_project/qPCR/
→analysis/WM/goi/'
# path_hkg = '/Users/zuzanavavrusova/Documents/PhD/UCSF/Science/Shh_project/qPCR/
→analysis/WM/hkg/'
# path_plot = '/Users/zuzanavavrusova/Documents/PhD/UCSF/Science/Shh_project/
→qPCR/analysis/WM/plots/'

```

```

# path_export = '/Users/zuzanavavrusova/Documents/PhD/UCSF/Science/Shh_project/
→qPCR/analysis/WM/pyth_export/'
# rna = '/Users/zuzanavavrusova/Documents/PhD/UCSF/Science/Shh_project/qPCR/
→analysis/WM/rna/'

# path =
# path_hkg =
# path_plot =
# path_export =
# rna =

os.chdir(path) #Change the current working directory
os.getcwd() #Prints the working directory which you are currently in

```

```
[424]: '/Users/zuzanavavrusova/Documents/PhD/UCSF/Science/Shh_project/qPCR/analysis/DF1
_201909_13_22_Gas10E_Dox_only_SHH_only/goi'
```

```
[425]: date = dt.datetime.today().strftime("%Y%m%d_%Hh%Mm%Ss")
#create a variable with today's date
print(date)
```

```
20200817_12h31m16s
```

```
[426]: rna
```

```
[426]: '/Users/zuzanavavrusova/Documents/PhD/UCSF/Science/Shh_project/qPCR/analysis/DF1
_201909_13_22_Gas10E_Dox_only_SHH_only/rna/'
```

3 ————— FUNCTIONS —————

3.1 Function to create mean values for hkg + E^Ct

```
[427]: def hkg_norm(filenamees, path, c1, c2):
    result = pd.DataFrame()
    all_files = pd.DataFrame()
    list_all_files_hkg = []
    for f in filenamees:
        dokument = f
        #     f = pd.DataFrame.from_csv(path + f)
        f = pd.read_csv(path + f)

        # Rename selected columns for condition1 and condition2 => used in foldu
        →change
        Condition(f, c1, c2)
    #     print(f)
```

```

#remove '/' from target values
Target_change(f)

#lists of different sample values
list_of_sample_values_all=list(set(f['Sample'].values))
list_of_std_values = list(filter(lambda x: str(x).startswith('1'),
                                list_of_sample_values_all))
list_of_neg_values = list(filter(lambda x: str(x).startswith('no'),
                                list_of_sample_values_all))

list_species=list(['Duck', 'Quail', 'Chick', 'Quck'])

#change sample name for negCTRLs to NTC (not necessary)
f.loc[f['Sample'].isin(list_of_neg_values), 'Sample'] = 'NTC'

#starting quantity dilution 1:x + logarithm(starting quantity dilution 1:
→x)
#   f['Log_qt'] = (np.log10(f['Starting Quantity (SQ)']))
#   f['St Qt'] = f['Starting Quantity (SQ)']/pow(10, 6)
#   f['Log_qt'] = -(np.log10(f['St Qt']))
Log_qt(f)

#create a sub data frame containing standards
f_std=f.loc[f['Sample'].isin(list_of_std_values)]
#   print(f_std)

#calculate means, standard dev., maxs, SEM, and mins of standards
f_std_mean = f_std.groupby(['Sample', 'Target'])['Cq'].aggregate([
    'mean', 'std', 'max', 'min'])
f_std_mean['Log_qt_mean'] = f_std.groupby(['Sample', 'Target'])[
    'Log_qt'].aggregate(['mean'])
f_std_mean = f_std_mean.dropna()
f_std_mean['SEM'] = f_std_mean['std']/math.sqrt(3)
#   print(f_std_mean)

print(dokument)
#slope, intercept, and efficiency
slope, intercept = np.polyfit(f_std_mean['Log_qt_mean'].values,
→f_std_mean['mean'].values, 1)

print('Slope')
print(slope)
print('Intercept')
print(intercept)
#   E = (pow(10, (1/slope))-1)*100 #E in %

```

```

#         E = pow(10,(-1/slope)) #E when plotting samples from highest Cq to
↳lowest
        E = (pow(10,(1/slope))) #E when plotting samples from lowest Cq to
↳highest
        print('Efficiency')
        print(E)
        print('-----')

        #normalizing Cq to the standards - Spenser's method
f['Norm_Cq'] = pow(10, -((f['Cq']-intercept)/slope))
#         print(f)

        #normalizing Cq with efficiency (used for Pffafl method)
#         hkg_mean = f.groupby(['Sample', 'Target', 'dox', 'species'])['Cq'].
↳aggregate(['mean'])
#         hkg_mean = f.groupby(['Sample', 'Target', 'condition1', 'species'])
↳)['Cq'].aggregate(['mean'])
        hkg_mean = f.groupby(['Sample', 'Target', 'condition1',
↳'condition2', 'species'])['Cq'].aggregate(['mean'])
        hkg_mean['E'] = E
        hkg_mean['E_pow_mean_cq'] = pow(E, (hkg_mean['mean']))
        hkg_mean['Spenser_Norm_Cq_hkg'] = pow(10, -((hkg_mean['mean']-intercept)/
↳slope))

#         print(hkg_mean)

        if all_files.empty:
            all_files = f
        else:
            all_files = all_files.append(f, ignore_index=True)

        list_all_files_hkg = list(set(filter(lambda x: str(x) not in ['nan',
↳'nocDNA', 'noRNA', 'NTC', 'no_cDNA'],
                                                all_files['Sample'].values)))

        if result.empty:
            result = hkg_mean
            hkg_name = dokument
        else:
            result = result.append(hkg_mean)

return result, dokument, list_all_files_hkg, c1, c2

```


3.2 Function to rename column of selected conditions to condition1 and condition2 - used for fold change

```
[428]: # Rename selected columns for condition1 and condition2 => used in fold change
def Condition(f, c1, c2):
    if c1 == '':
        f['condition1'] = 0
    else:
        f.rename(columns={ c1 : 'condition1'}, inplace=True)

    if c2 == '':
        f['condition2'] = 0
    else:
        f.rename(columns={ c2 : 'condition2'}, inplace=True)

    # print(f)
```

3.3 Functions to create a column for each sample based on the sample name

3.3.1 Target column

```
[429]: #Target column (original dataframe) changed if species spec. primers don't have
→the same target name for all species
def Target(f):
    tr = list(set(filter(lambda x: str(x)!='nan', f['Target'].values)))

    if '_D_' in tr[0]:
        f['Target'] = tr[0].replace('_D_', '_ss_')

    elif '_Q_' in tr[0]:
        f['Target'] = tr[0].replace('_Q_', '_ss_')

    elif '_C_' in tr[0]:
        f['Target'] = tr[0].replace('_C_', '_ss_')

    elif '_QD_' in tr[0]:
        f['Target'] = tr[0].replace('_QD_', '_ss_')

    else:
        f['Target'] = tr[0]
```

```
[430]: #Target column (original dataframe) changed if species spec. primers don't have
→the same target name for all species
def Target_change(f):
    tr = list(set(filter(lambda x: str(x)!='nan', f['Target'].values)))

    if '/' in tr[0]:
        f['Target'] = tr[0].replace('/', '')
```

```

else:
    f['Target'] = tr[0]

```

3.3.2 Logarithm of starting quantity dilution 1:x (Log_qt) column

```

[431]: def Log_qt(f):
#     f['Log_qt'] = (np.log10(f['Starting Quantity (SQ)']))
    f['St Qt'] = f['Starting Quantity (SQ)']/pow(10, 6)
#logarithm(starting quantity dilution 1:x)
    f['Log_qt'] = -(np.log10(f['St Qt']))

```

3.4 Gene of interest normalized to its efficiency ~ E^{Ct}, Spenser's norm Cq

```

[432]: def E_norm_cq(f, f_mean_norm, list_of_std_values):
    name = dokument #the csv file name - defined at the beginning of for loop
    →for all files
        #create a sub data frame containing standards
        f_std=f.loc[f['Sample'].isin(list_of_std_values)]
        #calculate means, standard dev., maxs, SEM, and mins of standards
        f_std_mean = f_std.groupby(['Sample', 'Target'])['Cq'].aggregate(['mean',
    →'std', 'max', 'min'])
        f_std_mean['Log_qt_mean'] = f_std.groupby(['Sample', 'Target'])['Log_qt'].
    →aggregate(['mean'])
        f_std_mean = f_std_mean.dropna()

        print(name)
        #slope, intercept, and efficiency
        slope, intercept = np.polyfit(f_std_mean['Log_qt_mean'].values,
    →f_std_mean['mean'].values, 1)
        print('Slope')
        print(slope)
        print('Intercept')
        print(intercept)
#     E = (pow(10, (1/slope))-1)*100 #E in %
#     E = pow(10, (-1/slope)) #E when plotting samples from highest Cq to lowest
E = (pow(10, (1/slope))) #E when plotting samples from lowest Cq to highest
        print('Efficiency')
        print(E)
        print('-----')

        #normalizing Cq with efficiency
        f_mean_norm['E'] = E
        f_mean_norm['E_pow_mean_cq'] = pow(E, (f_mean_norm['mean']))
        f_mean_norm['Spenser_Norm_Cq'] = pow(10, -((f_mean_norm['mean']-intercept)/
    →slope))

```

3.5 Gene of interest normalized to house keeping gene column - Spenser's method

```
[433]: #f_mean_norm['hkg_norm'] = f_mean_norm['mean']/tabulky['mean']
# function adding a column with values normalized to the housekeeping gene - use
→for GoI

# goi_hkg_norm(f_mean_norm, tabulky, list_of_sample_values_all_norm)

def goi_hkg_norm(f, f_hkg, list_of_sample_values_all):
#     f['Spenser_goi_hkg_norm'] = pd.Series()
#     for a in list_of_sample_values_all:
#         n = f_1.loc[a, 'Spenser_Norm_Cq']
#         m = f_hkg_1.loc[a, 'Spenser_Norm_Cq_hkg']
#         f.loc[a, 'Spenser_goi_hkg_norm'] = n.values[0]/m

f['Spenser_Norm_Cq_hkg'] = pd.Series()
f['Spenser_goi_hkg_norm'] = pd.Series()

for a in list_of_sample_values_all:
    goi = f.loc[a, 'Spenser_Norm_Cq']
#     print(goi)
#     print(goi.values[0])
    hkg = f_hkg.loc[a, 'Spenser_Norm_Cq_hkg']
#     print(hkg)
#     print(hkg.values[0])

    f.loc[a, 'Spenser_Norm_Cq_hkg'] =hkg.values[0]
    f.loc[a, 'Spenser_goi_hkg_norm'] = goi.values[0]/hkg.values[0]
```

3.6 Functions to create a column with fold change - choose dox, construct, and target which will be used as a reference ~ "set to 1"

3.6.1 Function used to get E[^]Ct(ctrl) / E[^]Ct(experimental) for both HKG as well as GoI

```
[434]: # def FC(df, l, condition1, species, target): # '15', 'Quail', always
→'18s_u_F2R2_SS' for hkg
def FC(df, l, condition1, condition2, species, target):

#     df_1 = df.reset_index(level=['condition1', 'species', 'Target'])
df_1 = df.reset_index(level=['condition1', 'condition2', 'species', 'Target'])

print(condition1)
print(condition2)
print(species)
print(target)

condition1_df = df_1.loc[df_1['condition1'].values==condition1]
```

```

#     print(condition1_df)

    condition2_df = condition1_df.loc[condition1_df['condition2']
→values==condition2]
#     print(condition2_df)

#     species_df = condition1_df.loc[condition1_df['species'].values==species]
species_df = condition2_df.loc[condition2_df['species'].values==species]
#     print(species_df)

    target_df = species_df.loc[species_df['Target'].values==target]
#     print(target_df)

    ctrl_mean = target_df.groupby(['Target'])['E_pow_mean_cq'].
→aggregate(['mean', 'std'])
#     print(ctrl_mean)

    df['E_ratio'] = pd.Series()
    targets=list(set(df_1['Target'].values))
#     print(targets)

    for a in l:
        for b in targets:
            if (a, b) not in df.index:
                continue
            m = df.loc[(a, b), 'E_pow_mean_cq']
#             print(a)
#             print(m.values[0])
            n = ctrl_mean.loc[target, 'mean']
#             print(n)
            df.loc[(a, b), 'E_ratio'] = n / m.values[0]

#     return targets, species, condition1, target
return targets, species, condition1, condition2, target

```

3.6.2 Pffaf method: used to calculate directly $E(\text{goi})^d \text{Ct}(\text{goi}) / E(\text{hkg})^d \text{Ct}(\text{hkg})$

```

[435]: # def FC_Pffaf(df, condition1, species, target): # '15', 'Quail', always_
→'18s_u_F2R2_SS' for hkg
def FC_Pffaf(df, condition1, condition2, species, target):

#     df_1 = df.reset_index(level=['condition1', 'species', 'Target'])
df_1 = df.reset_index(level=['condition1', 'condition2', 'species', 'Target'])

    print(condition1)

```

```

print(condition2)
print(species)
print(target)

condition1_df = df_1.loc[df_1['condition1'].values==condition1]
print(condition1_df)

condition2_df = condition1_df.loc[condition1_df['condition2'].
→values==condition2]
#     print(condition2_df)

species_df = condition1_df.loc[condition1_df['species'].values==species]
species_df = condition2_df.loc[condition2_df['species'].values==species]
print(species_df)

target_df = species_df.loc[species_df['Target'].values==target]
print(target_df)

ctrl_mean = target_df.groupby(['Target'])['mean'].aggregate(['mean', 'std'])
print(ctrl_mean)

ctrl_mean_hkg = target_df.groupby(['Target'])['Cq_hkg'].aggregate(['mean', 'std'])
→print(ctrl_mean_hkg)

n = ctrl_mean.loc[target, 'mean']
m = ctrl_mean_hkg.loc[target, 'mean']
print(n)
print(m)

df['dCt_goi'] = n - df['mean']
df['dCt_hkg'] = m - df['Cq_hkg']

df['FC_Pfaffl'] = (pow(df['E'], df['dCt_goi']))/(pow(df['E_hkg'],
→df['dCt_hkg']))

targets=list(set(df_1['Target'].values))
#     print(targets)

return targets

```

3.6.3 Livak method

```
[436]: # def FC_livak(df, condition1, species, target): # '15', 'Quail', always_
↳ '18s_u_F2R2_SS' for hkg
def FC_livak(df, condition1, condition2, species, target):

#     df_1 = df.reset_index(level=['condition1', 'species', 'Target'])
df_1 = df.reset_index(level=['condition1', 'condition2', 'species', 'Target'])
#     df['E_Livak'] = 2
#     df['dCt_Livak'] = df['mean'] - df['Cq_hkg']

print(condition1)
print(condition2)
print(species)
print(target)

condition1_df = df_1.loc[df_1['condition1'].values==condition1]
print(condition1_df)

condition2_df = condition1_df.loc[condition1_df['condition2'].
↳ values==condition2]
#     print(condition2_df)

#     species_df = condition1_df.loc[condition1_df['species'].values==species]
species_df = condition2_df.loc[condition2_df['species'].values==species]
print(species_df)

target_df = species_df.loc[species_df['Target'].values==target]
print(target_df)

ctrl_mean = target_df.groupby(['Target'])['dCt_Livak'].aggregate(['mean',
↳ 'std'])
print(ctrl_mean)

n = ctrl_mean.loc[target, 'mean']
print(n)

df['ddCt_Livak'] = df['dCt_Livak'] - n
df['FC_Livak'] = pow(2, -df['ddCt_Livak'])

targets=list(set(df_1['Target'].values))
#     print(targets)

return targets
```

3.6.4 Spenser's method fold change

```
[437]: # def FC_livak(df, condition1, species, target): # '15', 'Quail', always_
→ '18s_u_F2R2_SS' for hkg
def FC_Spenser(df, condition1, condition2, species, target):

#     df_1 = df.reset_index(level=['condition1', 'species', 'Target'])
df_1 = df.reset_index(level=['condition1', 'condition2', 'species', 'Target'])
#     df['E_Livak'] = 2
#     df['dCt_Livak'] = df['mean'] - df['Cq_hkg']

print(condition1)
print(condition2)
print(species)
print(target)

condition1_df = df_1.loc[df_1['condition1'].values==condition1]
print(condition1_df)

condition2_df = condition1_df.loc[condition1_df['condition2'].
→values==condition2]
#     print(condition2_df)

#     species_df = condition1_df.loc[condition1_df['species'].values==species]
species_df = condition2_df.loc[condition2_df['species'].values==species]
print(species_df)

target_df = species_df.loc[species_df['Target'].values==target]
print(target_df)

ctrl_mean = target_df.groupby(['Target'])['Spenser_goi_hkg_norm'].
→aggregate(['mean', 'std'])
print(ctrl_mean)

n = ctrl_mean.loc[target, 'mean']
print(n)

df['FC_Spenser'] = df['Spenser_goi_hkg_norm'] / n

targets=list(set(df_1['Target'].values))
#     print(targets)

return targets
```

3.6.5 Gene of interest normalized to house keeping gene fold change $E(\text{GoI})^{\text{dCt}} / E(\text{HKG})^{\text{dCt}}$

```
[438]: #E(GoI)dCt / E(HKG)dCt

def GER(f, f_hkg, list_of_sample_values_all):
    f['E_ratio_hkg'] = pd.Series()
    f['GER'] = pd.Series()
    f['Cq_hkg'] = pd.Series()
    f['E_hkg'] = pd.Series()
    # df_1 = f.reset_index(level=['condition1','species', 'Target'])
    df_1 = f.reset_index(level=['condition1', 'condition2','species', 'Target'])
    targets=list(set(df_1['Target'].values))

    for a in list_of_sample_values_all:
        for b in targets:
            if (a, b) not in f.index:
                continue
            # print(a)
            # print(b)
            goi = f.loc[(a, b), 'E_ratio']
            # print('goi')
            # print(goi.values[0])
            hkg = f_hkg.loc[a, 'E_ratio']
            # print('hkg')
            # print(hkg.values[0])
            cq_hkg = f_hkg.loc[a, 'mean']
            E_hkg = f_hkg.loc[a, 'E']

            f.loc[(a, b), 'Cq_hkg'] = cq_hkg.values[0]
            f.loc[(a, b), 'E_hkg'] = E_hkg.values[0]
            f.loc[(a, b), 'E_ratio_hkg'] = hkg.values[0]
            f.loc[(a, b), 'GER'] = goi.values[0]/hkg.values[0]
```

```
[439]: def hkg_values(f, f_hkg, list_of_sample_values_all):
    f['Cq_hkg'] = pd.Series()
    f['E_hkg'] = pd.Series()
    # df_1 = f.reset_index(level=['condition1','species', 'Target'])
    df_1 = f.reset_index(level=['condition1', 'condition2','species', 'Target'])
    targets=list(set(df_1['Target'].values))

    for a in list_of_sample_values_all:
        for b in targets:
            if (a, b) not in f.index:
                continue
            cq_hkg = f_hkg.loc[a, 'mean']
```



```

E_hkg = f_hkg.loc[a, 'E']

f.loc[(a, b), 'Cq_hkg'] = cq_hkg.values[0]
f.loc[(a, b), 'E_hkg'] = E_hkg.values[0]

```

3.7 Gene of interest multiplied by RNA extraction yields

```

[440]: # f_mean_norm['rna_yield'] = f_mean_norm['hkg_norm']*(rna['yield_um']/2)
# 'yield_um' is divided by 2 because 2uL of cDNA per well in the qPCR reaction
# f_yield ~ csv file with RNA yields for all samples

# rna_yield(all_files_mean_norm, rna_table, list_of_sample_values_all_norm)
def rna_yield(f, rna_table, list_of_sample_values_all_norm):
    f['FC_Spenser_rna_yield'] = pd.Series()
    f['Spenser_goi_hkg_norm_rna_yield'] = pd.Series()
    f['FC_Pfaffl_rna_yield'] = pd.Series()
    f['FC_Livak_rna_yield'] = pd.Series()
    t = rna_table.set_index('Sample')

    # print duplicate Sample values that are present in rna-table
    myset = set(rna_table['Sample'].values)
    for x in myset:
        c = list(rna_table['Sample'].values).count(x)
        if c > 1:
            print(x)

    for a in list_of_sample_values_all_norm:
#         print(a)
        n1 = f.loc[a, 'FC_Spenser']
#         print(n1)
        n4 = f.loc[a, 'Spenser_goi_hkg_norm']
#         print(n4)
        n2 = f.loc[a, 'FC_Pfaffl']
#         print(n2)
        n3 = f.loc[a, 'FC_Livak']
#         print(n3)

        m = t.loc[a, 'yield_ws']
#         print(m)

        f.loc[a, 'FC_Spenser_rna_yield'] = n1.values[0]*(m/2)
        f.loc[a, 'Spenser_goi_hkg_norm_rna_yield'] = n4.values[0]*(m/2)
        f.loc[a, 'FC_Pfaffl_rna_yield'] = n2.values[0]*(m/2)
        f.loc[a, 'FC_Livak_rna_yield'] = n3.values[0]*(m/2)
#         print(m)

```

4 DATA * PROCESSING

4.1 Read hkg files into jupyter

```
[441]: #find all csv files in a working directory
def find_csv_filenames( path_hkg, suffix=".csv" ):
    filenames_hkg = listdir(path_hkg)
    return [ filename for filename in filenames_hkg if filename.endswith( suffix_
    →) ]
```

```
[442]: filenames_hkg = find_csv_filenames(path_hkg)
for name in filenames_hkg:
    print(name)
```

r18s_u_F2R2_DF1_20190913.csv

4.2 Use function created above (hkg_norm) to get mean values for hkg

!! SET * CONDITION !!

```
[443]: # tabulky, hkg_name, list_all_files_hkg = hkg_norm(filenames_hkg, path_hkg)
tabulky, hkg_name, list_all_files_hkg, c1, c2 = hkg_norm(filenames_hkg,
    →path_hkg, 'dox', '')
```

r18s_u_F2R2_DF1_20190913.csv

Slope

3.3793850186130174

Intercept

8.9498571975

Efficiency

1.9765683116827863

```
[444]: tabulky
```

```
[444]:
```

					mean	E \
Sample	Target	condition1	condition2	species		
1:16_DF1	r18s_u_F2R2_SS	DF1_STD	0	std	13.044166	1.976568
1:256_DF1	r18s_u_F2R2_SS	DF1_STD	0	std	NaN	1.976568
1:4_DF1	r18s_u_F2R2_SS	DF1_STD	0	std	10.924775	1.976568
1:64_DF1	r18s_u_F2R2_SS	DF1_STD	0	std	15.056777	1.976568
1x_DF1	r18s_u_F2R2_SS	DF1_STD	0	std	8.981265	1.976568
A1	r18s_u_F2R2_SS	0	0	Gas1_C	12.509410	1.976568
A2	r18s_u_F2R2_SS	0.1	0	Gas1_C	12.609432	1.976568
A3	r18s_u_F2R2_SS	1	0	Gas1_C	12.689375	1.976568
A4	r18s_u_F2R2_SS	5	0	Gas1_C	12.962884	1.976568
A5	r18s_u_F2R2_SS	10	0	Gas1_C	11.538201	1.976568
A6	r18s_u_F2R2_SS	50	0	Gas1_C	12.915466	1.976568

B1	r18s_u_F2R2_SS	0	0	Gas1_C	12.522978	1.976568
B2	r18s_u_F2R2_SS	0.1	0	Gas1_C	12.380428	1.976568
B3	r18s_u_F2R2_SS	1	0	Gas1_C	12.669540	1.976568
B4	r18s_u_F2R2_SS	5	0	Gas1_C	12.753511	1.976568
B5	r18s_u_F2R2_SS	10	0	Gas1_C	11.912618	1.976568
B6	r18s_u_F2R2_SS	50	0	Gas1_C	12.963128	1.976568
C1	r18s_u_F2R2_SS	0	0	Gas1_Q	12.400953	1.976568
C2	r18s_u_F2R2_SS	0.1	0	Gas1_Q	12.029810	1.976568
C3	r18s_u_F2R2_SS	1	0	Gas1_Q	12.982646	1.976568
C4	r18s_u_F2R2_SS	5	0	Gas1_Q	13.077828	1.976568
C5	r18s_u_F2R2_SS	10	0	Gas1_Q	12.118152	1.976568
C6	r18s_u_F2R2_SS	50	0	Gas1_Q	12.616522	1.976568
D1	r18s_u_F2R2_SS	0	0	Gas1_Q	12.195742	1.976568
D2	r18s_u_F2R2_SS	0.1	0	Gas1_Q	10.873504	1.976568
D3	r18s_u_F2R2_SS	1	0	Gas1_Q	13.011662	1.976568
D4	r18s_u_F2R2_SS	5	0	Gas1_Q	12.495101	1.976568
D5	r18s_u_F2R2_SS	10	0	Gas1_Q	12.065826	1.976568
D6	r18s_u_F2R2_SS	50	0	Gas1_Q	12.229335	1.976568

E_pow_mean_cq \

Sample	Target	condition1	condition2	species	
1:16_DF1	r18s_u_F2R2_SS	DF1_STD	0	std	7243.077719
1:256_DF1	r18s_u_F2R2_SS	DF1_STD	0	std	NaN
1:4_DF1	r18s_u_F2R2_SS	DF1_STD	0	std	1709.110747
1:64_DF1	r18s_u_F2R2_SS	DF1_STD	0	std	28541.601853
1x_DF1	r18s_u_F2R2_SS	DF1_STD	0	std	454.634811
A1	r18s_u_F2R2_SS	0	0	Gas1_C	5031.324313
A2	r18s_u_F2R2_SS	0.1	0	Gas1_C	5386.169088
A3	r18s_u_F2R2_SS	1	0	Gas1_C	5687.693677
A4	r18s_u_F2R2_SS	5	0	Gas1_C	6852.842862
A5	r18s_u_F2R2_SS	10	0	Gas1_C	2595.912265
A6	r18s_u_F2R2_SS	50	0	Gas1_C	6634.970895
B1	r18s_u_F2R2_SS	0	0	Gas1_C	5078.053812
B2	r18s_u_F2R2_SS	0.1	0	Gas1_C	4608.028625
B3	r18s_u_F2R2_SS	1	0	Gas1_C	5611.340218
B4	r18s_u_F2R2_SS	5	0	Gas1_C	5941.753381
B5	r18s_u_F2R2_SS	10	0	Gas1_C	3350.307336
B6	r18s_u_F2R2_SS	50	0	Gas1_C	6853.980950
C1	r18s_u_F2R2_SS	0	0	Gas1_Q	4672.924216
C2	r18s_u_F2R2_SS	0.1	0	Gas1_Q	3628.801142
C3	r18s_u_F2R2_SS	1	0	Gas1_Q	6945.740023
C4	r18s_u_F2R2_SS	5	0	Gas1_Q	7411.120678
C5	r18s_u_F2R2_SS	10	0	Gas1_Q	3853.935436
C6	r18s_u_F2R2_SS	50	0	Gas1_Q	5412.253791
D1	r18s_u_F2R2_SS	0	0	Gas1_Q	4063.162671
D2	r18s_u_F2R2_SS	0.1	0	Gas1_Q	1650.435165
D3	r18s_u_F2R2_SS	1	0	Gas1_Q	7084.426106

D4	r18s_u_F2R2_SS	5	0	Gas1_Q	4982.508495
D5	r18s_u_F2R2_SS	10	0	Gas1_Q	3718.953762
D6	r18s_u_F2R2_SS	50	0	Gas1_Q	4157.237886

Sample	Target	condition1	condition2	species	Spenser_Norm_Cq_hkg
1:16_DF1	r18s_u_F2R2_SS	DF1_STD	0	std	0.061439
1:256_DF1	r18s_u_F2R2_SS	DF1_STD	0	std	NaN
1:4_DF1	r18s_u_F2R2_SS	DF1_STD	0	std	0.260374
1:64_DF1	r18s_u_F2R2_SS	DF1_STD	0	std	0.015592
1x_DF1	r18s_u_F2R2_SS	DF1_STD	0	std	0.978827
A1	r18s_u_F2R2_SS	0	0	Gas1_C	0.088448
A2	r18s_u_F2R2_SS	0.1	0	Gas1_C	0.082621
A3	r18s_u_F2R2_SS	1	0	Gas1_C	0.078241
A4	r18s_u_F2R2_SS	5	0	Gas1_C	0.064938
A5	r18s_u_F2R2_SS	10	0	Gas1_C	0.171427
A6	r18s_u_F2R2_SS	50	0	Gas1_C	0.067070
B1	r18s_u_F2R2_SS	0	0	Gas1_C	0.087634
B2	r18s_u_F2R2_SS	0.1	0	Gas1_C	0.096572
B3	r18s_u_F2R2_SS	1	0	Gas1_C	0.079305
B4	r18s_u_F2R2_SS	5	0	Gas1_C	0.074895
B5	r18s_u_F2R2_SS	10	0	Gas1_C	0.132826
B6	r18s_u_F2R2_SS	50	0	Gas1_C	0.064927
C1	r18s_u_F2R2_SS	0	0	Gas1_Q	0.095231
C2	r18s_u_F2R2_SS	0.1	0	Gas1_Q	0.122632
C3	r18s_u_F2R2_SS	1	0	Gas1_Q	0.064069
C4	r18s_u_F2R2_SS	5	0	Gas1_Q	0.060046
C5	r18s_u_F2R2_SS	10	0	Gas1_Q	0.115469
C6	r18s_u_F2R2_SS	50	0	Gas1_Q	0.082222
D1	r18s_u_F2R2_SS	0	0	Gas1_Q	0.109523
D2	r18s_u_F2R2_SS	0.1	0	Gas1_Q	0.269631
D3	r18s_u_F2R2_SS	1	0	Gas1_Q	0.062815
D4	r18s_u_F2R2_SS	5	0	Gas1_Q	0.089314
D5	r18s_u_F2R2_SS	10	0	Gas1_Q	0.119660
D6	r18s_u_F2R2_SS	50	0	Gas1_Q	0.107044

```
[445]: # tabulky.to_csv(path_export +
#           date + '_' +
#           'r18s' + '.csv'
#           )
```

————— **!! SET * CONDITION !!** —————

4.3 function definition: FC(df, l, condition1, condition2, species, target)

- condition1 ~ stage, dox, condition
- condition2 ~ initials, shh

```
[446]: # condition1 = '15', '18', '21', '24', '27', 'ctrl', '0', '0.1', '1', '5', '10', '50'
# condition2 = 0, 0.1, 1, 10, 100, 1000, 2000
# species = 'Chick', 'Duck', 'Quail', 'Quck', 'Gas1_C', 'Gas1_Q',

print(c1)
print(c2)
```

dox

```
[447]: # targets_hkg = FC(tabulky, list_all_files_hkg, '15', 0, 'Quail',
→ 'r18s_u_F2R2_SS') #wm

# targets_hkg = FC(tabulky, list_all_files_hkg, 'ctrl', 0, 'Quail',
→ 'r18s_u_F2R2_SS') #Hugo's files r18s_u_F2R2
# targets_hkg = FC(tabulky, list_all_files_hkg, 'ctrl', 0, 'Duck',
→ 'r18s_u_F2R2_SS') #Cmc, Dmc, Qmc
# targets_hkg = FC(tabulky, list_all_files_hkg, 'ctrl', 0, 'Chick',
→ 'r18s_u_F2R2_SS') #Cmc, Dmc, Qmc

# targets_hkg = FC(tabulky, list_all_files_hkg, '0', 0, 'Gas1_Q',
→ 'r18s_u_F2R2_SS') #DF1oe
targets_hkg = FC(tabulky, list_all_files_hkg, '0', 0, 'Gas1_C',
→ 'r18s_u_F2R2_SS') #DF1oe

# targets_hkg = FC(tabulky, list_all_files_hkg, '15', 0, 'Quail',
→ 'r18s_u_F2R2_SS')
```

```
0
0
Gas1_C
r18s_u_F2R2_SS
```

```
[448]: targets_hkg
```

```
[448]: (['r18s_u_F2R2_SS'], 'Gas1_C', '0', 0, 'r18s_u_F2R2_SS')
```

```
[449]: hkg_name
```

```
[449]: 'r18s_u_F2R2_DF1_20190913.csv'
```

4.4 Create hkg_target variable

```
[450]: #when using also Quck files
# hkg_name
hkg_target = hkg_name[:4]
```

```
print(hkg_name)
print(hkg_target)
```

```
r18s_u_F2R2_DF1_20190913.csv
r18s
```

4.5 Read goi files into jupyter

```
[451]: #find all csv files in a working directory
def find_csv_filenames( path, suffix=".csv" ):
    filenames = listdir(path)
    return [ filename for filename in filenames if filename.endswith( suffix )
    →and "allfiles" not in filename]
```

```
[452]: filenames = find_csv_filenames(path)
for name in filenames:
    print(name)
```

```
Gli1_C_F1R1_ES_DF1_20190913.csv
```

4.6 Normalizing Genes of Interest

```
[453]: all_files = pd.DataFrame()
all_files_mean = pd.DataFrame()
all_files_mean_norm = pd.DataFrame()
FC_df = pd.DataFrame()
list_all_files = []
list_of_targets = []
list_rna = []

for i, f in enumerate(filenames):
    dokument = f.replace(".csv", "")
    # f = pd.DataFrame.from_csv(path + f) - not working
    f = pd.read_csv(path + f)

    # Rename selected columns for condition1 and condition2 => used in fold
    →change
    Condition(f, c1, c2)

    #lists of different sample values
    list_of_sample_values_all=list(set(f['Sample'].values))
    list_of_std_values = list(filter(lambda x: str(x).startswith('1'),
    →list_of_sample_values_all))
    list_of_neg_values = list(filter(lambda x: str(x).startswith('no'),
    →list_of_sample_values_all))
    samples = list(filter(lambda x: str(x) not in ['nan', 'nocDNA',
    →'noRNA', 'NTC', 'no_cDNA'], list_of_sample_values_all))
```

```

list_of_sample_values_all_norm = list(filter(lambda x: str(x) not in
↳list_of_std_values, samples))
list_species=list(['Duck', 'Quail', 'Chick', 'Quack'])
#create list of targets
list_of_targets = list(set(filter(lambda x: str(x)!='nan', f['Target'].
↳values)))

#change Sample name for negCTRLs to NTC (not necessary)
f.loc[f['Sample'].isin(list_of_neg_values), 'Sample'] = 'NTC'

#remove '/' from target values
Target_change(f)

#change Target name for species spec. primers
Target(f)

#column logarithm(starting quantity dilution 1:x)
Log_qt(f)

# Create new table with Sample means for Cq values
# f_mean_norm = f.groupby(['Sample', 'Target', 'condition1', 'species'])['Cq'].
↳aggregate(['mean'])
f_mean_norm = f.groupby(['Sample', 'Target', 'condition1',
↳'condition2', 'species'])['Cq'].aggregate(['mean'])

#function to normalize Cq to the standards (print Efficiency)
E_norm_cq(f, f_mean_norm, list_of_std_values)
# print(f_mean_norm)

#function adding a column with values normalized to the housekeeping gene -
↳Spenser's method
#f_mean_norm['hkg_norm'] = f_mean_norm['mean']/tabulky['mean']
goi_hkg_norm(f_mean_norm, tabulky, list_of_sample_values_all_norm)

if all_files.empty:
    all_files = f
else:
    all_files = all_files.append(f, ignore_index=True)

list_all_files = list(set(filter(lambda x: str(x) not in ['nan', 'nocDNA',
↳'noRNA', 'NTC', 'no_cDNA'], all_files['Sample'].values)))
list_all_targets = list(set(all_files['Target'].values))

```

```

# list_rna_ = set(filter(lambda x: str(x).startswith('1'),
↳all_files['Sample'].values))
list_rna = set(filter(lambda x: str(x) not in ['nan', 'nocDNA',
↳'noRNA', 'NTC', 'no_cDNA'], all_files['Sample'].values)) - set(filter(lambda x:
↳str(x).startswith('1'), all_files['Sample'].values))

# list_rna = list(set(filter(lambda x: str(x) not in ['nan', 'nocDNA',
↳'noRNA', 'NTC', 'no_cDNA'], list_rna_)))
#
if all_files_mean_norm.empty:
    all_files_mean_norm = f_mean_norm
else:
    all_files_mean_norm = all_files_mean_norm.append(f_mean_norm)
#multiIndex-ed objects need to be sorted for effective slicing and indexing
all_files_mean_norm=all_files_mean_norm.sort_index()

#combine all csv files in 'path' directory into one big dataframe by adding rows
↳of each csv file at the end of the dataframe

```

```

Gli1_C_F1R1_ES_DF1_20190913
Slope
2.5033062679945015
Intercept
29.651365399999996
Efficiency
2.5088326664551324
-----

```

[454]: all_files_mean_norm

```

[454]:

```

Sample	Target	condition1	condition2	species	mean	E \
1:16_DF1	Gli1_ss_F1R1_ES	DF1_STD	0	std	32.442002	2.508833
1:256_DF1	Gli1_ss_F1R1_ES	DF1_STD	0	std	NaN	2.508833
1:4_DF1	Gli1_ss_F1R1_ES	DF1_STD	0	std	31.605795	2.508833
1:64_DF1	Gli1_ss_F1R1_ES	DF1_STD	0	std	NaN	2.508833
1x_DF1	Gli1_ss_F1R1_ES	DF1_STD	0	std	29.427721	2.508833
A1	Gli1_ss_F1R1_ES	0	0	Gas1_C	NaN	2.508833
A2	Gli1_ss_F1R1_ES	0.1	0	Gas1_C	32.159454	2.508833
A3	Gli1_ss_F1R1_ES	1	0	Gas1_C	32.782411	2.508833
A4	Gli1_ss_F1R1_ES	5	0	Gas1_C	32.011265	2.508833
A5	Gli1_ss_F1R1_ES	10	0	Gas1_C	31.248569	2.508833
A6	Gli1_ss_F1R1_ES	50	0	Gas1_C	32.544062	2.508833
B1	Gli1_ss_F1R1_ES	0	0	Gas1_C	32.195926	2.508833

B2	Gli1_ss_F1R1_ES	0.1	0	Gas1_C	33.153569	2.508833
B3	Gli1_ss_F1R1_ES	1	0	Gas1_C	33.032491	2.508833
B4	Gli1_ss_F1R1_ES	5	0	Gas1_C	32.137057	2.508833
B5	Gli1_ss_F1R1_ES	10	0	Gas1_C	32.228637	2.508833
B6	Gli1_ss_F1R1_ES	50	0	Gas1_C	33.928171	2.508833
C1	Gli1_ss_F1R1_ES	0	0	Gas1_Q	32.336660	2.508833
C2	Gli1_ss_F1R1_ES	0.1	0	Gas1_Q	32.124040	2.508833
C3	Gli1_ss_F1R1_ES	1	0	Gas1_Q	32.621752	2.508833
C4	Gli1_ss_F1R1_ES	5	0	Gas1_Q	32.313141	2.508833
C5	Gli1_ss_F1R1_ES	10	0	Gas1_Q	33.359558	2.508833
C6	Gli1_ss_F1R1_ES	50	0	Gas1_Q	32.759660	2.508833
D1	Gli1_ss_F1R1_ES	0	0	Gas1_Q	31.448287	2.508833
D2	Gli1_ss_F1R1_ES	0.1	0	Gas1_Q	31.030349	2.508833
D3	Gli1_ss_F1R1_ES	1	0	Gas1_Q	31.819967	2.508833
D4	Gli1_ss_F1R1_ES	5	0	Gas1_Q	32.459621	2.508833
D5	Gli1_ss_F1R1_ES	10	0	Gas1_Q	31.596858	2.508833
D6	Gli1_ss_F1R1_ES	50	0	Gas1_Q	32.901793	2.508833

Sample	Target	condition1	condition2	species	E_pow_mean_cq	\
1:16_DF1	Gli1_ss_F1R1_ES	DF1_STD	0	std	9.113006e+12	
1:256_DF1	Gli1_ss_F1R1_ES	DF1_STD	0	std		NaN
1:4_DF1	Gli1_ss_F1R1_ES	DF1_STD	0	std	4.222993e+12	
1:64_DF1	Gli1_ss_F1R1_ES	DF1_STD	0	std		NaN
1x_DF1	Gli1_ss_F1R1_ES	DF1_STD	0	std	5.695628e+11	
A1	Gli1_ss_F1R1_ES	0	0	Gas1_C		NaN
A2	Gli1_ss_F1R1_ES	0.1	0	Gas1_C	7.027352e+12	
A3	Gli1_ss_F1R1_ES	1	0	Gas1_C	1.246366e+13	
A4	Gli1_ss_F1R1_ES	5	0	Gas1_C	6.131889e+12	
A5	Gli1_ss_F1R1_ES	10	0	Gas1_C	3.040317e+12	
A6	Gli1_ss_F1R1_ES	50	0	Gas1_C	1.000994e+13	
B1	Gli1_ss_F1R1_ES	0	0	Gas1_C	7.267100e+12	
B2	Gli1_ss_F1R1_ES	0.1	0	Gas1_C	1.753526e+13	
B3	Gli1_ss_F1R1_ES	1	0	Gas1_C	1.568719e+13	
B4	Gli1_ss_F1R1_ES	5	0	Gas1_C	6.884061e+12	
B5	Gli1_ss_F1R1_ES	10	0	Gas1_C	7.489075e+12	
B6	Gli1_ss_F1R1_ES	50	0	Gas1_C	3.575561e+13	
C1	Gli1_ss_F1R1_ES	0	0	Gas1_Q	8.271424e+12	
C2	Gli1_ss_F1R1_ES	0.1	0	Gas1_Q	6.802127e+12	
C3	Gli1_ss_F1R1_ES	1	0	Gas1_Q	1.075144e+13	
C4	Gli1_ss_F1R1_ES	5	0	Gas1_Q	8.094412e+12	
C5	Gli1_ss_F1R1_ES	10	0	Gas1_Q	2.119333e+13	
C6	Gli1_ss_F1R1_ES	50	0	Gas1_Q	1.220554e+13	
D1	Gli1_ss_F1R1_ES	0	0	Gas1_Q	3.653427e+12	
D2	Gli1_ss_F1R1_ES	0.1	0	Gas1_Q	2.487404e+12	
D3	Gli1_ss_F1R1_ES	1	0	Gas1_Q	5.142524e+12	
D4	Gli1_ss_F1R1_ES	5	0	Gas1_Q	9.261891e+12	

D5	Gli1_ss_F1R1_ES	10	0	Gas1_Q	4.188424e+12
D6	Gli1_ss_F1R1_ES	50	0	Gas1_Q	1.391026e+13

Sample	Target	condition1	condition2	species	Spenser_Norm_Cq \
1:16_DF1	Gli1_ss_F1R1_ES	DF1_STD	0	std	0.076775
1:256_DF1	Gli1_ss_F1R1_ES	DF1_STD	0	std	NaN
1:4_DF1	Gli1_ss_F1R1_ES	DF1_STD	0	std	0.165676
1:64_DF1	Gli1_ss_F1R1_ES	DF1_STD	0	std	NaN
1x_DF1	Gli1_ss_F1R1_ES	DF1_STD	0	std	1.228399
A1	Gli1_ss_F1R1_ES	0	0	Gas1_C	NaN
A2	Gli1_ss_F1R1_ES	0.1	0	Gas1_C	0.099561
A3	Gli1_ss_F1R1_ES	1	0	Gas1_C	0.056135
A4	Gli1_ss_F1R1_ES	5	0	Gas1_C	0.114100
A5	Gli1_ss_F1R1_ES	10	0	Gas1_C	0.230124
A6	Gli1_ss_F1R1_ES	50	0	Gas1_C	0.069896
B1	Gli1_ss_F1R1_ES	0	0	Gas1_C	0.096276
B2	Gli1_ss_F1R1_ES	0.1	0	Gas1_C	0.039900
B3	Gli1_ss_F1R1_ES	1	0	Gas1_C	0.044600
B4	Gli1_ss_F1R1_ES	5	0	Gas1_C	0.101633
B5	Gli1_ss_F1R1_ES	10	0	Gas1_C	0.093423
B6	Gli1_ss_F1R1_ES	50	0	Gas1_C	0.019568
C1	Gli1_ss_F1R1_ES	0	0	Gas1_Q	0.084586
C2	Gli1_ss_F1R1_ES	0.1	0	Gas1_Q	0.102858
C3	Gli1_ss_F1R1_ES	1	0	Gas1_Q	0.065075
C4	Gli1_ss_F1R1_ES	5	0	Gas1_Q	0.086436
C5	Gli1_ss_F1R1_ES	10	0	Gas1_Q	0.033013
C6	Gli1_ss_F1R1_ES	50	0	Gas1_Q	0.057322
D1	Gli1_ss_F1R1_ES	0	0	Gas1_Q	0.191505
D2	Gli1_ss_F1R1_ES	0.1	0	Gas1_Q	0.281277
D3	Gli1_ss_F1R1_ES	1	0	Gas1_Q	0.136052
D4	Gli1_ss_F1R1_ES	5	0	Gas1_Q	0.075541
D5	Gli1_ss_F1R1_ES	10	0	Gas1_Q	0.167044
D6	Gli1_ss_F1R1_ES	50	0	Gas1_Q	0.050297

Sample	Target	condition1	condition2	species	Spenser_Norm_Cq_hkg \
1:16_DF1	Gli1_ss_F1R1_ES	DF1_STD	0	std	NaN
1:256_DF1	Gli1_ss_F1R1_ES	DF1_STD	0	std	NaN
1:4_DF1	Gli1_ss_F1R1_ES	DF1_STD	0	std	NaN
1:64_DF1	Gli1_ss_F1R1_ES	DF1_STD	0	std	NaN
1x_DF1	Gli1_ss_F1R1_ES	DF1_STD	0	std	NaN
A1	Gli1_ss_F1R1_ES	0	0	Gas1_C	0.088448
A2	Gli1_ss_F1R1_ES	0.1	0	Gas1_C	0.082621
A3	Gli1_ss_F1R1_ES	1	0	Gas1_C	0.078241
A4	Gli1_ss_F1R1_ES	5	0	Gas1_C	0.064938
A5	Gli1_ss_F1R1_ES	10	0	Gas1_C	0.171427

A6	Gli1_ss_F1R1_ES	50	0	Gas1_C	0.067070
B1	Gli1_ss_F1R1_ES	0	0	Gas1_C	0.087634
B2	Gli1_ss_F1R1_ES	0.1	0	Gas1_C	0.096572
B3	Gli1_ss_F1R1_ES	1	0	Gas1_C	0.079305
B4	Gli1_ss_F1R1_ES	5	0	Gas1_C	0.074895
B5	Gli1_ss_F1R1_ES	10	0	Gas1_C	0.132826
B6	Gli1_ss_F1R1_ES	50	0	Gas1_C	0.064927
C1	Gli1_ss_F1R1_ES	0	0	Gas1_Q	0.095231
C2	Gli1_ss_F1R1_ES	0.1	0	Gas1_Q	0.122632
C3	Gli1_ss_F1R1_ES	1	0	Gas1_Q	0.064069
C4	Gli1_ss_F1R1_ES	5	0	Gas1_Q	0.060046
C5	Gli1_ss_F1R1_ES	10	0	Gas1_Q	0.115469
C6	Gli1_ss_F1R1_ES	50	0	Gas1_Q	0.082222
D1	Gli1_ss_F1R1_ES	0	0	Gas1_Q	0.109523
D2	Gli1_ss_F1R1_ES	0.1	0	Gas1_Q	0.269631
D3	Gli1_ss_F1R1_ES	1	0	Gas1_Q	0.062815
D4	Gli1_ss_F1R1_ES	5	0	Gas1_Q	0.089314
D5	Gli1_ss_F1R1_ES	10	0	Gas1_Q	0.119660
D6	Gli1_ss_F1R1_ES	50	0	Gas1_Q	0.107044

Spenser_goi_hkg_norm

Sample	Target	condition1	condition2	species	
1:16_DF1	Gli1_ss_F1R1_ES	DF1_STD	0	std	NaN
1:256_DF1	Gli1_ss_F1R1_ES	DF1_STD	0	std	NaN
1:4_DF1	Gli1_ss_F1R1_ES	DF1_STD	0	std	NaN
1:64_DF1	Gli1_ss_F1R1_ES	DF1_STD	0	std	NaN
1x_DF1	Gli1_ss_F1R1_ES	DF1_STD	0	std	NaN
A1	Gli1_ss_F1R1_ES	0	0	Gas1_C	NaN
A2	Gli1_ss_F1R1_ES	0.1	0	Gas1_C	1.205038
A3	Gli1_ss_F1R1_ES	1	0	Gas1_C	0.717469
A4	Gli1_ss_F1R1_ES	5	0	Gas1_C	1.757070
A5	Gli1_ss_F1R1_ES	10	0	Gas1_C	1.342406
A6	Gli1_ss_F1R1_ES	50	0	Gas1_C	1.042126
B1	Gli1_ss_F1R1_ES	0	0	Gas1_C	1.098623
B2	Gli1_ss_F1R1_ES	0.1	0	Gas1_C	0.413157
B3	Gli1_ss_F1R1_ES	1	0	Gas1_C	0.562385
B4	Gli1_ss_F1R1_ES	5	0	Gas1_C	1.357008
B5	Gli1_ss_F1R1_ES	10	0	Gas1_C	0.703346
B6	Gli1_ss_F1R1_ES	50	0	Gas1_C	0.301378
C1	Gli1_ss_F1R1_ES	0	0	Gas1_Q	0.888221
C2	Gli1_ss_F1R1_ES	0.1	0	Gas1_Q	0.838747
C3	Gli1_ss_F1R1_ES	1	0	Gas1_Q	1.015698
C4	Gli1_ss_F1R1_ES	5	0	Gas1_Q	1.439498
C5	Gli1_ss_F1R1_ES	10	0	Gas1_Q	0.285902
C6	Gli1_ss_F1R1_ES	50	0	Gas1_Q	0.697162
D1	Gli1_ss_F1R1_ES	0	0	Gas1_Q	1.748543
D2	Gli1_ss_F1R1_ES	0.1	0	Gas1_Q	1.043193

D3	Gli1_ss_F1R1_ES 1	0	Gas1_Q	2.165913
D4	Gli1_ss_F1R1_ES 5	0	Gas1_Q	0.845787
D5	Gli1_ss_F1R1_ES 10	0	Gas1_Q	1.395991
D6	Gli1_ss_F1R1_ES 50	0	Gas1_Q	0.469875

```
[455]: list_rna
```

```
[455]: {'A1',
        'A2',
        'A3',
        'A4',
        'A5',
        'A6',
        'B1',
        'B2',
        'B3',
        'B4',
        'B5',
        'B6',
        'C1',
        'C2',
        'C3',
        'C4',
        'C5',
        'C6',
        'D1',
        'D2',
        'D3',
        'D4',
        'D5',
        'D6'}
```

```
[456]: list_all_targets[0]
```

```
[456]: 'Gli1_ss_F1R1_ES'
```

!! SET * CONDITION !!

```
- condition1 ~ stage, dox, condition
- condition2 ~ initials, shh
```

```
[457]: # condition1 = '15', '18', '21', '24', '27', 'ctrl', '0', '0.1', '1', '5', '10', '50'
# condition2 = 0, 0.1, 1, 10, 100, 1000, 2000, ZV, JF
# species = 'Chick', 'Duck', 'Quail', 'Quack', 'Gas1_C', 'Gas1_Q',
# target = 'Shh_u_F4R2', 'Gli2_u_F1R1_ES', 'Ptch1_u_F2R2', 'Gli3_u_F9R6',
→ 'Gas1_u_F1R2', 'Smo_u_F2R1',
# 'Boc_u_F3R2', 'Gli1_ss_F1R1_ES', 'CDON_u_F7R1', 'Cxcl14_ss_F3R3'
```

```

# condition1 = '15'
# condition1 = 'ctrl'
condition1 = '0'
print(condition1)

# condition2 = 0
condition2 = 0
print(condition2)

# species = 'Quail'
# species = 'Duck'
# species = 'Chick'
species = 'Gas1_C'
# species = 'Gas1_Q'
print(species)

# target = 'Gli1_ss_F1R1_ES'
target = list_all_targets[0]
print(target)

```

```

0
0
Gas1_C
Gli1_ss_F1R1_ES

```

4.7 Spenser_FC

```

[458]: # targets_Pffaf1 = FC_Pffaf1(all_files_mean_norm, condition1, species, target)
targets_Spenser = FC_Spenser(all_files_mean_norm, condition1, condition2, ↵
↪species, target)

```

```

0
0
Gas1_C
Gli1_ss_F1R1_ES

```

Sample	Target	condition1	condition2	species	mean	E \
A1	Gli1_ss_F1R1_ES	0	0	Gas1_C	NaN	2.508833
B1	Gli1_ss_F1R1_ES	0	0	Gas1_C	32.195926	2.508833
C1	Gli1_ss_F1R1_ES	0	0	Gas1_Q	32.336660	2.508833
D1	Gli1_ss_F1R1_ES	0	0	Gas1_Q	31.448287	2.508833

```

E_pow_mean_cq Spenser_Norm_Cq Spenser_Norm_Cq_hkg \
Sample
A1 NaN NaN 0.088448

```

```

B1      7.267100e+12      0.096276      0.087634
C1      8.271424e+12      0.084586      0.095231
D1      3.653427e+12      0.191505      0.109523

```

Spenser_goi_hkg_norm

Sample

```

A1      NaN
B1      1.098623
C1      0.888221
D1      1.748543

```

```

Target condition1 condition2 species mean E \

```

Sample

```

A1      Gli1_ss_F1R1_ES      0      0      Gas1_C      NaN      2.508833
B1      Gli1_ss_F1R1_ES      0      0      Gas1_C      32.195926      2.508833

```

```

E_pow_mean_cq Spenser_Norm_Cq Spenser_Norm_Cq_hkg \

```

Sample

```

A1      NaN      NaN      0.088448
B1      7.267100e+12      0.096276      0.087634

```

Spenser_goi_hkg_norm

Sample

```

A1      NaN
B1      1.098623

```

```

Target condition1 condition2 species mean E \

```

Sample

```

A1      Gli1_ss_F1R1_ES      0      0      Gas1_C      NaN      2.508833
B1      Gli1_ss_F1R1_ES      0      0      Gas1_C      32.195926      2.508833

```

```

E_pow_mean_cq Spenser_Norm_Cq Spenser_Norm_Cq_hkg \

```

Sample

```

A1      NaN      NaN      0.088448
B1      7.267100e+12      0.096276      0.087634

```

Spenser_goi_hkg_norm

Sample

```

A1      NaN
B1      1.098623
      mean std

```

Target

```

Gli1_ss_F1R1_ES 1.098623 NaN
1.09862326797986

```

```

[459]: # targets, species, condition1, target = FC(all_files_mean_norm, list_all_files,
      →condition1, species, target)
      targets, species, condition1, condition2, target = FC(all_files_mean_norm,
      →list_all_files, condition1, condition2, species, target)

```

```
0
0
Gas1_C
Gli1_ss_F1R1_ES
```

```
[460]: #GER(f, f_hkg, list_of_sample_values_all)
# GER(all_files_mean_norm, tabulky, list_all_files)
```

```
[461]: hkg_values(all_files_mean_norm, tabulky, list_all_files)
```

```
/usr/local/lib/python3.7/site-packages/ipykernel_launcher.py:2:
DeprecationWarning: The default dtype for empty Series will be 'object' instead
of 'float64' in a future version. Specify a dtype explicitly to silence this
warning.
```

```
/usr/local/lib/python3.7/site-packages/ipykernel_launcher.py:3:
DeprecationWarning: The default dtype for empty Series will be 'object' instead
of 'float64' in a future version. Specify a dtype explicitly to silence this
warning.
```

This is separate from the ipykernel package so we can avoid doing imports until

4.8 Livak

targets_Livak = FC_livak(all_files_mean_norm, condition1, species, target)

```
[462]: all_files_mean_norm['E_Livak'] = 2
all_files_mean_norm['dCt_Livak'] = all_files_mean_norm['mean'] -
→all_files_mean_norm['Cq_hkg']
```

```
[463]: targets_Livak = FC_livak(all_files_mean_norm, condition1, condition2, species,
→target)
```

```
0
0
Gas1_C
Gli1_ss_F1R1_ES
```

Sample	Target	condition1	condition2	species	mean	E	\
A1	Gli1_ss_F1R1_ES	0	0	Gas1_C	NaN	2.508833	
B1	Gli1_ss_F1R1_ES	0	0	Gas1_C	32.195926	2.508833	
C1	Gli1_ss_F1R1_ES	0	0	Gas1_Q	32.336660	2.508833	
D1	Gli1_ss_F1R1_ES	0	0	Gas1_Q	31.448287	2.508833	

Sample	E_pow_mean_cq	Spenser_Norm_Cq	Spenser_Norm_Cq_hkg	\
A1	NaN	NaN	0.088448	
B1	7.267100e+12	0.096276	0.087634	

C1	8.271424e+12	0.084586	0.095231
D1	3.653427e+12	0.191505	0.109523

Sample	Spenser_goi_hkg_norm	FC_Spenser	E_ratio	Cq_hkg	E_hkg	\
A1	NaN	NaN	NaN	12.509410	1.976568	
B1	1.098623	1.000000	1.000000	12.522978	1.976568	
C1	0.888221	0.808486	0.878579	12.400953	1.976568	
D1	1.748543	1.591577	1.989119	12.195742	1.976568	

Sample	E_Livak	dCt_Livak
A1	2	NaN
B1	2	19.672948
C1	2	19.935707
D1	2	19.252545

Sample	Target	condition1	condition2	species	mean	E	\
A1	Gli1_ss_F1R1_ES	0	0	Gas1_C	NaN	2.508833	
B1	Gli1_ss_F1R1_ES	0	0	Gas1_C	32.195926	2.508833	

Sample	E_pow_mean_cq	Spenser_Norm_Cq	Spenser_Norm_Cq_hkg	\
A1	NaN	NaN	0.088448	
B1	7.267100e+12	0.096276	0.087634	

Sample	Spenser_goi_hkg_norm	FC_Spenser	E_ratio	Cq_hkg	E_hkg	\
A1	NaN	NaN	NaN	12.509410	1.976568	
B1	1.098623	1.0	1.0	12.522978	1.976568	

Sample	E_Livak	dCt_Livak
A1	2	NaN
B1	2	19.672948

Sample	Target	condition1	condition2	species	mean	E	\
A1	Gli1_ss_F1R1_ES	0	0	Gas1_C	NaN	2.508833	
B1	Gli1_ss_F1R1_ES	0	0	Gas1_C	32.195926	2.508833	

Sample	E_pow_mean_cq	Spenser_Norm_Cq	Spenser_Norm_Cq_hkg	\
A1	NaN	NaN	0.088448	
B1	7.267100e+12	0.096276	0.087634	

Sample	Spenser_goi_hkg_norm	FC_Spenser	E_ratio	Cq_hkg	E_hkg	\
A1	NaN	NaN	NaN	12.509410	1.976568	


```
B1          1.098623          1.0          1.0  12.522978  1.976568
```

```

      E_Livak  dCt_Livak
Sample
A1          2          NaN
B1          2  19.672948
              mean  std
Target
Gli1_ss_F1R1_ES  19.672948  NaN
19.672947965

```

4.9 Pfaffl

targets_Pffaf1 = FC_Pffaf1(all_files_mean_norm, condition1, species, target)

```
[464]: targets_Pffaf1 = FC_Pffaf1(all_files_mean_norm, condition1, condition2, species,
↳target)
```

```

0
0
Gas1_C
Gli1_ss_F1R1_ES
      Target condition1  condition2 species          mean          E \
Sample
A1  Gli1_ss_F1R1_ES          0          0  Gas1_C          NaN  2.508833
B1  Gli1_ss_F1R1_ES          0          0  Gas1_C  32.195926  2.508833
C1  Gli1_ss_F1R1_ES          0          0  Gas1_Q  32.336660  2.508833
D1  Gli1_ss_F1R1_ES          0          0  Gas1_Q  31.448287  2.508833

```

```

      E_pow_mean_cq  Spenser_Norm_Cq  Spenser_Norm_Cq_hkg \
Sample
A1          NaN          NaN          0.088448
B1  7.267100e+12  0.096276          0.087634
C1  8.271424e+12  0.084586          0.095231
D1  3.653427e+12  0.191505          0.109523

```

```

      Spenser_goi_hkg_norm  FC_Spenser  E_ratio  Cq_hkg  E_hkg \
Sample
A1          NaN          NaN          NaN  12.509410  1.976568
B1          1.098623  1.000000  1.000000  12.522978  1.976568
C1          0.888221  0.808486  0.878579  12.400953  1.976568
D1          1.748543  1.591577  1.989119  12.195742  1.976568

```

```

      E_Livak  dCt_Livak  ddCt_Livak  FC_Livak
Sample
A1          2          NaN          NaN          NaN
B1          2  19.672948  0.000000  1.000000
C1          2  19.935707  0.262759  0.833493

```

```

D1          2  19.252545  -0.420403  1.338301
          Target condition1 condition2 species          mean          E \
Sample
A1  Gli1_ss_F1R1_ES          0          0  Gas1_C          NaN  2.508833
B1  Gli1_ss_F1R1_ES          0          0  Gas1_C  32.195926  2.508833

          E_pow_mean_cq  Spenser_Norm_Cq  Spenser_Norm_Cq_hkg \
Sample
A1          NaN          NaN          0.088448
B1  7.267100e+12  0.096276          0.087634

          Spenser_goi_hkg_norm  FC_Spenser  E_ratio          Cq_hkg          E_hkg \
Sample
A1          NaN          NaN          NaN  12.509410  1.976568
B1  1.098623          1.0          1.0  12.522978  1.976568

          E_Livak  dCt_Livak  ddCt_Livak  FC_Livak
Sample
A1          2          NaN          NaN          NaN
B1          2  19.672948          0.0          1.0

          Target condition1 condition2 species          mean          E \
Sample
A1  Gli1_ss_F1R1_ES          0          0  Gas1_C          NaN  2.508833
B1  Gli1_ss_F1R1_ES          0          0  Gas1_C  32.195926  2.508833

          E_pow_mean_cq  Spenser_Norm_Cq  Spenser_Norm_Cq_hkg \
Sample
A1          NaN          NaN          0.088448
B1  7.267100e+12  0.096276          0.087634

          Spenser_goi_hkg_norm  FC_Spenser  E_ratio          Cq_hkg          E_hkg \
Sample
A1          NaN          NaN          NaN  12.509410  1.976568
B1  1.098623          1.0          1.0  12.522978  1.976568

          E_Livak  dCt_Livak  ddCt_Livak  FC_Livak
Sample
A1          2          NaN          NaN          NaN
B1          2  19.672948          0.0          1.0

          mean  std
Target
Gli1_ss_F1R1_ES  32.195926  NaN
          mean          std
Target
Gli1_ss_F1R1_ES  12.516194  0.009594
32.1959259
12.5161938425

```

4.10 RNA yield

- function adding a column with fold change and normalized values multiplied by RNA extraction yields

`rna_yield(f_mean_norm, rna, list_of_sample_values_all_norm)`

```
[465]: print(list_rna)
```

```
{'C3', 'D2', 'D6', 'A2', 'A3', 'B4', 'C1', 'D3', 'B6', 'A6', 'B2', 'C6', 'D5',  
'A1', 'B1', 'A4', 'D4', 'B3', 'B5', 'C5', 'A5', 'C2', 'D1', 'C4'}
```

```
[466]: # all_files_mean_norm[all_files_mean_norm.index.duplicated()]
```

```
[467]: def rna_find_csv_filenames( rna, suffix=".csv" ):  
    rna_filenames = listdir(rna)  
    return [ rna_filenames for rna_filenames in rna_filenames if rna_filenames.  
    ↪endswith( suffix )]
```

```
[468]: # listdir(rna)
```

```
[469]: rna_filenames = rna_find_csv_filenames(rna)  
for name in rna_filenames:  
    print(name)
```

```
[470]: for i, f in enumerate(rna_filenames):  
    dokument = f.replace(".csv", "")  
    rna_table = pd.read_csv(rna + f)  
    print(rna_table)  
    # MAREK  
    rna_yield(all_files_mean_norm, rna_table, list_rna)
```

```
[471]: # rna_yield(all_files_mean_norm, rna_table, list_of_sample_values_all_norm)
```

5 DATA * EXPORT

5.1 Check table before exporting csv file

```
[472]: all_files_mean_norm
```

```
[472]:
```

Sample	Target	condition1	condition2	species	mean	E \
1:16_DF1	Gli1_ss_F1R1_ES	DF1_STD	0	std	32.442002	2.508833
1:256_DF1	Gli1_ss_F1R1_ES	DF1_STD	0	std	NaN	2.508833
1:4_DF1	Gli1_ss_F1R1_ES	DF1_STD	0	std	31.605795	2.508833
1:64_DF1	Gli1_ss_F1R1_ES	DF1_STD	0	std	NaN	2.508833
1x_DF1	Gli1_ss_F1R1_ES	DF1_STD	0	std	29.427721	2.508833

A1	Gli1_ss_F1R1_ES	0	0	Gas1_C	NaN	2.508833
A2	Gli1_ss_F1R1_ES	0.1	0	Gas1_C	32.159454	2.508833
A3	Gli1_ss_F1R1_ES	1	0	Gas1_C	32.782411	2.508833
A4	Gli1_ss_F1R1_ES	5	0	Gas1_C	32.011265	2.508833
A5	Gli1_ss_F1R1_ES	10	0	Gas1_C	31.248569	2.508833
A6	Gli1_ss_F1R1_ES	50	0	Gas1_C	32.544062	2.508833
B1	Gli1_ss_F1R1_ES	0	0	Gas1_C	32.195926	2.508833
B2	Gli1_ss_F1R1_ES	0.1	0	Gas1_C	33.153569	2.508833
B3	Gli1_ss_F1R1_ES	1	0	Gas1_C	33.032491	2.508833
B4	Gli1_ss_F1R1_ES	5	0	Gas1_C	32.137057	2.508833
B5	Gli1_ss_F1R1_ES	10	0	Gas1_C	32.228637	2.508833
B6	Gli1_ss_F1R1_ES	50	0	Gas1_C	33.928171	2.508833
C1	Gli1_ss_F1R1_ES	0	0	Gas1_Q	32.336660	2.508833
C2	Gli1_ss_F1R1_ES	0.1	0	Gas1_Q	32.124040	2.508833
C3	Gli1_ss_F1R1_ES	1	0	Gas1_Q	32.621752	2.508833
C4	Gli1_ss_F1R1_ES	5	0	Gas1_Q	32.313141	2.508833
C5	Gli1_ss_F1R1_ES	10	0	Gas1_Q	33.359558	2.508833
C6	Gli1_ss_F1R1_ES	50	0	Gas1_Q	32.759660	2.508833
D1	Gli1_ss_F1R1_ES	0	0	Gas1_Q	31.448287	2.508833
D2	Gli1_ss_F1R1_ES	0.1	0	Gas1_Q	31.030349	2.508833
D3	Gli1_ss_F1R1_ES	1	0	Gas1_Q	31.819967	2.508833
D4	Gli1_ss_F1R1_ES	5	0	Gas1_Q	32.459621	2.508833
D5	Gli1_ss_F1R1_ES	10	0	Gas1_Q	31.596858	2.508833
D6	Gli1_ss_F1R1_ES	50	0	Gas1_Q	32.901793	2.508833

Sample	Target	condition1	condition2	species	E_pow_mean_cq	\
1:16_DF1	Gli1_ss_F1R1_ES	DF1_STD	0	std	9.113006e+12	
1:256_DF1	Gli1_ss_F1R1_ES	DF1_STD	0	std	NaN	
1:4_DF1	Gli1_ss_F1R1_ES	DF1_STD	0	std	4.222993e+12	
1:64_DF1	Gli1_ss_F1R1_ES	DF1_STD	0	std	NaN	
1x_DF1	Gli1_ss_F1R1_ES	DF1_STD	0	std	5.695628e+11	
A1	Gli1_ss_F1R1_ES	0	0	Gas1_C	NaN	
A2	Gli1_ss_F1R1_ES	0.1	0	Gas1_C	7.027352e+12	
A3	Gli1_ss_F1R1_ES	1	0	Gas1_C	1.246366e+13	
A4	Gli1_ss_F1R1_ES	5	0	Gas1_C	6.131889e+12	
A5	Gli1_ss_F1R1_ES	10	0	Gas1_C	3.040317e+12	
A6	Gli1_ss_F1R1_ES	50	0	Gas1_C	1.000994e+13	
B1	Gli1_ss_F1R1_ES	0	0	Gas1_C	7.267100e+12	
B2	Gli1_ss_F1R1_ES	0.1	0	Gas1_C	1.753526e+13	
B3	Gli1_ss_F1R1_ES	1	0	Gas1_C	1.568719e+13	
B4	Gli1_ss_F1R1_ES	5	0	Gas1_C	6.884061e+12	
B5	Gli1_ss_F1R1_ES	10	0	Gas1_C	7.489075e+12	
B6	Gli1_ss_F1R1_ES	50	0	Gas1_C	3.575561e+13	
C1	Gli1_ss_F1R1_ES	0	0	Gas1_Q	8.271424e+12	
C2	Gli1_ss_F1R1_ES	0.1	0	Gas1_Q	6.802127e+12	
C3	Gli1_ss_F1R1_ES	1	0	Gas1_Q	1.075144e+13	

C4	Gli1_ss_F1R1_ES	5	0	Gas1_Q	8.094412e+12
C5	Gli1_ss_F1R1_ES	10	0	Gas1_Q	2.119333e+13
C6	Gli1_ss_F1R1_ES	50	0	Gas1_Q	1.220554e+13
D1	Gli1_ss_F1R1_ES	0	0	Gas1_Q	3.653427e+12
D2	Gli1_ss_F1R1_ES	0.1	0	Gas1_Q	2.487404e+12
D3	Gli1_ss_F1R1_ES	1	0	Gas1_Q	5.142524e+12
D4	Gli1_ss_F1R1_ES	5	0	Gas1_Q	9.261891e+12
D5	Gli1_ss_F1R1_ES	10	0	Gas1_Q	4.188424e+12
D6	Gli1_ss_F1R1_ES	50	0	Gas1_Q	1.391026e+13

Spenser_Norm_Cq \

Sample	Target	condition1	condition2	species	
1:16_DF1	Gli1_ss_F1R1_ES	DF1_STD	0	std	0.076775
1:256_DF1	Gli1_ss_F1R1_ES	DF1_STD	0	std	NaN
1:4_DF1	Gli1_ss_F1R1_ES	DF1_STD	0	std	0.165676
1:64_DF1	Gli1_ss_F1R1_ES	DF1_STD	0	std	NaN
1x_DF1	Gli1_ss_F1R1_ES	DF1_STD	0	std	1.228399
A1	Gli1_ss_F1R1_ES	0	0	Gas1_C	NaN
A2	Gli1_ss_F1R1_ES	0.1	0	Gas1_C	0.099561
A3	Gli1_ss_F1R1_ES	1	0	Gas1_C	0.056135
A4	Gli1_ss_F1R1_ES	5	0	Gas1_C	0.114100
A5	Gli1_ss_F1R1_ES	10	0	Gas1_C	0.230124
A6	Gli1_ss_F1R1_ES	50	0	Gas1_C	0.069896
B1	Gli1_ss_F1R1_ES	0	0	Gas1_C	0.096276
B2	Gli1_ss_F1R1_ES	0.1	0	Gas1_C	0.039900
B3	Gli1_ss_F1R1_ES	1	0	Gas1_C	0.044600
B4	Gli1_ss_F1R1_ES	5	0	Gas1_C	0.101633
B5	Gli1_ss_F1R1_ES	10	0	Gas1_C	0.093423
B6	Gli1_ss_F1R1_ES	50	0	Gas1_C	0.019568
C1	Gli1_ss_F1R1_ES	0	0	Gas1_Q	0.084586
C2	Gli1_ss_F1R1_ES	0.1	0	Gas1_Q	0.102858
C3	Gli1_ss_F1R1_ES	1	0	Gas1_Q	0.065075
C4	Gli1_ss_F1R1_ES	5	0	Gas1_Q	0.086436
C5	Gli1_ss_F1R1_ES	10	0	Gas1_Q	0.033013
C6	Gli1_ss_F1R1_ES	50	0	Gas1_Q	0.057322
D1	Gli1_ss_F1R1_ES	0	0	Gas1_Q	0.191505
D2	Gli1_ss_F1R1_ES	0.1	0	Gas1_Q	0.281277
D3	Gli1_ss_F1R1_ES	1	0	Gas1_Q	0.136052
D4	Gli1_ss_F1R1_ES	5	0	Gas1_Q	0.075541
D5	Gli1_ss_F1R1_ES	10	0	Gas1_Q	0.167044
D6	Gli1_ss_F1R1_ES	50	0	Gas1_Q	0.050297

Spenser_Norm_Cq_hkg \

Sample	Target	condition1	condition2	species	
1:16_DF1	Gli1_ss_F1R1_ES	DF1_STD	0	std	NaN
1:256_DF1	Gli1_ss_F1R1_ES	DF1_STD	0	std	NaN
1:4_DF1	Gli1_ss_F1R1_ES	DF1_STD	0	std	NaN

1:64_DF1	Gli1_ss_F1R1_ES	DF1_STD	0	std	NaN
1x_DF1	Gli1_ss_F1R1_ES	DF1_STD	0	std	NaN
A1	Gli1_ss_F1R1_ES	0	0	Gas1_C	0.088448
A2	Gli1_ss_F1R1_ES	0.1	0	Gas1_C	0.082621
A3	Gli1_ss_F1R1_ES	1	0	Gas1_C	0.078241
A4	Gli1_ss_F1R1_ES	5	0	Gas1_C	0.064938
A5	Gli1_ss_F1R1_ES	10	0	Gas1_C	0.171427
A6	Gli1_ss_F1R1_ES	50	0	Gas1_C	0.067070
B1	Gli1_ss_F1R1_ES	0	0	Gas1_C	0.087634
B2	Gli1_ss_F1R1_ES	0.1	0	Gas1_C	0.096572
B3	Gli1_ss_F1R1_ES	1	0	Gas1_C	0.079305
B4	Gli1_ss_F1R1_ES	5	0	Gas1_C	0.074895
B5	Gli1_ss_F1R1_ES	10	0	Gas1_C	0.132826
B6	Gli1_ss_F1R1_ES	50	0	Gas1_C	0.064927
C1	Gli1_ss_F1R1_ES	0	0	Gas1_Q	0.095231
C2	Gli1_ss_F1R1_ES	0.1	0	Gas1_Q	0.122632
C3	Gli1_ss_F1R1_ES	1	0	Gas1_Q	0.064069
C4	Gli1_ss_F1R1_ES	5	0	Gas1_Q	0.060046
C5	Gli1_ss_F1R1_ES	10	0	Gas1_Q	0.115469
C6	Gli1_ss_F1R1_ES	50	0	Gas1_Q	0.082222
D1	Gli1_ss_F1R1_ES	0	0	Gas1_Q	0.109523
D2	Gli1_ss_F1R1_ES	0.1	0	Gas1_Q	0.269631
D3	Gli1_ss_F1R1_ES	1	0	Gas1_Q	0.062815
D4	Gli1_ss_F1R1_ES	5	0	Gas1_Q	0.089314
D5	Gli1_ss_F1R1_ES	10	0	Gas1_Q	0.119660
D6	Gli1_ss_F1R1_ES	50	0	Gas1_Q	0.107044

Spenser_goi_hkg_norm \

Sample	Target	condition1	condition2	species	
1:16_DF1	Gli1_ss_F1R1_ES	DF1_STD	0	std	NaN
1:256_DF1	Gli1_ss_F1R1_ES	DF1_STD	0	std	NaN
1:4_DF1	Gli1_ss_F1R1_ES	DF1_STD	0	std	NaN
1:64_DF1	Gli1_ss_F1R1_ES	DF1_STD	0	std	NaN
1x_DF1	Gli1_ss_F1R1_ES	DF1_STD	0	std	NaN
A1	Gli1_ss_F1R1_ES	0	0	Gas1_C	NaN
A2	Gli1_ss_F1R1_ES	0.1	0	Gas1_C	1.205038
A3	Gli1_ss_F1R1_ES	1	0	Gas1_C	0.717469
A4	Gli1_ss_F1R1_ES	5	0	Gas1_C	1.757070
A5	Gli1_ss_F1R1_ES	10	0	Gas1_C	1.342406
A6	Gli1_ss_F1R1_ES	50	0	Gas1_C	1.042126
B1	Gli1_ss_F1R1_ES	0	0	Gas1_C	1.098623
B2	Gli1_ss_F1R1_ES	0.1	0	Gas1_C	0.413157
B3	Gli1_ss_F1R1_ES	1	0	Gas1_C	0.562385
B4	Gli1_ss_F1R1_ES	5	0	Gas1_C	1.357008
B5	Gli1_ss_F1R1_ES	10	0	Gas1_C	0.703346
B6	Gli1_ss_F1R1_ES	50	0	Gas1_C	0.301378
C1	Gli1_ss_F1R1_ES	0	0	Gas1_Q	0.888221

C2	Gli1_ss_F1R1_ES	0.1	0	Gas1_Q	0.838747
C3	Gli1_ss_F1R1_ES	1	0	Gas1_Q	1.015698
C4	Gli1_ss_F1R1_ES	5	0	Gas1_Q	1.439498
C5	Gli1_ss_F1R1_ES	10	0	Gas1_Q	0.285902
C6	Gli1_ss_F1R1_ES	50	0	Gas1_Q	0.697162
D1	Gli1_ss_F1R1_ES	0	0	Gas1_Q	1.748543
D2	Gli1_ss_F1R1_ES	0.1	0	Gas1_Q	1.043193
D3	Gli1_ss_F1R1_ES	1	0	Gas1_Q	2.165913
D4	Gli1_ss_F1R1_ES	5	0	Gas1_Q	0.845787
D5	Gli1_ss_F1R1_ES	10	0	Gas1_Q	1.395991
D6	Gli1_ss_F1R1_ES	50	0	Gas1_Q	0.469875

Sample	Target	condition1	condition2	species	FC_Spenser \
1:16_DF1	Gli1_ss_F1R1_ES	DF1_STD	0	std	NaN
1:256_DF1	Gli1_ss_F1R1_ES	DF1_STD	0	std	NaN
1:4_DF1	Gli1_ss_F1R1_ES	DF1_STD	0	std	NaN
1:64_DF1	Gli1_ss_F1R1_ES	DF1_STD	0	std	NaN
1x_DF1	Gli1_ss_F1R1_ES	DF1_STD	0	std	NaN
A1	Gli1_ss_F1R1_ES	0	0	Gas1_C	NaN
A2	Gli1_ss_F1R1_ES	0.1	0	Gas1_C	1.096862
A3	Gli1_ss_F1R1_ES	1	0	Gas1_C	0.653062
A4	Gli1_ss_F1R1_ES	5	0	Gas1_C	1.599338
A5	Gli1_ss_F1R1_ES	10	0	Gas1_C	1.221898
A6	Gli1_ss_F1R1_ES	50	0	Gas1_C	0.948574
B1	Gli1_ss_F1R1_ES	0	0	Gas1_C	1.000000
B2	Gli1_ss_F1R1_ES	0.1	0	Gas1_C	0.376068
B3	Gli1_ss_F1R1_ES	1	0	Gas1_C	0.511900
B4	Gli1_ss_F1R1_ES	5	0	Gas1_C	1.235190
B5	Gli1_ss_F1R1_ES	10	0	Gas1_C	0.640207
B6	Gli1_ss_F1R1_ES	50	0	Gas1_C	0.274323
C1	Gli1_ss_F1R1_ES	0	0	Gas1_Q	0.808486
C2	Gli1_ss_F1R1_ES	0.1	0	Gas1_Q	0.763453
C3	Gli1_ss_F1R1_ES	1	0	Gas1_Q	0.924519
C4	Gli1_ss_F1R1_ES	5	0	Gas1_Q	1.310275
C5	Gli1_ss_F1R1_ES	10	0	Gas1_Q	0.260237
C6	Gli1_ss_F1R1_ES	50	0	Gas1_Q	0.634578
D1	Gli1_ss_F1R1_ES	0	0	Gas1_Q	1.591577
D2	Gli1_ss_F1R1_ES	0.1	0	Gas1_Q	0.949546
D3	Gli1_ss_F1R1_ES	1	0	Gas1_Q	1.971479
D4	Gli1_ss_F1R1_ES	5	0	Gas1_Q	0.769861
D5	Gli1_ss_F1R1_ES	10	0	Gas1_Q	1.270673
D6	Gli1_ss_F1R1_ES	50	0	Gas1_Q	0.427694

Sample	Target	condition1	condition2	species	E_ratio	Cq_hkg \
1:16_DF1	Gli1_ss_F1R1_ES	DF1_STD	0	std	0.797443	13.044166

1:256_DF1	Gli1_ss_F1R1_ES	DF1_STD	0	std	NaN	NaN
1:4_DF1	Gli1_ss_F1R1_ES	DF1_STD	0	std	1.720841	10.924775
1:64_DF1	Gli1_ss_F1R1_ES	DF1_STD	0	std	NaN	15.056777
1x_DF1	Gli1_ss_F1R1_ES	DF1_STD	0	std	12.759083	8.981265
A1	Gli1_ss_F1R1_ES	0	0	Gas1_C	NaN	12.509410
A2	Gli1_ss_F1R1_ES	0.1	0	Gas1_C	1.034116	12.609432
A3	Gli1_ss_F1R1_ES	1	0	Gas1_C	0.583063	12.689375
A4	Gli1_ss_F1R1_ES	5	0	Gas1_C	1.185132	12.962884
A5	Gli1_ss_F1R1_ES	10	0	Gas1_C	2.390244	11.538201
A6	Gli1_ss_F1R1_ES	50	0	Gas1_C	0.725988	12.915466
B1	Gli1_ss_F1R1_ES	0	0	Gas1_C	1.000000	12.522978
B2	Gli1_ss_F1R1_ES	0.1	0	Gas1_C	0.414428	12.380428
B3	Gli1_ss_F1R1_ES	1	0	Gas1_C	0.463250	12.669540
B4	Gli1_ss_F1R1_ES	5	0	Gas1_C	1.055641	12.753511
B5	Gli1_ss_F1R1_ES	10	0	Gas1_C	0.970360	11.912618
B6	Gli1_ss_F1R1_ES	50	0	Gas1_C	0.203244	12.963128
C1	Gli1_ss_F1R1_ES	0	0	Gas1_Q	0.878579	12.400953
C2	Gli1_ss_F1R1_ES	0.1	0	Gas1_Q	1.068357	12.029810
C3	Gli1_ss_F1R1_ES	1	0	Gas1_Q	0.675919	12.982646
C4	Gli1_ss_F1R1_ES	5	0	Gas1_Q	0.897792	13.077828
C5	Gli1_ss_F1R1_ES	10	0	Gas1_Q	0.342896	12.118152
C6	Gli1_ss_F1R1_ES	50	0	Gas1_Q	0.595393	12.616522
D1	Gli1_ss_F1R1_ES	0	0	Gas1_Q	1.989119	12.195742
D2	Gli1_ss_F1R1_ES	0.1	0	Gas1_Q	2.921560	10.873504
D3	Gli1_ss_F1R1_ES	1	0	Gas1_Q	1.413139	13.011662
D4	Gli1_ss_F1R1_ES	5	0	Gas1_Q	0.784624	12.495101
D5	Gli1_ss_F1R1_ES	10	0	Gas1_Q	1.735044	12.065826
D6	Gli1_ss_F1R1_ES	50	0	Gas1_Q	0.522427	12.229335

Sample	Target	condition1	condition2	species	E_hkg	E_Livak \
1:16_DF1	Gli1_ss_F1R1_ES	DF1_STD	0	std	1.976568	2
1:256_DF1	Gli1_ss_F1R1_ES	DF1_STD	0	std	1.976568	2
1:4_DF1	Gli1_ss_F1R1_ES	DF1_STD	0	std	1.976568	2
1:64_DF1	Gli1_ss_F1R1_ES	DF1_STD	0	std	1.976568	2
1x_DF1	Gli1_ss_F1R1_ES	DF1_STD	0	std	1.976568	2
A1	Gli1_ss_F1R1_ES	0	0	Gas1_C	1.976568	2
A2	Gli1_ss_F1R1_ES	0.1	0	Gas1_C	1.976568	2
A3	Gli1_ss_F1R1_ES	1	0	Gas1_C	1.976568	2
A4	Gli1_ss_F1R1_ES	5	0	Gas1_C	1.976568	2
A5	Gli1_ss_F1R1_ES	10	0	Gas1_C	1.976568	2
A6	Gli1_ss_F1R1_ES	50	0	Gas1_C	1.976568	2
B1	Gli1_ss_F1R1_ES	0	0	Gas1_C	1.976568	2
B2	Gli1_ss_F1R1_ES	0.1	0	Gas1_C	1.976568	2
B3	Gli1_ss_F1R1_ES	1	0	Gas1_C	1.976568	2
B4	Gli1_ss_F1R1_ES	5	0	Gas1_C	1.976568	2
B5	Gli1_ss_F1R1_ES	10	0	Gas1_C	1.976568	2

B6	Gli1_ss_F1R1_ES	50	0	Gas1_C	1.976568	2
C1	Gli1_ss_F1R1_ES	0	0	Gas1_Q	1.976568	2
C2	Gli1_ss_F1R1_ES	0.1	0	Gas1_Q	1.976568	2
C3	Gli1_ss_F1R1_ES	1	0	Gas1_Q	1.976568	2
C4	Gli1_ss_F1R1_ES	5	0	Gas1_Q	1.976568	2
C5	Gli1_ss_F1R1_ES	10	0	Gas1_Q	1.976568	2
C6	Gli1_ss_F1R1_ES	50	0	Gas1_Q	1.976568	2
D1	Gli1_ss_F1R1_ES	0	0	Gas1_Q	1.976568	2
D2	Gli1_ss_F1R1_ES	0.1	0	Gas1_Q	1.976568	2
D3	Gli1_ss_F1R1_ES	1	0	Gas1_Q	1.976568	2
D4	Gli1_ss_F1R1_ES	5	0	Gas1_Q	1.976568	2
D5	Gli1_ss_F1R1_ES	10	0	Gas1_Q	1.976568	2
D6	Gli1_ss_F1R1_ES	50	0	Gas1_Q	1.976568	2

Sample	Target	condition1	condition2	species	dCt_Livak \
1:16_DF1	Gli1_ss_F1R1_ES	DF1_STD	0	std	19.397836
1:256_DF1	Gli1_ss_F1R1_ES	DF1_STD	0	std	NaN
1:4_DF1	Gli1_ss_F1R1_ES	DF1_STD	0	std	20.681019
1:64_DF1	Gli1_ss_F1R1_ES	DF1_STD	0	std	NaN
1x_DF1	Gli1_ss_F1R1_ES	DF1_STD	0	std	20.446456
A1	Gli1_ss_F1R1_ES	0	0	Gas1_C	NaN
A2	Gli1_ss_F1R1_ES	0.1	0	Gas1_C	19.550023
A3	Gli1_ss_F1R1_ES	1	0	Gas1_C	20.093036
A4	Gli1_ss_F1R1_ES	5	0	Gas1_C	19.048381
A5	Gli1_ss_F1R1_ES	10	0	Gas1_C	19.710368
A6	Gli1_ss_F1R1_ES	50	0	Gas1_C	19.628596
B1	Gli1_ss_F1R1_ES	0	0	Gas1_C	19.672948
B2	Gli1_ss_F1R1_ES	0.1	0	Gas1_C	20.773140
B3	Gli1_ss_F1R1_ES	1	0	Gas1_C	20.362952
B4	Gli1_ss_F1R1_ES	5	0	Gas1_C	19.383547
B5	Gli1_ss_F1R1_ES	10	0	Gas1_C	20.316018
B6	Gli1_ss_F1R1_ES	50	0	Gas1_C	20.965044
C1	Gli1_ss_F1R1_ES	0	0	Gas1_Q	19.935707
C2	Gli1_ss_F1R1_ES	0.1	0	Gas1_Q	20.094230
C3	Gli1_ss_F1R1_ES	1	0	Gas1_Q	19.639106
C4	Gli1_ss_F1R1_ES	5	0	Gas1_Q	19.235314
C5	Gli1_ss_F1R1_ES	10	0	Gas1_Q	21.241406
C6	Gli1_ss_F1R1_ES	50	0	Gas1_Q	20.143138
D1	Gli1_ss_F1R1_ES	0	0	Gas1_Q	19.252545
D2	Gli1_ss_F1R1_ES	0.1	0	Gas1_Q	20.156845
D3	Gli1_ss_F1R1_ES	1	0	Gas1_Q	18.808305
D4	Gli1_ss_F1R1_ES	5	0	Gas1_Q	19.964520
D5	Gli1_ss_F1R1_ES	10	0	Gas1_Q	19.531032
D6	Gli1_ss_F1R1_ES	50	0	Gas1_Q	20.672458

ddCt_Livak FC_Livak \

Sample	Target	condition1	condition2	species		
1:16_DF1	Gli1_ss_F1R1_ES	DF1_STD	0	std	-0.275112	1.210088
1:256_DF1	Gli1_ss_F1R1_ES	DF1_STD	0	std	NaN	NaN
1:4_DF1	Gli1_ss_F1R1_ES	DF1_STD	0	std	1.008071	0.497210
1:64_DF1	Gli1_ss_F1R1_ES	DF1_STD	0	std	NaN	NaN
1x_DF1	Gli1_ss_F1R1_ES	DF1_STD	0	std	0.773508	0.584993
A1	Gli1_ss_F1R1_ES	0	0	Gas1_C	NaN	NaN
A2	Gli1_ss_F1R1_ES	0.1	0	Gas1_C	-0.122925	1.088941
A3	Gli1_ss_F1R1_ES	1	0	Gas1_C	0.420088	0.747379
A4	Gli1_ss_F1R1_ES	5	0	Gas1_C	-0.624567	1.541748
A5	Gli1_ss_F1R1_ES	10	0	Gas1_C	0.037420	0.974396
A6	Gli1_ss_F1R1_ES	50	0	Gas1_C	-0.044352	1.031220
B1	Gli1_ss_F1R1_ES	0	0	Gas1_C	0.000000	1.000000
B2	Gli1_ss_F1R1_ES	0.1	0	Gas1_C	1.100192	0.466454
B3	Gli1_ss_F1R1_ES	1	0	Gas1_C	0.690004	0.619852
B4	Gli1_ss_F1R1_ES	5	0	Gas1_C	-0.289401	1.222133
B5	Gli1_ss_F1R1_ES	10	0	Gas1_C	0.643071	0.640349
B6	Gli1_ss_F1R1_ES	50	0	Gas1_C	1.292096	0.408357
C1	Gli1_ss_F1R1_ES	0	0	Gas1_Q	0.262759	0.833493
C2	Gli1_ss_F1R1_ES	0.1	0	Gas1_Q	0.421282	0.746761
C3	Gli1_ss_F1R1_ES	1	0	Gas1_Q	-0.033842	1.023735
C4	Gli1_ss_F1R1_ES	5	0	Gas1_Q	-0.437634	1.354382
C5	Gli1_ss_F1R1_ES	10	0	Gas1_Q	1.568458	0.337168
C6	Gli1_ss_F1R1_ES	50	0	Gas1_Q	0.470190	0.721869
D1	Gli1_ss_F1R1_ES	0	0	Gas1_Q	-0.420403	1.338301
D2	Gli1_ss_F1R1_ES	0.1	0	Gas1_Q	0.483897	0.715043
D3	Gli1_ss_F1R1_ES	1	0	Gas1_Q	-0.864642	1.820888
D4	Gli1_ss_F1R1_ES	5	0	Gas1_Q	0.291572	0.817011
D5	Gli1_ss_F1R1_ES	10	0	Gas1_Q	-0.141916	1.103369
D6	Gli1_ss_F1R1_ES	50	0	Gas1_Q	0.999510	0.500170

Sample	Target	condition1	condition2	species	dCt_goi	dCt_hkg \
1:16_DF1	Gli1_ss_F1R1_ES	DF1_STD	0	std	-0.246076	-0.527973
1:256_DF1	Gli1_ss_F1R1_ES	DF1_STD	0	std	NaN	NaN
1:4_DF1	Gli1_ss_F1R1_ES	DF1_STD	0	std	0.590131	1.591419
1:64_DF1	Gli1_ss_F1R1_ES	DF1_STD	0	std	NaN	-2.540583
1x_DF1	Gli1_ss_F1R1_ES	DF1_STD	0	std	2.768205	3.534928
A1	Gli1_ss_F1R1_ES	0	0	Gas1_C	NaN	0.006784
A2	Gli1_ss_F1R1_ES	0.1	0	Gas1_C	0.036472	-0.093238
A3	Gli1_ss_F1R1_ES	1	0	Gas1_C	-0.586486	-0.173181
A4	Gli1_ss_F1R1_ES	5	0	Gas1_C	0.184661	-0.446690
A5	Gli1_ss_F1R1_ES	10	0	Gas1_C	0.947357	0.977993
A6	Gli1_ss_F1R1_ES	50	0	Gas1_C	-0.348136	-0.399272
B1	Gli1_ss_F1R1_ES	0	0	Gas1_C	0.000000	-0.006784
B2	Gli1_ss_F1R1_ES	0.1	0	Gas1_C	-0.957643	0.135766
B3	Gli1_ss_F1R1_ES	1	0	Gas1_C	-0.836565	-0.153346

B4	Gli1_ss_F1R1_ES	5	0	Gas1_C	0.058869	-0.237317
B5	Gli1_ss_F1R1_ES	10	0	Gas1_C	-0.032711	0.603576
B6	Gli1_ss_F1R1_ES	50	0	Gas1_C	-1.732246	-0.446934
C1	Gli1_ss_F1R1_ES	0	0	Gas1_Q	-0.140734	0.115241
C2	Gli1_ss_F1R1_ES	0.1	0	Gas1_Q	0.071886	0.486384
C3	Gli1_ss_F1R1_ES	1	0	Gas1_Q	-0.425826	-0.466452
C4	Gli1_ss_F1R1_ES	5	0	Gas1_Q	-0.117215	-0.561634
C5	Gli1_ss_F1R1_ES	10	0	Gas1_Q	-1.163632	0.398042
C6	Gli1_ss_F1R1_ES	50	0	Gas1_Q	-0.563734	-0.100328
D1	Gli1_ss_F1R1_ES	0	0	Gas1_Q	0.747639	0.320452
D2	Gli1_ss_F1R1_ES	0.1	0	Gas1_Q	1.165577	1.642690
D3	Gli1_ss_F1R1_ES	1	0	Gas1_Q	0.375958	-0.495468
D4	Gli1_ss_F1R1_ES	5	0	Gas1_Q	-0.263695	0.021093
D5	Gli1_ss_F1R1_ES	10	0	Gas1_Q	0.599067	0.450367
D6	Gli1_ss_F1R1_ES	50	0	Gas1_Q	-0.705867	0.286859

Sample	Target	condition1	condition2	species	FC_Pfaffl
1:16_DF1	Gli1_ss_F1R1_ES	DF1_STD	0	std	1.142702
1:256_DF1	Gli1_ss_F1R1_ES	DF1_STD	0	std	NaN
1:4_DF1	Gli1_ss_F1R1_ES	DF1_STD	0	std	0.581864
1:64_DF1	Gli1_ss_F1R1_ES	DF1_STD	0	std	NaN
1x_DF1	Gli1_ss_F1R1_ES	DF1_STD	0	std	1.147605
A1	Gli1_ss_F1R1_ES	0	0	Gas1_C	NaN
A2	Gli1_ss_F1R1_ES	0.1	0	Gas1_C	1.101944
A3	Gli1_ss_F1R1_ES	1	0	Gas1_C	0.656088
A4	Gli1_ss_F1R1_ES	5	0	Gas1_C	1.606748
A5	Gli1_ss_F1R1_ES	10	0	Gas1_C	1.227559
A6	Gli1_ss_F1R1_ES	50	0	Gas1_C	0.952969
B1	Gli1_ss_F1R1_ES	0	0	Gas1_C	1.004633
B2	Gli1_ss_F1R1_ES	0.1	0	Gas1_C	0.377811
B3	Gli1_ss_F1R1_ES	1	0	Gas1_C	0.514272
B4	Gli1_ss_F1R1_ES	5	0	Gas1_C	1.240913
B5	Gli1_ss_F1R1_ES	10	0	Gas1_C	0.643173
B6	Gli1_ss_F1R1_ES	50	0	Gas1_C	0.275594
C1	Gli1_ss_F1R1_ES	0	0	Gas1_Q	0.812231
C2	Gli1_ss_F1R1_ES	0.1	0	Gas1_Q	0.766990
C3	Gli1_ss_F1R1_ES	1	0	Gas1_Q	0.928802
C4	Gli1_ss_F1R1_ES	5	0	Gas1_Q	1.316346
C5	Gli1_ss_F1R1_ES	10	0	Gas1_Q	0.261443
C6	Gli1_ss_F1R1_ES	50	0	Gas1_Q	0.637518
D1	Gli1_ss_F1R1_ES	0	0	Gas1_Q	1.598951
D2	Gli1_ss_F1R1_ES	0.1	0	Gas1_Q	0.953945
D3	Gli1_ss_F1R1_ES	1	0	Gas1_Q	1.980613
D4	Gli1_ss_F1R1_ES	5	0	Gas1_Q	0.773428
D5	Gli1_ss_F1R1_ES	10	0	Gas1_Q	1.276561
D6	Gli1_ss_F1R1_ES	50	0	Gas1_Q	0.429676

5.2 Change the columns names back from Condition1,2 to its original names

```
[473]: all_files_mean_norm = all_files_mean_norm.reset_index()
all_files_mean_norm.rename(columns={'condition1' : c1}, inplace=True)
all_files_mean_norm.rename(columns={'condition2' : c2}, inplace=True)
print(all_files_mean_norm)
```

	Sample	Target	dox	species	mean	E \
0	1:16_DF1	Gli1_ss_F1R1_ES	DF1_STD	0 std	32.442002	2.508833
1	1:256_DF1	Gli1_ss_F1R1_ES	DF1_STD	0 std	NaN	2.508833
2	1:4_DF1	Gli1_ss_F1R1_ES	DF1_STD	0 std	31.605795	2.508833
3	1:64_DF1	Gli1_ss_F1R1_ES	DF1_STD	0 std	NaN	2.508833
4	1x_DF1	Gli1_ss_F1R1_ES	DF1_STD	0 std	29.427721	2.508833
5	A1	Gli1_ss_F1R1_ES	0	0 Gas1_C	NaN	2.508833
6	A2	Gli1_ss_F1R1_ES	0.1	0 Gas1_C	32.159454	2.508833
7	A3	Gli1_ss_F1R1_ES	1	0 Gas1_C	32.782411	2.508833
8	A4	Gli1_ss_F1R1_ES	5	0 Gas1_C	32.011265	2.508833
9	A5	Gli1_ss_F1R1_ES	10	0 Gas1_C	31.248569	2.508833
10	A6	Gli1_ss_F1R1_ES	50	0 Gas1_C	32.544062	2.508833
11	B1	Gli1_ss_F1R1_ES	0	0 Gas1_C	32.195926	2.508833
12	B2	Gli1_ss_F1R1_ES	0.1	0 Gas1_C	33.153569	2.508833
13	B3	Gli1_ss_F1R1_ES	1	0 Gas1_C	33.032491	2.508833
14	B4	Gli1_ss_F1R1_ES	5	0 Gas1_C	32.137057	2.508833
15	B5	Gli1_ss_F1R1_ES	10	0 Gas1_C	32.228637	2.508833
16	B6	Gli1_ss_F1R1_ES	50	0 Gas1_C	33.928171	2.508833
17	C1	Gli1_ss_F1R1_ES	0	0 Gas1_Q	32.336660	2.508833
18	C2	Gli1_ss_F1R1_ES	0.1	0 Gas1_Q	32.124040	2.508833
19	C3	Gli1_ss_F1R1_ES	1	0 Gas1_Q	32.621752	2.508833
20	C4	Gli1_ss_F1R1_ES	5	0 Gas1_Q	32.313141	2.508833
21	C5	Gli1_ss_F1R1_ES	10	0 Gas1_Q	33.359558	2.508833
22	C6	Gli1_ss_F1R1_ES	50	0 Gas1_Q	32.759660	2.508833
23	D1	Gli1_ss_F1R1_ES	0	0 Gas1_Q	31.448287	2.508833
24	D2	Gli1_ss_F1R1_ES	0.1	0 Gas1_Q	31.030349	2.508833
25	D3	Gli1_ss_F1R1_ES	1	0 Gas1_Q	31.819967	2.508833
26	D4	Gli1_ss_F1R1_ES	5	0 Gas1_Q	32.459621	2.508833
27	D5	Gli1_ss_F1R1_ES	10	0 Gas1_Q	31.596858	2.508833
28	D6	Gli1_ss_F1R1_ES	50	0 Gas1_Q	32.901793	2.508833

	E_pow_mean_cq	Spenser_Norm_Cq	Spenser_Norm_Cq_hkg	...	E_ratio \
0	9.113006e+12	0.076775	NaN	...	0.797443
1	NaN	NaN	NaN	...	NaN
2	4.222993e+12	0.165676	NaN	...	1.720841
3	NaN	NaN	NaN	...	NaN
4	5.695628e+11	1.228399	NaN	...	12.759083
5	NaN	NaN	0.088448	...	NaN
6	7.027352e+12	0.099561	0.082621	...	1.034116
7	1.246366e+13	0.056135	0.078241	...	0.583063
8	6.131889e+12	0.114100	0.064938	...	1.185132

9	3.040317e+12	0.230124	0.171427	...	2.390244
10	1.000994e+13	0.069896	0.067070	...	0.725988
11	7.267100e+12	0.096276	0.087634	...	1.000000
12	1.753526e+13	0.039900	0.096572	...	0.414428
13	1.568719e+13	0.044600	0.079305	...	0.463250
14	6.884061e+12	0.101633	0.074895	...	1.055641
15	7.489075e+12	0.093423	0.132826	...	0.970360
16	3.575561e+13	0.019568	0.064927	...	0.203244
17	8.271424e+12	0.084586	0.095231	...	0.878579
18	6.802127e+12	0.102858	0.122632	...	1.068357
19	1.075144e+13	0.065075	0.064069	...	0.675919
20	8.094412e+12	0.086436	0.060046	...	0.897792
21	2.119333e+13	0.033013	0.115469	...	0.342896
22	1.220554e+13	0.057322	0.082222	...	0.595393
23	3.653427e+12	0.191505	0.109523	...	1.989119
24	2.487404e+12	0.281277	0.269631	...	2.921560
25	5.142524e+12	0.136052	0.062815	...	1.413139
26	9.261891e+12	0.075541	0.089314	...	0.784624
27	4.188424e+12	0.167044	0.119660	...	1.735044
28	1.391026e+13	0.050297	0.107044	...	0.522427

	Cq_hkg	E_hkg	E_Livak	dCt_Livak	ddCt_Livak	FC_Livak	dCt_goi	\
0	13.044166	1.976568	2	19.397836	-0.275112	1.210088	-0.246076	
1	NaN	1.976568	2	NaN	NaN	NaN	NaN	
2	10.924775	1.976568	2	20.681019	1.008071	0.497210	0.590131	
3	15.056777	1.976568	2	NaN	NaN	NaN	NaN	
4	8.981265	1.976568	2	20.446456	0.773508	0.584993	2.768205	
5	12.509410	1.976568	2	NaN	NaN	NaN	NaN	
6	12.609432	1.976568	2	19.550023	-0.122925	1.088941	0.036472	
7	12.689375	1.976568	2	20.093036	0.420088	0.747379	-0.586486	
8	12.962884	1.976568	2	19.048381	-0.624567	1.541748	0.184661	
9	11.538201	1.976568	2	19.710368	0.037420	0.974396	0.947357	
10	12.915466	1.976568	2	19.628596	-0.044352	1.031220	-0.348136	
11	12.522978	1.976568	2	19.672948	0.000000	1.000000	0.000000	
12	12.380428	1.976568	2	20.773140	1.100192	0.466454	-0.957643	
13	12.669540	1.976568	2	20.362952	0.690004	0.619852	-0.836565	
14	12.753511	1.976568	2	19.383547	-0.289401	1.222133	0.058869	
15	11.912618	1.976568	2	20.316018	0.643071	0.640349	-0.032711	
16	12.963128	1.976568	2	20.965044	1.292096	0.408357	-1.732246	
17	12.400953	1.976568	2	19.935707	0.262759	0.833493	-0.140734	
18	12.029810	1.976568	2	20.094230	0.421282	0.746761	0.071886	
19	12.982646	1.976568	2	19.639106	-0.033842	1.023735	-0.425826	
20	13.077828	1.976568	2	19.235314	-0.437634	1.354382	-0.117215	
21	12.118152	1.976568	2	21.241406	1.568458	0.337168	-1.163632	
22	12.616522	1.976568	2	20.143138	0.470190	0.721869	-0.563734	
23	12.195742	1.976568	2	19.252545	-0.420403	1.338301	0.747639	
24	10.873504	1.976568	2	20.156845	0.483897	0.715043	1.165577	
25	13.011662	1.976568	2	18.808305	-0.864642	1.820888	0.375958	

26	12.495101	1.976568	2	19.964520	0.291572	0.817011	-0.263695
27	12.065826	1.976568	2	19.531032	-0.141916	1.103369	0.599067
28	12.229335	1.976568	2	20.672458	0.999510	0.500170	-0.705867

	dCt_hkg	FC_Pfaffl
0	-0.527973	1.142702
1	NaN	NaN
2	1.591419	0.581864
3	-2.540583	NaN
4	3.534928	1.147605
5	0.006784	NaN
6	-0.093238	1.101944
7	-0.173181	0.656088
8	-0.446690	1.606748
9	0.977993	1.227559
10	-0.399272	0.952969
11	-0.006784	1.004633
12	0.135766	0.377811
13	-0.153346	0.514272
14	-0.237317	1.240913
15	0.603576	0.643173
16	-0.446934	0.275594
17	0.115241	0.812231
18	0.486384	0.766990
19	-0.466452	0.928802
20	-0.561634	1.316346
21	0.398042	0.261443
22	-0.100328	0.637518
23	0.320452	1.598951
24	1.642690	0.953945
25	-0.495468	1.980613
26	0.021093	0.773428
27	0.450367	1.276561
28	0.286859	0.429676

[29 rows x 22 columns]

5.3 Set 'Sample' as index (~first column)

```
[474]: all_files_mean_norm = all_files_mean_norm.set_index('Sample')
```

5.4 Export csv file

```
[475]: if c1 == '':
        safe = '_' + c2 + '_' + str(condition2)
    elif c2 == '':
        safe = '_' + c1 + '_' + str(condition1)
```

```
elif c1 and c2 == '':
    safe = '_'
else :
    safe = '_' + c1 + '_' + str(condition1) + '_' + c2 + '_' + str(condition2)

print(safe)
```

_dox_0

```
[478]: all_files_mean_norm.to_csv(path_export +
    date + '_' +
    'Sp_Li_Pf' + '_' +
    species +
    safe + '_' +
    target + '.csv'
    )
```


Chapter 5: Concluding remarks

Concluding remarks

Development and evolution are closely interconnected. Therefore, studies that identify changes in gene pathways and transcriptional regulation during evolution (i.e., by comparing different species) can provide insights into mechanisms of development and gene function without the need to create mutant lines. A major goal of my work has been to understand how genetic variation in nature can result in phenotypic variation especially regarding the scaling of body parts. The approach I have taken, which involved comparisons of three different species of birds (i.e., duck, chick, and quail), has allowed me to identify biologically relevant changes in gene expression for the SHH pathway. This strategy (i.e., comparative models) of exploiting the quail-duck chimeric system is very powerful tool to tease apart the countless signaling pathways and to resolve the connection between genotype and phenotype. There are still many unanswered questions about the mechanisms that NCM use to achieve craniofacial diversity in size as well as shape of different parts. Focusing on these questions by using closely related species (i.e., chick and quail) together with more distant species (i.e., duck) gives us the opportunity to decipher the development and evolution of key processes.

I found that *Gas1*, which is a member of the SHH pathway, likely plays a critical role in jaw evolution, since its expression is differentially regulated among chick, quail, and duck, and manipulating *Gas1* expression in NCM via overexpression or knockdown *in vivo* alters cell number and/or mandible size. I hypothesize that *Gas1* is responsible for differences in cell cycle length between different species (i.e., higher *Gas1* expression in duck results in longer cell cycle). NCM exhibits species-specific rates of proliferation, and there are species-specific differences in developmental rates, which lead to a larger NCM population in duck compared to quail at the same embryonic stages. Ultimately, this produces bigger mandibular primordia

in duck than in quail. Thus, species-specific jaw size is the result of a combination of multiple distinct developmental properties including the size of pre-migratory NCM population, proliferation rates, and developmental rate.

Much remains to be known about the mechanisms downstream of GAS1 that regulate the mandibular primordia size differences that I observed. Analyzing the expression dynamics of genes downstream of GAS1 such as the three Gli transcriptional regulators, interrogating the functions of different enhancers of *Gas1*, as well as characterizing any post-transcriptional and post-translational modifications of *Gas1* may enable a more complete understanding of mechanisms that are responsible for establishing species-specific size in the mandibular primordia. One strategy could be to use RNA-seq to assess changes in expression of target genes following a gain- or loss-of-function in *Gas1*.

Throughout my doctoral studies I have learned many new skills, but one of the most important ones is knowing how to form a hypothesis and to design experiments to test it. The choice of experimental techniques that I use will continue to be influenced by multiple factors including what is the most suitable as well as readily available (financially as well as on hand). Deciding when results are good enough to draw a biologically relevant conclusion is a critical step in the process. For example, this led to me using Vivo-morpholinos to knock-down *Gas1* expression (as described in Chapter 3). My reasons included the fact that *Gas1* is a very GC rich gene that is composed of only one exon in duck, chick, and quail, and also because I needed to deliver the Vivo-morpholinos unilaterally into the mandibular primordia at appropriate embryonic stage (HH18) to achieve gene knock-down during a developmental window of interest and not any earlier. Overall, I feel that through my thesis work, I have learned much about designing experiments and interpreting results, and I look forward to a career in the

field of developmental biology where many important questions remain to be answered.

References

- Abzhanov, A., Kuo, W.P., Hartmann, C., Grant, B.R., Grant, P.R., Tabin, C.J., 2006. The calmodulin pathway and evolution of elongated beak morphology in Darwin's finches. *Nature* 442, 563-567.
- Abzhanov, A., Protas, M., Grant, B.R., Grant, P.R., Tabin, C.J., 2004. Bmp4 and morphological variation of beaks in Darwin's finches. *Science* 305, 1462-1465.
- Abzhanov, A., Tabin, C.J., 2004. Shh and Fgf8 act synergistically to drive cartilage outgrowth during cranial development. *Dev Biol* 273, 134-148.
- Aguiar, D.P., Sghari, S., Creuzet, S., 2014. The facial neural crest controls fore- and midbrain patterning by regulating Foxg1 expression through Smad1 activity. *Development* 141, 2494-2505.
- Ahlgren, S.C., Bronner-Fraser, M., 1999. Inhibition of sonic hedgehog signaling in vivo results in craniofacial neural crest cell death. *Curr Biol* 9, 1304-1314.
- Ahlgren, S.C., Thakur, V., Bronner-Fraser, M., 2002. Sonic hedgehog rescues cranial neural crest from cell death induced by ethanol exposure. *Proc Natl Acad Sci U S A* 99, 10476-10481.
- Ainsworth, S.J., Stanley, R.L., Evans, D.J., 2010. Developmental stages of the Japanese quail. *J Anat* 216, 3-15.
- Alappat, S., Zhang, Z.Y., Chen, Y.P., 2003. Msx homeobox gene family and craniofacial development. *Cell Res* 13, 429-442.
- Alberch, P., 1985. Developmental constraints: Why St. Bernards often have an extra digit and poodles never do. *American Naturalist* 126, 430-433.
- Alberch, P., 1989. The logic of monsters: Evidence for internal constraint in development and evolution. *Geobios* 22, 21-57.
- Alberch, P., Gould, S.J., Oster, G.F., Wake, D.B., 1979. Size and shape in ontogeny and phylogeny. *Paleobiology* 5, 296-317.
- Allen, B.L., Song, J.Y., Izzi, L., Althaus, I.W., Kang, J.S., Charron, F., Krauss, R.S., McMahon, A.P., 2011. Overlapping roles and collective requirement for the coreceptors GAS1, CDO, and BOC in SHH pathway function. *Developmental cell* 20, 775-787.

Allen, B.L., Tenzen, T., McMahon, A.P., 2007. The Hedgehog-binding proteins Gas1 and Cdo cooperate to positively regulate Shh signaling during mouse development. *Genes Dev* 21, 1244-1257.

Almubarak, S., Nethercott, H., Freeberg, M., Beaudon, C., Jha, A., Jackson, W., Marcucio, R., Miclau, T., Healy, K., Bahney, C., 2016. Tissue engineering strategies for promoting vascularized bone regeneration. *Bone* 83, 197-209.

Andres, G., 1949. Untersuchungen an Chimären von Triton und Bombinator. *Genetica* 24, 387-534.

Appel, T.A., 1987. *The Cuvier-Geoffroy Debate: French Biology in the Decade before Darwin*. Oxford University Press, Oxford.

Ashique, A.M., Fu, K., Richman, J.M., 2002a. Endogenous bone morphogenetic proteins regulate outgrowth and epithelial survival during avian lip fusion. *Development* 129, 4647-4660.

Ashique, A.M., Fu, K., Richman, J.M., 2002b. Signalling via type IA and type IB bone morphogenetic protein receptors (BMPR) regulates intramembranous bone formation, chondrogenesis and feather formation in the chicken embryo. *Int J Dev Biol* 46, 243-253.

Atwood, S.X., Li, M., Lee, A., Tang, J.Y., Oro, A.E., 2013. GLI activation by atypical protein kinase C ζ/λ regulates the growth of basal cell carcinomas. *Nature* 494, 484-488.

Bae, G.U., Domené, S., Roessler, E., Schachter, K., Kang, J.S., Muenke, M., Krauss, R.S., 2011. Mutations in CDON, encoding a hedgehog receptor, result in holoprosencephaly and defective interactions with other hedgehog receptors. *Am J Hum Genet* 89, 231-240.

Bahney, C.S., Hu, D.P., Taylor, A.J., Ferro, F., Britz, H.M., Hallgrímsson, B., Johnstone, B., Miclau, T., Marcucio, R.S., 2014. Stem cell-derived endochondral cartilage stimulates bone healing by tissue transformation. *J Bone Miner Res* 29, 1269-1282.

Baker, C.V., Bronner-Fraser, M., 1997. The origins of the neural crest. Part I: embryonic induction. *Mechanisms of Development* 69, 3-11.

Balling, R., Mutter, G., Gruss, P., Kessel, M., 1989. Craniofacial abnormalities induced by ectopic expression of the homeobox gene Hox-1.1 in transgenic mice. *Cell* 58, 337-347.

Barkai, N., Ben-Zvi, D., 2009. 'Big frog, small frog'--maintaining proportions in embryonic development: delivered on 2 July 2008 at the 33rd FEBS Congress in Athens, Greece. *Febs j* 276, 1196-1207.

Barlow, A.J., Francis-West, P.H., 1997. Ectopic application of recombinant BMP-2 and BMP-4 can change patterning of developing chick facial primordia. *Development* 124, 391-398.

Baroffio, A., Dupin, E., Le Douarin, N.M., 1988. Clone-forming ability and differentiation potential of migratory neural crest cells. *Proc Natl Acad Sci U S A* 85, 5325-5329.

Beachy, P.A., Hymowitz, S.G., Lazarus, R.A., Leahy, D.J., Siebold, C., 2010. Interactions between Hedgehog proteins and their binding partners come into view. *Genes Dev* 24, 2001-2012.

Bee, J., Thorogood, P., 1980. The role of tissue interactions in the skeletogenic differentiation of avian neural crest cells. *Develop Biol* 78, 47-66.

Beresford, W.A., 1993. Cranial skeletal tissues: diversity and evolutionary trends, in: Hanken, J., Hall, B.K. (Eds.), *The Skull*. University of Chicago Press, Chicago, pp. 69-130.

Betancur, P., Bronner-Fraser, M., Sauka-Spengler, T., 2010. Assembling neural crest regulatory circuits into a gene regulatory network. *Annu Rev Cell Dev Biol* 26, 581-603.

Beverdam, A., Merlo, G.R., Paleari, L., Mantero, S., Genova, F., Barbieri, O., Janvier, P., Levi, G., 2002. Jaw transformation with gain of symmetry after *Dlx5/Dlx6* inactivation: mirror of the past? *Genesis* 34, 221-227.

Bhullar, B.A., Morris, Z.S., Sefton, E.M., Tok, A., Tokita, M., Namkoong, B., Camacho, J., Burnham, D.A., Abzhanov, A., 2015a. A molecular mechanism for the origin of a key evolutionary innovation, the bird beak and palate, revealed by an integrative approach to major transitions in vertebrate history. *Evolution* 69, 1665-1677.

Bhullar, B.A., Morris, Z.S., Sefton, E.M., Tok, A., Tokita, M., Namkoong, B., Camacho, J., Burnham, D.A., Abzhanov, A., 2015b. A molecular mechanism for the origin of a key evolutionary innovation, the bird beak and palate, revealed by an integrative approach to major transitions in vertebrate history. *Evolution*.

Bieler, J., Pozzorini, C., Naef, F., 2011. Whole-Embryo Modeling of Early Segmentation in *Drosophila* Identifies Robust and Fragile Expression Domains. *Biophysical Journal* 101, 287-296.

Billmyre, K.K., Klingensmith, J., 2015. Sonic hedgehog from pharyngeal arch 1 epithelium is necessary for early mandibular arch cell survival and later cartilage condensation differentiation. *Dev Dyn* 244, 564-576.

Braendle, C., Félix, M.A., 2008. Plasticity and errors of a robust developmental system in different environments. *Developmental cell* 15, 714-724.

Brigandt, I., 2006. Homology and heterochrony: the evolutionary embryologist Gavin Rylands de Beer (1899-1972). *J Exp Zool B Mol Dev Evol* 306, 317-328.

Briscoe, J., Ericson, J., 2001. Specification of neuronal fates in the ventral neural tube. *Curr Opin Neurobiol* 11, 43-49.

Briscoe, J., Théron, P.P., 2013. The mechanisms of Hedgehog signalling and its roles in development and disease. *Nature reviews. Molecular cell biology* 14, 416-429.

Brito, J.M., Teillet, M.A., Le Douarin, N.M., 2006. An early role for sonic hedgehog from foregut endoderm in jaw development: ensuring neural crest cell survival. *Proc Natl Acad Sci U S A* 103, 11607-11612.

Brito, J.M., Teillet, M.A., Le Douarin, N.M., 2008. Induction of mirror-image supernumerary jaws in chicken mandibular mesenchyme by Sonic Hedgehog-producing cells. *Development* 135, 2311-2319.

Bronner-Fraser, M., 1994. Neural crest cell formation and migration in the developing embryo. *Faseb Journal* 8, 699-706.

Bronner-Fraser, M., 2008. On the trail of the 'new head' in Les Treilles. *Development* 135, 2995-2999.

Brugmann, S.A., Goodnough, L.H., Gregorieff, A., Leucht, P., ten Berge, D., Fuerer, C., Clevers, H., Nusse, R., Helms, J.A., 2007. Wnt signaling mediates regional specification in the vertebrate face. *Development* 134, 3283-3295.

Brugmann, S.A., Powder, K.E., Young, N.M., Goodnough, L.H., Hahn, S.M., James, A.W., Helms, J.A., Lovett, M., 2010. Comparative gene expression analysis of avian embryonic facial structures reveals new candidates for human craniofacial disorders. *Hum Mol Genet* 19, 920-930.

Carballo, G.B., Honorato, J.R., de Lopes, G.P.F., Spohr, T., 2018. A highlight on Sonic hedgehog pathway. *Cell Commun Signal* 16, 11.

Cases, O., Perea-Gomez, A., Aguiar, D.P., Nykjaer, A., Amsellem, S., Chandellier, J., Umbhauer, M., Cereghini, S., Madsen, M., Collignon, J., Verroust, P., Riou, J.-F., Creuzet, S.E., Kozyraki, R., 2013. Cubilin, a High Affinity Receptor for Fibroblast Growth Factor 8, Is Required for Cell Survival in the Developing Vertebrate Head . *Journal of Biological Chemistry* 288, 16655-16670.

Catala, M., Ziller, C., Lapointe, F., Le Douarin, N.M., 2000. The developmental potentials of the caudalmost part of the neural crest are restricted to melanocytes and glia. *Mechanisms of Development* 95, 77-87.

- Cerny, R., Lwigale, P., Ericsson, R., Meulemans, D., Epperlein, H.H., Bronner-Fraser, M., 2004. Developmental origins and evolution of jaws: new interpretation of "maxillary" and "mandibular". *Dev Biol* 276, 225-236.
- Chang, D.T., López, A., von Kessler, D.P., Chiang, C., Simandl, B.K., Zhao, R., Seldin, M.F., Fallon, J.F., Beachy, P.A., 1994. Products, genetic linkage and limb patterning activity of a murine hedgehog gene. *Development* 120, 3339-3353.
- Chiang, C., Litingtung, Y., Lee, E., Young, K.E., Corden, J.L., Westphal, H., Beachy, P.A., 1996. Cyclopia and defective axial patterning in mice lacking Sonic hedgehog gene function. *Nature* 383, 407-413.
- Chong, H.J., Young, N.M., Hu, D., Jeong, J., McMahon, A.P., Hallgrimsson, B., Marcucio, R.S., 2012. Signaling by SHH rescues facial defects following blockade in the brain. *Dev Dyn* 241, 247-256.
- Choudhry, Z., Rikani, A.A., Choudhry, A.M., Tariq, S., Zakaria, F., Asghar, M.W., Sarfraz, M.K., Haider, K., Shafiq, A.A., Mobassarrah, N.J., 2014. Sonic hedgehog signalling pathway: a complex network. *Ann Neurosci* 21, 28-31.
- Chu, D., Nguyen, A., Smith, S.S., Vavrusova, Z., Schneider, R.A., 2020. Stable integration of an optimized inducible promoter system enables spatiotemporal control of gene expression throughout avian development. *Biology Open* 9.
- Cohn, M.J., Tickle, C., 1996. Limbs: a model for pattern formation within the vertebrate body plan. *Trends Genet* 12, 253-257.
- Cole, F., Krauss, R.S., 2003. Microform Holoprosencephaly in Mice that Lack the Ig Superfamily Member Cdon. *Curr Biol* 13, 411-415.
- Conrad, G.W., Bee, J.A., Roche, S.M., Teillet, M.-A., 1993. Fabrication of microscalpels by electrolysis of tungsten wire in a meniscus. *Journal of Neuroscience Methods* 50, 123-127.
- Coppinger, R.P., Schneider, R.A., 1995. Evolution of working dogs, in: Serpell, J. (Ed.), *The Domestic Dog*. Cambridge University Press, Cambridge, pp. 21-47.
- Cordero, D.R., Schneider, R.A., Helms, J.A., 2002. Morphogenesis of the Face, in: Lin, K.Y., Ogle, R.C., Jane, J.A. (Eds.), *Craniofacial Surgery: Science & Surgical Technique*. W. B. Saunders Company, Philadelphia, pp. 75-83.
- Couly, G., Creuzet, S., Bennaceur, S., Vincent, C., Le Douarin, N.M., 2002a. Interactions between Hox-negative cephalic neural crest cells and the foregut endoderm in patterning the facial skeleton in the vertebrate head. *Development* 129, 1061-1073.

- Couly, G., Creuzet, S., Bennaceur, S., Vincent, C., Le Douarin, N.M., 2002b. Interactions between Hox-negative cephalic neural crest cells and the foregut endoderm in patterning the facial skeleton in the vertebrate head. *Development* 129, 1061-1073.
- Couly, G., Grapin-Botton, A., Coltey, P., Le Douarin, N.M., 1996. The regeneration of the cephalic neural crest, a problem revisited: the regenerating cells originate from the contralateral or from the anterior and posterior neural fold. *Development* 122, 3393-3407.
- Couly, G., Le Douarin, N.M., 1988. The fate map of the cephalic neural primordium at the presomitic to the 3-somite stage in the avian embryo. *Development* 103, 101-113.
- Couly, G.F., Coltey, P.M., Le Douarin, N.M., 1992. The developmental fate of the cephalic mesoderm in quail-chick chimeras. *Development* 114, 1-15.
- Couly, G.F., Coltey, P.M., Le Douarin, N.M., 1993a. The triple origin of skull in higher vertebrates: a study in quail-chick chimeras. *Development* 117, 409-429.
- Couly, G.F., Coltey, P.M., Le Douarin, N.M., 1993b. The triple origin of skull in higher vertebrates: a study in quail-chick chimeras. *Development* 117, 409-429.
- Couly, G.F., Le Douarin, N.M., 1985. Mapping of the early neural primordium in quail-chick chimeras: I. Developmental relationships between placodes, facial ectoderm, and prosencephalon. *Develop Biol* 110, 422-439.
- Couly, G.F., Le Douarin, N.M., 1987. Mapping of the early neural primordium in quail-chick chimeras: II. The prosencephalic neural plate and neural folds: Implications for the genesis of cephalic human congenital abnormalities. *Develop Biol* 120, 198-214.
- Creuzet, S., Couly, G., Le Douarin, N.M., 2005a. Patterning the neural crest derivatives during development of the vertebrate head: insights from avian studies. *J Anat* 207, 447-459.
- Creuzet, S., Couly, G., Vincent, C., Le Douarin, N.M., 2002a. Negative effect of Hox gene expression on the development of the neural crest-derived facial skeleton. *Development* 129, 4301-4313.
- Creuzet, S., Couly, G., Vincent, C., Le Douarin, N.M., 2002b. Negative effect of Hox gene expression on the development of the neural crest-derived facial skeleton. *Development* 129, 4301-4313.
- Creuzet, S., Schuler, B., Couly, G., Le Douarin, N.M., 2004a. Reciprocal relationships between *Fgf8* and neural crest cells in facial and forebrain development. *Proc Natl Acad Sci U S A* 101, 4843-4847.

Creuzet, S., Schuler, B., Couly, G., Le Douarin, N.M., 2004b. Reciprocal relationships between *Fgf8* and neural crest cells in facial and forebrain development. *Proc Natl Acad Sci U S A* 101, 4843-4847.

Creuzet, S., Vincent, C., Couly, G., 2005b. Neural crest derivatives in ocular and periocular structures. *Int J Dev Biol* 49, 161-171.

Creuzet, S.E., 2009a. Neural crest contribution to forebrain development. *Seminars in cell & developmental biology* 20, 751-759.

Creuzet, S.E., 2009b. Regulation of pre-otic brain development by the cephalic neural crest. *Proceedings of the National Academy of Sciences* 106, 15774-15779.

Creuzet, S.E., Martinez, S., Le Douarin, N.M., 2006. The cephalic neural crest exerts a critical effect on forebrain and midbrain development. *Proceedings of the National Academy of Sciences* 103, 14033-14038.

Creuzet, S.E., Viallet, J.P., Ghawitian, M., Torch, S., Thélu, J., Alrajeh, M., Radu, A.G., Bouvard, D., Costagliola, F., Borgne, M.L., Buchet-Poyau, K., Aznar, N., Buschlen, S., Hosoya, H., Thibert, C., Billaud, M., 2016. *LKB1* signaling in cephalic neural crest cells is essential for vertebrate head development. *Develop Biol* 418, 283-296.

Crump, J.G., Maves, L., Lawson, N.D., Weinstein, B.M., Kimmel, C.B., 2004. An essential role for *Fgfs* in endodermal pouch formation influences later craniofacial skeletal patterning. *Development* 131, 5703-5716.

D'amico-Martel, A., Noden, D.M., 1983. Contributions of placodal and neural crest cells to avian cranial peripheral ganglia. *American Journal of Anatomy* 166, 445-468.

Darwin, C., 1859. *The Origin of Species*, 1962 ed. The Crowell-Collier Publishing Co., New York.

DasGupta, R., Fuchs, E., 1999. Multiple roles for activated LEF/TCF transcription complexes during hair follicle development and differentiation. *Development* 126, 4557-4568.

de Beer, G.R., 1930. *Embryology and Evolution*. Clarendon Press, Oxford.

de Beer, G.R., 1937. *The Development of the Vertebrate Skull*. University of Chicago Press, Chicago.

de Beer, G.R., 1940. *Embryos and ancestors*. Clarendon Press, Oxford,.

de Beer, G.R., 1954. Embryos and ancestors, Revised ed. Clarendon Press, Oxford.

de Beer, G.R., 1958. Embryos and Ancestors, Third (1958) ed. Oxford University Press, Oxford.

Del Sal, G., Ruaro, E.M., Utrera, R., Cole, C.N., Levine, A.J., Schneider, C., 1995. Gas1-induced growth suppression requires a transactivation-independent p53 function. *Mol Cell Biol* 15, 7152-7160.

Del Sal, G., Ruaro, M.E., Philipson, L., Schneider, C., 1992. The growth arrest-specific gene, *gas1*, is involved in growth suppression. *Cell* 70, 595-607.

Delloye-Bourgeois, C., Rama, N., Brito, J., Le Douarin, N., Mehlen, P., 2014. Sonic Hedgehog promotes the survival of neural crest cells by limiting apoptosis induced by the dependence receptor CDON during branchial arch development. *Biochem Biophys Res Commun* 452, 655-660.

Depew, M.J., Compagnucci, C., 2008. Tweaking the hinge and caps: testing a model of the organization of jaws. *J Exp Zool B Mol Dev Evol* 310, 315-335.

Depew, M.J., Liu, J.K., Long, J.E., Presley, R., Meneses, J.J., Pedersen, R.A., Rubenstein, J.L., 1999. *Dlx5* regulates regional development of the branchial arches and sensory capsules. *Development* 126, 3831-3846.

Depew, M.J., Lufkin, T., Rubenstein, J.L., 2002. Specification of jaw subdivisions by *Dlx* genes. *Science* 298, 381-385.

Depew, M.J., Olsson, L., 2008. Symposium on the evolution and development of the vertebrate head. *Journal of experimental zoology. Part B, Molecular and developmental evolution* 310, 287-293.

Depew, M.J., Simpson, C.A., Morasso, M., Rubenstein, J.L., 2005. Reassessing the *Dlx* code: the genetic regulation of branchial arch skeletal pattern and development. *J Anat* 207, 501-561.

Dessaud, E., McMahon, A.P., Briscoe, J., 2008. Pattern formation in the vertebrate neural tube: a sonic hedgehog morphogen-regulated transcriptional network. *Development* 135, 2489-2503.

Dimitrov, P., Zucker, S.W., 2006. A constant production hypothesis guides leaf venation patterning. *Proceedings of the National Academy of Sciences* 103, 9363-9368.

Diogo, R., Kelly, R.G., Christiaen, L., Levine, M., Ziermann, J.M., Molnar, J.L., Noden, D.M., Tzahor, E., 2015. A new heart for a new head in vertebrate cardiopharyngeal evolution. *Nature* 520, 466-473.

Douarin, N.L., Dieterlen-Lièvre, F., Creuzet, S., Teillet, M.A., 2008. Chapter 2 Quail-Chick Transplantations, *Methods in cell biology*. Academic Press, pp. 19-58.

Doufexi, A.E., Mina, M., 2008. Signaling pathways regulating the expression of Prx1 and Prx2 in the chick mandibular mesenchyme. *Dev Dyn* 237, 3115-3127.

Driever, W., Nüsslein-Volhard, C., 1988. The bicoid protein determines position in the *Drosophila* embryo in a concentration-dependent manner. *Cell* 54, 95-104.

Dunlop, L.L., Hall, B.K., 1995. Relationships between cellular condensation, preosteoblast formation and epithelial-mesenchymal interactions in initiation of osteogenesis. *International Journal of Developmental Biology* 39, 357-371.

Dupin, E., Calloni, G.W., Le Douarin, N.M., 2010. The cephalic neural crest of amniote vertebrates is composed of a large majority of precursors endowed with neural, melanocytic, chondrogenic and osteogenic potentialities. *Cell cycle* 9, 238-249.

Ealba, E.L., Jheon, A.H., Hall, J., Curantz, C., Butcher, K.D., Schneider, R.A., 2015. Neural crest-mediated bone resorption is a determinant of species-specific jaw length. *Dev Biol*.

Ealba, E.L., Schneider, R.A., 2013. A simple PCR-based strategy for estimating species-specific contributions in chimeras and xenografts. *Development* 140, 3062-3068.

Eames, B.F., Schneider, R.A., 2005. Quail-duck chimeras reveal spatiotemporal plasticity in molecular and histogenic programs of cranial feather development. *Development* 132, 1499-1509.

Eames, B.F., Schneider, R.A., 2008. The genesis of cartilage size and shape during development and evolution. *Development* 135, 3947-3958.

Eames, B.F., Sharpe, P.T., Helms, J.A., 2004. Hierarchy revealed in the specification of three skeletal fates by Sox9 and Runx2. *Dev Biol* 274, 188-200.

Echelard, Y., Epstein, D.J., St-Jacques, B., Shen, L., Mohler, J., McMahon, J.A., McMahon, A.P., 1993. Sonic hedgehog, a member of a family of putative signaling molecules, is implicated in the regulation of CNS polarity. *Cell* 75, 1417-1430.

Echevarría-Andino, M.L., Allen, B.L., 2020. The hedgehog co-receptor BOC differentially regulates SHH signaling during craniofacial development. *Development* 147.

- Etchevers, H.C., Couly, G., Vincent, C., Le Douarin, N.M., 1999a. Anterior cephalic neural crest is required for forebrain viability. *Development* 126, 3533-3543.
- Etchevers, H.C., Couly, G., Vincent, C., Le Douarin, N.M., 1999b. Anterior cephalic neural crest is required for forebrain viability. *Development* 126, 3533-3543.
- Etchevers, H.C., Vincent, C., Le Douarin, N.M., Couly, G.F., 2001. The cephalic neural crest provides pericytes and smooth muscle cells to all blood vessels of the face and forebrain. *Development* 128, 1059-1068.
- Evans, D.J., Noden, D.M., 2006. Spatial relations between avian craniofacial neural crest and paraxial mesoderm cells. *Dev Dyn* 235, 1310-1325.
- Eyal-Giladi, H., Kochav, S., 1976. From cleavage to primitive streak formation: A complementary normal table and a new look at the first stages of the development of the chick: I. General morphology. *Develop Biol* 49, 321-337.
- Ferguson, C.A., Tucker, A.S., Sharpe, P.T., 2000. Temporospatial cell interactions regulating mandibular and maxillary arch patterning. *Development* 127, 403-412.
- Feulgren, R., Rossenbeck, H., 1924. Mikroskopisch-chemischer Nachweis einer Nucleinsäure vom Typus der Thymonucleinsäure und die- darauf beruhende elektive Färbung von Zellkernen in mikroskopischen Präparaten. 135, 203-248.
- Fish, J.L., Schneider, R.A., 2014a. Assessing species-specific contributions to craniofacial development using quail-duck chimeras. *J Vis Exp* 87, 1-6.
- Fish, J.L., Schneider, R.A., 2014b. Chapter 6 - Neural Crest-Mediated Tissue Interactions During Craniofacial Development: The Origins of Species-Specific Pattern, in: Trainor, P.A. (Ed.), *Neural Crest Cells*. Academic Press, Boston, pp. 101-124.
- Fish, J.L., Schneider, R.A., 2014c. On the origins of species-specific size, *The Node*, February 25 ed. The Company of Biologists, Cambridge.
- Fish, J.L., Sklar, R.S., Woronowicz, K.C., Schneider, R.A., 2014. Multiple developmental mechanisms regulate species-specific jaw size. *Development* 141, 674-684.
- Fish, J.L., Villmoare, B., Kobernick, K., Compagnucci, C., Britanova, O., Tarabykin, V., Depew, M.J., 2011. *Satb2*, modularity, and the evolvability of the vertebrate jaw. *Evol Dev* 13, 549-564.
- Foppiano, S., Hu, D., Marcucio, R.S., 2007. Signaling by bone morphogenetic proteins directs formation of an ectodermal signaling center that regulates craniofacial development. *Dev Biol* 312, 103-114.

Francis-West, P., Ladher, R., Barlow, A., Graveson, A., 1998. Signalling interactions during facial development. *Mechanisms of Development* 75, 3-28.

Francis-West, P.H., Robson, L., Evans, D.J., 2003. Craniofacial development: the tissue and molecular interactions that control development of the head. *Adv Anat Embryol Cell Biol* 169, III-VI, 1-138.

Gammill, L.S., Gonzalez, C., Bronner-Fraser, M., 2007. Neuropilin 2/semaphorin 3F signaling is essential for cranial neural crest migration and trigeminal ganglion condensation. *Dev Neurobiol* 67, 47-56.

Gans, C., Northcutt, R.G., 1983. Neural Crest and the Origin of Vertebrates: A New Head. *Science* 220, 268-273.

Garcez, R.C., Le Douarin, N.M., Creuzet, S.E., 2014. Combinatorial activity of Six1-2-4 genes in cephalic neural crest cells controls craniofacial and brain development. *Cell Mol Life Sci* 71, 2149-2164.

Garstang, W., 1922. The theory of recapitulation: a critical restatement of the biogenic law. *Journal of the Linnean Society of London, Zoology* 35, 81-101.

Gayon, J., 2000. History of the Concept of Allometry. *American Zoologist* 40, 748-758.

Gendron-Maguire, M., Mallo, M., Zhang, M., Gridley, T., 1993. Hoxa-2 mutant mice exhibit homeotic transformation of skeletal elements derived from cranial neural crest. *Cell* 75, 1317-1331.

Golding, J.P., Trainor, P., Krumlauf, R., Gassmann, M., 2000. Defects in pathfinding by cranial neural crest cells in mice lacking the neuregulin receptor ErbB4. *Nat Cell Biol* 2, 103-109.

Goldschmidt, R., 1938. *Physiological Genetics*. McGraw Hill, New York.

Gomez-Gavira, M.V., Balaban, E., Bocancea, D., Lorrio, M.T., Pompeiano, M., Desco, M., Ripoll, J., Vaquero, J.J., 2017. Optimized CUBIC protocol for three-dimensional imaging of chicken embryos at single-cell resolution. *Development* 144, 2092-2097.

Goodrich, E.S., 1913. Metameric Segmentation and Homology. *Quarterly Journal of Microscopical Science* 59, 227-248.

Goodrich, E.S., 1930. *Studies on the Structure and Development of Vertebrates*. University of Chicago Press, Chicago.

Gould, S.J., 1966. Allometry and Size in Ontogeny and Phylogeny. *Biol Rev* 41, 587-640.

Gould, S.J., 1977. *Ontogeny and Phylogeny*. Harvard University Press, Cambridge.

Gould, S.J., 1981. *The Mismeasure of Man*. W. W. Norton & Company, New York.

Grammatopoulos, G.A., Bell, E., Toole, L., Lumsden, A., Tucker, A.S., 2000. Homeotic transformation of branchial arch identity after *Hoxa2* overexpression. *Development* 127, 5355-5365.

Grant, P.R., Grant, B.R., Abzhanov, A., 2006. A developing paradigm for the development of bird beaks. *Biological Journal of the Linnean Society* 88, 17-22.

Grenier, J., Teillet, M.A., Grifone, R., Kelly, R.G., Duprez, D., 2009. Relationship between neural crest cells and cranial mesoderm during head muscle development. *PLoS One* 4, e4381.

Griffin, J.N., Compagnucci, C., Hu, D., Fish, J., Klein, O., Marcucio, R., Depew, M.J., 2013. *Fgf8* dosage determines midfacial integration and polarity within the nasal and optic capsules. *Dev Biol* 374, 185-197.

Haldane, J.B.S., 1926. On Being the Right Size, *Harper's Magazine*.

Hall, B., 1980a. Chondrogenesis and Osteogenesis of Cranial Neural Crest Cells, in: Pratt/Christiansen (Ed.), *Current Research Trends in Prenatal Craniofacial Development*. Elsevier North Holland, Inc., pp. 47-63.

Hall, B.K., 1980b. Tissue interactions and the initiation of osteogenesis and chondrogenesis in the neural crest-derived mandibular skeleton of the embryonic mouse as seen in isolated murine tissues and in recombinations of murine and avian tissues. *Journal of Embryology and Experimental Morphology* 58, 251-264.

Hall, B.K., 1981. The induction of neural crest-derived cartilage and bone by embryonic epithelia: an analysis of the mode of action of an epithelial-mesenchymal interaction. *Journal of Embryology and Experimental Morphology* 64, 305-320.

Hall, B.K., 1982. The Role of Tissue Interactions in the Growth of Bone, in: Dixon, A.D., Sarnat, B.G. (Eds.), *Factors and Mechanisms Influencing Bone Growth*. Alan R. Liss, Inc., New York, pp. 205-215.

Hall, B.K., 1984. Developmental processes underlying heterochrony as an evolutionary mechanism. *Canadian Journal of Zoology* 62, 1-7.

Hall, B.K., 1987. Tissue Interactions in the Development and Evolution of the Vertebrate Head, in: Maderson, P.F.A. (Ed.), *Developmental and Evolutionary Aspects of the Neural Crest*. John Wiley & Sons, New York, pp. 215-260.

Hall, B.K., 2000a. Balfour, Garstang and de Beer: The first century of evolutionary embryology. *American Zoologist* 40, 718-728.

Hall, B.K., 2000b. The neural crest as a fourth germ layer and vertebrates as quadroblastic not triploblastic. *Evol Dev* 2, 3-5.

Hall, B.K., 2005a. *Bones and cartilage : developmental and evolutionary skeletal biology*. Elsevier Academic Press, San Diego, Calif.

Hall, B.K., 2005b. Consideration of the neural crest and its skeletal derivatives in the context of novelty/innovation. *Journal of Experimental Zoology Part B: Molecular and Developmental Evolution* 304B, 548-557.

Hall, B.K., Miyake, T., 1992. The membranous skeleton: the role of cell condensations in vertebrate skeletogenesis. *Anat Embryol (Berl)* 186, 107-124.

Hall, B.K., Miyake, T., 2000. All for one and one for all: condensations and the initiation of skeletal development. *Bioessays* 22, 138-147.

Hall, J., Jheon, A.H., Ealba, E.L., Eames, B.F., Butcher, K.D., Mak, S.S., Ladher, R., Alliston, T., Schneider, R.A., 2014. Evolution of a developmental mechanism: Species-specific regulation of the cell cycle and the timing of events during craniofacial osteogenesis. *Dev Biol* 385, 380-395.

Hall, W.G., Williams, C.L., 1983. Suckling isn't feeding, or is it? A search for developmental continuities. *Advances in the Study of Behavior* 13, 219-254.

Hamburger, V., Hamilton, H.L., 1951. A series of normal stages in the development of the chick embryo. *Journal of Morphology* 88, 49-92.

Hamilton, H.L., 1965. *Lillie's Development of the Chick: An Introduction to Embryology*, Third ed. Holt, Rinehart and Winston, New York.

Hanken, J., Hall, B.K., 1984. Variation and timing of the cranial ossification sequence of the Oriental fire-bellied toad, *Bombina orientalis* (Amphibia, Discoglossidae). *Journal of Morphology* 182, 245-255.

Hanken, J., Hall, B.K., 1993. *The Skull, Volume 3: Functional and Evolutionary Mechanisms*. University of Chicago Press.

Havens, B.A., Velonis, D., Kronenberg, M.S., Lichtler, A.C., Oliver, B., Mina, M., 2008. Roles of FGFR3 during morphogenesis of Meckel's cartilage and mandibular bones. *Dev Biol* 316, 336-349.

Helms, J.A., Schneider, R.A., 2003. Cranial skeletal biology. *Nature* 423, 326-331.

Hersh, A.H., 1934. Evolutionary allometric growth in the titanotheres. *American Naturalist* 68, 537-561.

His, W., 1868. Untersuchungen über die erste Anlage des Wirbelthierleibes : die erste Entwicklung des Hühnchens im Ei. F.C.W. Vogel, Leipzig :.

Holloway, D.M., 2010. The role of chemical dynamics in plant morphogenesis(1). *Biochemical Society transactions* 38, 645-650.

Hong, M., Krauss, R.S., 2018. Modeling the complex etiology of holoprosencephaly in mice. *American Journal of Medical Genetics Part C: Seminars in Medical Genetics* 178, 140-150.

Hong, M., Srivastava, K., Kim, S., Allen, B.L., Leahy, D.J., Hu, P., Roessler, E., Krauss, R.S., Muenke, M., 2017. BOC is a modifier gene in holoprosencephaly. *Human Mutation* 38, 1464-1470.

Hörstadius, S., 1950. The neural crest: its properties and derivatives in the light of experimental research. Hafner Publishing Company.

Hörstadius, S., Hörstadius, S.O., 1950. The Neural Crest: Its Properties and Derivatives in the Light of Experimental Research. Oxford University Press.

Hu, D., Marcucio, R.S., 2009a. A SHH-responsive signaling center in the forebrain regulates craniofacial morphogenesis via the facial ectoderm. *Development* 136, 107-116.

Hu, D., Marcucio, R.S., 2009b. Unique organization of the frontonasal ectodermal zone in birds and mammals. *Develop Biol* 325, 200-210.

Hu, D., Marcucio, R.S., 2012. Neural crest cells pattern the surface cephalic ectoderm during FEZ formation. *Dev Dyn* 241, 732-740.

Hu, D., Marcucio, R.S., Helms, J.A., 2003. A zone of frontonasal ectoderm regulates patterning and growth in the face. *Development* 130, 1749-1758.

Hu, D., Young, N.M., Li, X., Xu, Y., Hallgrímsson, B., Marcucio, R.S., 2015a. A dynamic Shh expression pattern, regulated by SHH and BMP signaling, coordinates fusion of primordia in the amniote face. *Development* 142, 567-574.

Hu, D., Young, N.M., Xu, Q., Jamniczky, H., Green, R.M., Mio, W., Marcucio, R.S., Hallgrímsson, B., 2015b. Signals from the brain induce variation in avian facial shape. *Dev Dyn.*

Huelsken, J., Vogel, R., Erdmann, B., Cotsarelis, G., Birchmeier, W., 2001. beta-Catenin controls hair follicle morphogenesis and stem cell differentiation in the skin. *Cell* 105, 533-545.

Hunt, P., Clarke, J.D., Buxton, P., Ferretti, P., Thorogood, P., 1998. Stability and plasticity of neural crest patterning and branchial arch Hox code after extensive cephalic crest rotation. *Develop Biol* 198, 82-104.

Hunt, P., Gulisano, M., Cook, M., Sham, M.H., Faiella, A., Wilkinson, D., Boncinelli, E., Krumlauf, R., 1991. A distinct Hox code for the branchial region of the vertebrate head. *Nature* 353, 861-864.

Hunt, P., Krumlauf, R., 1992. Hox codes and positional specification in vertebrate embryonic axes. *Annu Rev Cell Biol* 8, 227-256.

Huxley, J.S., 1924. Constant Differential Growth-Ratios and their Significance. *Nature* 114, 895-896.

Huxley, J.S., 1932. *Problems of Relative Growth*. Methuen, London.

Huxley, J.S., 1950. *Relative Growth and Form Transformation*. Proceedings of the Royal Society of London. Series B, Biological Sciences 137, 465-469.

Huxley, J.S., Teissier, G., 1936. Terminology of Relative Growth. *Nature* 137, 780-781.

Ingham, P.W., McMahon, A.P., 2001. Hedgehog signaling in animal development: paradigms and principles. *Genes Dev* 15, 3059-3087.

Izzi, L., Levesque, M., Morin, S., Laniel, D., Wilkes, B.C., Mille, F., Krauss, R.S., McMahon, A.P., Allen, B.L., Charron, F., 2011. Boc and Gas1 each form distinct Shh receptor complexes with Ptch1 and are required for Shh-mediated cell proliferation. *Developmental cell* 20, 788-801.

Jeong, J., Li, X., McEvelly, R.J., Rosenfeld, M.G., Lufkin, T., Rubenstein, J.L., 2008. Dlx genes pattern mammalian jaw primordium by regulating both lower jaw-specific and upper jaw-specific genetic programs. *Development* 135, 2905-2916.

Jeong, J., Mao, J., Tenzen, T., Kottmann, A.H., McMahon, A.P., 2004. Hedgehog signaling in the neural crest cells regulates the patterning and growth of facial primordia. *Genes Dev* 18, 937-951.

Jessell, T.M., 2000. Neuronal specification in the spinal cord: inductive signals and transcriptional codes. *Nat Rev Genet* 1, 20-29.

Jheon, A.H., Schneider, R.A., 2009. The cells that fill the bill: neural crest and the evolution of craniofacial development. *J Dent Res* 88, 12-21.

Jiang, T.X., Jung, H.S., Widelitz, R.B., Chuong, C.M., 1999. Self-organization of periodic patterns by dissociated feather mesenchymal cells and the regulation of size, number and spacing of primordia. *Development* 126, 4997-5009.

Jiang, X., Iseki, S., Maxson, R.E., Sucov, H.M., Morriss-Kay, G.M., 2002. Tissue origins and interactions in the mammalian skull vault. *Dev Biol* 241, 106-116.

Jing, Y., Zhou, X., Han, X., Jing, J., von der Mark, K., Wang, J., de Crombrughe, B., Hinton, R.J., Feng, J.Q., 2015. Chondrocytes Directly Transform into Bone Cells in Mandibular Condyle Growth. *J Dent Res* 94, 1668-1675.

Jung, H.S., Francis-West, P.H., Widelitz, R.B., Jiang, T.X., Ting-Berreth, S., Tickle, C., Wolpert, L., Chuong, C.M., 1998. Local inhibitory action of BMPs and their relationships with activators in feather formation: implications for periodic patterning. *Dev Biol* 196, 11-23.

Kaesler, S., Lüscher, B., Rütter, U., 2000. Transcriptional activity of GLI1 is negatively regulated by protein kinase A. *Biol Chem* 381, 545-551.

Kalmar, T., Lim, C., Hayward, P., Muñoz-Descalzo, S., Nichols, J., Garcia-Ojalvo, J., Martinez Arias, A., 2009. Regulated Fluctuations in Nanog Expression Mediate Cell Fate Decisions in Embryonic Stem Cells. *PLOS Biology* 7, e1000149.

Kant, I., 1790. *Kritik der Urteilskraft*.

Kauffman, S., Shymko, R., Trabert, K., 1978. Control of sequential compartment formation in *Drosophila*. *Science* 199, 259-270.

Kimmel, C.B., Ullmann, B., Walker, C., Wilson, C., Currey, M., Phillips, P.C., Bell, M.A., Postlethwait, J.H., Cresko, W.A., 2005. Evolution and development of facial bone morphology in threespine sticklebacks. *Proc Natl Acad Sci U S A* 102, 5791-5796.

Kinzler, K.W., Ruppert, J.M., Bigner, S.H., Vogelstein, B., 1988. The GLI gene is a member of the Kruppel family of zinc finger proteins. *Nature* 332, 371-374.

Kinzler, K.W., Vogelstein, B., 1990. The GLI gene encodes a nuclear protein which binds specific sequences in the human genome. *Mol Cell Biol* 10, 634-642.

Kondo, S., Asai, R., 1995. A reaction-diffusion wave on the skin of the marine angelfish *Pomacanthus*. *Nature* 376, 765-768.

Kondo, S., Miura, T., 2010. Reaction-Diffusion Model as a Framework for Understanding Biological Pattern Formation. *Science* 329, 1616-1620.

Kontges, G., Lumsden, A., 1996. Rhombencephalic neural crest segmentation is preserved throughout craniofacial ontogeny. *Development* 122, 3229-3242.

Köntges, G., Lumsden, A., 1996. Rhombencephalic neural crest segmentation is preserved throughout craniofacial ontogeny. *Development* 122, 3229-3242.

Koressaar, T., Remm, M., 2007. Enhancements and modifications of primer design program Primer3. *Bioinformatics* 23, 1289-1291.

Krauss, S., Concordet, J.P., Ingham, P.W., 1993. A functionally conserved homolog of the *Drosophila* segment polarity gene *hh* is expressed in tissues with polarizing activity in zebrafish embryos. *Cell* 75, 1431-1444.

Kulesa, P., Ellies, D.L., Trainor, P.A., 2004. Comparative analysis of neural crest cell death, migration, and function during vertebrate embryogenesis. *Dev Dyn* 229, 14-29.

Kuraku, S., Takio, Y., Sugahara, F., Takechi, M., Kuratani, S., 2010. Evolution of oropharyngeal patterning mechanisms involving *Dlx* and endothelins in vertebrates. *Dev Biol* 341, 315-323.

Kuratani, S., 2005. Craniofacial development and the evolution of the vertebrates: the old problems on a new background. *Zool Sci* 22, 1-19.

Kuratani, S., 2012. Evolution of the vertebrate jaw from developmental perspectives. *Evol Dev* 14, 76-92.

Kuratani, S., Adachi, N., Wada, N., Oisi, Y., Sugahara, F., 2013. Developmental and evolutionary significance of the mandibular arch and prechordal/premandibular cranium in vertebrates: revising the heterotopy scenario of gnathostome jaw evolution. *J Anat* 222, 41-55.

Kvon, E.Z., Kamneva, O.K., Melo, U.S., Barozzi, I., Osterwalder, M., Mannion, B.J., Tissières, V., Pickle, C.S., Plajzer-Frick, I., Lee, E.A., Kato, M., Garvin, T.H., Akiyama, J.A., Afzal, V., Lopez-Rios, J., Rubin, E.M., Dickel, D.E., Pennacchio, L.A., Visel, A., 2016.

Progressive Loss of Function in a Limb Enhancer during Snake Evolution. *Cell* 167, 633-642.e611.

Lamichhane, S., Berglund, J., Almen, M.S., Maqbool, K., Grabherr, M., Martinez-Barrio, A., Promerova, M., Rubin, C.J., Wang, C., Zamani, N., Grant, B.R., Grant, P.R., Webster, M.T., Andersson, L., 2015. Evolution of Darwin's finches and their beaks revealed by genome sequencing. *Nature* 518, 371-375.

Landge, A.N., Jordan, B.M., Diego, X., Müller, P., 2020. Pattern formation mechanisms of self-organizing reaction-diffusion systems. *Develop Biol* 460, 2-11.

Le Douarin, N., 1969. [Details of the interphase nucleus in Japanese quail (*Coturnix coturnix japonica*)]. *Bull Biol Fr Belg* 103, 435-452.

Le Douarin, N., Kalcheim, C., 1999. *The neural crest*, 2nd ed. Cambridge University Press, Cambridge, UK ; New York, NY.

Le Douarin, N.M., Creuzet, S., Couly, G., Dupin, E., 2004. Neural crest cell plasticity and its limits. *Development* 131, 4637-4650.

Le Lièvre, C., Le Douarin, N., 1974. [Ectodermic origin of the derma of the face and neck, demonstrated by interspecific combinations in the bird embryo]. *C R Acad Hebd Seances Acad Sci D* 278, 517-520.

Le Lièvre, C.S., 1978. Participation of neural crest-derived cells in the genesis of the skull in birds. *J Embryol Exp Morphol* 47, 17-37.

Le Lièvre, C.S., Le Douarin, N.M., 1975a. Mesenchymal derivatives of the neural crest: analysis of chimaeric quail and chick embryos. *Journal of Embryology and Experimental Morphology* 34, 125-154.

Le Lièvre, C.S., Le Douarin, N.M., 1975b. Mesenchymal derivatives of the neural crest: analysis of chimaeric quail and chick embryos. *J Embryol Exp Morphol* 34, 125-154.

Leary, S., Underwood, W., Anthony, R., Cartner, S., Corey, D., Grandin, T., Greenacre, C., Gwaltney-Brant, S., McCrackin, M.A., Meye, R., Miller, D., Shearer, J., Yanong, R., Golab, G.C., Patterson-Kane, E., 2013. *AVMA Guidelines for the Euthanasia of Animals: 2013 Edition*, American Veterinary Medical Association, Schaumburg, IL.

Lee, C.S., Buttitta, L., Fan, C.M., 2001a. Evidence that the WNT-inducible growth arrest-specific gene 1 encodes an antagonist of sonic hedgehog signaling in the somite. *Proc Natl Acad Sci U S A* 98, 11347-11352.

- Lee, C.S., Fan, C.M., 2001. Embryonic expression patterns of the mouse and chick Gas1 genes. *Mech Dev* 101, 293-297.
- Lee, K.K., Leung, A.K., Tang, M.K., Cai, D.Q., Schneider, C., Brancolini, C., Chow, P.H., 2001b. Functions of the growth arrest specific 1 gene in the development of the mouse embryo. *Dev Biol* 234, 188-203.
- Lee, S.H., Fu, K.K., Hui, J.N., Richman, J.M., 2001c. Noggin and retinoic acid transform the identity of avian facial prominences. *Nature* 414, 909-912.
- Lescroart, F., Hamou, W., Francou, A., Théveniau-Ruissy, M., Kelly, R.G., Buckingham, M., 2015. Clonal analysis reveals a common origin between nonsomite-derived neck muscles and heart myocardium. *Proc Natl Acad Sci U S A* 112, 1446-1451.
- Liu, J.K., Ghattas, I., Liu, S., Chen, S., Rubenstein, J.L., 1997. Dlx genes encode DNA-binding proteins that are expressed in an overlapping and sequential pattern during basal ganglia differentiation. *Developmental Dynamics* 210, 498-512.
- Liu, W., Selever, J., Murali, D., Sun, X., Brugger, S.M., Ma, L., Schwartz, R.J., Maxson, R., Furuta, Y., Martin, J.F., 2005. Threshold-specific requirements for Bmp4 in mandibular development. *Dev Biol* 283, 282-293.
- Liu, Y., May, N.R., Fan, C.M., 2001. Growth arrest specific gene 1 is a positive growth regulator for the cerebellum. *Dev Biol* 236, 30-45.
- Livak, K.J., Schmittgen, T.D., 2001. Analysis of relative gene expression data using real-time quantitative PCR and the 2(-Delta Delta C(T)) Method. *Methods* 25, 402-408.
- Longo, G., Montévil, M., 2014. Scaling and Scale Symmetries in Biological Systems, Perspectives on Organisms: Biological time, Symmetries and Singularities. Springer Berlin Heidelberg, Berlin, Heidelberg, pp. 23-73.
- Lopez-Rios, J., Duchesne, A., Speziale, D., Andrey, G., Peterson, K.A., Germann, P., Unal, E., Liu, J., Floriot, S., Barbey, S., Gallard, Y., Müller-Gerbl, M., Courtney, A.D., Klopp, C., Rodriguez, S., Ivanek, R., Beisel, C., Wicking, C., Iber, D., Robert, B., McMahon, A.P., Duboule, D., Zeller, R., 2014. Attenuated sensing of SHH by Ptch1 underlies evolution of bovine limbs. *Nature* 511, 46-51.
- Lufkin, T., Mark, M., Hart, C., Dollé, P., Lemeur, M., Chambon, P., 1992. Homeotic transformation of the occipital bones of the skull by ectopic expression of a homeobox gene. *Nature* 359, 835-841.
- Lumer, H., 1940. Evolutionary allometry in the skeleton of the domesticated dog. *The American Naturalist* 76, 439-467.

Lumer, H., Anderson, B.G., Hersh, A.H., 1942. On the Significance of the Constant b in the Law of Allometry $y = bx^a$. *The American Naturalist* 76, 364-375.

Lwigale, P.Y., Schneider, R.A., 2008. Other chimeras: quail-duck and mouse-chick. *Methods in cell biology* 87, 59-74.

MacDonald, M.E., Abbott, U.K., Richman, J.M., 2004. Upper beak truncation in chicken embryos with the cleft primary palate mutation is due to an epithelial defect in the frontonasal mass. *Dev Dyn* 230, 335-349.

Mallarino, R., Grant, P.R., Grant, B.R., Herrel, A., Kuo, W.P., Abzhanov, A., 2011. Two developmental modules establish 3D beak-shape variation in Darwin's finches. *Proc Natl Acad Sci U S A* 108, 4057-4062.

Marconi, A., Hancock-Ronemus, A., Gillis, J.A., 2020. Adult chondrogenesis and spontaneous cartilage repair in the skate, *Leucoraja erinacea*. *Elife* 9.

Marcucio, R.S., Cordero, D.R., Hu, D., Helms, J.A., 2005. Molecular interactions coordinating the development of the forebrain and face. *Dev Biol* 284, 48-61.

Martinelli, D.C., Fan, C.-M., 2007. The Role of Gas1 in Embryonic Development and its Implications for Human Disease. *Cell cycle* 6, 2650-2655.

McBratney-Owen, B., Iseki, S., Bamforth, S.D., Olsen, B.R., Morriss-Kay, G.M., 2008. Development and tissue origins of the mammalian cranial base. *Dev Biol* 322, 121-132.

McLellan, J.S., Zheng, X., Hauk, G., Ghirlando, R., Beachy, P.A., Leahy, D.J., 2008. The mode of Hedgehog binding to Ihog homologues is not conserved across different phyla. *Nature* 455, 979-983.

McLennan, R., Schumacher, L.J., Morrison, J.A., Teddy, J.M., Ridenour, D.A., Box, A.C., Semerad, C.L., Li, H., McDowell, W., Kay, D., Maini, P.K., Baker, R.E., Kulesa, P.M., 2015a. Neural crest migration is driven by a few trailblazer cells with a unique molecular signature narrowly confined to the invasive front. *Development* 142, 2014-2025.

McLennan, R., Schumacher, L.J., Morrison, J.A., Teddy, J.M., Ridenour, D.A., Box, A.C., Semerad, C.L., Li, H., McDowell, W., Kay, D., Maini, P.K., Baker, R.E., Kulesa, P.M., 2015b. VEGF signals induce trailblazer cell identity that drives neural crest migration. *Dev Biol* 407, 12-25.

Meinhardt, H., 2012. Turing's theory of morphogenesis of 1952 and the subsequent discovery of the crucial role of local self-enhancement and long-range inhibition. *Interface Focus* 2, 407-416.

- Meinhardt, H., Fowler, D.R., Prusinkiewicz, P., 2003. Algorithmic Beauty of Sea Shells. Springer-Verlag.
- Merrill, A.E., Eames, B.F., Weston, S.J., Heath, T., Schneider, R.A., 2008. Mesenchyme-dependent BMP signaling directs the timing of mandibular osteogenesis. *Development* 135, 1223-1234.
- Mina, M., Upholt, W.B., Kollar, E.J., 1994. Enhancement of avian mandibular chondrogenesis in vitro in the absence of epithelium. *Archives of Oral Biology* 39, 551-562.
- Mina, M., Wang, Y.H., Ivanisevic, A.M., Upholt, W.B., Rodgers, B., 2002. Region- and stage-specific effects of FGFs and BMPs in chick mandibular morphogenesis. *Dev Dyn* 223, 333-352.
- Minoux, M., Rijli, F.M., 2010. Molecular mechanisms of cranial neural crest cell migration and patterning in craniofacial development. *Development* 137, 2605-2621.
- Mitsiadis, T.A., Caton, J., Cobourne, M., 2006. Waking-up the sleeping beauty: recovery of the ancestral bird odontogenic program. *J Exp Zool B Mol Dev Evol* 306, 227-233.
- Mitsiadis, T.A., Cheraud, Y., Sharpe, P., Fontaine-Perus, J., 2003. Development of teeth in chick embryos after mouse neural crest transplantations. *Proc Natl Acad Sci U S A* 100, 6541-6545.
- Momose, T., Tonegawa, A., Takeuchi, J., Ogawa, H., Umesono, K., Yasuda, K., 1999. Efficient targeting of gene expression in chick embryos by microelectroporation. *Development, Growth & Differentiation* 41, 335-344.
- Moore, W.J., 1981. *The Mammalian Skull*. Cambridge University Press, Cambridge.
- Morris, V.B., Cowan, R., 1995. An analysis of the growth of the retinal cell population in embryonic chicks yielding proliferative ratios, numbers of proliferative and non-proliferative cells and cell-cycle times for successive generations of cell cycles. *Cell Prolif* 28, 373-391.
- Morris, V.B., Cowan, R., Culpin, D., 1979. Variability of cell cycle times measured in vivo in embryonic chick retina by continuous labelling with BUdR. *Nature* 280, 68-71.
- Morriss-Kay, G.M., 2001. Derivation of the mammalian skull vault. *J Anat* 199, 143-151.
- Muramatsu, T., Shibata, O., Ryoki, S., Ohmori, Y., Okumura, J.-i., 1997. Foreign Gene Expression in the Mouse Testis by Localized in Vivo Gene Transfer. *Biochemical and Biophysical Research Communications* 233, 45-49.

- Nagorcka, B.N., Mooney, J.R., 1982. The role of a reaction-diffusion system in the formation of hair fibres. *Journal of Theoretical Biology* 98, 575-607.
- Nagorcka, B.N., Mooney, J.R., 1985. The role of a reaction-diffusion system in the initiation of primary hair follicles. *J Theor Biol* 114, 243-272.
- Nakamasu, A., Takahashi, G., Kanbe, A., Kondo, S., 2009. Interactions between zebrafish pigment cells responsible for the generation of Turing patterns. *Proceedings of the National Academy of Sciences* 106, 8429-8434.
- Needham, J., Lerner, M.I., 1940. Terminology of Relative Growth-Rates. *Nature* 146, 618.
- Newman, S., Frisch, H., 1979. Dynamics of skeletal pattern formation in developing chick limb. *Science* 205, 662-668.
- Nikitina, N., Sauka-Spengler, T., Bronner-Fraser, M., 2008. Dissecting early regulatory relationships in the lamprey neural crest gene network. *Proc Natl Acad Sci U S A* 105, 20083-20088.
- Noden, D.M., 1978a. The Control of Avian Cephalic Neural Crest Cytodifferentiation: II. Neural Tissues. *Develop Biol* 67, 313-329.
- Noden, D.M., 1978b. The control of avian cephalic neural crest cytodifferentiation. I. Skeletal and connective tissues. *Develop Biol* 67, 296-312.
- Noden, D.M., 1983a. The Embryonic Origins of Avian Cephalic and Cervical Muscles and Associated Connective Tissues. *Am J Anat* 168, 257-276.
- Noden, D.M., 1983b. The Role of the Neural Crest in Patterning of Avian Cranial Skeletal, Connective, and Muscle Tissues. *Develop Biol* 96, 144-165.
- Noden, D.M., 1988. Interactions and fates of avian craniofacial mesenchyme. *Development* 103, 121-140.
- Noden, D.M., Francis-West, P., 2006. The differentiation and morphogenesis of craniofacial muscles. *Dev Dyn* 235, 1194-1218.
- Noden, D.M., Marcucio, R., Borycki, A.G., Emerson, C.P., Jr., 1999. Differentiation of avian craniofacial muscles: I. Patterns of early regulatory gene expression and myosin heavy chain synthesis. *Developmental Dynamics* 216, 96-112.
- Noden, D.M., Schneider, R.A., 2006a. Neural Crest Cells and the Community of Plan for Craniofacial Development: Historical Debates and Current Perspectives, in: Saint-

Jeannet, J.-P. (Ed.), Neural crest induction and differentiation. Landes Bioscience, Georgetown, Tex., pp. 1-23.

Noden, D.M., Schneider, R.A., 2006b. Neural crest cells and the community of plan for craniofacial development: historical debates and current perspectives. *Adv Exp Med Biol* 589, 1-23.

Noden, D.M., Trainor, P.A., 2005. Relations and interactions between cranial mesoderm and neural crest populations. *J Anat* 207, 575-601.

Northcutt, R.G., 2005. The new head hypothesis revisited. *Journal of Experimental Zoology Part B: Molecular and Developmental Evolution* 304B, 274-297.

Northcutt, R.G., Gans, C., 1983. The Genesis of Neural Crest and Epidermal Placodes. *Quarterly Review of Biology* 58, 1-27.

Nusslein-Volhard, C., Wieschaus, E., 1980. Mutations affecting segment number and polarity in *Drosophila*. *Nature* 287, 795-801.

Ogino, H., Yasuda, K., 1998. Induction of Lens Differentiation by Activation of a bZIP Transcription Factor, L-Maf. *Science* 280, 115-118.

Olesnick Killian, E.C., Birkholz, D.A., Artinger, K.B., 2009. A role for chemokine signaling in neural crest cell migration and craniofacial development. *Dev Biol* 333, 161-172.

Olsson, L., Falck, P., Lopez, K., Cobb, J., Hanken, J., 2001. Cranial neural crest cells contribute to connective tissue in cranial muscles in the anuran amphibian, *Bombina orientalis*. *Dev Biol* 237, 354-367.

Oster, G., Alberch, P., 1982. Evolution and bifurcation of developmental programs. *Evolution* 36, 444-459.

Owen, R., 1848. *On the Archetype and Homologies of the Vertebrate Skeleton*. John Van Voorst, Paternoster Row, London.

Padovan-Merhar, O., Nair, Gautham P., Biaesch, Andrew G., Mayer, A., Scarfone, S., Foley, Shawn W., Wu, Angela R., Churchman, L.S., Singh, A., Raj, A., 2015. Single Mammalian Cells Compensate for Differences in Cellular Volume and DNA Copy Number through Independent Global Transcriptional Mechanisms. *Molecular Cell* 58, 339-352.

Paré, A.C., Vichas, A., Fincher, C.T., Mirman, Z., Farrell, D.L., Mainieri, A., Zallen, J.A., 2014. A positional Toll receptor code directs convergent extension in *Drosophila*. *Nature* 515, 523-527.

- Park, J., Gebhardt, M., Golovchenko, S., Perez-Branguli, F., Hattori, T., Hartmann, C., Zhou, X., deCrombrughe, B., Stock, M., Schneider, H., von der Mark, K., 2015. Dual pathways to endochondral osteoblasts: a novel chondrocyte-derived osteoprogenitor cell identified in hypertrophic cartilage. *Biol Open* 4, 608-621.
- Parsons, T.E., Schmidt, E.J., Boughner, J.C., Jamniczky, H.A., Marcucio, R.S., Hallgrímsson, B., 2011. Epigenetic integration of the developing brain and face. *Dev Dyn* 240, 2233-2244.
- Pasqualetti, M., Ori, M., Nardi, I., Rijli, F.M., 2000. Ectopic *Hoxa2* induction after neural crest migration results in homeosis of jaw elements in *Xenopus*. *Development* 127, 5367-5378.
- Patterson, C., 1977. Cartilage bones, dermal bones, and membrane bones, or the exoskeleton versus the endoskeleton, in: Andrews, S., Miles, R., Walker, A. (Eds.), *Problems in Vertebrate Evolution*. Academic Press, London, pp. 77-121.
- Pekarik, V., Bourikas, D., Miglino, N., Joset, P., Preiswerk, S., Stoeckli, E.T., 2003. Screening for gene function in chicken embryo using RNAi and electroporation. *Nature Biotechnology* 21, 93-96.
- Pfaffl, M.W., 2001. A new mathematical model for relative quantification in real-time RT-PCR. *Nucleic Acids Res* 29, e45.
- Phillips, N.E., Mandic, A., Omid, S., Naef, F., Suter, D.M., 2019. Memory and relatedness of transcriptional activity in mammalian cell lineages. *Nature Communications* 10, 1208.
- Primm, D.R., Norris, W.E., Carlson, G.J., Keynes, R.J., Stern, C.D., 1989. Periodic segmental anomalies induced by heat shock in the chick embryo are associated with the cell cycle. *Development* 105, 119-130.
- Qiu, M., Bulfone, A., Ghattas, I., Meneses, J.J., Christensen, L., Sharpe, P.T., Presley, R., Pedersen, R.A., Rubenstein, J.L., 1997. Role of the *Dlx* homeobox genes in proximodistal patterning of the branchial arches: mutations of *Dlx-1*, *Dlx-2*, and *Dlx-1* and *-2* alter morphogenesis of proximal skeletal and soft tissue structures derived from the first and second arches. *Development* 125, 165-184.
- Qiu, M., Bulfone, A., Martinez, S., Meneses, J.J., Shimamura, K., Pedersen, R.A., Rubenstein, J.L., 1995. Null mutation of *Dlx-2* results in abnormal morphogenesis of proximal first and second branchial arch derivatives and abnormal differentiation in the forebrain. *Genes & Development* 9, 2523-2538.

Raspopovic, J., Marcon, L., Russo, L., Sharpe, J., 2014. Modeling digits. Digit patterning is controlled by a Bmp-Sox9-Wnt Turing network modulated by morphogen gradients. *Science* 345, 566-570.

Ribeiro, L.A., Queizi, R.G., Nascimento, A., Bertolacini, C.P., Richieri-Costa, A., 2010. Holoprosencephaly and holoprosencephaly-like phenotype and GAS1 DNA sequence changes: Report of four Brazilian patients. *American Journal of Medical Genetics Part A* 152A, 1688-1694.

Richardson, M.K., Hornbruch, A., Wolpert, L., 1990. Mechanisms of pigment pattern formation in the quail embryo. *Development* 109, 81-89.

Richman, J.M., Herbert, M., Matovinovic, E., Walin, J., 1997. Effect of fibroblast growth factors on outgrowth of facial mesenchyme. *Develop Biol* 189, 135-147.

Richman, J.M., Lee, S.H., 2003. About face: signals and genes controlling jaw patterning and identity in vertebrates. *Bioessays* 25, 554-568.

Richman, J.M., Tickle, C., 1989. Epithelia are interchangeable between facial primordia of chick embryos and morphogenesis is controlled by the mesenchyme. *Develop Biol* 136, 201-210.

Richman, J.M., Tickle, C., 1992. Epithelial-mesenchymal interactions in the outgrowth of limb buds and facial primordia in chick embryos. *Develop Biol* 154, 299-308.

Ricklefs, R.E., Starck, J.M., 1998. Embryonic Growth and Development, in: Starck, J.M., Ricklefs, R.E. (Eds.), *Avian growth and development : evolution within the altricial-precocial spectrum*. Oxford University Press, New York, pp. 31-58.

Riddihough, G., Ish-Horowicz, D., 1991. Individual stripe regulatory elements in the *Drosophila* hairy promoter respond to maternal, gap, and pair-rule genes. *Genes Dev* 5, 840-854.

Riddle, R.D., Johnson, R.L., Laufer, E., Tabin, C., 1993. Sonic hedgehog mediates the polarizing activity of the ZPA. *Cell* 75, 1401-1416.

Ridley, M., 1985. Embryology and classical zoology in Great Britain, in: Horder, T.J., Witkowski, J., Wylie, C.C. (Eds.), *A history of embryology : the Eighth Symposium of the British Society for Developmental Biology*. Cambridge University Press, Cambridge, pp. 35-67.

Rijli, F.M., Mark, M., Lakkaraju, S., Dierich, A., Dolle, P., Chambon, P., 1993. A homeotic transformation is generated in the rostral branchial region of the head by disruption of *Hoxa-2*, which acts as a selector gene. *Cell* 75, 1333-1349.

Rinon, A., Lazar, S., Marshall, H., Buchmann-Moller, S., Neufeld, A., Elhanany-Tamir, H., Taketo, M.M., Sommer, L., Krumlauf, R., Tzahor, E., 2007. Cranial neural crest cells regulate head muscle patterning and differentiation during vertebrate embryogenesis. *Development* 134, 3065-3075.

Roelink, H., Augsburger, A., Heemskerk, J., Korzh, V., Norlin, S., Ruiz i Altaba, A., 1994. Floor plate and motor neuron induction by *vhh-1*, a vertebrate homolog of hedgehog expressed by the notochord. *Cell* 76, 761-775.

Rowe, A., Richman, J.M., Brickell, P.M., 1992. Development of the spatial pattern of retinoic acid receptor-beta transcripts in embryonic chick facial primordia. *Development* 114, 805-813.

Roycroft, A., Mayor, R., 2016. Molecular basis of contact inhibition of locomotion. *Cell Mol Life Sci* 73, 1119-1130.

Ruhin, B., Creuzet, S., Vincent, C., Benouaiche, L., Le Douarin, N.M., Couly, G., 2003. Patterning of the hyoid cartilage depends upon signals arising from the ventral foregut endoderm. *Developmental Dynamics* 228, 239-246.

Russell, E.S., 1916. *Form and Function: A Contribution to the History of Animal Morphology*. John Murray Publishers Ltd., London.

Sacilotto, N., Castillo, J., Riffo-Campos, Á.L., Flores, J.M., Hibbitt, O., Wade-Martins, R., López, C., Rodrigo, M.I., Franco, L., López-Rodas, G., 2015. Growth Arrest Specific 1 (*Gas1*) Gene Overexpression in Liver Reduces the In Vivo Progression of Murine Hepatocellular Carcinoma and Partially Restores Gene Expression Levels. *PLOS ONE* 10, e0132477.

Sadaghiani, B., Thiebaud, C.H., 1987. Neural crest development in the *Xenopus laevis* embryo, studied by interspecific transplantation and scanning electron microscopy. *Dev Biol* 124, 91-110.

Saint-Jeannet, J.-P., 2006. *Neural crest induction and differentiation*. Springer Science+Business Media ;

Landes Bioscience/Eurekah.com, New York, N.Y.

Georgetown, Tex.

Sambasivan, R., Kuratani, S., Tajbakhsh, S., 2011. An eye on the head: the development and evolution of craniofacial muscles. *Development* 138, 2401-2415.

Sánchez-Villagra, M.R., Smith, K.K., 1997. Diversity and Evolution of the Marsupial Mandibular Angular Process. *Journal of Mammalian Evolution* 4, 119-144.

Sarkar, S., Poon, C.C., Mirzaei, R., Rawji, K.S., Hader, W., Bose, P., Kelly, J., Dunn, J.F., Yong, V.W., 2018. Microglia induces Gas1 expression in human brain tumor-initiating cells to reduce tumorigenicity. *Scientific Reports* 8, 15286.

Sasaki, H., Nishizaki, Y., Hui, C., Nakafuku, M., Kondoh, H., 1999. Regulation of Gli2 and Gli3 activities by an amino-terminal repression domain: implication of Gli2 and Gli3 as primary mediators of Shh signaling. *Development* 126, 3915-3924.

Sato, T., Kurihara, Y., Asai, R., Kawamura, Y., Tonami, K., Uchijima, Y., Heude, E., Ekker, M., Levi, G., Kurihara, H., 2008. An endothelin-1 switch specifies maxillomandibular identity. *Proc Natl Acad Sci U S A* 105, 18806-18811.

Schilling, T.F., 1997. Genetic analysis of craniofacial development in the vertebrate embryo. *Bioessays* 19, 459-468.

Schneider, C., King, R.M., Philipson, L., 1988. Genes specifically expressed at growth arrest of mammalian cells. *Cell* 54, 787-793.

Schneider, R.A., 1999. Neural crest can form cartilages normally derived from mesoderm during development of the avian head skeleton. *Develop Biol* 208, 441-455.

Schneider, R.A., 2005. Developmental mechanisms facilitating the evolution of bills and quills. *J Anat* 207, 563-573.

Schneider, R.A., 2007. How to tweak a beak: molecular techniques for studying the evolution of size and shape in Darwin's finches and other birds. *Bioessays* 29, 1-6.

Schneider, R.A., 2015. Regulation of Jaw Length During Development, Disease, and Evolution. *Curr Top Dev Biol* 115, 271-298.

Schneider, R.A., 2018a. Cellular Control of Time, Size, and Shape in Development and Evolution, in: Hall, B.K., Moody, S. (Eds.), *Cells in Evolutionary Biology: Translating Genotypes into Phenotypes – Past, Present, Future*. CRC Press, Taylor & Francis Group, Boca Raton, pp. 167-212.

Schneider, R.A., 2018b. Neural crest and the origin of species-specific pattern. *Genesis* 56, e23219.

Schneider, R.A., Helms, J.A., 2003. The cellular and molecular origins of beak morphology. *Science* 299, 565-568.

Schneider, R.A., Hu, D., Helms, J.A., 1999. From head to toe: conservation of molecular signals regulating limb and craniofacial morphogenesis. *Cell and Tissue Research* 296, 103-109.

Schneider, R.A., Hu, D., Rubenstein, J.L., Maden, M., Helms, J.A., 2001. Local retinoid signaling coordinates forebrain and facial morphogenesis by maintaining FGF8 and SHH. *Development* 128, 2755-2767.

Schoenebeck, J.J., Hutchinson, S.A., Byers, A., Beale, H.C., Carrington, B., Faden, D.L., Rimbault, M., Decker, B., Kidd, J.M., Sood, R., Boyko, A.R., Fondon, J.W., 3rd, Wayne, R.K., Bustamante, C.D., Ciruna, B., Ostrander, E.A., 2012. Variation of BMP3 contributes to dog breed skull diversity. *PLoS genetics* 8, e1002849.

Schowing, J., 1968. Influence inductrice de l'encéphale embryonnaire sur le développement du crâne chez le Poulet. *Journal of Embryology and Experimental Morphology* 19, 9-32.

Selleck, M.A., Bronner-Fraser, M., 1995. Origins of the avian neural crest: the role of neural plate-epidermal interactions. *Development* 121, 525-538.

Selleck, M.A., Bronner-Fraser, M., 1996. The genesis of avian neural crest cells: a classic embryonic induction. *Proc Natl Acad Sci U S A* 93, 9352-9357.

Seppala, M., Depew, M.J., Martinelli, D.C., Fan, C.M., Sharpe, P.T., Cobourne, M.T., 2007. Gas1 is a modifier for holoprosencephaly and genetically interacts with sonic hedgehog. *J Clin Invest* 117, 1575-1584.

Seppala, M., Xavier, G.M., Fan, C.M., Cobourne, M.T., 2014. Boc modifies the spectrum of holoprosencephaly in the absence of Gas1 function. *Biol Open* 3, 728-740.

Sheehan-Rooney, K., Swartz, M.E., Lovely, C.B., Dixon, M.J., Eberhart, J.K., 2013. Bmp and Shh signaling mediate the expression of satb2 in the pharyngeal arches. *PLoS One* 8, e59533.

Shellard, A., Mayor, R., 2016. Chemotaxis during neural crest migration. *Seminars in cell & developmental biology* 55, 111-118.

Shen, H., Wilke, T., Ashique, A.M., Narvey, M., Zerucha, T., Savino, E., Williams, T., Richman, J.M., 1997. Chicken transcription factor AP-2: cloning, expression and its role in outgrowth of facial prominences and limb buds. *Develop Biol* 188, 248-266.

Sheth, R., Marcon, L., Bastida, M.F., Junco, M., Quintana, L., Dahn, R., Kmita, M., Sharpe, J., Ros, M.A., 2012. *Hox* Genes Regulate Digit Patterning by Controlling the Wavelength of a Turing-Type Mechanism. *Science* 338, 1476-1480.

Shigetani, Y., Nobusada, Y., Kuratani, S., 2000. Ectodermally derived FGF8 defines the maxillomandibular region in the early chick embryo: epithelial-mesenchymal

interactions in the specification of the craniofacial ectomesenchyme. *Dev Biol* 228, 73-85.

Shigetani, Y., Sugahara, F., Kawakami, Y., Murakami, Y., Hirano, S., Kuratani, S., 2002. Heterotopic shift of epithelial-mesenchymal interactions in vertebrate jaw evolution. *Science* 296, 1316-1319.

Shimeld, S.M., van den Heuvel, M., Dawber, R., Briscoe, J., 2007. An amphioxus Gli gene reveals conservation of midline patterning and the evolution of hedgehog signalling diversity in chordates. *PLoS One* 2, e864.

Sick, S., Reinker, S., Timmer, J., Schlake, T., 2006. WNT and DKK Determine Hair Follicle Spacing Through a Reaction-Diffusion Mechanism. *Science* 314, 1447-1450.

Small, S., Kraut, R., Hoey, T., Warrior, R., Levine, M., 1991. Transcriptional regulation of a pair-rule stripe in *Drosophila*. *Genes Dev* 5, 827-839.

Smith, F.J., Percival, C.J., Young, N.M., Hu, D., Schneider, R.A., Marcucio, R.S., Hallgrímsson, B., 2015. Divergence of craniofacial developmental trajectories among avian embryos. *Dev Dyn*.

Smith, J.L., Schoenwolf, G.C., 1987. Cell cycle and neuroepithelial cell shape during bending of the chick neural plate. *Anat Rec* 218, 196-206.

Smith, K.K., Schneider, R.A., 1998. Have Gene Knockouts Caused Evolutionary Reversals in the Mammalian First Arch? *BioEssays* 20, 245-255.

Smith, L., Thorogood, P., 1983. Transfilter studies on the mechanism of epithelio-mesenchymal interaction leading to chondrogenic differentiation of neural crest cells. *Journal of Embryology and Experimental Morphology* 75, 165-188.

Smith, M.M., Hall, B.K., 1993. A Development Model for Evolution of the Vertebrate Exoskeleton and Teeth: The Role of Cranial and Trunk Neural Crest, in: Max, H.K. (Ed.), *Evolutionary Biology*. Plenum Press, New York, pp. 387-449.

Solem, R.C., Eames, B.F., Tokita, M., Schneider, R.A., 2011. Mesenchymal and mechanical mechanisms of secondary cartilage induction. *Dev Biol* 356, 28-39.

Solnica-Krezel, L., Sepich, D., 2012. Gastrulation: making and shaping germ layers. *Annu Rev Cell Dev Biol* 28, 687-717.

Song, Y., Hui, J.N., Fu, K.K., Richman, J.M., 2004. Control of retinoic acid synthesis and FGF expression in the nasal pit is required to pattern the craniofacial skeleton. *Dev Biol* 276, 313-329.

- Sosa, J.M., Huber, D.E., Welk, B., Fraser, H.L., 2014. Development and application of MIPAR™: a novel software package for two- and three-dimensional microstructural characterization. *Integrating Materials and Manufacturing Innovation* 3, 123-140.
- Spemann, H., 1938. *Embryonic development and induction*. Yale University Press, New Haven.
- Spemann, H., Mangold, H., 1924. Induction of embryonic primordia by implantation of organizers from a different species. Hafner, New York.
- Starck, J.M., Ricklefs, R.E., 1998. *Avian growth and development : evolution within the altricial-precocial spectrum*. Oxford University Press, New York.
- Stern, D.L., Emlen, D.J., 1999. The developmental basis for allometry in insects. *Development* 126, 1091-1101.
- Stoeckli, E.T., 2006. Production of dsRNA for RNAi in avian embryos. *Cold Spring Harbor Protocols* 2006, pdb. prot4503.
- Strickland, L., 2005. How Modern Was Leibniz's Biology? *Studia Leibnitiana* 37, 186-207.
- Szabo-Rogers, H.L., Geetha-Loganathan, P., Nimmagadda, S., Fu, K.K., Richman, J.M., 2008. FGF signals from the nasal pit are necessary for normal facial morphogenesis. *Dev Biol* 318, 289-302.
- Talbot, J.C., Johnson, S.L., Kimmel, C.B., 2010. *hand2* and *Dlx* genes specify dorsal, intermediate and ventral domains within zebrafish pharyngeal arches. *Development* 137, 2507-2517.
- Tenzen, T., Allen, B.L., Cole, F., Kang, J.S., Krauss, R.S., McMahon, A.P., 2006. The cell surface membrane proteins *Cdo* and *Boc* are components and targets of the Hedgehog signaling pathway and feedback network in mice. *Developmental cell* 10, 647-656.
- Theveneau, E., Mayor, R., 2012. Neural crest delamination and migration: from epithelium-to-mesenchyme transition to collective cell migration. *Dev Biol* 366, 34-54.
- Thompson, D.W., 1917. *On growth and form*. University press, Cambridge [Eng.].
- Thorogood, P., 1983. Morphogenesis of Cartilage, in: Hall, B.K. (Ed.), *Cartilage*. Academic Press, Inc., New York, pp. 223-253.

Thorogood, P., 1987. Mechanisms of morphogenetic specification in skull development, in: J.R. Wolff, J.S.M.B. (Ed.), *Mesenchymal-Epithelial Interactions in Neural Development*. Springer-Verlag, Berlin, pp. 141-152.

Thorogood, P., Bee, J., Mark, K.v.d., 1986. Transient expression of collagen type II at epitheliomesenchymal interfaces during morphogenesis of the cartilaginous neurocranium. *Develop Biol* 116, 497-509.

Tokita, M., Schneider, R.A., 2009. Developmental origins of species-specific muscle pattern. *Dev Biol* 331, 311-325.

Tosney, K.W., 1982. The segregation and early migration of cranial neural crest cells in the avian embryo. *Develop Biol* 89, 13-24.

Tostevin, F., ten Wolde, P.R., Howard, M., 2007. Fundamental limits to position determination by concentration gradients. *PLoS Comput Biol* 3, e78.

Trainor, P.A., Krumlauf, R., 2000. Patterning the cranial neural crest: hindbrain segmentation and Hox gene plasticity. *Nat Rev Neurosci* 1, 116-124.

Trainor, P.A., Krumlauf, R., 2001. Hox genes, neural crest cells and branchial arch patterning. *Curr Opin Cell Biol* 13, 698-705.

Trainor, P.A., Sobieszczuk, D., Wilkinson, D., Krumlauf, R., 2002. Signalling between the hindbrain and paraxial tissues dictates neural crest migration pathways. *Development* 129, 433-442.

Trainor, P.A., Tam, P.P., 1995. Cranial paraxial mesoderm and neural crest cells of the mouse embryo: co-distribution in the craniofacial mesenchyme but distinct segregation in branchial arches. *Development* 121, 2569-2582.

Trainor, P.A., Tan, S.S., Tam, P.P., 1994. Cranial paraxial mesoderm: regionalisation of cell fate and impact on craniofacial development in mouse embryos. *Development* 120, 2397-2408.

Tucker, A.S., Lumsden, A., 2004. Neural crest cells provide species-specific patterning information in the developing branchial skeleton. *Evol Dev* 6, 32-40.

Turing, A.M., 1952. The Chemical Basis of Morphogenesis. *Philosophical Transactions of the Royal Society of London. Series B, Biological Sciences* 237, 37-72.

Tyler, M.S., 1978. Epithelial influences on membrane bone formation in the maxilla of the embryonic chick. *Anatomical Record* 192, 225-233.

Tyler, M.S., 1983. Development of the frontal bone and cranial meninges in the embryonic chick: an experimental study of tissue interactions. *Anatomical Record* 206, 61-70.

Tyler, M.S., Hall, B.K., 1977. Epithelial influences on skeletogenesis in the mandible of the embryonic chick. *Anatomical Record* 188.

Untergasser, A., Cutcutache, I., Koressaar, T., Ye, J., Faircloth, B.C., Remm, M., Rozen, S.G., 2012. Primer3--new capabilities and interfaces. *Nucleic Acids Res* 40, e115.

Uygur, A., Young, J., Huycke, T.R., Koska, M., Briscoe, J., Tabin, C.J., 2016. Scaling Pattern to Variations in Size during Development of the Vertebrate Neural Tube. *Developmental cell* 37, 127-135.

Venters, S.J., Hultner, M.L., Ordahl, C.P., 2008. Somite cell cycle analysis using somite-staging to measure intrinsic developmental time. *Dev Dyn* 237, 377-392.

von Bonin, G., 1937. Brain-Weight and Body-Weight of Mammals. *Journal of General Psychology* 16, 379-389.

Waddington, C.H., 1940. *Organisers & genes*. University Press, Cambridge Eng.

Waddington, C.H., 1942. CANALIZATION OF DEVELOPMENT AND THE INHERITANCE OF ACQUIRED CHARACTERS. *Nature* 150, 563-565.

Waddington, C.H., 1957. *The Strategy of the Genes: A Discussion of Some Aspects of Theoretical Biology*. George Allan Unwin, London.

Wagner, A., 2005. *Robustness and Evolvability in Living Systems*. Princeton University Press.

Wagner, G., 1959. Untersuchungen an Bombinator-Triton-Chimaeren. *Roux' Archiv für Entwicklungsmechanik der Organismen* 151, 136-158.

Watanabe, M., Kondo, S., 2015. Is pigment patterning in fish skin determined by the Turing mechanism? *Trends Genet* 31, 88-96.

Wilkinson, D.G., Bhatt, S., Cook, M., Boncinelli, E., Krumlauf, R., 1989. Segmental expression of Hox-2 homoeobox-containing genes in the developing mouse hindbrain. *Nature* 341, 405-409.

Wilson, C.W., Chuang, P.T., 2010. Mechanism and evolution of cytosolic Hedgehog signal transduction. *Development* 137, 2079-2094.

Wilson, J., Tucker, A.S., 2004. Fgf and Bmp signals repress the expression of Bapx1 in the mandibular mesenchyme and control the position of the developing jaw joint. *Dev Biol* 266, 138-150.

Wolpert, L., 1969. Positional information and the spatial pattern of cellular differentiation. *J Theor Biol* 25, 1-47.

Wolpert, L., 1996. One hundred years of positional information. *Trends Genet* 12, 359-364.

Woronowicz, K.C., Gline, S.E., Herfat, S.T., Fields, A.J., Schneider, R.A., 2018. FGF and TGFbeta signaling link form and function during jaw development and evolution. *Dev Biol* 444 Suppl 1, S219-S236.

Woronowicz, K.C., Schneider, R.A., 2019. Molecular and cellular mechanisms underlying the evolution of form and function in the amniote jaw. *EvoDevo* 10, 17.

Wu, P., Jiang, T.X., Shen, J.Y., Widelitz, R.B., Chuong, C.M., 2006. Morphoregulation of avian beaks: comparative mapping of growth zone activities and morphological evolution. *Dev Dyn* 235, 1400-1412.

Wu, P., Jiang, T.X., Suksaweang, S., Widelitz, R.B., Chuong, C.M., 2004. Molecular shaping of the beak. *Science* 305, 1465-1466.

Xavier, G.M., Seppala, M., Barrell, W., Birjandi, A.A., Geoghegan, F., Cobourne, M.T., 2016. Hedgehog receptor function during craniofacial development. *Dev Biol* 415, 198-215.

Xu, Q., Jamniczky, H., Hu, D., Green, R.M., Marcucio, R.S., Hallgrímsson, B., Mio, W., 2015. Correlations Between the Morphology of Sonic Hedgehog Expression Domains and Embryonic Craniofacial Shape. *Evol Biol* 42, 379-386.

Yamaguchi, M., Yoshimoto, E., Kondo, S., 2007. Pattern regulation in the stripe of zebrafish suggests an underlying dynamic and autonomous mechanism. *Proceedings of the National Academy of Sciences* 104, 4790-4793.

Yang, G., Zhu, L., Hou, N., Lan, Y., Wu, X.M., Zhou, B., Teng, Y., Yang, X., 2014a. Osteogenic fate of hypertrophic chondrocytes. *Cell Res* 24, 1266-1269.

Yang, L., Tsang, K.Y., Tang, H.C., Chan, D., Cheah, K.S., 2014b. Hypertrophic chondrocytes can become osteoblasts and osteocytes in endochondral bone formation. *Proc Natl Acad Sci U S A* 111, 12097-12102.

Ye, J., Coulouris, G., Zaretskaya, I., Cutcutache, I., Rozen, S., Madden, T.L., 2012. Primer-BLAST: a tool to design target-specific primers for polymerase chain reaction. *BMC Bioinformatics* 13, 134.

Yoshida, T., Vivatbutstiri, P., Morriss-Kay, G., Saga, Y., Iseki, S., 2008. Cell lineage in mammalian craniofacial mesenchyme. *Mech Dev* 125, 797-808.

Young, N.M., Chong, H.J., Hu, D., Hallgrímsson, B., Marcucio, R.S., 2010. Quantitative analyses link modulation of sonic hedgehog signaling to continuous variation in facial growth and shape. *Development* 137, 3405-3409.

Young, N.M., Hu, D., Lainoff, A.J., Smith, F.J., Diaz, R., Tucker, A.S., Trainor, P.A., Schneider, R.A., Hallgrímsson, B., Marcucio, R.S., 2014. Embryonic bauplans and the developmental origins of facial diversity and constraint. *Development* 141, 1059-1063.

Zacchei, A.M., 1961. The embryonic development of the Japanese quail (*Coturnix coturnix japonica*). *Arch. Ital. Anat. Embriol.* 66, 36-62.

Zallen, J.A., Wieschaus, E., 2004. Patterned gene expression directs bipolar planar polarity in *Drosophila*. *Developmental cell* 6, 343-355.

Zamorano, A., Mellström, B., Vergara, P., Naranjo, J.R., Segovia, J., 2004. Glial-specific retrovirally mediated gas1 gene expression induces glioma cell apoptosis and inhibits tumor growth in vivo. *Neurobiol Dis* 15, 483-491.

Zhang, L., Lander, A.D., Nie, Q., 2012. A reaction-diffusion mechanism influences cell lineage progression as a basis for formation, regeneration, and stability of intestinal crypts. *BMC Syst Biol* 6, 93.

Zhang, W., Hong, M., Bae, G.U., Kang, J.S., Krauss, R.S., 2011. Cdo modifies the holoprosencephaly spectrum of Cdo mutant mice. *Dis Model Mech* 4, 368-380.

Zhang, W., Kang, J.S., Cole, F., Yi, M.J., Krauss, R.S., 2006. Cdo functions at multiple points in the Sonic Hedgehog pathway, and Cdo-deficient mice accurately model human holoprosencephaly. *Developmental cell* 10, 657-665.

Zhou, X., von der Mark, K., Henry, S., Norton, W., Adams, H., de Crombrughe, B., 2014. Chondrocytes transdifferentiate into osteoblasts in endochondral bone during development, postnatal growth and fracture healing in mice. *PLoS genetics* 10, e1004820.

Zusi, R.L., 1993. Patterns of Diversity in the Avian Skull, in: Hanken, J., Hall, B.K. (Eds.), *The Skull*, First ed. University of Chicago Press, Chicago, pp. 391-437.

Appendix I: Additional methods

Introduction

This section includes additional techniques that I developed in order to image large cleared samples on an available light sheet microscope.

CUBIC clearing

Dissected mandibular primordia intended for volumetric analysis were cleared using CUBIC clearing protocol (*Gomez-Gaviro et al., 2017*). The original protocol was modified, and steps for sample processing were following:

Day 1

Samples were re-hydrated by incubating for 5 minutes at room temperature in 75 %, 50 %, and 25 % methanol in 1x PBS, made from 10X RNase-free stock solution (cat. No. BP3991, Fisher Scientific, Hanover Park, IL, USA) and two times for 10 minutes in 1x PBS.

Cubic reagent 1 (CR1) was prepared as described in *Gómez-Gaviro et al.* using MilliQ (cat. No. CDUFBI001, Emd Millipore Lab Water, MilliporeSigma, St. Louis, MO, USA) water, urea (cat. No. U15-500, Fisher Chemical, Fisher Scientific, Hanover Park, IL, USA), N N N 'N 'tetrakis(2-hydroxy-propyl)ethylenediamine (cat. No. 122262, Sigma-Aldrich, MilliporeSigma, St. Louis, MO, USA) and Triton X-100 (cat. No. BP151-500, Fisher Bioreagent, Fisher Scientific, Hanover Park, IL, USA). 1x PBS was removed and replaced with CR1 making sure that the CR1 volume was at least 20 times the sample volume. Samples were incubated in CR1 overnight at 37 °C on a rocker.

Day 2

CR1 was carefully removed and samples were washed twice for 10 minutes at room

temperature in 1x PBS. Samples were incubated for one hour at room temperature in DRAQ5™ (Lot# GR3335847-1 and GR3237708-1, cat No. ab108410, Abcam, Cambridge, MA, USA) diluted 1:1000 in 1x PBS. Next samples were washed twice for 10 minutes at room temperature in 1x PBS. Then samples were dehydrated by incubating for 20 minutes at room temperature in 20 % sucrose (cat. No. BP220-1, Fisher Bioreagent, Fisher Scientific, Hanover Park, IL, USA) solution in 1x PBS that was filter sterilized through 0.2 µm filter (cat. No. 568-0020, Thermo Scientific, Fisher Scientific, Hanover Park, IL, USA).

Cubic reagent 2 (CR2) was prepared as described in Gómez-Gavero *et al.* using MilliQ (cat. No. CDUFBI001, Emd Millipore Lab Water, MilliporeSigma, St. Louis, MO, USA) water, triethanolamine (cat. No. 421630025, Acros Organics, Fisher Scientific, Hanover Park, IL, USA), D-Sucrose (cat. No. BP220-1, Fisher Bioreagent, Fisher Scientific, Hanover Park, IL, USA), and urea (cat. No. U15-500, Fisher Chemical, Fisher Scientific, Hanover Park, IL, USA). 20 % sucrose solution was removed and replaced with CR2 making sure that the CR2 volume was at least 20 times the sample volume. Samples were incubated in CR2 overnight at 37 °C on a rocker.

Day 3

Samples were embedded in 1 % low gelling temperature Agarose (cat. No. A4018, Sigma-Aldrich, MilliporeSigma, St. Louis, MO, USA). The agarose solution was made in 20 % sucrose and filter sterilized through 0.2 µm filter. Agarose was heated up to about 65 °C in a water bath to liquified and kept at about 40 °C during embedding. To embed samples, 5 x 5 x 4 millimeters mold was 3D printed, mold was positioned onto a glass microscope slide (cat. No. 1255015, Fisher Scientific, Hanover Park, IL, USA), mandibular primordia was transferred from CR2 using a glass Pasteur pipet (cat. No. 1367820C, Fisher Scientific, Hanover Park, IL, USA)

with as little CR2 as possible and positioned in the center of the mold aboral side facing up, and 5 drops of liquid agarose solution was pipetted into the mold. Sample was covered with aluminum foil and kept at room temperature for 5 minutes (i.e., until the agarose is mostly solidified). Then the mold containing the sample was carefully flipped and one extra drop of liquid agarose was added onto the oral side of the mandibular primordia and left at room temperature covered in dark for another 5 minutes. Embedded sample was then carefully transferred back into the tube containing CR2 and incubated for at least 15 hours at 35 °C. Samples embedded in agarose in CR2 can be kept in dark at room temperature for at least 3 weeks before imaging.

Cleared sample embedded in agarose was loaded into 3D printed sample holder and imaged on a custom build SPIM microscope or sample in agarose was transferred into a 15 mm sylgard bottom Petri dish and imaged using Nikon AZ100 Laser Scanning Macro Confocal Microscope.

It is important to prepare CR1 and CR2 ahead of time to ensure proper dissolving of solid chemicals as well as limit the amount of air bubbles in solutions.

Imaging – Selective Plane Illumination Microscope

Cleared mandibular primordia embedded in cleared agarose matrix (prepared and processed as described) were imaged using a Selective Plane Illumination Microscope (SPIM). The SPIM is designed to rapidly collect 3D volumes of cleared samples. It uses a galvo mirror (ThorLabs, Newton, NJ, USA) to create a thin light sheet from a Gaussian beam. A beam splitter allows dual-sided illumination of the sample to reduce scattering artifacts. The lasers are guided by a series of mirrors and lenses through an Olympus Plan N 4x/0.10 objective to the sample. Hardware includes 3-visible laser lines: 488 nm, 561 nm, 642 nm (Vortran VersaLase™, Vortran

Laser Technology, Roseville, CA, USA) with 525/45 nm, 609/54 nm, and 680/42 nm emission bandpass filters (Semrock, IDEX Health & Science, Rochester, NY, USA), an OrcaFlash 4.0 camera (cat. No. C11440-22CU, Hamamatsu photonics K.K, Hamamatsu City, Japan), a multi-micromanipulator system (model MPC-200, Sutter Instrument Co., Novato, CA, USA) used as a 3-axis stage, and an Olympus UMPlanFL N 20x/0.5 W objective (Olympus corporation, San Jose, CA, USA).

Micro-Magellan, a μ Manager plugin (<https://micro-manager.org/wiki/MicroMagellan>), was used for device control and image acquisition. Explore acquisitions were used for sample navigation in XY and Z to quickly build a 3D map of the sample with minimal photobleaching. The "Surfaces" feature allowed us to define non-cuboidal regions of interest for sample acquisition. Sample volumes were imaged with 200 – 500 ms exposure times and 1-2 μ m step size. ImaRiCumpiler, a FIJI plugin utility was used to compile Micro-Magellan data and convert it to Imaris files for further analysis. Both, Micro-Magellan and ImaRiCumpiler software are freely available to download from GitHub and necessary information for installation is available on the BIDC (Biological Imaging Development CoLab) website in the code repository (<https://bidc.ucsf.edu/code-repository>).

Appendix II: Other publications

METHODS & TECHNIQUES

Stable integration of an optimized inducible promoter system enables spatiotemporal control of gene expression throughout avian development

Daniel Chu, An Nguyen*, Spenser S. Smith*, Zuzana Vavrušová* and Richard A. Schneider[‡]

ABSTRACT

Precisely altering gene expression is critical for understanding molecular processes of embryogenesis. Although some tools exist for transgene misexpression in developing chick embryos, we have refined and advanced them by simplifying and optimizing constructs for spatiotemporal control. To maintain expression over the entire course of embryonic development we use an enhanced *piggyBac* transposon system that efficiently integrates sequences into the host genome. We also incorporate a DNA targeting sequence to direct plasmid translocation into the nucleus and a D4Z4 insulator sequence to prevent epigenetic silencing. We designed these constructs to minimize their size and maximize cellular uptake, and to simplify usage by placing all of the integrating sequences on a single plasmid. Following electroporation of stage HH8.5 embryos, our tetracycline-inducible promoter construct produces robust transgene expression in the presence of doxycycline at any point during embryonic development *in ovo* or in culture. Moreover, expression levels can be modulated by titrating doxycycline concentrations and spatial control can be achieved using beads or gels. Thus, we have generated a novel, sensitive, tunable, and stable inducible-promoter system for high-resolution gene manipulation *in vivo*.

KEY WORDS: Gene expression, *PiggyBac* transposon, Tet-inducible, Avian embryos

INTRODUCTION

For thousands of years, birds have been used to study development. The ability to ‘window’ and reseal the egg shell, the comparatively large size of the embryo, the straightforward process of stage-matching diverse embryos, the ease of starting and arresting embryogenesis at any time, and the commercial availability of fertilized eggs have significantly advanced the utilization of birds for a broad range of experiments (Stern, 2005; Jheon and Schneider, 2009). Birds remain particularly applicable for questions that are best answered through microsurgical manipulations (e.g. tissue recombination, transplants, ablation, or extirpations), cell labeling and live imaging (e.g. fluorescent dyes and other agents, *ex ovo*

culture, or immunochemical detection of engrafted cells), gain- and loss-of-function strategies (e.g. implantation of reagent-soaked beads, insertion of cell pellets, injection of biochemicals, infection with retroviruses, or electroporation of constructs) and other experimental approaches (Johnston, 1966; Noden, 1975; Serbedzija et al., 1989; Fekete and Cepko, 1993b; Stocker et al., 1993; Bronner-Fraser, 1996; Chen et al., 1999; Kulesa and Fraser, 2000; Larsen et al., 2001; Nakamura and Funahashi, 2001; Schneider et al., 2001; Garcia-Castro et al., 2002; Trainor et al., 2002; Cerny et al., 2004; Krull, 2004; Lwigale et al., 2004; Lwigale et al., 2005; Schneider, 2007; Bronner-Fraser and Garcia-Castro, 2008; Lwigale and Schneider, 2008; Sauka-Spengler and Barenbaum, 2008; Fish and Schneider, 2014; Fish et al., 2014; Ealba et al., 2015; Woronowicz et al., 2018). Overall, such strategies have been indispensable to understanding numerous dynamic aspects of development including cell fate decisions, tissue interactions, pattern formation, morphogenesis, and gene function and regulatory networks (Le Douarin and McLaren, 1984; Noden, 1984; Le Douarin et al., 1996; Clarke and Tickle, 1999; Schneider, 1999; Eames and Schneider, 2005; Noden and Schneider, 2006; Sauka-Spengler and Bronner-Fraser, 2008; Tokita and Schneider, 2009; Betancur et al., 2010; Le Douarin and Dieterlen-Lièvre, 2013; Martik and Bronner, 2017; Abramyan and Richman, 2018; Schneider, 2018; Gammill et al., 2019; Núñez-León et al., 2019).

However, there are limitations to what can be done with avian embryos. For example, compared to mouse or zebrafish model systems, birds have limited genetic tools, transgenic lines are expensive to maintain, and targeted mutagenesis followed by forward genetics is difficult. While some transgenic chick and quail lines have been generated (McGrew et al., 2004; Chapman et al., 2005; Koo et al., 2006; van de Lavoie et al., 2006a,b; Sato et al., 2010; Bower et al., 2011; Huss et al., 2015; June Byun et al., 2017; Tsujino et al., 2019), the technical challenges and expense of making transgenics, the low efficiency of transgene inheritance due to epigenetic silencing or selection against transgenic germ cells/gametes, combined with the logistics of keeping sufficient transgenic flocks has limited the broad application of this approach (Sang, 2006; Park et al., 2010; Macdonald et al., 2012; Liu et al., 2013; Bednarczyk et al., 2018). Nonetheless, the ability to create genetic mutations through CRISPR/Cas9 technology has already made the prospects of genome engineering much easier in avians (Ahn et al., 2017; Gandhi et al., 2017; Morin et al., 2017; Williams et al., 2018).

Given the challenges of germ line transgenesis, proxies for studying gene function in avian model systems have predominantly involved a range of alternative strategies. For example, transgenes can be delivered efficiently using retroviral vectors (Fekete and Cepko, 1993a; Morgan and Fekete, 1996; Logan and Tabin, 1998; Chen et al., 1999; Kardon et al., 2003; Hughes, 2004) especially the

Department of Orthopaedic Surgery, University of California at San Francisco, 513 Parnassus Avenue, S-1164, San Francisco, CA 94143-0514, USA.

*These authors contributed equally and are listed alphabetically

[‡]Author for correspondence (rich.schneider@ucsf.edu)

 R.A.S., 0000-0002-2626-3111

This is an Open Access article distributed under the terms of the Creative Commons Attribution License (<https://creativecommons.org/licenses/by/4.0>), which permits unrestricted use, distribution and reproduction in any medium provided that the original work is properly attributed.

Received 24 July 2020; Accepted 27 August 2020

replication-competent RCAS and RCASBP retroviruses. Some advantages of these vectors include their ability to spread widely throughout host tissues, which in turn allows for broad misexpression of a given transgene, and the ease at preparing large quantities of high-titer viral stocks (Logan and Tabin, 1998). But some limitations of retroviral vectors include the size of the gene insert that they can carry (up to approximately 2.4 kb), as well as their inability to infect most strains of chickens and other birds because of immunity arising from prior exposure to avian sarcoma-leukosis viruses (Hughes, 2004). A further drawback of retroviral-based strategies is their general lack of precise control over the timing, spatial domains, and levels of gene misexpression. Oftentimes, to achieve sufficient amounts of viral spread, infection must be performed at very early stages, which means that the transgene has to be expressed continuously throughout development regardless if there is a specific stage desired for expressing genes of interest.

Another approach for transiently misexpressing genes in a given location or for a certain period of time relies on electroporation of promoter-driven DNA constructs. Electroporation, which is very effective in avian embryos, involves placing electrodes to generate a pulsed electric field that transiently alters the plasma membrane and allows DNA constructs to be introduced into cells (Funahashi et al., 1999; Itasaki et al., 1999; Momose et al., 1999; Nakamura and Funahashi, 2001; Swartz et al., 2001; Chen et al., 2004; Krull, 2004; Simkin et al., 2014; Reberšek, 2017; McLennan and Kulesa, 2019). Electroporation is a very effective technique for introducing expression constructs into the premigratory cephalic NCM particularly by targeting the neural folds in stage HH8.5 embryos (Creuzet et al., 2002; Krull, 2004; McLennan and Kulesa, 2007; Hall et al., 2014). Several DNA constructs containing a robust chicken β -actin promoter, a CMV promoter, an internal ribosome entry site (IRES), and a bicistronic reporter with green fluorescent protein (GFP) have been widely adopted including pMES, pCIG, and pCA β (Swartz et al., 2001; Megason and McMahon, 2002; McLarren et al., 2003; Sauka-Spengler and Barembaum, 2008; Jhingory et al., 2010; Hall et al., 2014; Yang et al., 2014; Gammill et al., 2019; Wu and Taneyhill, 2019). Electroporation can also efficiently enable gene repression using RNA interference (RNAi) and antisense morpholino oligonucleotides (Tucker, 2001; Kos et al., 2003; Chesnutt and Niswander, 2004; Krull, 2004; Nakamura et al., 2004; Rao et al., 2004; Das et al., 2006; Sauka-Spengler and Barembaum, 2008; Gammill et al., 2019). However, due to the extrachromosomal nature of these vectors such treatments are only transient since plasmids and short oligonucleotides degrade and dilute following the proliferation of transfected cells, and misexpression is almost entirely eliminated by 72 to 96 h (Sauka-Spengler and Barembaum, 2008; Wang et al., 2011; Hall et al., 2014; Bourgeois et al., 2015). Moreover, the promoters in these widely used plasmids cannot be induced to control the timing or levels of gene expression. Thus, there has remained a need for highly versatile vectors that can achieve both long-term and conditional expression in avian embryos. To this end, one transgene expression system was created that uses *Tol2* transposon-mediated gene transfer (Koga et al., 1996) to enable stable integration of a given transgene into the avian genome (Kawakami, 2007), and that leverages a tetracycline (tet)-dependent inducible promoter (Sato et al., 2007; Watanabe et al., 2007; Takahashi et al., 2008). This system has been useful, for example, for studying the behavior and activity of neural crest mesenchyme (NCM) during later stages of embryogenesis (Yokota et al., 2011).

Building on the clear advantages of inducible promoter systems for exerting spatiotemporal control over gene expression and the

ability of transposable elements to integrate into the avian genome and facilitate long-term expression throughout development (Wang et al., 2011; Macdonald et al., 2012; Serralbo et al., 2013; Bourgeois et al., 2015), we endeavored to design a new gene delivery system that advances this technology. Our goal was to streamline and minimize the number of components, to optimize the delivery and detection features, and to achieve efficient and more robust transgene expression. To do so, we generated a constitutively active mNeonGreen (GFP) (Shaner et al., 2013) and doxycycline (dox)-inducible (Gossen et al., 1995; Loew et al., 2010; Heinz et al., 2011) mScarlet-I (RFP) (Bindels et al., 2017) construct. Then, to maintain expression of our electroporated constructs throughout embryonic development, we combined our dox-inducible system with an enhanced *piggyBac* transposon system, which allows for stable semi-random integration so that the construct is replicated along with the host genome (Lacoste et al., 2009; Lu et al., 2009; Yusa et al., 2011; Liu et al., 2013; Jordan et al., 2014; Yusa, 2015). We further improved this construct by adding a D4Z4 genetic insulator sequence to block transcriptional repression (Bire et al., 2013) and a DNA targeting sequence (DTS) to direct transport of the plasmids into the nucleus (Dean et al., 1999; Bai et al., 2017). We find that this construct is sensitive to induction by dox both *in ovo* and in culture, integrates stably into the genome of chick and duck, and enables expression in embryonic tissues at any desired time or place. Here we demonstrate for example, that presumptive NCM can be electroporated at embryonic stage (HH) 8.5 and then gene expression can be induced at HH15, HH30, or later. Also, we show that transgene expression levels can be modulated by titrating the concentration of dox, and precise spatial control over transgene activation can be achieved by implanting beads or gels that release dox locally. Thus, our optimized and integrating inducible-promoter system can control the timing, spatial domains, and levels of gene misexpression throughout avian development, which will be useful for a broad range of experimental contexts.

RESULTS AND DISCUSSION

Design of the small plasmid pNano

To maximize transfection and electroporation efficiency we aimed to generate plasmids as small as possible. Smaller plasmids have been shown to transfect and electroporate more efficiently than large plasmids (Yin et al., 2005). Moreover, large plasmids have been found to be toxic when introduced into cells independent of transgene expression from the plasmid (Lesueur et al., 2016). To minimize the size of our constructs we generated a new plasmid, pNano, only including a plasmid origin of replication and β -lactamase resistance (BlaR) sequence with a minimal multicloning site containing EcoRI, EcoRV, and XhoI restriction enzyme sites. The plasmid is 1562 bp (Fig. 1A) and serves as the backbone for the other constructs generated. To our knowledge, pNano is the smallest plasmid with BlaR selection.

Choosing a promoter

We chose the PGK1 promoter over other commonly used promoters due to its relatively small size at 500 bp and its consistent expression across different cell types (Qin et al., 2010; Huss et al., 2015). Moreover, the PGK1 promoter does not contain any viral sequences, which are prone to epigenetic silencing and loss of expression over time (Brooks et al., 2004; Xia et al., 2007; Normman et al., 2010).

Choosing a transposon

Transient transfections and electroporations with standard plasmids only enable transgene over-expression for up to 5 days, which is

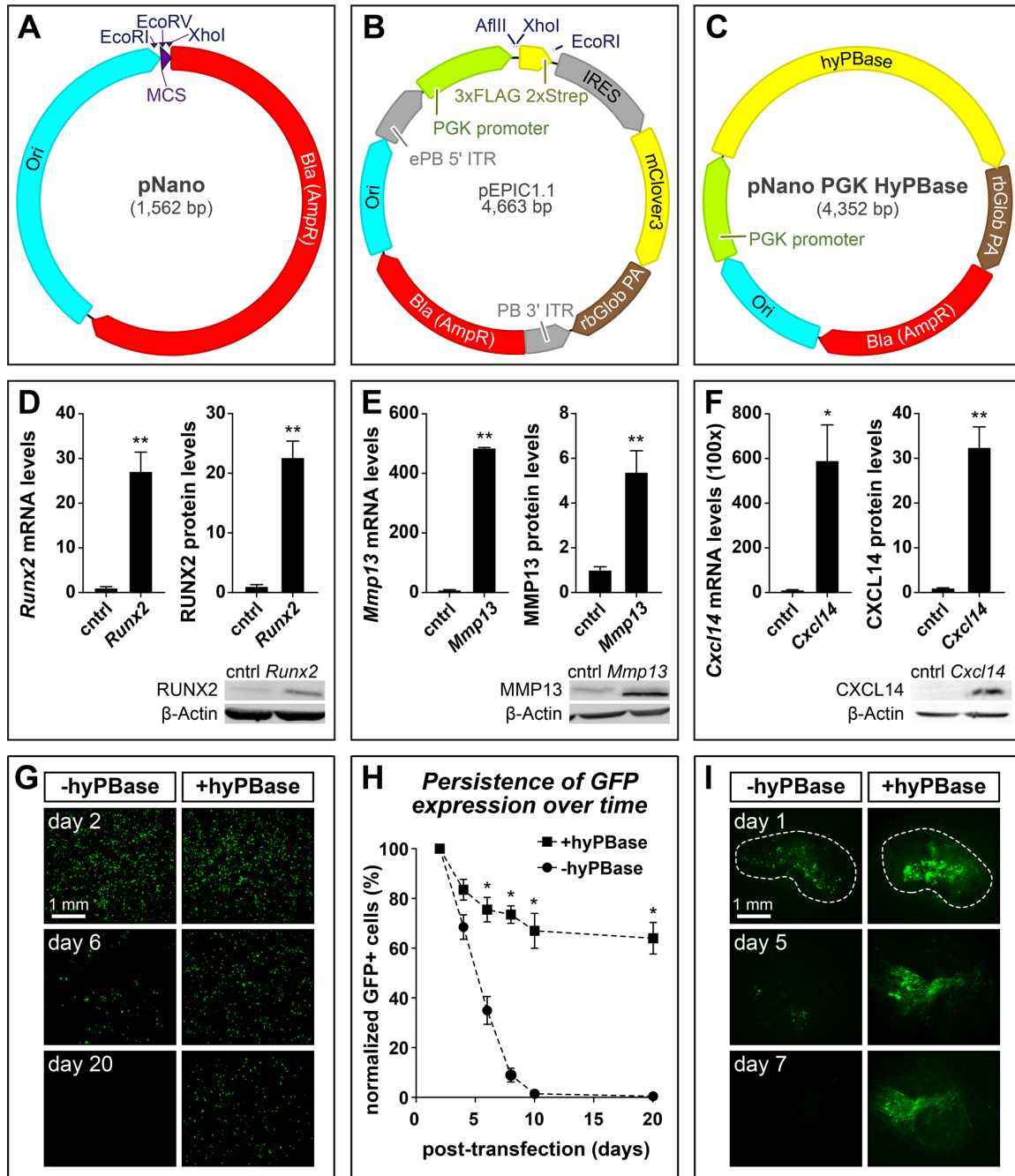


Fig. 1. See next page for legend.

much shorter than the time required to span *in ovo* development (e.g. 21 days for chick and 28 days for duck). To ensure stable and robust expression over the course of embryogenesis, we used a type II transposon (cut and paste) system to integrate sequences into the genome (Curcio and Derbyshire, 2003; Hickman et al., 2010; Yuan

and Wessler, 2011). Several transposable systems currently exist including *Tol2* (Koga et al., 1996; Kawakami, 2007), *Sleeping Beauty* (Ivics et al., 1997), and *piggyBac* (Fraser et al., 1983, 1996; Ding et al., 2005). We chose *piggyBac* because previously published work has demonstrated several advantages over other

Fig. 1. Plasmid maps and over-expression analyses. (A) Map of the pNano minimal cloning vector showing restriction sites for cloning, multicloning sites (MCS) in purple, bacterial origin of replication (Ori) in cyan, and bacterial β -lactamase (Bla) resistance gene (AmpR) in red. (B) Map of the pEPIC1.1 *piggyBac*-integrating constitutively-active expression vector showing *piggyBac* ITRs and IRES sequences in grey, PGK promoter sequences in green, terminator sequences in brown, and coding sequences in yellow. The pEPIC1.1 vector constitutively expresses mClover3, a GFP. (C) Map of the pNano-hyPBase expression vector used to integrate *piggyBac* sequences into host genome. (D) Over-expression of *Runx2*, (E) *Mmp13*, and (F) *Cxcl14* with pEPIC1.1. DF-1 cells were transfected with control (cntrl) empty pEPIC1.1 or pEPIC1.1 plus *Runx2*, *Mmp13*, or *Cxcl14* coding sequences and harvested 3 days post-transfection. Relative mRNA levels were measured by qPCR and normalized using 18S. Relative protein levels were measured by western blot (WB) and normalized using β -Actin. Representative WBs are shown below. There were four biological replicates for *Runx2* and *Mmp13*, and two for *Cxcl14*. (G) Fluorescent images showing a time course of DF-1 cells transfected with pEPIC1.1. Cells were transfected either without pNano-hyPBase (left column) or with (right column). Cells were passaged every 2 days and imaged at 2, 6, and 20 days post-transfection. (H) Quantification of GFP positive cells as a fraction of the total number of DF-1 cells transfected with pEPIC1.1 with or without pNano-hyPBase and normalized to 2 days post-transfection. There were two biological replicates for each group. (I) Fluorescent images showing a time course of HH21 chick mandibular primordia electroporated with pEPIC1.1-*Cxcl14* either without pNano-hyPBase (left column) or with (right column) cultured, and imaged at day 1, 5, and 7. All qPCR was performed in technical duplicate. A two-tailed *t*-test was used for all statistical analyses. Error bars represent standard error of the mean (s.e.m.). (* $P < 0.05$; ** $P < 0.005$).

transposon systems. Most importantly, *piggyBac* shows higher transposition activity than *Tol2* or *Sleeping Beauty* in human and chick (Wu et al., 2006; Lu et al., 2009; Huang et al., 2010) and there are improved versions of both the *piggyBac* transposon and transposase (Lacoste et al., 2009; Yusa et al., 2011). The efficiency of *piggyBac* integration is relatively size independent up to at least 10 kb (Ding et al., 2005) and *piggyBac* can deliver cargos in the hundreds of kb (Li et al., 2011; Rostovskaya et al., 2013), whereas *Sleeping Beauty* has reduced integration efficiency with cargo sizes above 5 kb (Geurts et al., 2003). *PiggyBac* integrates into genomes semi-randomly at sites of open chromatin while *Sleeping Beauty*'s integration pattern appears more random (Huang et al., 2010). In general, successful transposition events into silenced or heterochromatic regions may show no transgene expression due to epigenetic silencing. *PiggyBac* has lower rates of transgene silencing than *Sleeping Beauty* or *Tol2* (Meir and Wu, 2011) and for this reason, the *piggyBac* system can be adapted to enable the expression of transgenes of interest only when they integrate into the genome at a position permissive to transcription (Kumamoto et al., 2020). The *piggyBac* system is also relatively insensitive to the ratio of transposon to transposase while *Sleeping Beauty* and *Tol2* require titration to determine the optimal ratios (Meir et al., 2011). *PiggyBac* has consistent transposition activity across different cell lines (Wu et al., 2006) and has been utilized in many different organisms including yeast, mice, rats, humans, goat, pig, macaque, chick, rice, and several species of protists and insects (Yusa, 2015). This allows for the same construct to be used among different organisms compared to viral methods, which have species-specificity.

Generating the pEPIC1.1 construct for constitutive expression

To enable long-term constitutive transgene expression, we generated pEPIC1.1 (enhanced *piggyBac* IRES mClover3) (Fig. 1B). This construct drives transgene expression under the

constitutive PGK promoter. To improve translational efficiency, we included a Kozak sequence directly upstream of the translational start site (Kozak, 1986). As a marker for expression, we used a minimal encephalomyocarditis virus IRES (Bochkov and Palmenberg, 2006) to express a bicistronic transcript containing the over-expressed transgene and mClover3 (GFP) (Bajar et al., 2016). An optional C-terminal tandem affinity purification (TAP) tag consisting of 3xFLAG peptide sequences and 2xStrep-tag II sequences (Dalvai et al., 2015) can be added to enhance detection or pulldown. Sequences can be cloned either untagged by digesting pEPIC1.1 with AflIII and EcoRI or tagged by digesting with AflIII and XhoI. Sustained expression over long time periods is maintained by flanking the over-expression cassette with *piggyBac* inverted terminal repeat sequences (ITR). The ITRs in the presence of *piggyBac* transposase (PBase) semi-randomly integrates into the host genome at sequences containing a TAA motif through a cut and paste mechanism. We used the enhanced *piggyBac* sequence which contains two point mutations in the left '5' ITR that increase transposition efficiency (Lacoste et al., 2009). To express PBase we also generated a complementary plasmid, pNano-hyPBase (Fig. 1C). This plasmid expresses a hyperactive version of PBase (hyPBase) (Yusa et al., 2011) under the PGK promoter.

As a proof-of-concept and to test our ability to over-express a diverse range of gene types, we cloned coding sequences of a transcription factor (i.e. *Runx2*, 1419 bp), an extracellular matrix molecule (i.e. *Mmp13*, 1416 bp), and a cytokine (i.e. *Cxcl14*, 297 bp), into pEPIC1.1. We first confirmed that pEPIC1.1 constructs could over-express our genes of interest by transfecting them into a chick fibroblast cell line (DF-1). We found that pEPIC1.1-*Runx2*, pEPIC1.1-*Mmp13*, and pEPIC1.1-*Cxcl14* all induce strong over-expression compared to empty pEPIC1.1 (Fig. 1D–F). The pEPIC1.1-*Runx2* construct increased *Runx2* mRNA levels 27 \pm 4.3 times by qPCR ($P < 0.005$) and RUNX2 protein levels 23 \pm 2.7 times by WB compared to pEPIC1.1 ($P < 0.005$) (Fig. 1D). The pEPIC1.1-*Mmp13* construct increased *Mmp13* mRNA levels 480 \pm 2.4 times by qPCR ($P < 0.005$) and the MMP13 protein levels 5 \pm 0.96 times by WB compared to pEPIC1.1 ($P < 0.005$) (Fig. 1E). The pEPIC1.1-*Cxcl14* construct increased *Cxcl14* mRNA levels 59,000 \pm 16,000 times by qPCR ($P < 0.02$) and the CXCL14 protein levels 32 \pm 4.6 times by WB compared to pEPIC1.1 ($P < 0.005$) (Fig. 1F).

To confirm stable expression, we transfected DF-1 cells with pEPIC1.1 with or without pNano-hyPBase. Following transfection, cells were allowed to express GFP for 2 days to determine the baseline transfection efficiency. We then passaged the cells every 2 days for 20 days, to determine the stability of expression. We found that cells transfected without pNano-hyPBase rapidly lost GFP expression while those transfected with pNano-hyPBase initially had a small drop in GFP expression, which then stabilized over time. At 6 days post-transfection, cells with pNano-hyPBase retained higher levels of GFP expression compared to those without pNano-hyPBase (75% \pm 5 compared to 35% \pm 6, respectively, $P < 0.05$) (Fig. 1G,H). By day 20, 70% \pm 6 of cells transfected with pNano-hyPBase still expressed GFP, compared to <1% of cells without pNano-hyPBase.

We next confirmed that the pEPIC1.1 construct is functional at the tissue level. Mandibular primordia (i.e. 'mandibles') were dissected from HH24 chick embryos, injected with a plasmid solution containing pEPIC1.1-*Cxcl14* with or without hyPBase, and then electroporated. Mandibles were then cultured over 7 days. After 5 days of culture, mandibles electroporated with pNano-hyPBase retained strong GFP expression while mandibles without

pNano-hyPBase had greatly reduced expression compared to 1-day post-electroporation (Fig. 1I). After 7 days of culture mandibles electroporated without pNano-hyPBase had no detectable GFP expression.

Generating the pPID2 *piggyBac* cloning vector

To enhance the versatility of our *piggyBac* vectors we generated a general *piggyBac* cloning vector pPID2 (*piggyBac*, insulator, DTS) (Fig. 2A). pPID2 uses the pNano backbone to maintain a minimal vector footprint and contains the enhanced *piggyBac* mutations (Lacoste et al., 2009), a DTS, insulator sequence, and a multicloning site with over 20 restriction enzyme sites including HindIII, PstI, Sall, XhoI, EcoRI, PstI, NcoI, NgoMV, NheI, SpeI, MscI, and BglII, for ease of cloning.

When cells are transfected or electroporated with plasmids, transport from the cytoplasm to the nucleus is required for both expression and transposition into the genome. Plasmid entry into the nucleus generally occurs either during mitosis when the nuclear envelope breaks down, allowing for passive diffusion of plasmids into the nuclear space, or when the intracellular plasmid concentration is very high (10^4 – 10^6 molecules of plasmid DNA per cell) (Utvik et al., 1999; Young et al., 2003; Bai et al., 2017). To overcome potential nuclear import barriers, we added a DTS (Dean et al., 1999, 2005). A DTS functions by binding to transcription factors, which are then actively transported into the nucleus. We chose to use the simian virus 40 (SV40) 72 bp promoter DTS (Dean et al., 1999) because it can function in a wide variety of cell types (Dean, 1997; Young et al., 2003), is small, uses endogenously expressed transcription factors (Miller et al., 2009), and does not require expression of viral proteins (Dean et al., 2005). The DTS only directs plasmid entry into the nucleus and does not affect transgene localization. Alternatively, if nuclear entry is low even with a DTS, addition of trans-cyclohexane-1,2-diol reversibly increases the permeability of the nuclear pore complex allowing plasmids to diffuse into the nucleus (Vandenbroucke et al., 2007; De la Rossa and Jabaudon, 2015; Cervia et al., 2018).

Epigenetic and heterochromatic silencing of foreign DNA inserted into the host genome represent an obstacle for efficient transgene expression both at the time of insertion and over long-term expression (Garrison et al., 2007). Genomic insertions containing viral sequences are known to be actively silenced (Pannell and Ellis, 2001; Ellis, 2005; Wen et al., 2014; Hudecek et al., 2017). An insertion in a heterochromatic region or region that subsequently becomes heterochromatic may result in transgene inactivation (Janssen et al., 2018). To prevent this epigenetic silencing, we added a genetic insulator that blocks the spread of repressive epigenetic marks and heterochromatin (Ali et al., 2016). Moreover, insulator sequences help to protect endogenous sequences from epigenetic activation or silencing caused by the transposition (Hollister and Gaut, 2009). We used the D4Z4 insulator, which is only 65 bp and has been shown to efficiently protect *piggyBac* transgene expression (Ottaviani et al., 2009; Bire et al., 2013). pPID2 contains two D4Z4 insulator sequences contained within the *piggyBac* ITRs flanking the multicloning site (Fig. 2A).

Generating the pPIDNB doxycycline-inducible system

We also added a dox-inducible component to our over-expression constructs, which provides several advantages, including increased temporal control of expression. Without such precise temporal control, the premature and continuous expression of a gene of interest may disrupt development in ways that cause phenotypes

unrelated to the processes under study. A dox-based strategy has several advantages over other inducible systems in that dox is extremely cheap and effective at low concentrations. Additionally, dox is able to diffuse efficiently through tissues allowing for induction past the surface level (Agwuh and MacGowan, 2006; Sato et al., 2007) and the use of dox-soaked beads or gels can allow for spatial control of expression.

We generated the pPIDNB (*piggyBac*, insulator, DTS, mNeonGreen, bi-directional) construct as a minimal dox-inducible plasmid (Fig. 2B). This plasmid is based upon the pPID2 backbone and includes the DTS, insulator, and *piggyBac* sequences. In addition, pPIDNB constitutively expresses the reverse tetracycline (tet) transactivator (rtTA) and mNeonGreen (GFP) under the PGK promoter (Shaner et al., 2013). The rtTA and mNeonGreen coding sequences are bicistronic and are separated by a porcine teschovirus-1 2A (P2A) site, which causes them to be expressed as two different peptide sequences (Szymczak et al., 2004; Kim et al., 2011). When bound to dox, the rtTA undergoes a conformational shift allowing binding and activation of the bidirectional tet promoter (Gossen et al., 1995; Das et al., 2016). We chose to use the rtTA-V16 variant of rtTA, which is both sensitive to dox and can induce strong expression (Das et al., 2016). Because the rtTA-V16 variant is under a constitutively active PGK promoter and not autoregulated, varying levels of dox can have a graded effect on gene expression at the cellular level rather than simply modulate expression like a binary switch (Herr et al., 2011; Heinz et al., 2013; Roney et al., 2016). On one side of the bidirectional promoter is mScarlet-1 (RFP) serving as a marker for dox induction (Bindels et al., 2017). On the other side of the bidirectional promoter is the cloning site containing AflII and PstI sites for dox-inducible expression of the gene of interest. Combining both the rtTA and tet promoter into a single construct enables stable inducible-expression with one integrating plasmid and one transposase-expressing plasmid. Moreover, for experiments that would benefit from the ability to detect nuclear localization, we also generated pPIDNB2, which has histone H2B fused to GFP to label nuclei (Bourgeois et al., 2015), in contrast to the pPIDNB plasmid where GFP localization is diffuse throughout the cell (Fig. 2C).

To evaluate the sensitivity of the pPIDNB plasmid to induction by dox, we transfected DF-1 cells and performed a dose-response analysis with dox for 24 h. In the absence of dox, there was a very low basal level of RFP expression, with only 0.15%±0.2% of the GFP positive cells also expressing detectable levels of RFP expression (Fig. 2D,E). After treating cells with 2.5 ng/ml dox, 52%±1.1% of the GFP positive cells also expressed RFP. We found that the percent of RFP expressing cells as a fraction of the GFP positive cells maxed out at a dose of 10 ng/ml dox at 88%±2.7% with cells treated at 50 ng/ml and 250 ng/ml dox expressing RFP at 80%±2.7% and 84%±7.3%, respectively (Fig. 2E). While the fraction of cells expressing RFP did not increase at dox concentrations greater than 10 ng/ml, the intensity of RFP did increase with higher concentrations of dox (Fig. 2D).

We next tested the ability of pPIDNB to drive exogenous gene expression by cloning in the coding sequences for *Cxcl14*, *Gas1* (a plasma membrane receptor, 945 bp), *Rumx2*, and *Mmp13*. We first transfected DF-1 cells with pPIDNB-*Cxcl14*, treated with various doses of dox, and found that *Cxcl14* expression correlated with the concentration of dox (Fig. 2F). We found DF-1 cells treated with 2.5, 10, 50, and 250 ng/ml dox for 24 h increased *Cxcl14* mRNA expression by 27±6.4 ($P<0.05$), 96±23 ($P<0.05$), 149±34 ($P<0.05$), and 178±20 ($P<0.005$) times, respectively, compared to

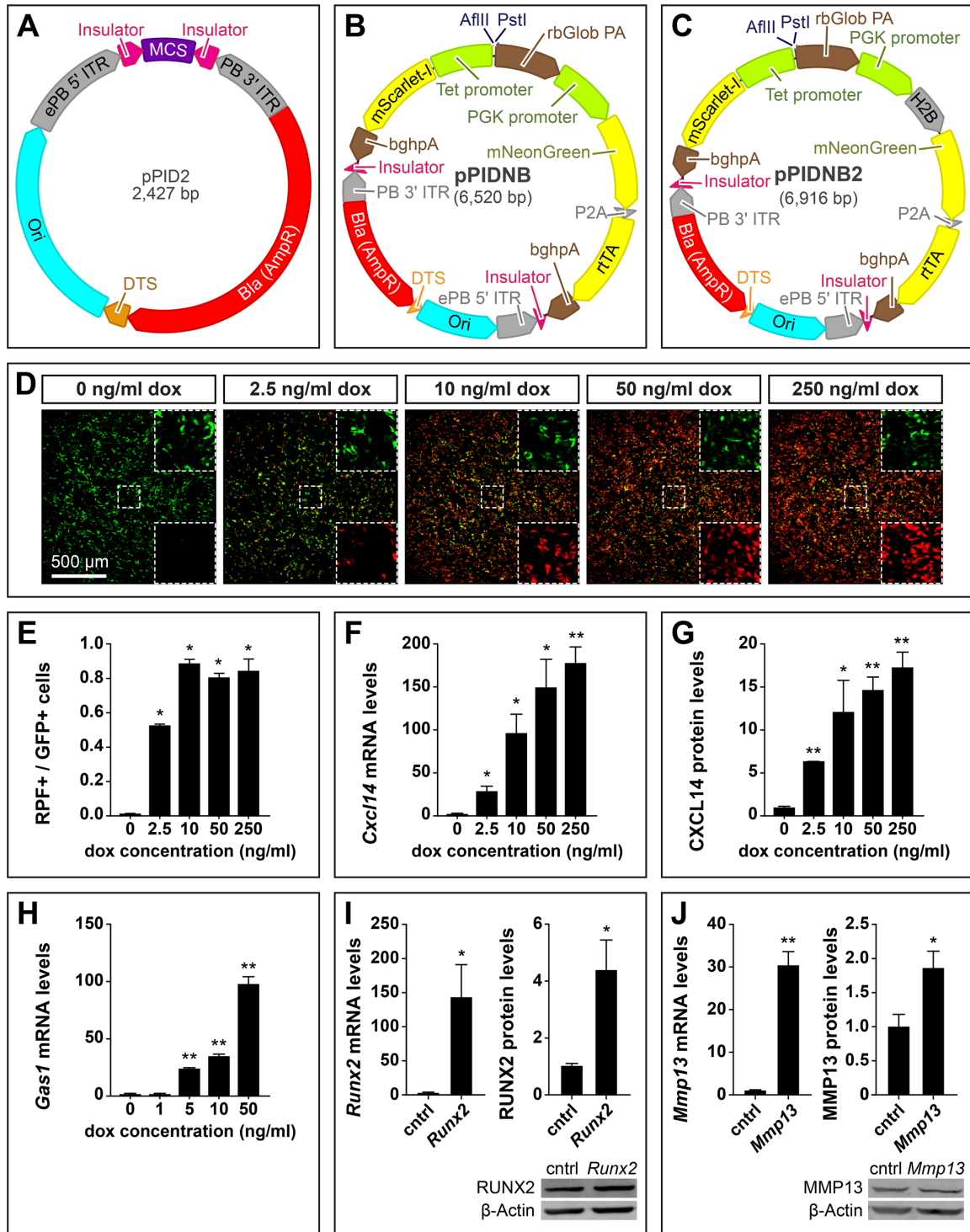


Fig. 2. See next page for legend.

Fig. 2. Maps of doxycycline (dox)-inducible plasmids and over-expression analyses. (A) Map of the pPID2 *piggyBac* cloning vector showing insulators (Ori) in magenta; a DTS in orange; MCS in purple; bacterial origin of replication (Ori) in cyan; bacterial β -lactamase (Bla) resistance gene (AmpR) in red; and *piggyBac* ITRs, IRES, and P2A sequences in grey. (B) Map of the pPIDNB *piggyBac* dox-inducible vector showing restriction sites for cloning, coding sequences in yellow, terminator sequences in brown, and promoter sequences in green. pPIDNB constitutively expresses mNeonGreen (GFP) and coding sequences can be cloned into the plasmid under a bidirectional tetracycline (tet) inducible promoter using the AflIII and PstI restriction sites. mScarlet-I, a red fluorescent protein (RFP), is expressed on the alternate side of the bidirectional tet promoter. (C) Map of the pPIDNB2 vector, which is identical to pPIDNB except that GFP is localized to the nucleus using histone H2B. (D) DF-1 cells transfected with pPIDNB constitutively express GFP and differentially express RFP in response to varying concentrations of dox after 24 h. Higher resolution split channel image insets of the center area outlined by dashed lines show the GFP channel (top right) and RFP channel (bottom right). (E) RFP-positive (i.e. dox-induced) cells relative to total number of GFP-positive (i.e. transfected) cells. There were two biological replicates for each group. (F) Dox induction was measured in DF-1 cells on the mRNA level. There are three biological replicates for each group. (G) Dox dose response of protein levels for *Cxcl14*. There are three biological replicates for each group except for the 2.5 ng/ml treatment, which has two biological replicates. (H) Dox dose response of *Gas1* mRNA. There were four biological replicates for each group. Levels are relative to 0 ng/ml of dox and normalized to 18S for mRNA and β -Actin for protein. (I) Over-expression of *Runx2* and (J) *Mmp13* with pPIDNB. DF-1 cells were transfected with control (cntrl) empty pPIDNB or pPIDNB plus *Runx2* or *Mmp13* coding sequence and treated with 50 ng/ml of dox for 24 h. mRNA levels were normalized using 18S and protein using β -Actin. Representative WBs are shown below. There were four biological replicates for each group. All qPCRs were performed in technical duplicate. A two-tailed *t*-test was used for all statistical analyses. When multiple comparisons were made, *P*-values were adjusted using the Holm–Bonferroni method. All bar graphs are shown as mean \pm s.e.m. (**P*<0.05; ***P*<0.005).

cells not treated with dox (Fig. 2F). WB analysis also showed a dose response with 2.5, 10, 50, and 250 ng/ml dox with CXCL14 protein levels increasing by 6.3 \pm 0.053 (*P*<0.005), 12 \pm 3.8 (*P*<0.05), 15 \pm 1.6 (*P*<0.005), and 17 \pm 1.9 (*P*<0.005) times, respectively, compared to cells not treated with dox (Fig. 2G). These results in conjunction with the RFP data above suggest that dox dose-response is effectively tunable per unit cell and not simply a binary threshold response to increased dox concentrations that causes more cells to express RFP. These observations are consistent with previously published work demonstrating that varying the concentration of dox can have a graded effect on gene expression at the cellular level (Herr et al., 2011; Heinz et al., 2013; Roney et al., 2016).

To determine if pPIDNB can stably integrate into the genome and express a transgene, we transfected DF-1 cells with pPIDNB-*Gas1* and pNano-hyPBBase. DF-1 cells were passaged over 4 weeks and then fluorescence-activated cell sorted (FACS) for GFP to confirm pPIDNB-*Gas1* could be stably integrated into the host genome and remain dox-inducible. We treated cells with dox and found that they were induced in a dose-response manner. After treating cells with 1, 5, 10, and 50 ng/ml dox for 24 h, *Gas1* mRNA expression increased by 1.1 \pm 0.16 (*P*>0.05), 23 \pm 0.99 (*P*<0.005), 34 \pm 2.7 (*P*<0.005), and 97 \pm 7.6 times (*P*<0.005), respectively, compared to cells not treated with dox (Fig. 2H). To confirm that pPIDNB can over-express different types of genes we also transfected DF-1 cells with either with empty pPIDNB, pPIDNB-*Runx2*, or pPIDNB-*Mmp13*. Transfected cells were treated with 50 ng/ml of dox for 24 h. The pPIDNB-*Runx2* and pPIDNB-*Mmp13* transfected cells expressed 140 \pm 47 (*P*<0.05) times more *Runx2* mRNA and 30 \pm 3.2 (*P*<0.005) times more *Mmp13* mRNA than cells transfected with empty

pPIDNB, respectively (Fig. 2I,J). WB analyses also showed over-expression with pPIDNB-*Runx2* and pPIDNB-*Mmp13* expressing 4.4 \pm 1.1 (*P*<0.05) and 1.9 \pm 0.25 (*P*<0.05) times more RUNX2 and MMP13 protein than pPIDNB alone, respectively.

Even though we found that 10 ng/ml of dox provides for high levels of induction, in order to achieve prolonged and robust gene expression in our subsequent long-term experiments, we decided to use 50 ng/ml dox. This higher concentration takes into account the half-life of dox, which is between 24–48 h in culture (based on estimates from the manufacturer), and our need to maintain gene expression for extended periods of time (like up to 10 days) without having to re-introduce additional dox, especially *in ovo*, so that we can minimize the number of times we handle samples.

Spatiotemporal control of expression in cell culture

To confirm that we could exert spatiotemporal control over transgene expression using pPIDNB, DF-1 cells were transfected with pNano-hyPBBase and either pPIDNB-*Gas1* or pPIDNB2-*Gas1*. Cells were passaged for 4 weeks and then sorted for GFP to generate stable lines with either pPIDNB-*Gas1* or pPIDNB2-*Gas1* integrated into their genomes. Cells with integrated pPIDNB-*Gas1* or pPIDNB2-*Gas1* were visualized by GFP. pPIDNB-*Gas1* cells showed GFP localized throughout the entire cell while pPIDNB2-*Gas1* showed nuclear localization of GFP (Fig. 3A,B). Cells were then treated with 50 ng/ml dox and imaged at 0, 6, and 12 h post-dox treatment. After 6 h of dox treatment, cells began to express detectable levels of RFP and by 12 h the RFP signal was robust.

To determine if we could control the spatial localization of transgene expression, we applied minocycline microspheres to DF-1 cells transfected with pPIDNB-*Gas1*. These microspheres slowly release minocycline, a tetracycline (dox) analog, and induce the tet expression system (Chtarto et al., 2003; Zhou et al., 2006). We applied minocycline microspheres directly to a localized area in the well and cells were imaged at 0, 6, and 12 h after treatment. After 6 h, we observed low levels of RFP expression, and after 12 h RFP expression levels were high in areas adjacent to the microspheres but not in areas further away (Fig. 3C).

For experiments that could benefit from the ability to monitor dynamic changes in the cell cycle, we added a DNA helicase B (DHB) cell cycle sensor sequence (Spencer et al., 2013; Kohrman et al., 2020) to the dox-inducible RFP of pPIDNB2. The DHB cell cycle sensor translocates to the nucleus at G0/G1. During S phase, DHB localizes to both the nucleus and the cytoplasm and during M-phase DHB primarily localizes to the cytoplasm. The nuclear localization of GFP in pPIDNB2 allows for the determination of how much of the DHB signal is nuclear versus cytoplasmic. We transfected DF-1 cells with pPIDNB2 DHB and treated them with 50 ng/ml of dox and imaged them after 12 h. We found that we could identify cells in different phases of the cell cycle with nuclear-localized DHB (G0/G1), nuclear- and cytoplasm-localized DHB (S phase), and cytoplasm localized DHB (M phase) (Fig. 3D).

Temporal and spatial control of gene expression during development

To exert spatiotemporal control over gene expression in embryonic tissues, we unilaterally electroporated the presumptive cephalic NCM of HH8.5 chick embryos with pPIDNB and pNano-hyPBBase. At HH10, we assayed for the extent of electroporation by visualizing GFP-positive cells *in ovo* in migrating NCM destined for the mandibular primordia (Fig. 4A). These embryos were then incubated until HH30, at which point the mandibular primordia

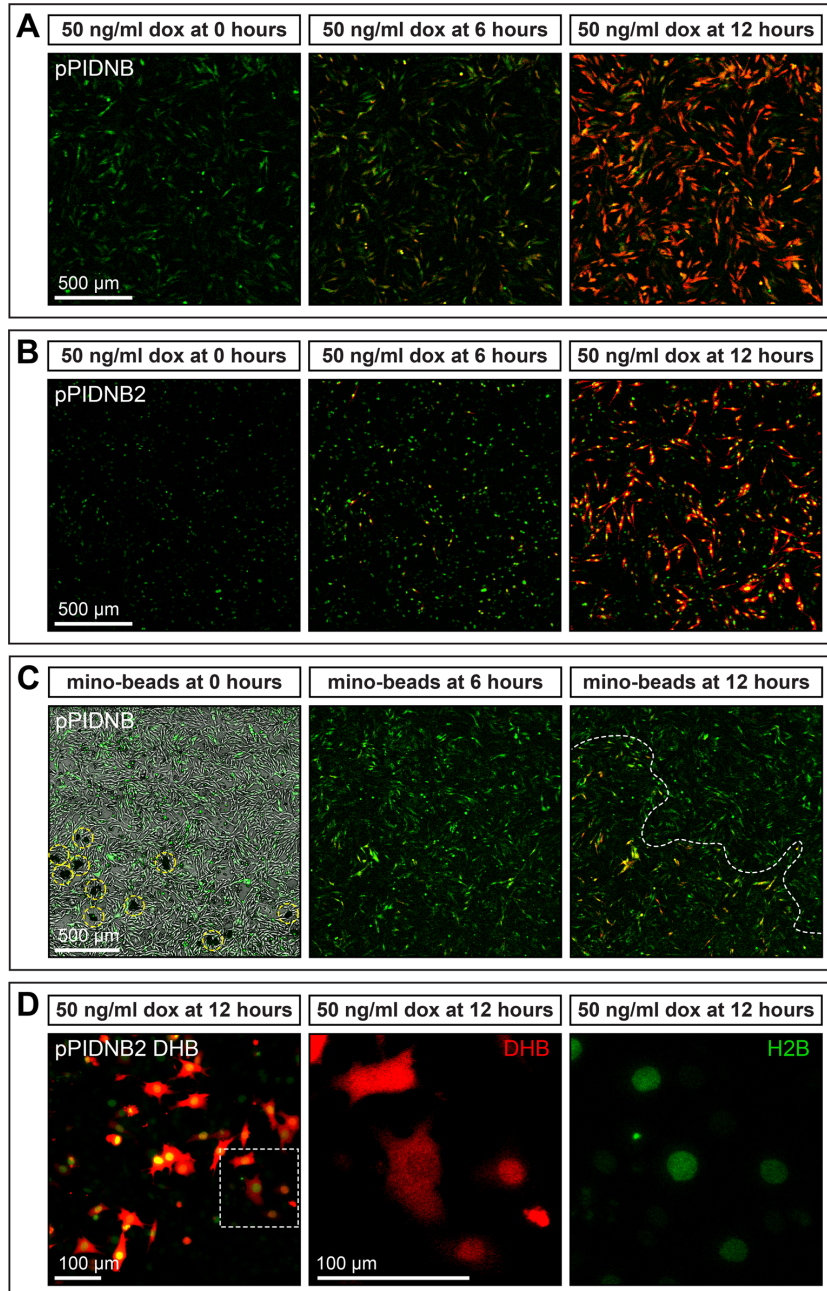


Fig. 3. *In vitro* induction of gene expression in cells. (A) DF-1 cells stably transfected with pPIDNB constitutively express mNeonGreen (GFP) and begin to express mScarlet-1 (RFP) over time in response to treatment with 50 ng/ml doxycycline (dox). Cells were imaged at 0, 6, and 12 h post-treatment. (B) DF-1 cells stably transfected with pPIDNB2 constitutively express GFP in the nucleus and begin to express RFP over time in response to treatment with 50 ng/ml dox. Cells were imaged at 0, 6, and 12 h post-treatment. (C) DF-1 cells transfected with pPIDNB constitutively express GFP and begin to express RFP over time in response to treatment with minocycline microspheres. Cells were imaged at 0, 6, and 12 h post-treatment. Microspheres are circled in yellow and a boundary between cells that are induced versus those that are not is indicated by a white dashed line. (D) DF-1 cells transfected with pPIDNB2 DHB (DNA Helicase B) constitutively express GFP in the nucleus and the DHB cell cycle sensor is tagged with RFP and induced in response to 50 ng/ml dox as seen at 12 h post-treatment. White-dashed inset box indicates cells shown at higher magnification where RFP marks DHB localization and GFP marks nuclei. DHB localization appears enriched in the nucleus, cytoplasm, or diffused throughout the cell.

were dissected out, cultured with 50 ng/ml of dox, and imaged at 0, 12, and 24 h post-treatment. As evidence of the stable genomic integration and induction of the plasmids in embryos, we observe the electroporated side of the mandible expressing GFP, with the contralateral side showing little to no GFP expression. After 12 h, treatment with dox results in strong RFP signal that is co-localized with GFP and this RFP expression intensifies further by 24 h (Fig. 4A; Movie 1).

Additionally, some duck embryos were bilaterally electroporated at HH8.5 with pPIDNB-*Gas1* and pNano-hyPBase and were treated with 50 ng/ml dox *in ovo* at HH15. By HH24, we observed RFP expression throughout the mandibular primordia (Fig. 4B). To confirm that *in ovo* dox treatment would work efficiently even during later stages of development, some chick embryos were unilaterally electroporated at HH8.5 with pPIDNB and pNano-hyPBase, incubated for 7 days, and then were treated *in ovo* with a

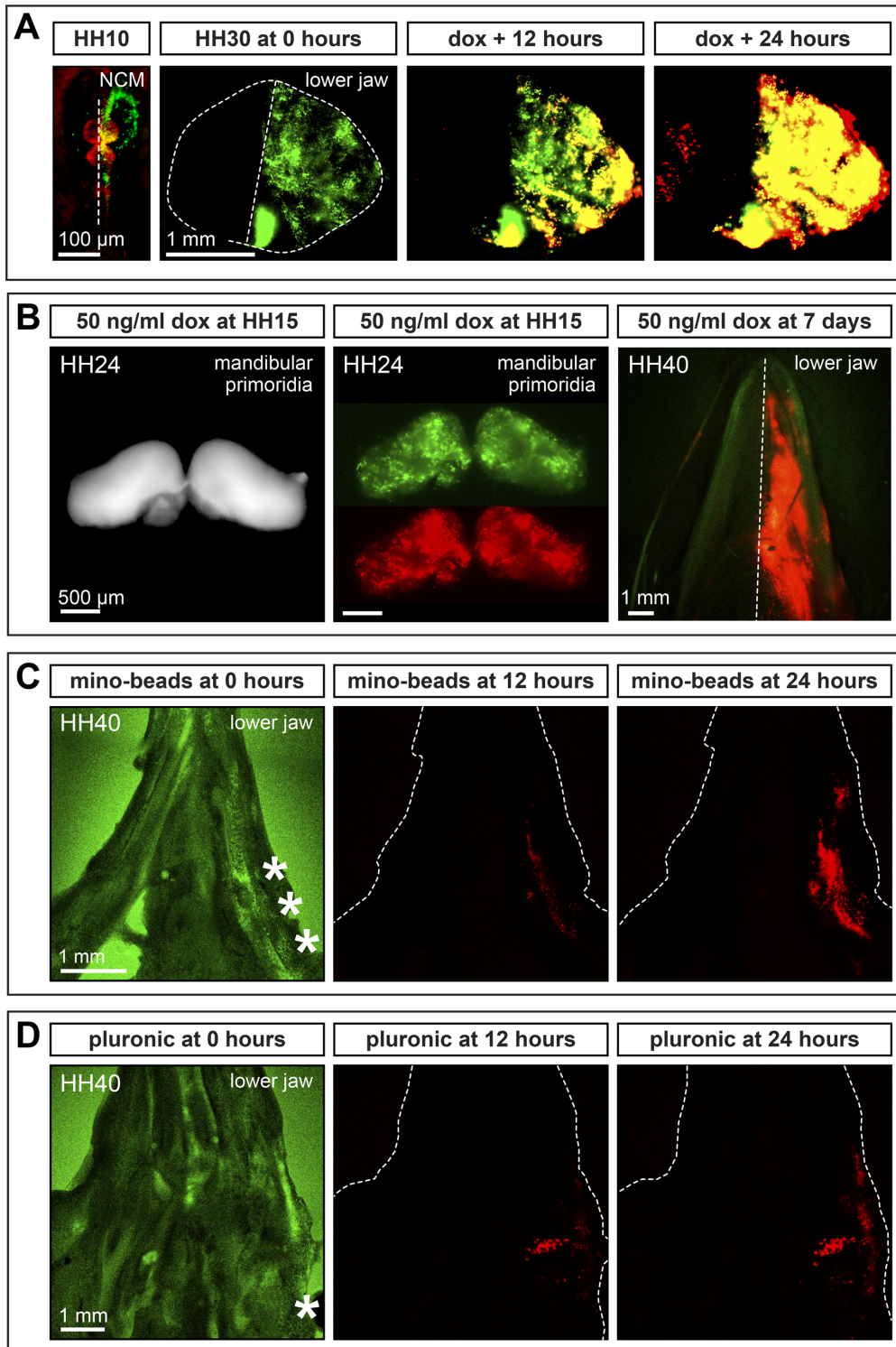


Fig. 4. See next page for legend.

Fig. 4. *In ovo* and *ex vivo* induction of gene expression in the lower jaw. (A) Presumptive cephalic NCM electroporated unilaterally with pPIDNB and pNano-hyPBase in a chick embryo at HH8.5 constitutively expresses mNeonGreen (GFP) as shown at HH10 (counterstained red with neutral red). At HH30, the lower jaw shows unilateral GFP expression in NCM-derived tissues. After 12 and 24 h in culture, NCM express mScarlet (RFP) in response to treatment with 50 ng/ml doxycycline (dox). (B) Presumptive NCM bilaterally electroporated with pPIDNB and pNano-hyPBase in a duck embryo at HH8.5 shows RFP expression on both sides of the lower jaw at HH24 (after bilateral electroporation) when treated *in ovo* with 50 ng/ml dox at HH15. Presumptive NCM bilaterally electroporated with pPIDNB and pNano-hyPBase in a chick embryo at HH8.5 shows RFP expression on one side of the lower jaw at HH40 (after unilateral electroporation) when treated *in ovo* with 50 ng/ml dox 7 days after electroporation and imaged 9 days after treatment. (C) Presumptive NCM electroporated bilaterally with pPIDNB-*Gas1* and pNano-hyPBase in a duck embryo at HH8.5 shows RFP expression in the lower jaw (white dashed area) 12 and 24 h after being injected in culture with minocycline microspheres at HH40 (white asterisks). (D) Presumptive NCM electroporated unilaterally with pPIDNB-*Gas1* and pNano-hyPBase in a duck embryo at HH8.5 shows RFP expression in the lower jaw 12 and 24 h after being treated at HH40 with 35% Pluronic F-127 gel containing 50 ng/ml dox (white asterisk). GFP and RFP channels shown at t=0. RFP channel shown for 12 and 24 h post-dox treatment. The margin of the lower jaw is represented by the white dashed line.

single dose of dox (50 ng/ml). These embryos were then allowed to develop for 9 more days (to around HH40), at which point we observed robust unilateral RFP expression in the lower jaw (Fig. 4B).

To exert more precise spatial control over gene expression, some embryos were bilaterally electroporated at HH8.5 with pPIDNB-*Gas1* and pNano-hyPBase and incubated until HH40. Their lower jaws were then harvested and either injected along the right side with minocycline microspheres or with dox gel (Pluronic F-127). Pluronic F-127 is a liquid at low temperatures (4°C) but solidifies at higher temperatures (37°C) and has been used for delivering drugs to different tissues (Harris et al., 2004; Giovagnoli et al., 2010). Whereas before treatment we observe GFP on both sides of the jaw, after 12 h of treatment with either minocycline microspheres or with dox gel, we observe RFP expression localized on the right side of the jaw, which becomes more elevated by 24 h (Fig. 4C,D).

Conclusion

In this study, we generated an ‘all-in-one’ *piggyBac* dox-inducible system. The pPIDNB plasmid is designed to be as small as possible to optimize cellular uptake while incorporating critical features to maximize its functionality. The DTS and insulator sequences serve to promote expression by directing nuclear entry of the plasmid and block heterochromatic silencing expression. We used mutated *piggyBac* and hyPBase sequences to increase genome integration efficiency. We have also incorporated a constitutively expressed GFP to mark cells that have taken in plasmid DNA and RFP to mark dox-induced cells. Our system facilitates precise temporal control of gene induction and is easily adapted for *in vitro* or *in ovo*. Spatial control of gene expression can be achieved by electroporating regions of interest and/or by applying beads or gels to localize the distribution of dox. This especially allows for electroporation of early avian embryos when ease of access and electroporation efficiency are highest. Embryos can then develop to their desired stage and the region of interest can be induced in a precise and rapid manner using dox-soaked beads or gel. Although we only tested induction in the lower jaw as a proof-of-concept, this same technique should be readily applicable to other accessible tissues in a developing avian embryo such as the limb buds, somites, neural tube, eyes, and heart.

The pPIDNB system is able to induce expression quickly and its reliance on a low dose of dox is important because dox has biological effects beyond antimicrobial activity including affecting matrix metalloproteinase activity, inflammation, the NF-κB pathway, and the nervous system (Bahrami et al., 2012; Alexander-Savino et al., 2016). High concentrations of dox (e.g. 1000 ng/ml) are cytotoxic in culture and have strong proliferative and metabolic effects, and some cell types are affected at even lower concentrations (e.g. 100–200 ng/ml) (Ermak et al., 2003; Ahler et al., 2013; Alexander-Savino et al., 2016). By using a low dose of dox (i.e. 50 ng/ml) we have likely minimized any off-target effects of dox treatment.

Based on the reasons described above, we were motivated to design the pPIDNB system even though other systems have been effective previously for achieving stable transgene expression in chick embryos. For example, *piggyBac* combined with heterologous promoters and *Cre/loxP* technology has enabled temporal control of transgene expression and cell-type-specific labeling in the neural tube (Lu et al., 2009). *Tol2*-based dox-inducible systems have also been generated (Sato et al., 2007; Watanabe et al., 2007; Takahashi et al., 2008) and applied to study NCM (Yokota et al., 2011). However, these systems require the integration of multiple plasmids in the same cell to function properly. While transposon integration is highly efficient, the likelihood of two or more different plasmids integrating is less than for a single plasmid. Our system only requires a single integrating plasmid, which both simplifies and improves the efficiency of electroporations. Another transposon-based integration method involves an ‘integration-coupled On’ (iOn) genetic switch, which has the advantage of being drug-free and limiting expression to productive transposition events (Kumamoto et al., 2020). However, in its current form the iOn system is not inducible at a given timepoint or location, which was a prerequisite for our experimental strategy. Specifically, for ongoing and future work, we want to electroporate NCM at HH8.5, perform transplants of electroporated NCM between quail and duck embryos at HH9.5, and then exert precise spatiotemporal control over transgene activation at HH34 or later by implanting beads that slowly and locally release dox. We imagine that equivalent approaches could be used to electroporate other avian tissues such as the somites for example at HH15 (Krull, 2004; Scaal et al., 2004; Pourquié, 2018), and then induce transgene expression in the developing limbs at any subsequent stage to investigate skeletal muscle patterning (Wang et al., 2011; Bourgeois et al., 2015).

While in the present study, we designed the pPIDNB construct for transgene over-expression, we envision that future applications will include different types of experiments such as gene knockdown using CRISPRi (Qi et al., 2013; Mandegar et al., 2016). For example, catalytically inactive *Cas9* could be placed with transcriptional repressors under an inducible tet promoter (Qi et al., 2013; Yeo et al., 2018). Constitutively active U6 promoters would drive expression of single guide RNAs (Cong et al., 2013; Gandhi et al., 2017; Williams et al., 2018). Using similar protocols for over-expression and knockdown would reduce the number of variables between experiments and help limit the confounding effects from different constructs. Overall, a great strength of avian model systems has been the combination of experimental embryology and modern genetic techniques. Our sensitive, stable, and robust inducible-promoter system builds on this strength and joins an arsenal of tools for manipulating gene expression in avians that will likely be useful to the broader community for addressing classic and current questions in developmental biology.

MATERIALS AND METHODS

Plasmids

To generate pNano, the Ori and BlaR from pJet1.2 (Thermo Fisher Scientific, Waltham, MA, USA, K1231) were amplified using Q5 Hot Start High-Fidelity DNA Polymerase (NEB, Ipswich, MA, USA, M0493L). Fragments were cloned together using NEBuilder HiFi DNA Assembly Master Mix (NEB, Ipswich, MA, USA, E2621L). EcoRI, XhoI, and EcoRV restriction enzyme sites were incorporated as tails added to the primers. To generate pEPIC1.1, the enhanced *piggyBac* ITRs, PGK promoter, 3× FLAG 2× Strep tag, IRES, mClover3, rabbit Beta globin terminator sequence, pNano were amplified by PCR using Q5 Hot Start High-Fidelity DNA Polymerase and cloned together using NEBuilder HiFi DNA Assembly Master Mix. The enhanced *piggyBac* ITRs were ordered as gBlocks (IDT, Coralville, IA, USA). The 3× FLAG 2× Strep tag sequence was amplified from AAVS1 Puro Tet3G 3× FLAG Twin Strep (Addgene, Watertown, MA, USA, 92099) (Dalvai et al., 2015). mClover3 sequence was amplified from pKancMV-mClover3-mRuby3 (Addgene, Watertown, MA, USA, 74252) (Bajar et al., 2016). To generate pNano-hyPBase, the PGK promoter, hyPBase, and rabbit β-Globin poly A sequences were amplified by PCR using Q5 Hot Start High-Fidelity DNA Polymerase and cloned together using NEBuilder HiFi DNA Assembly Master Mix. To generate pPID2, the SV40 72 bp DTS and two 65 bp insulator sequences flanking MCS were ordered as gBlocks (IDT, Coralville, IA, USA). The enhanced *piggyBac* ITRs, Ori, and BlaR were amplified using Q5 Hot Start High-Fidelity DNA Polymerase and cloned together with the DTS and insulator gBlocks using NEBuilder HiFi DNA Assembly Master Mix. To generate pPIDNB, the bovine growth hormone poly A, mScarlet-I, bi-directional tet promoter, rabbit β-Globin poly A, PGK promoter, mNeonGreen P2A, and rTA sequences were amplified by PCR using Q5 Hot Start High-Fidelity DNA Polymerase and then cloned together using NEBuilder HiFi DNA Assembly Master Mix. The bi-directional tet promoter and rTA sequences were amplified from AAVS1 Puro Tet3G 3xFLAG Twin Strep (Addgene, Watertown, MA, USA, 92099). The mScarlet-I sequence was amplified from pmScarlet-i_C1 (Addgene, Watertown, MA, USA, 85044) (Bindels et al., 2017). To generate pPIDNB2, H2B was amplified using Q5 Hot Start High-Fidelity DNA Polymerase and then cloned into pPIDNB with QuikChange (Liu and Naismith, 2008) using KOD Xtreme Hot Start DNA Polymerase (MilliporeSigma, Burlington, MA, USA, 71975-3). To generate pPIDNB2-DHB, DHB was ordered as a gBlock and cloned into pPIDNB2 digested with XhoI (NEB, Ipswich, MA, USA, R0146S) and NotI (NEB, Ipswich, MA, USA, R3189S).

RNA extractions

For *Runx2*, *Mmp13*, and *Cxcl14*, RNA was extracted from DF-1 cells and HH27 whole chick heads using the RNeasy Plus Kit (Qiagen, Hilden, Germany, 74136) following the manufacturer's directions. Whole heads and DF-1 cells were resuspended in 600 µl of RTL plus buffer supplemented with 1% β-mercaptoethanol. Homogenization was carried out in a Bead Mill 24 (Thermo Fisher Scientific, Waltham, MA, USA, 15-340-163) at 5 m/s for 30 s. Following purification of total RNA, residual genomic DNA was removed using TURBO DNA-free Kit (Invitrogen, Carlsbad, CA, USA, AM1907). For RNA extractions involving *Gas1*, the PicoPure RNA Isolation Kit (Applied Biosystems, Foster City, CA, USA, KIT0204) was used following the manufacturer's directions and homogenization was carried out in a Bead Mill 24 (Fisher Scientific Waltham, MA, USA, 15-340-163) at 4 m/s for 15 s.

Cloning coding sequences

Full length cDNA synthesis from RNA was carried out using Maxima H-reverse transcriptase (Thermo Fisher Scientific, Waltham, MA, USA, K1651) following the manufacturer's directions with 2 µg of total RNA and 100 pmol of d(T)20 VN primer. The cDNA synthesis reaction was carried out at 50°C for 30 min, 55°C for 10 min, 60°C for 10 min, 65°C for 10 min, and 85°C for 5 min. Full length *Runx2*, *Mmp13*, *Cxcl14*, and *Gas1* were amplified by PCR using Q5 Hot Start High-Fidelity DNA Polymerase (NEB, Ipswich, MA, USA, M0493L) and cloned using CloneJET PCR Cloning Kit (Thermo Fisher Scientific, Waltham, MA, USA, K1231). Following confirmation of cloning of full length coding sequences by Sanger

sequencing, *Runx2*, *Mmp13*, *Cxcl14*, and *Gas1* were cloned into pEPIC1.1 digested with AflII (NEB, Ipswich, MA, USA, R0520S) and EcoRI (NEB, Ipswich, MA, USA, R3101S) or pPIDNB digested with AflII (NEB, Ipswich, MA, USA, R0520S) and PstI (NEB, Ipswich, MA, USA, R3140S) using NEBuilder HiFi DNA Assembly Master Mix. All constructs were verified by Sanger sequencing and midprep for electroporation and transfection using PureLink Fast Low-Endotoxin Midi Kit (Invitrogen, Carlsbad, CA, USA, A36227).

Avian embryos and cell culture

Fertilized eggs of chicken (*Gallus gallus*) and duck (*Anas platyrhynchos*) were purchased from AA Lab Eggs (Westminster, CA, USA) and incubated at 37.5°C in a humidified chamber (GQF Hova-Bator, Savannah, GA, USA, 1588) until they reached embryonic stages appropriate for manipulation and/or analyses. For all experiments, we adhered to accepted practices for the humane treatment of avian embryos as described in S3.4.4 of the AVMA Guidelines for the Euthanasia of Animals: 2013 Edition (Leary et al., 2013). Embryos were matched at equivalent stages using the Hamburger and Hamilton (HH) staging system, a well-established standard which utilizes an approach based on external morphological characters and that is independent of body size and incubation time (Hamburger and Hamilton, 1951; Hamilton, 1965; Ricklefs and Starck, 1998; Starck and Ricklefs, 1998). For late embryonic stages, we relied primarily on growth of the limbs, facial primordia, feather buds, and eyes (Eames and Schneider, 2005, 2008; Merrill et al., 2008).

Embryonic chick fibroblasts (DF-1) were purchased (ATCC, Manassas, VA, USA, CRL-12203) and cultured in Dulbecco's Modified Eagle's Medium (DMEM, Corning, NY, USA, 10-013-CV) supplemented with 10% FBS (VWR, Radnor, PA, USA, 97068-085, Lot# 283K18) and 1× penicillin-streptomycin (Thermo Fisher Scientific, Waltham, MA, USA, 15140122) at 37°C with 5% CO₂. These cells were confirmed to be chicken cells via PCR and by sequencing *Runx2*. Cells were passaged twice a week and monitored for mycoplasma contamination every 4 weeks. Cells were transfected with lipofectamine 3000 (Thermo Fisher Scientific, Waltham, MA, USA, L3000008) according to the manufacturer's instructions. Transfections for integrating *piggyBac* vectors were carried out in six-well plates with 5 µg *piggyBac* plasmid, 5 µg of pNano-hyPBase, and 20 µl of P3000.

Electroporations

Electroporations were performed by injecting a solution of pEPIC1.1-Cxcl14 and pNano-hyPBase at 3 µg/µl and 1 µg/µl, respectively, with a small amount of Fast Green dye. DNA was injected with a Pneumatic PicoPump (World Precision Instruments, Sarasota County, FL, USA, PV830) into dissected HH21 mandibular primordia using thin wall borosilicate glass micropipettes (O.D. 1.0 mm, I.D. 0.75 mm, Sutter Instrument Company, Novato, CA, USA, B100-75-10) pulled on a micropipette puller (Sutter Instrument Company, Novato, CA, USA, P-97 Flaming/Brown). Mandibles were placed between two gold plate electrodes 0.5 cm apart submerged in Hanks' balanced salt solution (HBSS, Thermo Fisher Scientific, Waltham, MA, USA, 14170120). Electroporations were carried out by delivering five square pulses at 25 V for 50 ms spaced 500 ms apart (CUY21EDITII Next Generation Electroporator, BEX CO, Ltd). Mandibles were then cultured in BgJB medium (Thermo Fisher Scientific, Waltham, MA, USA, 12591038) supplemented with 10% FBS (VWR, Radnor, PA, USA, 97068-085, Lot# 283K18) and 1× penicillin-streptomycin (Thermo Fisher Scientific, Waltham, MA, USA, 15140122).

In ovo electroporations were performed using a solution of pPIDNB and pNano-hyPBase at 3 µg/µl and 1 µg/µl, respectively. With the addition of Fast Green tracer dye, DNA solution was injected into HH8.5 chick neural tubes with a Pneumatic PicoPump using thin wall borosilicate glass micropipettes pulled on a micropipette puller. Platinum electrodes were positioned on each side of the area pellucida, centered along the neural folds of the midbrain-hindbrain boundary as done previously to target the presumptive NCM destined for the mandibular arch (Creuzet et al., 2002; Krull, 2004; McLennan and Kulesa, 2007; Hall et al., 2014). For unilateral electroporations, we delivered three square pulses at 50 V for 1 ms spaced 50 ms apart followed by five square pulses at 10 V for 50 ms spaced 50 ms

apart. For bilateral electroporations, we delivered three square pulses at 50 V for 1 ms spaced 50 ms apart, three square pulses at 50 V for 1 ms spaced 50 ms apart in the reverse polarity, five square pulses at 10 V for 50 ms spaced 50 ms apart followed by, five square pulses at 10 V for 50 ms spaced 50 ms apart in the reverse polarity.

qPCR

DNase RNA was reverse-transcribed using iSCRIPT (Bio-Rad, Hercules, CA, USA, 1708841). Gene expression was quantified by qPCR with iQ SYBR Green Supermix (Bio-Rad, Hercules, CA, USA, 1708882) and normalized to 18S rRNA following previously published protocols (Dole et al., 2015; Smith et al., 2016). Primer sets were designed and optimized as described previously (Ealba and Schneider, 2013) and are listed in Table S1. Each sample was assayed in technical duplicate.

Western blot

DF-1 cells were lysed with 1× RIPA lysis buffer (MilliporeSigma, Burlington, MA, USA, 20-188) containing Halt protease inhibitors (Thermo Fisher Scientific, Waltham, MA, USA, 78430). A BCA assay (Thermo Fisher Scientific, Waltham, MA, USA, 23225) using a SpectraMax M5 plate reader (Molecular Devices, San Jose, CA, USA) was performed to quantify protein, and 40 µg protein was electrophoresed on a 10% SDS polyacrylamide gel following a published protocol (Smith et al., 2016). Proteins were transferred to an Immobilon-PVDF membrane (MilliporeSigma, Burlington, MA, USA, IPVH00010). Membranes were probed with rabbit anti-chick RUNX2 primary antibody (1:1000, Abcam Burlingame, CA, USA, #ab23981), custom made rabbit anti-chick MMP13 antibody (1 µg/ml, GenScript, Piscataway, NJ, USA), rabbit anti-CXCL14 (0.2 µg/ml, PeproTech, Rocky Hill, NJ, USA, 500-P237), mouse anti-chick β-actin antibody (1:4000, Novus Biologicals, Littleton, CO, USA, NB600-501), goat anti-rabbit IRDye 800CW (1:15000, LI-COR, Lincoln, NE, USA, 925-32211), and donkey anti-mouse IRDye 680RD antibody (1:15,000, LI-COR, Lincoln, NE, USA, 925-68072). Fluorescent signal was captured using the Odyssey Imaging System (Thermo Fisher Scientific, Waltham, MA, USA). Quantifications of protein bands were performed using Image Studio Lite. RUNX2, MMP13, and CXCL14 levels were normalized to β-actin.

Doxycycline treatment

Stock solutions of doxycycline hyclate (Acros Organics, Fair Lawn, NJ, USA, 446060250) were made to a final concentration of 1 mg/ml in water, filter sterilized, and stored at −20°C as single use aliquots. DF-1 cells and mandibles were treated in culture with the stock solution diluted in DMEM, with minocycline microspheres (Arrestin) added directly to each well, or by suspending microspheres in PBS and injecting them into the lower jaw with a 30-gauge needle. Pluronic F-127 (MilliporeSigma, Burlington, MA, USA, P2443-250G) was dissolved at a final concentration of 35% (w/v) in DMEM growth medium rocking at 4°C for 48 h. Dox was added to Pluronic F-127 for a final concentration of 500 ng/ml and injected into the lower jaw with an 18-gauge needle. For *in ovo* treatments, 2.5 µl (for chick) and 3.75 µl (for duck) of the 1 mg/ml dox stock solution was diluted with 750 µl of HBSS. This solution was then gently pipetted into the egg adjacent to the embryo and allowed to diffuse.

Imaging

DF-1 cells were imaged using a macroconfocal (Nikon, Minato City, Tokyo, Japan, AZ100 C2+). Time-lapse experiments were carried out in a custom-made stage top incubator (Okolab, Ambridge, PA, USA) set to 37°C, 95% humidity and 5% CO₂. All DF-1 experiments were carried out in six-well plates (Corning, Corning, NY, USA, 08-772-1B) with 2 ml of DMEM. Lower jaw time-lapse experiments were carried out on six-well transwell membranes (VWR, Radnor, PA, USA, 10769-192) with 2 ml of DMEM. Brightfield and fluorescent images of duck HH24 mandibular primordia were captured on an epifluorescent stereomicroscope (Leica, Wetzlar, Germany, MZFLIII).

Fluorescence-activated cell sorting (FACS)

DF-1 cells were washed with 2 ml of Trypsin followed by 3ml fresh wash. Trypsin activity was inhibited by adding 5 ml of DMEM with 10% FBS.

Cells were pipetted and passed through 70 µm filter. Cells were sorted on FACSAriaII Flow Cytometer (BD Biosciences, San Jose, CA, USA). For all sorts, debris and dead cells were eliminated using FSC-A and SSC-A gating, doublets were excluded via gating discrimination using FSC-H and FSC-W, and only GFP+ cells were collected.

Statistical analysis

Statistical analysis carried out using Student's *t*-test was performed (GraphPad Prism version 8.4.3, GraphPad Software, La Jolla, CA, USA). When multiple comparisons were made, *P*-values were adjusted using the Holm–Bonferroni method (Holm, 1979). We aimed to have at least three biological replicates for each experiment.

Acknowledgements

We thank Tony Qu, Austen Lucena, Paul Asfour, Kate Woronowicz, and Jessye Aggleton for laboratory assistance and/or comments on the manuscript; T. Dam at AA Lab Eggs for fertilized chick and duck eggs; and the UCSF Biological Imaging Development Core (BIDC) for microscopy support. The pmScarlet-I_C1 was a gift from Dorus Gadella (Addgene, #85044). The AAVS1 Puro Tet3G 3xFLAG Twin Strep was a gift from Yannick Doyon (Addgene, #92099). The pKanCMV-mClover3-mRuby3 was a gift from Michael Lin (Addgene, #74252). The pCAG-Cre-IRES2-GFP was a gift from Anjen Chenn (Addgene, #26646). The pCMV-hyPBBase was provided by the Wellcome Trust Sanger Institute. The mNeonGreen was provided by Allele Biotechnology & Pharmaceuticals. The DHB was a gift from Dave Matus. The PGK promoter was a gift from Jonathan Brunger via Tamara Alliston.

Competing interests

The authors declare no competing or financial interests.

Author contributions

Conceptualization: R.A.S.; Methodology: D.C.; Validation: D.C., A.N., S.S.S., Z.V.; Formal analysis: D.C., A.N., S.S.S., Z.V.; Investigation: D.C., A.N., S.S.S., Z.V.; Resources: D.C.; Writing - original draft: D.C., R.A.S.; Writing - review & editing: D.C., A.N., S.S.S., Z.V., R.A.S.; Visualization: D.C., A.N., S.S.S., Z.V., R.A.S.; Supervision: R.A.S.; Project administration: R.A.S.; Funding acquisition: R.A.S.

Funding

This work was supported in part by National Institutes of Health (NIH)/National Institute for Dental Research (NIDCR) F30 DE027616 to A.N.; F31 DE027283 to S.S.S.; and R01 DE016402, R01 DE025668, and Office of the Director S10 OD021664 to R.A.S.

Data availability

Datasets supporting the results of this study are available upon reasonable request from the corresponding author (R.A.S.). Plasmids are also available upon request subject to the terms of the original licenses under which they were obtained. GenBank accession numbers for nucleotide sequences are as follows: Runx2 (MW036689), Mmp13 (MW036690), Gas1 (MW036691), and Cxcl14 (MW036692).

Supplementary information

Supplementary information available online at <https://bio.biologists.org/lookup/doi/10.1242/bio.055343.supplemental>

References

- Abramyan, J. and Richman, J. M. (2018). Craniofacial development: discoveries made in the chicken embryo. *Int. J. Dev. Biol.* **62**, 97-107. doi:10.1387/ijdb.170321ja
- Agwuh, K. N. and MacGowan, A. (2006). Pharmacokinetics and pharmacodynamics of the tetracyclines including glycylicyclines. *J. Antimicrob. Chemother.* **58**, 256-265. doi:10.1093/jac/dkl224
- Ahler, E., Sullivan, W. J., Cass, A., Braas, D., York, A. G., Bensinger, S. J., Graeber, T. G. and Christofk, H. R. (2013). Doxycycline alters metabolism and proliferation of human cell lines. *PLoS ONE* **8**, e64561. doi:10.1371/journal.pone.0064561
- Ahn, J., Lee, J., Park, J. Y., Oh, K. B., Hwang, S., Lee, C.-W. and Lee, K. (2017). Targeted genome editing in a quail cell line using a customized CRISPR/Cas9 system. *Poult. Sci.* **96**, 1445-1450. doi:10.3382/ps/pew435
- Alexander-Savino, C. V., Hayden, M. S., Richardson, C., Zhao, J. and Poligone, B. (2016). Doxycycline is an NF-κB inhibitor that induces apoptotic cell death in malignant T-cells. *Oncotarget* **7**, 75954-75967. doi:10.18632/oncotarget.12488
- Ali, T., Renkawitz, R. and Bartkuhn, M. (2016). Insulators and domains of gene expression. *Curr. Opin. Genet. Dev.* **37**, 17-26. doi:10.1016/j.gde.2015.11.009

- Bahrami, F., Morris, D. L. and Pourgholami, M. H. (2012). Tetracyclines: drugs with huge therapeutic potential. *Mini Rev. Med. Chem.* **12**, 44-52. doi:10.2174/138955712798868977
- Bai, H., Lester, G. M. S., Petishnok, L. C. and Dean, D. A. (2017). Cytoplasmic transport and nuclear import of plasmid DNA. *Biosci. Rep.* **37**, BSR20160616. doi:10.1042/BSR20160616
- Bajar, B. T., Wang, E. S., Lam, A. J., Kim, B. B., Jacobs, C. L., Howe, E. S., Davidson, M. W., Lin, M. Z. and Chu, J. (2016). Improving brightness and photostability of green and red fluorescent proteins for live cell imaging and FRET reporting. *Sci. Rep.* **6**, 20889. doi:10.1038/srep20889
- Bednarczyk, M., Kozłowska, I., Łakota, P., Szczerba, A., Stadnicka, K. and Kuwana, T. (2018). Generation of transgenic chickens by the non-viral, cell-based method: effectiveness of some elements of this strategy. *J. Appl. Genet.* **59**, 81-89. doi:10.1007/s13353-018-0429-6
- Betancur, P., Bronner-Fraser, M. and Sauka-Spengler, T. (2010). Assembling neural crest regulatory circuits into a gene regulatory network. *Annu. Rev. Cell Dev. Biol.* **26**, 581-603. doi:10.1146/annurev.cellbio.042308.113245
- Bindels, D. S., Haarbosch, L., van Weeren, L., Postma, M., Wiese, K. E., Mastop, M., Aumonier, S., Gotthard, G., Royant, A., Hink, M. A. et al. (2017). mScarlet: a bright monomeric red fluorescent protein for cellular imaging. *Nat. Methods* **14**, 53-56. doi:10.1038/nmeth.4074
- Bire, S., Gosset, D., Jégot, G., Midoux, P., Pichon, C. and Rouleux-Bonnin, F. (2013). Exogenous mRNA delivery and bioavailability in gene transfer mediated by piggyBac transposition. *BMC Biotechnol.* **13**, 75. doi:10.1186/1472-6750-13-75
- Bochkov, Y. A. and Palmenberg, A. C. (2006). Translational efficiency of EMCV IRES in bicistronic vectors is dependent upon IRES sequence and gene location. *BioTechniques* **41**, 283-284, 286, 288 passim. doi:10.2144/000112243
- Bourgeois, A., Esteves de Lima, J., Charvet, B., Kawakami, K., Stricker, S. and Duprez, D. (2015). Stable and bicistronic expression of two genes in somite- and lateral plate-derived tissues to study chick limb development. *BMC Dev. Biol.* **15**, 39. doi:10.1186/s12861-015-0088-3
- Bower, D. V., Sato, Y. and Lansford, R. (2011). Dynamic lineage analysis of embryonic morphogenesis using transgenic quail and 4D multispectral imaging. *Genesis* **49**, 619-643. doi:10.1002/dvg.20754
- Bronner-Fraser, M. (1996). Manipulations of neural crest cells or their migratory pathways. *Methods Cell Biol.* **51**, 61-79. doi:10.1016/S0091-679X(08)06622-6
- Bronner-Fraser, M. and Garcia-Castro, M. (2008). Manipulations of neural crest cells or their migratory pathways. *Methods Cell Biol.* **87**, 75-96. doi:10.1016/S0091-679X(08)00204-5
- Brooks, A. R., Harkins, R. N., Wang, P., Qian, H. S., Liu, P. and Rubanyi, G. M. (2004). Transcriptional silencing is associated with extensive methylation of the CMV promoter following adenoviral gene delivery to muscle. *J. Gene Med.* **6**, 395-404. doi:10.1002/jgm.516
- Cerny, R., Lwigale, P., Ericsson, R., Meulemans, D., Epperlein, H.-H. and Bronner-Fraser, M. (2004). Developmental origins and evolution of jaws: new interpretation of "maxillary" and "mandibular". *Dev. Biol.* **276**, 225-236. doi:10.1016/j.ydbio.2004.08.046
- Cervia, L. D., Chang, C.-C., Wang, L., Mao, M. and Yuan, F. (2018). Enhancing electrotransfection efficiency through improvement in nuclear entry of plasmid DNA. *Mol. Ther. Nucleic Acids* **11**, 263-271. doi:10.1016/j.omtn.2018.02.009
- Chapman, S. C., Lawson, A., Macarthur, W. C., Wiese, R. J., Loehel, R. H., Burgos-Trinidad, M., Wakefield, J. K., Ramabhadran, R., Mauch, T. J. and Schoenwolf, G. C. (2005). Ubiquitous GFP expression in transgenic chickens using a lentiviral vector. *Development* **132**, 935-940. doi:10.1242/dev.01652
- Chen, C.-M. A., Smith, D. M., Peters, M. A., Samson, M. E. S., Zitz, J., Tabin, C. J. and Cepko, C. L. (1999). Production and design of more effective avian replication-incompetent retroviral vectors. *Dev. Biol.* **214**, 370-384. doi:10.1006/dbio.1999.9432
- Chen, Y. X., Krull, C. E. and Reneker, L. W. (2004). Targeted gene expression in the chicken eye by *in ovo* electroporation. *Mol. Vis.* **10**, 874-883.
- Chesnutt, C. and Niswander, L. (2004). Plasmid-based short-hairpin RNA interference in the chicken embryo. *Genesis* **39**, 73-78. doi:10.1002/gene.20028
- Ch tarto, A., Tenenbaum, L., Velu, T., Brotchi, J., Levivier, M. and Blum, D. (2003). Minocycline-induced activation of tetracycline-responsive promoter. *Neurosci. Lett.* **352**, 155-158. doi:10.1016/j.neulet.2003.08.067
- Clarke, J. D. W. and Tickle, C. (1999). Fate maps old and new. *Nat. Cell Biol.* **1**, E103-E109. doi:10.1038/12105
- Cong, L., Ran, F. A., Cox, D., Lin, S., Barretto, R., Habib, N., Hsu, P. D., Wu, X., Jiang, W., Marraffini, L. A. et al. (2013). Multiplex genome engineering using CRISPR/Cas systems. *Science* **339**, 819-823. doi:10.1126/science.1231143
- Creuzet, S., Couly, G., Vincent, C. and Le Douarin, N. M. (2002). Negative effect of Hox gene expression on the development of the neural crest-derived facial skeleton. *Development* **129**, 4301-4313.
- Curcio, M. J. and Derbyshire, K. M. (2003). The outs and ins of transposition: from mu to kangaroo. *Nat. Rev. Mol. Cell Biol.* **4**, 865-877. doi:10.1038/nrm1241
- Daivai, M., Loehr, J., Jacquet, K., Huard, C. C., Roques, C., Herst, P., Côté, J. and Doyon, Y. (2015). A scalable genome-editing-based approach for mapping multiprotein complexes in human cells. *Cell Rep.* **13**, 621-633. doi:10.1016/j.celrep.2015.09.009
- Das, R. M., Van Hateren, N. J., Howell, G. R., Farrell, E. R., Bangs, F. K., Porteous, V. C., Manning, E. M., McGrew, M. J., Ohyama, K., Sacco, M. A. et al. (2006). A robust system for RNA interference in the chicken using a modified microRNA operon. *Dev. Biol.* **294**, 554-563. doi:10.1016/j.ydbio.2006.02.020
- Das, A. T., Tenenbaum, L. and Berkhout, B. (2016). Tet-on systems for doxycycline-inducible gene expression. *Curr. Gene Ther.* **16**, 156-167. doi:10.2174/1566523216666160524144041
- De la Rossa, A. and Jabaudon, D. (2015). *In vivo* rapid gene delivery into postmitotic neocortical neurons using iontoporation. *Nat. Protoc.* **10**, 25-32. doi:10.1038/nprot.2015.001
- Dean, D. A. (1997). Import of plasmid DNA into the nucleus is sequence specific. *Exp. Cell Res.* **230**, 293-302. doi:10.1006/excr.1996.3427
- Dean, D. A., Dean, B. S., Muller, S. and Smith, L. C. (1999). Sequence requirements for plasmid nuclear import. *Exp. Cell Res.* **253**, 713-722. doi:10.1006/excr.1999.4716
- Dean, D. A., Strong, D. D. and Zimmer, W. E. (2005). Nuclear entry of nonviral vectors. *Gene Ther.* **12**, 881-890. doi:10.1038/sj.gt.3302534
- Ding, S., Wu, X., Li, G., Han, M., Zhuang, Y. and Xu, T. (2005). Efficient transposition of the piggyBac (PB) transposon in mammalian cells and mice. *Cell* **122**, 473-483. doi:10.1016/j.cell.2005.07.013
- Dole, N. S., Kapinas, K., Kessler, C. B., Yee, S.-P., Adams, D. J., Pereira, R. C. and Delany, A. M. (2015). A single nucleotide polymorphism in osteonectin 3' untranslated region regulates bone volume and is targeted by miR-433. *J. Bone Miner. Res.* **30**, 723-732. doi:10.1002/jbmr.2378
- Ealba, E. L. and Schneider, R. A. (2013). A simple PCR-based strategy for estimating species-specific contributions in chimeras and xenografts. *Development* **140**, 3062-3068. doi:10.1242/dev.092676
- Ealba, E. L., Jheon, A. H., Hall, J., Curantz, C., Butcher, K. D. and Schneider, R. A. (2015). Neural crest-mediated bone resorption is a determinant of species-specific jaw length. *Dev. Biol.* **408**, 151-163. doi:10.1016/j.ydbio.2015.10.001
- Eames, B. F. and Schneider, R. A. (2005). Quail-duck chimeras reveal spatiotemporal plasticity in molecular and histogenic programs of cranial feather development. *Development* **132**, 1499-1509. doi:10.1242/dev.01719
- Eames, B. F. and Schneider, R. A. (2008). The genesis of cartilage size and shape during development and evolution. *Development* **135**, 3947-3958. doi:10.1242/dev.023309
- Ellis, J. (2005). Silencing and variegation of gammaretrovirus and lentivirus vectors. *Hum. Gene Ther.* **16**, 1241-1246. doi:10.1089/hum.2005.16.1241
- Ermak, G., Cancasci, V. J. and Davies, K. J. A. (2003). Cytotoxic effect of doxycycline and its implications for tet-on gene expression systems. *Anal. Biochem.* **318**, 152-154. doi:10.1016/S0003-2697(03)00166-0
- Fekete, D. M. and Cepko, C. L. (1993a). Replication-competent retroviral vectors encoding alkaline phosphatase reveal spatial restriction of viral gene expression/transduction in the chick embryo. *Mol. Cell. Biol.* **13**, 2604-2613. doi:10.1128/MCB.13.4.2604
- Fekete, D. M. and Cepko, C. L. (1993b). Retroviral infection coupled with tissue transplantation limits gene transfer in the chicken embryo. *Proc. Natl. Acad. Sci. USA* **90**, 2350-2354. doi:10.1073/pnas.90.6.2350
- Fish, J. L. and Schneider, R. A. (2014). Assessing species-specific contributions to craniofacial development using quail-duck chimeras. *J. Vis. Exp.* **87**, 1-6. doi:10.3791/51534
- Fish, J. L., Sklar, R. S., Woronowicz, K. C. and Schneider, R. A. (2014). Multiple developmental mechanisms regulate species-specific jaw size. *Development* **141**, 674-684. doi:10.1242/dev.100107
- Fraser, M. J., Smith, G. E. and Summers, M. D. (1983). Acquisition of host cell DNA sequences by baculoviruses: relationship between host DNA insertions and FP mutants of *Autographa californica* and *Galleria mellonella* nuclear polyhedrosis viruses. *J. Virol.* **47**, 287-300. doi:10.1128/JVI.47.2.287-300.1983
- Fraser, M. J., Cliszczon, T., Elick, T. and Bauser, C. (1996). Precise excision of TTA-specific lepidopteran transposons piggyBac (IFP2) and tagalong (TFP3) from the baculovirus genome in cell lines from two species of Lepidoptera. *Insect Mol. Biol.* **5**, 141-151. doi:10.1111/j.1365-2583.1996.tb00048.x
- Funahashi, J., Okafuji, T., Ohuchi, H., Noji, S., Tanaka, H. and Nakamura, H. (1999). Role of Pax-5 in the regulation of a mid-hindbrain organizer's activity. *Dev. Growth Differ.* **41**, 59-72. doi:10.1046/j.1440-169x.1999.00401.x
- Gammill, L. S., Jacques-Fricke, B. and Roffers-Agarwal, J. (2019). Embryological and genetic manipulation of chick development. *Methods Mol. Biol.* **1920**, 75-97. doi:10.1007/978-1-4939-9009-2_6
- Gandhi, S., Piacentino, M. L., Vieceli, F. M. and Bronner, M. E. (2017). Optimization of CRISPR/Cas9 genome editing for loss-of-function in the early chick embryo. *Dev. Biol.* **432**, 86-97. doi:10.1016/j.ydbio.2017.08.036
- Garcia-Castro, M. I., Marcelle, C. and Bronner-Fraser, M. (2002). Ectodermal Wnt function as a neural crest inducer. *Science* **13**, 13.
- Garrison, B. S., Yant, S. R., Mikkelsen, J. G. and Kay, M. A. (2007). Postintegrative gene silencing within the Sleeping Beauty transposon system. *Mol. Cell. Biol.* **27**, 8824-8833. doi:10.1128/MCB.00498-07
- Geurts, A. M., Yang, Y., Clark, K. J., Liu, G., Cui, Z., Dupuy, A. J., Bell, J. B., Largaespada, D. A. and Hackett, P. B. (2003). Gene transfer into genomes of human cells by the sleeping beauty transposon system. *Mol. Ther.* **8**, 108-117. doi:10.1016/S1525-0016(03)00099-6

- Giovagnoli, S., Tsai, T. and DeLuca, P. P. (2010). Formulation and release behavior of doxycycline-alginate hydrogel microparticles embedded into pluronic F127 thermogels as a potential new vehicle for doxycycline intradermal sustained delivery. *AAPS PharmSciTech* 11, 212-220. doi:10.1208/s12249-009-9361-8
- Gossen, M., Freundlieb, S., Bender, G., Muller, G., Hillen, W. and Bujard, H. (1995). Transcriptional activation by tetracyclines in mammalian cells. *Science* 268, 1766-1769. doi:10.1126/science.7792603
- Hall, J., Jheon, A. H., Ealba, E. L., Eames, B. F., Butcher, K. D., Mak, S.-S., Lather, R., Alliston, T. and Schneider, R. A. (2014). Evolution of a developmental mechanism: Species-specific regulation of the cell cycle and the timing of events during craniofacial osteogenesis. *Dev. Biol.* 385, 380-395. doi:10.1016/j.ydbio.2013.11.011
- Hamburger, V. and Hamilton, H. L. (1951). A series of normal stages in the development of the chick embryo. *J. Morphol.* 88, 49-92. doi:10.1002/jmor.1050880104
- Hamilton, H. L. (1965). *Lillie's Development of the Chick: An Introduction to Embryology*, 3rd edn. New York: Holt, Rinehart and Winston.
- Harris, M. P., Linkhart, B. L. and Fallon, J. F. (2004). Bmp7 mediates early signaling events during induction of chick epidermal organs. *Dev. Dyn.* 231, 22-32. doi:10.1002/dvdy.20096
- Heinz, N., Schambach, A., Galla, M., Maetzig, T., Baum, C., Loew, R. and Schiedlmeier, B. (2011). Retroviral and transposon-based tet-regulated all-in-one vectors with reduced background expression and improved dynamic range. *Hum. Gene Ther.* 22, 166-176. doi:10.1089/hum.2010.099
- Heinz, N., Hennig, K. and Loew, R. (2013). Graded or threshold response of the tet-controlled gene expression: all depends on the concentration of the transactivator. *BMC Biotechnol.* 13, 5. doi:10.1186/1472-6750-13-5
- Herr, R., Wührle, F. U., Danke, C., Berens, C. and Brummer, T. (2011). A novel MCF-10A line allowing conditional oncogene expression in 3D culture. *Cell Commun. Signal.* 9, 17. doi:10.1186/1478-811X-9-17
- Hickman, A. B., Chandler, M. and Dyda, F. (2010). Integrating prokaryotes and eukaryotes: DNA transposases in light of structure. *Crit. Rev. Biochem. Mol. Biol.* 45, 50-69. doi:10.3109/10409230903505596
- Hollister, J. D. and Gaut, B. S. (2009). Epigenetic silencing of transposable elements: a trade-off between reduced transposition and deleterious effects on neighboring gene expression. *Genome Res.* 19, 1419-1428. doi:10.1101/gr.091678.109
- Holm, S. (1979). A Simple Sequentially Rejective Multiple Test Procedure. *Scandinavian Journal of Statistics* 6, 65-70.
- Huang, X., Guo, H., Tammana, S., Jung, Y.-C., Mellgren, E., Bassi, P., Cao, Q., Tu, Z. J., Kim, Y. C., Ekker, S. C. et al. (2010). Gene transfer efficiency and genome-wide integration profiling of Sleeping Beauty, Tol2, and piggyBac transposons in human primary T cells. *Mol. Ther.* 18, 1803-1813. doi:10.1038/mt.2010.141
- Hudecek, M., Izsvák, Z., Johnen, S., Renner, M., Thumann, G. and Ivics, Z. (2017). Going non-viral: the Sleeping Beauty transposon system breaks on through to the clinical side. *Crit. Rev. Biochem. Mol. Biol.* 52, 355-380. doi:10.1080/10409238.2017.1304354
- Hughes, S. H. (2004). The RCAS vector system. *Folia biologica* 50, 107-119.
- Huss, D., Benazeraf, B., Wallingford, A., Filla, M., Yang, J., Fraser, S. E. and Lansford, R. (2015). A transgenic quail model that enables dynamic imaging of amniote embryogenesis. *Development* 142, 2850-2859. doi:10.1242/dev.121392
- Itasaki, N., Bel-Vialar, S. and Krumlauf, R. (1999). 'Shocking' developments in chick embryology: electroporation and in ovo gene expression. *Nat. Cell Biol.* 1, E203-E207. doi:10.1038/70231
- Ivics, Z., Hackett, P. B., Plasterk, R. H. and Izsvák, Z. (1997). Molecular reconstruction of Sleeping Beauty, a Tc1-like transposon from fish, and its transposition in human cells. *Cell* 91, 501-510. doi:10.1016/S0092-8674(00)80436-5
- Janssen, A., Colmenares, S. U. and Karpen, G. H. (2018). Heterochromatin: guardian of the genome. *Annu. Rev. Cell Dev. Biol.* 34, 265-288. doi:10.1146/annurev-cellbio-100617-062653
- Jheon, A. H. and Schneider, R. A. (2009). The cells that fill the bill: neural crest and the evolution of craniofacial development. *J. Dent. Res.* 88, 12-21. doi:10.1177/0022034508327757
- Jhingory, S., Wu, C.-Y. and Taneyhill, L. A. (2010). Novel insight into the function and regulation of α N-catenin by Snail2 during chick neural crest cell migration. *Dev. Biol.* 344, 896-910. doi:10.1016/j.ydbio.2010.06.006
- Johnston, M. C. (1966). A radioautographic study of the migration and fate of cranial neural crest cells in the chick embryo. *Anat. Rec.* 156, 143-155. doi:10.1002/ar.1091560204
- Jordan, B. J., Vogel, S., Stark, M. R. and Beckstead, R. B. (2014). Expression of green fluorescent protein in the chicken using in vivo transfection of the piggyBac transposon. *J. Biotechnol.* 173, 86-89. doi:10.1016/j.jbiotec.2014.01.016
- June Byun, S., Yuk, S.-S., Jang, Y.-J., Choi, H., Jeon, M.-H., Erdene-Ochir, T. O., Kwon, J.-H., Noh, J.-Y., Sun Kim, J., Gyu Yoo, J. et al. (2017). Transgenic chickens expressing the 3D8 single chain variable fragment protein suppress avian influenza transmission. *Sci. Rep.* 7, 5938. doi:10.1038/s41598-017-05270-8
- Kardon, G., Harfe, B. D. and Tabin, C. J. (2003). A Tcf4-positive mesodermal population provides a prepattern for vertebrate limb muscle patterning. *Dev. Cell* 5, 937-944. doi:10.1016/S1534-5807(03)00360-5
- Kawakami, K. (2007). Tol2: a versatile gene transfer vector in vertebrates. *Genome Biol.* 8 Suppl. 1, S7. doi:10.1186/gb-2007-8-s1-s7
- Kim, J. H., Lee, S.-R., Li, L.-H., Park, H.-J., Park, J.-H., Lee, K.-Y., Kim, M.-K., Shin, B. A. and Choi, S.-Y. (2011). High cleavage efficiency of a 2A peptide derived from porcine teschovirus-1 in human cell lines, zebrafish and mice. *PLoS ONE* 6, e18556. doi:10.1371/journal.pone.0018556
- Koga, A., Suzuki, M., Inagaki, H., Bessho, Y. and Hori, H. (1996). Transposable element in fish. *Nature* 383, 30. doi:10.1038/383030a0
- Kohrman, A. Q., Adikes, R. C., Martinez, M. A. Q., Palmisano, N. J., Smith, J. J., Medwig-Kinney, T. N., Min, M., Sallee, M. D., Ahmed, O. B., Kim, N. et al. (2020). Visualizing the metazoan proliferation-terminal differentiation decision in vivo. *bioRxiv*, 2019.2012.2018.881888.
- Koo, B. C., Kwon, M. S., Choi, B. R., Kim, J. H., Cho, S. K., Sohn, S. H., Cho, E. J., Lee, H. T., Chang, W., Jeon, I. et al. (2006). Production of germ-line transgenic chickens expressing enhanced green fluorescent protein using a MoMLV-based retrovirus vector. *FASEB J.* 20, 2251-2260. doi:10.1096/fj.06-5866com
- Kos, R., Tucker, R. P., Hall, R., Duong, T. D. and Erickson, C. A. (2003). Methods for introducing morpholinos into the chicken embryo. *Dev. Dyn.* 226, 470-477. doi:10.1002/dvdy.10254
- Kozak, M. (1986). Point mutations define a sequence flanking the AUG initiator codon that modulates translation by eukaryotic ribosomes. *Cell* 44, 283-292. doi:10.1016/0092-8674(86)90762-2
- Krull, C. E. (2004). A primer on using in ovo electroporation to analyze gene function. *Dev. Dyn.* 229, 433-439. doi:10.1002/dvdy.10473
- Kulesa, P. M. and Fraser, S. E. (2000). In ovo time-lapse analysis of chick hindbrain neural crest cell migration shows cell interactions during migration to the branchial arches. *Development* 127, 1161-1172.
- Kumamoto, T., Maurinot, F., Barry-Martinet, R., Vaslin, C., Vandormael-Pournin, S., Le, M., Lerat, M., Niculescu, D., Cohen-Tannoudji, M., Rebsam, A. et al. (2020). Direct Readout of Neural Stem Cell Transgenesis with an Integration-Coupled Gene Expression Switch. *Neuron* 107, 617-630 e616.
- Lacoste, A., Berenshteyn, F. and Brivanlou, A. H. (2009). An efficient and reversible transposable system for gene delivery and lineage-specific differentiation in human embryonic stem cells. *Cell Stem Cell* 5, 332-342. doi:10.1016/j.stem.2009.07.011
- Larsen, C. W., Zeltser, L. M. and Lumsden, A. (2001). Boundary formation and compartment in the avian diencephalon. *J. Neurosci.* 21, 4699-4711. doi:10.1523/JNEUROSCI.21-13-04699.2001
- Le Douarin, N. and McLaren, A. (1984). *Chimeras in Developmental Biology*. London; Orlando: Academic Press.
- Le Douarin, N. M. and Dieterlen-Lièvre, F. (2013). How studies on the avian embryo have opened new avenues in the understanding of development: a view about the neural and hematopoietic systems. *Dev. Growth Differ.* 55, 1-14. doi:10.1111/dgd.12015
- Le Douarin, N. M., Dieterlen-Lievre, F. and Teillet, M. (1996). Quail-chick transplantations. In *Methods in Avian Embryology* (ed. M. Bronner-Fraser), pp. 23-59. San Diego: Academic Press.
- Leary, S., Underwood, W., Anthony, R., Cartner, S., Corey, D., Grandin, T., Greenacre, C., Gwaltney-Brant, S., McCrackin, M. A., Meye, R. et al. (2013). *AVMA Guidelines for the Euthanasia of Animals*. 2013 edn. Schaumburg, IL: American Veterinary Medical Association.
- Lesueur, L. L., Mir, L. M. and André, F. M. (2016). Overcoming the specific toxicity of large plasmids electrotransfer in primary cells in vitro. *Mol. Ther. Nucleic Acids* 5, e291. doi:10.1038/mtna.2016.4
- Li, M. A., Turner, D. J., Ning, Z., Yusa, K., Liang, Q., Eckert, S., Rad, L., Fitzgerald, T. W., Craig, N. L. and Bradley, A. (2011). Mobilization of giant piggyBac transposons in the mouse genome. *Nucleic Acids Res.* 39, e148. doi:10.1093/nar/gkr764
- Liu, H. and Naismith, J. H. (2008). An efficient one-step site-directed deletion, insertion, single and multiple-site plasmid mutagenesis protocol. *BMC Biotechnol.* 8, 91. doi:10.1186/1472-6750-8-91
- Liu, X., Li, N., Hu, X., Zhang, R., Li, Q., Cao, D., Liu, T., Zhang, Y. and Liu, X. (2013). Efficient production of transgenic chickens based on piggyBac. *Transgenic Res.* 22, 417-423. doi:10.1007/s11248-012-9642-y
- Loew, R., Heinz, N., Hampf, M., Bujard, H. and Gossen, M. (2010). Improved Tet-responsive promoters with minimized background expression. *BMC Biotechnol.* 10, 81. doi:10.1186/1472-6750-10-81
- Logan, M. and Tabin, C. (1998). Targeted gene misexpression in chick limb buds using avian replication-competent retroviruses. *Methods* 14, 407-420. doi:10.1006/meth.1998.0595
- Lu, Y., Lin, C. and Wang, X. (2009). PiggyBac transgenic strategies in the developing chicken spinal cord. *Nucleic Acids Res.* 37, e141. doi:10.1093/nar/gkp686
- Lwigale, P. Y. and Schneider, R. A. (2008). Other chimeras: quail-duck and mouse-chick. *Methods Cell Biol.* 87, 59-74. doi:10.1016/S0091-679X(08)00203-3
- Lwigale, P. Y., Conrad, G. W. and Bronner-Fraser, M. (2004). Graded potential of neural crest to form cornea, sensory neurons and cartilage along the rostrocaudal axis. *Development* 131, 1979-1991. doi:10.1242/dev.01106

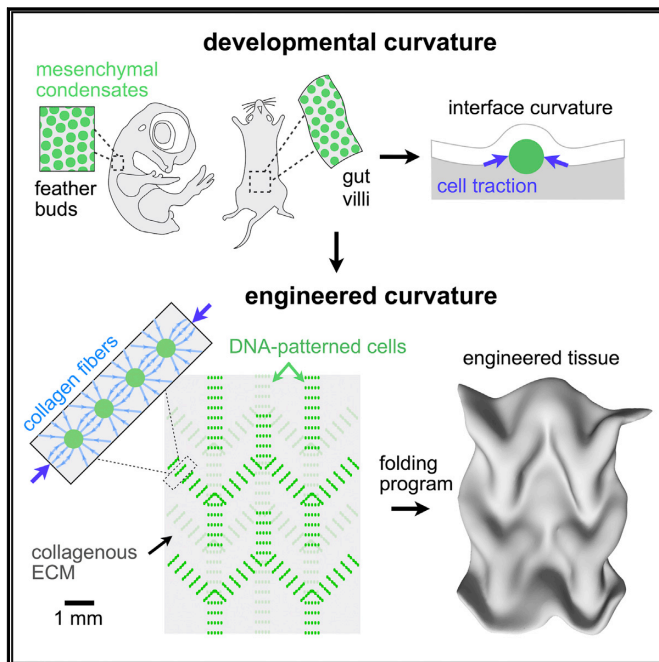
- Lwigale, P. Y., Cressy, P. A. and Bronner-Fraser, M. (2005). Corneal keratocytes retain neural crest progenitor cell properties. *Dev. Biol.* **288**, 284-293. doi:10.1016/j.ydbio.2005.09.046
- Macdonald, J., Taylor, L., Sherman, A., Kawakami, K., Takahashi, Y., Sang, H. M. and McGrew, M. J. (2012). Efficient genetic modification and germ-line transmission of primordial germ cells using piggyBac and Tol2 transposons. *Proc. Natl. Acad. Sci. USA* **109**, E1466-E1472. doi:10.1073/pnas.1118715109
- Mandegar, M. A., Huebsch, N., Frolov, E. B., Shin, E., Truong, A., Olvera, M. P., Chan, A. H., Miyaoka, Y., Holmes, K., Spencer, C. I. et al. (2016). CRISPR interference efficiently induces specific and reversible gene silencing in human iPSCs. *Cell Stem Cell* **18**, 541-553. doi:10.1016/j.stem.2016.01.022
- Martik, M. L. and Bronner, M. E. (2017). Regulatory logic underlying diversification of the neural crest. *Trends Genet.* **33**, 715-727. doi:10.1016/j.tig.2017.07.015
- McGrew, M. J., Sherman, A., Ellard, F. M., Lillico, S. G., Gilhooley, H. J., Kingsman, A. J., Mitrophanous, K. A. and Sang, H. (2004). Efficient production of germline transgenic chickens using lentiviral vectors. *EMBO Rep.* **5**, 728-733. doi:10.1038/sj.embor.7400171
- McLarren, K. W., Litsiou, A. and Streit, A. (2003). DLX5 positions the neural crest and preplacode region at the border of the neural plate. *Dev. Biol.* **259**, 34-47. doi:10.1016/S0012-1606(03)00177-5
- McLennan, R. and Kulesa, P. M. (2007). In vivo analysis reveals a critical role for neuropilin-1 in cranial neural crest cell migration in chick. *Dev. Biol.* **301**, 227-239. doi:10.1016/j.ydbio.2006.08.019
- McLennan, R. and Kulesa, P. M. (2019). In ovo electroporation of plasmid DNA and morpholinos into specific tissues during early embryogenesis. *Methods Mol. Biol.* **1976**, 71-82. doi:10.1007/978-1-4939-9412-0_6
- Megason, S. G. and McMahon, A. P. (2002). A mitogen gradient of dorsal midline Wnts organizes growth in the CNS. *Development* **129**, 2087-2098.
- Meir, Y. J. and Wu, S. C. (2011). Transposon-based vector systems for gene therapy clinical trials: challenges and considerations. *Chang Gung Med. J.* **34**, 565-579.
- Meir, Y.-J. J., Weirauch, M. T., Yang, H.-S., Chung, P.-C., Yu, R. K. and Wu, S. C.-Y. (2011). Genome-wide target profiling of piggyBac and Tol2 in HEK 293: pros and cons for gene discovery and gene therapy. *BMC Biotechnol.* **11**, 28. doi:10.1186/1472-6750-11-28
- Merrill, A. E., Eames, B. F., Weston, S. J., Heath, T. and Schneider, R. A. (2008). Mesenchyme-dependent BMP signaling directs the timing of mandibular osteogenesis. *Development* **135**, 1223-1234. doi:10.1242/dev.015933
- Miller, A. M., Munkonge, F. M., Alton, E. W. F. W. and Dean, D. A. (2009). Identification of protein cofactors necessary for sequence-specific plasmid DNA nuclear import. *Mol. Ther.* **17**, 1897-1903. doi:10.1038/mt.2009.127
- Momose, T., Tonegawa, A., Takeuchi, J., Ogawa, H., Umesono, K. and Yasuda, K. (1999). Efficient targeting of gene expression in chick embryos by microelectroporation. *Dev. Growth Differ.* **41**, 335-344. doi:10.1046/j.1440-169X.1999.413437.x
- Morgan, B. A. and Fekete, D. M. (1996). Manipulating gene expression with replication-competent retroviruses. In *Methods in Avian Embryology* (ed. M. Bronner-Fraser), pp. 186-217. San Diego: Academic Press.
- Morin, V., Véron, N. and Marcelle, C. (2017). CRISPR/Cas9 in the chicken embryo. In *Avian and Reptilian Developmental Biology: Methods and Protocols* (ed. G. Sheng), p. 1 online resource (xii, 365 pages). New York: Humana Press: Springer.
- Nakamura, H. and Funahashi, J.-I. (2001). Introduction of DNA into chick embryos by in ovo electroporation. *Methods* **24**, 43-48. doi:10.1006/meth.2001.1155
- Nakamura, H., Katahira, T., Sato, T., Watanabe, Y. and Funahashi, J.-I. (2004). Gain- and loss-of-function in chick embryos by electroporation. *Mech. Dev.* **121**, 1137-1143. doi:10.1016/j.mod.2004.05.013
- Noden, D. M. (1975). An analysis of the migratory behavior of avian cephalic neural crest cells. *Dev. Biol.* **42**, 106-130. doi:10.1016/0012-1606(75)90318-8
- Noden, D. M. (1984). The use of chimeras in analyses of craniofacial development. In *Chimeras in Developmental Biology* (ed. N. Le Douarin and A. McLaren), pp. 241-280. London; Orlando: Academic Press.
- Noden, D. M. and Schneider, R. A. (2006). Neural crest cells and the community of plan for craniofacial development: historical debates and current perspectives. *Adv. Exp. Med. Biol.* **589**, 1-23. doi:10.1007/978-0-387-46954-6_1
- Norrmann, K., Fischer, Y., Bonnamy, B., Wolfhagen Sand, F., Ravassard, P. and Semb, H. (2010). Quantitative comparison of constitutive promoters in human ES cells. *PLoS ONE* **5**, e12413. doi:10.1371/journal.pone.0012413
- Núñez-León, D., Aguirre-Fernández, G., Steiner, A., Nagashima, H., Jensen, P., Stoekli, E., Schneider, R. A. and Sánchez-Villagra, M. R. (2019). Morphological diversity of integumentary traits in fowl domestication: insights from disparity analysis and embryonic development. *Dev. Dyn.* **248**, 1044-1058. doi:10.1002/dvdy.105
- Ottaviani, A., Rival-Gervier, S., Boussouar, A., Foerster, A. M., Rondier, D., Sacconi, S., Desnuelle, C., Gilson, E. and Magdinier, F. (2009). The D4Z4 macrosatellite repeat acts as a CTCF and A-type lamins-dependent insulator in facio-scapulo-humeral dystrophy. *PLoS Genet.* **5**, e1000394. doi:10.1371/journal.pgen.1000394
- Pannell, D. and Ellis, J. (2001). Silencing of gene expression: implications for design of retrovirus vectors. *Rev. Med. Virol.* **11**, 205-217. doi:10.1002/rmv.316
- Park, S. H., Kim, J. N., Park, T. S., Lee, S. D., Kim, T. H., Han, B. K. and Han, J. Y. (2010). CpG methylation modulates tissue-specific expression of a transgene in chickens. *Theriogenology* **74**, 805-816.e801. doi:10.1016/j.theriogenology.2010.04.005
- Pourquié, O. (2018). Somite formation in the chicken embryo. *Int. J. Dev. Biol.* **62**, 57-62. doi:10.1387/ijdb.180036op
- Qi, L. S., Larson, M. H., Gilbert, L. A., Doudna, J. A., Weissman, J. S., Arkin, A. P. and Lim, W. A. (2013). Repurposing CRISPR as an RNA-guided platform for sequence-specific control of gene expression. *Cell* **152**, 1173-1183. doi:10.1016/j.cell.2013.02.022
- Qin, J. Y., Zhang, L., Cliff, K. L., Hulus, I., Xiang, A. P., Ren, B.-Z. and Lahn, B. T. (2010). Systematic comparison of constitutive promoters and the doxycycline-inducible promoter. *PLoS ONE* **5**, e10611. doi:10.1371/journal.pone.0010611
- Rao, M., Baraban, J. H., Rajaii, F. and Sockanathan, S. (2004). In vivo comparative study of RNAi methodologies by in ovo electroporation in the chick embryo. *Dev. Dyn.* **231**, 592-600. doi:10.1002/dvdy.20161
- Reberšek, M. (2017). Beyond electroporation pulse parameters: from application to evaluation. In *Handbook of Electroporation* (ed. D. Miklavcic), pp. 1-21. Cham: Springer International Publishing.
- Ricklefs, R. E. and Starck, J. M. (1998). Embryonic growth and development. In *Avian Growth and Development: Evolution within the Altricial-Precocial Spectrum* (ed. J. M. Starck and R. E. Ricklefs), pp. 31-58. New York: Oxford University Press.
- Roney, I. J., Rudner, A. D., Couture, J.-F. and Kærn, M. (2016). Improvement of the reverse tetracycline transactivator by single amino acid substitutions that reduce leaky target gene expression to undetectable levels. *Sci. Rep.* **6**, 27697. doi:10.1038/srep27697
- Rostovskaya, M., Naumann, R., Fu, J., Obst, M., Mueller, D., Stewart, A. F. and Anastassiadis, K. (2013). Transposon mediated BAC transgenesis via pronuclear injection of mouse zygotes. *Genesis* **51**, 135-141. doi:10.1002/dvg.22362
- Sang, H. (2006). Transgenesis sunny-side up. *Nat. Biotechnol.* **24**, 955-956. doi:10.1038/nbt0806-955
- Sato, Y., Kasai, T., Nakagawa, S., Tanabe, K., Watanabe, T., Kawakami, K. and Takahashi, Y. (2007). Stable integration and conditional expression of electroporated transgenes in chicken embryos. *Dev. Biol.* **305**, 616-624. doi:10.1016/j.ydbio.2007.01.043
- Sato, Y., Poynter, G., Huss, D., Filla, M. B., Czirok, A., Rongish, B. J., Little, C. D., Fraser, S. E. and Lansford, R. (2010). Dynamic analysis of vascular morphogenesis using transgenic quail embryos. *PLoS ONE* **5**, e12674. doi:10.1371/journal.pone.0012674
- Sauka-Spengler, T. and Barembaum, M. (2008). Gain- and loss-of-function approaches in the chick embryo. *Methods Cell Biol.* **87**, 237-256. doi:10.1016/S0091-679X(08)00212-4
- Sauka-Spengler, T. and Bronner-Fraser, M. (2008). A gene regulatory network orchestrates neural crest formation. *Nat. Rev. Mol. Cell Biol.* **9**, 557-568. doi:10.1038/nrm2428
- Scaal, M., Gros, J., Lesbros, C. and Marcelle, C. (2004). In ovo electroporation of avian somites. *Dev. Dyn.* **229**, 643-650. doi:10.1002/dvdy.10433
- Schneider, R. A. (1999). Neural crest can form cartilages normally derived from mesoderm during development of the avian head skeleton. *Dev. Biol.* **208**, 441-455. doi:10.1006/dbio.1999.9213
- Schneider, R. A. (2007). How to tweak a beak: molecular techniques for studying the evolution of size and shape in Darwin's finches and other birds. *BioEssays* **29**, 1-6. doi:10.1002/bies.20517
- Schneider, R. A. (2018). Neural crest and the origin of species-specific pattern. *Genesis* **56**, e23219. doi:10.1002/dvg.23219
- Schneider, R. A., Hu, D., Rubenstein, J. L., Maden, M. and Helms, J. A. (2001). Local retinoid signaling coordinates forebrain and facial morphogenesis by maintaining FGF8 and SHH. *Development* **128**, 2755-2767.
- Serbedžija, G. N., Bronner-Fraser, M. and Fraser, S. E. (1989). A vital dye analysis of the timing and pathways of avian trunk neural crest cell migration. *Development* **106**, 809-816.
- Serralbo, O., Picard, C. A. and Marcelle, C. (2013). Long-term, inducible gene loss-of-function in the chicken embryo. *Genesis* **51**, 372-380. doi:10.1002/dvg.12388
- Shaner, N. C., Lambert, G. G., Chammas, A., Ni, Y., Cranfill, P. J., Baird, M. A., Sell, B. R., Allen, J. R., Day, R. N., Israelsson, M. et al. (2013). A bright monomeric green fluorescent protein derived from Branchiostoma lanceolatum. *Nat. Methods* **10**, 407-409. doi:10.1038/nmeth.2413
- Simkin, J. E., Zhang, D., Ighaniyan, S. and Newgreen, D. F. (2014). Parameters affecting efficiency of in ovo electroporation of the avian neural tube and crest. *Dev. Dyn.* **243**, 1440-1447. doi:10.1002/dvdy.24163
- Smith, S. S., Dole, N. S., Franceschetti, T., Hrdlicka, H. C. and Delany, A. M. (2016). MicroRNA-433 dampens glucocorticoid receptor signaling, impacting circadian rhythm and osteoblastic gene expression. *J. Biol. Chem.* **291**, 21717-21728. doi:10.1074/jbc.M116.737890
- Spencer, S. L., Cappell, S. D., Tsai, F.-C., Overton, K. W., Wang, C. L. and Meyer, T. (2013). The proliferation-quiescence decision is controlled by a bifurcation in CDK2 activity at mitotic exit. *Cell* **155**, 369-383. doi:10.1016/j.cell.2013.08.062

- Starck, J. M. and Ricklefs, R. E. (1998). *Avian Growth and Development: Evolution within the Altricial-Precocial Spectrum*. New York: Oxford University Press.
- Stern, C. D. (2005). The chick: a great model system becomes even greater. *Dev. Cell* **8**, 9-17. doi:10.1016/S1534-5807(04)00425-3
- Stocker, K. M., Brown, A. M. C. and Ciment, G. (1993). Gene transfer of LacZ into avian neural tube and neural crest by retroviral infection of grafted embryonic tissues. *J. Neurosci. Res.* **34**, 135-145. doi:10.1002/jnr.490340114
- Swartz, M., Eberhart, J., Mastick, G. S. and Krull, C. E. (2001). Sparking new frontiers: using in vivo electroporation for genetic manipulations. *Dev. Biol.* **233**, 13-21. doi:10.1006/dbio.2001.0181
- Szymczak, A. L., Workman, C. J., Wang, Y., Vignali, K. M., Dilioglou, S., Vanin, E. F. and Vignali, D. A. (2004). Correction of multi-gene deficiency in vivo using a single 'self-cleaving' 2A peptide-based retroviral vector. *Nat. Biotechnol.* **22**, 589-594. doi:10.1038/nbt957
- Takahashi, Y., Watanabe, T., Nakagawa, S., Kawakami, K. and Sato, Y. (2008). Transposon-mediated stable integration and tetracycline-inducible expression of electroporated transgenes in chicken embryos. *Methods Cell Biol.* **87**, 271-280. doi:10.1016/S0091-679X(08)00214-8
- Tokita, M. and Schneider, R. A. (2009). Developmental origins of species-specific muscle pattern. *Dev. Biol.* **331**, 311-325. doi:10.1016/j.ydbio.2009.05.548
- Trainor, P. A., Ariza-McNaughton, L. and Krumlauf, R. (2002). Role of the isthmus and FGFs in resolving the paradox of neural crest plasticity and prepatternning. *Science* **295**, 1288-1291. doi:10.1126/science.1064540
- Tsujino, K., Okuzaki, Y., Hibino, N., Kawamura, K., Saito, S., Ozaki, Y., Ishishita, S., Kuroiwa, A., Iijima, S., Matsuda, Y. et al. (2019). Identification of transgene integration site and anatomical properties of fluorescence intensity in a EGFP transgenic chicken line. *Dev. Growth Differ.* **61**, 393-401. doi:10.1111/dgd.12631
- Tucker, R. P. (2001). Abnormal neural crest cell migration after the in vivo knockdown of tenascin-C expression with morpholino antisense oligonucleotides. *Dev. Dyn.* **222**, 115-119. doi:10.1002/dvdy.1171
- Utvik, J. K., Nja, A. and Gundersen, K. (1999). DNA injection into single cells of intact mice. *Hum. Gene Ther.* **10**, 291-300. doi:10.1089/10430349950019075
- van de Lavoie, M.-C., Diamond, J. H., Leighton, P. A., Mather-Love, C., Heyer, B. S., Bradshaw, R., Kerchner, A., Hooi, L. T., Gessaro, T. M., Swanberg, S. E. et al. (2006a). Germline transmission of genetically modified primordial germ cells. *Nature* **441**, 766-769. doi:10.1038/nature04831
- van de Lavoie, M.-C., Mather-Love, C., Leighton, P., Diamond, J. H., Heyer, B. S., Roberts, R., Zhu, L., Winters-Digiacinto, P., Kerchner, A., Gessaro, T. et al. (2006b). High-grade transgenic somatic chimeras from chicken embryonic stem cells. *Mech. Dev.* **123**, 31-41. doi:10.1016/j.mod.2005.10.002
- Vandenbroucke, R. E., Lucas, B., Demeester, J., De Smedt, S. C. and Sanders, N. N. (2007). Nuclear accumulation of plasmid DNA can be enhanced by non-selective gating of the nuclear pore. *Nucleic Acids Res.* **35**, e86. doi:10.1093/nar/gkm440
- Wang, H., Bonnet, A., Delfini, M. C., Kawakami, K., Takahashi, Y. and Duprez, D. (2011). Stable, conditional, and muscle-fiber-specific expression of electroporated transgenes in chick limb muscle cells. *Dev. Dyn.* **240**, 1223-1232. doi:10.1002/dvdy.22498
- Watanabe, T., Saito, D., Tanabe, K., Suetsugu, R., Nakaya, Y., Nakagawa, S. and Takahashi, Y. (2007). Tet-on inducible system combined with in ovo electroporation dissects multiple roles of genes in somitogenesis of chicken embryos. *Dev. Biol.* **305**, 625-636. doi:10.1016/j.ydbio.2007.01.042
- Wen, S., Zhang, H., Li, Y., Wang, N., Zhang, W., Yang, K., Wu, N., Chen, X., Deng, F., Liao, Z. et al. (2014). Characterization of constitutive promoters for piggyBac transposon-mediated stable transgene expression in mesenchymal stem cells (MSCs). *PLoS ONE* **9**, e94397. doi:10.1371/journal.pone.0094397
- Williams, R. M., Senanayake, U., Artibani, M., Taylor, G., Wells, D., Ahmed, A. A. and Sauka-Spengler, T. (2018). Genome and epigenome engineering CRISPR toolkit for in vivo modulation of cis-regulatory interactions and gene expression in the chicken embryo. *Development* **145**, dev160333. doi:10.1242/dev.160333
- Woronowicz, K. C., Gline, S. E., Herfat, S. T., Fields, A. J. and Schneider, R. A. (2018). FGF and TGFbeta signaling link form and function during jaw development and evolution. *Dev. Biol.* **444** Suppl. 1, S219-S236. doi:10.1016/j.ydbio.2018.05.002
- Wu, C. Y. and Taneyhill, L. A. (2019). Cadherin-7 mediates proper neural crest cell-placodal neuron interactions during trigeminal ganglion assembly. *Genesis* **57**, e23264. doi:10.1002/dvg.23264
- Wu, S. C.-Y., Meir, Y.-J. J., Coates, C. J., Handler, A. M., Pelczar, P., Moisyadi, S. and Kaminski, J. M. (2006). piggyBac is a flexible and highly active transposon as compared to sleeping beauty, Tol2, and Mos1 in mammalian cells. *Proc. Natl. Acad. Sci. USA* **103**, 15008-15013. doi:10.1073/pnas.0606979103
- Xia, X., Zhang, Y., Ziehl, C. R. and Zhang, S.-C. (2007). Transgenes delivered by lentiviral vector are suppressed in human embryonic stem cells in a promoter-dependent manner. *Stem Cells Dev.* **16**, 167-176. doi:10.1089/scd.2006.0057
- Yang, C. Q., Li, X. Y., Li, Q., Fu, S. L., Li, H., Guo, Z. K., Lin, J. T. and Zhao, S. T. (2014). Evaluation of three different promoters driving gene expression in developing chicken embryo by using in vivo electroporation. *Genet. Mol. Res.* **13**, 1270-1277. doi:10.4238/2014.February.27.12
- Yeo, N. C., Chavez, A., Lance-Byrne, A., Chan, Y., Menn, D., Milanova, D., Kuo, C.-C., Guo, X., Sharma, S., Tung, A. et al. (2018). An enhanced CRISPR repressor for targeted mammalian gene regulation. *Nat. Methods* **15**, 611-616. doi:10.1038/s41592-018-0048-5
- Yin, W., Xiang, P. and Li, Q. (2005). Investigations of the effect of DNA size in transient transfection assay using dual luciferase system. *Anal. Biochem.* **346**, 289-294. doi:10.1016/j.ab.2005.08.029
- Yokota, Y., Saito, D., Tadokoro, R. and Takahashi, Y. (2011). Genomically integrated transgenes are stably and conditionally expressed in neural crest cell-specific lineages. *Dev. Biol.* **353**, 382-395. doi:10.1016/j.ydbio.2011.02.001
- Young, J. L., Benoit, J. N. and Dean, D. A. (2003). Effect of a DNA nuclear targeting sequence on gene transfer and expression of plasmids in the intact vasculature. *Gene Ther.* **10**, 1465-1470. doi:10.1038/sj.gt.3302021
- Yuan, Y.-W. and Wessler, S. R. (2011). The catalytic domain of all eukaryotic cut-and-paste transposase superfamilies. *Proc. Natl. Acad. Sci. USA* **108**, 7884-7889. doi:10.1073/pnas.1104208108
- Yusa, K. (2015). piggyBac Transposon. *Microbiol. Spectr.* **3**, MDNA3-0028-2014. doi:10.1128/microbiolspec.MDNA3-0028-2014
- Yusa, K., Zhou, L., Li, M. A., Bradley, A. and Craig, N. L. (2011). A hyperactive piggyBac transposase for mammalian applications. *Proc. Natl. Acad. Sci. USA* **108**, 1531-1536. doi:10.1073/pnas.1008322108
- Zhou, X., Vink, M., Klaver, B., Berkhout, B. and Das, A. T. (2006). Optimization of the Tet-On system for regulated gene expression through viral evolution. *Gene Ther.* **13**, 1382-1390. doi:10.1038/sj.gt.3302780

Developmental Cell

Engineered Tissue Folding by Mechanical Compaction of the Mesenchyme

Graphical Abstract



Authors

Alex J. Hughes, Hikaru Miyazaki, Maxwell C. Coyle, ..., Richard A. Schneider, Ophir D. Klein, Zev J. Gartner

Correspondence

zev.gartner@ucsf.edu

In Brief

A key challenge for tissue engineering is to harness the organizational principles that generate complex tissue topography *in vivo*. Hughes et al. find that mesenchymal compaction processes are sufficient to generate curvature at tissue interfaces and develop a framework to engineer curvature trajectories of reconstituted tissues via patterns of mesenchymal condensates.

Highlights

- Mesenchymal condensation involves myosin II-dependent compaction of ECM
- Reconstituted condensates compact ECM and drive curvature at tissue interfaces
- Finite element modeling of condensation mechanics predicts tissue folding patterns
- Arrays of condensates encode complex curvature profiles of reconstituted tissues



Hughes et al., 2018, *Developmental Cell* 44, 165–178
 January 22, 2018 © 2017 Elsevier Inc.
<https://doi.org/10.1016/j.devcel.2017.12.004>

CellPress

Engineered Tissue Folding by Mechanical Compaction of the Mesenchyme

Alex J. Hughes,^{1,2,11} Hikaru Miyazaki,^{1,3,4} Maxwell C. Coyle,⁵ Jesse Zhang,^{1,3,9} Matthew T. Laurie,⁶ Daniel Chu,⁷ Zuzana Vavrušová,⁷ Richard A. Schneider,⁷ Ophir D. Klein,^{4,10} and Zev J. Gartner^{1,2,3,8,12,*}

¹Department of Pharmaceutical Chemistry, University of California, San Francisco, CA 94143, USA

²Center for Cellular Construction, University of California, San Francisco, CA 94143, USA

³Graduate Program in Bioengineering, University of California, Berkeley, CA, USA

⁴Program in Craniofacial Biology and Department of Orofacial Sciences, University of California, San Francisco, CA 94143, USA

⁵Department of Molecular and Cell Biology, University of California, Berkeley, CA 94720, USA

⁶Department of Biochemistry and Molecular Biology, University of California, San Francisco, CA 94143, USA

⁷Department of Orthopaedic Surgery, University of California, San Francisco, CA 94143, USA

⁸Chan Zuckerberg Biohub, San Francisco, CA 94158, USA

⁹Department of Bioengineering and Therapeutic Sciences, University of California, San Francisco, CA 94143, USA

¹⁰Department of Pediatrics and Institute for Human Genetics, University of California, San Francisco, CA 94143, USA

¹¹Present address: Department of Bioengineering, University of Pennsylvania, Philadelphia, PA, USA

¹²Lead Contact

*Correspondence: zev.gartner@ucsf.edu

<https://doi.org/10.1016/j.devcel.2017.12.004>

SUMMARY

Many tissues fold into complex shapes during development. Controlling this process *in vitro* would represent an important advance for tissue engineering. We use embryonic tissue explants, finite element modeling, and 3D cell-patterning techniques to show that mechanical compaction of the extracellular matrix during mesenchymal condensation is sufficient to drive tissue folding along programmed trajectories. The process requires cell contractility, generates strains at tissue interfaces, and causes patterns of collagen alignment around and between condensates. Aligned collagen fibers support elevated tensions that promote the folding of interfaces along paths that can be predicted by modeling. We demonstrate the robustness and versatility of this strategy for sculpting tissue interfaces by directing the morphogenesis of a variety of folded tissue forms from patterns of mesenchymal condensates. These studies provide insight into the active mechanical properties of the embryonic mesenchyme and establish engineering strategies for more robustly directing tissue morphogenesis *ex vivo*.

INTRODUCTION

Engineered tissues have applications in basic sciences, drug testing, and regenerative medicine (Bajaj et al., 2014; Clevers, 2016; Huch et al., 2017). A key challenge for tissue engineers is to build or grow tissues *in vitro* that reproducibly incorporate key structural motifs of the corresponding tissue *in vivo* (Gjorevski et al., 2016; Huh et al., 2010; Lancaster and Knoblich, 2014; Lancaster et al., 2017; Warmflash et al., 2014). Tissue folds are a

widespread and crucially important structural motif because they contribute to tissue function in adults. However, the trajectory of folding during development also contributes to changes in the detailed structure of a tissue, through processes such as cell identity specification and the emergence of anisotropies in the distribution of cells and extracellular matrix (ECM) fibers (Kim et al., 2015; Li et al., 2017; Shyer et al., 2015). Thus, the gross folded form of a tissue as well as the trajectory of tissue folding can both be important for mature tissue function.

While tissue folding *in vivo* can be highly reproducible and robust (Nelson, 2016; Savin et al., 2011), folding remains difficult to reconstitute or control *in vitro* (Huch et al., 2017; Li et al., 2017; Varner and Nelson, 2014b). For example, many popular organoid models can faithfully reproduce epithelial architecture and composition across tens to hundreds of micrometers, but the size and shape of folded architectures can vary considerably from organoid to organoid, particularly over larger length scales (Huch et al., 2017; Takebe et al., 2015). Folding is difficult to control *in vitro* because it emerges from spatially patterned cell dynamics that span micro- to millimeter scales. Moreover, folding is critically reliant on boundary conditions and often requires interactions between more than one tissue layer (Nelson, 2016; Gladman et al., 2016). In principle, engineers could guide the formation of folds from simpler structures by combining top-down engineering with the intrinsic self-organizing properties of cells and ECM. According to this strategy, engineers would use top-down tools to define the initial conditions of a culture (Qi et al., 2013; Wang et al., 2017; Zhang and Khademhosseini, 2017) and then leverage the autonomous cellular processes underlying tissue self-organization to drive folding along a single trajectory.

To implement such a strategy for engineering the formation of precisely folded tissues, we considered the physical mechanisms through which folding occurs in living systems. Folds form when initially planar regions of tissue bend or buckle to form more complex 3D shapes. Here, the concave surface of a tissue layer experiences negative strain (reduction in dimension)



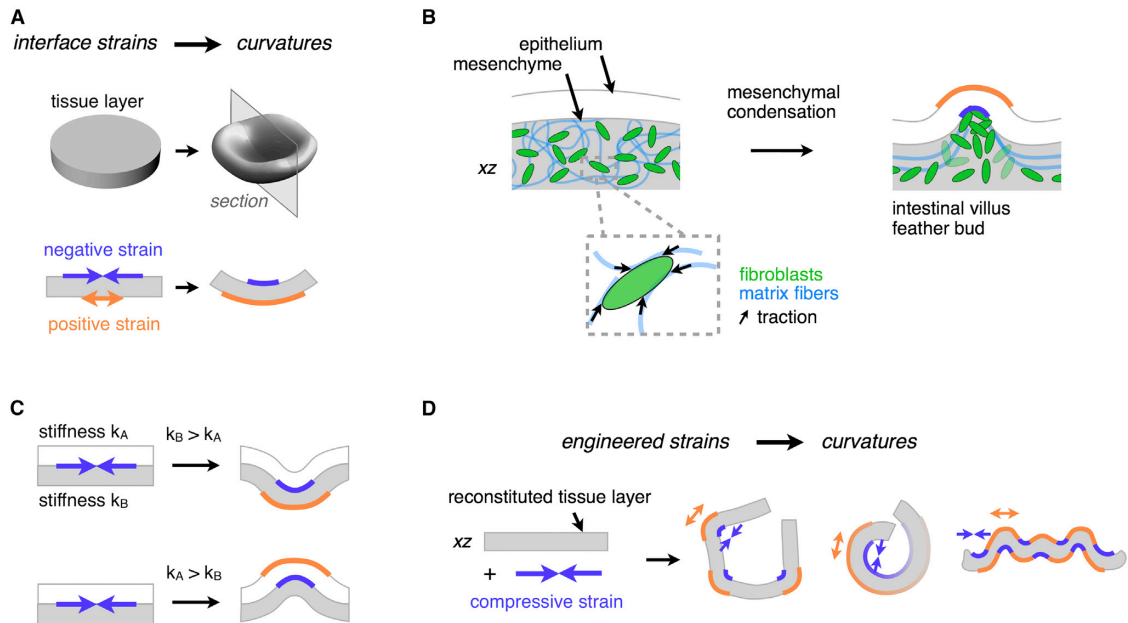


Figure 1. Tissue Folding Requires Patterns of Negative and Positive Strain at Tissue Interfaces

(A) Curvature at tissue interfaces is associated with a decrease in length (negative strain) at concave interfaces and an increase in length (positive strain) at convex interfaces.

(B) Traction forces generated by mesenchymal cells on ECM at the epithelial-mesenchymal interface could account for strains that drive curvature in the intestinal villus and avian feather bud.

(C) Negative strain at the interface between two tissue layers can drive invagination or evagination according to the relative bending stiffnesses of the adhered layers (see also Figure S1).

(D) Patterns of mesenchymal condensates could be mapped to corresponding patterns of tissue strains, creating a programmable approach to engineered folding of reconstituted tissues.

and the convex surface experiences positive strain (increase in dimension), Figure 1A (Timoshenko and Woinowsky-Krieger, 1959). Negative and positive strains are perceived by cells as a net compression or stretching of the surrounding tissue, respectively. Tissue folding derives from a mismatch in strains between two adjacent tissue layers, which in vertebrate embryos are often an epithelium and the underlying ECM in a loose connective tissue layer known as the mesenchyme (Hay, 2013). The requisite strains arise in response to stresses (force per unit cross-sectional area) accumulated during developmental processes that can be generated in wildly different ways. For example, compressive or tensile stresses can act across entire organ systems to generate patterns of folding through buckling processes (Nelson, 2016; Shyer et al., 2013), or they can act across smaller regions of a tissue, for example, when smaller groups of cells proliferate or exert cytoskeletal forces locally against surrounding tissue (Kim et al., 2015; Mammoto et al., 2013; Odell et al., 1981; Panousopoulou and Green, 2016; Wen et al., 2017). While both classes of folding are in principle amenable to engineering, we focused on mechanisms that act at the level of local cell-generated forces. These mechanisms are readily integrated with top-down patterning technologies such as optogenetics, micromolding, and printing approaches that control cellular and ECM tissue composition at specific locations (Bhattacharjee

et al., 2015; Hinton et al., 2015; Miller et al., 2012; Oakes et al., 2017; Stevens et al., 2013; Warmflash et al., 2014).

In order to identify cellular processes that could be used to direct tissue folding downstream of patterning technologies, we looked to developmental systems where the pattern of folding is tightly linked to patterns of cell dynamics. For example, the patterns of folds that emerge during the morphogenesis of feathers (Eames and Schneider, 2005; Jiang et al., 1999; Wessells and Evans, 1968) and mouse gut villi (Walton et al., 2012) are both spatially and temporally coupled to corresponding patterns of cellular condensates in the neighboring mesenchyme (Figure 1B). In particular, experiments using explants of the developing mouse intestine suggest that mesenchymal condensates forming at the epithelial-mesenchymal interface contribute to the early stages of the folding of the gut to form villi, because they can be physically isolated from surrounding tissue without disrupting the initiation of local folds (Walton et al., 2016b). Similar observations have also been made for feather bud formation during culture of chick skin (Davidson, 1983), and recent reports indicate that the patterning of condensates in the chick skin is also tightly coupled to the mechanics of a compacting mesenchyme (Shyer et al., 2017). We therefore hypothesized that mechanical strains sufficient to produce local curvature at these interfaces could be generated directly by mesenchymal

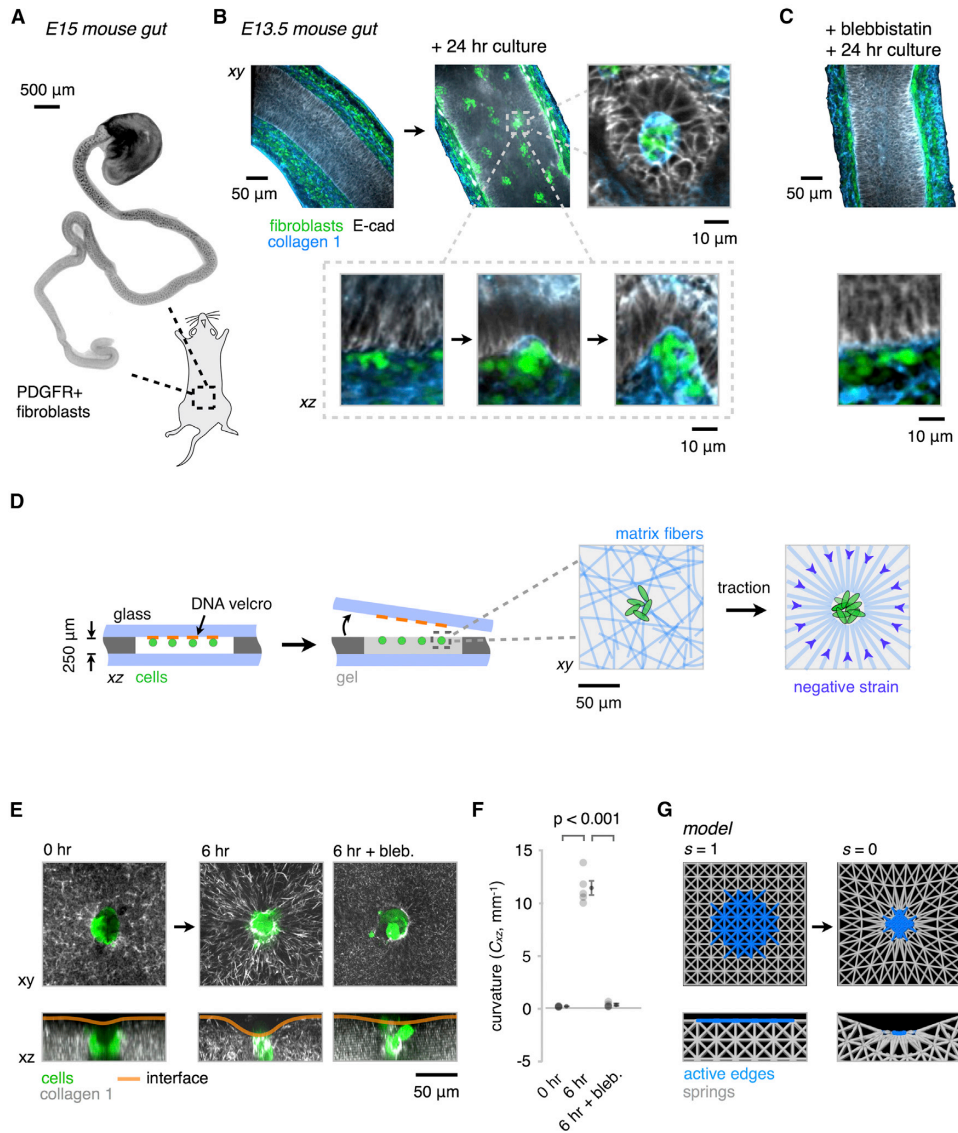


Figure 2. Signatures of Mesenchymal Condensation in the Mouse Gut and Their Reconstitution *In Vitro* and *In Silico*

(A) Whole-mount wide-field fluorescence microscopy image of the embryonic day 15 (E15) mouse intestine showing PDGFR+ fibroblast clusters forming in an anterior to posterior wave.

(B) Optical sections from whole-mount confocal immunofluorescence images showing PDGFR+ cells (green) and collagen I fibers (blue) in E13.5 explants cultured for 0 or 24 hr *in vitro*. Detail shows intermediate stages of PDGFR+ cluster formation against the basal surface of the epithelium (E-cadherin, gray), along the wave of condensation. Successive stages of cluster formation show progressive collagen I accumulation and localized curvature at the basal surface of the epithelium (see also Figure S2).

(C) Intestine explant cultures as in (B) show reduced cell clustering, collagen I accumulation, and interface curvature in the presence of 30 μM blebbistatin (a myosin II inhibitor). See Figures S2A–S2C for further quantitation.

(D) Schematic of reconstitution strategy using DNA-programmed assembly of cells (DPAC) to build loose clusters of mesenchymal cells near the surface of ECM gels containing collagen I and Matrigel. Detail at right illustrates the hypothesized traction-mediated compaction and alignment of ECM fibers around cell clusters.

(legend continued on next page)

condensation, since local tissue mechanical properties change at the site of condensation (Mammoto et al., 2011; Shyer et al., 2017). In this model, invagination (inward bending) or evagination (outward bending) would arise from the relative stiffness of the two conjoined layers (Oster and Alberch, 1982). Folding would occur away from the material with the higher bending modulus (Figures 1C and S1), which may frequently be the epithelial layer, given that these tissues are often pre-stressed due to a combination of forces both intrinsic and extrinsic to the tissue (Inger, 2006).

Here, we develop an engineering framework for guiding autonomous tissue folding along prescribed trajectories by using patterns of mesenchymal condensates to program corresponding patterns of strains into slabs of ECM gels (Figure 1D). We begin by providing evidence that cell dynamics associated with mesenchymal condensation can bend nearby epithelial-mesenchymal interfaces. Specifically, we observe that mesenchymal condensation in the developing mouse intestine and chick skin is associated with non-muscle myosin II-dependent compaction of the collagenous ECM. This compaction is associated with alignment of nearby collagen fibers and tissue interface curvature. To provide evidence that condensate formation through a mechanical compaction of the mesenchyme is sufficient to direct tissue folding, we use an *in vitro* reconstitution approach. Reconstituted condensates generate similar patterns of aligned collagen and interface curvature. We perform quantitative measurements relating initial cell patterns to tissue strains and interface curvatures. These observations are supported by folding trajectories predicted through linear finite element modeling. Finally, we utilize this system to drive the folding of complex 3D structures that mimic *in vivo*-relevant and other, more stylized folding motifs.

RESULTS

Signatures of Mesenchymal Condensation Mechanics

We sought to identify patterns of cell dynamics that could be leveraged to drive folding of reconstituted tissues. We first focused on embryonic villus formation in the mouse gut. Previous reports suggest that condensates in the embryonic intestine are tightly associated with the folding of the epithelial-mesenchymal interface (Walton et al., 2012, 2016b). Consistent with these reports, we found that folding initiated in the mouse gut at the basal surface of the epithelium and was tightly associated with the appearance of clusters of PDGFR+ mesenchymal fibroblasts. Collagen I accumulated around these PDGFR+ foci during folding. Importantly, cell condensation, collagen accumulation, and tissue folding were blocked by treatment with blebbistatin, an inhibitor of myosin II activity (Figures 2A–2C and S2A–S2C). Blebbistatin also blocked feather bud formation and curvature in chick skin (Figures S2D–S2H). These observa-

tions are consistent with a role for mechanical condensation of the mesenchyme along the epithelial-mesenchymal interface in driving the folding of nearby tissue interfaces. They further suggest that if reconstituted *in vitro*, the mechanics of the condensation process could be leveraged to direct the local folding of tissue interfaces.

In Vitro Reconstitution of Mesenchymal Condensation Mechanics

To more rigorously investigate whether the cell dynamics observed *in vivo* were sufficient to direct tissue folding, as would be necessary to place the folding process under engineering control, we reconstituted a simulacrum of the mesenchymal-epithelial tissue interface, devoid of the overlying epithelium. We used a 3D cell-patterning technology called DNA-programmed assembly of cells (DPAC) to prepare loose clusters of GFP-expressing mouse embryonic fibroblasts (MEFs) positioned just below the surface of 250- μm -thick slabs of fluorescently labeled collagen I in Matrigel (Figure 2D) (Todhunter et al., 2015). We attached these slabs to glass coverslips and tracked cell and ECM dynamics within them using time-lapse confocal microscopy. Previous studies have shown that cells in these types of gels generate traction forces that strain and align matrix fibers (Baker et al., 2015; Harris et al., 1981; Sawhney and Howard, 2002; Vader et al., 2009). Consistent with these reports, MEF clusters compacted over 6 hr in culture, concentrating fluorescently labeled collagen near the cluster surface, and producing patterns of radially aligned collagen fibers in their local microenvironment (Figures 2E and S3A–S3E, Movie S1). Examination of the gel-media interface revealed local curvature and invagination of the ECM gel proximal to the condensing MEFs. This curvature motif was similar, but of opposite polarity, to that seen in the mouse gut, possibly due to the absence of a stiff overlying epithelium. Indeed, culture of MEF clusters at the interface between two gel layers of different modulus resulted in the reproducible folding of the interface toward the more compliant layer (Figure S1). As in the intestinal gut explants, cluster compaction, collagen alignment, and interfacial curvature were inhibited by treatment with blebbistatin (Figures 2E and 2F). These observations suggest that key features of condensation can be reconstituted *in vitro* and that condensates themselves could act as mechanical actuators of tissue interface curvature (Oster et al., 1983). Indeed, a two-parameter finite element model (FEM) consisting of an isotropic contractile node within a grid of unit cells constructed from elastic springs captured aspects of elastic edge (ECM fiber) compaction, alignment, and interface invagination seen in the *in vivo* and *in vitro* systems (Figure 2G).

ECM compaction and cell motility have both been implicated in mesenchymal cell condensation (Mammoto et al., 2011; Oster et al., 1983). While both processes could contribute to

(E) GFP-expressing MEF clusters (green) were patterned in AF555-labeled collagen I-containing gels (gray) as in (D). Live confocal microscopy of condensing clusters and collagen I reveals ECM compaction, radial collagen I fiber alignment, and the emergence of curvature of the gel-medium interface (see also Figure S3). These phenomena are blocked by treatment with 30 μM blebbistatin (bleb.).

(F) Quantification of the interfacial curvatures proximal to the condensates shown in (E) (mean \pm SEM, $n = 5$, one-way ANOVA with Holm-Sidak's multiple comparisons test).

(G) Snapshots from a finite element model containing passive elastic elements (gray) and active edges (blue) whose lengths can be reduced to simulate local gel strains by cell clusters.

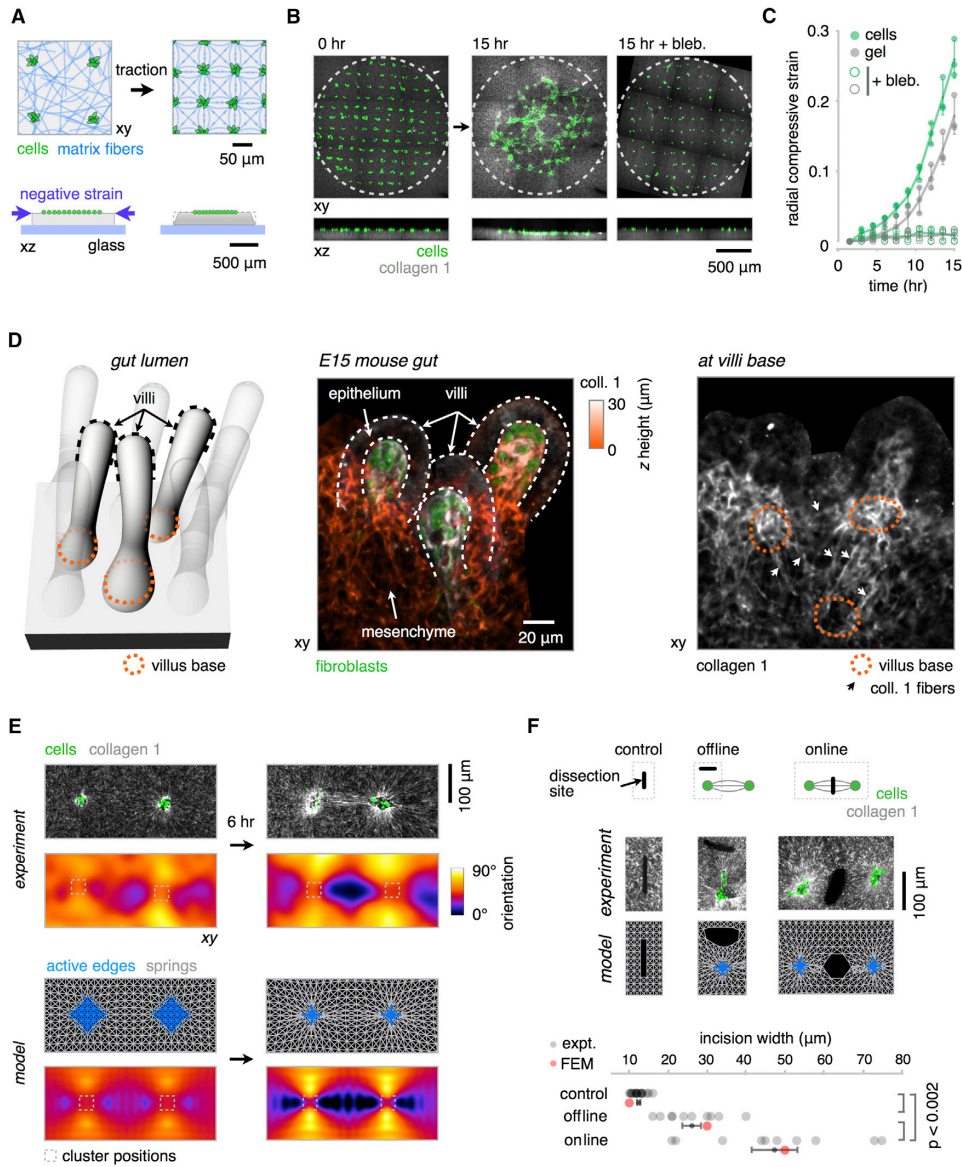


Figure 3. Mechanical Coupling between Mesenchymal Condensates *In Vivo* and *In Vitro*

(A) Schematic for measuring cell migration and ECM compaction contributions to reconstituted tissue condensation. A grid of GFP-expressing MEF clusters (green) is patterned just below the surface of a gel containing collagen I (gray), and the motion of fluorescent collagen fibers and cells is tracked by time-lapse confocal microscopy.

(B) Maximum intensity projections and xz sections from a representative time-lapse confocal microscopy experiment showing (left) untreated MEF cluster grid (green) and AF555-labeled collagen I (gray) converging toward a central focus over 15 hr (middle) and in the presence of 30 μM blebbistatin (bleb.; right). The dotted lines mark the initial spatial extent of the grid.

(C) Quantification of the data in (B), showing radial strain of the cell grid (green) and ECM (gray) in the presence and absence of 30 μM blebbistatin (mean \pm SEM, $n = 3$).

(D) (Left) Schematic illustrating the developing mouse intestine shown in the images to the right. Dark dotted lines indicate the location of three villi “caps,” and orange dotted lines indicate the position of three villi bases. (Center) Immunofluorescence image of the embryonic day 15 (E15) mouse intestine showing three representative villi as in the diagram to the left. Data are shown as a maximum intensity projection of labeled collagen I fibers within these villi, color coded

(legend continued on next page)

condensation, ECM compaction among them could account for strains at nearby tissue interfaces sufficient to explain their folding. To evaluate the relative contribution of cell motility and ECM compaction to the condensation process *in vitro*, we prepared circular grids of closely spaced MEF clusters at the ECM surface using DPAC (Figure 3A). MEFs in this configuration condense radially into aggregates over short periods of time in culture. Condensation occurs in a manner that resembles cell motility, which could also be interpreted as a mechanical compaction of the ECM. To distinguish between these two scenarios, we measured the radial strain (shrinkage) of the cell grid by tracking individual cells, and of the surrounding ECM by tracking fluorescent collagen I fibers dispersed in the underlying matrix (Figure 3B). We found that as the cell grid condensed toward a central focus, the radial strain observed in the reference frame of the cells is largely accounted for by the strain observed in the compacting underlying ECM fibers (compare gray and green curves in Figure 3C). Further, the strain in both the cell and the ECM reference frames was abolished by inhibiting myosin II with blebbistatin. These data are consistent with a model wherein reconstituted cell condensates act as mechanical actuators by compacting the surrounding ECM and imposing local strains at tissue interfaces.

Strain Engineering among Mechanically Coupled Arrays of Condensates

Condensates occur in arrays in a variety of embryonic systems, where they can become mechanically coupled through networks of aligned ECM fibers. For example, we observed distinct patterns of collagen alignment between adjacent feather buds in chick skin (confirming previous reports; Stuart and Moscona, 1967; Figure S2H) and additionally observed aligned collagen fibers spanning the basal plane of nascent villi in the developing mouse intestine (Figure 3D). We hypothesized that these regions of aligned matrix fibers were a consequence of the condensation process and were under elevated tension. We reasoned that if similar patterns could be reconstituted *in vitro* without the physical constraints found *in vivo*, they could be used to coordinate tissue folding over much larger distances and into complex 3D geometries.

To explore the mechanical coupling between networks of condensates, we used DPAC to prepare pairs of loose MEF clusters at set distances from one another. As the paired clusters condensed and remodeled the surrounding ECM over 6 hr, collagen fibers were initially radially aligned around each condensate and then formed regions of amplified collagen fiber alignment (“straps”) along the axis between them (Figures 3E and S4A–S4E). These straps were similar to the aligned collagen tracts seen in chick and mouse tissues (Figures 3D and S2,

Movie S2) (Sawhney and Howard, 2002). An FEM simulation of this process qualitatively captured the same pattern of aligned elastic elements between nodes and suggested that these regions coincided with higher tensile stresses relative to regions having less strongly aligned collagen fibers. To evaluate whether straps were under elevated tension compared with other regions of the gel, we mapped the local distribution of forces around interacting condensates by measuring recoil of the ECM surface upon cutting. Biophysical studies suggest that regions of gel under elevated tensile stresses should undergo a damped elastic recoil in proportion to the local tension orthogonal to the incision (Bonnet et al., 2012; Kumar et al., 2006; Legoff et al., 2013) (see Method Details in the STAR Methods). Indeed, in both experiments and the FEM, significantly greater recoil of the gel surface occurred upon ablation with a focused UV laser at straps in comparison with regions having only radially aligned collagen or with control regions distant from condensate pairs (Figure 3F). These data suggest that nearby condensates are mechanically coupled and can promote the alignment of collagen fibers along their axes of interaction. Moreover, the data suggest that these aligned collagen fibers are under elevated tension compared with the surrounding tissue.

From an engineering perspective, the same phenomena that drive changes in curvature around individual cell clusters could be harnessed to program the curvature of deformable tissue interfaces across considerably larger distances. In such a scenario, the positions and density of condensing mesenchymal cells would determine tension patterns borne by aligned collagen straps. Without physical constraints on the geometry of the gel, these tensions would drive patterns of interfacial strains, thereby having a direct, predictable, and reproducible relationship with the final folded architecture of the tissue. However, implementing such a strategy would require that straps among patterned condensates formed in a predictable pattern, for example, between nearest neighbors, similar to the patterns observed among feather buds in the developing chick.

We explored how networks of condensates mechanically couple by studying the relationship between the initial pattern of interacting condensates and the resulting pattern of force-transmitting collagen straps. We again used DPAC to place loose clusters of MEFs in either isotropic grids (with the same densities along the horizontal and vertical axes, ρ_x and ρ_y) or anisotropic grids (unequal ρ_x and ρ_y) at the surface of ECM gels adhered to the culture surface. We found that collagen straps formed preferentially between nearest neighbor clusters as they condense, with closely spaced clusters forming straps more rapidly than sparsely spaced clusters (Figures 4A and S4C). Straps persisted in orientation for as long as neighboring aggregates did not merge with each other during the

according to their height in the confocal stack. PDGFR+ fibroblast clusters (green) are also shown. (Right) One section from the base of the stack illustrating regions of collagen I alignment (white arrows) around villi bases (orange dotted lines).

(E) (Top) GFP-expressing MEF clusters (green) were patterned using DPAC at fixed distances within a gel containing collagen I (gray). Collagen alignment is evident after 6 hr; the pixel-wise angle of average orientation was used to generate the heatmaps below each microscopy image (see also Figure S4). (Bottom) Qualitatively similar patterns of elastic edge alignment (gray) were observed between contractile nodes (blue) in the finite element model (FEM).

(F) (Top) Schematic of an assay for retraction of the gel surface after laser ablation in three regions around pairs of interacting condensates. (Middle, top) Confocal micrographs of gel surface in three corresponding regions after cutting with a UV laser. (Middle, bottom) Similar views from a 2D FEM with simulated cuts. (Bottom) Qualitatively similar retraction behavior in the FEM implies that collagen straps bear greater tension than the less aligned regions of the gel (mean \pm SEM, $n > 9$ incisions per group, one-way ANOVA with Holm-Sidak’s multiple comparisons test).

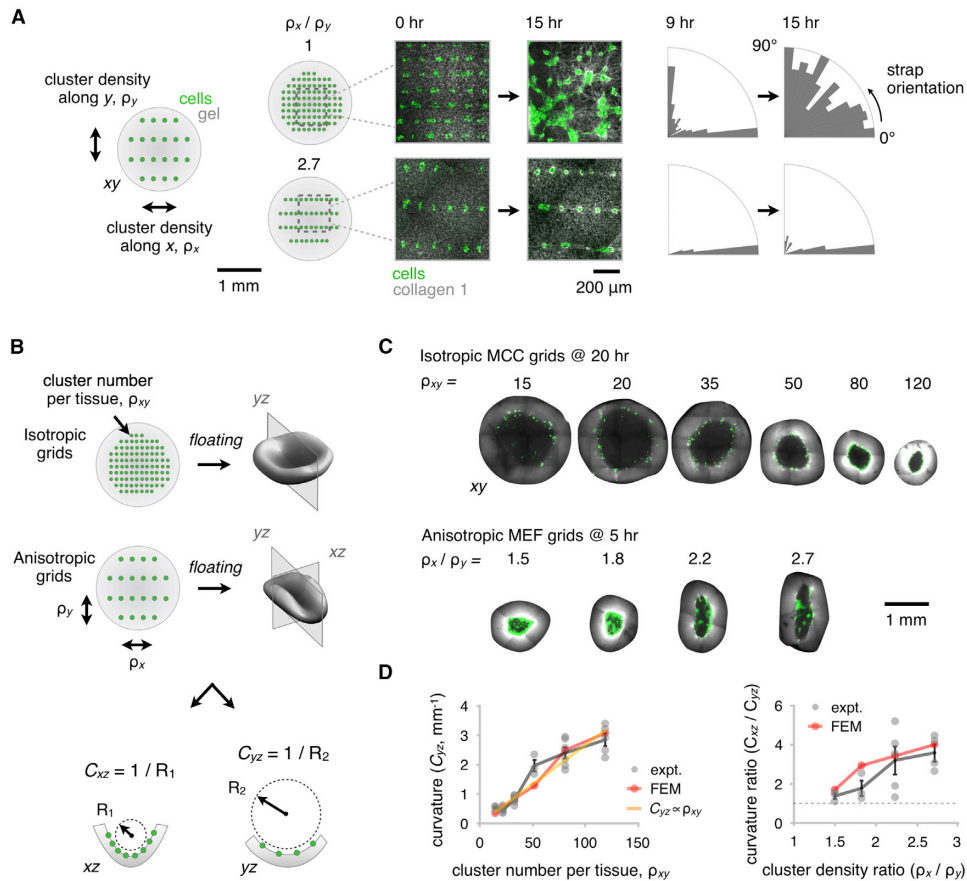


Figure 4. Patterns of Condensates Mechanically Couple over Large Distances and Quantitatively Encode the Trajectory of Tissue Curvature

(A) (Left) Isotropic and anisotropic grids of GFP-expressing MEF clusters (green) were patterned using DPAC into gels containing AF555-labeled collagen I (gray), adhered to a glass substrate, and imaged using time-lapse confocal microscopy. The densities of clusters along the horizontal and vertical axes are denoted ρ_x and ρ_y , respectively. The emergence of collagen straps (center) was observed over 9 to 15 hr (see also Figure S5). (Right) Radial bar charts illustrating the alignment of tension-bearing straps relative to the horizontal axis at 9 and 15 hr. Straps extend only between nearest neighbors in the vertical and horizontal directions, until later time points when the clusters begin to merge.

(B) Schematic depicting how curvature is measured in the xz and yz planes of floating gels containing either isotropic cell cluster grids (with cell cluster number per tissue ρ_{xy}) or anisotropic grids.

(C) Representative confocal microscopy sections through the mid-plane of invaginating reconstituted tissues patterned with different total cluster densities and combinations of densities in the horizontal and vertical directions. Graded patterns of curvature emerge for the indicated density and anisotropy of cell clusters. MCC, mammary carcinoma cell.

(D) Curvature measurements for the experimental data shown in (C). (Left) Curvature as a function of total cluster density and (right) curvature anisotropy as a function of anisotropy in cluster density along x and y . These data constitute quantitative calibration relationships (mean \pm SEM, $n > 2$ per grid geometry) that parameterize a finite element model (FEM) relating “blueprint” patterns of contractile nodes to folding trajectories of reconstituted tissues.

condensation process, suggesting that the spatial pattern of forces imposed at reconstituted tissue interfaces could be predictably encoded by the geometry of initial MEF cluster positions.

Engineering Control of Interfacial Curvature in Reconstituted Tissues

Given that strains at tissue interfaces can be relieved by out-of-plane buckling (Armon et al., 2011), we hypothesized that grids of

condensing MEFs would drive reconstituted tissue folding if they were released from the geometric constraints imposed by the glass substrate. We therefore studied the global curvatures of MEF grids placed at the surface of free-floating, rather than substrate-anchored, ECM gels (Figure 4B). We found that gels followed predictable trajectories as they underwent morphogenesis from planar to curved 3D geometries. Specifically, gel layers carrying grids of loose cell clusters formed radially symmetric invaginations (Figure 4C). Moreover, by patterning a range of cell

types with different contractile properties, we found that the initial curvature rates of the invaginating gels were proportional to the rates at which the cells strained the surrounding ECM, with curvature dynamics spanning timescales of ~ 5 to >40 hr (Figures S5A–S5F).

We chose relatively slower-folding reconstituted tissues bearing isotropic grids of mesenchymal-like mammary carcinoma cells (MCCs) to enable detailed measurement of the temporal dynamics of folding by confocal microscopy, as we were unable to capture the rapid folding dynamics of isotropic MEF tissues at higher cluster numbers using confocal microscopy. We found that the gel curvature C at a given time point increased approximately linearly with the cell cluster number per tissue (ρ_{xy} , Figures 4C and 4D). The experimental C versus ρ_{xy} data were adequately fit by both a proportional scaling relationship describing bending induced by constant strain-rate actuators (Holmes et al., 2011; Timoshenko and Woinowsky-Krieger, 1959) ($R^2 = 0.8$, see Method Details in STAR Methods) and by a 3D implementation of our FEM. We additionally found that the emergence of curvature coincided with extensive and irreversible gel remodeling since pre-folded tissues unfolded by less than 40% upon inducing apoptosis of cells using staurosporine (Figures S5G and S5H).

Beyond radially symmetric invaginations, we predicted that anisotropic grids of MEF clusters having a greater density along the horizontal relative to the vertical axis ($\rho_x > \rho_y$) would program a fold running vertically, since tension-bearing collagen straps would be concentrated along the more densely packed horizontal axis. Indeed, anisotropic MEF grids consistently folded gels along the expected axis, and curvature anisotropy in x and y was approximately proportional to cluster density anisotropy (Figures 4C and 4D). Surprisingly, identical grids actuated by less contractile and more migratory MCCs did not form controlled anisotropic folds along a predictable axis (Figure S5I). We found that the ratio of folding rate to cell migration rate for a given condensing cell type was critical in determining the fidelity with which anisotropic folds could be specified, because rapidly migrating cells quickly scramble the initial cluster pattern imposed by DPAC (see Method Details in STAR Methods, Figures S5J and S5K).

We continued to explore the generality and robustness with which different patterns of mesenchymal condensates could encode the morphogenesis of reconstituted tissues into a variety of complex 3D folding motifs (Figures 5, S6, and Movie S3). These included the isotropic and anisotropic motifs already discussed, as well as a compound curvature motif (spatially graded curvature) and an opposing curvature motif (neighboring tissue regions with curvatures of opposite polarity, Figure S6A). We first elaborated the anisotropic folding motif to generate a coiled tissue conceptually similar to several biological forms, including the looping of the small intestine. To drive coiling, we placed anisotropic grids of MEF clusters at a 45° angle to the long axis of a rectangular ECM substrate, encoding a partially enclosed helical shape with a pitch of 1 mm and radius of $200 \mu\text{m}$ (with comparable values of 1.2 mm and $220 \mu\text{m}$ in a member of the corresponding FEM family; Figures 5A, 5B, S6B, and S6C).

Tubular structures are ubiquitous in the body, where ducts and vessels serve to carry fluids within and among organ systems.

We reasoned that we could roll a tube from an initially planar sheet by combining anisotropic and compound curvature motifs. Specifically, a gradient in curvature along the horizontal axis was encoded using MEF clusters patterned horizontally with log-distributed spacings from 80 to $250 \mu\text{m}$, each row being set apart by $300 \mu\text{m}$ along the vertical axis (Movie S4). The folded tube was hollow along its entire length, with an inner diameter of $550 \mu\text{m} \pm 9\%$ CV lengthwise ($555 \mu\text{m} \pm 4\%$ by FEM).

A number of tissues incorporate neighboring folds with opposing polarity. For example, the folds of the cerebral cortex and developing chick gut pass through intermediates having a locally zigzag architecture in which three folds of positive curvature and another of negative curvature converge at a point. We reconstructed this pattern by incorporating an opposing curvature motif into a four-fold vertex shape (Movie S5). We found that these more complex opposing fold patterns were surprisingly robust to errors in cell patterning. More specifically, folding was robust to “pop-through” defects so long as the cluster densities encoding adjacent folds were comparable (see Method Details in STAR Methods, Figures S7A–S7C).

The folding of flat surfaces into 3D shapes has fundamental physical constraints, since “non-developable” surfaces that are curved in more than one direction at a given location require that the material stretch or compress (Modes et al., 2010). Residual stresses not relieved by deformations in the material can lead to unintended folding outcomes (Armon et al., 2011; Kim et al., 2012). *In vivo*, these residual stresses could be relieved by additional out-of-plane buckling, or by in-plane changes in cell shape, size, intercalation geometry, proliferation, or ECM compaction (Humphrey and Dufresne, 2014; Legoff et al., 2013). Indeed, when we prepared a non-developable fold consisting of two adjacent isotropic folding motifs of opposite polarity in a single ECM gel, local folds emerged as expected, but additional buckling events occurred, consistent with the FEM-predicted accumulation of unresolved in-plane stresses (Figures S6D and S6E). In such cases, targeted modification of tissue boundary conditions by strategic cutting of surfaces prior to folding can enable the construction of more complex shapes without additional non-programmed buckling events, for example, spherical and cubic tissues (as in the kirigami art form) (Sussman et al., 2015; Zhang et al., 2015). We built both tissue architectures using laser microdissection of gel substrates prior to folding (Figures 5C, 5D, S6F, and S6G), in the latter case relying on anisotropic curvature at cube creases to actuate folding.

Finally, we combined anisotropic, compound, and opposing curvature motifs to generate a corrugation of pitch 1.6 mm and amplitude $130 \mu\text{m}$ (1.6 mm and $115 \mu\text{m}$ by FEM; Figures 5E, 5F, S6H, and S6I). These corrugated objects model periodic curvature patterns seen *in vivo*, for example, at the dermal-epidermal junction in the skin, in the trachea, and in a transient folding pattern of the luminal surface of the chick gut (Shyer et al., 2013).

Reconstituting Tissues with Multiple Cell Types and Tessellated Curvature Motifs

The process of morphogenesis often results in the tessellation of architectural motifs, such as the repeated copies of nephrons in the kidney and the alveoli of the lung. We reasoned that

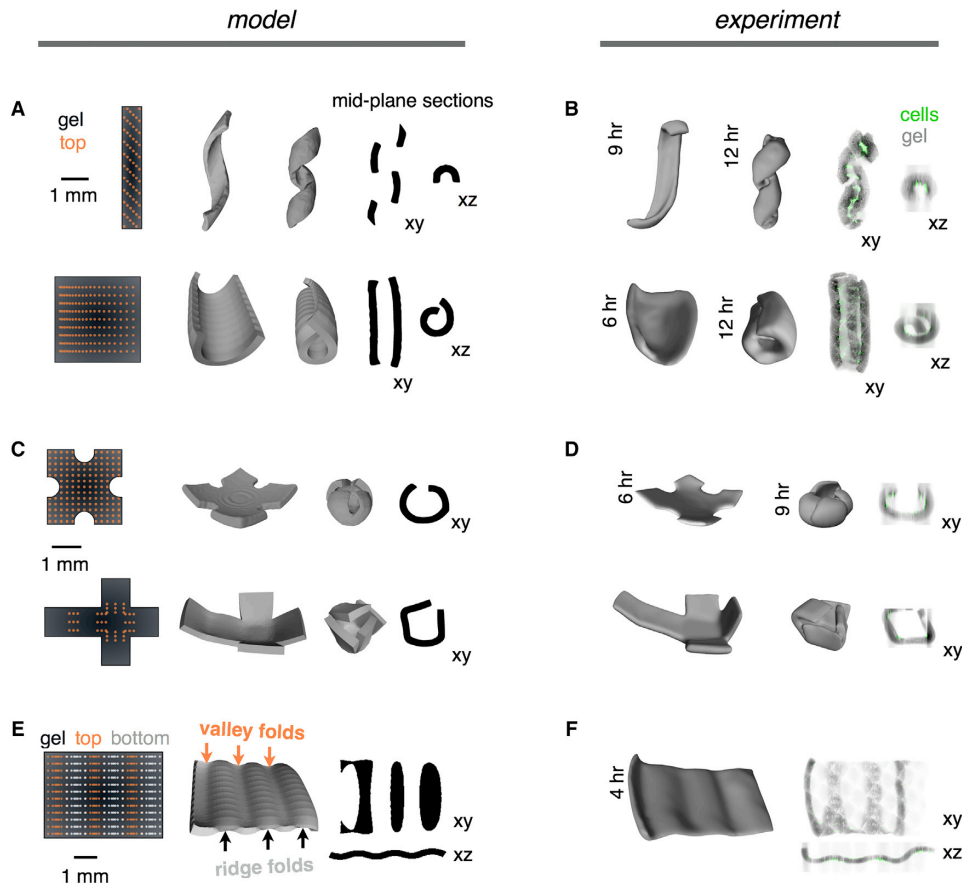


Figure 5. Networks of Mechanically Active Mesenchymal Condensates Program the Autonomous Folding of Diverse 3D Tissue Architectures

(A) (Left) DPAC blueprints of MEF cluster positions in x and y for a coiled object (top) and rolled tube object (bottom). (Center) Snapshots from the FEM showing intermediates along the predicted folding trajectories. (Right) Mid-plane sections from the FEM snapshots (see also Figure S6). (B) Shell surfaces and mid-plane sections of reconstituted tissues corresponding to the model objects in (A) at two imaging time points. Shell surfaces were reconstructed from confocal micrographs (MEFs, green; AF555-labeled collagen I, gray). (C and D) Spherical and cubic FEM objects and corresponding reconstituted tissues, imaged and analyzed as in (A) and (B). (E) (Left) DPAC blueprint encoding an opposing curvature motif incorporates MEF clusters on both the top (orange) and the bottom (white) surfaces of the gel. (Center) FEM showing predicted opposing ridge and valley folds, and (right) mid-plane sections. (F) Shell surface and mid-plane sections of a reconstituted tissue corresponding to the model in (E).

the simple folding patterns described above could be tiled as repeating subunits to construct reconstituted tissue architectures of even greater size and complexity. Inspired by the zigzag-shaped luminal surface of the embryonic day 13–16 (E13–16) chick gut (Shyer et al., 2013), we sought to engineer a similar pattern of folding but through an entirely different mechanism directed by mesenchymal condensates rather than global tissue buckling. We therefore designed a tessellation of the four-fold junction analogous to the Miura origami fold (Figure 6A). The Miura fold has several unusual geometric features, including the capability to be fit generically to complex target surfaces (Dudte et al., 2016). Finite element modeling of the Miura design predicted a folding trajectory with similarity to the folding pattern

of the chick gut, but directed by cell-generated forces of an entirely synthetic design (Figure 6B; Movie S4B). Consistent with the model, the reconstituted Miura tissue autonomously emerged from a 6×8 mm flat sheet to a 4×6 mm zigzag structure at 15 hr with all 31 folds having the correct orientation and similar periodicity and amplitude to those in the FEM.

A remarkable aspect of tissue folding processes during development is that curvature trajectories are generally robust, even within microenvironments with complex cellular compositions (Nelson, 2016; Savin et al., 2011). Such robustness would also be important for engineering tissue folding, particularly when incorporating the additional cell types necessary to build a functional tissue. We therefore tested the robustness of

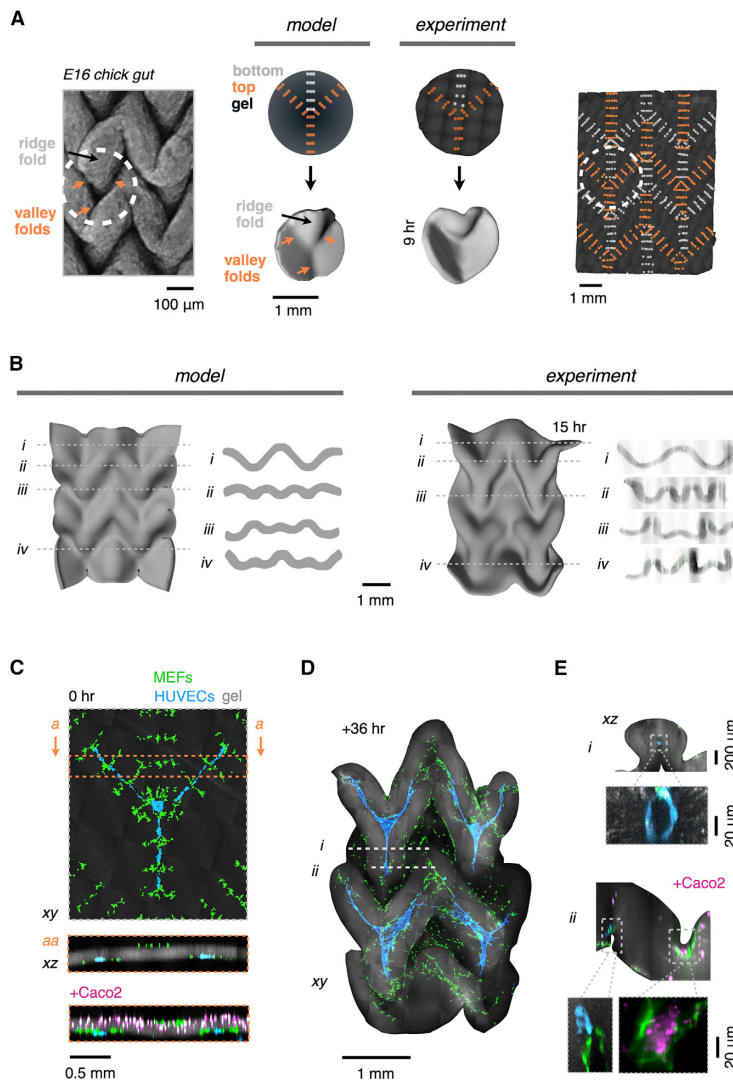


Figure 6. Mesenchymal Condensates Drive the Autonomous Folding of Tesselated Tissue Patterns Incorporating Multiple Cell Types

(A) (Left) Macro-confocal micrograph of ethidium bromide-stained embryonic day 16 (E16) chick gut lumen exhibiting a tessellated four-fold vertex pattern that incorporates three valley folds (arrows) and one ridge fold converging on a single point (see also Figure S7). (Middle) FEM and as-printed DPAC blueprints, FEM snapshot, and shell surface of a reconstituted four-fold vertex tissue (AF555-labeled collagen I in gel, dark gray). (Right) As-printed DPAC blueprint encoding a tessellated architecture similar to the chick gut lumen and Miura origami fold.

(B) (Left) FEM snapshot and cross sections of the Miura object. (Right) Shell surface and cross sections of the corresponding reconstituted tissue after 15 hr *in vitro*.

(C) Confocal micrographs and sections showing the DPAC output for a Miura folding pattern as in (B), but incorporating human umbilical vein endothelial cells (HUVECs) patterned as three-pronged cords at programmed folds and/or Caco2 cells distributed uniformly at the top surface of the gel. (D) Maximum intensity confocal projection of the folded architecture of HUVEC-containing gel after 36 hr in culture.

(E) (Top, *i*) Representative confocal cross sections of the object in (D) showing lumenized HUVEC cords enveloped by Miura folds and (bottom, *ii*) Caco2 cells in a different HUVEC-containing Miura tissue deposited as in (C, bottom). Caco2 cell clusters form atop contractile fibroblasts within concave folds.

juxtaposition with condensing mesenchyme raised the intriguing possibility that the behavior of passenger cells themselves would be altered by the dynamics of the surrounding tissue architecture as it folded over the course of the experiment (Mammoto et al., 2013; Shyer et al., 2015).

To test these hypotheses, we patterned multiple cell types in reconstituted tissues directed to fold into the Miura pattern previously described (Figures 6C–6E, S7E, and S7F; Movie S6). Three-pronged HUVEC cords were positioned underneath incipient folds; while Caco2 cells (a colon carcinoma cell line) were deposited on top by embedding them uniformly near the tissue surface. We found that the folded shapes of these passenger cell-laden Miura tissues were similar to those predicted by FEM, confirming that the properties of the condensing MEFs dominated folding trajectories (Figures 6B and 6D). We additionally found that HUVEC migration was biased along incipient folds, suggesting that emerging tissue topography and ECM compaction induced by tissue folding feed back on the behavior of passenger cells (Figures S7G and S7H). At later time points, the HUVEC cords became fully encapsulated within the zigzag folds and were lumenized across 100- to 200- μ m tracts after

mesenchymal condensation-driven folding in reconstituted tissues incorporating other cell types as “passengers.” We reasoned that a given folding trajectory predicted by FEM would not be disrupted if the rate of strain that passenger cells induced on their surrounding ECM was significantly lower than that of condensing mesenchymal cells. We therefore screened seven cell types for their ability to contract ECM droplets, finding that MEFs and primary human mammary fibroblasts contracted the ECM at a much higher rate than other common cell types, including endothelial and epithelial lines (Figure S7D). These data suggested that the latter cell types, themselves critical components of most tissues, would not interfere with folding trajectories dominated by the properties of the mesenchyme. In addition, our ability to include additional cell types in

36 hr. Finally, we found that Caco2 cells, which form 3D cysts in Matrigel (Ivanov et al., 2008), became concentrated at the base of valley folds on top of the network of fibroblasts. This completely synthetic folded architecture had a gross similarity to the developing small intestine (Walton et al., 2016a), indicating that mesenchymal compaction of the ECM may represent a general strategy for engineering folds into tissues with complex cellular compositions.

DISCUSSION

Animal development involves the stepwise elaboration of tissue structure at multiple length scales. Each step of morphogenesis acts upon and remodels the architecture formed in preceding steps. Thus, tissues are inherently imprinted with a developmental history that contributes to the anisotropy in their ECM, cell shape, and topography—architectural features that are critical for sculpting local cell-fate decisions and for directing subsequent self-organization processes that determine tissue function (Brownfield et al., 2013; Cerchiarì et al., 2015; Engler et al., 2006). Mesenchymal condensation is an example of a core vertebrate developmental program underlying this imprinting process, acting at key steps of development in multiple tissues to remodel the topography, ECM anisotropy, and ECM density at the interface of the epithelium and mesenchyme (Kim et al., 2015; Li et al., 2015; Mammoto et al., 2013; Oster et al., 1983; Walton et al., 2012). The events that coincide with the emergence of curvature during mesenchymal condensation are complex, involving changes in both the mechanics and the paracrine signaling microenvironment between multiple cellular components in each layer (Eames and Schneider, 2005; Varner and Nelson, 2014a; Walton et al., 2012). Recent evidence suggests a role for mechanics in the pattern of condensate formation in developing chick skin and possibly the mouse gut (Shyer et al., 2017; Walton et al., 2016a, 2016b). However, the contribution of cell mechanics during condensation in directing the initiation of tissue curvature has not been studied in detail, a process that is often hypothesized to be driven by forces generated by epithelial cell behaviors such as migration, localized growth, or shape change (Lecuit et al., 2011; Panousopoulou and Green, 2016). We find that in the context of a loose and fibrous ECM composite, the mechanics and dynamics of condensing mesenchymal cells are sufficient to explain a variety of shape transitions in nearby tissue interfaces. In these cases, the mesenchyme behaves like an active composite material, with cells straining and compacting the ECM, aligning ECM fibers between regions of compaction, and encoding forces in the material along regions of maximum fiber alignment. These forces lead to bending of the material at tissue interfaces along trajectories that can be predicted using finite element modeling. While additional experiments will be necessary to demonstrate that the mechanics of condensate formation directly act to initiate tissue folding in the gut and other systems, our experiments suggest a framework from which to investigate these processes.

Importantly, the predictable relationship between strain and curvature observed in these cell-ECM composites allowed us to program the autonomous folding of tissues into a variety of 3D architectures bearing striking similarity to structures found *in vivo*, as well as into entirely novel geometries. The folding pro-

cess is analogous to the autonomous folding of abiotic materials into complex shapes (Cangialosi et al., 2017; Holmes et al., 2011; Kim et al., 2012; Na et al., 2014; Gladman et al., 2016; Tallinen et al., 2016). Moreover, the self-organizing and dynamic properties of a mesenchymal cell-ECM composite bear striking similarity to phenomena observed in reconstituted actomyosin networks (Köster et al., 2016; Linsmeier et al., 2016), suggesting these active materials may adhere to common physical principles.

Our finite element modeling approach has several characteristic limitations, including simple, arbitrary boundary conditions of either floating or anchored vertices, elastic material properties, and a coarse spatial resolution suited to tracking overall tissue shape rather than matrix mechanics at the scale of individual cells or matrix fibers. Despite these simplifications, it broadly captures local curvature phenomena observed in our reconstituted tissue models, allowing an iterative approach to the “forward problem” of mapping local cell cluster mechanics to tissue shape at a millimeter-centimeter scale. One key aspect of our model is that it does not invoke any physical property of overlying tissue layers, such as an epithelium. However, it predicts that these properties would affect the magnitude and polarity of tissue folding. Here, reconstituted tissues and FEMs treat the overlying material as having negligible bending modulus. Thus, a condensation near the upper surface of reconstituted tissues always forms a region of concave curvature, and we leverage this idea to pattern complex folds by placing condensing cells at either the upper or lower surface of an ECM slab. However, if the overlying material has a higher bending modulus than the mesenchyme, modeling predicts an inversion of the curvature direction, converting an invagination into an evagination (Figure S1). Indeed, our preliminary experiments with MEF clusters placed at the interface between adhered gel layers of different stiffness confirm this (Figure S1). The model further suggests a coincident lateral compaction of the overlying layer during a condensation event, forming a placode-like structure (Oster and Alberch, 1982). These studies leave open an intriguing possibility: that paracrine signaling originating in the mesenchyme could serve to set the mechanical properties of an overlying epithelium, thereby determining the direction and magnitude of folding during a condensation event *in vivo*. Such a view of mesenchymal-epithelial interaction could explain how different combinations of epithelium and mesenchyme transition to markedly different tissue architectures through an interplay between tissue mechanics and paracrine signaling. Combined with the established roles of the epithelium in tissue buckling, our results suggest that a combination of mechanically active tissue components could collaborate to initiate and reinforce the pattern, polarity, and magnitude of tissue folding (Hirashima, 2014; Lecuit et al., 2011; Nelson, 2016; Odell et al., 1981; Oster and Alberch, 1982; Savin et al., 2011; Shyer et al., 2013; Tallinen et al., 2016; Varner et al., 2015). These possibilities warrant further investigation.

Apart from its relevance to developmental biology, our study raises the possibility that dynamic control over both the material and physical properties of cell-ECM composites is readily achievable. In this view, building tissues *de novo* is a 4D process where initial tissue structures and boundary conditions are assembled in 3D but evolve in time across multiple length scales

according to specific developmental principles, converging ultimately on a new 3D structure with more defined and life-like structural features. This approach could significantly improve the structure, maturation, and vascularization of organoid tissue models at mesoscale (Lancaster and Knoblich, 2014; Takebe et al., 2015) and should be incorporated as a design criterion for 3D printed tissues. We believe these efforts have important implications for the engineering of *in vitro* models of disease, for regenerative medicine, and for future applications of living active materials such as in soft robotics.

STAR★METHODS

Detailed methods are provided in the online version of this paper and include the following:

- KEY RESOURCES TABLE
- CONTACT FOR REAGENT AND RESOURCE SHARING
- EXPERIMENTAL MODEL AND SUBJECT DETAILS
 - Animals
 - Cell Lines
- METHOD DETAILS
 - Cell Treatments
 - Reconstituted Tissue Fabrication
 - Adhered-Layer Tissues and Stiffness
 - Droplet Contraction
 - Measuring ECM Gel Strain by Single Cells
 - Collagen Fiber and Strap Orientation Analysis
 - Laser Ablation of ECM Gel
 - Reconstituted Tissue Imaging
 - Spatial Reconstruction of Tissues from Images
 - Example Immunofluorescence Protocol
 - Mouse Gut Explant Culture and Immunostaining
 - Chick Gut Explants
 - Chick Skin Explants
 - Finite Element Modeling
 - Inferring Tension from Local Retraction after Ablation in Reconstituted Tissues
 - Scaling Analysis of Isotropic Reconstituted Tissue Curvature
 - Fidelity of Anisotropic Folds
 - Robustness of Adjacent Opposing Folds to Pop-Through
- QUANTIFICATION AND STATISTICAL ANALYSIS
- DATA AND SOFTWARE AVAILABILITY

SUPPLEMENTAL INFORMATION

Supplemental Information includes seven figures and six movies and can be found with this article online at <https://doi.org/10.1016/j.devcel.2017.12.004>.

ACKNOWLEDGMENTS

We thank J. Liu, A. Paulson, C. Krishnamurthy, J. Farlow, M. LaBarge, and J. Debnath for providing reagents and cells; M. Chung for technical assistance with chick gut dissection and imaging; A. Long and S. Dumont for discussion and assistance with laser ablation studies; and A. Cerchiarì, M. Thompson, and J. Spence for critical discussion. This work was funded by a Jane Coffin Childs postdoctoral fellowship to A.J.H., NIH grants R01 DE016402 and S10 OD021664 to R.A.S., the Department of Defense Breast Cancer Research Program (W81XWH-10-1-1023 and W81XWH-13-1-0221 to Z.J.G.), the NIH

Common Fund (DP2 HD080351-01 to Z.J.G.), the Chan-Zuckerberg Biohub Investigator Program (to Z.J.G.), the NSF (MCB-1330864 to Z.J.G.), the UCSF Program in Breakthrough Biomedical Research, and the UCSF Center for Cellular Construction (DBI-1548297), an NSF Science and Technology Center.

AUTHOR CONTRIBUTIONS

A.J.H. and Z.J.G. conceived the project. A.J.H. built reconstituted tissues. A.J.H. and M.T.L. imaged and characterized reconstituted tissue morphology. A.J.H. and J.Z. developed finite element models. M.C.C. did gel contraction assays. A.J.H. and H.M. did mouse gut assays. A.J.H., D.C., and Z.V. did chick skin and gut assays. R.A.S. and O.D.K. assisted with experiment design. All authors analyzed data and wrote the manuscript.

DECLARATION OF INTERESTS

A.J.H. and Z.J.G. are inventors on intellectual property related to engineered tissue folding.

Received: July 15, 2017

Revised: September 22, 2017

Accepted: December 1, 2017

Published: December 28, 2017

REFERENCES

- Armon, S., Efrati, E., Kupferman, R., and Sharon, E. (2011). Geometry and mechanics in the opening of chiral seed pods. *Science* 333, 1726–1730.
- Bajaj, P., Schweller, R.M., Khademhosseini, A., West, J.L., and Bashir, R. (2014). 3D biofabrication strategies for tissue engineering and regenerative medicine. *Annu. Rev. Biomed. Eng.* 16, 247–276.
- Baker, B.M., Trappmann, B., Wang, W.Y., Sakar, M.S., Kim, I.L., Shenoy, V.B., Burdick, J.A., and Chen, C.S. (2015). Cell-mediated fibre recruitment drives extracellular matrix mechanosensing in engineered fibrillar microenvironments. *Nat. Mater.* 14, 1262–1268.
- Bender, J., Müller, M., Otaduy, M.A., Teschner, M., and Macklin, M. (2014). A survey on position-based simulation methods in computer graphics. *Comput. Graph. Forum* 33, 228–251.
- Bhattacharjee, T., Zehnder, S.M., Rowe, K.G., Jain, S., Nixon, R.M., Sawyer, W.G., and Angelini, T.E. (2015). Writing in the granular gel medium. *Sci. Adv.* 1, e1500655.
- Bonnet, I., Marcq, P., Bosveld, F., Fetler, L., Bellaïche, Y., and Graner, F. (2012). Mechanical state, material properties and continuous description of an epithelial tissue. *J. R. Soc. Interface* 9, 2614–2623.
- Brownfield, D.G., Venugopalan, G., Lo, A., Mori, H., Tanner, K., Fletcher, D.A., and Bissell, M.J. (2013). Patterned collagen fibers orient branching mammary epithelium through distinct signaling modules. *Curr. Biol.* 23, 703–709.
- Cangialosi, A., Yoon, C., Liu, J., Huang, Q., Guo, J., Nguyen, T.D., Gracias, D.H., and Schulman, R. (2017). DNA sequence-directed shape change of photopatterned hydrogels via high-degree swelling. *Science* 357, 1126–1130.
- Cerchiarì, A.E., Garbe, J.C., Jee, N.Y., Todhunter, M.E., Broaders, K.E., Pehel, D.M., Desai, T.A., LaBarge, M.A., Thomson, M., and Gartner, Z.J. (2015). A strategy for tissue self-organization that is robust to cellular heterogeneity and plasticity. *Proc. Natl. Acad. Sci. USA* 112, 2287–2292.
- Clevers, H. (2016). Modeling development and disease with organoids. *Cell* 165, 1586–1597.
- Davidson, D. (1983). The mechanism of feather pattern development in the chick. 1. The time of determination of feather position. *J. Embryol. Exp. Morphol.* 74, 245–259.
- Debnath, J., Muthuswamy, S.K., and Brugge, J.S. (2003). Morphogenesis and oncogenesis of MCF-10A mammary epithelial acini grown in three-dimensional basement membrane cultures. *Methods* 30, 256–268.
- Dudte, L.H., Vouga, E., Tachi, T., and Mahadevan, L. (2016). Programming curvature using origami tessellations. *Nat. Mater.* 15, 583–588.

- Eames, B.F., and Schneider, R.A. (2005). Quail-duck chimeras reveal spatio-temporal plasticity in molecular and histogenic programs of cranial feather development. *Development* 132, 1499–1509.
- Engler, A.J., Sen, S., Sweeney, H.L., and Discher, D.E. (2006). Matrix elasticity directs stem cell lineage specification. *Cell* 126, 677–689.
- Gjorevski, N., Sachs, N., Manfrin, A., Giger, S., Bragina, M.E., Ordóñez-Morán, P., Clevers, H., and Lutolf, M.P. (2016). Designer matrices for intestinal stem cell and organoid culture. *Nature* 539, 560–564.
- Gladman, A.S., Matsumoto, E.A., Nuzzo, R.G., Mahadevan, L., and Lewis, J.A. (2016). Biomimetic 4D printing. *Nat. Mater.* 15, 413–418.
- Hamilton, T.G., Klinghoffer, R.A., Corrin, P.D., and Soriano, P. (2003). Evolutionary divergence of platelet-derived growth factor alpha receptor signaling mechanisms. *Mol. Cell. Biol.* 23, 4013–4025.
- Harris, A.K., Stopak, D., and Wild, P. (1981). Fibroblast traction as a mechanism for collagen morphogenesis. *Nature* 290, 249–251.
- Hatch, J., and Mukoyama, Y. (2015). Spatiotemporal mapping of vascularization and innervation in the fetal murine intestine. *Dev. Dyn.* 244, 56–68.
- Hay, E.D. (2013). *Cell Biology of Extracellular Matrix* (Springer Science & Business Media).
- Hinton, T.J., Jallerat, Q., Palchesko, R.N., Park, J.H., Grodzicki, M.S., Shue, H.J., Ramadan, M.H., Hudson, A.R., and Feinberg, A.W. (2015). Three-dimensional printing of complex biological structures by freeform reversible embedding of suspended hydrogels. *Sci. Adv.* 1, e1500758.
- Hirashima, T. (2014). Pattern formation of an epithelial tubule by mechanical instability during epididymal development. *Cell Rep.* 9, 866–873.
- Holmes, D.P., Roché, M., Sinha, T., and Stone, H.A. (2011). Bending and twisting of soft materials by non-homogenous swelling. *Soft Matter* 7, 5188–5193.
- Huch, M., Knoblich, J.A., Lutolf, M.P., and Martinez-Arias, A. (2017). The hope and the hype of organoid research. *Development* 144, 938–941.
- Huh, D., Matthews, B.D., Mammoto, A., Montoya-Zavala, M., Hsin, H.Y., and Ingber, D.E. (2010). Reconstituting organ-level lung functions on a chip. *Science* 328, 1662–1668.
- Humphrey, J.D., and Dufresne, E.R. (2014). Mechanotransduction and extracellular matrix homeostasis. *Nat. Rev. Mol. Cell Biol.* 15, 802–812.
- Ingber, D.E. (2006). Cellular mechanotransduction: putting all the pieces together again. *FASEB J.* 20, 811–827.
- Ivanov, A.I., Hopkins, A.M., Brown, G.T., Gerner-Smidt, K., Babbin, B.A., Parkos, C.A., and Nusrat, A. (2008). Myosin II regulates the shape of three-dimensional intestinal epithelial cysts. *J. Cell Sci.* 121, 1803–1814.
- Jiang, T.X., Jung, H.S., Widelitz, R.B., and Chuong, C.M. (1999). Self-organization of periodic patterns by dissociated feather mesenchymal cells and the regulation of size, number and spacing of primordia. *Development* 126, 4997–5007.
- Kim, H.Y., Pang, M.F., Varner, V.D., Kojima, L., Miller, E., Radisky, D.C., and Nelson, C.M. (2015). Localized smooth muscle differentiation is essential for epithelial bifurcation during branching morphogenesis of the mammalian lung. *Dev. Cell* 34, 719–726.
- Kim, J., Hanna, J.A., Byun, M., Santangelo, C.D., and Hayward, R.C. (2012). Designing responsive buckled surfaces by halftone gel lithography. *Science* 335, 1201–1205.
- Köster, D.V., Husain, K., Iljazi, E., Bhat, A., Bieling, P., Mullins, R.D., Rao, M., and Mayor, S. (2016). Actomyosin dynamics drive local membrane component organization in an in vitro active composite layer. *Proc. Natl. Acad. Sci. USA* 113, E1645–E1654.
- Kumar, S., Maxwell, I.Z., Heisterkamp, A., Polte, T.R., Lele, T.P., Salanga, M., Mazur, E., and Ingber, D.E. (2006). Viscoelastic retraction of single living stress fibers and its impact on cell shape, cytoskeletal organization, and extracellular matrix mechanics. *Biophys. J.* 90, 3762–3773.
- Lancaster, M.A., and Knoblich, J.A. (2014). Organogenesis in a dish: modeling development and disease using organoid technologies. *Science* 345, 1247125.
- Lancaster, M.A., Corsini, N.S., Wolfinger, S., Gustafson, E.H., Phillips, A.W., Burkard, T.R., Otani, T., Livesey, F.J., and Knoblich, J.A. (2017). Guided self-organization and cortical plate formation in human brain organoids. *Nat. Biotechnol.* 35, 659–666.
- Lecuit, T., Lenne, P.F., and Munro, E. (2011). Force generation, transmission, and integration during cell and tissue morphogenesis. *Annu. Rev. Cell Dev. Biol.* 27, 157–184.
- Legoff, L., Rouault, H., and Lecuit, T. (2013). A global pattern of mechanical stress polarizes cell divisions and cell shape in the growing *Drosophila* wing disc. *Development* 140, 4051–4059.
- Li, J., Feng, J., Liu, Y., Ho, T.V., Grimes, W., Ho, H.A., Park, S., Wang, S., and Chai, Y. (2015). BMP-SHH signaling network controls epithelial stem cell fate via regulation of its niche in the developing tooth. *Dev. Cell* 33, 125–135.
- Li, Y., Muffat, J., Omer, A., Bosch, I., Lancaster, M.A., Sur, M., Gehrke, L., Knoblich, J.A., and Jaenisch, R. (2017). Induction of expansion and folding in human cerebral organoids. *Cell Stem Cell* 20, 385–396.e3.
- Linsmeier, I., Banerjee, S., Oakes, P.W., Jung, W., Kim, T., and Murrell, M.P. (2016). Disordered actomyosin networks are sufficient to produce cooperative and telescopic contractility. *Nat. Commun.* 7, 12615.
- Liu, J.S., Farlow, J.T., Paulson, A.K., LaBarge, M.A., and Gartner, Z.J. (2012). Programmed cell-to-cell variability in Ras activity triggers emergent behaviors during mammary epithelial morphogenesis. *Cell Rep.* 2, 1461–1470.
- Mammoto, T., Mammoto, A., and Ingber, D.E. (2013). Mechanobiology and developmental control. *Annu. Rev. Cell Dev. Biol.* 29, 27–61.
- Mammoto, T., Mammoto, A., Torisawa, Y.-S., Tat, T., Gibbs, A., Derda, R., Mannix, R., de Bruijn, M., Yung, C.W., Huh, D., et al. (2011). Mechanochemical control of mesenchymal condensation and embryonic tooth organ formation. *Dev. Cell* 21, 758–769.
- Meshel, A.S., Wei, Q., Adelstein, R.S., and Sheetz, M.P. (2005). Basic mechanism of three-dimensional collagen fibre transport by fibroblasts. *Nat. Cell Biol.* 7, 157–164.
- Miller, J.S., Stevens, K.R., Yang, M.T., Baker, B.M., Nguyen, D.-H.T., Cohen, D.M., Toro, E., Chen, A.A., Galle, P.A., Yu, X., et al. (2012). Rapid casting of patterned vascular networks for perfusable engineered three-dimensional tissues. *Nat. Mater.* 11, 768–774.
- Modes, C.D., Bhattacharya, K., and Warner, M. (2010). Gaussian curvature from flat elastica sheets. *Proc. R. Soc. A Math. Phys. Eng. Sci.* 467, 1121–1140.
- Na, J.H., Evans, A.A., Bae, J., Chiappelli, M.C., Santangelo, C.D., Lang, R.J., Hull, T.C., and Hayward, R.C. (2014). Programming reversibly self-folding origami with micropatterned photo-crosslinkable polymer trilayers. *Adv. Mater.* 27, 79–85.
- Nelson, C.M. (2016). On buckling morphogenesis. *J. Biomech. Eng.* 138, 021005.
- Oakes, P.W., Wagner, E., Brand, C.A., Probst, D., Linke, M., Schwarz, U.S., Glotzer, M., and Gardel, M.L. (2017). Optogenetic control of RhoA reveals zyxin-mediated elasticity of stress fibres. *Nat. Commun.* 8, 15817.
- Odell, G.M., Oster, G., Alberch, P., and Burnside, B. (1981). The mechanical basis of morphogenesis. I. Epithelial folding and invagination. *Dev. Biol.* 85, 446–462.
- Oster, G., and Alberch, P. (1982). Evolution and bifurcation of developmental programs. *Evolution* 36, 444–459.
- Oster, G.F., Murray, J.D., and Harris, A.K. (1983). Mechanical aspects of mesenchymal morphogenesis. *J. Embryol. Exp. Morphol.* 78, 83–125.
- Panousoyopoulou, E., and Green, J.B.A. (2016). Invagination of ectodermal placodes is driven by cell intercalation-mediated contraction of the suprabasal tissue canopy. *PLoS Biol.* 14, e1002405.
- Püspöki, Z., Storath, M., Sage, D., and Unser, M. (2016). Transforms and operators for directional bioimage analysis: a survey. In *Focus on Bio-Image Informatics*, W.H. De Vos, S. Munck, and J.-P. Timmermans, eds. (Springer), pp. 69–93.
- Qi, H., Ghodousi, M., Du, Y., Grun, C., Bae, H., Yin, P., and Khademhosseini, A. (2013). DNA-directed self-assembly of shape-controlled hydrogels. *Nat. Commun.* 4, 2275.

- Savin, T., Kurpios, N.A., Shyer, A.E., Florescu, P., Liang, H., Mahadevan, L., and Tabin, C.J. (2011). On the growth and form of the gut. *Nature* **476**, 57–62.
- Sawhney, R.K., and Howard, J. (2002). Slow local movements of collagen fibers by fibroblasts drive the rapid global self-organization of collagen gels. *J. Cell Biol.* **157**, 1083–1092.
- Schindelin, J., Arganda-Carreras, I., Frise, E., Kaynig, V., Longair, M., Pietzsch, T., Preibisch, S., Rueden, C., Saalfeld, S., Schmid, B., et al. (2012). Fiji: an open-source platform for biological-image analysis. *Nat. Methods* **9**, 676–682.
- Schneider, R.A. (1999). Neural crest can form cartilages normally derived from mesoderm during development of the avian head skeleton. *Dev. Biol.* **208**, 441–455.
- Shyer, A.E., Huycke, T.R., Lee, C., Mahadevan, L., and Tabin, C.J. (2015). Bending gradients: how the intestinal stem cell gets its home. *Cell* **161**, 569–580.
- Shyer, A.E., Rodrigues, A.R., Schroeder, G.G., Kassianidou, E., Kumar, S., and Harland, R.M. (2017). Emergent cellular self-organization and mechanosensation initiate follicle pattern in the avian skin. *Science* **357**, 811–815.
- Shyer, A.E., Tallinen, T., Nerurkar, N.L., Wei, Z., Gil, E.S., Kaplan, D.L., Tabin, C.J., and Mahadevan, L. (2013). Villification: how the gut gets its villi. *Science* **342**, 212–218.
- Stevens, K.R., Ungrin, M.D., Schwartz, R.E., Ng, S., Carvalho, B., Christine, K.S., Chaturvedi, R.R., Li, C.Y., Zandstra, P.W., Chen, C.S., et al. (2013). InVERT molding for scalable control of tissue microarchitecture. *Nat. Commun.* **4**, 1847.
- Stuart, E.S., and Moscona, A.A. (1967). Embryonic morphogenesis: role of fibrous lattice in the development of feathers and feather patterns. *Science* **157**, 947–948.
- Sussman, D.M., Cho, Y., Castle, T., Gong, X., Jung, E., Yang, S., and Kamien, R.D. (2015). Algorithmic lattice kirigami: a route to pluripotent materials. *Proc. Natl. Acad. Sci. USA* **112**, 7449–7453.
- Takebe, T., Enomura, M., Yoshizawa, E., Kimura, M., Koike, H., Ueno, Y., Matsuzaki, T., Yamazaki, T., Toyohara, T., Osafune, K., et al. (2015). Vascularized and complex organ buds from diverse tissues via mesenchymal cell-driven condensation. *Stem Cell* **16**, 556–565.
- Tallinen, T., Chung, J.Y., Rousseau, F., Girard, N., Lefèvre, J., and Mahadevan, L. (2016). On the growth and form of cortical convolutions. *Nat. Phys.* **12**, 588–593.
- Tanner, K., Boudreau, A., Bissell, M.J., and Kumar, S. (2010). Dissecting regional variations in stress fiber mechanics in living cells with laser nanosurgery. *Biophys. J.* **99**, 2775–2783.
- Timoshenko, S.P., and Woinowsky-Krieger, S. (1959). *Theory of Plates and Shells* (McGraw-Hill).
- Todhunter, M.E., Jee, N.Y., Hughes, A.J., Coyle, M.C., Cerchiari, A., Farlow, J., Garbe, J.C., LaBarge, M.A., Desai, T.A., and Gartner, Z.J. (2015). Programmed synthesis of three-dimensional tissues. *Nat. Methods* **12**, 975–981.
- Tseng, Q., Duchemin-Pelletier, E., Deshiere, A., Balland, M., Guillou, H., Filhol, O., and Théry, M. (2012). Spatial organization of the extracellular matrix regulates cell-cell junction positioning. *Proc. Natl. Acad. Sci. USA* **109**, 1506–1511.
- Vader, D., Kabla, A., Weitz, D., and Mahadevan, L. (2009). Strain-induced alignment in collagen gels. *PLoS One* **4**, e5902.
- Varner, V.D., and Nelson, C.M. (2014a). Cellular and physical mechanisms of branching morphogenesis. *Development* **141**, 2750–2759.
- Varner, V.D., and Nelson, C.M. (2014b). Toward the directed self-assembly of engineered tissues. *Annu. Rev. Chem. Biomol. Eng.* **5**, 507–526.
- Varner, V.D., Gleghorn, J.P., Miller, E., Radisky, D.C., and Nelson, C.M. (2015). Mechanically patterning the embryonic airway epithelium. *Proc. Natl. Acad. Sci. USA* **112**, 9230–9235.
- Walton, K.D., and Kolterud, A. (2014). Mouse fetal whole intestine culture system for ex vivo manipulation of signaling pathways and three-dimensional live imaging of villus development. *J. Vis. Exp.* e51817.
- Walton, K.D., Freddo, A.M., Wang, S., and Gumucio, D.L. (2016a). Generation of intestinal surface: an absorbing tale. *Development* **143**, 2261–2272.
- Walton, K.D., Kolterud, A., Czerwinski, M.J., Bell, M.J., Prakash, A., Kushwaha, J., Grosse, A.S., Schnell, S., and Gumucio, D.L. (2012). Hedgehog-responsive mesenchymal clusters direct patterning and emergence of intestinal villi. *Proc. Natl. Acad. Sci. USA* **109**, 15817–15822.
- Walton, K.D., Whidden, M., Kolterud, A., Shoffner, S.K., Czerwinski, M.J., Kushwaha, J., Parmar, N., Chandrasekhar, D., Freddo, A.M., Schnell, S., et al. (2016b). Villification in the mouse: bmp signals control intestinal villus patterning. *Development* **143**, 427–436.
- Wang, Y., Gunasekara, D.B., Reed, M.I., DiSalvo, M., Bultman, S.J., Sims, C.E., Magness, S.T., and Allbritton, N.L. (2017). A microengineered collagen scaffold for generating a polarized crypt-villus architecture of human small intestinal epithelium. *Biomaterials* **128**, 44–55.
- Warmflash, A., Sorre, B., Etoc, F., Siggia, E.D., and Brivanlou, A.H. (2014). A method to recapitulate early embryonic spatial patterning in human embryonic stem cells. *Nat Methods* **11**, 847–854.
- Weber, R.J., Liang, S.I., Selden, N.S., Desai, T.A., and Gartner, Z.J. (2014). Efficient targeting of fatty-acid modified oligonucleotides to live cell membranes through stepwise assembly. *Biomacromolecules* **15**, 4621–4626.
- Wen, F.-L., Wang, Y.-C., and Shibata, T. (2017). Epithelial folding driven by apical or basal-lateral modulation: geometric features, mechanical inference, and boundary effects. *Biophys. J.* **112**, 2683–2695.
- Wessells, N.K., and Evans, J. (1968). The ultrastructure of oriented cells and extracellular materials between developing feathers. *Dev. Biol.* **18**, 42–61.
- Zhang, Y., Yan, Z., Nan, K., Xiao, D., Liu, Y., Luan, H., Fu, H., Wang, X., Yang, Q., Wang, J., et al. (2015). A mechanically driven form of Kirigami as a route to 3D mesostructures in micro/nanomembranes. *Proc. Natl. Acad. Sci. USA* **112**, 11757–11764.
- Zhang, Y.S., and Khademhosseini, A. (2017). Advances in engineering hydrogels. *Science* **356**, eaaf3627.

STAR★METHODS

KEY RESOURCES TABLE

REAGENT or RESOURCE	SOURCE	IDENTIFIER
Antibodies		
rat anti-mouse E-cadherin	Abcam	Cat#ab11512; RRID: AB_298118
rabbit anti-mouse Collagen I	Abcam	Cat#ab34710; RRID: AB_731684
AlexaFluor 647-labeled goat anti-rat IgG	ThermoFisher Scientific	Cat#A21247; RRID: AB_141778
AlexaFluor 568-labeled goat anti-rabbit IgG	ThermoFisher Scientific	Cat#A11011; RRID: AB_143157
Chemicals, Peptides, and Recombinant Proteins		
Staurosporine	Sigma-Aldrich	Cat#S5921
(-)-Blebbistatin	Sigma-Aldrich	Cat#B0560
Alexa Fluor 555-NHS	ThermoFisher Scientific	Cat# A20009
Alexa Fluor 647-NHS	ThermoFisher Scientific	Cat#A20006
Turbo DNase	ThermoFisher Scientific	Cat#AM2238
Experimental Models: Cell Lines		
Mouse: Embryonic fibroblasts (MEFs)	Jay Debnath Lab, UCSF	N/A
Human: MCF10A cells	(Liu et al., 2012)	ATCC Cat#CRL-10317; RRID: CVCL_0598
Human: MCF10AT cells (MCCs)	(Liu et al., 2012)	N/A
Human: HUVECs	Lonza	Cat#CC-2517
Human: 998 mammary fibroblasts	Mark LaBarge Lab, City of Hope	N/A
Canine: MDCK epithelial cells	UCSF cell culture facility	N/A
Human: Jurkat T-cells	ATCC	ATCC Cat#TIB-152; RRID:CVCL_0367
Human: Caco2 cells	UCSF cell culture facility	N/A
Experimental Models: Organisms/Strains		
White leghorn chicken	AA Lab Eggs, Westminster, CA	N/A
Mouse: PDGFR α ^{EGFP/+}	Ophir Klein Lab, UCSF (Hamilton et al., 2003)	N/A
Oligonucleotides		
A-lipid: 5'-C24 lipid (lignoceric acid)-GTAACGATCCAGC TGCTCACT-T ₆₀ - ACTGACTGACTGACTGACTG-3'	(Todhunter et al., 2015; Weber et al., 2014)	N/A
Aprime-lipid: 5'-C24 lipid (lignoceric acid)- GTAACGATCC AGCTGCTCACT-T ₆₀ - CAGTCAGTCAGTCAGTCAGT-3'	(Todhunter et al., 2015; Weber et al., 2014)	N/A
F-lipid: 5'-C24 lipid (lignoceric acid)-GTAACGATCCAGCT GTCAC-T ₆₀ - AGAAGAAGAACGAAGAAGAA-3'	(Todhunter et al., 2015; Weber et al., 2014)	N/A
Fprime-lipid: 5'-C24 lipid (lignoceric acid)-GTAACGATCC AGCTGCTCACT-T ₆₀ - TTCTTCTTCGTTCTTCTTCT-3'	(Todhunter et al., 2015; Weber et al., 2014)	N/A
Co-anchor-lipid: 3'-C16 lipid (palmitic acid)-CATTGCTAG GTCGACAGTGA-5'	(Weber et al., 2014)	N/A
A-amine: 5'-amine-ACTGACTGACTGACTGACTG-3'	(Todhunter et al., 2015; Weber et al., 2014), Glen Research	custom order
Aprime-amine: 5'-amine-CAGTCAGTCAGTCAGTCAGT-3'	(Todhunter et al., 2015; Weber et al., 2014), Glen Research	custom order
F-amine: 5'-amine-AGAAGAAGAACGAAGAAGAA-3'	(Todhunter et al., 2015; Weber et al., 2014), Glen Research	custom order
Fprime-amine: 5'-amine-TTCTTCTTCGTTCTTCTTCT-3'	(Todhunter et al., 2015; Weber et al., 2014), Glen Research	custom order

(Continued on next page)

Continued

REAGENT or RESOURCE	SOURCE	IDENTIFIER
Recombinant DNA		
pSicoR-Ef1a-mCh-Puro	Addgene	Cat#31845
pSicoR-Ef1a-maxGFP-Puro	This paper	From Addgene # 31845
pHIV-H2B-eGFP	(Liu et al., 2012)	From Addgene #18982
Software and Algorithms		
Fiji	(Schindelin et al., 2012)	www.fiji.sc
MATLAB	The Mathworks, Inc.	https://www.mathworks.com/products/matlab.html
Rhinoceros 3D	Robert McNeel & Associates	https://www.rhino3d.com
Grasshopper: Algorithmic Modeling for Rhino	David Rutten, Robert McNeel & Associates	http://www.grasshopper3d.com
Kangaroo Physics	Daniel Piker, independent researcher	http://www.grasshopper3d.com/group/kangaroo
Prism 7	GraphPad	https://www.graphpad.com/scientific-software/prism/
Source code for building curvature-mapped meshes; example interactive FEM model.	This paper	https://github.com/ahug030/tissue-origami
Other		
Aldehyde-silanized glass slides	Schott	Cat#1064874
Laser cutter	Universal Laser Systems	Model VLS3.5
Microfluidic droplet printer	Bioforce Nanosciences	NanoEnabler
Microarray hybridization cassette	ArrayIt	Cat#AHC1X16
Craft cutter	Silhouette	N/A

CONTACT FOR REAGENT AND RESOURCE SHARING

Further information and requests for resources and reagents should be directed to and will be fulfilled by the Lead Contact, Zev Gartner (zev.gartner@ucsf.edu).

EXPERIMENTAL MODEL AND SUBJECT DETAILS**Animals**

Fertilized white Leghorn chicken eggs (AA Lab Eggs, Westminster, CA) were incubated, windowed, and otherwise handled as previously described (Schneider, 1999). PDGFR α ^{EGFP/+} mice were group-housed and genotyped as previously published (Hamilton et al., 2003). All embryos were staged by embryonic day and pregnant females were euthanized by CO₂ administration followed by cervical dislocation for embryo harvesting. Embryos were used without determining sex. All animal experiments were approved by the Institutional Animal Care and Use Committee of the University of California, San Francisco.

Cell Lines

Mouse embryonic fibroblasts (MEFs, male and female mixed, gift of Jay Debnath, UCSF) expressing maxGFP via pSicoR-Ef1a-maxGFP-Puro (gift of Justin Farlow, Serotiny Bio), human MCF10A cells (female) expressing H2B-GFP (Liu et al., 2012), human MCF10AT (Liu et al., 2012) (mesenchymal-like carcinoma cells, MCCs, female bulk population and clones) expressing H2B-GFP and constitutively active H-Ras^{V12}, human umbilical vein endothelial cells (HUVECs, male, Lonza) expressing mCherry after transduction with lentivirus made with pSicoR-Ef1a-mCh-Puro (Addgene 31845), human 998 mammary fibroblasts (female, gift of Mark LaBarge, LBNL) expressing maxGFP, Madin-Darby canine kidney epithelial cells (MDCK, female, UCSF cell culture facility), Jurkat immortalized human T-cells (male, American Type Culture Collection), and Caco2 human epithelial colorectal adenocarcinoma cells (male, UCSF cell culture facility) were cultured on polystyrene plates and flasks at 37° C and 5% CO₂ (Corning). MCCs and MCF10A cells were cultured as previously described (Debnath et al., 2003). HUVECs were maintained in EGM-2 medium (Lonza). Jurkat cells were maintained in Roswell Park Memorial Institute (RPMI) medium with 10% fetal bovine serum (FBS). MEFs, 998 fibroblasts, MDCKs and Caco2 cells were maintained in Dulbecco's modified Eagle's medium (DMEM) with 10% FBS and 1x non-essential amino acids. All cell lines were used without formal authentication.

METHOD DETAILS

Cell Treatments

Staurosporine (Sigma-Aldrich S5921) was prepared by serial dilution from a 10 mM DMSO stock. Cell lines without endogenous fluorescent markers were labeled with CellTracker Deep Red or Blue CMHC dyes according to manufacturer protocols (ThermoFisher Scientific C34565 and C2111 respectively). Cell viability was measured via microplate-based PrestoBlue assay according to manufacturer instructions (ThermoFisher Scientific A13261).

Reconstituted Tissue Fabrication

Microfluidic flow cells were constructed by sandwiching aldehyde-silanized glass slides (Schott 1064874) against a polydimethylsiloxane (PDMS) membrane gasket (0.01" thick, SSP M823) cut with a craft cutter (Silhouette). Prior to sandwiching, through-holes in the top slide were made using 20 passes of a 50 W etching laser at 100% power, 15% speed, 350 pulses per inch (VLS3.5, Universal Laser Systems). Fiducial marks were etched into both glass slides to aid alignment by light microscopy before cell patterning. Etched slides were used as substrates for DNA-programmed assembly of cells (DPAC), as detailed previously (Todhunter et al., 2015; Weber et al., 2014). To summarize, after etching, amine-modified oligonucleotides (5'-amine-X₂₀-3', see Key Resources Table) were printed onto the slides using a microfluidic cantilever (NanoEnabler, Bioforce Nanosciences) and covalently attached by reductive amination. Printing locations were specified in bitmap files. Slides were treated with hydrophobic silane and blocked for 1 hr in 3% bovine serum albumin in PBS before being assembled against the PDMS gasket. Immediately prior to sandwiching, PBS was added to gaps in the gasket to prime flow cells and reduce the tendency to trap bubbles between the slides. Slight pressure was applied to the sandwich using a microarray hybridization cassette (AHC1X16, ArrayIt). The positions of through-holes in the top glass slide and voids in the PDMS gasket were matched to the dimensions of the cassette such that 16 flow cells could be independently addressed through pairs of through-holes.

Cells to be assembled on the top and bottom flow cell walls were lifted from plates using a PBS wash followed by 0.05% trypsin and labelled with lipid-modified oligonucleotides (5'-lipid-Y₂₀-T₆₀-X₂₀-3' followed by a 3'-lipid-Y₂₀-5' "co-anchor", see Key Resources Table) as previously described (Todhunter et al., 2015; Weber et al., 2014) (with the exception of Caco2 cells, see below). With the flow cell cassette on ice, cells in suspensions of $\sim 10 \times 10^6$ cells/ml were introduced to flow cells by gentle pipetting on top of one of the pair of through-holes and adhered to DNA spots on the glass. A further round of cellular assembly was used to generate clusters of 5-8 cells at each DNA spot. After cell patterning, liquid gel precursor was introduced in two aliquots of 20 μ l per flow cell and the cassette placed at 37° C for 20 min to set the precursor. Reconstituted tissue gels consist of a composite of fluorescently-labeled collagen I fibers in matrigel. To prepare the gel precursor, 200 μ l of ~ 8.5 mg/ml rat tail collagen I in 0.02 M acetic acid (Corning 354249) was labeled using 5 μ l of 1 mg/ml Alexa Fluor 555- or 647-NHS ester in DMSO (ThermoFisher Scientific A20009 and A20006; chosen to avoid spectral overlap with cell labels in a given experiment) that was added immediately prior to neutralization with 10 μ l 20x PBS and 4 μ l 3 M NaOH on ice. After 10 min on ice, 70 μ l of this collagen stock was added to a second stock consisting of 415 μ l of ~ 9 mg/ml matrigel (Corning 354234) and 15 μ l of Turbo DNase (ThermoFisher Scientific AM2238). This 500 μ l precursor solution was sufficient to build reconstituted tissues in 8-10 flow cells.

The flow cell cassette was then disassembled gently, and the slide sandwich submerged in the appropriate cell media at room temperature. A razor blade was used to gently pry apart the glass slides. Reconstituted tissues consisting of cell clusters carried along with the ECM gel typically floated spontaneously into the media or could be gently detached from one of the glass slides with a micro-spatula (Fine Science Tools 110089-11). Floating tissues were then manually cut out using either a biopsy punch or razor blade, or by laser microdissection (Zeiss PALM MicroBeam). Finished tissues were transferred to glass coverslip-bottomed 24-well plates (Greiner) using a P1000 pipet trimmed to a ~ 7 mm diameter. If reconstituted tissues were intended to undergo folding, the glass in each well was coated with 1% agarose in PBS prior to adding tissues to prevent them from adhering. For imaging studies of collagen strain/alignment, cell migration, and non-folding controls, or prior to microdissection, reconstituted tissues were encouraged to adhere to the bottom of coverslip wells by 10 min 37° C incubation in a semi-dry state (with media temporarily withdrawn).

Rather than being assembled by DPAC, a semi-confluent layer of Caco2 cells was assembled at the lower tissue surface by pre-mixing them at 4×10^6 cells/ml in gel precursor such that they settled onto the bottom of the flow cell prior to setting at 37° C.

Reconstituted tissues that contained HUVECs were cultured in EGM-2 with 200 ng/ml each of IL-3, stromal-cell derived factor 1a (SDF-1a) and stem-cell factor (SCF) to encourage lumenization. Tissues with a single passenger cell type were cultured for 12 hours in the appropriate fibroblast medium, and transferred to the passenger cell type's medium thereafter. 3-cell type reconstituted tissues (containing MEFs, HUVECs, and Caco2 cells) were similarly transferred to 50:50 HUVEC:Caco2 media after 12 hours. We anticipate that significant optimization of media conditions will be required depending on the targeted endpoints relevant to cell types of interest.

Adhered-Layer Tissues and Stiffness

For single and two-layer interface deflection studies in Figure S1, plain gel layers lacking cell clusters were fabricated in microfluidic flow cells as described above. MEF clusters were separately assembled by centrifugation into 100 μ m-diameter agarose microwells as previously described (Cerchiari et al., 2015). Microwells were washed several times with media and incubated for 3 hr until clusters condensed into microtissues. Microtissues were freed from microwells by pipetting and placed on top of single gel layers prior to incubation and imaging at the indicated timepoints, or for two-layer experiments, placed on a single layer and subsequently

sandwiched with a second layer. Layers were adhered by incubating in a semi-dry state for 10 min as described above, before adding media, incubating, and imaging.

Gel layer stiffness was approximated according to the protocol in (Varner et al., 2015), briefly, roughly cylindrical fluorescently-tagged gel samples were fabricated in PDMS molds and subjected to a uniaxial compression by applying a 10 mm diameter coverslip of known weight. Gels in a semi-dry state were imaged via confocal microscopy before and after application of the coverslip to determine their initial cross-sectional area and height, and their final height in the compressed state. The elastic modulus E was inferred by assuming an elastic material model of the form $E = FL_0/A\Delta L$. Where F is the weight of the coverslip, L_0 is the initial gel height, A is its initial cross-sectional area, and ΔL is its change in height after application of the coverslip.

Droplet Contraction

Rapid screening for cell contractility was performed by setting 1 μ l droplets of ECM gel containing 10^6 cells/ml on coverslip-bottomed microwells at 37° C for 20 min. Media was then added and droplets detached by gentle pipetting prior to timelapse imaging.

Measuring ECM Gel Strain by Single Cells

ECM strain in the vicinity of single cells was determined by particle image velocimetry (PIV ImageJ plugin (Tseng et al., 2012)). 30 μ l aliquots of reconstituted tissue gel precursor with 1 μ m red fluorescent polystyrene beads at 8×10^6 per ml (ThermoFisher Scientific F13083) and unlabeled collagen fibers were set in wells of a 96-well plate at 37° C for 20 min. 3,000 cells per well were then settled on the gel underlay and imaged every 60 min by confocal microscopy for bead displacement.

Collagen Fiber and Strap Orientation Analysis

Collagen fiber orientation and FEM edge orientation were measured using OrientationJ in ImageJ (Püspöki et al., 2016). The absolute value of pixels in orientation images was taken to put orientations in the 0-90° range. Orientation images were then smoothed using Gaussian blur on a length-scale of ~ 0.1 times the cell cluster spacing to enable interpretation. Average projections of aligned orientation images were used to visually summarize replicates.

Collagen strap orientation was determined in ImageJ by manual annotation. Straps that showed collagen fluorescence above a signal-to-noise ratio of 3 (measured from fluorescence profiles taken orthogonal to strap axes) were included in orientation plots.

Laser Ablation of ECM Gel

Gel rebound was measured 30 min after ablation of $\sim 100 \mu$ m x 10 μ m tracks by laser microdissection (Zeiss PALM MicroBeam, see later in Method Details). Laser power was adjusted in control regions distant from cell clusters to ensure cutting through the entire gel thickness.

Reconstituted Tissue Imaging

3D timelapses of reconstituted tissue folding were recorded at 37°C and 5% CO₂ with a 10x objective via tiled confocal microscopy. Images were acquired through Zeiss Zen 2012 software with 30 μ m z slice spacing using a Zeiss Observer.Z1 with a Yokogawa CSUX1 spinning disk and Photometrics Evolve 512 EMCCD camera.

Spatial Reconstruction of Tissues from Images

Confocal image stacks were segmented in ImageJ either manually or by semi-automated thresholding. Binary image stacks were then read into MATLAB (MathWorks) and converted to isosurface meshes via marching cubes. Meshes were smoothed and face colors assigned to local mean curvatures using custom scripts.

Curvatures of isotropic reconstituted tissues were generated by radially reslicing and thresholding image stacks in ImageJ after manually picking the center of tissues to serve as origin points. Radial slices were read into MATLAB and least-squares fitted to circles using custom scripts. Anisotropic curvatures were similarly generated for the indicated cutting planes and folds.

Example Immunofluorescence Protocol

Reconstituted tissues were transferred to a fresh 24-well plate and fixed in 2% paraformaldehyde for 45 min at room temperature. All pipetting was done while observing by light microscopy to avoid mechanical disruption with the pipet tip. Reconstituted tissues were washed three times with 100 mM glycine in PBS for 20 min per wash and permeabilized in 0.5% Triton X-100 in PBS for 15 min, all at room temperature; and blocked overnight at 4°C in 0.1% bovine serum albumin, 0.2% Triton X-100, 0.04% Tween-20, 10% goat serum (ThermoFisher Scientific 16210064) including a 1:50 dilution of goat anti-mouse IgG fab fragment (Jackson ImmunoResearch 115-007-003) in PBS. Reconstituted tissues were probed with primary antibodies in blocking buffer overnight at 4°C and washed three times for 1 hour per wash in blocking buffer. This process was repeated for secondary antibodies. Reconstituted tissue were then imaged in FocusClear (CedarLane FC-101).

Mouse Gut Explant Culture and Immunostaining

Embryonic intestines were harvested in cold DPBS or BGJb medium. Embryonic day 13.5 intestines were cut into approximately 5mm segments and either fixed immediately or cultured on 8.0 μm pore-size transwell membranes (Corning, 353182) (Walton and Kolterud, 2014). Explants were cultured at 37°C and 5% CO_2 in medium with or without 30 μM (-)-Blebbistatin (Sigma-Aldrich, B0560), with media changed twice daily.

Explants were fixed overnight at 4°C in 2% paraformaldehyde in PBS. Whole mount immunostaining was performed as previously described (Hatch and Mukoyama, 2015). In brief, tissues were blocked with blocking buffer (10% heat-inactivated goat serum and 0.2% Triton X-100 in PBS) overnight at 4°C. The tissues were then incubated overnight at 4°C with primary antibodies diluted in the blocking buffer and washed five times for 25 minutes per wash in washing buffer (2% heat-inactivated goat serum and 0.2% Triton X-100 in PBS). The same process was repeated for secondary antibodies. Tissues were then placed on glass slides and incubated with FocusClear for 10-40 mins at room temperature prior to confocal imaging (as for reconstituted tissues). Primary antibodies were rat anti-mouse E-cadherin (1:100, Abcam ab11512) and rabbit anti-mouse Collagen I (1:100, Abcam ab34710). Secondary antibodies were AlexaFluor 647-labeled goat anti-rat IgG and AlexaFluor 568-labeled goat anti-rabbit IgG (1:250, ThermoFisher Scientific A21247 and A11011 respectively).

Chick Gut Explants

Embryos were decapitated and dissected at the indicated embryonic day to remove the gut tube. Tubes were cut into rough 2 mm segments and then longitudinally to expose the luminal surface. Tissues were fixed in 4% paraformaldehyde, washed 3 times in PBS for 5 min per wash, stained in 2 $\mu\text{g}/\text{ml}$ ethidium bromide in PBS for 15 min, and washed similarly, all at room temperature (Eames and Schneider, 2005). The luminal surface was imaged using a macro confocal microscope (Nikon AZ-C2Si) at 2x magnification.

Chick Skin Explants

Chick embryos were similarly dissected by removing the prospective pterygia with fine forceps and pinning the skin to an underlay of 1% agarose. Explants were incubated in DMEM with 10% FBS and 1x pen/strep (with or without blebbistatin) at 37°C and 5% CO_2 . Explants were fixed and prepared for immunofluorescence studies as for mouse gut explants.

Finite Element Modeling

Reconstituted tissues were modeled using Kangaroo2, a position-based dynamics solver within the Rhinoceros Grasshopper (Robert McNeel & Associates) algorithmic modeling environment (Bender et al., 2014). We took a form-finding FEM approach to enable interactive, rapid prototyping, although this sacrificed high-resolution simulation of matrix deformations in the immediate vicinity of individual cell clusters. Cuboidal unit cells were constructed from quad mesh faces with two diagonals per quad. Unit cells were assembled to model 3D tissues at a scale of 100 μm per unit edge length and 2D tissues at 10 μm per unit edge length, balancing spatial resolution and simulation time. All edges were modeled as linear elastic elements with stiffness k_1 and rest lengths equal to their initial lengths. Since cell cluster positions were specified at 10x higher resolution for DPAC than for mesh vertices in 3D models, *contractile nodes* to be specified on the upper or lower model faces were generated by rescaling and rounding DPAC cell cluster coordinates. The edges in the xy plane coincident with these nodes were specified as *active edges* with a >3x-higher spring constant k_2 relative to other edges in the spring network, and with rest length s manipulated by the user.

Models constructed in this way had two parameters – the stiffness of non-active edges k_1 , and the active edge rest length s . $k_1 = 100 \text{ Nm}^{-1}$ was fitted such that 3D model isotropic caps with $\rho_{xy} = 170$ per tissue would reach the maximal observed curvature of $\sim 3 \text{ mm}^{-1}$ at $s = 0$ (Figure S5B); and $k_1 = 20 \text{ Nm}^{-1}$ was fitted for 2D models by manually iterating it for $s = 0$ to approximate the local matrix orientation generated by single MEF clusters at a sampling distance $r = 50 \mu\text{m}$ away and $t \sim 6$ hours (Figure S3B). These values of k_1 were then used for all subsequent simulations. 3D tissues were typically simulated for 10 values of s in the range of 0-1 to produce a family of objects at intermediate folding states for each design. Simulated tissue models were exported from Rhino as stereolithography files, remeshed in Zbrush (Pixologic) to remove mesh face orientation defects, read into MATLAB, voxelized, converted to isosurface meshes, smoothed and face colors mapped to local curvatures using custom scripts.

Since s is not directly analogous to tissue folding time *in vitro*, models intended for visual and local curvature comparison to reconstituted tissues at a given time-point were chosen from object families based on qualitative similarity.

Inferring Tension from Local Retraction after Ablation in Reconstituted Tissues

Since real-time imaging of retraction at the gel surface was limited by a mismatch in the appropriate length-scales of cutting and confocal microscopy, we made dissections and imaged resulting incisions within approximately 30 min. We expected that strain due to elastic tissue rebound would be fully realized within seconds (Bonnet et al., 2012), while continued strain due to active pulling at cell clusters would be limited to less than $\sim 10 \mu\text{m}$ along collagen straps within 30 min (Figure S5F, Movie S2A). We consider ablation of tissues to be analogous to severing an elastic spring under tension, discarding time-dependent dynamics from the Kelvin-Voigt model typically used to study viscoelastic retraction in live biological contexts (Bonnet et al., 2012; Kumar et al., 2006; Tanner et al., 2010). Therefore, the pre-tension force orthogonal to an ablated incision $F \propto (L - L_0)$, where L is the relaxed incision width at the gel surface after ablation, and L_0 is the width of gel immediately destroyed by laser irradiation (in practice, the incision width in control gels lacking cell clusters).

Scaling Analysis of Isotropic Reconstituted Tissue Curvature

We approximate reconstituted tissues as synclastic elastic plates, such that for small curvatures (deflections smaller than plate thickness), the strain in the yz plane at an arbitrary vertical distance z from the midplane of the plate is given by:

$$\varepsilon_{yz} = zC_{yz} \quad (\text{Equation 1})$$

where C_{yz} is the curvature of the midplane parallel to the yz plane (Timoshenko and Woinowsky-Krieger, 1959). We assume that arrays of isotropic actuators on reconstituted tissues generate spatially homogeneous strains tangential to gel surfaces at a given time-point t in proportion to their total number per tissue ρ_{xy} such that:

$$\varepsilon_{yz} \sim \rho_{xy} \dot{\varepsilon}_{yz} t \quad (\text{Equation 2})$$

where $\dot{\varepsilon}_{yz}$ is the collagen matrix strain rate of a cell cluster. Experimentally measured values of $\dot{\varepsilon}_{yz}$ appear to be approximately constant over time for large ranges in local and global collagen gel deformation (Meshel et al., 2005). Thus, combining [Equation 1] and [Equation 2] suggests a first-order model of the form $C_{yz} \propto \rho_{xy}$ to fit calibration data describing folding of isotropic reconstituted tissues at intermediate time-points.

Fidelity of Anisotropic Folds

We hypothesized that cell-type specific differences in migration rate would predict the fidelity with which initial cluster positions encode anisotropic curvatures. We found that mesenchymal-like carcinoma cells (MCCs) migrated to a characteristic distance of half the cluster pair spacing $d/2$ of 80 μm in a characteristic time $\tau_{d/2}$ of 7.5 hr, while mouse embryonic fibroblasts (MEFs) reached this threshold in 11 hr (Figure S5J). Because the folding times for isotropic reconstituted tissues with grids of similar spacing were approximately 10 hr and 5 hr for MCC and MEF cell types, respectively, these data suggest that MCC clusters disperse from their initial positions before significant folding occurs, whereas MEFs do not. This dispersal of cells away from their intended positions during folding would tend to produce spatially uncontrolled strains, and thus uncontrolled curvatures.

To further investigate this hypothesis, we measured the angle at which tensile collagen straps formed between clusters (relative to the horizontal axis) in isotropic or highly anisotropic grids (Figure S5K). At 9 hours in culture, straps between clusters were primarily oriented towards nearest neighbors along 0 and 90 degree angles in isotropic grids, regardless of cell type. At 15 hours, however, strap orientation had become randomly distributed due to the disorganizing effect of cell migration away from initial cluster positions.

For anisotropic grids, straps between clusters were also primarily oriented towards nearest neighbors at 9 hr, focused at 0° along the horizontal axis. At 15 hours, however, straps were more frequently oriented away from this axis (i.e. were more disorganized) in anisotropic MCC grids when compared to MEF grids, consistent with extensive MCC migration away from initial cluster positions. These data suggest that a threshold in the ratio of cell strain rate to migration rate determines the extent to which a given cell type actuates reconstituted tissues with sufficient fidelity.

Robustness of Adjacent Opposing Folds to Pop-Through

Of central concern for the design of adjacent folds of alternating negative and positive curvature (i.e. opposing folds) is their robustness to “pop-through” defects, in which out of plane deformations can emerge in the unintended orientation. Opposing folds can be built by placing cell clusters on opposite sides of the ECM sheet at spatially distinct regions in the xy plane. To study the robustness of our reconstituted tissues to such defects, we built four-fold vertex tissues that have three folds of the same orientation and one in the opposite orientation that converge at a single point. We hypothesized that for opposing folds to form successfully, they would need to be actuated by similar numbers of cell clusters so that the orientation of a particular fold would not be determined by a more radically curved neighboring fold. Indeed, a critical threshold at which the opposing fold formed in the incorrect orientation emerged when the number of clusters in the opposing fold was less than around half the average number in the two adjacent folds (Figure S7B). However, for values of this ratio above ~ 0.75 , the opposing fold always popped into the correct orientation, demonstrating that adjacent opposing folds form robustly if spatial strain profiles are properly managed.

QUANTIFICATION AND STATISTICAL ANALYSIS

Data were analyzed for statistically significant differences between sample means after checking and considering normality and equal variance assumptions via ordinary one-way ANOVA with Holm-Sidak’s multiple comparisons test in Prism 7 (GraphPad). Other statistical details relating to sample size, central tendency, and spread are noted in figure legends where applicable.

DATA AND SOFTWARE AVAILABILITY


Source code for building curvature-mapped meshes (MATLAB license required) and an example interactive FEM model (Rhino license required, with Grasshopper and Kangaroo Physics add-ons) are freely available at <https://github.com/ahug030/tissue-origami>.

RESEARCH ARTICLE

Open Access



Natural selection in bats with historical exposure to white-nose syndrome

Markéta Harazim^{1,2}, Ivan Horáček³, Lucie Jakešová², Kristína Luermann⁴, Jiří C. Moravec¹, Shannon Morgan^{5,9}, Jiri Pikula⁶, Petr Sosík⁷, Zuzana Vavrušová⁴, Alexandra Zahradníková Jr.^{1,8,10}, Jan Zukal^{1,2} and Natália Martínková^{1,4*} 

Abstract

Background: Hibernation allows animals to survive periods of resource scarcity by reducing their energy expenditure through decreased metabolism. However, hibernators become susceptible to psychrophilic pathogens if they cannot mount an efficient immune response to infection. While Nearctic bats infected with white-nose syndrome (WNS) suffer high mortality, related Palearctic taxa are better able to survive the disease than their Nearctic counterparts. We hypothesised that WNS exerted historical selective pressure in Palearctic bats, resulting in genomic changes that promote infection tolerance.

Results: We investigated partial sequences of 23 genes related to water metabolism and skin structure function in nine Palearctic and Nearctic hibernating bat species and one non-hibernating species for phylogenetic signals of natural selection. Using maximum likelihood analysis, we found that eight genes were under positive selection and we successfully identified amino acid sites under selection in five encoded proteins. Branch site models revealed positive selection in three genes. Hibernating bats exhibit signals for positive selection in genes ensuring tissue regeneration, wound healing and modulation of the immune response.

Conclusion: Our results highlight the importance of skin barrier integrity and healing capacity in hibernating bats. The protective role of skin integrity against both pathophysiology and WNS progression, in synergy with down-regulation of the immune reaction in response to the *Pseudogymnoascus destructans* infection, improves host survival. Our data also suggest that hibernating bat species have evolved into tolerant hosts by reducing the negative impact of skin infection through a set of adaptations, including those at the genomic level.

Keywords: Skin, Fungal infection, Wound healing, Immunity, Gene evolution

Background

Emergence of a novel infectious disease or pathogen transmission to a naïve population leads to allele frequency changes in populations experiencing disease outbreaks with high mortality [1, 2]. Carriers of alleles that facilitate less serious disease manifestation have a higher chance of survival, while gene variants causing increased susceptibility to the infection or more severe diseases are more likely to vanish from the population gene pool. Pathogens serve as a selective force in susceptible hosts, directing changes in host population genetic diversity.

Alterations in host genetic structure driven by pathogens are detectable in coding DNA sequences as signals for natural selection. While equal rates of both substitution types occur during neutral evolution, a higher rate of non-synonymous substitutions (d_N) than synonymous substitutions (d_S) is a sign of predominant positive selective pressure ($d_N/d_S > 1$) and, conversely, higher rates of synonymous substitutions are a sign of predominant negative selective pressure ($d_N/d_S < 1$) [3, 4].

White-nose syndrome (WNS), a fungal infection of hibernating bats, potentially applies strong selection pressure on bat populations in the Nearctic. Since its emergence in 2006, WNS has caused the death of millions of bats across the eastern part of North America [5]. Indeed, WNS has led to the near extirpation of some of the most common hibernating *Myotis* species due to local declines exceeding 90% per year [6, 7]. In comparison, Palearctic bat species

* Correspondence: martinkova@ivb.cz

¹Institute of Vertebrate Biology, The Czech Academy of Sciences, Brno, Czech Republic

⁴Institute of Biostatistics and Analyses, Masaryk University, Brno, Czech Republic

Full list of author information is available at the end of the article



© The Author(s). 2018 **Open Access** This article is distributed under the terms of the Creative Commons Attribution 4.0 International License (<http://creativecommons.org/licenses/by/4.0/>), which permits unrestricted use, distribution, and reproduction in any medium, provided you give appropriate credit to the original author(s) and the source, provide a link to the Creative Commons license, and indicate if changes were made. The Creative Commons Public Domain Dedication waiver (<http://creativecommons.org/publicdomain/zero/1.0/>) applies to the data made available in this article, unless otherwise stated.

suffering from WNS show greater survival, with no reports of population declines attributable to WNS [8, 9] despite sporadic mortality [10, 11].

The difference in survival rate of infected Nearctic and Palearctic bats is most likely connected to species-specific pathophysiological impacts during host-pathogen interaction. The infective agent of the disease, the psychrophilic fungus *Pseudogymnoascus destructans*, invades deep into living skin layers on the hibernating bat's nose, ears, limbs and membranes [10–14]. The disease may subsequently have a negative effect on ion and blood gas balance [15, 16], evaporative loss of water [17] and overall hibernation behaviour [18]. Frequent arousals from hibernation in infected, moribund bats [19] may also contribute to loss of energy reserves essential for survival. Following arousal from torpor, the host's infection response will exacerbate tissue damage by immunopathology [20] and reaction to fungal metabolite accumulation. In particular, riboflavin produced by *P. destructans*, which hyperaccumulates in skin lesions during hibernation, causes oxidative tissue damage [14] and triggers a cytotoxic immune response when presented to the innate immune system [21].

The recent emergence of WNS in the Nearctic resulting in high mortality rates, and later recognition of the pathogen in the Palearctic with differing disease manifestation, suggests spatio-temporal variation in host-pathogen coevolution [22]. Recent evidence demonstrates that *P. destructans* infection occurred in Palearctic bats prior to its emergence in the Nearctic [23, 24]. Coupled with current disease tolerance in the Palearctic, historical exposure to the pathogen has given rise to the hypothesis that WNS may have caused mass mortality events in the Palearctic in the past. Martínková et al. [8] speculated that the large fossil deposits of bat species now rare in underground hibernacula may have accumulated due to a WNS epidemic in the Pleistocene. Based on the assumption that Palearctic bats were exposed to the lethal skin infection prior to the Holocene, we hypothesised that Palearctic bat species may have evolved inheritable mechanisms leading to tolerance toward the disease. If so, any alteration in genetic information should be detectable in genes encoding proteins interacting with the pathogen in a manner dependent on infection pathophysiology. Identification of those genes targeted by positive selection should enhance our understanding of disease pathogenesis. Considering the disease's etiology and close functional connection to acid-base and electrolyte homeostasis and skin layer damage during disease progression, we hypothesise that genes involved in water metabolism and skin function in hibernating bat species are most likely to display signatures of positive selection.

Results

Annotated sequences of 23 genes were retrieved from the NCBI database for species in the Vespertilionidae and

Miniopteridae families, namely *acad10*, *acp5*, *anxa1*, *aqp3*, *aqp4*, *aqp7*, *aqp9*, *bcam*, *ctnmb1*, *fads1*, *fgf10*, *guca2b*, *has2*, *hyal2*, *hyal3*, *krt8*, *lrp4*, *psen2*, *ptch2*, *pxn*, *sncg*, *tgm1*, and *tnfrsf13* (Additional file 1). We sequenced five genes in seven bat species using PacBio SMRT technology (GenBank Accession Numbers: MH178037–MH178081) and supplemented the datasets from the public database with 71 phased partial coding sequences. In other species (Additional file 2), PacBio sequences were not of sufficient quality to provide at least 10× coverage. In total, we analysed 11 bat species with 1–23 genes available per species, and partial coding sequences of 23 genes available in 3–9 species (Additional file 1).

Using a maximum likelihood framework [25], we estimated the rate ratio of non-synonymous to synonymous substitutions $\omega = d_N/d_S$ for the available coding sequences. We used the likelihood ratio test (LRT) to differentiate between nested models of DNA sequence evolution, where twice the difference in model log-likelihoods ($2\Delta\ln L$) approximately follows a χ^2 distribution with degrees of freedom equal to the difference in the number of model parameters. Comparison of M0 and M3 nested models of DNA sequence evolution (testing for variability of ω between sites) revealed 13 of the 23 genes to be significant after correction for multiple testing with false discovery rate (FDR) (Table 1). Comparison of M1 to M2 and M7 to M8 model pairs (differentiating between neutral and positive selection) revealed significance in seven genes. Statistically significant support for positive selection (FDR adjusted $p < 0.05$) was detected in genes encoding annexin A1 (*anxa1*), tartrate resistant acid phosphatase 5 (*acp5*), aquaporin 3 (*aqp3*), the basal cell adhesion molecule (*bcam*), LDL receptor related protein 4 (*lrp4*), patched 2 (*ptch2*) and synuclein gamma (*sncg*) (Table 1).

In those genes showing positive selection, we used Bayes empirical Bayes (BEB) to identify specific amino acids encoding sites under significant positive selection (Fig. 1). We identified four sites under positive selection in *acp5*, seven sites in *anxa1* (with one additional site identified from a comparison of the M7 and M8 models), one site in *aqp3*, one site recognised from both model comparisons and one additional site identified by comparing M7 to M8 in *ptch2*. All six sites identified in *bcam* were supported by the M7 to M8 comparison (Table 2, Fig. 1).

Amino acid sites under positive selection were mapped onto predicted 3D protein structure models of four genes (Fig. 2). In tartrate resistant acid phosphatase (TRAP; encoded within the *acp5* gene), the selected sites were spread along the protein sequence, while in ANXA1, the selected sites were accumulated in the N-terminal region of the protein (six out of eight sites detected occurred within the range 17–27; Fig. 1). The sole AQP3 site under selection was located within a transmembrane helix, and four out of six sites identified under positive selection in

Table 1 Maximum likelihood analysis of positive selection in DNA-encoding proteins linked to water metabolism and skin structure

Gene	Protein	<i>n</i>		M0-M3		M1-M2			M7-M8		
		sp.	ind.	LRT	<i>p</i>	ω (prop.)	LRT	<i>p</i>	ω (prop.)	LRT	<i>p</i>
<i>acad10</i>	ACAD10	4	4	19.6	0.495	1.01 (0%)	0.0	1.000	1.36 (13.3%)	1.4	0.877
<i>acp5</i>	TRAP	9	26	191.5	0.001	6.16 (2.0%)	34.4	0.001	6.05 (2.0%)	38.1	0.001
<i>anxa1</i>	ANXA1	9	16	157.4	0.001	8.57 (15.3%)	57.2	0.001	8.03 (15.5%)	59.1	0.001
<i>aqp3</i>	AQP3	8	28	69.7	0.001	9.22 (1.1%)	14.8	0.004	9.19 (1.1%)	17.1	0.001
<i>aqp4</i>	AQP4	3	3	1.3	1.000	1.00 (3.0%)	0.0	1.000	14.87 (2.5%)	0.6	1.000
<i>aqp7</i>	AQP7	3	3	0.1	1.000	1.00 (5.1%)	0.0	1.000	1.00 (0%)	0.0	1.000
<i>aqp9</i>	AQP9	4	4	12.2	0.028	3.19 (15.5%)	4.3	0.292	3.19 (15.5%)	4.6	0.226
<i>bcam</i>	BCAM/Lu	6	8	73.5	0.004	5.81 (5.2%)	10.5	0.025	5.32 (5.8%)	11.1	0.018
<i>ctnnb1</i>	CTNNB1	4	4	0.0	1.000	1.00 (0%)	0.0	1.000	1.00 (0%)	0.0	1.000
<i>fads1</i>	FADS1	3	3	18.0	0.03	13.40 (1.5%)	7.0	0.085	13.46 (1.6%)	7.2	0.081
<i>fgf10</i>	FGF10	5	5	7.7	0.155	1.00 (1.7%)	0.0	1.000	1.00 (1.8%)	0.1	1.000
<i>guca2b</i>	GUCA2B	7	12	29.1	0.001	3.53 (5.1%)	3.6	0.345	3.23 (6.3%)	5.4	0.172
<i>has2</i>	HAS2	4	4	0.0	1.000	1.00 (0%)	0.0	1.000	1.01 (0%)	0.0	1.000
<i>hyal2</i>	HYAL2	5	5	17.8	0.003	1.00 (2.9%)	0.0	1.000	1.00 (2.9%)	0.0	1.000
<i>hyal3</i>	HYAL3	4	4	0.4	1.000	1.00 (8.2%)	0.0	1.000	1.01 (0%)	0.0	1.000
<i>krt8</i>	KRT8	4	4	0.0	1.000	1.00 (0%)	0.0	1.000	1.00 (0%)	0.0	1.000
<i>lrp4</i>	LRP4	4	4	14.1	0.015	52.96 (1.11%)	9.3	0.035	52.95 (1.11%)	10.1	0.021
<i>psen2</i>	PSEN2	3	3	12.98	0.001	11.39 (1.1%)	4.1	0.351	10.95 (1.2%)	3.9	0.226
<i>ptch2</i>	PTCH2	4	4	67.2	0.001	10.75 (0.4%)	9.110	0.035	10.45 (1.2%)	10.7	0.018
<i>pxn</i>	PXN	4	4	6.6	0.225	1.00 (0%)	0.000	1.000	1.00 (0%)	0.0	1.000
<i>sncg</i>	SNCG	3	3	13.2	0.020	84.38 (1.1%)	11.506	0.018	85.32 (1.1%)	11.8	0.016
<i>tgm1</i>	TGM1	5	5	6.7	0.620	1.00 (4.8%)	0.000	1.000	1.00 (0%)	0.0	1.000
<i>tnfsf13</i>	TNFSF13/APRIL	4	4	12.1	0.028	14.26 (0.6%)	3.286	0.370	8.6 (1.1%)	3.1	0.404

The table shows ω values indicating the ratio of non-synonymous to synonymous substitution rates. *n* = sample size; sp. - species; ind. - individuals; LRT likelihood ratio test statistic, given as $\Delta 2\ln L$ in the nested models compared (M0-M3, M1-M2 and M7-M8); prop. - proportion of sites with $\omega > 1$; and *p*-values (adjusted for multiple testing with FDR; significant at $\alpha = 0.05$) for the corresponding tests. Tests indicating signals of natural selection are in bold

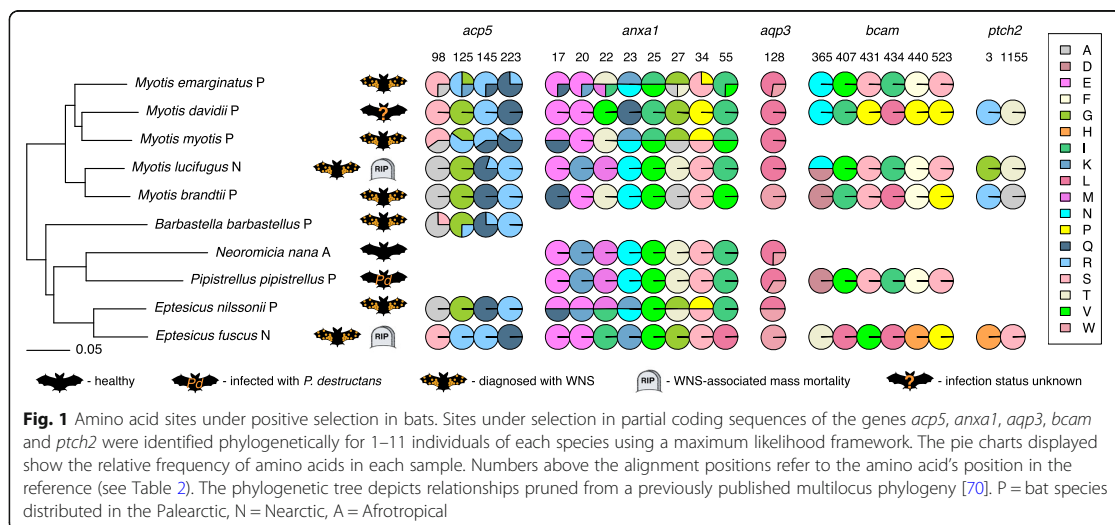


Fig. 1 Amino acid sites under positive selection in bats. Sites under selection in partial coding sequences of the genes *acp5*, *anxa1*, *aqp3*, *bcam* and *ptch2* were identified phylogenetically for 1–11 individuals of each species using a maximum likelihood framework. The pie charts displayed show the relative frequency of amino acids in each sample. Numbers above the alignment positions refer to the amino acid's position in the reference (see Table 2). The phylogenetic tree depicts relationships pruned from a previously published multilocus phylogeny [70]. P = bat species distributed in the Palearctic, N = Nearctic, A = Afrotropical

Table 2 Bat amino acid sites under selection

Gene	M1-M2					M7-M8				
	pos	aa	<i>p</i>	mean	SE	pos	aa	<i>p</i>	mean	SE
<i>acp5</i>	98	S/A	0.003	6.542	1.424	98	S/A	0.0001	7.299	1.384
XP_006104612.1	125	G/R/K	0.0001	6.559	1.394	125	G/R/K	0.0001	7.304	1.372
	145	R/Q	0.0001	6.557	1.396	145	R/Q	0.0001	7.304	1.373
	223	Q/R	0.017	6.454	1.554	223	Q/R	0.006	7.261	1.461
<i>anxa1</i>	17	E/Q	0.024	8.227	1.718	17	E/Q	0.002	7.841	1.296
XP_014396764.1	20	E/K	0.009	8.420	1.297	20	E/K	0.009	7.792	1.410
	22	T/M/V/I	0.0001	8.420	1.297	22	T/M	0.0001	7.857	1.255
	23	K/N	0.0001	8.420	1.299	23	K/N	0.0001	7.857	1.255
	25	I/V	0.020	8.261	1.653	25	I/V	0.002	7.842	1.318
	27	G/A/T	0.0001	8.420	1.297	27	G/A/T	0.0001	7.857	1.255
	34	P/S	0.002	8.403	1.345	34	P/S	0.0001	7.856	1.259
	55	I/V	0.012	8.325	1.526	55	I/V	0.002	7.846	1.285
<i>aqp3</i>	128	L/W	0.001	8.693	1.604	128	L/W	0.0001	8.027	1.895
XP_006758647.1										
<i>bcam</i>						365	N/D	0.038	6.850	1.934
XP_015416692.1						407	V/I	0.012	7.019	1.678
						431	S/N/P	0.008	7.046	1.628
						434	I/L	0.013	7.013	1.690
						440	F/H	0.035	6.866	1.902
						523	S/P	0.009	7.040	1.641
<i>ptch2</i>						3	R/G/H	0.028	2.806	1.006
XP_014319265.1	1155	T/S/A	0.046	4.57	1.778	1155	T/S/A		2.842	0.963

Amino acid sites under positive selection were analysed using Bayes empirical Bayes. Position (pos) refers to the position of an amino acid (aa) mapped against the reference sequence stated in the table. The calculation is based on both M1-M2 and M7-M8 comparisons and shows the M1-M2 comparison as more strict

BCAM lay in the 2nd Ig-like C2 type domain (Fig. 2). It was not possible to model the structure of PTCH2, the fifth protein with sites under positive selection. We assume that the two sites under positive selection were both located in the intracellular partition of the protein.

The branch site test of positive selection compared the two nested models identifying the branch under positive selection (A1 and A). A significant difference between the models indicated positive selection in *Eptesicus fuscus* ($p = 0.001$) and *E. nilssonii* ($p = 0.001$) in *acp5* (Table 3).

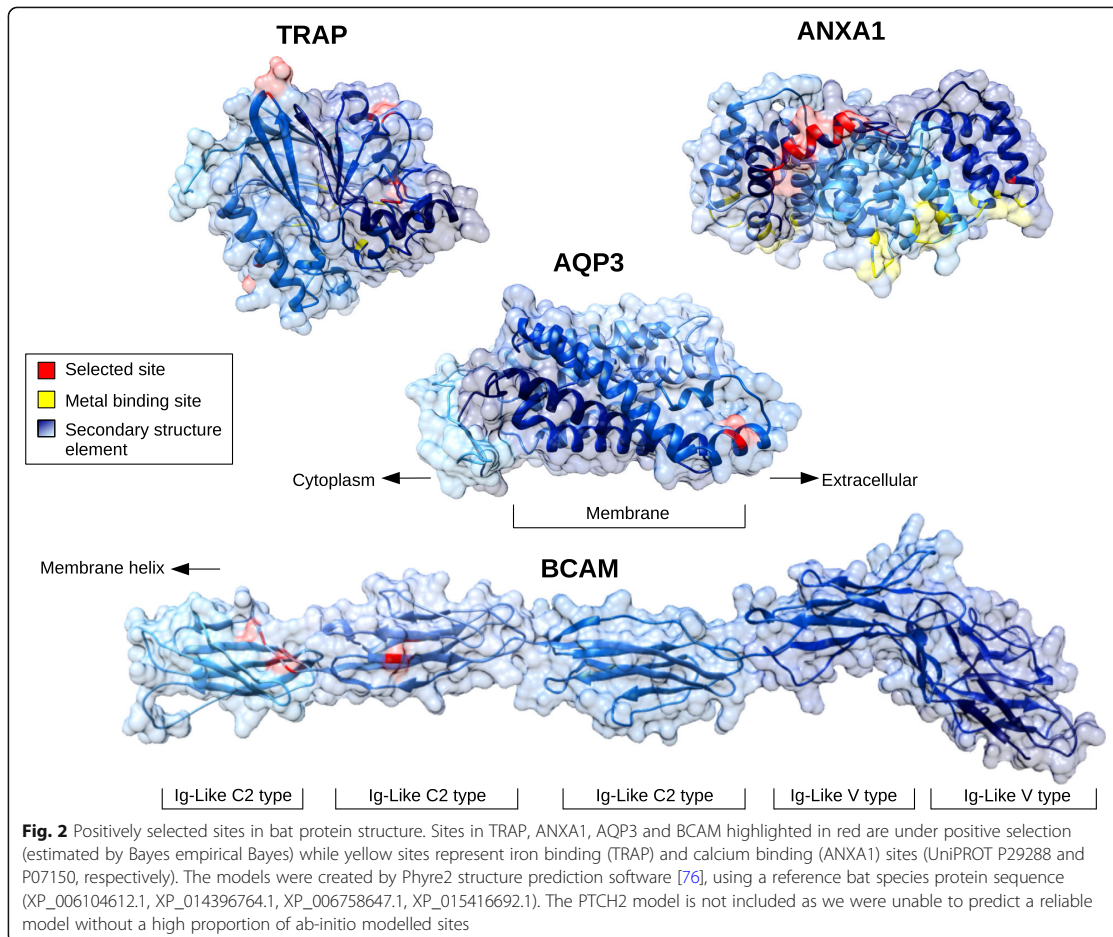
We then tested for positive selection on species in a Palearctic monophyletic clade that included *Myotis davidii*, *Myotis emarginatus* and *Myotis myotis*. Three genes under selection were available for the clade (Fig. 1, Additional file 1). Clade model C vs. M2a_rel revealed positive selection in *acp5* for the species ($p = 0.005$), but no significant evidence of selection in *anxa1* and *aqp3* ($p > 0.05$).

Discussion

Hibernation is a strategy used by temperate-zone bats to increase survival rate under conditions of constrained energy reserves [26, 27]. Exposure of hibernating individuals to

additional stressors, such as pathogen pressure, could result in health-related costs decreasing their ability to overwinter. Mounting an immune response at times of low activity, low body temperature and reduced possibility of regulation and energy uptake is a risky defence mechanism against potential microbial threats as it may contribute to mortality through depletion of fat reserves [19, 28] or overwhelming inflammation [20]. Frequency changes in functionally important single nucleotide polymorphisms in histocompatibility antigens, cytokines and toll-like receptors have been recorded in *Myotis lucifugus* populations that survived the initial *P. destructans* epidemic front associated with population decline [2]. Considering the risks associated with immune response investment in hibernators, tolerance of the pathogen at a molecular level is likely to be the best possible approach to infection in hibernation.

WNS pathophysiology is directly connected to the bat's hibernation ability. Assuming that a) Palearctic bats have been historically exposed to *P. destructans* [23, 24], b) Nearctic bats represent naïve animals with no historical influence of infection, and c) Afrotropic bats remain healthy as they live in an environment too warm for pathogen growth [29], it should be possible to detect



selective changes in the bat genome testifying to the consequences to infection-related mortality, this serving as a selective pressure favouring beneficial mutations over the ancestral genetic sequence.

Infection by *P. destructans* is dependent on low temperatures as the fungus is unable to grow at temperatures greater than 20 °C [29]. At environmental temperatures prevalent in hibernacula, the fungus invades the host's skin from the epidermis to the deeper skin layers [20, 30, 31]. An ability to protect the skin from lesions and functional disruption is critical to the bat's survival, and even more so as regards the skin forming the wing (considered the bat's largest organ). Of the genes signalling positive selection, many are involved in maintaining skin homeostasis and promoting wound healing (Table 1, Fig. 3). While proving a direct causal link between selection on particular genes (Table 1) and historical *P. destructans* exposure is impossible without experimental manipulation, the molecular function of genes under selection may be interpreted in relation to a skin infection.

Sites under positive selection in the Patched 2 protein (PTCH2) were located in the protein intracellular partition (Fig. 1). PTCH2 is functionally similar to its homologue, PTCH1, both of which serve as receptors in the Sonic hedgehog pathway, crucial in embryonic development and adult tissue homeostasis [32, 33]. While PTCH2 appears to be redundant in embryonic development, it preserves a crucial role as regards the adult epidermis [34, 35], though the molecular mechanism remains unclear. Synuclein gamma protein (SNCG) is expressed in stratum granulosum, both in embryonic development and in adults, where it functions as a keratin network modulator in the epidermis [36]. The basal cell adhesion molecule (BCAM/Lu), a membrane-bound molecule expressed by keratinocytes in inflammatory states [37], may contribute to anti-infection reactions in the bat's skin. The accumulation of sites under positive selection in the 2nd Ig-like C2 type domain in BCAM (Fig. 2) may indicate the importance of this domain as regards molecular functioning in skin pathology, though

Table 3 Branch site tests for proteins undergoing positive selection

Gene/Foreground branch	n foreground ind.	2ΔlnL	p
<i>acp5</i>			
<i>Eptesicus fuscus</i>	1	73	0.001
<i>Eptesicus nilssonii</i>	1	27.5	0.001
<i>Myotis davidii</i>	1	0.7	1.000
<i>Myotis myotis</i>	5	0.7	1.000
<i>Myotis brandtii</i>	1	0.0	1.000
<i>Barbastella barbastellus</i>	4	0.0	1.000
<i>Myotis emarginatus</i>	8	0.0	1.000
<i>Myotis lucifugus</i>	5	-0.7	1.000
<i>anxa1</i>			
<i>Myotis davidii</i>	1	8.1	0.153
<i>Myotis emarginatus</i>	4	8.1	0.153
<i>Myotis brandtii</i>	1	3.1	1.000
<i>Eptesicus fuscus</i>	1	3.1	1.000
<i>Neoromicia nana</i>	1	1.9	1.000
<i>Eptesicus nilssonii</i>	2	0.0	1.000
<i>Myotis lucifugus</i>	1	0.0	1.000
<i>Myotis myotis</i>	4	0.0	1.000
<i>Pipistrellus pipistrellus</i>	1	-1.8	1.000
<i>aqp3</i>			
<i>Eptesicus fuscus</i>	1	0.9	1.000
<i>Myotis myotis</i>	4	0.8	1.000
<i>Eptesicus nilssonii</i>	2	0.0	1.000
<i>Myotis brandtii</i>	1	0.0	1.000
<i>Myotis davidii</i>	1	0.0	1.000
<i>Myotis emarginatus</i>	11	0.0	1.000
<i>Myotis lucifugus</i>	1	0.0	1.000
<i>Neoromicia nana</i>	4	0.0	1.000
<i>Pipistrellus pipistrellus</i>	3	0.0	1.000
<i>bcam</i>			
<i>Eptesicus fuscus</i>	1	0.1	1.000
<i>Myotis brandtii</i>	1	0.0	1.000
<i>Myotis davidii</i>	1	0.0	1.000
<i>Myotis emarginatus</i>	1	0.0	1.000
<i>Myotis lucifugus</i>	2	0.0	1.000
<i>Pipistrellus pipistrellus</i>	2	0.0	1.000
<i>lrp4</i>			
<i>Eptesicus fuscus</i>	1	0.7	1.000
<i>Myotis lucifugus</i>	1	0.2	1.000
<i>Myotis brandtii</i>	1	0.0	1.000
<i>Myotis davidii</i>	1	0.0	1.000

Table 3 Branch site tests for proteins undergoing positive selection (Continued)

Gene/Foreground branch	n foreground ind.	2ΔlnL	p
<i>ptch2</i>			
<i>Eptesicus fuscus</i>	1	0.7	1.000
<i>Myotis lucifugus</i>	1	0.2	1.000
<i>Myotis brandtii</i>	1	0.0	1.000
<i>Myotis davidii</i>	1	0.0	1.000
<i>sncg</i>			
<i>Myotis davidii</i>	1	0.8	1.000
<i>Eptesicus fuscus</i>	1	0.0	1.000
<i>Myotis brandtii</i>	1	0.0	1.000

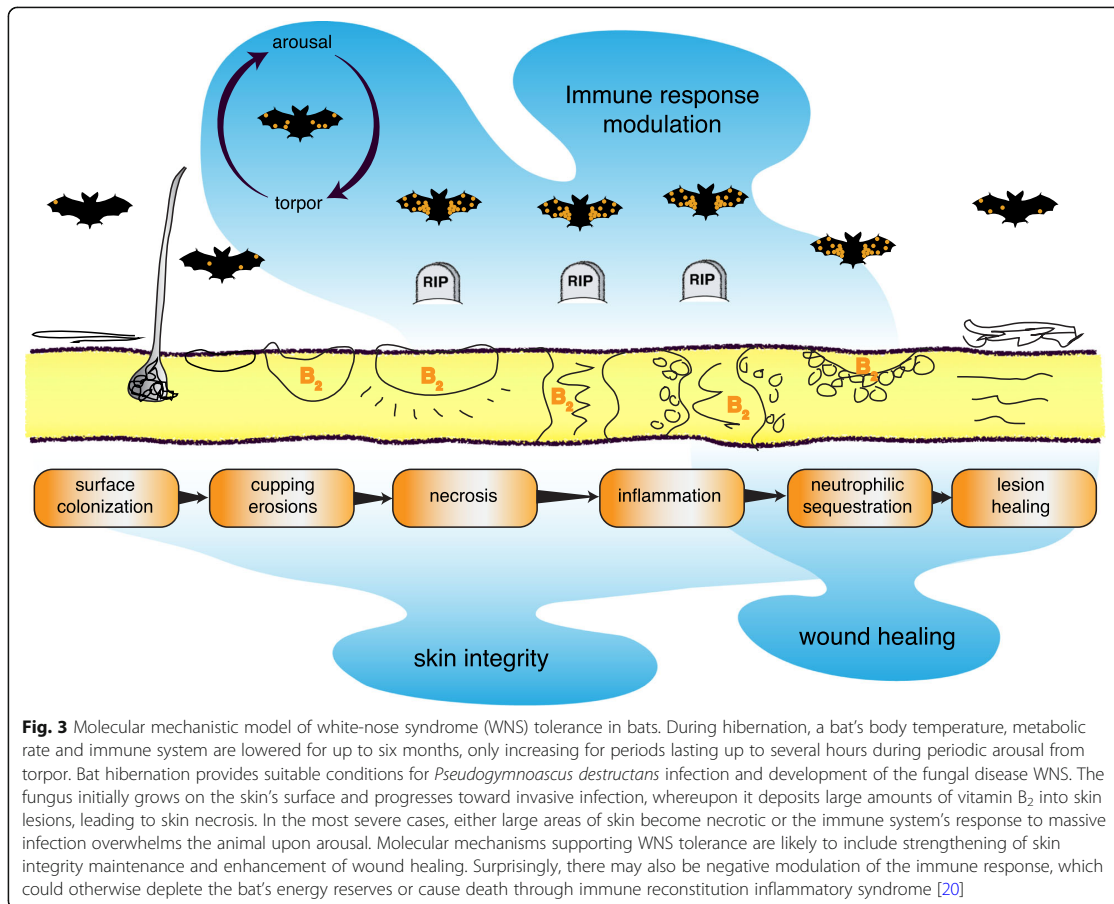
Proteins were tested for positive selection using the likelihood ratio test (A-model as alternative hypothesis and A1-model with ω = 1 as null hypothesis). p-values (FDR corrected; significant at α = 0.05) indicating signals of natural selection are marked in bold

the molecular mechanism for BCAM activity remains unclear.

LDL receptor protein 4 (LRP4) belongs to a family of LDL receptor proteins that, in dimeric form (LRP5/LRP6), serve as activating receptors for the Wnt/β-catenin pathway. Apart from its role in embryogenesis, this pathway is reactivated in adults and mediates tissue regeneration following injury [38], its role lying in negative regulation against activation of the Wnt/β-catenin pathway [39, 40]. While LRP4 shares the general structural motifs of the family, it lacks some binding motifs. LRP4 mutations severely alter pathway signalling. Bats with skin disruptions are most likely affected by changes in LRP4 structure and its subsequent effect on the Wnt/β-catenin pathway during wound healing.

Aquaporin 3 (AQP3) is expressed in keratinocytes [41] and epidermal tissues and is involved in the regulation of water and glycerol content in skin [41], thereby influencing wound healing. By regulating water flow, AQP3 facilitates epidermal cell migration and proliferation [42]. AQP3 has been shown to have a role in the healing of cutaneous burn wounds [43], which are similar to the skin disruption caused by riboflavin accumulation, tissue necrosis and subsequent oxidative stress contributing to WNS pathology [14]. The site under selection in AQP3 possibly affects the shape (and thus function) of the porin through its position in the transmembrane helix (Fig. 2).

Skin barrier integrity is an important factor in WNS pathology and survival (Fig. 3). Diseased and moribund bats with WNS skin lesions arouse from hibernation more frequently than healthy animals [19, 28]. During arousal, body temperature rises and is followed by a notable increase in activity and metabolism, following which the immune system mounts a response to the chronic infection. This reaction is often uncontrolled, causing



tissue damage [20]. Annexin A1 (ANXA1), which is positively selected for in bats, acts as a mediator of glucocorticoid anti-inflammatory activity [44], and hence may be able to down-regulate such an immune response. ANXA1, which is produced by innate immunity cells such as neutrophils, has an autocrine and paracrine effect on the innate immunity cells through inhibition of vascular attachment and extravasation [45]. ANXA1 also plays an important role in adaptive immunity against chronic infectious disease [46], modulating T-cell adaptive response and directing the immune response towards the Th1/Th17 response [47, 48]. Increased expression of *il-17* and *il-6* [49] directs proliferation of Th17 and Th1/Th17 cells, the latter T-cells also being affected by *ifn γ* , which is highly variable in post-WNS populations [2]. The observed decrease in neutrophil adhesion and inefficient antibody-mediated immune response [50] may be an effect of a predominating protective Th1/Th17 response to the pathogen in later stages of the infection. The overall character of the immune reaction supports our proposal

for an important role of ANXA1 in infection pathology and regulation of the immune response. As a regulator of inflammation, ANXA1 also plays a role in the outcome of inflammatory processes, wound repair and epithelial recovery [51]. The selected sites in ANXA1 are accumulated in the N-terminal region of the protein (Figs. 1 and 2) and, while they do not overlay the binding sites, they point to the importance of the area.

Similarly, TRAP also serves as an innate immune regulator, participating in the macrophage immune response and impacting on pathogen clearance from the host, most likely by affecting innate immune cell activity at the site of infection [52] by catalysing production of reactive oxygen species [53]. It also participates in down-regulation of the immune system and modulation of the Th1 response [54], which may contribute to Th1/Th17 modulation of the immune response by ANXA1. Metal binding sites in TRAP are spread along the protein sequence and do not directly coincide with the selected sites; hence, the effect of selected sites on binding

capacity cannot be evaluated from a simple sequence comparison and would require further study.

The amino acid sites under positive selection do not necessarily reflect the active or binding sites of proteins. In fact, it is more probable that protein function is maintained through purifying selection ($\omega < 1$), with a higher proportion of synonymously mutated sites conserving the active amino acid site. While a positively selected active site is unlikely, it is possible, most notably in cases of protein co-evolution with a ligand. Variable regions in the sequence are located on the protein's surface and influence structural folding. Protein structure influences affinity and interaction to partners, which is probably the case as regards the sites detected in this study. Just as with the shape of a folded protein, protein interaction barriers may affect their biological function; hence, an absence of mechanical barriers in the area surrounding the active site is essential for physical interaction of the proteins, and positive selection in these regions may facilitate inter-protein contact.

The signal for positive selection in a protein can be allocated to specific branches on a phylogeny and can be identified at sites in the DNA sequence. Nested branch-site models require differences in the natural selection signal at an a priori defined branch, compared with the remaining diversity, which is presumed to be under purifying selection in the model. We detected positive selection in the *acp5* gene in both Nearctic and Palearctic *Eptesicus* and in a clade of Palearctic *Myotis*. The Nearctic bat species *Eptesicus fuscus* shows limited levels of resistance to WNS infection [55], while the Palearctic species *Eptesicus nilssonii* rarely develops severe WNS pathology [10]. Palearctic *M. myotis* and *M. emarginatus* are representative of those species displaying a high fungal load and severe WNS pathology [10, 22], though they are able to tolerate the infection [22]; information on infection status of the third species in the Palearctic clade, *M. davidii*, is presently unavailable. While the mechanisms exerting selective pressure on *acp5* may differ from *P. destructans* infection, it may now provide protection against WNS progression.

We were unable to locate branches of positive selection in some genes, most likely due to a lack of available sequences ($n_{\text{lrp4}} = 4$, $n_{\text{ptch2}} = 4$, $n_{\text{sneg}} = 3$) and, therefore, low sequence variability in the data set. It has also been shown that, with an increased proportion of synonymous mutations (d_s), the branch site test for positive selection is more prone to false negative results [56]. Lack of selection signal heterogeneity in branches could also be assigned to host-unspecific characteristics of the pathogen, where the selective pressure would affect all species in the analysis. However, as the number of sequences in the analysis increases with additional sequencing effort (e.g. [57]), so the chances of detecting significant signs of positive selection in at least some branches increases, thus detection of a lack of positive selection in the analysis is more likely.

Inability to detect a specific branch under selection may also be affected by the use of two different haplotypes from each individual during sequence analysis, while the relationship between the two haplotypes remains unevaluated. In cases where one haplotype dominates, presence of the second haplotype in the sequence analysis may mask the signal of a positively selected haplotype in the species.

Since the protein products of genes for which positive selection has been detected are relevant to the pathology and pathophysiology of WNS, we expect them to play a role in skin integrity, wound healing and immune suppression. Hence, we can hypothesise that the selected genes contribute to the mechanism of infection tolerance in Palearctic bat species infected with WNS (Fig. 3).

Extrapolating from the devastating effects on Nearctic bat populations not previously exposed to skin injuries caused by *P. destructans* [6], WNS has to be the historical factor exerting enormous selection pressure on Palearctic bats. Not only could WNS have influenced genetic changes in skin integrity it has probably also influenced other rearrangements capable of preventing the devastating effects of the disease. Clear differences between Nearctic and Palearctic bats indicate at least two such rearrangements. The first is a much higher tolerance to mite and insect ectoparasites in Palearctic bats (typically 100% prevalence in breeding colonies) [58–60]. This results in habituation to the stress of skin injuries, which may also act as a feedback factor reducing neural sensitivity to such stimuli and their effect upon arousal from torpidity. The second difference between Palearctic and Nearctic bats relates to hibernation tactics. Most hibernating Palearctic bats disperse into a large number of less populated hibernacula rather than forming giant clusters in a single mass hibernaculum, characteristic for multiple Nearctic species [61, 62]. While this behavioural pattern appears to have declined after the WNS invasion front [63], repeated arousal caused by the grooming of infected individuals could still lead to an unintentional domino effect of multiple arousals [64]. This results in the breakdown of the core advantage of such hibernation tactics, i.e. socially controlled thermal homeostasis reducing demands on fat reserves and the need of individual behavioural skills for hibernation performance.

The above factors, suggested by the differences between Nearctic and Palearctic bats, illustrate the complex nature of skin infection and the intricacies involved in an adaptive response to an infectious agent. We show that positive selection at the genetic level is combined with the effects of increased tolerance to a parasite load and behavioural rearrangements, reducing the bat's capacity to perform advanced hibernation tactics.

Conclusions

During hibernation, bats conserve energy by maintaining a low body temperature and minimising metabolism.

While this strategy enables them to survive periods of resource scarcity, they become vulnerable to infection as their immune system fails to actively battle against infection while in torpor. Once it had invaded living tissue, the pathogen causes major damage, forming lesions and depositing metabolites that lead to necrosis. The accumulation of physiological consequences starts a cascade of adverse effects that culminates in the death of the diseased animal. We found that genes involved in the development, structure and maintenance of skin show signs of positive selection. With respect to lethal dermal infection, the epidermis likely protects heterotherms by acting as a passive barrier against infection during hibernation, a time when the animal cannot invest energy into immune reactions. The genes identified in this study may provide inspiration in designing targeted treatments for skin infections and for elucidating mechanisms involved in disease tolerance and resistance to other fungal infections, such as snake fungal disease or amphibian chytridiomycosis.

Methods

Identification of putative genes

We first selected genes with water metabolism and skin functions in the Gene Ontology database [65], then used the keywords 'water' and 'epidermis' to find genes with functions related to these keywords in *Rattus norvegicus* (223 genes found). We then searched UniProtKB for orthologous proteins in the Vespertilionidae and Miniopteridae families (50 genes found).

To identify genes expressed in Vespertilionidae during natural *P. destructans* infection, we analysed Illumina reads of *M. myotis* transcriptome (Accession numbers: SRX2270325, SRX2266671) by mapping them in Geneious mapper onto the reference nucleotide sequences of the selected genes with high sensitivity. We mapped the reads to the reference sequences using Geneious software version 6.1.6 (Biomatters Ltd., Auckland, New Zealand).

From the set of 50 protein orthologs in Vespertilionidae, we identified a subset of mRNA sequences for 30 selected genes expressed in *M. myotis*. Sequences of 23 of the 30 genes identified were found in more than two species of Palearctic and Nearctic bats infected by *P. destructans* by name and taxa search in the NCBI Nucleotide database, and these were used for further analysis. We avoided searching for orthologs with BLAST due to the non-negligible possibility of gene tree to species tree discordance between paralogs and orthologs in closely related species caused by incomplete lineage sorting [66].

Assembled coding DNA sequences expressed in *M. myotis* were then aligned with the reference to identify conserved regions flanking a variable region in order to design primers within an exon. Primers for amplification of the selected coding regions were designed in Primer3web 4.0.0

[67, 68]. Forward and reverse gene primers were supplemented with an M13 oligonucleotide tail at the 5' end to facilitate barcoding, forming Primer set 1. Primer set 2 contained paired barcodes and a complementary sequence to the flanking M13 tails of Primer set 1 at the 3' end. The paired barcode sequences conformed to the barcoding protocol in SMRT Analysis 1.4 (Pacific Biosciences, Menlo Park, CA, USA).

Sample collection and DNA processing

Samples were obtained from ethanol-stored tissue collections at the Institute of Vertebrate Biology of the Czech Academy of Sciences, National Animal Genetic Bank, Studenec, Czech Republic. DNA was extracted using the DNeasy® Blood & Tissue Kit (Qiagen, Hilden, Germany) according to the manufacturer's protocol, additional DNA samples being obtained from the Griffin Rabies Laboratory at the State of New York Department of Health, Wadsworth, NY, USA. In total, 240 samples representing 32 species from Europe, North America and Africa were amplified with nested PCR (Additional file 2). In the first PCR, coding regions of the selected genes were amplified with the gene-specific primers, forming PCR set 1. The master mix for each gene contained 1× buffer, 0.2 mM dNTP, 0.2 μM of forward and reverse primers, 0.05 U Platinum Taq DNA polymerase (Invitrogen, Carlsbad, CA, USA) and 1 μl of DNA. Each reaction was supplemented with MgCl₂ at final concentrations given in Additional file 3. The PCR was initialised with a hot-start at 95 °C for 3 min, followed by 35 cycles at annealing temperatures and annealing and extension (72 °C) times specified in Additional file 3, after which the reaction was finalised at 72 °C for 3 min. The PCR product was diluted 33× and used as a template for the second PCR. In the second PCR, Primer set 2 was used for all genes, taking care that individual samples were amplified with a unique barcode combination. The PCR reaction was identical to the first PCR, with 1.5 mM of MgCl₂ and the 35 cycles using the 95–53–72 °C temperature profile for 40–40-*ext* seconds, where *ext* represents extension times per gene (Additional file 3). The PCR product concentration was estimated from 2% agarose gels stained with GoldView relative to a 100 bp DNA Ladder standard (Invitrogen, available from Life Technologies, Prague, Czech Republic) in the GenoSoft 4.0 program (VWR International BVBA, Leuven, Belgium). The PCR product concentration enabled equimolar pooling of all samples for each gene. The PCR product pooled for all samples was separated on a gel, the band of expected length excised and DNA purified with the High Pure PCR Purification Kit (Roche Diagnostics GmbH, Mannheim, Germany). The gene products were pooled equimolarly with a final concentration of 29 ng μl⁻¹ and the DNA samples were sequenced commercially on a SMRT (single molecule real-time) platform (Pacific Biosciences) in two technical

replicates. The DNA template library was prepared with the PacBio DNA Template Prep Kit 2.0 according to the PacBio protocol for 10 kb Template Preparation and Sequencing. The DNA template library was bound to the DNA polymerase with the PacBio DNA/Polymerase Binding Kit P4 for the first replicate, and P5 for the second replicate. Sequencing on the PacBio RS II sequencer was performed with the PacBio DNA Sequencing Kit, using C2 and C3 chemistry for the two replicates, respectively. Sequencing was performed on 2 SMRT Cells with a 180-min movie time per SMRT Cell.

Data processing

The reads were de-multiplexed as part of the commercial raw data analysis during sequencing. Data obtained from SMRT gene sequencing were assembled to the reference sequences in Geneious with coverage > 10× and percent similarity in the alignment > 50%. Processed sequence data were aligned using MAFFT version 7.307 [69] to an annotated sequence reference obtained from the NCBI database. Alignments were edited in Geneious to contain only coding sequences of the gene fitting the appropriate open reading frame from the sequence reference annotation.

Data analysis

A maximum-likelihood phylogeny of Chiropteran species obtained in a previous study [70] was used for phylogenetic analysis of positive selection. The tree was unrooted and subset to contain species present in each corresponding sequence alignment (Additional file 1). In genes where more than one individual per species was sequenced, the respective tree tip was populated with a polytomy with zero-length branches to fit the number of individuals per species analysed in the alignment.

We tested the codons in alignment for signs of positive selection, defined as rate ratio of non-synonymous and synonymous substitutions ($\omega = d_N/d_S$). We used the CODEML program from the PAML 4.9 package [25] to estimate ω for the respective partial gene sequences, and variability between sites using the maximum likelihood method. Signals for positive selection were estimated from a comparison of nested models implemented in PAML using the likelihood ratio test (LRT).

The one ratio model (M0) [71, 72] sets one ω for all sites along the tested gene. A corresponding alternative model, the discrete model (M3) [4], allows a predefined number of site classes to vary in ω . While the nearly neutral model (M1) [73] does not allow ω to vary, the rate of synonymous mutations may vary at each site, with the rate of non-synonymous mutations being equal to the synonymous or equal to 0. An alternative to M1, the positive selection model (M2) [73], is derived from the neutral (M1) model and allows the rate of non-synonymous mutations to exceed the rate of synonymous mutations ($\omega > 1$). In

the beta M7 model [71], ω distribution in sites is limited to interval [0,1], meaning that the signal for predominant positive selection cannot be detected. The alternative nested model, beta& ω (M8) [74], allows the values of ω to be larger than 1.

A comparison of the one ratio (M0) model and the discrete (M3) model was used to test whether ω varied between sites. To test for positive selection signals in the codon sequence data, we paired the nearly neutral (M1) and positive selection (M2) models and the beta (M7) and beta& ω (M8) models, with the first model pair used as a null model.

The nested model's likelihood values were compared using the LRT (twice the difference between the log-likelihoods; $2\Delta\ln L$) of the null and alternative models. The $2\Delta\ln L$ values were then compared to χ^2 distributions for M0 - M3, M1 - M2 and M7 - M8 comparisons. We corrected significance of those analyses with false discovery rates (FDR) and accepted the adjusted levels of significance at 5% as significant.

Proteins with significant results in locus-level selection were analysed for sites under positive selection, identified based on the Bayes empirical Bayes method (BEB) [75] implemented in PAML for site tests of positive selection M1 - M2 and M7 - M8. The BEB method incorporates uncertainty in maximum likelihood estimates of parameters of the ω distribution by integrating over their prior distribution. By correcting for the uncertainty in parameter estimates, BEB is well suited for small datasets [75]. For visualisation of sites within the protein structure, Phyre2 structure prediction software [76] was used to predict protein models using a reference bat species protein sequence (XP_006104612.1, XP_014396764.1, XP_006758647.1, XP_015416692.1).

In genes with sites undergoing positive selection, we identified phylogeny branches under selection using the branch-site test of positive selection [75, 77]. The branch site test is used to detect branches under positive selection pre-specified in the tested phylogeny (foreground branches), where the other background branches would undergo purifying selection. In every tree, we tested each individual branch as a foreground branch for signs of positive selection. The branch site test is performed by comparing modified branch site model A, allowing ω to vary between branches, with null model A1 where $\omega = 1$. The nested models were tested by LRT and compared to χ^2 distribution with $df = 2$ and p -values were adjusted with the FDR.

The monophyletic clade of Palearctic species including *M. davidii*, *M. emarginatus* and *M. myotis* was modelled by clade model C [78] as a foreground tested clade, which was compared to a null model M2a_rel [79]. The nested models were tested by LRT and compared to χ^2 distribution with $df = 1$, with p -values adjusted by the FDR.

Additional files

Additional file 1: Accession numbers of bat DNA sequences and their respective phylogeny. The coding sequences of the respective genes (alignment length in parentheses) were used for maximum likelihood analysis of natural selection in bats. The guide tree was pruned from a previously published multilocus phylogeny [70]. The scale bar is in substitutions bp^{-1} . (PDF 189 kb)

Additional file 2: Bat samples amplified in this study. Populations were considered as hibernating (+) or non-hibernating (-) in the country of sample origin. Species were considered infected when *Pseudogymnoascus destructans* was detected in at least one individual using molecular genetic or culture experiments and positive for WNS when *P. destructans* was confirmed and diagnostic lesions found on skin histopathology [10, 22]. (XLSX 42 kb)

Additional file 3: Primers and amplification conditions for genes with a skin integrity or water metabolism function. Primer pairs were designed for genes expressed in *Myotis myotis* with white-nose syndrome (Accession numbers: SRX2270325, SRX2266671). (XLSX 47 kb)

Abbreviations

BEB: Bayes empirical Bayes; FDR: False discovery rate; LRT: Likelihood ratio test; WNS: White-nose syndrome

Acknowledgements

The authors acknowledge Anna Bryjová for study design consultation; Dagmar Šoukalová and Petra Rabušicová for laboratory assistance; Josef Bryja and Alena Fornůšková from the Institute of Vertebrate Biology (Brno), Petra Hájková and Barbora Zemanová from the National Animal Genetic Bank, Studenec; and Robert Rudd and April Davis from the Griffin Rabies Laboratory for the State of New York Department of Health, Wadsworth, NY, for providing DNA and tissue material used in this study.

Funding

This study was supported by the Czech Science Foundation (17-20286S) and by the Ministry of Education, Youth and Sports of the Czech Republic through the National Programme of Sustainability Project IT4 Innovations - Excellence in Science (LQ1602). The funders played no role in the study design, data collection and analysis, decision to publish or preparation of the manuscript.

Availability of data and materials

The datasets generated and analysed during this study are available in the NCBI Nucleotide repository, MH178037-MH178081.

Authors' contributions

IH, SM, JP, JZ and NM conceived and conceptualised the idea; ZV and NM designed the study; IH, SM, JP, JZ and NM collected the material; LJ, AZjr. and NM performed the laboratory analysis; MH, KL, JCM, PS and NM analysed the data; MH and NM wrote the manuscript, to which all authors contributed.

Ethics approval

The authors are authorised to handle free-living bats under Czech Certificate of Competency (No. CZ01341; §17, Act No. 246/1992 Coll.). The Czech Academy of Science's Ethics Committee has reviewed and approved the Animal Use Protocol No. 169/2011 in compliance with Act No. 312/2008 Coll. on Protection of Animals against Cruelty, as adopted by the Parliament of the Czech Republic. Non-lethal bat sampling complied with Act No. 114/1992 Coll. on Nature and Landscape Protection, and was based on permits 01662/MK/2012S/00775/MK/2012, 866/JS/2012 and 00356/KK/2008/AOPK, issued by the Nature Conservation Agency of the Czech Republic.

Consent for publication

Not applicable.

Competing interests

The authors declare that they have no competing interests.

Publisher's Note

Springer Nature remains neutral with regard to jurisdictional claims in published maps and institutional affiliations.

Author details

¹Institute of Vertebrate Biology, The Czech Academy of Sciences, Brno, Czech Republic. ²Department of Botany and Zoology, Faculty of Science, Masaryk University, Brno, Czech Republic. ³Department of Zoology, Faculty of Science, Charles University in Prague, Prague, Czech Republic. ⁴Institute of Biostatistics and Analyses, Masaryk University, Brno, Czech Republic. ⁵Department of Biological Sciences, University at Albany, State University of New York, Albany, NY, USA. ⁶Department of Ecology and Diseases of Game, Fish and Bees, University of Veterinary and Pharmaceutical Sciences Brno, Brno, Czech Republic. ⁷Research Institute of the Innovations Centre of Excellence, Silesian University in Opava, Opava, Czech Republic. ⁸Department of Muscle Cell Research, Centre of Biosciences, Institute of Molecular Physiology and Genetics, Slovak Academy of Sciences, Bratislava, Slovakia. ⁹Present address: Public Health Microbiologist for the State of Alaska, Department of Health and Social Services at the Alaska State Virology Lab in Fairbanks, Fairbanks, AK, USA. ¹⁰Present address: Department of Cellular Cardiology, Institute of Experimental Endocrinology, Biomedical Research Center, Slovak Academy of Sciences, Bratislava, Slovakia.

Received: 16 March 2018 Accepted: 16 August 2018

Published online: 29 August 2018

References

- Altizer S, Harvell D, Friedle E. Rapid evolutionary dynamics and disease threats to biodiversity. *Trends Ecol Evol.* 2003;18:589–96. <https://doi.org/10.1016/j.tree.2003.08.013>.
- Donaldson ME, Davy CM, Willis CKR, McBurney S, Park A, Kyle CJ. Profiling the immunome of little brown myotis provides a yardstick for measuring the genetic response to white-nose syndrome. *Evol Appl.* 2017;10:1076–90. <https://doi.org/10.1111/evo.12514>.
- Kimura M. Preponderance of synonymous changes as evidence for the neutral theory of molecular evolution. *Nature.* 1977;267:275–6.
- Yang Z, Bielawski JP. Statistical methods for detecting molecular adaptation. *Trends Ecol Evol.* 2000;15:496–503. [https://doi.org/10.1016/S0169-5347\(00\)01994-7](https://doi.org/10.1016/S0169-5347(00)01994-7).
- Blehert DS, Hicks AC, Behr M, Meteyer CU, Berlowski-Zier BM, Buckles EL, et al. Bat white-nose syndrome: an emerging fungal pathogen? *Science.* 2009;323:227. <https://doi.org/10.1126/science.1163874>.
- Frick WF, Pollock JF, Hicks AC, Langwig KE, Reynolds DS, Turner GG, et al. An emerging disease causes regional population collapse of a common north American bat species. *Science.* 2010;329:679–82. <https://doi.org/10.1126/science.1188594>.
- Hoyt JR, Langwig KE, Sun K, Lu G, Parise KL, Jiang T, et al. Host persistence or extinction from emerging infectious disease: insights from white-nose syndrome in endemic and invading regions. *Proc R Soc B Biol Sci.* 2016;283:20152861. <https://doi.org/10.1098/rspb.2015.2861>.
- Martínková N, Bačkor P, Bartonička T, Blažková P, Červený J, Falteisek L, et al. Increasing incidence of *Geomyces destructans* fungus in bats from the Czech Republic and Slovakia. *PLoS One.* 2010;5:e13853. <https://doi.org/10.1371/journal.pone.0013853>.
- Van der Meij T, Van Strien AJ, Haysom KA, Dekker J, Russ J, Biala K, et al. Return of the bats? A prototype indicator of trends in European bat populations in underground hibernacula. *Mamm Biol - Z Für Säugetierkd.* 2015;80:170–7. <https://doi.org/10.1016/j.mambio.2014.09.004>.
- Pikula J, Amelon SK, Bandouchova H, Bartonička T, Berkova H, Brichta J, et al. White-nose syndrome pathology grading in Nearctic and Palearctic bats. *PLoS One.* 2017;12:e0180435. <https://doi.org/10.1371/journal.pone.0180435>.
- Pikula J, Bandouchova H, Novotný L, Meteyer CU, Zukal J, Irwin NR, et al. Histopathology confirms white-nose syndrome in bats in Europe. *J Wildl Dis.* 2012;48:207–11. <https://doi.org/10.7589/0090-3558-48.1.207>.
- Gargas A, Trest MT, Christensen M, Volk TJ, Blehert DS. *Geomyces destructans* sp nov associated with bat white-nose syndrome. *Mycotaxon.* 2009;108:147–54. <https://doi.org/10.5248/108.147>.
- Lorch JM, Meteyer CU, Behr MJ, Boyles JG, Cryan PM, Hicks AC, et al. Experimental infection of bats with *Geomyces destructans* causes white-nose syndrome. *Nature.* 2011;480:376–U129. <https://doi.org/10.1038/nature10590>.
- Flieger M, Bandouchova H, Cerny J, Chudíčková M, Kolarik M, Kovacova V, et al. Vitamin B₂ as a virulence factor in *Pseudogymnoascus destructans* skin infection. *Sci Rep.* 2016;6 <https://doi.org/10.1038/srep33200>.
- Warnecke L, Turner JM, Bollinger TK, Misra V, Cryan PM, Blehert DS, et al. Pathophysiology of white-nose syndrome in bats: a mechanistic model

- linking wing damage to mortality. *Biol Lett*. 2013;9:20130177. <https://doi.org/10.1098/rsbl.2013.0177>.
16. Verant ML, Meteyer CU, Speakman JR, Cryan PM, Lorch JM, Blehert DS. White-nose syndrome initiates a cascade of physiologic disturbances in the hibernating bat host. *BMC Physiol*. 2014;14 <https://doi.org/10.1186/s12899-014-0010-4>.
 17. Willis CKR, Menzies AK, Boyles JG, Wojciechowski MS. Evaporative water loss is a plausible explanation for mortality of bats from white-nose syndrome. *Integr Comp Biol*. 2011;51:364–73. <https://doi.org/10.1093/icb/ocr076>.
 18. Bohn SJ, Turner JM, Warnecke L, Mayo C, McGuire LP, Misra V, et al. Evidence of 'sickness behaviour' in bats with white-nose syndrome. *Behaviour*. 2016;153:981–1003. <https://doi.org/10.1163/1568539X-00003384>.
 19. Reeder DM, Frank CL, Turner GG, Meteyer CU, Kurta A, Britzke ER, et al. Frequent arousal from hibernation linked to severity of infection and mortality in bats with white-nose syndrome. *PLoS One*. 2012;7:e38920. <https://doi.org/10.1371/journal.pone.0038920>.
 20. Meteyer CU, Barber D, Mandl JN. Pathology in euthermic bats with white nose syndrome suggests a natural manifestation of immune reconstitution inflammatory syndrome. *Virulence*. 2012;3:583–8. <https://doi.org/10.4161/viru.22330>.
 21. Kjer-Nielsen L, Patel O, Corbett AJ, Le Nours J, Meehan B, Liu L, et al. MR1 presents microbial vitamin B metabolites to MAIT cells. *Nature*. 2012;491:717–23.
 22. Zukal J, Bandouchova H, Brichta J, Cmokova A, Jaron KS, Kolarik M, et al. White-nose syndrome without borders: *Pseudogymnoascus destructans* infection tolerated in Europe and Palearctic Asia but not in North America. *Sci Rep*. 2016;6. doi:<https://doi.org/10.1038/srep19829>.
 23. Campana MG, Kurata NP, Foster JT, Helgen LE, Reeder DM, Fleischer RC, et al. White-nose syndrome fungus in a 1918 bat specimen from France. *Emerg Infect Dis*. 2017;23:1611–2. <https://doi.org/10.3201/eid2309.170875>.
 24. Zahradniková A, Kovacova V, Martinková N, Orlova MV, Orlov OL, Piacek V, et al. Historic and geographic surveillance of *Pseudogymnoascus destructans* possible from collections of bat parasites. *Transbound Emerg Dis*. 2017. doi:<https://doi.org/10.1111/tbed.12773>.
 25. Yang Z. PAML 4: phylogenetic analysis by maximum likelihood. *Mol Biol Evol*. 2007;24:1586–91. <https://doi.org/10.1093/molbev/msm088>.
 26. Humphries MM, Thomas DW, Speakman JR. Climate-mediated energetic constraints on the distribution of hibernating mammals. *Nature*. 2002;418:313–6. <https://doi.org/10.1038/nature00828>.
 27. Turbill C, Bieber C, Ruf T. Hibernation is associated with increased survival and the evolution of slow life histories among mammals. *Proc Biol Sci*. 2011;278:3355–63. <https://doi.org/10.1098/rspb.2011.0190>.
 28. Lilley TM, Johnson JS, Ruokolainen L, Rogers EJ, Wilson CA, Schell SM, et al. White-nose syndrome survivors do not exhibit frequent arousals associated with *Pseudogymnoascus destructans* infection. *Front Zool*. 2016;13:12. <https://doi.org/10.1186/s12983-016-0143-3>.
 29. Verant ML, Boyles JG, Waldrep W, Wibbelt G, Blehert DS. Temperature-dependent growth of *Geomyces destructans*, the fungus that causes bat white-nose syndrome. *PLoS One*. 2012;7 <https://doi.org/10.1371/journal.pone.0046280>.
 30. Bandouchova H, Bartonicka T, Berkova H, Brichta J, Cerny J, Kovacova V, et al. *Pseudogymnoascus destructans*: evidence of virulent skin invasion for bats under natural conditions, Europe. *Transbound Emerg Dis*. 2015;62:1–5. <https://doi.org/10.1111/tbed.12282>.
 31. Wibbelt G, Puechmaile SJ, Ohlendorf B, Mühlendorfer K, Bosch T, Görföl T, et al. Skin lesions in European hibernating bats associated with *Geomyces destructans*, the etiologic agent of white-nose syndrome. *PLoS One*. 2013;8. doi:<https://doi.org/10.1371/journal.pone.0074105>.
 32. Motoyama J, Takabatake T, Takeshima K, Hui C. *Ptch2*, a second mouse patched gene is co-expressed with sonic hedgehog. *Nat Genet*. 1998;18:104. <https://doi.org/10.1038/ng0298-104>.
 33. Takabatake T, Ogawa M, Takahashi TC, Mizuno M, Okamoto M, Takeshima K. Hedgehog and patched gene expression in adult ocular tissues. *FEBS Lett*. 1997;410:485–9. [https://doi.org/10.1016/S0014-5793\(97\)00645-5](https://doi.org/10.1016/S0014-5793(97)00645-5).
 34. Adolphe C, Nieuwenhuis E, Villani R, Li ZJ, Kaur P, Hui C, et al. Patched 1 and patched 2 redundancy has a key role in regulating epidermal differentiation. *J Invest Dermatol*. 2014;134:1981–90. <https://doi.org/10.1038/jid.2014.63>.
 35. Nieuwenhuis E, Motoyama J, Barnfield PC, Yoshikawa Y, Zhang X, Mo R, et al. Mice with a targeted mutation of patched2 are viable but develop alopecia and epidermal hyperplasia. *Mol Cell Biol*. 2006;26:6609–22. <https://doi.org/10.1128/MCB.00295-06>.
 36. Ninkina NN, Privalova EM, Pinön LGP, Davies AM, Buchman VL. Developmentally regulated expression of Persyn, a member of the Synuclein family, in skin. *Exp Cell Res*. 1999;246:308–11. <https://doi.org/10.1006/excr.1998.4292>.
 37. Schön M, Hogenkamp V, Gregor Wienrich B, Schön MP, Eberhard Klein C, Kaufmann R. Basal-cell adhesion molecule (*β-CAM*) is induced in epithelial skin tumors and inflammatory epidermis, and is expressed at cell–cell and cell–substrate contact sites. *J Invest Dermatol*. 2000;115:1047–53. <https://doi.org/10.1046/j.1523-1747.2000.00189.x>.
 38. Saito-Diaz K, Chen TW, Wang X, Thorne CA, Wallace HA, Page-McCaw A, et al. The way Wnt works: components and mechanism. *Growth Factors Chur Switz*. 2013;31:1–31. <https://doi.org/10.3109/08977194.2012.752737>.
 39. Johnson EB, Hammer RE, Herz J. Abnormal development of the apical ectodermal ridge and polysyndactyly in *Megf7*-deficient mice. *Hum Mol Genet*. 2005;14:3523–38.
 40. Ahn Y, Sims C, Murray MJ, Kuhlmann PK, Fuentes-Antrás J, Weatherbee SD, et al. Multiple modes of *Lrp4* function in modulation of Wnt/ β -catenin signaling during tooth development. *Dev Camb Engl*. 2017;144:2824–36.
 41. Qin H, Zheng X, Zhong X, Shetty AK, Elias PM, Bollag WB. Aquaporin-3 in keratinocytes and skin: its role and interaction with phospholipase D2. *Arch Biochem Biophys*. 2011;508:138–43. <https://doi.org/10.1016/j.abb.2011.01.014>.
 42. Hara-Chikuma M, Verkman AS. Aquaporin-3 facilitates epidermal cell migration and proliferation during wound healing. *J Mol Med*. 2008;86:221–31. <https://doi.org/10.1007/s00109-007-0272-4>.
 43. Sebastian R, Chau E, Fillmore P, Matthews J, Price LA, Sidhaye V, et al. Epidermal aquaporin-3 is increased in the cutaneous burn wound. *Burns*. 2015;41:843–7. <https://doi.org/10.1016/j.burns.2014.10.033>.
 44. Perretti M, D'Acquisto F. Annexin A1 and glucocorticoids as effectors of the resolution of inflammation. *Nat Rev Immunol*. 2009;9:62. <https://doi.org/10.1038/nri2470>.
 45. Lim LH, Solito E, Russo-Marie F, Flower RJ, Perretti M. Promoting detachment of neutrophils adherent to murine postcapillary venules to control inflammation: effect of lipocortin 1. *Proc Natl Acad Sci U S A*. 1998;95:14535–9.
 46. Vanessa KHQ, Julia MG, Wenwei L, Michelle ALT, Zarina ZRS, Lina LHK, et al. Absence of Annexin A1 impairs host adaptive immunity against *Mycobacterium tuberculosis* in vivo. *Immunobiology*. 2015;220:614–23. <https://doi.org/10.1016/j.imbio.2014.12.001>.
 47. D'Acquisto F, Merghani A, Lecona E, Rosignoli G, Raza K, Buckley CD, et al. Annexin-1 modulates T-cell activation and differentiation. *Blood*. 2007;109:1095–102. <https://doi.org/10.1182/blood-2006-05-022798>.
 48. Yang YH, Song W, Deane JA, Kao W, Ooi JD, Ngo D, et al. Deficiency of annexin A1 in CD4+ T cells exacerbates T cell-dependent inflammation. *J Immunol Baltim Md 1950*. 2013;190:997–1007. <https://doi.org/10.4049/jimmunol.1202236>.
 49. Lilley TM, Prokko JM, Johnson JS, Rogers EJ, Gronsky S, Kurta A, et al. Immune responses in hibernating little brown myotis (*Myotis lucifugus*) with white-nose syndrome. *Proc R Soc B*. 2017;284:20162232. <https://doi.org/10.1098/rspb.2016.2232>.
 50. Johnson JS, Reeder DM, Lilley TM, Cziriák GÁ, Voigt CC, McMichael JW, et al. Antibodies to *Pseudogymnoascus destructans* are not sufficient for protection against white-nose syndrome. *Ecol Evol*. 2015;5:2203–14. <https://doi.org/10.1002/ece3.1502>.
 51. Leoni G, Neumann P-A, Kamaly N, Quiros M, Nishio H, Jones HR, et al. Annexin A1-containing extracellular vesicles and polymeric nanoparticles promote epithelial wound repair. *J Clin Invest*. 2015;125:1215–27. <https://doi.org/10.1172/JCI76693>.
 52. Bune AJ, Hayman AR, Evans MJ, Cox TM. Mice lacking tartrate-resistant acid phosphatase (Acp 5) have disordered macrophage inflammatory responses and reduced clearance of the pathogen, *Staphylococcus aureus*. *Immunology*. 2001;102:103–13. <https://doi.org/10.1046/j.1365-2567.2001.01145.x>.
 53. Räisänen SR, Alatalo SL, Ylipahkala H, Halleen JM, Cassidy AJ, Hume DA, et al. Macrophages overexpressing tartrate-resistant acid phosphatase show altered profile of free radical production and enhanced capacity of bacterial killing. *Biochem Biophys Res Commun*. 2005;331:120–6. <https://doi.org/10.1016/j.bbrc.2005.03.133>.
 54. Lausch E, Jancke A, Bros M, Trojandt S, Alanay Y, De Laet C, et al. Genetic deficiency of tartrate-resistant acid phosphatase associated with skeletal dysplasia, cerebral calcifications and autoimmunity. *Nat Genet*. 2011;43:132–7. <https://doi.org/10.1038/ng.749>.

55. Frank CL, Michalski A, McDonough AA, Rahimian M, Rudd RJ, Herzog C. The resistance of a north American bat species (*Eptesicus fuscus*) to white-nose syndrome (WNS). *PLoS One*. 2014;9:e113958. <https://doi.org/10.1371/journal.pone.0113958>.
56. Gharib WH, Robinson-Rechavi M. The branch-site test of positive selection is surprisingly robust but lacks power under synonymous substitution saturation and variation in GC. *Mol Biol Evol*. 2013;30:1675–86. <https://doi.org/10.1093/molbev/mst062>.
57. Teeling EC, Vernes SC, Dávalos LM, Ray DA, Gilbert MTP, Myers E and. Bat biology, genomes, and the Bat1K project: to generate chromosome-level genomes for all living bat species. *Annu Rev Anim Biosci*. 2018;6:23–46. <https://doi.org/10.1146/annurev-animal-022516-022811>.
58. Horáček I, Bartonička T, Lučan RK. Macroecological characteristics of bat geomycosis in the Czech Republic: results of five years of monitoring. *Vespertilio*. 2014;17:65–77.
59. Lucan RK. Relationships between the parasitic mite *Spinturnix andegavinus* (Acari: Spinturnicidae) and its bat host, *Myotis daubentonii* (Chiroptera: Vespertilionidae): seasonal, sex- and age-related variation in infestation and possible impact of the parasite on the host condition and roosting behaviour. *Folia Parasitol (Praha)*. 2006;53:147–52. <https://doi.org/10.14411/fp.2006.019>.
60. Webber QM, Czenze ZJ, Willis CK. Host demographic predicts ectoparasite dynamics for a colonial host during pre-hibernation mating. *Parasitology*. 2015;142:1260–9. <https://doi.org/10.1017/S0031182015000542>.
61. Fenton MB. Population studies of *Myotis lucifugus* (Chiroptera: Vespertilionidae) in Ontario. Toronto: Royal Ontario Museum; 1970. <http://archive.org/details/populationstudies00fent>. Accessed 7 Jun 2018
62. Boratyński JS, Rusiński M, Kokurewicz T, Bereszyński A, Wojciechowski MS. Clustering behavior in wintering greater mouse-eared bats *Myotis myotis* — the effect of micro-environmental conditions. *Acta Chiropterologica*. 2012; 14:417–24. <https://doi.org/10.3161/150811012X661738>.
63. Frick WF, Puechmaile SJ, Hoyt JR, Nickel BA, Langwig KE, Foster JT, et al. Disease alters macroecological patterns of north American bats. *Glob Ecol Biogeogr*. 2015;24:741–9. <https://doi.org/10.1111/geb.12290>.
64. Hayman DTS, Cryan PM, Fricker PD, Dannemiller NG. Long-term video surveillance and automated analyses reveal arousal patterns in groups of hibernating bats. *Methods Ecol Evol*. 2017;8:1813–21. <https://doi.org/10.1111/2041-210X.12823>.
65. Ashburner M, Ball CA, Blake JA, Botstein D, Butler H, Cherry JM, et al. Gene ontology: tool for the unification of biology. The Gene Ontology Consortium. *Nat Genet*. 2000;25:25–9. <https://doi.org/10.1038/75556>.
66. Altenhoff AM, Boeckmann B, Capella-Gutierrez S, Dalquen DA, DeLuca T, Forslund K, et al. Standardized benchmarking in the quest for orthologs. *Nat Methods*. 2016;13:425–30. <https://doi.org/10.1038/nmeth.3830>.
67. Koressaar T, Remm M. Enhancements and modifications of primer design program Primer3. *Bioinformatics*. 2007;23:1289–91. <https://doi.org/10.1093/bioinformatics/btm091>.
68. Untergasser A, Cutcutache I, Koressaar T, Ye J, Faircloth BC, Remm M, et al. Primer3—new capabilities and interfaces. *Nucleic Acids Res*. 2012;40:e115. <https://doi.org/10.1093/nar/gks596>.
69. Katoh K, Standley DM. MAFFT multiple sequence alignment software version 7: improvements in performance and usability. *Mol Biol Evol*. 2013; 30:772–80. <https://doi.org/10.1093/molbev/mst010>.
70. Zukal J, Bandouchova H, Bartonička T, Berkova H, Brack V, Brichta J, et al. White-nose syndrome fungus: a generalist pathogen of hibernating bats. *PLoS One*. 2014;9:e97224. <https://doi.org/10.1371/journal.pone.0097224>.
71. Yang Z, Nielsen R, Hasegawa M. Models of amino acid substitution and applications to mitochondrial protein evolution. *Mol Biol Evol*. 1998;15:1600–11.
72. Goldman N, Yang Z. Codon-based model of nucleotide substitution for protein-coding DNA-sequences. *Mol Biol Evol*. 1994;11:725–36.
73. Nielsen R, Yang Z. Likelihood models for detecting positively selected amino acid sites and applications to the HIV-1 envelope gene. *Genetics*. 1998;148:929–36. <https://doi.org/10.1093/oxfordjournals.molbev.a040153>.
74. Yang Z. Maximum likelihood estimation on large phylogenies and analysis of adaptive evolution in human influenza virus a. *J Mol Evol*. 2000;51:423–32. <https://doi.org/10.1007/s002390010105>.
75. Yang Z, Wong WS, Nielsen R. Bayes empirical Bayes inference of amino acid sites under positive selection. *Mol Biol Evol*. 2005;22:1107–18. <https://doi.org/10.1016/j.tree.2003.08.013>.
76. Kelley LA, Mezulis S, Yates CM, Wass MN, Sternberg MJE. The Phyre2 web portal for protein modeling, prediction and analysis. *Nat Protoc*. 2015;10: 845. <https://doi.org/10.1038/nprot.2015.053>.
77. Zhang J. Evaluation of an improved branch-site likelihood method for detecting positive selection at the molecular level. *Mol Biol Evol*. 2005;22: 2472–9. <https://doi.org/10.1093/molbev/msi237>.
78. Bielawski JP, Yang Z. A maximum likelihood method for detecting functional divergence at individual codon sites, with application to gene family evolution. *J Mol Evol*. 2004;59:59–121.
79. Weadick CJ, Chang BSW. An improved likelihood ratio test for detecting site-specific functional divergence among clades of protein-coding genes. *Mol Biol Evol*. 2012;29:1297–300. <https://doi.org/10.1093/molbev/msr311>.

Ready to submit your research? Choose BMC and benefit from:

- fast, convenient online submission
- thorough peer review by experienced researchers in your field
- rapid publication on acceptance
- support for research data, including large and complex data types
- gold Open Access which fosters wider collaboration and increased citations
- maximum visibility for your research: over 100M website views per year

At BMC, research is always in progress.

Learn more biomedcentral.com/submissions



Appendix III: Synthèse

Les animaux appartenant à un taxon donné partagent généralement un plan corporel conservé qui contient des structures équivalentes (i.e., homologues). Souvent, de telles structures semblent d'être des versions itératives d'un modèle commun qui varie en taille relative et/ou en proportions dans les limites d'une distribution normale, ce qui est un phénomène connu sous le nom d'allométrie (Gayon, 2000; Gould, 1966; Huxley, 1932; Huxley and Teissier, 1936; Schneider, 2018a; Stern and Emlen, 1999; Thompson, 1917; Woodger, 1945; Young et al., 2014). Pour maintenir de la morphologie fonctionnelle, la croissance appropriée des structures est maintenue au cours du développement des individus même si la taille de ces mêmes structures peut varier énormément à la fois au sein d'une espèce et parmi les membres des taxons apparentés (Russell, 1916; Haldane, 1926; Smith et al., 2015). De plus, les expériences de régénération tissulaire et de transplantation indiquent que les structures conservent des mécanismes intrinsèques leur permettant de connaître leur taille appropriée et de réguler la croissance (Leevers and McNeill, 2005 ; Allard et Tabin, 2009 ; Fish et al., 2014 ; Uygur et al., 2016 ; Schneider, 2018b). Mais comment ces mécanismes intrinsèques fonctionnent et comment ils potentialisent une variation phénotypique normale à anormale, est mal compris. De plus, les processus moléculaires et cellulaires qui permettent aux embryons précoces d'établir des trajectoires de croissance à l'appui de la forme et de la fonction adultes requises restent à identifier, en particulier comme un moyen pour comprendre les étiologies des maladies et les mécanismes d'évolution (Schneider, 2015 ; Woronowicz et Schneider, 2019).

Au niveau moléculaire, l'allométrie implique probablement des modulations spécifiques à l'espèce aux niveaux intrinsèques et aux niveaux de la localisation d'expression génique qui affectent les comportements des cellules résultant en variation de la croissance des tissus correspondants et des organes. De telles idées ont émergé dans la première moitié du

vingtième siècle avec la découverte des gènes responsable du début, de l'échelonnement et du taux de développement (Huxley, 1932 ; Goldschmidt, 1938 ; Goldschmidt, 1940 ; de Beer, 1954), telles ont conduit à des théories et des analyses quantitatives pendant la renaissance de la biologie de l'évolution et du développement dans les années 1970, prédisant comment même de très petits changements affectant le temps et les taux de développement pourraient générer d'importantes variations phénotypiques et des transformations de taille (Gould, 1977 ; Alberch et al., 1979 ; Hall, 1984 ; McKinney, 1988 ; Klingenberg, 1998 ; Smith, 2003 ; Keyte et Smith, 2014). Dans ce contexte, les molécules qui agissent comme des morphogènes semblent jouer un rôle clé, en particulier lorsque des changements génétiques modifient leurs niveaux d'expression, la source (i.e., les cellules qui produisent le morphogène), la distribution (i.e., la libération du morphogène), le transport (i.e., la diffusion du morphogène) et la détection (i.e., la sensibilité cellulaire au morphogène) dans l'environnement local (Oster et al., 1988; Gurdon et al., 1999; Gurdon et Bourillot, 2001; Dessaud et al., 2007; Tostevin et al., 2007 ; Ribes et Briscoe, 2009 ; Ben-Zvi et Barkai, 2010 ; Cheung et al., 2014). Un exemple bien étudié est le morphogène classique Sonic Hedgehog (SHH), qui provoque des réponses de prolifération ou de différenciation cellulaire d'une manière dépendante de la concentration qui est responsable de la croissance et morphogenèse des organes tels que le bourgeon de membre, le tube neural et les primordia cranio-faciaux (Summerbell et al., 1973; Echelard et al., 1993; Riddle et al., 1993; Laufer et al., 1994; Ericson et al., 1995; López-Martínez et al., 1995; Ericson et al., 1997; Yang et al. , 1997; Briscoe et al., 2001; Schneider et al., 2001; Zeng et al., 2001; Dessaud et al., 2007; Dessaud et al., 2008; McLellan et al., 2008; Hu et Marcucio, 2009 ; Young et al., 2010 ; Xu et al., 2015 ; Uygur et al., 2016).

SHH se lie au récepteur canonique PaTCHed (PTCH1) et aux corécepteurs Cell adhesion

molecule-related/Downregulated by ONcogenes (CDON) et Brother Of Cdon (BOC), ainsi qu'à Growth Arrest-Specific 1 (GAS1) (Tenzen et al., 2006 ; Beachy et al., 2010 ; Izzi et al., 2011 ; Choudhry et al., 2014). La liaison de PTCH1 par SHH entraîne une dé-répression et une accumulation de SMOothened (SMO) résultant d'une transduction du signal via les facteurs de transcription Glioma-associated oncogene (GLI) (van den Heuvel et Ingham, 1996 ; Alcedo et Noll, 1997 ; Quirk et al., 1997 ; Murone et al., 1999 ; Taipale et al., 2002 ; Wilson et Chuang, 2010). GLI2 et GLI3 sont des facteurs de transcription bi-fonctionnels qui peuvent soit activer soit inhiber la transcription alors que GLI1 n'a pas de domaine répresseur et ne peut fonctionner qu'en tant qu'activateur transcriptionnel (Marigo et al., 1996; Lee et al., 1997; Mo et al., 1997 ; Matisse et Joyner, 1999 ; Wang et al., 2000 ; Bai et Joyner, 2001 ; Bai et al., 2002 ; Hui et Angers, 2011). La liaison de CDON, BOC et GAS1 par SHH favorise la survie, la prolifération et la différenciation cellulaires, ce qui peut finalement affecter la taille et la forme des organes (Allen et al., 2007 ; Martinelli et Fan, 2007 ; Izzi et al., 2011 ; Delloye-Bourgeois et al., 2014).

Dans la présente étude, nous avons testé si la régulation différentielle de la voie SHH peut expliquer la régulation de la taille de la mandibule spécifique à l'espèce au cours du développement en comparant l'expression des membres de la voie SHH chez le canard, le poussin et la caille, ce qui sont trois espèces d'oiseaux ayant la taille de la mandibule et les taux de maturation nettement différente. Nous analysons les stades embryonnaires à partir du moment où le mésenchyme de la crête neurale (NCM), qui sont les cellules précurseurs de la mâchoire (Jheon et Schneider, 2009 ; Le Lièvre, 1978 ; Noden, 1978), arrivent dans les primordia mandibulaires puis subissent de la croissance. NCM contrôle la taille de la mandibule spécifique à l'espèce (Schneider, 2005; Schneider, 2015; Schneider, 2018b; Schneider et Helms,

2003) et précédemment, nous avons montré que les mécanismes contribuant à la plus grande taille de la mâchoire du canard par rapport à la caille incluent l'allocation d'environ 15% plus de cellules progénitrices de la mâchoire aux primordia mandibulaires pendant les premiers stades de la migration et un cycle cellulaire plus long (13,5 heures chez le canard et 11,0 heures chez la caille). Lorsqu'on prend un intervalle du développement équivalents pour le canard et la caille nous avons une période de 45 heures chez le canard par rapport à 32 heures chez la caille (i.e., la quantité de temps absolu nécessaire pour chaque espèce d'oiseau), cela se traduit par une différence du double du nombre de cellules des primordia mandibulaires par HH20 (Fish et al., 2014). Le NCM exerce également un contrôle spécifique à l'espèce sur de multiples voies de signalisation au cours des stades ultérieurs de la prolifération cellulaire et de la différenciation squelettique qui affectent directement la taille de la mâchoire (Ealba et al., 2015 ; Eames et Schneider, 2008 ; Fish et Schneider, 2014b ; Hall et al., 2014, Merrill et al., 2008). Les interactions de signalisation entre le NCM et l'épithélium de l'endoderme pharyngé, qui sécrète la protéine SHH, favorisent la croissance des primordia mandibulaires et établissent la polarité antéropostérieure du squelette de la mâchoire (Abzhanov et Tabin, 2004 ; Brito et al., 2006 ; Couly et al., 2002 ; Graham et al., 2005 ; Helms et Schneider, 2003 ; Moore-Scott et Manley, 2005). De même, SHH est associé à la forme et à la croissance du visage spécifiques à l'espèce (Hu et Marcucio, 2012; Hu et al., 2015a; Hu et al., 2015b; Schneider et al., 2001; Young et al., 2010) et les perturbations des corécepteurs SHH ainsi que d'autres membres de ce voie peuvent entraîner une micrognathie et d'autres défauts de la mâchoire, en particulier en association avec l'holoprosencéphalie (Allen et al., 2011 ; Bae et al., 2011 ; Cole et Krauss, 2003 ; Dennis et al. , 2012 ; Echevarría-Andino et Allen, 2020 ; Hong et al., 2017 ; Hui et Angers, 2011 ; Melnick et al., 2005 ; Mo et al., 1997 ; Pineda-Alvarez et al., 2012 ; Ribeiro et al., 2010 ; Roessler

et Muenke, 2010 ; Seppala et al., 2007 ; Seppala et al., 2014 ; Xavier et al., 2016 ; Zhang et al., 2011 ; Zhang et al., 2006). Mais la mesure dans laquelle la voie SHH est régulée différemment par le NCM et si des modifications de sa régulation pourraient affecter la croissance spécifique à l'espèce des primordia mandibulaires ne sont toujours pas claires.

Nous avons effectué une analyse comparative des primordia mandibulaires au cours du développement du canard, du poussin et de la caille, particulièrement des stades embryonnaires (HH) 15 à HH27 (Hamburger et Hamilton, 1951) et nous avons trouvé des différences spécifiques à l'espèce en regardant la taille de la population de NCM à chaque stade et aussi en quantifiant de l'ARN totale. Nous avons quantifié l'expression de *Shh*, *Ptch1*, *Cdon*, *Boc*, *Smo*, *Gas1*, *Gli1*, *Gli2* et *Gli3* dans les primordia mandibulaires de canard, de poussin, de caille et de chimères dans lesquels nous avons transplanté NCM de la caille au canard (i.e., quack). Notre stratégie découvre les niveaux d'expression spécifiques au stade et à l'espèce pour les membres clés de la voie SHH, identifie les niveaux d'activation de la voie spécifiques au stade et à l'espèce, et révèle que ces différences sont médiées par le NCM puisque le NCM donneur maintient son expression semblable à celle de la caille dans le canard (i.e., le récepteur du greffon). Nous testons également si le canard, le poussin et la caille ont une réponse intrinsèque spécifique à l'espèce à la signalisation SHH en cultivant des explants de primordia mandibulaires et en les traitant avec différents niveaux de la protéine SHH ou d'un inhibiteur (i.e., la cyclopamine). Ces expériences d'activation et d'inhibition de la voie révèlent une réponse spécifique à l'espèce à la signalisation SHH, le corécepteur SHH Gas1 étant le plus sensible aux manipulations. Ceci contraste avec les études *in vitro* que nous réalisons en parallèle sur des fibroblastes de poulet où nous observons une réponse minimale aux mêmes traitements, ce qui indique que la sensibilité à la signalisation SHH et la réponse

de *Gas1* dépendent du contexte. La surexpression *in ovo* et le knockdown de *Gas1* dans le NCM modifient le nombre de cellules et/ou la taille de la mandibule. Dans l'ensemble, nos travaux suggèrent que les changements spécifiques à l'espèce dans la réponse de NCM à la signalisation SHH et la régulation différentielle de l'expression de *Gas1* peuvent être un mécanisme par lequel NCM contrôle la taille de la mâchoire pendant le développement, la maladie et l'évolution.

Titre : Le rôle de la signalisation SHH dans la régulation de la taille de la mandibule spécifique à l'espèce

Mots clés : SHH, Gas1, crête neurale, arc branchial, spécifique à l'espèce, taille des primordia mandibulaires

Résumé : Les changements de la taille de la mandibule au cours de l'évolution ont été cruciaux pour le rayonnement adaptatif des vertébrés. Cependant, une variation anormale est associée à des malformations congénitales humaines et à des maladies. L'évolution des différences de la taille de la mandibule spécifiques à l'espèce est causée en partie par des mécanismes du développement précoces qui sont régulés par le mésenchyme de la crête neurale (MCN). Un de ces mécanismes implique des interactions précisément déterminées entre le MCN et l'épithélium adjacent qui facilitent la croissance de la mandibule spécifique à l'espèce. Ces interactions sont médiées par des multiples voies de signalisation, y compris Sonic Hedgehog (SHH). La signalisation SHH joue un rôle dans une variété des processus de développement, y compris la prolifération cellulaire. Nous examinons les embryons du canard, du poussin et de la caille et constatons que le canard a la population progénitrice de NCM migrant dans l'arc branchial la plus grande et a une dynamique de prolifération distincte, avec

un cycle cellulaire plus long. Nous émettons l'hypothèse que la réponse du MCN à la signalisation SHH est spécifique à l'espèce, et celui affecte la prolifération ce qui génère des différences dans la taille de la mandibule. Nous testons notre hypothèse *in vivo* en quantifiant l'expression des membres de la voie SHH chez le canard, le poussin, la caille et les chimères caille-canard. Nous constatons que le MCN est le médiateur des niveaux d'expression spécifiques à l'espèce pour les membres clés de la voie. Nous testons, *in vitro*, si la réponse à la signalisation SHH dans MCN est intrinsèquement spécifique à l'espèce. Nous traitons les mandibules avec des différents concentrations de la protéine SHH ou un inhibiteur de la voie SHH (i.e., la cyclopamine). Également, nous surexprimons un corécepteur de la protéine SHH ce qui résulte en une altération de la taille de la mandibule et son knock-down en une asymétrie mandibulaire. Nos résultats révèlent que les différences spécifiques à l'espèce dans la signalisation SHH sont médiées par MCN et sont autonomes des cellules.

Title: The role of SHH signaling in regulating species-specific jaw size

Keywords: SHH, Gas1, neural crest, branchial arch, species-specific, mandibular primordia size

Abstract: Changes in jaw size during evolution have been crucial for the adaptive radiation of vertebrates. However, abnormal variation in jaw size is associated with human birth defects and disease. The evolution of species-specific jaw size is due in part, to early developmental mechanisms that are regulated by neural crest mesenchyme (NCM). One such mechanism involves precisely timed interactions between NCM and adjacent epithelium. These interactions are mediated by multiple signaling pathways including Sonic Hedgehog (SHH). SHH signaling plays a role in a variety of developmental processes including cell proliferation. We examine duck, chick, and quail embryos and find that duck start with more NCM in their mandibular arch and have longer cell cycle. We hypothesize that the

response of NCM to SHH signaling is species-specific, which affects proliferation and generates differences in jaw size. We test our hypothesis *in vivo* by quantifying expression of SHH pathway members in duck, chick, quail, and quail-duck chimeras. We find that NCM mediates species-specific expression for key pathway members. We also test, *in vitro*, if the response to SHH signaling in NCM is intrinsically species-specific. We treat mandibles with different levels of recombinant SHH protein or a pathway inhibitor (i.e., cyclopamine). We also overexpress a SHH binding protein, which alters jaw size and its knock-down results in jaw asymmetry. These experiments reveal that species-specific differences in SHH signaling are mediated by NCM and are cell-autonomous.